Universitat de Girona

DEVELOPMENT AND APPLICATION OF NEW METHODOLOGIES FOR CHEMICAL BONDING ANALYSIS

Martí Gimferrer Andrés

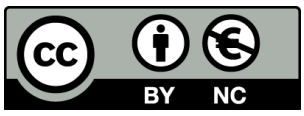

DOCTORAL THESIS

DEVELOPMENT AND APPLICATION OF NEW METHODOLOGIES FOR CHEMICAL BONDING ANALYSIS

Martí Gimferrer Andrés

2023

DOCTORAL THESIS

DEVELOPMENT AND APPLICATION OF NEW METHODOLOGIES FOR CHEMICAL BONDING ANALYSIS

Martí Gimferrer Andrés

· 2023 ·

DOCTORAL PROGRAMME IN CHEMISTRY

Supervised by:

Dr. Pedro Salvador Sedano

Tutor:

Dr. Pedro Salvador Sedano

Presented to obtain the degree of PhD at the University of Girona

Universitat de Girona

Dr. Pedro Salvador Sedano, from the Universitat de Girona,

I DECLARE:

That this thesis entitled "**Development and application of new methodologies for chemical bonding analysis**" presented by **Martí Gimferrer Andrés** to obtain the doctoral degree has been completed under my supervision and meets the requirements to opt for an International Doctorate.

For all intents and purposes, I hereby sign this document

Dr. Pedro Salvador Sedano

Girona, 27 February 2023

A la Dajana i als meus pares
Aquesta tesi és resultat del suport incondicional i educació que m'heu brindat

Acknowledgements

Arribat el moment final, ara és quan un és conscient del suport que ha rebut per part de qui l'ha acompanyat en aquest trajecte. En el meu cas han sigut molts més dels que esperava de bones a primeres, els quals intentaré esmentar a continuació (i demano disculpes anticipades als que em deixi!).

A Pedro Salvador, el meu supervisor de tesi, per ensenyar-me a programar i adoptar-me com a estudiant des de finals de segon de carrera. Hem treballat molts anys junts sent més que supervisor-estudiant i potser per aquest motiu hem tingut els nostres "alts i baixos" tant a nivell personal com professional. M'has ensenyat a ser exigent i rigorós en la "nostra" recerca (fins al punt tenir discussions amb professors externs per defensar el meu punt de vista) i espero en un futur ser capaç de demostrar-t'ho. Gràcies per guiar-me en aquest camí, el qual no m'hagues ni plantejat si no fos per tu.

A l'Albert Poater, per les dures i políticament incorrectes discussions sobre la vida personal i acadèmica, i a la Montse Rodríguez. Sempre m'heu tractat com un "fill", per lo bo i lo dolent i us estaré sempre agraït.

To Prof. Martin Head-Gordon, to host me in his research group during my first predoctoral research stay at the University of California Berkeley, to make me feel like a member of the MHG group from the very first meeting and to always demonstrate interest in the projects I was involved even after my comeback to Girona due to the start of the Covid pandemy.

To Dr. Diego M. Andrada, por aguantarme durante tantos meses en tu grupo y sobrevivir a que siempre diese mi opinión personal, hasta sobre porqué creo que un entrecot de ternera es mejor "poco hecho".

From Germany to Kike, Jule, Nicola, Manutai, Tanja, Stavi, Ilgin and Anjana, for the good times both at university and in beergardens, to Prof. Dominik Munz for the always considering relevant my opinion about the chemical bonding of sophisticated compounds (even though 90% of the times we disagreed) and to Christopher Stein and Alex Zech for the excursions, dinners and poker nights we had in California.

De Girona, primer a tots els membres que hem compartit hores al despatx 177 (vella nomenclatura), incloent a Artigas, Gibu, Pareras, Pau, Sergio, Gerard, Leila i Marc. Menció especial a Dani, l'IQCC no seria el mateix sense tu (tot i que t'has estovat amb els anys, opinió personal) i per totes les hores que hem invertit en discutir sobre videojocs, tecnologia i calers, entre altres. A la Silvia, pel teu suport (tant "científic" com personal) al llarg dels anys. A les "besties" Ricard i Joel, amics fora de la pista, enemics de pàdel. També a Yago, Stuart, Anthony, Germano, Ferran i Marc per totes les batalletes i consells sobre el món acadèmic. Finalment, als fundadors de QuantumBTT, Duran i Solà, per cada sortida que hem fet els diumenges i els racons de Girona que m'heu ensenyat.

Special mention to Julian, Sergi and Àlex for not only sharing and discuss about our research projects but also for the beautiful friendship (I clarify it for Sergi, he tends to confuse things...) we formed along the years, which I hope will continue for many more!

Als amics de Banyoles (i rodalies), Adri, Mariscot, Reyes, Ferrer, Colomer, Toni, pels soparets i moments de desconecció viscuts.

Per acabar, als meus pares, Toni i Francesca, per sempre haver intentat entendre què feia a la universitat i treure més pit de que "el meu fill ha tret un article" que jo mateix. A la meva germana, Nuri (+ Paul!), per apretar-me a fer una tesi doctoral quan va surgir l'oportunitat i viure enganyada pensant que sóc més llest que ella. I a la Dajana, la persona que m'acompanya en els meus millors i pitjors moments, tant personals com professionals, aconseguint treure el millor de mi (en cas que hi hagi) en cada moment (com diria l'Albert... Pobre noia, es mereix el cel!).

The projects of the Thesis were realized thanks to the Generalitat de Catalunya and Fons Social Europeu for the predoctoral fellowship (2018 FI_B 01120), the Ministerio de Ciencia, Innovación y Universidades (grant number PGC2018-098212-B-C22), the EC Research Innovation Action under the H2020 Programme for the HPCEUROPA3 for the mobility grant (INFRAIA-2016-1-730897), the program of Ajuts Complementaris per la Mobilitat d'investigadors of the Universitat de Girona for the mobility grant (MOB2019) and the Institut de Química Computacional i Catàlisi (IQCC) for the facilities and material resources provided.

Full list of Publications

This thesis is presented as a compendium of publications.

Published articles included in this Thesis:

- Gimferrer, M.; Salvador, P.; Poater, A. Computational Monitoring of Oxidation States in Olefin Metathesis. *Organometallics* **2019**, 38, 24, 4585-4592. (IF: 3.804; JCR Ranking: 6/45; Q1 in Chemistry, Inorganic & Nuclear).
  Contribution: *M.G participated in the design of the project, performed all calculations, collected the data, analyzed the results, wrote the first draft and co-wrote the manuscript.*

- Gimferrer, M.; Comas-Vilà G.; Salvador, P. Can We Safely Obtain Formal Oxidation States from Centroids of Localized Orbitals? *Molecules* **2020**, 25, 234. (IF: 4.412; JCR Ranking: 63/178; Q2 in Chemistry, Multidisciplinary).
  Contribution: *M.G implemented the software, performed all calculations, collected the data, co-analyzed the results and co-wrote the manuscript.*

- Gimferrer, M.; Van der Mynsbrugge, J.; Bell, A. T.; Salvador, P.; Head-Gordon, M. Facing the Challenges of Borderline Oxidation State Assignments Using State-of-the-Art Computational Methods. *Inorg. Chem.* **2020**, 59, 20, 15410-15420. (IF: 5.165; JCR Ranking: 5/45; Q1 in Chemistry, Inorganic & Nuclear).
  Contribution: *M.G participated in the design of the project, performed all calculations, collected the data, analyzed the results, wrote the first draft and co-wrote the manuscript.*

- Gimferrer, M.; Danés, S.; Andrada, D. M.; Salvador, P. Unveiling the Electronic Structure of the Bi(+1)/Bi(+3) Redox Couple on NCN and NNN Pincer Complexes. *Inorg. Chem.* **2021**, 60, 23, 17657-17668. (IF: 5.436; JCR Ranking: 5/46; Q1 in Chemistry, Inorganic & Nuclear).
  Contribution: *M.G participated in the design of the project, performed half of the calculations, collected the data, co-analyzed the results, wrote the first draft and co-wrote manuscript.*

- Gimferrer, M.; Aldossary, A.; Salvador, P.; Head-Gordon, M. Oxidation State Localized Orbitals: A Method for Assigning Oxidation States Using Optimally Fragment-Localized Orbitals and a Fragment Orbital Localization Index. *J. Chem. Theory Comput.* **2022**, 18, 1, 309-322. (IF: 6.578; JCR Ranking: 7/36; Q1 in Physics, Atomic, Molecular & Chemical).
  Contribution: *M.G participated in the design of the project, implemented the software, performed most of the calculations, collected the data, co-analyzed the results, wrote the first draft and co-wrote the manuscript.*

- Gimferrer, M.; Danés, S.; Vos, E.; Yildiz, C. B.; Corral, I.; Jana, A.; Salvador, P.; Andrada, D. M. The oxidation state in low-valent beryllium and magnesium compounds. *Chem. Sci.* **2022**, 13, 6583-6591. (IF: 9.969; JCR Ranking: 25/179; Q1 in Chemistry, Multidisciplinary).
  Contribution: *M.G performed all calculations, collected the data, co-analyzed the results, wrote the first draft and co-wrote the manuscript.*

Submitted for Publication articles included in this Thesis:

- Gimferrer, M.; Danés, S.; Andrada, D. M.; Salvador, P. Merging the Energy Decomposition Analysis with the Interaction Quantum Atoms Approaches. **2023**, *Submitted.*
  Contribution: *M.G implemented the software, performed all calculations, collected the data, co-analyzed the results and co-wrote the manuscript.*
- Gimferrer, M.; Salvador, P. Towards a Unified Treatment of Spin-Polarization in Wavefunction Analysis. **2023**, *Submitted.*
  Contribution: *M.G participated in the design of the project, implemented the software, performed all calculations, collected the data, co-analyzed the results and co-wrote the manuscript.*
- Gimferrer, M.; Salvador, P. Exact Decompositions of the Total KS-DFT Exchange-Correlation Energy into One- and Two-Center Terms. **2023**, *Submitted.*
  Contribution: *M.G participated in the design of the project, implemented the software, performed all calculations, collected the data, analyzed the results, wrote the first draft and co-wrote the manuscript.*

Other publications by the author not included in this thesis:

- Skara, G.; Gimferrer, M.; De Proft, F.; Salvador, P.; Pinter, B. Scrutinizing the Noninnocence of Quinone Ligands in Ruthenium Complexes: Insights from Structural, Electronic, Energy, and Effective Oxidation State Analyses. *Inorg. Chem.* **2016**, 55, 5, 2185-2199.
- Luque-Urrutia, J.; Gimferrer, M.; Casals-Cruañas E.; Poater A. In Silico Switch from Second- to First-Row Transition Metals in Olefin Metathesis: From Ru to Fe and from Rh to Co. *Catalysts* **2017**, 7, 389.
- Gimferrer, M.; Minami, Y.; Noguchi, Y.; Hiyama, T.; Poater, A. Monitoring of the Phosphine Role in the Mechanism of Palladium-Catalyzed Benzosilole Formation from Aryloxyethynyl Silanes. *Organometallics* **2018**, 37, 9, 1456-1461.
- Naji-Rad, E.; Gimferrer, M.; Bahri-Laleh, N.; Nekoomanesh-Haghighi, M.; Jamjah, R.; Poater, A. Exploring Basic Components Effect on the Catalytic Efficiency of Chevron-Phillips Catalyst in Ethylene Trimerization. *Catalysts* **2018**, 8, 224.
- Poater, J.; Gimferrer, M.; Poater, A. Covalent and Ionic Capacity of MOFs To Sorb Small Gas Molecules. *Inorg. Chem.* **2018**, 57, 12, 6981-6990.
- Masdemont, M.; Luque-Urrutia, J.; Gimferrer, M.; Milstein, D.; Poater, A. Mechanism of Coupling of Alcohols and Amines To Generate Aldimines and H2 by a Pincer Manganese Catalyst. *ACS Catal.* **2019**, 9, 3, 1662-1669.

- Ramos, M.; Poater, J.; Villegas-Escobar, N.; Gimferrer, M.; Toro-Labbé, A.; Cavallo, L.; Poater, A. Phenoxylation of Alkynes through Mono- and Dual Activation Using Group 11 (Cu, Ag, Au) Catalysts. *Eur. J. Inorg. Chem.* **2020**, 1123-1134.

- Gimferrer, M.; D'Alterio, M. C.; Talarico, G.; Minami, Y.; Hiyama, T.; Poater, A. Allyl Monitorization of the Regioselective Pd-Catalyzed Annulation of Alkylnyl Aryl Ethers Leading to Bismethylenechromanes. *J. Org. Chem.* **2020**, 85, 19, 12262-12269.

- Gimferrer, M.; Joly, N.; Escayola, S.; Viñas, E.; Gaillard, S.; Solà, M.; Renaud, J. L.; Salvador, P.; Poater, A. Knölker Iron Catalysts for Hydrogenation Revisited: A Nonspectator Solvent and Fine-Tuning. *Organometallics* **2022**, 41, 10, 1204-1215.

- Grünwald, A.; Goswami, B.; Breitwieser, K.; Morgenstern, B.; Gimferrer, M.; Heinemann, F. W.; Momper, D. M.; Kay, C. W. M.; Munz, D. Palladium Terminal Imido Complexes with Nitrene Character. *J. Am. Chem. Soc.* **2022**, 144, 20, 8897-8901.

List of Abbreviations

3c-2e	Three-center two-electron
3D	Three-dimensional
a.u.	Atomic units
AIM	Atom in a molecule
ALMO	Absolutely localized molecular orbital
AO	Atomic orbital
B88	Becke88 exchange functional
BA	Basin-allegiance
BOD	Bond order density
BS	Broken-symmetry
BSSE	Basis set superposition error
CA	Closest-atom
cAAC	Cyclic(alkyl)(amino) carbene
CASSCF	Complete active space self-consistent field
CECA	Chemical energy component analysis
CHA	Chemical Hamiltonian approach
CI	Configuration interaction
CI_a	Clarity index
CISD	Configuration interaction with single and double excitations
CISDT	Configuration interaction with single, double and triple excitations
CSS	Closed-shell singlet
DFT	Density functional theory
DI	Delocalization index
ECP	Effective core potential
EDA	Energy decomposition analysis
EDF	Electron distribution function
eff-AO	Effective atomic orbital
EFO	Effective fragment orbital
EOS	Effective oxidation state
ER	Edminston-Ruedenberg
FB	Foster-Boys
FCI	Full configuration interaction
FOLI	Fragment orbital localization index
FU	First unoccupied

GGA	Generalized gradient approximation
HF	Hartree-Fock
HONO	Highest occupied natural orbital
IA	Ionic approximation
IAO	Intrinsic atomic orbital
I-Hirshfeld	Iterative Hirshfeld
IQA	Interacting quantum atoms
IUPAC	International union of pure and applied chemistry
KS	Kohn-Sham
KS-DFT	Kohn-Sham density functional theory
LCAO	Linear combination of atomic orbitals
LDA	Local density approximation
LI	Localization index
LO	Lowest occupied
LMO	Localized molecular orbital
LOBA	Localized orbitals bonding analysis
LSA	Local spin analysis
LSDA	Local spin density approximation
LUNO	Lowest unoccupied natural orbital
LYP	Lee-Yang-Parr correlation functional
MBO	Mayer bond order
MBS	Minimal basis set
MLWF	Maximally localized Wannier function
MM	Molecular mechanics
MO	Molecular orbital
MP2	Moller-Plesset of second order
MUD	Mean unsigned deviation
NAO	Natural atomic orbital
NBO	Natural bond orbital
NEDA	Natural energy decomposition analysis
NHC	N-heterocyclic carbene
NLMO	Natural localized molecular orbital
NO	Natural orbital
NOCV	Natural orbitals for chemical valence
NOF	Natural orbital functional
NPA	Natural population analysis
OS	Oxidation state
OSLO	Oxidation state localized orbital
OSS	Open-shell singlet
PA	Proton affinity
PM	Pipek-Mezey
QM	Quantum mechanics
QTAIM	Quantum theory of atoms in molecules
R(%)	Reliability index

RASSCF	Restricted active space self-consistent field
RDM1	First-order reduced density matrix
RDM2	Second-order reduced density matrix
RHF	Restricted Hartree-Fock
SAD	Superposition of atomic density
SAPT	Symmetry adapted perturbation theory
SD	Slater determinant
T	Triplet
TFVC	Topological fuzzy Voronoi cells
TM	Transition metal
VWN	Vosko-Wilk-Nusair correlation functional
WBI	Wiberg bond index
xc	Exchange-correlation
ZES	Zero-error scheme
ZORA	Zeroth-order regular approximation
ZPE	Zero-point energy

Contents

List of Figures

List of Tables

Summary

The chemical bond is one -if not the most- important concept in chemistry, recurrently used in the discussion of molecular structure, reactivity and properties. While unravelling the physical origin of a particular chemical bond is inaccessible directly from experiment, computational chemistry fills the gap with different approaches that can be used, some of them scrutinized and introduced in this Thesis.

In the last decades, electronic structure methods have been crucial for chemists to achieve deeper insight into chemistry itself and to make predictions before performing the actual experiments. The development of computational approaches for chemical bonding analysis ultimately aims at performing predictions before running the electronic structure calculations.

This Thesis is devoted to both development and application of tools for chemical bonding analysis, attempting to bridge the "physical" and "chemical" worlds and making a contribution to extract chemical information from wavefunction analysis. For this aim, we present the new computational tools developed, mainly focused in the topics of oxidation states (Chapter 4) and energy decomposition schemes (Chapter 5), together with application to enlighten the chemical bonding picture of chemically-interesting, borderline and challenging molecular systems (Chapter 6).

Regarding to method development, we first evaluated the performance of centroids of localized molecular orbitals to assign oxidation states (Section 4.1), using the established distance (closest-atom) criterion, and a new introduced electronic criterion based on Bader's basins. The later performed much better when assigning electrons from rather simple systems, but both failed in the TM-carbene classification. Second, we introduced a new fragment-based localization procedure for single-determinant wavefunctions. The localized molecular orbitals are associated to the fragments, thus affording also the electron count necessary for oxidation state assignation (Section 4.2). The introduced scheme showed very good performance for all systems tested, in particular for TM-carbene systems and coping with ligand's non-innocence. Third, we explored a generalization of the effective oxidation states (EOS) method, that readily affords homolytic splitting of bond electrons driven by static correlation (e.g. diradicaloids). This was a limitation of the original EOS scheme, that has now been surpassed with the uEOS scheme (Section 4.3). Fourth, we proposed a new scheme to merges the two main families of energy decomposition schemes, namely energy decomposition analysis (EDA) and interacting quantum atoms (IQA). In particular, in Section 5.1 we apply the IQA decomposition to each term from an EDA calculation. Finally, we developed a strategy to numerically integrate the two-electron energy components from the IQA approaches in the context of overlapping atoms achieving zero error, and we performed a comparison between the two reported schemes that are able to decompose the exchange-correlation energy term from a density functional theory calculation into both one- and two-center terms (Section 5.2).

Regarding to applications, we first performed a critical comparison between two (at that time) state-of-the-art oxidation states elucidation techniques, the localized orbitals bonding analysis (LOBA) and EOS method (Section 6.1), that also lead on improvement of the former and further developments such as the aforementioned OSLO approach. Second, we tackled Ru(+2)/Ru(+4) debate in the olefin metathesis catalysts by means of the EOS analysis, unveiling that the +2 oxidation state is preferred along the reaction pathway in exception of the metallacycle species, which presents character in between Ru(+2) and Ru(+4) (Section 6.2). Third, we proved that validity of the EOS analysis to scrutinize the electronic structure of Bi-based complexes and tackled the Bi(+1)/Bi(+3) conundrum in redox-active bismuth-based compounds with pincer ligands, together with the explanation and quantification of their Lewis acid/base character and reactivity (Section 6.3). Finally, we studied the nature of low-valent Mg(carbene)$_2$ and Be(carbene)$_2$ (carbene = NHC and cAAC) compounds by applying our toolbox of wavefunction analysis. Contrary to previous interpretations, the Be(+2)-diradicaloid picture clearly emerged from the study, highlighting the relevance of high-level correlated wavefunctions. The inadequacy of the commonly adopted energy-based criterion for oxidation state assignation within EDA was also exposed (Section 6.4).

Resum

L'enllaç químic és un dels conceptes més importants de la química, si no el que més, i s'utilitza per l'elucidació i discussió d'estructures, reactivitat i propietats moleculars. Mentre desentranyar l'origen físic d'un enllaç químic concret és inaccessible experimentalment de manera immediata, la química computacional omple el buit amb les diferents metodologies que poden emprar-se, algunes de les quals es mencionen en aquesta Tesi.

En les últimes dècades, la química computacional ha sigut crucial per aconseguir una visió més profunda de la pròpia química i per dur a terme prediccions abans de realitzar els experiments. Per això el desenvolupament de noves metodologies computacionals d'anàlisi de l'enllaç químic és fonamental.

Aquesta Tesi està dedicada tant al desenvolupament com a l'aplicació d'eines d'anàlisi de l'enllaç químic, intentant establir nexes d'unió entre els mons "físic" i "químic" i contribuir a l'extracció d'informació química mitjançant l'análisi de la funció d'ona. Amb aquesta finalitat, presentem les noves eines computacionals desenvolupades, centrades principalment en els temes dels estats d'oxidació (Capítol 4) i els esquemes de descomposició de l'energia (Capítol 5), i llavors reportem la seva aplicació per desvelar la imatge de l'enllaç químic de sistemes moleculars químicament interessants i desafiants (Capítol 6).

En quant al desenvolupament de mètode, primer avaluem l'ús dels centroides d'orbitals localitzats per l'assignació d'estats d'oxidació (Secció 4.1), emprant el criteri de distància establert (àtom més proper), i un nou criteri electrònic introduït basat en les conques de Bader. Aquest últim funciona molt millor per l'assignació d'electrons de sistemes relativament senzills, però ambdós fallen en la classificació de carbens. En segon lloc, s'ha introduït un nou procediment de localització d'orbitals basat en fragments per funcions d'ona monodeterminants. Els orbitals localitzats s'associen als fragments, proporcionant així també el recompte d'electrons necessari per l'assignació d'estats d'oxidació (Secció 4.2). L'esquema introduït ha presentat molt bon rendiment per tots els sistemes provats, en particular pels carbens i pels sistemes amb lligants no innocents. En tercer lloc, s'ha explorat una generalització del mètode dels estats d'oxidació efectius (EOS), que permet fàcilment la divisió homolítica dels electrons d'enllaç impulsat per la correlació estàtica (per exemple, diradicaloids). Aquesta era una limitació de l'esquema EOS original, essent ara superada amb l'esquema uEOS (Secció 4.3). En quart lloc, s'ha proposat un nou esquema que fusiona les dues principals famílies d'esquemes de descomposició de l'energia: anàlisi de la descomposició de l'energia (EDA) i àtoms quàntics interactuants (IQA). En particular, en la Secció 5.1 descomponem cada terme d'un càlcul EDA en els components procedents de IQA. Finalment, s'ha desenvolupat una estratègia per integrar numèricament els components bielectrònics de l'energia de les aproximacions IQA aconseguint un error de formalment zero, i s'ha realitzat una comparació entre els dos esquemes reportats capaços de descompondre el terme de l'energia d'intercanvi-correlació d'un càlcul de teoria del funcional de la densitat en termes atòmics i diatòmics (Secció 5.2).

En quant a les aplicacions, primerament s'ha realitzar una comparació entre les dues tècniques d'elucidació d'estats d'oxidació d'última generació (en aquell moment), l'anàlisi d'enllaç d'orbitals localitzats (LOBA) i el mètode EOS (Secció 6.1), que també ha portat a millorar el primer i a desenvolupaments posteriors com l'anteriorment mencionat OSLO. En segon lloc, s'ha abordat el debat Ru(+2)/Ru(+4) en els catalitzadors de metàtesi d'olefines mitjançant EOS, revelant que l'estat d'oxidació +2 és el preferit al llarg del mecanisme de reacció excepte l'espècie metal·lacicle, que presenta un caràcter entre Ru(+2) i Ru(+4) (Secció 6.2). En tercer lloc, s'ha demostrat la validesa de l'anàlisi EOS per elucidar l'estructura electrònica dels complexes basats en Bi (grup principal) i s'ha abordat l'enigma Bi(+1)/Bi(+3) en compostos redox-actius basats en bismut amb lligants pinça, juntament amb l'explicació del seu caràcter àcid/base de Lewis (i reactivitat) a partir dels valors d'ocupació de l'EFO $6p_z$ del Bi (Secció 6.3). Per últim, s'ha estudiat la naturalesa dels compostos Mg(carbè)$_2$ i Be(carbè)$_2$ de baix estat d'oxidació (carbè = NHC y cAAC) aplicant un conjunt d'eines computacionals per l'anàlisi de l'enllaç químic, incloent l'anàlisi de l'espí local, EOS i EDA, on es va exposar el risc d'emprar el criteri energètic comunament emprat per l'assignació d'estats d'oxidació (Secció 6.4).

Resumen

El enlace químico es uno de los conceptos más importantes de la química, si no el que más, y se utiliza en la elucidación y discusión de estructuras, reactividad y propiedades moleculares. Mientras que desentrañar el origen físico de un enlace químico concreto es inaccesible experimentalmente de manera inmediata, la química computacional llena ese vacío con las diferentes metodologías que pueden utilizarse, algunos de los cuales se mencionan en esta Tesis.

En las últimas décadas, la química computacional ha sido crucial para alcanzar una visión más profunda de la propia química y para realizar predicciones antes de llevar a cabo los experimentos. De ahí que el desarrollo de nuevas metodologías computacionales para el análisis del enlace químico sea una tarea fundamental.

Esta Tesis está dedicada tanto al desarrollo como a la aplicación de herramientas para el análisis del enlace químico, intentando tender un puente entre los mundos "físico" y "químico" y contribuyendo a la extracción de información química a partir del análisis de la función de onda. Con este fin, presentamos las nuevas herramientas computacionales desarrolladas, centradas principalmente en los temas de los estados de oxidación (Capítulo 4) y los esquemas de descomposición de la energía (Capítulo 5), y luego reportamos su aplicación para revelar la imagen del enlace químico de sistemas moleculares químicamente interesantes y desafiantes (Capítulo 6).

En cuanto al desarrollo del método, primero evaluamos el uso de los centroides de orbitales localizados para asignar estados de oxidación (Sección 4.1), utilizando el criterio de distancia establecido (átomo más cercano), y un nuevo criterio electrónico introducido basado en las cuencas de Bader. Este último funcionó mucho mejor al asignar electrones de sistemas relativamente simples, pero ambos fallaron en clasificar carbenos. En segundo lugar, introdujimos un nuevo procedimiento de localización basado en fragmentos para funciones de onda monodeterminantales. Los orbitales localizados se asocian a los fragmentos, proporcionando así también el recuento de electrones necesario para la asignación del estado de oxidación (Sección 4.2). El esquema introducido mostró muy buen rendimiento para todos los sistemas probados, en particular para los carbenos y para sistemas con ligandos no inocentes. En tercer lugar, exploramos una generalización del método de los estados de oxidación efectivos (EOS), que permite fácilmente la división homolítica de los electrones de enlace impulsada por la correlación estática (por ejemplo, diradicaloides). Esta era una limitación del esquema EOS original, que ahora se ha superado con el esquema uEOS (Sección 4.3). En cuarto lugar, propusimos un nuevo esquema que fusiona las dos familias principales de esquemas de descomposición de energía: análisis de descomposición de energía (EDA) y átomos cuánticos interactuantes (IQA). En particular, en la Sección 5.1 descomponemos cada término de un cálculo EDA en los componentes de IQA. Finalmente, desarrollamos una estrategia para integrar numéricamente los componentes bielectrónicos de la energía de

las aproximaciones IQA consiguiendo un error de formalmente cero, y realizamos una comparación entre los dos esquemas reportados que son capaces de descomponer el término de energía de intercambio-correlación de un cálculo de teoría del funcional de la densidad en términos atómicos y interatómicos (Sección 5.2).

En cuanto a las aplicaciones, en primer lugar realizamos una comparación entre las dos técnicas de elucidación de estados de oxidación de última generación (en aquel momento), el análisis de enlace de orbitales localizados (LOBA) y el método EOS (Sección 6.1), que también condujo a la mejora del primero y a desarrollos posteriores como el enfoque OSLO mencionado anteriormente. En segundo lugar, abordamos el debate Ru(+2)/Ru(+4) en los catalizadores de metátesis de olefinas mediante el análisis EOS, desvelando que el estado de oxidación +2 es el preferido a lo largo del mecanismo reacción a excepción de la especie metalaciclo, que presenta un carácter intermedio entre Ru(+2) y Ru(+4) (Sección 6.2). En tercer lugar, demostramos la validez del anális EOS para elucidar la estructura electrónica de complejos basados en Bi (grupo principal) y abordamos el enigma Bi(+1)/Bi(+3) en compuestos redox-activos basados en bismuto con ligandos pinza, junto con la explicación de su carácter ácido/base de Lewis (y reactividad) a partir de los valores de ocupación del EFO $6p_z$ del Bi (Sección 6.3). Por último, estudiamos la naturaleza de los compuestos Mg(carbeno)$_2$ y Be(carbeno)$_2$ de bajo estado oxidación (carbeno = NHC y cAAC) aplicando un conjunto de herramientas computacionales para el análisis del enlace químico, incluyendo el análisis del espín local, EOS y EDA, donde se expuso el riesgo de usar el criterio energético comúnmente utilizado para la asignación del estado de oxidación (Sección 6.4).

Chapter 1

Introduction

The chemical bond is one -if not the most- important concept in chemistry, used in the elucidation and discussion of molecular structures, reactivity and its associated properties.[1,2] However, there is no unique approach to unambiguously characterize it, neither from experimental nor from computational analysis. While unravelling the physical origin of a particular chemical bond is inaccessible directly from experiment, computational chemistry fills the gap with different approaches that can be used, some of them reviewed in the current Thesis. Most of them rely on the definition of the atom in a molecule (AIM), following the phylosophy of understanding chemical bonding as electron-pair interactions between atoms or fragments introduced by Pauling.[3] The chemical bond, together with the bonding models associated to it, i.e. ionic, covalent and metallic bonding, resonance, conjugation and hyperconjugation, aromaticity and donor-acceptor interaction, to name a few, are considered chemical *unicorns* as most of these concepts lack of a *solid* quantum theory-based root because there is no observable behind them.[4] However, they are crucial in the chemistry community for the classification of systems, helping to identify, understand and predict chemical reactivity.

Computational chemistry makes use of computers to produce data which, for example, simulate experimental results or molecular properties. In the last decades it has been crucial for chemists to achieve deeper insight into chemistry itself and to make predictions before running the actual experiments. Furthermore, the accuracy of the electronic structure methods, together with the computational power, has importantly increased, growing as consequence the reliability on the predicted properties. Hence, the development of new computational approaches for chemical bonding analysis is a fundamental task. In this Thesis, we focus not only in the development of chemical bonding tools but also on its applications for state-of-the-art molecular systems, attempting thus to be a bridge between the "physical" and "chemical" worlds and making our contribution to extract chemical information from wavefunction analysis. For this aim, first we will briefly introduce the electronic structure methods, focusing on the wavefunction-based ones (both single- and multi-determinant) and density functional theory (DFT), the AIM definitions and some of the most relevant computational chemistry tools for chemical bonding analysis. Then, we present the new computational tools developed during the Thesis, mainly focused in the topics of oxidation states and energy decomposition schemes. In particular, the decomposition of the total energy of a molecular system into one- and two-center contributions. Finally, we report the scientific works in which the introduced computational schemes are applied to enlight the chemical bonding picture of chemically-interesting, borderline and challenging molecular systems. With this, we also pretend (to some extend) to show the performance of more sophisticated, and more importantly, more robust techniques that the commonly used in the bibliography.

1.1 Electronic structure methods

In quantum mechanics, the fundamental postulate declare that the state of any chemical system is completely described by the so-called wavefunction, $\Psi(\mathbf{q}, t)$, which depends on the position of all particles $\mathbf{q}$, and time t. Operators (mostly Hermitian), $\hat{O}$, can act on the wavefunction providing as eigenvalue, e, the associated observable property of the system

$$\hat{O}\Psi(\mathbf{q}, t) = e\Psi(\mathbf{q}, t). \tag{1.1}$$

When the operator applied is the Hamiltonian operator, $\hat{H}$, the resulting eigenvalue corresponds to the electronic energy of the system, E, leading to the time-dependent form of the Schrödinger equation [5]

$$\hat{H}\Psi(\mathbf{q}, t) = E\Psi(\mathbf{q}, t). \tag{1.2}$$

Typically, the Hamiltonian operator takes into account five energy contributions to the total energy. In particular, the kinetic energy of both nuclei and electrons, the electron-nuclei attraction, and the electron-electron and nuclei-nuclei repulsions

$$\begin{aligned}\hat{H} = &-\sum_{A}^{N_{At}} \frac{\hbar^2}{2m_A}\nabla_A^2 - \sum_{i}^{N} \frac{\hbar^2}{2m_e}\nabla_i^2 \\ &- \sum_{i}^{N}\sum_{A}^{N_{At}} \frac{e^2 Z^A}{|\mathbf{r}_i - \mathbf{R}_A|} + \sum_{i,j>i}^{N} \frac{e^2}{|\mathbf{r}_i - \mathbf{r}_j|} + \sum_{A,B>A}^{N_{At}} \frac{e^2 Z^A Z^B}{|\mathbf{R}_A - \mathbf{R}_B|}.\end{aligned} \tag{1.3}$$

In Eq. 1.3, $\hbar$ is the Planck constant divided by 2π, Z^A is the atomic number of nucleus A, e is the electron charge, $\mathbf{r}_k$ and $\mathbf{R}_C$ are the position of electron k and nucleus C, respectively, m_e and m_A are the mass of the electron and nucleus A, respectively, the ∇^2 operator is the Laplacian and summations run over the number of electrons (N) and nuclei (N_{At}), respectively.

One can find more sophisticated Hamiltonian operators if desires to take into consideration (scalar) relativistic effects, spin-orbit coupling or for when the molecular system is under the presence of an electric and/or magnetic field.

Solving *exactly* the Schrödinger equation is not possible beyond two electron systems. Hence, the energy evaluation for "chemical" systems, usually composed of tens of electron and atoms, require to make use of some approximations. The most common one was proposed in 1927 by Born and Oppenheimer, being named the Born-Oppenheimer approximation in their honor. [6] The authors proposed to assume that the motion of the nuclei and electrons are independent (decoupled). Such assumption is originated by the large mass difference between the nuclei and the electrons. As the electrons are much lighter than the nuclei, the speed of the nuclei speed is negligible compared to that of the electrons. In other words, the nuclei positions are considered fixed. As consequence, the electrostatic repulsion between nuclei is now constant (V_{NN}) and the nuclei kinetic energy is equal to zero. With this, and considering all terms in atomic units (a.u.), the Hamiltonian operator from Eq. 1.3 is simplified to

$$\hat{H} = \sum_{i}^{N} \hat{h}_i^{(1)} + \sum_{i,j>i}^{N} \hat{V}_{ee,ij}^{(2)} + V_{NN}, \tag{1.4}$$

where $\hat{h}_i^{(1)}$ is constituted by the sum of the already introduced (Eqs. 1.3) electronic kinetic energy, $\hat{T}_i^{(1)}$, and electron-nuclei attraction, $\hat{U}_i^{(1)}$, operators

$$\begin{aligned} &\hat{h}_i^{(1)} = \hat{T}_i^{(1)} + \hat{U}_i^{(1)}, \\ &\hat{T}_i^{(1)} = -\frac{1}{2}\nabla^2(\mathbf{r}_i);\ \hat{U}_i^{(1)} = -\sum_{B}^{N_{At}} \frac{Z^B}{|\mathbf{r}_i - \mathbf{R}_B|}, \end{aligned} \tag{1.5}$$

$\hat{V}_{ee,ij}^{(2)}$ is the two-electron operator that accounts for the interelectronic repulsion.

$$\hat{V}_{ee,ij}^{(2)} = r_{ij}^{-1} = \frac{1}{|\mathbf{r}_i - \mathbf{r}_j|}, \tag{1.6}$$

and V_{NN} is computed from the fixed atomic positions as

$$V_{NN} = \sum_{A,B>A}^{N_{At}} \frac{Z^A Z^B}{R_{AB}}. \tag{1.7}$$

Within the Born-Oppenheimer approximation, and in the time-independent case, the (time-independent) electronic Schrödinger equation for an N-electron system reads as

$$\hat{H}\Psi(\mathbf{q}_1, \mathbf{q}_2, ..., \mathbf{q}_N) = E\Psi(\mathbf{q}_1, \mathbf{q}_2, ..., \mathbf{q}_N), \tag{1.8}$$

where the electronic wavefunction Ψ here depends on $4N$ coordinates (three spatial $\mathbf{r}_i$ and one spin coordinate σ_i for each electron where $\mathbf{q}_i = (\mathbf{r}_i, \sigma_i)$), and parametrically on the nuclear coordinates $\mathbf{R}_A, A = 1, N_{At}$. Importantly, the wavefunction must fulfill the antisymmetry principle, thus being antisymmetric when the coordinates of any two electrons interchange

$$\Psi(\mathbf{q}_1, \mathbf{q}_2, \mathbf{q}_3, ..., \mathbf{q}_N) = -\Psi(\mathbf{q}_3, \mathbf{q}_2, \mathbf{q}_1, ..., \mathbf{q}_N). \tag{1.9}$$

The determinant is the simplest mathematical object that fulfills the condition from Eq. 1.9. For this reason, in 1929 Slater proposed to construct the simplest but antisymmetric wavefunction based on a determinant, namely the Slater determinant (SD).[7] The SD, conforming an electronic configuration k, is constructed in terms of a set of N (occupied) spin molecular orbitals (MO), $\phi_i(\mathbf{q})$, respecting the antisymmetric nature of the electrons (and thus the wavefunction) as

$$\psi_k(\mathbf{q}_1, \mathbf{q}_2, ..., \mathbf{q}_N) = \frac{1}{\sqrt{N!}} \begin{vmatrix} \phi_1(\mathbf{q}_1) & \phi_1(\mathbf{q}_2) & \cdots & \phi_1(\mathbf{q}_N) \\ \phi_2(\mathbf{q}_1) & \phi_2(\mathbf{q}_2) & \cdots & \phi_2(\mathbf{q}_N) \\ \vdots & \vdots & \ddots & \vdots \\ \phi_N(\mathbf{q}_1) & \phi_N(\mathbf{q}_2) & \cdots & \phi_N(\mathbf{q}_N) \end{vmatrix}. \tag{1.10}$$

Each one of these MOs is usually constructed, approximately, as a linear combination of basis functions. Commonly, the basis functions have shape of the orbitals from the isolated atoms, also named atomic orbitals (AO) χ_μ, and mathematically are expressed using Gaussian- or Slater-type functions. The procedure of

building the MOs as a linear combination of AOs is the so-called linear combination of atomic orbitals (LCAO) approach

$$\phi_i = \sum_{\mu=1}^{N_{AO}} c_{\mu i}\chi_\mu, \tag{1.11}$$

where N_{AO} corresponds to the number of AOs and $c_{\mu i}$ to the expansion coefficient of the μth AO in the ith MO. With this approach, one obtains as many MOs as AOs used to build them ($N_{MO} = N_{AO}$), being N considered occupied and the rest unnoccupied (virtual). Note that in Eq. 1.11 the origin (location) of the basis functions is not specified. This is because the LCAO approach is not limited to basis functions centered in a particular location/object, e.g. centered on the atomic positions. For a variety of reasons, most of the quantum-chemistry packages make use of atom-centered basis sets but it is not mandatory, i.e. bond functions, floating functions or the plane-waves used in packages with periodic boundary conditions to simulate materials.

The construction of the wavefunction considering only one electronic configuration (single-determinant) do not always accurately describe the *exact* wavefunction. Alternatively, one can build the wavefunction as a linear combination of n_C SDs

$$\Psi(\mathbf{q}_1, \mathbf{q}_2, ..., \mathbf{q}_N) = \sum_{k=1}^{n_C} c_k\psi_k(\mathbf{q}_1, \mathbf{q}_2, ..., \mathbf{q}_N);\ \sum_{k=1}^{n_C} |c_k|^2 = 1, \tag{1.12}$$

where the SD involved represent the ground-state and each of the excited-state electronic configurations. Then, one can rewrite Eq. 1.12 depending on the nature of the electronic excitation

$$\begin{aligned}\Psi(\mathbf{q}_1, \mathbf{q}_2, ..., \mathbf{q}_N) = c_0\psi_{(0)}(\mathbf{q}_1, \mathbf{q}_2, ..., \mathbf{q}_N) + \sum_a \sum_r c_a^r\psi_a^r(\mathbf{q}_1, \mathbf{q}_2, ..., \mathbf{q}_N) \\ + \sum_{ab} \sum_{rs} c_{ab}^{rs}\psi_{ab}^{rs}(\mathbf{q}_1, \mathbf{q}_2, ..., \mathbf{q}_N) + \sum_{abc} \sum_{rst} c_{abc}^{rst}\psi_{abc}^{rst}(\mathbf{q}_1, \mathbf{q}_2, ..., \mathbf{q}_N) + \ ...,\end{aligned} \tag{1.13}$$

where (a, b, c) and (r, s, t) are indices for the occupied and virtual MOs, respectively, ψ_0 is the SD of the ground-state electronic configuration, ψ_a^r corresponds to the single-electron excitation from the ath occupied MO to the rth virtual ($a \rightarrow r$), ψ_{ab}^{rs} to the simultaneous $a \rightarrow r$ and $b \rightarrow s$ double-electron excitation and so forth.

Considering all plausible electronic configurations, hence constructing the electronic wavefunction as linear combination of all possible SDs (Eqs. 1.12 and 1.13), and determining the c coefficients variationally leads to the *exact* electronic energy for the particular atomic basis set used. This procedure is the so-called Full Configuration Interaction (FCI) method[8,9] and its computationally highly expensive as the number of SDs to consider rapidly increase with the number of basis functions

$$N_{SD} = \binom{2N_{AO}}{N} = \frac{2N_{AO}!}{N!(2N_{AO} - N)!}. \tag{1.14}$$

As illustrative example, the water molecule ($N = 10$) with a minimal atomic basis set ($N_{AO} = 7$) require involving 1.0×10^3 Slater determinants, while $N_{SD} = 1.3 \times 10^7$ for a still rather small double-ζ basis set ($N_{AO} = 14$). This makes the FCI method solely applicable for small molecules coupled to a small atomic

basis set and in practice unafforable for most of the systems. Thus, the development and use of wavefunction methods which accurately approach the *exact* electronic energy at a lower computational cost is required. Different methods have been developed over the years for this aim, including the truncated Configuration Interaction (CI) family[10] and the Complete (or Restricted) Active Space Self-Consistent Field (CASSCF[11] and RASSCF,[12] respectively) methods, to name a few. In the truncated CI methods, the wavefunction from Eq. 1.13 is obtained by selecting the included Slater determinants according to the nature of the electronic configurations, and using a set of MOs optimized for the ground-state electronic configuration (usually obtained at the Hartree-Fock level) to construct each of the Slater determinants. Once the initial wavefunction is constructed, the c coefficients from Eq. 1.13 are variationally obtained, but keeping the reference MOs. Truncating Eq. 1.13 to include only single- and double-electron excitations or single-, double- and triple-electron excitations leads to the expressions of the CISD and CISDT methods, respectively. Let us note that the CI methods fail to provide accurate electronic energies when the system to study presents some multi(reference/configurational) character. Its origin is the use of the Hartree-Fock optimized MOs to build all electronic configurations without allowing them to relax along the minimization procedure. In such a case, one requires to make use of methods that variationally optimize both the c coefficients from Eq. 1.12 and the MOs, being CASSCF the most famous one. In CASSCF, the SDs used to construct the CASSCF wavefunction are selected differently to the CI methods. The CASSCF method divides the molecular orbitals in three subspaces: internal, active and external (see Figure 1.1 (a)). The internal and external MOs are considered frozen, which means that always present occupancies of 2 and 0, respectively, but are allowed to rotate to keep the complete set of occupied MOs orthogonal. For the active MOs (also known as active space) all possible electronic configurations (FCI) are considered.

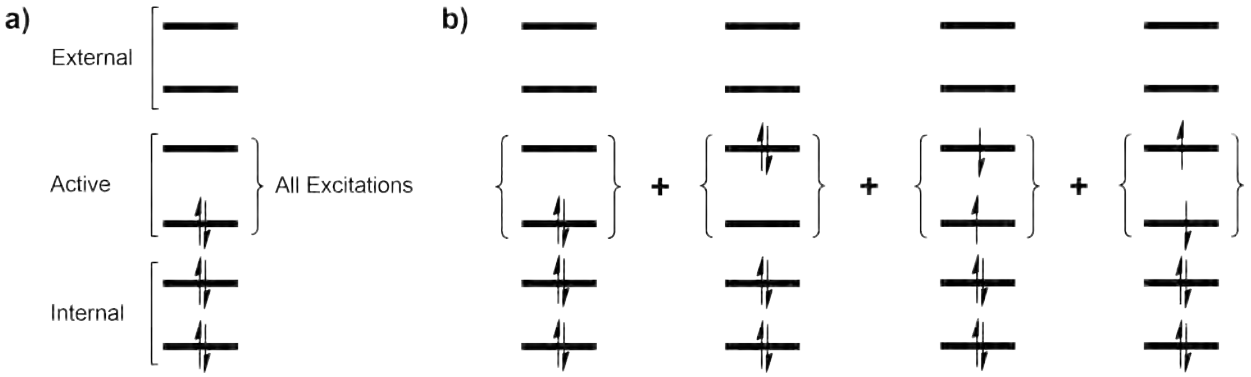

Figure 1.1: Example CASSCF(2,2) MO subspaces (a) and electronic configurations involved in Slater determinant basis (b).

Then, the CASSCF wavefunction is constructed with the Slater determinants corresponding to the FCI electronic configurations within the active space. We represented in Figure 1.1 (b) an example for a system containing 2 electrons in 2 MOs (CASSCF(2,2)). Let us mention that CASSCF is not a black-box method and the results obtained depends on the active-space selection.

From the wavefunction, and independently of its nature (single- or multi-determinant), one can build the N-density matrix by multiplying the wavefunction with its complex conjugate

$$\rho_N(\mathbf{q}_1, ..., \mathbf{q}_N; \mathbf{q}'_1, ..., \mathbf{q}'_N) = \Psi^*(\mathbf{q}_1, ..., \mathbf{q}_N)\Psi(\mathbf{q}'_1, ..., \mathbf{q}'_N), \tag{1.15}$$

whose diagonal elements ($\mathbf{q}'_1 = \mathbf{q}_1$) are related with the probability density distribution for the electrons. For instance, $\rho_N(\mathbf{q}_1, ..., \mathbf{q}_N; \mathbf{q}_1, ..., \mathbf{q}_N)$ provides the probability of finding *simultaneously* electron 1 in $\mathbf{q}_1$, electron 2 in $\mathbf{q}_2$, etc.

Lower in rank density matrices can be obtained upon integration of the appropriate coordinates. [13] For the purpose of this Thesis we focus solely into the first- and second-order (reduced) density matrices, henceforth named RDM1 and RDM2, respectively. The RDM1, $\rho_1(\mathbf{q}_1; \mathbf{q}'_1)$, is obtained from the wavefunction itself as

$$\rho_1(\mathbf{q}_1; \mathbf{q}'_1) = N \int \Psi^*(\mathbf{q}_1, \mathbf{q}_2, ..., \mathbf{q}_N)\Psi(\mathbf{q}'_1, \mathbf{q}_2, ..., \mathbf{q}_N)d\mathbf{q}_2, ..., \mathbf{q}_N. \tag{1.16}$$

Integration by the spin coordinate $\sigma = (\alpha, \beta)$ of the RDM1 leads to the first-order spin-less density, $\rho_1(\mathbf{r}_1; \mathbf{r}'_1)$, composed by the α and β parts of the RDM1 as

$$\rho_1(\mathbf{r}_1; \mathbf{r}'_1) = \int \rho_1(\mathbf{q}_1; \mathbf{q}'_1)|_{\sigma'_1=\sigma_1} d\sigma_1 = \rho_1^\alpha(\mathbf{r}_1; \mathbf{r}'_1) + \rho_1^\beta(\mathbf{r}_1; \mathbf{r}'_1), \tag{1.17}$$

which solely depends on the spatial coordinates of electron 1 in $\mathbf{r}_1$ and $\mathbf{r}'_1$. Substraction of its spin components (Eq. 1.17) gives the first-order spin density

$$\rho_1^s(\mathbf{r}_1; \mathbf{r}'_1) = \rho_1^\alpha(\mathbf{r}_1; \mathbf{r}'_1) - \rho_1^\beta(\mathbf{r}_1; \mathbf{r}'_1). \tag{1.18}$$

In the $\mathbf{r}'_1 = \mathbf{r}_1$ case, Eqs. 1.17 and 1.18 yield the spinless one-electron density, $\rho(\mathbf{r}_1)$, its spin components, $\rho^\alpha(\mathbf{r}_1)$ and $\rho^\beta(\mathbf{r}_1)$, and the spin density

$$\rho^s(\mathbf{r}_1) = \rho^\alpha(\mathbf{r}_1) - \rho^\beta(\mathbf{r}_1). \tag{1.19}$$

One can generally express the RDM1 in terms of the MOs as

$$\rho_1(\mathbf{r}_1; \mathbf{r}'_1) = \sum_{ij}^{N_{orb}} D_{ij}\phi_j^*(\mathbf{r}_1)\phi_i(\mathbf{r}'_1), \tag{1.20}$$

where the matrix $\mathbf{D}$ is the representation of the first-order density matrix in the MO basis and N_{orb} is the number of MOs. For open-shells, the α and β parts of the density matrix ($\mathbf{D}^\alpha$ and $\mathbf{D}^\beta$) are independent

$$\rho_1(\mathbf{r}_1; \mathbf{r}'_1) = \sum_{ij}^{N_{orb,\alpha}} D_{ij}^\alpha \phi_j^{*,\alpha}(\mathbf{r}_1)\phi_i^\alpha(\mathbf{r}'_1) + \sum_{ij}^{N_{orb,\beta}} D_{ij}^\beta \phi_j^{*,\beta}(\mathbf{r}_1)\phi_i^\beta(\mathbf{r}'_1). \tag{1.21}$$

In the single-determinant case, $\mathbf{D}$ is diagonal with $D_{ii} = 2, 0$ and $D_{ii}^\sigma = 1, 0$ values for the restricted closed- and open-shell cases, respectively. Thus, Eq. 1.20 and 1.21 reduce to

$$\rho(\mathbf{r}_1; \mathbf{r}'_1) = 2\sum_{i}^{N_{occ}} \phi_i^*(\mathbf{r}_1)\phi_i(\mathbf{r}'_1), \tag{1.22}$$

and

$$\rho(\mathbf{r}_1; \mathbf{r}'_1) = \sum_{i}^{N_\alpha} \phi_i^{*,\alpha}(\mathbf{r}_1)\phi_i^\alpha(\mathbf{r}'_1) + \sum_{i}^{N_\beta} \phi_i^{*,\beta}(\mathbf{r}_1)\phi_i^\beta(\mathbf{r}'_1), \tag{1.23}$$

where N_{occ} is the number of doubly-occupied MOs, and N_α and N_β the number of singly-occupied α and β spin MOs, respectively.

For multi-determinant wavefunctions, **D** is non-diagonal (Eq. 1.20), and the orbitals that diagonalize it are the so-called natural orbitals (NO)

$$\rho(\mathbf{r}_1;\mathbf{r}'_1) = \sum_{i}^{N_{orb}} n_i \phi_i^{*,NO}(\mathbf{r}_1)\phi_i^{NO}(\mathbf{r}'_1), \tag{1.24}$$

where n_i corresponds to the occupancy number of the ith NO.

In 1978, Takatsuka *et al.* defined the effective number of unpaired electrons function, namely $u(\mathbf{r}_1)$, from the one-electron density and the first-order density matrix

$$u(\mathbf{r}_1) = 2\rho(\mathbf{r}_1) - \int \rho_1(\mathbf{r}_1;\mathbf{r}'_1)\rho_1(\mathbf{r}'_1;\mathbf{r}_1)d\mathbf{r}'_1, \tag{1.25}$$

accounting for the deviation from idempotency of the first-order density matrix and playing the role of the spin density when the latter vanishes.[14] In fact, in the case of a restricted open-shell wavefunction, $u(\mathbf{r}_1) = \rho^s(\mathbf{r}_1)$. In a more general case, $u(\mathbf{r}_1)$ is conveniently expressed in the NO basis as

$$u(\mathbf{r}_1) = \sum_{i} n_i(2-n_i)\phi_i^{*,NO}(\mathbf{r}_1)\phi_i^{NO}(\mathbf{r}_1), \tag{1.26}$$

and upon integration one obtains the effective number of unpaired electrons

$$N_u = \int u(\mathbf{r}_1)d\mathbf{r}_1. \tag{1.27}$$

Takatsuka's definition presents as main drawback that upon integration can yield a number of unpaired electrons larger than the total number of electrons (with maximum asymptotic value $N_u = 2N$), which is nonphysical. As example, in the dissociation of a singlet O_2 molecule into two triplet oxygen atoms one expects $N_u = 4$, but Ramos-Cordoba *et al.* showed that Takatsuka's definition leads at the dissociation limit to $N_u = 5$, i.e. five effectively unpaired electrons.[15]

In 2003, Head-Gordon introduced an alternative definition of $u(\mathbf{r}_1)$, expressed in the NO basis as

$$u(\mathbf{r}_1) = \sum_{i} \left(1 - abs(1-n_i)\right) \phi_i^{*,NO}(\mathbf{r}_1)\phi_i^{NO}(\mathbf{r}_1). \tag{1.28}$$

The rather simple new definition fulfills that $u(\mathbf{r}_1) = 0$ when $n_i = 2, 0$ and $u(\mathbf{r}_1) = 1$ for $n_i = 1$, it provides $N_u \leq N$ values and, recovering the dissociation of the O_2 molecule, it provides the expected $N_u = 4$ at dissociation.[16] However, as the author already pinpointed in his work, such definition is not unique as many functions fulfill the aforementioned conditions.

The RDM2, $\rho_2(\mathbf{q}_1,\mathbf{q}_2;\mathbf{q}'_1,\mathbf{q}'_2)$ is again obtained from the wavefunction as

$$\rho_2(\mathbf{q}_1,\mathbf{q}_2;\mathbf{q}'_1,\mathbf{q}'_2) = N(N-1)\int \Psi^*(\mathbf{q}_1,\mathbf{q}_2,...,\mathbf{q}_N)\Psi(\mathbf{q}'_1,\mathbf{q}'_2,...,\mathbf{q}_N)d\mathbf{q}_3...d\mathbf{q}_N, \tag{1.29}$$

where $N(N-1)$ corresponds to the number of unsorted electron pairs, also known as McWeeny's normalization.[13] Other authors normalize it to the number of sorted electron pairs, $N(N-1)/2$, known as Löwdin normalization. In the $\mathbf{q}'_1 = \mathbf{q}_1$ and $\mathbf{q}'_2 = \mathbf{q}_2$ case, the RDM2 is related (proportional to) with the proba-

bility of finding electron 1 in $\mathbf{q}_1$ and electron 2 in $\mathbf{q}_2$, independently of the position of the other $N-2$ electrons.

Upon integration of Eq. 1.29 by spin, one obtains the spinless form of the RDM2

$$\rho_2(\mathbf{r}_1,\mathbf{r}_2;\mathbf{r}'_1,\mathbf{r}'_2) = \iint \rho_2(\mathbf{q}_1,\mathbf{q}_2;\mathbf{q}'_1,\mathbf{q}'_2)|_{\substack{\sigma'_1=\sigma_1\\ \sigma'_2=\sigma_2}} d\sigma_1 d\sigma_2, \tag{1.30}$$

which can be conveniently expressed from the RDM1 (Eq. 1.17), the first-order spin density (Eq. 1.18) and an additional two-electron dependent term, namely the cumulant of the second-order density matrix, $\Gamma(\mathbf{r}_1,\mathbf{r}_2;\mathbf{r}'_1,\mathbf{r}'_2)$, as

$$\begin{aligned}\rho_2(\mathbf{r}_1,\mathbf{r}_2;\mathbf{r}'_1,\mathbf{r}'_2) = \rho_1(\mathbf{r}_1;\mathbf{r}'_1)\rho_1(\mathbf{r}_2,\mathbf{r}'_2) - \frac{1}{2}\rho_1(\mathbf{r}_1;\mathbf{r}'_2)\rho_1(\mathbf{r}_2;\mathbf{r}'_1)\\ - \frac{1}{2}\rho_1^s(\mathbf{r}_1;\mathbf{r}'_2)\rho_1^s(\mathbf{r}_2;\mathbf{r}'_1) + \Gamma(\mathbf{r}_1,\mathbf{r}_2;\mathbf{r}'_1,\mathbf{r}'_2).\end{aligned} \tag{1.31}$$

Usually, the two last terms of Eq. 1.31 are gathered together into the spinfree cumulant of the RDM2 [17,18]

$$\Lambda(\mathbf{r}_1,\mathbf{r}_2;\mathbf{r}'_1,\mathbf{r}'_2) = -\frac{1}{2}\rho_1^s(\mathbf{r}_1;\mathbf{r}'_2)\rho_1^s(\mathbf{r}_2;\mathbf{r}'_1) + \Gamma(\mathbf{r}_1,\mathbf{r}_2;\mathbf{r}'_1,\mathbf{r}'_2), \tag{1.32}$$

being Eq. 1.32 simplified to

$$\rho_2(\mathbf{r}_1,\mathbf{r}_2;\mathbf{r}'_1,\mathbf{r}'_2) = \rho_1(\mathbf{r}_1;\mathbf{r}'_1)\rho_1(\mathbf{r}_2,\mathbf{r}'_2) - \frac{1}{2}\rho_1(\mathbf{r}_1;\mathbf{r}'_2)\rho_1(\mathbf{r}_2;\mathbf{r}'_1) + \Lambda(\mathbf{r}_1,\mathbf{r}_2;\mathbf{r}'_1,\mathbf{r}'_2). \tag{1.33}$$

It can be easily seen that in the single-determinant case the RDM2 can be expressed solely in terms of the RDM1. In other words, the cumulant $\Gamma(\mathbf{r}_1,\mathbf{r}_2;\mathbf{r}'_1,\mathbf{r}'_2)$ is zero. Thus, the RDM2 expression (Eq. 1.31) is reduced to

$$\rho_2(\mathbf{r}_1,\mathbf{r}_2;\mathbf{r}'_1,\mathbf{r}'_2) = \rho_1(\mathbf{r}_1;\mathbf{r}'_1)\rho_1(\mathbf{r}_2,\mathbf{r}'_2) - \frac{1}{2}\rho_1(\mathbf{r}_1;\mathbf{r}'_2)\rho_1(\mathbf{r}_2;\mathbf{r}'_1) - \frac{1}{2}\rho_1^s(\mathbf{r}_1;\mathbf{r}'_2)\rho_1^s(\mathbf{r}_2;\mathbf{r}'_1). \tag{1.34}$$

Let us mention that for closed-shell wavefunctions the later term from Eq. 1.34 also vanishes as the spin density is zero.

Recovering Eq. 1.8 coupled with the Hamiltonian from Eq. 1.4 and using the aforementioned density matrices, the expectation value of the electronic energy in wavefunction theory is generally written as

$$E = \int \hat{h}_1^{(1)}\rho_1(\mathbf{r}_1;\mathbf{r}'_1)|_{\mathbf{r}'_1=\mathbf{r}_1} d\mathbf{r}_1 + \frac{1}{2}\iint \rho_2(\mathbf{r}_1,\mathbf{r}_2)\hat{V}_{ee,12}^{(2)} d\mathbf{r}_1 d\mathbf{r}_2, \tag{1.35}$$

with the one- and two-electron operators introduced in Eqs. 1.5 and 1.6, respectively. Hence, even the wavefunction depends explicitly on the coordinates of N electrons, one can express the total system energy in terms of one- and two-electron operators, being the dimensionality (and thus computational cost) highly reduced.

With this, the one-electron dependent expressions of the electronic kinetic energy (T) and electron-nuclei attraction (U) terms are

$$T = -\frac{1}{2}\int \nabla^2\rho_1(\mathbf{r}_1;\mathbf{r}'_1)|_{\mathbf{r}'_1=\mathbf{r}_1} d\mathbf{r}_1, \tag{1.36}$$

and

$$U = -\sum_{B}^{N_{At}} \int \frac{Z^B}{|\mathbf{r}_1 - \mathbf{R}_B|} \rho(\mathbf{r}_1) d\mathbf{r}_1. \tag{1.37}$$

Note that to compute the kinetic energy it is required to use the RDM1. This is justified for the ∇^2 operator first acts on $\mathbf{r}_1$ and then $\mathbf{r}'_1 = \mathbf{r}_1$ before integration over $\mathbf{r}_1$. Contrarily, U (Eq. 1.37) can be directly expressed in terms of the one-electron density.

The inclusion of Eq. 1.33 into the second term of Eq. 1.35 yields the electron-electron interaction, V_{ee}, constituted by the three following terms

$$\begin{aligned} V_{ee} = &\frac{1}{2} \iint \rho(\mathbf{r}_1)\rho(\mathbf{r}_2) r_{12}^{-1} d\mathbf{r}_1 d\mathbf{r}_2 + \frac{1}{2} \iint \Gamma(\mathbf{r}_1, \mathbf{r}_2) r_{12}^{-1} d\mathbf{r}_1 d\mathbf{r}_2 \\ &- \frac{1}{4} \iint \left(\rho_1(\mathbf{r}_1;\mathbf{r}_2)\rho_1(\mathbf{r}_2;\mathbf{r}_1) + \rho_1^s(\mathbf{r}_1;\mathbf{r}_2)\rho_1^s(\mathbf{r}_2;\mathbf{r}_1)\right) r_{12}^{-1} d\mathbf{r}_1 d\mathbf{r}_2. \end{aligned} \tag{1.38}$$

The first contribution corresponds to the Coulombic repulsion, E_{Coul}, and involves the quotient between the product of the one-electron densities of electrons 1 and 2 at the $\mathbf{r}_1$ and $\mathbf{r}_2$ positions, respectively, and their interelectronic distance. The second term is in charge of providing the correlation energy between electrons, E_c, and the third is the so-called exchange energy, E_x, which contains the self-interaction of the electrons and is originated from the antisymmetric nature of the electronic wavefunction. From its expression, one can define the exchange density, $\rho^x(\mathbf{r}_1, \mathbf{r}_2)$, as

$$\rho^x(\mathbf{r}_1, \mathbf{r}_2) = \frac{1}{2} \left(\rho_1(\mathbf{r}_1;\mathbf{r}_2)\rho_1(\mathbf{r}_2;\mathbf{r}_1) - \rho_1^s(\mathbf{r}_1;\mathbf{r}_2)\rho_1^s(\mathbf{r}_2;\mathbf{r}_1)\right). \tag{1.39}$$

Finally, to recover the total system energy, E_{tot}, is required the addition of the repulsion between nuclei V_{NN} to the electronic energy, $E_{tot} = E + V_{NN}$, which within the BO approximation is trivially evaluated as in Eq. 1.7.

As it was aforementioned, in the single-determinant case, such as in Hartree-Fock (HF) theory, the RDM2 expression is simplified as the cumulant term is missing (Eq. 1.34). As consequence, the electronic repulsion energy V_{ee}, is solely expressed from the one-electron and exchange densities

$$V_{ee} = \frac{1}{2} \iint \rho(\mathbf{r}_1)\rho(\mathbf{r}_2) r_{12}^{-1} d\mathbf{r}_1 d\mathbf{r}_2 - \frac{1}{2} \iint \rho^x(\mathbf{r}_1, \mathbf{r}_2) r_{12}^{-1} d\mathbf{r}_1 d\mathbf{r}_2, \tag{1.40}$$

where the exchange density can be generally expressed from the MOs using Eq. 1.22 for the closed-shell

$$\rho^x(\mathbf{r}_1, \mathbf{r}_2) = 2 \sum_{ij}^{N_{occ}} \phi_i^*(\mathbf{r}_1)\phi_j^*(\mathbf{r}_2)\phi_j(\mathbf{r}_1)\phi_i(\mathbf{r}_2), \tag{1.41}$$

and Eq. 1.23 for the open-shell scenario

$$\rho^x(\mathbf{r}_1,\mathbf{r}_2) = \sum_{ij}^{N_\alpha} \phi_i^{*,\alpha}(\mathbf{r}_1)\phi_j^{*,\alpha}(\mathbf{r}_2)\phi_j^{\alpha}(\mathbf{r}_1)\phi_i^{\alpha}(\mathbf{r}_2) + \sum_{ij}^{N_\beta} \phi_i^{*,\beta}(\mathbf{r}_1)\phi_j^{*,\beta}(\mathbf{r}_2)\phi_j^{\beta}(\mathbf{r}_1)\phi_i^{\beta}(\mathbf{r}_2). \tag{1.42}$$

In both cases, the integration of the exchange density over both $\mathbf{r}_1$ and $\mathbf{r}_2$ coordinates yields its normalization

$$\iint \rho^x(\mathbf{r}_1,\mathbf{r}_2)d\mathbf{r}_1 d\mathbf{r}_2 = N. \tag{1.43}$$

Lastly, the use of Eqs. 1.41 and 1.42 in the second term of Eq. 1.40 yield the so-called HF exchange energy, which in the closed-shell case reads as

$$E_x^{HF} = -\sum_{ij}^{N_{occ}} \iint \phi_i^*(\mathbf{r}_1)\phi_j^*(\mathbf{r}_2)\phi_j(\mathbf{r}_1)\phi_i(\mathbf{r}_2)r_{12}^{-1}d\mathbf{r}_1 d\mathbf{r}_2, \tag{1.44}$$

and in the open-shell one as

$$E_x^{HF} = -\frac{1}{2}\left(\sum_{ij}^{N_\alpha} \iint \phi_i^{*,\alpha}(\mathbf{r}_1)\phi_j^{*,\alpha}(\mathbf{r}_2)\phi_j^{\alpha}(\mathbf{r}_1)\phi_i^{\alpha}(\mathbf{r}_2)r_{12}^{-1}d\mathbf{r}_1 d\mathbf{r}_2 + \sum_{ij}^{N_\beta} \iint \phi_i^{*,\beta}(\mathbf{r}_1)\phi_j^{*,\beta}(\mathbf{r}_2)\phi_j^{\beta}(\mathbf{r}_1)\phi_i^{\beta}(\mathbf{r}_2)r_{12}^{-1}d\mathbf{r}_1 d\mathbf{r}_2 \right). \tag{1.45}$$

Let us mention that the expressions and thus the evaluation of the other energy components are equivalent for both single- (HF) and multi-determinant wavefunctions.

An alternative to the wavefunction-based methods is the density functional theory, based on the Hohenberg-Kohn theorems. In 1964, Hohenberg and Kohn proved that the electronic energy of a system in its (non-degenerate) ground state is completely determined by the one-electron density,[19] stating that:

- **The exact electronic energy of a non-degenerated ground state is functional of the one-electron density**. Thus, that it exists a one-electron density functional which *exactly* determines both the energy, and any other observable, $E_{exact} = E[\rho_{exact}(\mathbf{r})]$. However, *the functional that connects the ground state energy of a system with its one-electron density function is not known.*

- **The energy of a system in its ground state reaches a minimum value when the exact electronic density is considered**. That is, if the energy functional is applied to a one-electron density different to the exact one, the obtained energy is higher or equal to the exact, $E[\rho_{exact}(\mathbf{r})] \leq E[\rho(\mathbf{r})]$. In other words, the energy density functional is bowed to the variational principle.

Later on, Kohn and Sham introduced a practical approach to apply DFT which can be related with the Hartree-Fock approach.[20] The Kohn-Sham implementation of DFT (KS-DFT) is rooted to a single-

determinant wavefunction, and its energy expression compared to HF solely differs in the exchange contribution. Thus, in KS-DFT the kinetic energy is expressed as in Eq. 1.36 instead of as a functional of the one-electron density and the HF exchange energy from Eq. 1.44 is formally replaced by the exchange-correlation term, E_{xc}^{DFT}, which attempts to approximate the *exact* exchange-correlation (plus kinetic correlation) energy as

$$E_{xc}^{DFT} = \int \epsilon^{xc}(\mathbf{r}_1) d\mathbf{r}_1 = \int \epsilon^{xc}[\rho(\mathbf{r}_1), \nabla\rho(\mathbf{r}_1), ...] d\mathbf{r}_1. \tag{1.46}$$

Here, $\epsilon^{xc}(\mathbf{r}_1)$ corresponds to the exchange-correlation energy density and is commonly functional of the electron density and its derivatives $\epsilon^{xc}[\rho(\mathbf{r}_1), \nabla\rho(\mathbf{r}_1), ...]$. In Eq. 1.46 both the exchange and correlation energy terms are gathered together, but in fact the KS-DFT functionals usually are expressed as combination of exchange and correlation, independently, $\epsilon^{xc}(\mathbf{r}_1) = \epsilon^{x}(\mathbf{r}_1) + \epsilon^{c}(\mathbf{r}_1)$. Even the *exact* functional ϵ^{xc} should exist, its mathematical expression has not *yet* been found. Thus, there is a plethora of KS-DFT functionals developed to date. Some of them are based on providing the mathematically exact solution for a particular system or under some conditions, e.g. the local density approximation exchange functional (LDA) is the exact solution of the exchange for the uniform electron gas. Alternatively, the expression of others is build upon parametrization according to experimentally or computationally obtained data. Anyway, and as it was aforementioned, all of them are approximations to the *exact* E_{xc}, and its accuracy depends on the complexity of the functional itself and the purpose of its development, e.g. some functionals are parametrized to provide accurate spin states but may fail in other properties.

Commonly, the KS-DFT functionals are classified according to its nature (complexity), being the most popular classification the so-called Jacob ladder of the density functional approximations introduced by Perdew.[21] According to such classification, the lowers rung on the ladder corresponds to the functionals which solely depends on the one-electron density, giving name to the local spin density approximation (LSDA) family. The method complexity, and thus rung in the Jacob's ladder, increases upon inclusion of the first (gradient) and second (Laplacian) derivative of the one-electron density (or kinetic energy density for the later), known as generalized gradient approximation (GGA) and meta-GGA, respectively. The three families of approximations, namely the LSDA, GGA and meta-GGA, are considered *pure* as only depends on the density and its derivatives, and *local* due to solely depend on the position at one point of the space. The following step on the ladder corresponds to the functionals which include a percentage of HF-type exchange, Eq. 1.44 but evaluated with the MOs obtained at the KS-DFT level, in the exchange functional expression, leading to the so-called *hybrid* methods. Among them, one (if not the most) renowned (and extensively used) is the B3LYP method,[22,23] which combines using only 3 parameters: Hartree-Fock, the Becke88 (B88)[24] formulae and the Dirac expression of exact exchange of the homogeneous electron gas (LDA)[25,26] to evaluate the exchange energy, and the Lee, Yang, Parr (LYP)[23] with the Vosko, Wilk, Nusair (VWN)[27] expressions for correlation

$$\begin{aligned} E_{xc}^{B3LYP} = E_x^{LDA} + a_0(E_x^{HF} - E_x^{LDA}) + a_x(E_x^{B88} - E_x^{LDA}) \\ + E_c^{VWN} + a_c(E_c^{LYP} - E_c^{VWN}), \end{aligned} \tag{1.47}$$

$$a_0 = 0.2, \;\; a_x = 0.72, \;\; a_c = 0.81.$$

An extension comes with the tuning of the HF-type exchange inclusion as function of the interelectronic distance, leading to the so-called long-range corrected functionals. In a last step, it comes the design of the most sophisticated functionals, involving also the admixture of a portion of perturbation theory-obtained (Moller-Plesset of second order, MP2) correlation energy to the correlation expression of the functional, being categorized as *double-hybrids*. Further details about the KS-DFT approximations, together with the fundamentals of density functional theory, are out of the scope of the Thesis. Then, we guide the reader to the following references in case of interest about the topic.[21,28–30]

1.2 The definition of the atom within the molecule

Nowadays it is well accepted that, from a genuine chemical perspective, every molecule is conceived as a system constructed by interacting atoms, the elementary units (building blocks) in chemistry. Grounding chemistry and its rationalization based on the concept of an atom in a molecule was originated by Lewis in 1916, where he attempted to rationalize the behaviour and properties of many systems according to the "electronic structure" (the author tag it as *atomic kernel*) of the constituting atoms.[31] The theory at that moment was considering fixed atomic kernels by fulfilling a series of postulates, such as the octet rule. However, the fact that different Manganese- or Cobalt-based complexes presents different colour but shares the same central element made Lewis pinpoint that, in his opinion, the kernel of an atom is not *unique* and permanently defined. Currently, it is undeniable that every atom from two molecular systems, even being of the same type, is electronically different if the chemical environment from both is not the same. This may affect into the properties and reactivity showed by the systems even constructed with the same type of building blocks. For example, the carbon atoms, and as consequence also the hydrogen ones, of two rather simple organic systems like ethane (C_2H_6) and ethyne (C_2H_2) are (and behave) completely different, i.e. the H atoms on ethyne are much more acidic ($pKa = 25$) than in ethane ($pKa = 50$), the C-C bond presents a single multiplicity in ethane, while triple in ethyne, etc. Thus, the electronic structure characterization of any molecular systems requires to distinguish and unveil the role of the atoms that form that particular system. For this aim, one needs a well-defined methodology that subdivides the global system (also known as supersystem) into its constituting atoms, namely an atom in molecule definition. The AIM definition, also known as atomic partition, allows not only to define atomic properties useful to rationalize the electronic structure of the system, but also to decompose a molecular property into atomic and interatomic contributions, providing the required information to understand its chemical bonding picture. Unfortunately, the atoms are not quantum mechanical observables, being the *exact* AIM definition non-existent, and leading to a plethora of atomic partitioning methods. As consequence, all chemical concepts such as bond orders,[32–37] partial atomic charges,[38–41] oxidation states,[42,43] energy decomposition,[44–52] aromaticity indexes[53,54] and steric/electronic repulsions,[55] to name a few, entirely rely on the AIM definition used to evaluate them.

Several AIM schemes have been developed over the years, being classified into two main families: Hilbert- and real-space. To some extent all atomic definitions are arbitrary, being important to know the pros and cons, together with the limitations of each AIM scheme before its application. In the next sections we briefly introduce the most renowned AIMs from both families, together with some insights about their strong and weak points.

1.2.1 Hilbert-space analysis

In Section 1.1 we pinpointed that by following the LCAO approach the MOs are expanded on a finite set of AOs (Eq. 1.11), and its origin of coordinates may be a nuclear position or elsewhere. Herein, and justified by its use in all scientific contributions compiled in this Thesis, we will use atom-centered basis functions as AOs. Then, Eq. 1.11 can be rewritten as

$$\phi_i(\mathbf{r}_1) = \sum_{\mu=1}^{N_{AO}} c_{\mu i}\chi_\mu(\mathbf{r}_1), \tag{1.48}$$

where the $\chi(\mathbf{r}_1)$ contains a set of atom-centered AOs for every atom constituting the molecular system. Each of these sets is known as an atomic Hilbert subspace, $\{\chi_\mu(\mathbf{r}_1)\}_{\mu\in A}$. This allows one to define the atom as its nucleus and its associated Hilbert subspace, being any well-defined molecular quantity decomposable into atomic and interatomic terms. Lets take for instance the one-electron density, that can be written in the AO basis as

$$\rho(\mathbf{r}_1) = \sum_{\mu\nu}^{N_{AO}} D_{\mu\nu}\chi^*_\nu(\mathbf{r}_1)\chi_\mu(\mathbf{r}_1), \tag{1.49}$$

where $\mathbf{D}$ is the density matrix in the AO basis. Upon integration of Eq. 1.49 one recovers the total number of electrons

$$N = \int \rho(\mathbf{r}_1)d\mathbf{r}_1 = \sum_{\mu\nu}^{N_{AO}} D_{\mu\nu}\int \chi^*_\nu(\mathbf{r}_1)\chi_\mu(\mathbf{r}_1) = \sum_{\mu\nu}^{N_{AO}} D_{\mu\nu}S_{\nu\mu}, \tag{1.50}$$

being $\mathbf{S}$ the overlap matrix in the AO basis

$$\mathbf{S} \;=\; \langle\chi_\mu|\chi_\nu\rangle \;=\int \chi_\mu(\mathbf{r}_1)\chi_\nu(\mathbf{r}_1)d\mathbf{r}_1. \tag{1.51}$$

By grouping the summation according to the introduced Hilbert subspaces

$$N = \sum_{AB}^{N_{At}}\sum_{\mu\in A}^{N_{AO}}\sum_{\nu\in B}^{N_{AO}} D_{\mu\nu}S_{\nu\mu} = \sum_{A}^{N_{At}} N_{AA} + \sum_{A,B\neq A}^{N_{At}} N_{AB}, \tag{1.52}$$

one obtains the Mulliken net atomic (N_{AA}) and overlap populations ($N_{AB}+N_{BA}$), respectively.[38] Alternatively, one can rewrite Eq. 1.50 as

$$N = \sum_{\mu\nu}^{N_{AO}} D_{\mu\nu}S_{\nu\mu} = \sum_{\mu\mu}^{N_{AO}} (\mathbf{DS})_{\mu\mu} = tr(\mathbf{DS}), \tag{1.53}$$

and decompose it only in atomic terms

$$N = \sum_{A}^{N_{At}}\sum_{\mu\in A}^{N_{AO}} (DS)_{\mu\mu} = \sum_{A}^{N_{At}} N_A. \tag{1.54}$$

Such decomposition, and using the original basis set to construct the overlap matrix, is the so-called Mulliken gross atomic (N_A) populations. By simple substraction of the atomic electron population (N_A) from the corresponding atomic number (Z_A), one obtains the partial atomic charge

$$Q_A = Z_A - N_A, \tag{1.55}$$

which are extensively used within the computational chemistry community.

Mayer proposed to decompose the exchange density from a single-determinant wavefunction similarly to the Mulliken overlap population.[34,35] As we already illustrated in Eq. 1.42, the exchange density recovers its normalization upon integration, which in the AO basis read as

$$N = \iint \rho_x(\mathbf{r}_1, \mathbf{r}_2) d\mathbf{r}_1 d\mathbf{r}_2 = \sum_{\mu\nu}^{N_{AO}} \left[(\mathbf{DS})_{\mu\nu}(\mathbf{DS})_{\nu\mu} + (\mathbf{D}^s\mathbf{S})_{\mu\nu}(\mathbf{D}^s\mathbf{S})_{\nu\mu} \right], \tag{1.56}$$

where $\mathbf{D}^s = \mathbf{D}^\alpha - \mathbf{D}^\beta$ corresponds to the spin density matrix in the AO basis. Then, by grouping the summations from Eq. 1.56 by Hilbert subspaces one obtains for every pair of atoms A and B the so-called Mayer bond order (MBO)

$$B_{AB} = \sum_{\mu\in A}^{N_{AO}} \sum_{\mu\in B}^{N_{AO}} \left[(\mathbf{DS})_{\mu\nu}(\mathbf{DS})_{\nu\mu} + (\mathbf{D}^s\mathbf{S})_{\mu\nu}(\mathbf{D}^s\mathbf{S})_{\nu\mu} \right], \tag{1.57}$$

which are related with the bond multiplicities, i.e. $B_{AB} = 1$ for a single bond, $B_{AB} = 2$ double, etc. In 2012, Mayer improved the MBO definition for correlated wavefunctions by changing the term on the r.h.s of Eq. 1.58 for a similar one which depends on the Takatsuka definition of the $\mathbf{u}$ function (Eq. 1.25)

$$B_{AB} = \sum_{\mu\in A}^{N_{AO}} \sum_{\mu\in B}^{N_{AO}} \left[(\mathbf{DS})_{\mu\nu}(\mathbf{DS})_{\nu\mu} + (\mathbf{RS})_{\mu\nu}(\mathbf{RS})_{\nu\mu} \right], \tag{1.58}$$

where

$$\mathbf{R} = \mathbf{S}^{-\frac{1}{2}} (\mathbf{u}^\lambda)^{-\frac{1}{2}} \mathbf{S}^{-\frac{1}{2}}, \tag{1.59}$$

and λ denotes that the quantity is in the Löwdin orthogonalized basis (see below). Mayer showed that the original bond order definition (Eq. 1.57) explicitly depends of the m_s (spin) value, providing different B_{AB} values for a triplet ($S = 1$) with $m_s = 1$ and $m_s = 0$, being corrected with tha later definition (Eq. 1.58). Furthermore, the latter definition presented very similar results to the obtained with the original formulae, and the appropriate behaviour at dissociation.[37] Let us mention that from Mayer's point of view the bond order should be computed using the exchange density, while other authors consider that one should use the exchange-correlation density, instead, as directly provide values independent of m_s.

The use of the untransformed AOs to define the Hilbert subspaces presents a battery of drawbacks, including:

- **Basis set dependency**. The results obtained for a decomposed quantity are highly affected by the size (and type) of basis set used. This flaw was already pinpointed by Baker in 1985, where he evaluated atomic charges and bond orders for a variety of systems using basis sets from the minimal (STO-3G) to double-ζ (6-31G**).[56] As conclusion, the author propose the use of Löwdin partition (see below) instead of Mulliken's one. Note that the basis sets used at that time were rather small compared to the used nowadays. More recently, similar studies has been performed for extended basis sets. As example, in 2005 Martin and

Zipse studied the basis set effect on the atomic populations of the oxygen atom of the water molecule.[57] The authors obtained very large differences (up to half electron) depending on the basis set used and small differences with the method. Selected illustrative results are collected in Table 1.1.

Table 1.1: Partial charge (Mulliken's) of the oxygen atom in the water molecule computed at different levels of theory. Results extracted from Ref. 57.

Basis set	HF	B3LYP	MP2	QCISD
STO-3G	-0.3664	-0.3687	-0.3481	-0.3369
6-31G(d,p)	-0.6736	-0.6100	-0.6415	-0.6319
6-311G(d,p)	-0.4985	-0.4753	-0.4740	-0.4611
cc-pVTZ	-0.4826	-0.4322	-0.4720	-0.4611
cc-pV5Z	-0.5611	-0.5578	-0.5097	-
cc-pV6Z	-0.3912	-0.4207	-0.3234	-
aug-cc-pV5Z	-0.8239	-0.8752	-0.7835	-

- **Unphysical behaviour for large basis sets which include diffuse-type AOs**. Increasing the basis set size, together with including AOs of different type benefits the construction of the MOs (much more flexibility) and thus the wavefunction itself. However, the diffuse-type AOs, even being atom-centered, do not present large atomic character. Thus, they are included within atomic Hilbert subspaces which formally they should not contribute to. As consequence, the decomposition of any quantity will be contaminated, presenting larger values than expected. As example, in 2003 Fonseca-Guerra *et al.* showed that for basis sets including diffuse functions the overlap populations became larger and as consequence Mulliken's partition yielded totally unphysical atomic charges.[58] One may (erratically) think that a plausible solution is directly erase the diffuse-type functions from the basis set. However, their use is crucial for properly describing many molecular systems such as anions.

It is important to mention that such flaws will be present to the decomposition of *any* quantity as are rooted to the AIM definition itself. For this reason, several groups attempted to develop Hilbert-space AIM definitions that surpass (at least) the two first drawbacks, originated by including in the atomic Hilbert subspaces AOs (and thus MOs) that are not formally contributing to the *belonging* atom. The main problem is not only the AO size, i.e. a 6p-type AO is probably too large (expanded) to consider that it entirely contributes to its originator, but more importantly the shape of the AOs constituting the Hilbert subspace. For the later, one may be able to find a transformation of the original AOs which provides satisfactory results. Generally, one performs a unitary transformation to the original basis

$$|\varphi^T\rangle \;=\; \mathbf{U}|\chi\rangle, \tag{1.60}$$

where $\mathbf{U}$ is a unitary matrix, $\mathbf{U}^\dagger\mathbf{U} = \mathbf{I}$. In 1950 Löwdin proposed to use $\mathbf{U} = (\mathbf{S})^{-1/2}$ as transformation matrix, being $\mathbf{S}$ the overlap matrix in the AO basis, constructing then a set of symmetrically orthogonalized orbitals (φ^{Low})

$$|\varphi^{Low}\rangle \;=\; \mathbf{S}^{-1/2}|\chi\rangle. \tag{1.61}$$

This procedure is the so-called Löwdin symmetric orthogonalization of the original basis to the Löwdin basis.[59] A set of orthogonal orbitals fulfill that its overlap matrix is diagonal with terms, $\langle\varphi_\mu^{Low}|\varphi_\mu^{Low}\rangle = \delta_{\mu\nu}$. By using, for example, the Löwdin (or any orthogonal) basis to evaluate atomic electron populations, Eq. 1.54 simplifies to

$$N_A = \sum_{\mu \in A}^{N_{AO}} D_{\mu\mu}, \tag{1.62}$$

leading to Löwdin's atomic populations. Note that in the orthogonal basis the overlap populations from Eq. 1.52 are zero and net and gross populations are equivalent.

Similarly, one can also express the bond order (Eq. 1.57) in an orthogonal basis

$$B_{AB} = \sum_{\mu \in A}^{N_{AO}} \sum_{\mu \in B}^{N_{AO}} |D_{\mu\nu}|^2, \tag{1.63}$$

being known as the Wiberg bond index (WBI).[33]

In general, the results obtained for both atomic charges and bond orders obtained using the Löwdin basis give much satisfactory results than the Mulliken ones, being less (but still) basis set dependent.[56]

An extension of this method is the so-called weighted (or occupancy weighted) Löwdin family of schemes, which rely on the use of a "weighting" matrix, $\mathbf{W}$, to construct the transformation matrix as

$$\mathbf{U} = \mathbf{W}(\mathbf{WSW})^{-1/2}. \tag{1.64}$$

Then, each definition of $\mathbf{W}$ leads to a different set of transformed orbitals (and as consequence to a different AIM). Among them, a famous (if not the most) basis is the natural atomic orbitals (NAO) introduced by Weinhold and coworkers in 1985.[60,61] Using the NAO basis to extract atomic charges give name to the extensively used Natural Population Analysis (NPA),[61] which presents much robust results regarding to basis set dependency than the aforementioned schemes not only for atomic charges but also for spin populations.[58,62]

Alternatively, other Hilbert-space methods rely on the use of a reference minimal basis set, which contains for each atom as many basis functions as its number of core and valence electrons, to *exactly* span the occupied (MOs) space.[63–66] Among them, the Intrinsic Atomic Orbitals (IAO) from Knizia gained particular interest.[66,67] The IAO, φ^{IAO}, construction is a rather convoluted procedure based on projection to a reference (and *minimal*) basis. Starting from a converged SCF solution, one projects the occupied MO coefficients, $\mathbf{C}_{occ} = c_{\mu i}$, into the (small) reference minimal basis and back to the big basis as

$$\tilde{\mathbf{C}}_{occ} = ortho(\mathbf{R}_{ls}\mathbf{R}_{sl}\mathbf{C}_{occ}), \tag{1.65}$$

where the $\mathbf{R}_{sl} = \mathbf{s}^{-1}\mathbf{S}_{sl}$ matrix is the projector from the large to the small basis, $\mathbf{S}$ and $\mathbf{s}$ are the overlap matrices in the large and small basis, respectively, and $\mathbf{S}_{sl}$ corresponds to the overlap matrix between AOs in the small and large basis sets. $\mathbf{R}_{ls} = \mathbf{S}^{-1}\mathbf{S}_{ls}$ projects back from the small to the big basis and then symmetric orthogonalization (*ortho*, Eq. 1.65) is required to restore the orthonormality and obtain the so-called depolarized orbitals, $\tilde{\mathbf{C}}_{occ}$.

Then, the transformation matrix $\mathbf{A}_{ls}$ from the large basis, χ_μ, to the IAO basis, $\varphi_\alpha^{IAO} = \sum_\mu \chi_\mu A_{\mu\alpha}$, is constructed by following a double projection step

$$\mathbf{A}_{ls} = ortho(\mathbf{PS\tilde{P}S}_{ls} + \mathbf{QS\tilde{Q}S}_{ls}). \tag{1.66}$$

Here, $\mathbf{P}$ and $\tilde{\mathbf{P}}$ are the density matrices of the occupied original and depolarized MOs, respectively, and $\mathbf{P}$ and $\tilde{\mathbf{Q}}$ their orthogonal complements

$$\mathbf{P} = \mathbf{C}_{occ}\mathbf{C}_{occ}^{T};\ \tilde{\mathbf{P}} = \tilde{\mathbf{C}}_{occ}\tilde{\mathbf{C}}_{occ}^{T};\ \mathbf{Q} = \mathbf{S}^{-1} - \mathbf{P};\ \tilde{\mathbf{Q}} = \mathbf{S}^{-1} - \tilde{\mathbf{P}}. \tag{1.67}$$

It is important to remark that the IAO procedure forms a set of orthonormalized (and of minimal size) basis which *exactly* express the MOs (and thus the density) in terms of the resulting IAOs. Regarding to the minimal basis, this procedure make use of the so-called MinAO basis set, which is a manual truncation of the cc-pVTZ basis to a minimal one. In case of requiring the use of effective core potentials (ECP) in the calculation, the core AOs are also excluded from the truncated cc-pVTZ, leading to the so-called MinAO-PP basis. The main limitation of this basis is that fails to be valid for ECPs of different sizes, i.e. smaller or larger core, which is crucial for transition metal based complexes.

The IAO partition showed successful performance and robustness for population analysis, being to date one of the best performing Hilbert-space AIMs.[66–68]

Let us remind that, even the new schemes provides chemically-satisfactory results, Hilbert-space analysis presents one intrinsic drawback; its non-applicability if the MOs are not expanded using atom-centered AOs. In that case, like in periodic systems where they commonly use plane waves as basis, the definition of atomic Hilbert subspaces is not possible. As consequence, the property decomposition in atomic and interatomic contributions is also non-possible. This drawback is not present in the real-space AIM definitions, introduced in the following Section.

1.2.2 Real-space analysis

Alternatively to the Hilbert-space, one can divide the physical three-dimensional (3D) space into atomic regions, commonly defined according to the electron density topology, and then define the atom as its nucleus and the region of the real-space that belongs to it. This type of AIM definitions give name to the real-space atomic partitioning methods, being the most important ones the Quantum Theory of Atoms in Molecules (QTAIM) and the family of schemes known as fuzzy atoms.

In the real-space formalism, a given quantity (F) expressed as a one-electron integral naturally decompose into one-center (atomic) contributions by restricting the integration over the atomic domain, Ω_A, or by introducing an atomic weight function, $w_A(\mathbf{r}_1)$, once

$$\begin{aligned} F_A &= \int_{\Omega_A} f(\mathbf{r}_1)d\mathbf{r}_1 \equiv \int w_A(\mathbf{r}_1)f(\mathbf{r}_1)d\mathbf{r}_1; \\ F &= \sum_{A}^{N_{At}} F_A = \sum_{A}^{N_{At}} \int w_A(\mathbf{r}_1)f(\mathbf{r}_1)d\mathbf{r}_1. \end{aligned} \tag{1.68}$$

The aforementioned weight function measures to which extent the $\mathbf{r}_1$ point contributes to a given atom A, and must satisfy the following two conditions

$$\sum_{A}^{N_{At}} w_A(\mathbf{r}_1) = 1; \;\; w_A(\mathbf{r}_1) \geq 0. \tag{1.69}$$

As illustrative example, by inserting the one-electron density as one-electron function in Eq. 1.68, the electron population of the atom A, N_A, is obtained and the total number of electrons is then recovered by simple summation

$$\begin{aligned} N &= \sum_{A}^{N_{At}} N_A = \sum_{A}^{N_{At}} \int w_A(\mathbf{r}_1)\rho(\mathbf{r}_1)d\mathbf{r}_1; \\ N_A &= \int_{\Omega_A} \rho(\mathbf{r}_1)d\mathbf{r}_1 = \int w_A(\mathbf{r}_1)\rho(\mathbf{r}_1)d\mathbf{r}_1. \end{aligned} \tag{1.70}$$

Similarly, two-electron integrals naturally decompose into both one- and two-center (diatomic) contributions, depending if both electrons lie on the same atomic domain or in different ones, respectively. By means of the weight function, this is achieved by introducing it twice

$$\begin{aligned} F_{AA} &= \int_{\Omega_A}\int_{\Omega_A} f(\mathbf{r}_1,\mathbf{r}_2)d\mathbf{r}_1d\mathbf{r}_2 \equiv \iint w_A(\mathbf{r}_1)w_A(\mathbf{r}_2)f(\mathbf{r}_1,\mathbf{r}_2)d\mathbf{r}_1d\mathbf{r}_2; \\ F_{AB} &= \int_{\Omega_A}\int_{\Omega_B} f(\mathbf{r}_1,\mathbf{r}_2)d\mathbf{r}_1d\mathbf{r}_2 \equiv \iint w_A(\mathbf{r}_1)w_B(\mathbf{r}_2)f(\mathbf{r}_1,\mathbf{r}_2)d\mathbf{r}_1d\mathbf{r}_2, \end{aligned} \tag{1.71}$$

and then the total quantity F is recovered by summation of both atomic and diatomic components

$$F = \sum_{A}^{N_{At}} F_{AA} + \sum_{A}^{N_{At}}\sum_{B}^{N_{At}} F_{AB}. \tag{1.72}$$

For instance, one can insert the single-determinant exchange density expression (Eq. 1.41) into Eq. 1.71, obtaining

$$\lambda_A = \int_{\Omega_A}\int_{\Omega_A} \rho^x(\mathbf{r}_1,\mathbf{r}_2)d\mathbf{r}_1d\mathbf{r}_2 \equiv \iint w_A(\mathbf{r}_1)w_B(\mathbf{r}_2)\rho^x(\mathbf{r}_1,\mathbf{r}_2)d\mathbf{r}_1d\mathbf{r}_2, \tag{1.73}$$

that measures the number of electrons localized on atom A, and the MBO (B_{AB}) generalization in the real-space formalism

$$\begin{aligned} B_{AB} &= \int_{\Omega_A}\int_{\Omega_B} \rho^x(\mathbf{r}_1,\mathbf{r}_2)d\mathbf{r}_1d\mathbf{r}_2 + \int_{\Omega_B}\int_{\Omega_A} \rho^x(\mathbf{r}_1,\mathbf{r}_2)d\mathbf{r}_1d\mathbf{r}_2 \\ &\equiv \iint (w_A(\mathbf{r}_1)w_B(\mathbf{r}_2) + w_B(\mathbf{r}_1)w_A(\mathbf{r}_2))\rho^x(\mathbf{r}_1,\mathbf{r}_2)d\mathbf{r}_1d\mathbf{r}_2, \end{aligned} \tag{1.74}$$

which again quantifies the number of electron pairs *covalently* shared between a pair of atoms A and B. Thus, if the bond of that particular atom pair is governed by electrostatic interactions, i.e. ionically bonded systems, it will not be reflected in the B_{AB} (low) value. In the context of QTAIM (see below), the number of electron pairs localized in an atom A and delocalized between a pair of atoms A and B are known as the localization and delocalization indices (LI and DI), respectively. Contrarily to the MBO, the DI is defined from the exchange-correlation density, expressed from the RDM2 (Eq. 1.31) as

$$\rho^{xc}(\mathbf{r}_1,\mathbf{r}_2) = \frac{1}{2}\left(\rho_1(\mathbf{r}_1;\mathbf{r}_2)\rho_1(\mathbf{r}_2;\mathbf{r}_1) + \rho_1^s(\mathbf{r}_1;\mathbf{r}_2)\rho_1^s(\mathbf{r}_2;\mathbf{r}_1)\right) - \Gamma(\mathbf{r}_1,\mathbf{r}_2), \tag{1.75}$$

decomposing also into one-

$$LI_A = \int_{\Omega_A}\int_{\Omega_A} \rho^{xc}(\mathbf{r}_1,\mathbf{r}_2)d\mathbf{r}_1 d\mathbf{r}_2 \equiv \iint w_A(\mathbf{r}_1)w_A(\mathbf{r}_2)\rho^{xc}(\mathbf{r}_1,\mathbf{r}_2)d\mathbf{r}_1 d\mathbf{r}_2, \tag{1.76}$$

and two-center terms

$$\begin{aligned} DI_{AB} &= \int_{\Omega_A}\int_{\Omega_B} \rho^{xc}(\mathbf{r}_1,\mathbf{r}_2)d\mathbf{r}_1 d\mathbf{r}_2 + \int_{\Omega_B}\int_{\Omega_A} \rho^{xc}(\mathbf{r}_1,\mathbf{r}_2)d\mathbf{r}_1 d\mathbf{r}_2 \\ &\equiv \iint (w_A(\mathbf{r}_1)w_B(\mathbf{r}_2) + w_B(\mathbf{r}_1)w_A(\mathbf{r}_2))\rho^{xc}(\mathbf{r}_1,\mathbf{r}_2)d\mathbf{r}_1 d\mathbf{r}_2. \end{aligned} \tag{1.77}$$

It can be easily seen that the MBO and DI expressions converge in the single-determinant case. For correlated (multi-determinant) wavefunctions their expressions differ, but the obtained valued are used for the same purpose.

Similarly, one can attempt to express the overlap populations in the real-space formalism upon inclusion of the weight function twice

$$N_{AB} = 2\sum_{\mu,\nu}^{N_{AO}} D_{\mu\nu}\int w_A(\mathbf{r}_1)w_B(\mathbf{r}_1)\chi_\nu^*(\mathbf{r}_1)\chi_\mu(\mathbf{r}_1)d\mathbf{r}_1, \tag{1.78}$$

but note that this decomposition is unnatural according to Eq. 1.68 and in case of non-overlapping domains (similarly to Hilbert-space analyses using orthogonal basis), N_{AB} is always zero.

The difference between real-space AIMs arises from how one defines the atomic domains (or atomic weight functions). In the QTAIM framework,[69] the atomic regions and their boundaries are determined from the *zero-flux* surface condition of the gradient of the electron density

$$\nabla\rho(\mathbf{r}_1)\cdot\vec{n}(\mathbf{r}_1) = \vec{0};\ \ \forall\mathbf{r}_1 \in S(\mathbf{r}_1), \tag{1.79}$$

where $\vec{n}(\mathbf{r}_1)$ corresponds to the unit vector perpendicular to zero-flux surface $S(\mathbf{r}_1)$, also known as separatrix. Then, each point of the space solely belongs to a given atom, being the atomic regions non-overlapping. The set of points from a particular atom conforms its atomic domain, Ω_A. In terms of the aforementioned weight function, $w(\mathbf{r}_1) = 1$ if $\mathbf{r}_1$ belongs to the atom and $w(\mathbf{r}_1) = 0$ otherwise. Contrarily, the fuzzy atom schemes allow the atomic domains to overlap, being the $w(\mathbf{r}_1)$ values within the $[0, 1]$ range.

In the fuzzy atom framework, there is a plethora of schemes that differs on how they identify the atomic $w(\mathbf{r}_1)$ functions, including Hirshfeld,[70] Iterative Hirshfeld (I-Hirshfeld),[71,72] Becke,[73] Becke-rho[74] and Topological Fuzzy Voronoi Cells (TFVC),[75] to name a few.

Starting by the Hirshfeld method,[70] the atomic weight function is defined as the ratio between the isolated (reference) atom density, $\rho_A^0(\mathbf{r}_1)$, and the promolecular density, $\sum_A^{N_{At}}\rho_A^0(\mathbf{r}_1)$, typically evaluated using the spherically average densities of the isolated atoms at their ground state, and superposed at the *exactly* same geometry as the actual molecule

$$w_A(\mathbf{r}_1) = \frac{\rho_A^0(\mathbf{r}_1)}{\sum_B^{N_{At}} \rho_B^0(\mathbf{r}_1)}. \tag{1.80}$$

Along the years, the Hirshfeld atomic definition has been applied to evaluate quantities such as partial atomic charges, dipole moments and Fukui functions,[39,40,76] and also to decompose the total HF energy into atomic[77] and also interatomic terms,[46] to name a few. For instance, in 1985 Maslen and Spackman compared the Hirshfeld atomic charges and atomic dipole moments against the, named at that moment, Bader charges for a large set of organic compounds.[39] The authors found that in the H-X case, where X corresponds to a series of functional groups frequently found in organic molecules, the atomic charges correlates ($R^2 = 0.945$) with the electronegativity difference obtained using Pauling's electronegativity scale after exclusion of the fluorinated systems. Almost perfect correlation was also obtained when correlating the atomic dipole molents instead of the atomic charges ($R^2 = 0.939$). Some years later, Rousseau *et al.* studied the basis set dependency of the Hilshfeld atomic charges, obtaining very robust results independently of the basis set used compared to Mulliken and CHELPG, among others.[40] More recently, de Proft *et al.* also extracted atomic charges, dipole moments and Fukui functions using Hirshfeld partition obtaining, for a large set of organic systems, the expected bond polarities but smaller in magnitude compared to other real-space AIMs.[76] As last example, Mandado *et al.* decomposed the HF electronic energy into (only) atomic contributions and found that the correlation between the H-atom electron population and its atomic energies is useful to study the proton acidity.[77]

The main drawback of the Hirshfeld partition is that requires to arbitrarily choose the electronic structure of the isolated fragments. This can highly affect (and influence) the results obtained, being an extreme case that, depending on the isolated atoms electronic structure, the chemical bonding picture is one or another. As plausible solution, Bultinck et a. introduced in 2009 the Iterative Hirshfeld procedure,[72] in which they impose the condition that the density of the isolated atoms must integrate to the *same* atomic population within the actual molecule

$$N_A = \int \rho_A^0(\mathbf{r}_1) d\mathbf{r}_1 = \int w_A(\mathbf{r}_1)\rho(\mathbf{r}_1) d\mathbf{r}_1. \tag{1.81}$$

This condition is fulfilled iteratively by constructing the isolated atomic densities upon interpolation of isolated atom densities evaluated considering different number of electrons as

$$\rho_A^{0,N_A}(\mathbf{r}_1) = (uint(N_A) - N_A)\rho_A^{0,lint(N_A)}(\mathbf{r}_1) - (lint(N_A) - N_A)\rho_A^{0,uint(N_A)}(\mathbf{r}_1), \tag{1.82}$$

where $lint(N_A)$ and $uint(N_A)$ corresponds to the lower and upper integer values of the fractional population of the atom (N_A) *in* the actual molecule. The obtained interpolated isolated atomic densities, Eq. 1.82, at a given step of the iterative procedure are used for building the new promolecular density and, by using it in Eq. 1.80, the new atomic weights. This procedure is repeated until fulfilling (within a numerical threshold) for each atom the condition from Eq. 1.81.

Among the extended list of applications of the Iterative Hishfeld AIM, in 2007 Bultinck and coworkers numerically proved the basis set independence of the I-Hirshfeld atomic charges, together with the independency of the Hirshfeld charges on the promolecule chosen.[78] Later on, in 2009 Van Damme *et al.* showed the remarkably good performance of them, compared to other AIMs, when computing electrostatic potentials.[79] Furthermore, this methodology has been used as base to recently construct more sophisticated Hirshfeld-

based AIMs.[80]

On the other hand, the Becke's scheme relies on the use of the so-called Voronoi polyhedra to evaluate the atomic weights.[73] Considering first a molecular system consisting on only two atoms, the aforementioned Voronoi polyhedra can be mathematically expressed using the two-center coordinate system known as confocal elliptical coordinates (λ, μ, ϕ). Coordinate ϕ corresponds to the angle of the internuclear axis, and λ and μ are defined as

$$\lambda = \frac{r_A + r_B}{R_{AB}};\ \ \mu = \frac{r_A - r_B}{R_{AB}}, \tag{1.83}$$

with ranges

$$0 \leq \phi \leq 2\pi;\ \ 1 \leq \lambda \leq \infty;\ \ -1 \leq \mu_{AB} \leq 1, \tag{1.84}$$

where r_A, r_B and R_{AB} from Eq. 1.83 note the distance between any point in the space and nucleus A and nucleus B, and between the pair of nuclei AB.

The Voronoi polihedron on nucleus A is described by a function, $s(\mu_{AB})$, known as the step function

$$s(\mu_{AB}) = \begin{cases} 1, & -1 \leq \mu_{AB} \leq 0 \\ 0, & 0 < \mu_{AB} \leq 1 \end{cases}. \tag{1.85}$$

By evaluating the step functions for each other atomic center in the system, $B \neq A$, one can construct a "cell function" as

$$P_A(\mathbf{r}_1) = \prod_{B \neq A} s(\mu_{AB}), \tag{1.86}$$

where $P_A(\mathbf{r}_1)$ vanishes if the $\mathbf{r}_1$ point lies outside the Voronoi cell and equals to unity when $\mathbf{r}_1$ lies inside. Then, these functions can be used to calculate the atomic weight functions for a Voronoi polyhedra as

$$w_A(\mathbf{r}_1) = \frac{P_A(\mathbf{r}_1)}{\sum_B^{N_{At}} P_B(\mathbf{r}_1)}. \tag{1.87}$$

Up to this point, the Voronoi polyhedra presents boundaries and conditions analogous to QTAIM, being the atomic domains non-overlapping. To make these boundaries fuzzy, and thus allowing the Voronoi cells to overlap, it is required to substitute the current step function (Eq. 1.85) for the appropriate continuous analog $f(\mu_{AB})$. In his original work, Becke imposed that $f(\mu_{AB})$ must fulfill the following conditions

$$\begin{aligned} &f(-1) = -1;\ \ f(1) = 1; \\ &\frac{df(-1)}{d\mu_{AB}} = \frac{df(1)}{d\mu_{AB}} = 0, \end{aligned} \tag{1.88}$$

obtaining a new step (cutoff) function $s(\mu_{AB})$ as

$$s(\mu_{AB}) = \frac{1}{2}\left(1 - f(\mu_{AB})\right). \tag{1.89}$$

The simplest possible $f(\mu_{AB})$ that satisfy the imposed constrains (Eq. 1.88) is the two-term polynomial

$$p(\mu_{AB}) = \frac{3}{2}\mu_{AB} - \frac{1}{2}\mu_{AB}. \tag{1.90}$$

Polynomial $p(\mu_{AB})$ varies smoothly between the end points -1 and 1, but its sharpness can be controlled upon iteration as

$$f_1(\mu_{AB}) = p(\mu_{AB}), f_2(\mu_{AB}) = p\left[p(\mu_{AB})\right], f_3(\mu_{AB}) = p\left[p\left[p(\mu_{AB})\right]\right], \ldots, \tag{1.91}$$

where the iteration order k is known as stiffness parameter. Illustratively, one can depict the shape of the cutoff function for different values of the stiffness parameter (Figure 1.2), and observe that the larger the k value, the sharper the cutoff function.

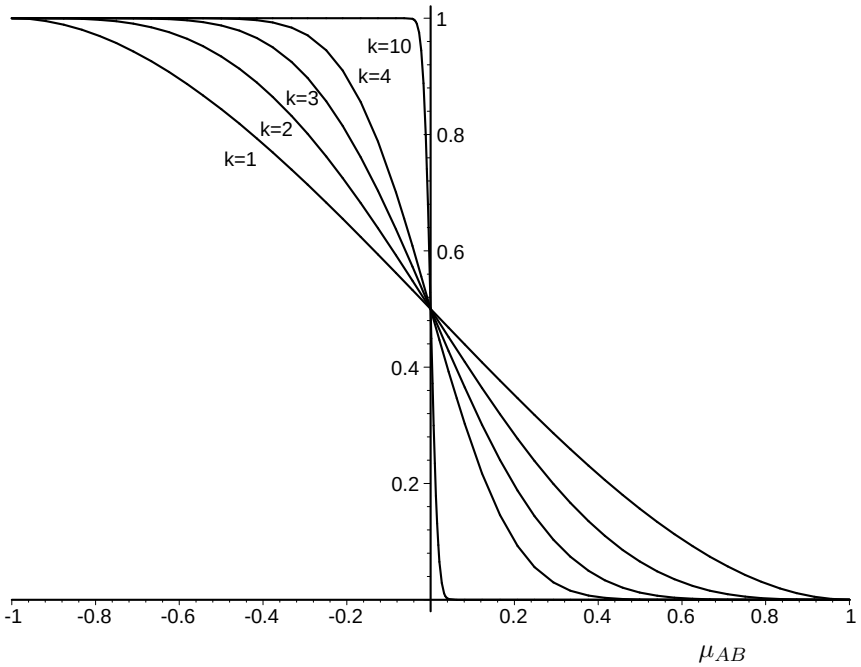

Figure 1.2: Shape of the cutoff function μ_{AB} for different stiffness parameter (k) values, extracted from Ref. 75.

This definition of the Fuzzy Voronoi Cells can lead to unsatisfactory results in heteronuclear systems as does not account for the different atomic sizes and thus the cell faces exactly bisect the internuclear axis between a pair of neighboring atoms. As solution, a shifted cutoff profile can be obtained by using as argument the following transformed coordinate

$$\mu'_{AB} = \mu_{AB} + \alpha_{AB}(1 + \mu_{AB}^2), \tag{1.92}$$

where $-\frac{1}{2} \leq \alpha_{AB} \leq \frac{1}{2}$ in order to ensure that $-1 \leq \mu_{AB} \leq 1$. The α_{AB} parameter allows to control the position of the cell boundary, which in the new coordinates is given by the $\mu'_{AB} = 0$ condition. Then, at the intersection between the cell boundary and the interatomic plane, one has

$$\mu'_{AB} = \frac{r_A - r_B}{r_A + r_B}. \tag{1.93}$$

In Becke's scheme, the r_A/r_B ratio is related with the relative size of atoms A and B, making use of a

reference set of fixed atomic radii R_A^0 and R_B^0, as

$$\frac{r_A}{r_B} = \frac{R_A^0}{R_B^0} = \chi_{AB}, \tag{1.94}$$

thus successfully expanding the atomic definition for heteroatomic systems. Note that while using a set of fixed atomic radii the atoms of the same type will be equally truncated independently of the chemical environment. This is a relevant limitation of the model. As solution, one can use an internal criterion to determine the cell boundaries between every pair of neighboring atoms, establishing thus a strategy to determine a new set of χ_{AB} values which do not depend on a fixed set of atomic radii. In this direction, in 2004 Salvador and Mayer explored using the position of the extremum (typically the minimum) of the electron density along the internuclear axis between every pair of neighboring atoms to locate the cell boundaries.[36] The resulting scheme, termed as Becke-rho, was later introduced by Matito *et al.* in 2007.[74] However, the shifting applied to the cell boundary has a maximum, when the ratio $\chi_{AB} = 1 + \sqrt{2}$, that cannot be surpassed. Then, when the atomic electronegativity or effective radii differences are very large, the position of the boundary will not coincide with the extremum of the density, being an intrinsic limitation of the method. To fully accommodate the criterion behind the original Becke and Becke-rho AIMs, in 2013 Salvador and Ramos-Cordoba introduced an alternative transformation to μ_{AB} (Eq. 1.92)

$$\mu'_{AB} = \frac{1 + \mu_{AB} - \chi_{AB}(1 - \mu_{AB})}{1 + \mu_{AB} + \chi_{AB}(1 - \mu_{AB})}, \tag{1.95}$$

leading to the so-called Topological Fuzzy Voronoi Cells (TFVC) atomic definition.[75] This transformation fulfills that $\mu'_{AB} = \mu_{AB}$ at the limit values $\mu_{AB} = -1$ and $\mu_{AB} = 1$, and also if $\chi_{AB} = 1$. Furthermore, for any value of χ_{AB} the cutoff is monotonic, being applicable to shift the cell boundary to any position along the internuclear axis. In their work, the authors found that by playing with the aforementioned stiffness parameter very similar results to QTAIM can be obtained but at much lower computational cost. In particular, atomic charges and delocalization indices obtained using both TFVC and QTAIM AIMs correlate almost perfectly with $k = 4$ (see Figure 1.3).

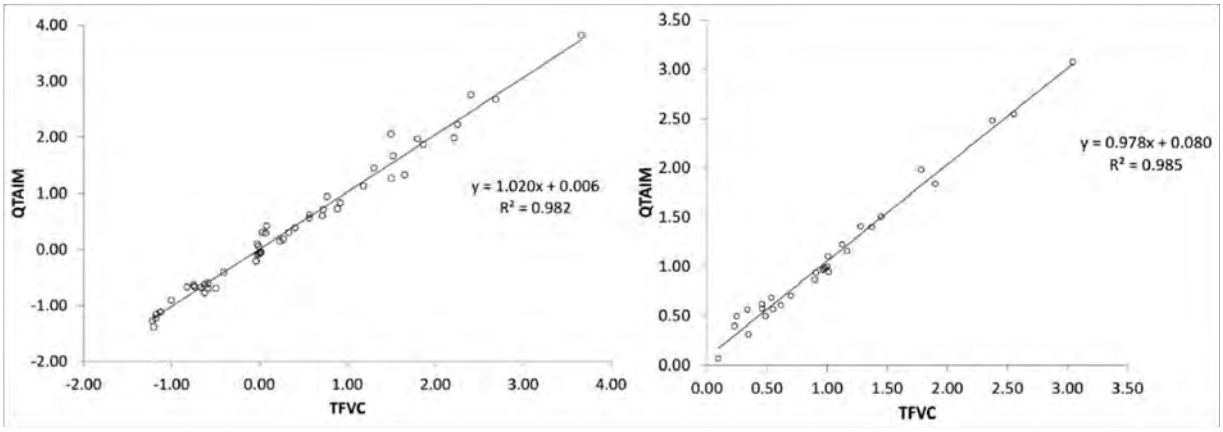

Figure 1.3: Correlation between QTAIM and TFVC ($k = 4$) atomic charges (left) and delocalization indices (right). Figure adapted from Ref. 75.

The TFVC AIM has been applied to decompose a wide range of molecular properties, including the evaluation of atomic charges,[41] delocalization[81] and aromaticity indices,[53,54,82] atomic static polarizabilities,[83] local spin[84,85] and oxidation states,[42,43] to name a few. In most cases, TFVC presented robust and very sim-

ilar results compared to other state-of-the-art atomic partitioning methods such as QTAIM, or sophisticated Hirshfeld-based methods.[41,75] In fact, Martin and coworkers showed for an extensive and representative number of systems (W4-17 benchmark set) that, as already pinpointed by Salvador *et al.*,[75] QTAIM- and TFVC-obtained atomic charges almost perfectly correlate ($R^2 = 0.97$).[41,86] However, the scheme struggles to properly set the boundary between a pair of neighbouring atoms when the interatomic density is very flat. Such scenario is found, for example, in the H-S bond in H_2S, where planar cell boundaries of TFVC versus the curved ones in QTAIM lead to somewhat different numerical results.[75]

The fact that the decomposition of *any* quantity requires the definition of the atom in a molecule means that there are as many analysis methods as AIM definitions. In the case of the population analysis, the atomic populations, and thus the partial atomic charges, are highly sensible to the chosen AIM and, as Fonseca-Guerra *et al.* showed using QTAIM and Mulliken, evaluating them with different AIMs sometimes yields results difficult to reconcile. There are AIMs more sophisticated and robust than anothers, and that two AIMs provide contrarily results *may* be an artifact of one of the AIMs (or not). It is the responsability of the chemist itself to do an unbiased selection of the AIM to use, based on the strong and weak points of each one of them. It has been already pinpointed in the literature, starting from Baker almost 40 years ago,[56] and briefly commented in the current Thesis that the Mulliken and Löwdin decomposed quantities are highly basis set dependent and overcount when diffuse-type functions are included (crucial for anions, transition metal complexes, etc), providing unreliable results. However, they are still extensively used to elucidate the electronic structure of molecular systems due to its simplicity.

1.3 Modern chemical bonding descriptors from first principles

1.3.1 Local spin analysis

The characterization of the local spin distribution in molecular systems such as organic diradicaloids, metallic complexes ferro- or anti-ferromagnetically coupled or systems which present spin-polarized bonds has been matter of interest to better understand the spin-spin interactions and also due to the properties and reactivity they present. Commonly, its computational characterization is performed by means of the spin density, and its decomposition into atoms/fragments. However, spin densities are globally and locally zero for singlet spin-state systems at both closed-shell single-determinant or multireference level. A plausible solution is to make use of broken-symmetry (BS) approaches, but this strategy presents two main drawbacks. First, it is required to find a stable BS solution, which in most of the cases do not exist, and second its use is less appealing than multireference approaches because, contrarily to BS, the later properly describe the multiconfigurational nature of these systems. Alternatively, one can appeal to the computational tools that decompose the total $< S^2 >$ value, namely the local spin analysis (LSA), into both atomic and diatomic components

$$< S^2 > = \sum_A < S^2 >_A + \sum_A \sum_{B \neq A} < S^2 >_{AB} . \tag{1.96}$$

Many different expressions of the local spin, and its decomposition, has been proposed along the years.[87–92] In 2001, Clark and Davidson proposed to define atomic spin operators ($\hat{S}_A$) obtained by projections of the overall spin vector operator,[87] construct spin-squared operators as product of atomic ($\hat{S}_A^2$) and diatomic

operators ($\hat{S}_A\hat{S}_B$) and consider its expectation value as atomic ($< \hat{S}_A^2 >$) and diatomic ($< \hat{S}_A\hat{S}_B >$) components, respectively. However, this definition presents non-zero local-spin values for genuine closed-shell diamagnetic systems, e.g. H_2 at the RHF level of theory. In 2009, Alcoba *et al.* proposed to express for a single-determinant wavefunction the components of $< S^2 >$ in terms of the spin density matrix, being thus the decomposition non-satisfactory for singlet spin-state systems.[88] Later on, Mayer proposed its formulation for correlated wavefunctions based on some physical requirements, paving the way for subsequent decompositions.[89] Mayer stated that (1) all local spins terms, $< S^2 >_A$ and $< S^2 >_{AB}$, must be zero for closed-shell wavefunctions, (2) they should present proper asymptotic behaviour. Hence, upon dissociation the atom/fragment values ($< S^2 >_A$) must lead to the $< S^2 >$ of the isolated atom/fragment and (3) the expressions of $< S^2 >_A$ and $< S^2 >_{AB}$ for a general wavefunction must reduce to the single-determinant ones if applied to a single-determinant wavefunction.

For a general wavefunction, $< S^2 >$ can be expressed from the spinless first- and second-order RDMs as

$$\begin{aligned} < S^2 > = & \frac{3}{4}\int \rho_1(\mathbf{r}_1;\mathbf{r}_1)d\mathbf{r}_1 \\ & - \frac{1}{4}\iint \rho_2(\mathbf{r}_1,\mathbf{r}_2;\mathbf{r}_1,\mathbf{r}_2)d\mathbf{r}_1 d\mathbf{r}_2 - \frac{1}{2}\iint \rho_2(\mathbf{r}_1,\mathbf{r}_2;\mathbf{r}_2,\mathbf{r}_1)d\mathbf{r}_1 d\mathbf{r}_2, \end{aligned} \tag{1.97}$$

considering that they are normalized to N and $N(N-1)$, respectively. By using the expressions of the RDM2 and the effective number of unpaired electrons function (Eqs. 1.33 and 1.25, respectively), one can rewrite Eq. 1.97 as

$$< S^2 > = \frac{3}{8}\int u(\mathbf{r}_1)d\mathbf{r}_1 - \frac{1}{4}\iint \Lambda(\mathbf{r}_1,\mathbf{r}_2)d\mathbf{r}_1 d\mathbf{r}_2 - \frac{1}{2}\iint \Lambda(\mathbf{r}_1,\mathbf{r}_2;\mathbf{r}_2,\mathbf{r}_1)d\mathbf{r}_1 d\mathbf{r}_2, \tag{1.98}$$

where $\Lambda(\mathbf{r}_1,\mathbf{r}_2) \equiv \Lambda(\mathbf{r}_1,\mathbf{r}_2;\mathbf{r}_1,\mathbf{r}_2)$.

In 2011 Alcoba *et al.* proposed a similar general expression for $< S^2 >$,[91] being

$$< S^2 > = \frac{1}{2}\int u(\mathbf{r}_1)d\mathbf{r}_1 - \frac{1}{2}\iint \Lambda(\mathbf{r}_1,\mathbf{r}_2;\mathbf{r}_2,\mathbf{r}_1)d\mathbf{r}_1 d\mathbf{r}_2. \tag{1.99}$$

Both Eqs. 1.98 and 1.99 can be generally expressed by including a parameter a as

$$< S^2 > = a\int u(\mathbf{r}_1)d\mathbf{r}_1 - (1-2a)\iint \Lambda(\mathbf{r}_1,\mathbf{r}_2)d\mathbf{r}_1 d\mathbf{r}_2 - \frac{1}{2}\iint \Lambda(\mathbf{r}_1,\mathbf{r}_2;\mathbf{r}_2,\mathbf{r}_1)d\mathbf{r}_1 d\mathbf{r}_2, \tag{1.100}$$

reducing to Alcoba's expression for $a = 1/2$ and to Eq. 1.98 when $a = 3/8$.

Independently of the selected a parameter, in the real-space the $< S^2 >$ expression (Eq. 1.100) decompose into both one- and two-center terms by using the atomic weight functions (Eqs. 1.68 and 1.71) as

$$< S^2 >_A = a \int w_A(\mathbf{r}_1) u(\mathbf{r}_1) d\mathbf{r}_1 - (1-2a) \iint w_A(\mathbf{r}_1) w_A(\mathbf{r}_2) \Lambda(\mathbf{r}_1, \mathbf{r}_2) d\mathbf{r}_1 d\mathbf{r}_2 - \frac{1}{2} \iint w_A(\mathbf{r}_1) w_A(\mathbf{r}_2) \Lambda(\mathbf{r}_1, \mathbf{r}_2; \mathbf{r}_2, \mathbf{r}_1) d\mathbf{r}_1 d\mathbf{r}_2, \tag{1.101}$$

and

$$< S^2 >_{AB} = -(1-2a) \iint w_A(\mathbf{r}_1) w_B(\mathbf{r}_2) \Lambda(\mathbf{r}_1, \mathbf{r}_2) d\mathbf{r}_1 d\mathbf{r}_2 - \frac{1}{2} \iint w_A(\mathbf{r}_1) w_B(\mathbf{r}_2) \Lambda(\mathbf{r}_1, \mathbf{r}_2; \mathbf{r}_2, \mathbf{r}_1) d\mathbf{r}_1 d\mathbf{r}_2. \tag{1.102}$$

The most satisfactory decomposition of $< S^2 >$ is rooted to based on what one selects the value of the a parameter. In 2012, Ramos-Cordoba *et al.* proposed to make use a value of $a = 3/4$ based on the behaviour of Eqs. 1.100 and 1.101 for a one-electron system.[92] In particular, the authors showed that in the single-electron case most of the terms from Eq. 1.100 disappear, being reduced to

$$< S^2 >= a \int \rho(\mathbf{r}_1) d\mathbf{r}_1, \tag{1.103}$$

as $u(\mathbf{r}_1) = \rho(\mathbf{r}_1)$ due to the idempotency of the RDM1. Then, and considering that a single spin (doublet) should provide a total $< S^2 >$ value of 3/4, the selection of a seems straightforward ($a = 3/4$). This definition of the local spin, together with its decomposition, showed promising results.[92] In their original work, the authors evaluated using different a values a set of representative molecular systems and the dissociation curves of several diatomic molecules, obtaining for $a = 3/4$ the correct behaviour upon dissociation and, compared to other methods, very low $< S_A^2 >$ and $< S_{AB}^2 >$ values for diamagnetic systems at the correlated level. Later on, Ramos-Cordoba *et al.* applied it to measure how much the bond in main-group diatomic molecules deviates from a perfect covalent bond.[15] The authors showed that the C_2 system in its ground state present $< S^2 >_C$ values of 0.81, higher than the value of 0.75 expected for a perfectly localized unpaired spin, being thus categorized as diradical. The same year Ponec *et al.* shed light into the chemical bonding picture of a model copper-sulfur complex present in multiple enzymes, $[Cu_3S_2]^{3+}$, finding significant local spin on both Cu and S centers but almost negligible diatomic terms, concluding thus that the Cu–S bonding is not caused by the antiferromagnetic coupling of unpaired electrons.[93] More recently, Salvador *et al.* showed its usefulness to characterize the $NaBH_3^-$ system, which present diradical(oid) character between spins antiferromagnetically coupled located on bonded atoms. The resulting chemical bonding scenario lead to a new type of bond, namely the spin-polarized bond.[94] Many applications of the LSA are present in the literature, showing its usefulness in the characterization of unpaired spins and its coupling from multideterminant wavefunctions, i.e. characterization of di- and poli-radical character in molecular systems,[84,85] the definition of new constrains for the cumulant matrix[95] to develop new natural orbital functionals (NOF) and for the development of indicators of dynamic and non-dynamic electron correlation,[96] among others. However, in 2021 Pendas *et al.* showed their disagreement in using a one-electron system to fix conditions for the expression of the $< S^2 >$ decomposition.[97,98] The autors made use of the electron distribution functions (EDF) to evaluate the local spins, reducing to Davidson's decomposition.

For Thesis purposes, let us illustrate the expected behaviour of the local spin decomposition when de-

composing the total $< S^2 >$ of a collinear system consisting on three fragments (Figure 1.4). In the singlet spin-state case, and having one electron perfectly localized on each ligand (L), one expects a local spin value of $< S^2 >_E = 0$ for the central moiety (E) and $< S^2 >_L = 3/4$ for each ligand. The nature of the spin-coupling between unpaired electrons is captured by the sign of the inter-fragment contribution, being negative and positive for anti- and ferro-magnetic couplings, respectively. The value of this term will depend on the total $< S^2 >$ value being $< S^2 >_{L1-L2} = -3/4$ in this particular case. The same scenario but in the triplet spin-state leads to the same fragment local spin values with an inter-fragment contribution of $< S^2 >_{L1-L2} = 1/4$, indicating the parallel alignment of the spins (see Figure 1.4b).

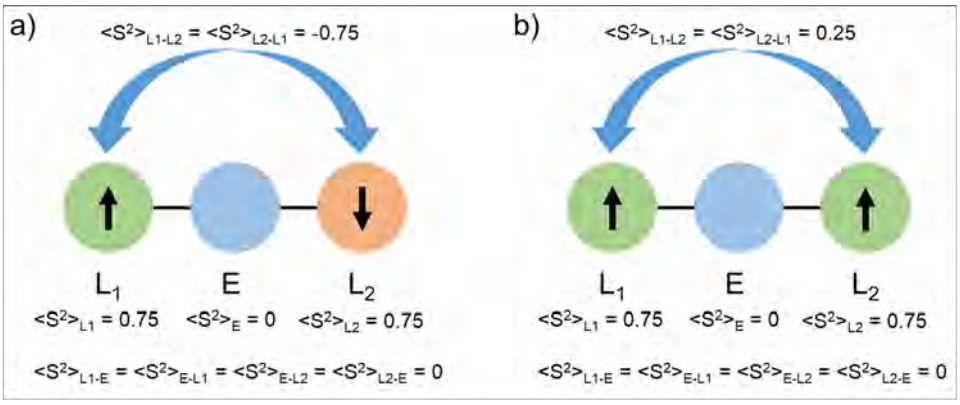

Figure 1.4: Schematic representation of the E-L_2 system local spin decomposition in an ideal singlet (a) and triplet (b) state diradical(oid)s with unpaired spins localized on the L fragments.

The values of the local spin, both intra- and inter-fragment (or atomic), obtained with the Ramos-Cordoba[92] and Pendas[97] definitions are clearly different in *ideal* cases, and thus may slightly differ numerically for systems with less pronounced radical (or poliradical) character. In our opinion both schemes are equally plausible to be applied to chemically-relevant (and more complex) molecular system, but a proper comparison between them has not been realized yet.

1.3.2 Effective atomic/fragment orbitals

Within the computational chemistry community, the use of the chemical notion that atoms forms molecules with their s-, p- and d-type orbitals of the appropriate symmetry is widely extended to understand the chemical bonding picture of molecular systems. However, these traditional descriptions are difficult to acquire by evaluating the shape of the molecular orbitals from a quantum mechanical calculation. One can apply orbital localization *a posteriori* and evaluate the bonding, non-bonding, and symmetry of the resulting localized molecular orbitals (LMO). However, even being more localized that the original MOs, they are still *molecular*.

In 1995, Mayer introduced a formalism that re-obtains the traditional AO-based description of the chemical bond from *ab initio* calculations, producing distorted but with AO shape orbitals, namely the effective atomic orbitals (eff-AO).[99,100] The eff-AOs are constructed for each atom upon diagonalization of its corresponding atom's net density. Instead of atoms, one can define fragments within the system, i.e. the metal center and each one of its ligands in case of a transition metal system, obtaining the so-called effective fragment orbitals (EFO). The procedure for obtaining both is *exactly* the same, and for Thesis purposes we will proceed tagging them as EFOs. In the real-space formalism, Q_{ij}^A is obtained using the intra-fragment part of the MOs, $\phi_i^A = w_A(\mathbf{r})\phi_i(\mathbf{r})$, as

$$Q_{ij}^{A} = \int \phi_i^{*,A}(\mathbf{r})\phi_j^{A}(\mathbf{r})d\mathbf{r} = \int w_A(\mathbf{r})w_A(\mathbf{r})\phi_i^{*}(\mathbf{r})\phi_j(\mathbf{r})d\mathbf{r}, \tag{1.104}$$

and the diagonalization of $\mathbf{Q}^A$ is performed by unitary matrix U^A transformation

$$\mathbf{U}^A\mathbf{Q}^A\mathbf{U}^A = diag\{\lambda_\mu^A\}, \tag{1.105}$$

where λ_μ^A is a diagonal matrix that contains the occupancies of the resulting EFOs. Let us remind that the fragment net density does not integrate to an integer number of electrons, being thus the EFO occupancies fractionary and within the [0, 2] range. The EFOs, $\varphi_\mu^{EFO,A}(\mathbf{r})$, are then constructed by linear combination of the intra-fragment parts of the MOs

$$\varphi_\mu^{EFO,A}(\mathbf{r}) = \frac{1}{\sqrt{\lambda_\mu^A}}\sum_{i=1}^{n_A} U_{i,\mu}^A\phi_i^A(\mathbf{r}), \tag{1.106}$$

being n_A the number of EFOs with occupancy values larger than zero (usually, the zero is given by a numerical threshold). The EFOs can be seen as the fragment natural hybrid orbitals within the molecular system that originate from the one-electron density. In case of the fragment being an atom, their shape recover the notions of core, valence and virtual atomic orbitals with the corresponding symmetry. If the fragment is a ligand, they resemble the isolated ligand MOs. The core and lone pairs present occupancy values close to 2 while the EFOs involved in the bonding between fragments suffer an occupancy decrease due to electron sharing. Interestingly, most of the EFOs have occupancies very close to zero, being thus irrelevant for the chemical bonding analysis, and independently of the size of the basis set used in the calculation. Thus, the EFOs can be considered an **effective** minimal basis, being very appealing for the construction of, for example, reference minimal basis sets.[100,101]

In the open-shell case, the EFOs are constructed for each spin case, independently. From the $\sigma = \alpha, \beta$ parts of the one-electron density, one first obtains

$$Q_{ij}^{A,\sigma} = \int \phi_i^{*,A,\sigma}(\mathbf{r})\phi_j^{\sigma,A}(\mathbf{r})d\mathbf{r} = \int w_A(\mathbf{r})w_A(\mathbf{r})\phi_i^{*,\sigma}(\mathbf{r})\phi_j^{\sigma}(\mathbf{r})d\mathbf{r}, \tag{1.107}$$

then perform its diagonalization

$$\mathbf{U}^A\mathbf{Q}^{A,\sigma}\mathbf{U}^A = diag\{\lambda_\mu^{A,\sigma}\}, \tag{1.108}$$

and finally reconstruct the spin-separated EFOs

$$\varphi_\mu^{EFO,A,\sigma}(\mathbf{r}) = \frac{1}{\sqrt{\lambda_\mu^{A,\sigma}}}\sum_{i=1}^{n_A} U_{i,\mu}^A\phi_i^{A,\sigma}(\mathbf{r}). \tag{1.109}$$

Here, the occupancy values obtained, $\lambda_\mu^{A,\sigma}$, are within the [0, 1] range.

Interestingly, in 2013 Mayer demonstrated that the Hilbert-space analysis performed in the EFO basis reproduces *exactly* the real-space obtained results.[102] In particular, the author showed that the Mulliken bond orders, and the net and overlap atomic populations, extracted in the EFO basis coincide with the corresponding bond order, and net and overlap populations, from real-space.

1.4 Oxidation states from wavefunction analysis

The oxidation state (OS) is one of the most fundamental chemical concepts due to its use for the rationalization, characterization, categorization and prediction of the properties and reactivity of inorganic compounds.[103–105] It reaches back to the early days of chemistry where the "oxydationsstufe" was introduced to rationalize the products obtained after reacting with oxygen. The electron-gathering tendency of oxygen is represented by its most common OS of -2 in compounds with ionic interactions, which is one of the generally accepted counting rules to assign OSs in Oxygen-containing systems. Even it is universally taught and used, a well-established definition for the OS concept is still lacking. Informally, the OS of an element (typically a metal) is the net charge that results from an ionic division of the electrons and electron pairs between the selected element and the rest of the molecule. For years, its assignment has been performed by applying a set of "agreed upon" rules, but without having an explicit definition of the concept.

After thorough revision of the OS concept lead by Karen, in 2014 a new generic definition of OS entered into the IUPAC's Gold Book, reading as *the atom's charge after ionic approximation of its heteronuclear bonds*, while homonuclear bonds must be always equally divided, independently of the chemical environment.[104] Together with the new definition, the authors also provided an algorithm to assign OSs, namely IUPAC's ionic approximation (IA).[105] The algorithm proceeds as follows: One starts by establishing the appropriate Lewis structure of the selected molecule to assign the OSs. Then, the electron pair from each bond between a pair of bonded atoms is heterolytically assigned to the more electronegative one, according to Allen's electronegativity scale.[106] Finally, as one knows the number of electrons assigned to each atom, simple substraction to the corresponding atomic numbers gives the OSs. For illustrative purposes, we depicted in Figure 1.5 the OS assignment according to IUPAC's IA for some selected (and trivial) systems.

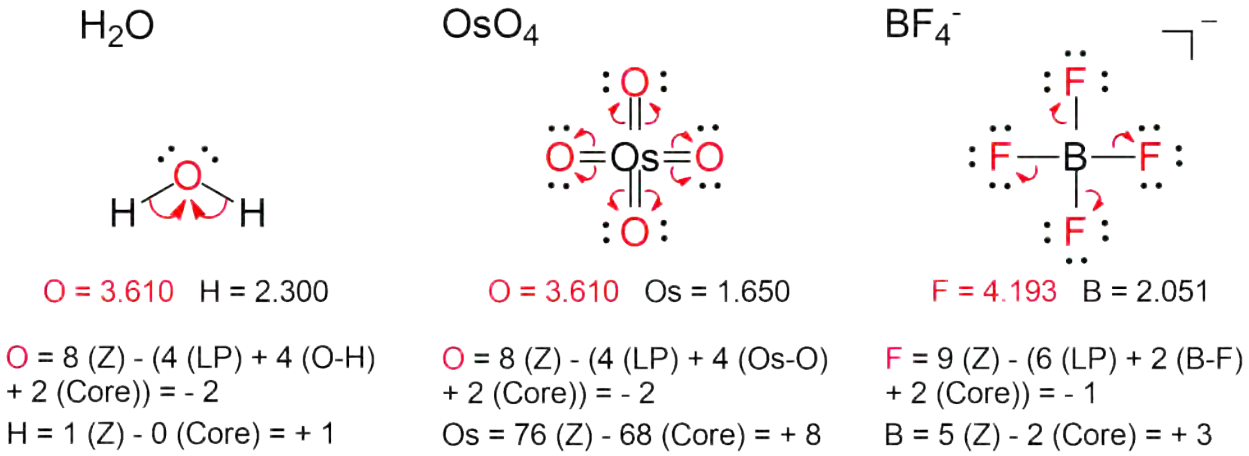

Figure 1.5: Example of application of the IUPAC IA for the H_2O, OsO_4 and BF_4^- systems. LP = lone pair and Core = Core electrons.

The new OSs definition is a large improvement compared to the previous set of rules and the rather simple recipe to assign them works generally well. For this reason, it should be used as the first resort in assigning the OSs of new compounds of interest. However, several authors already exposed some limitations.[42,107,108] One example is the case of the π-adducted systems. In 2018, Postils *et al.* showed that in π-adducts the spin state of the π-system is who determines its formal charge, and as consequence the OS of the transition metal.[42] For instance, the cycloheptatryenil (C_7H_7) moiety in the singlet spin-state fulfills the Hückel aromaticity rule when it is found on the +1 or -3 OSs, but the -1 OS is also plausible if it is a local triplet as

fulfills Baird's rule. Another example is the transition metal carbenes case, where the carbon atom from the carbene unit exhibits formally a double bond with the metal center. Due to electronegativity differences, the four electrons from both the σ- and π-type M-C interaction are assigned to C, leading to a formally -2 carbene moiety. Hence, all transition metal-based carbenes are classified as Schrock-type.[109] Alternative assignments, and thus other types of carbenes,[110] can not be reconciled using the IUPAC winner-takes-it-all rule. For instance, the Fischer-type carbenes presents a neutral carbene unit, requiring to consider the σ-type bond polarized towards the carbon and the π-type to the metal center, giving two electrons to each one of them.[111] This view requires approaches beyond IUPAC's IA. As last example we include the systems containing nitrosyl (NO) as ligand. The bonding of the nitrosyl to a transition metal relies on three different interactions: one formally σ-type donor bond from the ligand to the metal M $\leftarrow$ NO^+ and two M-π^*(NO) bonds with character that can vary between two limiting scenarios: M $\leftarrow$ NO^- and M $\rightarrow$ NO^+.[108] According to the ionic approximation, the electron pair from the first interaction is assigned to the NO moiety, and the two pairs from the other two M-π^*(NO) interactions can not be unambiguously assigned due to its high covalency. Moreover, according to IUPAC's algorithm the NO ligand will never present the 0 OS.

The majority of the ambiguities and caveats present in the IUPAC's scheme are originated by the inability of Allen's (or any other) atomic electronegativity scale to account for the different chemical environment of atoms of the same type within the molecule. A plausible solution is the definition of atom-types, similarly to the classical force fields for molecular dynamics but with electronegativity values. However, the complexity of the algorithm would rapidly increase, diminishing its practical utility. From our point of view, the OS must be connected to the electron distribution around the atoms, being computational chemistry the natural candidate to elucidate OSs, at least for the non-trivial cases. Electronic structure calculations provides an accurate description of the electron density, offering an ideal starting point for probing the borderline cases. Nowadays, there is still the misconception that partial atomic charges from population analysis are a non-integer form of the OS. Vivid discussions in the literature on the basis of partial atomic charges or atomic spin populations computed one way or another can still be found.[112–115] An illustrative example is the series of iron-based compounds compiled in Table 1.2.[43,116] Focusing in the extreme cases, the $[Fe(PyTACN)(OH)_2]^+$ system presents larger partial charge ($q_{Fe} = +1.68$) of the iron center at its +3 OS than for $[Fe(PyTACN)O(OH)]^{2+}$ ($q_{Fe} = +1.50$), where the OS is formally +5. For these systems, the partial atomic charges do not even correlate with the OSs, and the atomic spin densities might be useful as far as the system is not singlet or presents values very close between two local spin-states, e.g. a doublet system with $\rho^s_{TM} \approx 0.5$. Thus, there is particular interest in going beyond the simple, but clearly unsatisfactory, use of partial atomic charges or spin densities to extract OSs from quantum mechanical calculations. Let us remark that, even we focus on molecular systems, the same issue exists for OS assignments in solid state materials.[115,117–119]

Table 1.2: Iron partial charges (q_{Fe}) and spin populations (ρ^s_{Fe}) from a series of [Fe(PyTACN)] complexes obtained using the TFVC atomic definition. PyTACN = 1-(2'-pyridylmethyl)-4,7-dimethyl-1,4,7-triazacyclononane. Results extracted from Ref. 43.

System	OS	q_{Fe}	ρ^s_{Fe}	ρ^s_{Fe} (ideal)
$[Fe(PyTACN)(H_2O)_2]^{2+}$	+2	+1.28	-	-
$[Fe(PyTACN)(H_2O)(OH)]^{+}$	+2	+1.24	-	-
$[Fe(PyTACN)(OH)_2]^{+}$	+3	+1.68	4.10	5
$[Fe(PyTACN)(OH)_2]^{2+}$	+4	+1.51	1.88	2
$[Fe(PyTACN)O(H_2O)]^{2+}$	+4	+1.45	1.30	2
$[Fe(PyTACN)O(OH)]^{+}$	+4	+1.52	3.14	4
$[Fe(PyTACN)O(OH)]^{2+}$	+5	+1.50	2.10	3

Along the years, several research groups have been developing density-based approaches for OSs purposes based on assigning each electron pair (or individual electrons in case of open-shell systems/wavefunctions) to one atom or ligand within the system based on some strategy that generalizes simple counting approaches such as the IUPAC definition. Alternatively, one may attempt to assign OSs based on the fragment electronic structure which minimizes a selected energetic criterion. Focusing on the density-based methods, some schemes rely on the use of LMOs.[120–122] The orbital localization procedure is not unique as, for single determinant wavefunctions, one can perform unitary transformations to the occupied MOs and obtain different LMOs, according to some criterion, without changing neither the wavefuntion nor the energy

$$\phi_n^{loc} = \sum_i^{nocc} U_{in}\phi_i. \tag{1.110}$$

This transformation usually involves the maximization or minimization of the expectation value of the specific of each method localization operator $\hat{\mathbf{L}}$ as

$$< \hat{L} >=< \phi_i|\hat{\mathbf{L}}|\phi_i > . \tag{1.111}$$

In the case of Pipek-Mezey (PM),[123] one minimizes the spread functional Ω, which is evaluated as

$$\Omega = \sum_n^{nocc}[< \phi_n^{loc}|r^2|\phi_n^{loc} > - < \phi_n^{loc}|r|\phi_n^{loc} >^2]. \tag{1.112}$$

Other localization schemes exist, including Foster-Boys (FB),[124,125] Edminston-Ruedenberg (ER)[126] and more recent improved formulations produce LMOs by minimizing some atomic spread functional.[66,127,128] A different strategy is used to obtain the so-called natural bond orbitals (NBO), based on sequentially finding the one- and two-center LMOs which most closely represent the Lewis structure of the system.[129] Differently to the rest, the NBOs are not strictly doubly-occupied (i.e., do not span the occupied space) but the (exact) double-occupancy can be restored, leading to the natural localized molecular orbitals (NLMOs).[130] If the system is properly described by a single Lewis structure, one expects LMOs of three types: core and fully atomic LMOs, bonding orbitals shared (not equally, depending on their electronegativity difference and the chemical environment) between a pair of atoms and nonbonding orbitals completely localized on the atoms (e.g. lone pairs). More complex bonding patterns can be encountered, like delocalized molecular orbitals shared between more than two atoms, being the task to assign the electrons from a LMO to an atomic center/fragment complicated without coupling the orbital localization to another technique. Furthermore, the arbitrary selection of the orbital localization procedure might affect the quality of orbitals obtained and thus the resulting OSs. For these reasons, in 2009 Thom *et al.* proposed to combine orbital localization

with atomic population analysis to extract the OSs of transition metal complexes, leading to the so-called localized orbitals bonding analysis (LOBA) scheme.[120] In the LOBA scheme, one first localized the occupied MOs using the desired localization procedure. Then, atomic populations are evaluated for each LMO, assigning the number of electrons from the LMO to the metal center if its population surpasses a given threshold. After evaluating a battery of systems, the authors concluded that the threshold that better suit is 60% by coupling Pipek-Mezey orbital localization with Löwdin population analysis. Thus, if the atomic population from a given LMO of the metal center surpasses the 60%, the metal keeps its electrons, if not the electrons are formally assigned to the "rest" of the system. If one desires to assign fragment (ligand) oxidation states, it is required to evaluate the shape of the LMOs and their associated atomic populations. To use this method there are some arbritrary choices that one must perform, i.e. selection of localization procedure and population analysis schemes. For this reason, together with that a rigid threshold for the electron assignment is considered, it is recommended to check the important (bonding) localized molecular orbitals to ensure both the quality of localization and of the electron assignment. The LOBA scheme represents a nice computational mapping of IUPAC's algorithm of assigning bonds, and even proved to be robust few use has been made of it. To name a few of its applications, in 2012 Sundstrom *et al.* employed the LOBA to analize the Molybdenum OS, and to assess to which extend the Mo electrons are delocalized, throughout the catalytic cycle of hydrogen formation from water by means of a Molybdenum-Oxo electrocatalyst.[131] Some years later, Jurss *et al.* designed and characterized a Co-based compound with a ligand with non-innocence character in multielectron processes.[132] In 2016, Panetier *et al.* employed LOBA to probe the Co OS in a cobalt-bis(diaryldithiolene)-catalyzed proton reduction in non-aqueous media,[133] and more recently, Van der Mynsbrugge *et al.* characterized the OS of the Pd ions absorbed inside a Pd/CHA-type zeolite depending on how the Pd coordinates to the zeolite walls.[134]

In 2011, Sit *et al.* developed another strategy to assign OSs using maximally localized Wannier functions (MLWF) as LOs in the framework of plane-waves, and its corresponding centroids (Wannier centers).[121] In their work, the authors make use of the centroids position to assign the electron pair of the LMO to the closest atom. As the MLWF (plane-waves) reduce to the FB localized molecular orbitals (atom-centered basis sets), atom-centered basis sets can be used. This motivated Vidossich *et al.* in 2014 to apply the same strategy for molecular systems, but relying on the PM localized molecular orbitals as allow for σ and π separation.[122] The use of centroids to assign electrons is very appealing due to its simplicity and they can be used for both molecular systems or solid state. Furthermore, by following the trajectory of the centroids along a chemical reaction one recovers the curly arrow picture of Robinson,[135] but from quantum-mechanical calculations. Its application for assigning OSs has not been fully tested yet, and many problems may arise when assigning the electrons from assigning LMOs electrons to the closest atom if the atom sizes are very different.

In 2015, Ramos-cordoba *et al.* introduced an alternative and straightforward methodology to derive OSs of atoms and/or molecular fragments (ligands) from the analysis of the first-order density matrix.[43] The scheme, named effective oxidation states (EOS) analysis, is applicable in equal footing to single- and multi-determinant wavefunctions. EOS relies on the occupancies of the already introduced Mayer EFOs and aims to provide the most appropriate integer electronic configuration of the atoms within the molecule.[100,136] In EOS, one first constructs a set of EFOs for each fragment defined and sort them by decreasing occupancy number independently of the originating fragment. Then, individual electron (or pairs in closed-shell systems) are assigned, following the *aufbau* principle, to the hybrids with highest occupancy until reaching the total number of electrons. This procedure leads to an effective configuration of the atoms/fragments defined

within the molecule and simple substraction of the assigned fragment electrons from the sum of nuclear charges directly determines its corresponding OS. As there are more EFOs than electrons to assign, the last occupied (LO) and first unoccupied (FU) EFOs (belonging to different fragments) make up the frontier EFOs. From their corresponding occupancies, one can define a reliability index, $R\,(\%)$, that quantifies how close the actual electron distribution is to the formal ionic picture given by the OS

$$R\,(\%) = 100\; min(1, max(0, \lambda^{\sigma}_{LO} - \lambda^{\sigma}_{FU} + 0.5)). \tag{1.113}$$

From its definition (Eq. 1.113), if the occupancy difference between frontier EFOs exceeds half electron (one electron in the closed-shell case) the assignment is considered undisputable and $R\,(\%) = 100$. The worst-case scenario is when two (or more) frontier EFOs from different fragments are pseudodegenerated (in occupancy). In this situation, there are two (or more) different and equally plausible OS distributions with $R\,(\%) = 50$ and the algorithm covalently assign the remaining electrons (homolitic splitting of the electrons) between the involved EFOs. This pseudodegeneracy is controlled by a numerical threshold, being $5 \cdot 10^{-3}$ the default value. However, and similarly to the LOBA scheme, in closed-call scenarios it is highly recommended to evaluate the shape and the occupancies of the EFOs to not only assign the electrons but also to enlight the chemical bonding picture of the system.

To date, the EOS scheme is the one (if not the only) methodology capable to assign OSs from both single-determinant and multireference wavefunctions, but presents some conceptual problems when dealing with spin-polarization at the correlated level. To enlight them, in Figure 1.6 we represented the EOS behaviour for a diradical molecular system (AB) constituting of two non-symmetric fragments (A and B) in its singlet spin-state using restricted single-determinant, unrestricted broken-symmetry and correlated (CASSCF) wavefunctions.

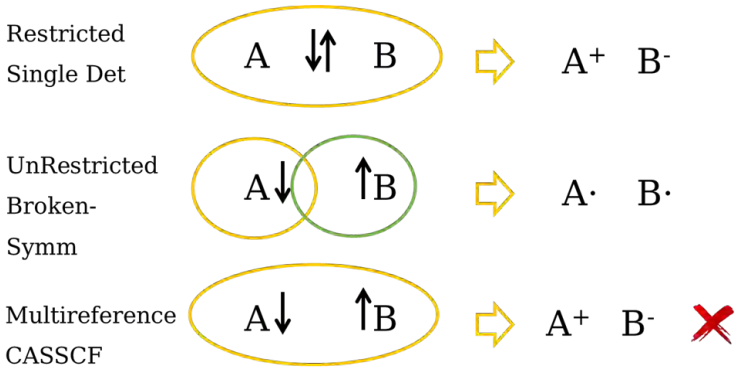

Figure 1.6: EOS assignment for a singlet diradical(oid) system consisting on two fragments depending on the wavefunction nature: (a) restricted single-determinant, (b) unrestricted broken-symmetry and (c) multireference CASSCF wavefunctions.

In the restricted single-determinant case (Figure 1.6a), the electron pair which describes the A-B bonding interaction is be entirely assigned to the one EFO from fragment A or another from fragment B that presents the larger occupancy. Thus, the resulting chemical bonding picture from EOS is or either $A^{+}\;B^{-}$ or $A^{-}\;B^{+}$. The unique scenario that leads into the $A\cdot\;\;\cdot B$ picture is if the frontier EFOs pseudodegenerated, being very rare if fragment A and B are non-symmetric. Instead, in the broken-symmetry case (Figure 1.6b), the $A\cdot\;\;\cdot B$ picture is naturally recovered as the α and β electrons are assigned independently. However, the broken-symmetry wavefunctions are not very appealing for the aforementioned reasons and also due to spin-

contamination. Finally, the most appropriate wavefunction is the multireference one (CASSCF for example, Figure 1.6c), but faces the same scenario than the restricted single-determinant case as electrons are treated by pairs. Thus, EOS cannot properly characterize non-symmetric singlet spin-state diradical(oid)s when using the wavefunction that describes them best (correlated).

1.5 Energy decomposition schemes

1.5.1 Energy decomposition analysis

The accurate evaluation of the total energy of a molecular system is one of the most important challenges in quantum chemistry. However, the value of the energy itself provides little immediate chemical bonding information. To extract this information from the energy one can make use of computational tools which operate on the energetics of the bond/interaction formation, in particular the schemes which decompose the molecular/formation energy into chemically meaningful terms. One of the most typical energy decomposition schemes is the so-called Energy Decomposition Analysis (EDA) developed by Ziegler and Rauk [137,138] as extension of the pioneering work of Kitaura and Morokuma. [139]

Generally, the energy of formation of a molecular system AB from the isolated fragments A and B in their ground states, also known as stabilization energy, reads as

$$\Delta E_{Stab} = E(AB^{AB}) - (E(A^{A}) + E(B^{B})), \tag{1.114}$$

where $E(X^{Y})$ corresponds to the energy of the state X at the optimized geometry of Y and basis set superposition error (BSSE) correction has not been included.

In EDA, the stabilization energy from Eq. 1.114 is further decomposed into the so-called interaction (ΔE_{Int}) and preparation (ΔE_{Prep}) energy terms, defined as

$$\begin{aligned} \Delta E_{Int} &= E(AB^{AB}) - (E(A^{0,AB}) + E(B^{0,AB})) = -D_e; \\ \Delta E_{Prep} &= E(A^{0,AB}) + E(B^{0,AB}) - (E(A^{A}) + E(B^{B})). \end{aligned} \tag{1.115}$$

Here, $E(A^{0,AB})$ corresponds to the energy of fragment A with the A^0 electronic configuration evaluated at the optimized geometry of the system AB. Let us remark that A^0 does not necessarily corresponds to the ground state electronic configuration of the isolated fragment. According to Eq. 1.115, ΔE_{Int} is the interaction between the unrelaxed fragments A and B while forming system AB. This term will be negative/attractive if the interaction between fragments is favourable and its value changed of sign give name to the dissociation energy (D_e). Regarding to ΔE_{Prep}, it contains both the geometrical distortion of the fragments upon formation of system AB, and the energy to promote the fragment A and B electronic ground-states to the selected A^0 and B^0, respectively. By definition, the preparation energy will always be positive as $E(A^{A})$ and $E(B^{B})$ are ground state energies both electronically and geometrically.

The interaction energy can be further decomposed by introducing additional intermediate states and pseudostates constructed at the optimized geometry of system AB. In classical EDA, it decomposes into classical electrostatics (ΔE_{Elec}), Pauli repulsion (ΔE_{Pauli}) and orbital interaction (ΔE_{Orbint})

$$\Delta E_{Int} = \Delta E_{Elec} + \Delta E_{Pauli} + \Delta E_{Orbint}. \tag{1.116}$$

In detail, first one constructs a pseudostate based on the superposition of the undeformed (frozen) densities from the fragments in the A^0 and B^0 states at the AB geometry, namely $A^{0,AB} \cup B^{0,AB}$, with associate energy $E(A^{0,AB} \cup B^{0,AB})$. The energy difference between the created pseudostate, tagged as such because it does not have a well-defined antisymmetric wavefunction associated to it, and the energies of the deformed fragments reads as

$$\Delta \tilde{E}^{0,AB} = E(A^{0,AB} \cup B^{0,AB}) - (E(A^{0,AB}) + E(B^{0,AB})), \tag{1.117}$$

which is formally constituted by the classical electrostatics energy plus an exchange-correlation contribution

$$\Delta \tilde{E}^{0,AB} = \Delta E_{Elec} + \Delta \tilde{E}^{0,AB}_{xc}. \tag{1.118}$$

In practice, the classical electrostatics ΔE_{Elec} accounts for the electrostatic interaction of the unrelaxed one-electron density of A with the nuclei of B, and *viceversa*, the electronic (Coulombic) repulsion between both densities and the nuclear repulsion between atoms of A and B

$$\begin{aligned} \Delta E_{Elec} = &- \sum_{i \in B} \int \rho^0_A(\mathbf{r}) \frac{Z_i}{\mathbf{r} - \mathbf{R}_i} d\mathbf{r} - \sum_{i \in A} \int \rho^0_B(\mathbf{r}) \frac{Z_i}{\mathbf{r} - \mathbf{R}_i} d\mathbf{r} + \\ &\iint \frac{\rho^0_A(\mathbf{r}_1)\rho^0_B(\mathbf{r}_2)}{|\mathbf{r}_1 - \mathbf{r}_2|} + \sum_{i \in A} \sum_{j \in B} \frac{Z_i Z_j}{|\mathbf{R}_i - \mathbf{R}_j|}. \end{aligned} \tag{1.119}$$

In a next step, an intermediate state, namely $A^{0,AB}B^{0,AB}$, is constructed via Löwdin orthogonalization of the the occupied MOs of the A^0 and B^0 states. This leads into a proper antisymmetrized wavefunction with associated energy $E(A^{0,AB}B^{0,AB})$. The energy difference between this and the previous pseudostate reads as

$$\Delta \tilde{E}_{Pauli} = E(A^{0,AB}B^{0,AB}) - E(A^{0,AB} \cup B^{0,AB}), \tag{1.120}$$

and by combining Eqs. 1.118 and 1.120 one obtains the so-called Pauli repulsion energy term

$$\Delta E_{Pauli} = \Delta \tilde{E}_{Pauli} + \Delta \tilde{E}^{0,AB}_{xc}. \tag{1.121}$$

Thus, the classical electrostatics together with the Pauli repulsion, known as the frozen energy term in other energy decomposition schemes such as the absolutely localized molecular orbitals EDA (see below), accounts for the energetic change of going from the geometrically and electronically prepared fragments to a *true* intermediate state with a properly antisymmetrized wavefunction but unrelaxed MOs

$$\Delta E_{Elec} + \Delta E_{Pauli} = E(A^{0,AB}B^{0,AB}) - (E(A^{0,AB}) + E(B^{0,AB})). \tag{1.122}$$

In a last step, the orthogonal MOs from the previous intermediate step are allowed to relax to the ground state of the AB system. The energy lowering associated to the orbital relaxation is the so-called orbital interaction ΔE_{Orbint}, which is *always* negative/stabilizing

$$\Delta E_{Orbint} = E(AB^{AB}) - E(A^{0,AB}B^{0,AB}). \tag{1.123}$$

A graphical summary of all steps of the EDA procedure is depicted in Figure 1.7.

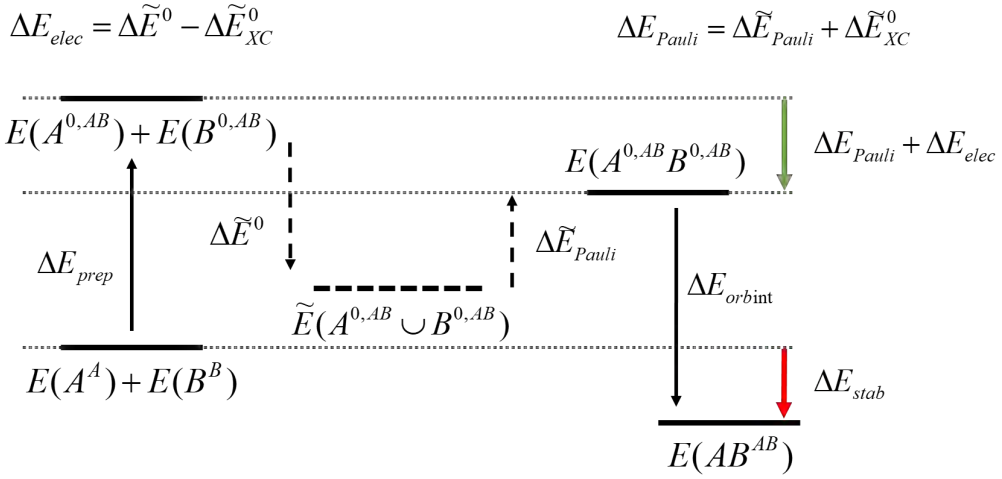

Figure 1.7: Illustrative representation of the EDA procedure with their corresponding states, pseudostates and associated energies.

It is possible to make use of localized molecular orbitals in this type of energy decompositions. One example was introduced by Head-Gordon's group where they make use of the absolutely localized molecular orbitals (ALMOs), to decompose the interaction energy into chemically meaninful terms.[140–144] In this scheme, tagged as ALMO-EDA, the interaction energy is further decomposed into frozen, polarization and charge-transfer energy terms by using the block-localized (and variationally optimized) orbitals. Interestingly, the ALMO-EDA scheme avoids the definition and use of intermediate pseudostates. Another example is the natural EDA (NEDA),[145] which use the natural bond orbitals.[129,146] In this Thesis we focus on the Ziegler-Rauk EDA, and further details about other EDA-like schemes can be found in the following references.[147,148]

1.5.2 Interacting quantum atoms approaches

The EDA-like schemes are mainly developed to study a particular A-B interaction from the pair of fragments A and B and requiring to define the fragment electronic configuration which *presumably* will better describe the system. Alternatively to that, there are methods that decompose the total energy of a molecular system into intra- and inter-atomic (or fragment) contributions solely using the wavefunction from the optimized AB system

$$E = \sum_{A} \varepsilon_A + \sum_{A,B>A} \varepsilon_{AB}. \tag{1.124}$$

They require to define the AIM, which as it has been previously mentioned it is not unique. In the Hilbert-space, in 1983 Mayer introduced the chemical Hamiltonian approach (CHA),[149] which make use of atomic projector operators to decompose the Hamiltonian into one- and two-center terms, leading finally in 2000 into the chemical energy component analysis (CECA) method.[150] Much more simple, but with some associated numerical error, is to use real-space atomic definitions as one- and two-electron dependent energy terms naturally decompose into one- and two-center contributions. The first complete real-space energy decomposition scheme was introduced in 2001 by Mayer and Hamza[44] and implemented by Salvador and Mayer[45] for the Hartree-Fock energy and using QTAIM, being later expanded to fuzzy atoms.[46] Then, in

2005 Blanco *et al.* proposed its decomposition from CASSCF/CI wavefunctions, giving name to the nowadays known as interacting quantum atoms (IQA) approach.[47] More recently, the IQA-type decompositions for the MP2,[151,152] coupled cluster[153–155] and some approximations for the KS-DFT (see below) wavefunctions has been reported.[48–51] The main problem with the IQA-type decompositions is that their definition depends on the electronic structure method used to compute the energy to decompose, and curiously the KS-DFT case is the most conflictive one due to the nature of the exchange-correlation energy (see below).

In wavefunction theory, the total energy of any molecular system can be expressed in terms of one- and two-electron dependent energy functions (Eq. 1.35). Thus, IQA naturally affords its decomposition into one- and two-center (energy) contributions. In particular, one-electron energy functions naturally decompose only into one-center (atomic) terms while two-electron ones provides both intra- and inter-atomic contributions (Eqs. 1.68 and 1.71). From the one-electron part of Eq. 1.35, the kinetic energy (Eq. 1.36) decompose in atomic terms as

$$T^A = -\frac{1}{2}\int w_A(\mathbf{r}_1)\nabla^2\rho_1(\mathbf{r}_1';\mathbf{r}_1)|_{\mathbf{r}_1'=\mathbf{r}_1}d\mathbf{r}_1. \tag{1.125}$$

The electron-nuclei attraction (Eq. 1.37), even formally being a one-electron quantity, provides both one- and two-center terms as the nuclei and the electron are not constrained to belong to the same atomic basin

$$\begin{aligned} U^A &= -\int \frac{Z^A}{|\mathbf{r}_1-\mathbf{R}_A|}w_A(\mathbf{r}_1)\rho(\mathbf{r}_1)d\mathbf{r}_1; \\ U^{AB} &= -\int \frac{Z^A}{|\mathbf{r}_1-\mathbf{R}_A|}w_B(\mathbf{r}_1)\rho(\mathbf{r}_1)d\mathbf{r}_1 - \int \frac{Z^B}{|\mathbf{r}_1-\mathbf{R}_B|}w_A(\mathbf{r}_1)\rho(\mathbf{r}_1)d\mathbf{r}_1. \end{aligned} \tag{1.126}$$

Regarding to the two-electron part of Eq. 1.35, all three energy quantities (Coulomb, exchange and correlation, Eq. 1.38) decompose into both intra- and inter-atomic terms, leading to the following terms for Coulomb

$$\begin{aligned} E_{Coul}^{AA} &= \frac{1}{2}\iint \frac{w_A(\mathbf{r}_1)\rho(\mathbf{r}_1)w_A(\mathbf{r}_2)\rho(\mathbf{r}_2)}{|\mathbf{r}_1-\mathbf{r}_2|}d\mathbf{r}_1d\mathbf{r}_2; \\ E_{Coul}^{AB} &= \iint \frac{w_A(\mathbf{r}_1)\rho(\mathbf{r}_1)w_B(\mathbf{r}_2)\rho(\mathbf{r}_2)}{|\mathbf{r}_1-\mathbf{r}_2|}d\mathbf{r}_1d\mathbf{r}_2, \end{aligned} \tag{1.127}$$

exchange

$$\begin{aligned} E_{x}^{AA} &= -\frac{1}{2}\iint \frac{w_A(\mathbf{r}_1)\rho^x(\mathbf{r}_1,\mathbf{r}_2)w_A(\mathbf{r}_2)}{|\mathbf{r}_1-\mathbf{r}_2|}d\mathbf{r}_1d\mathbf{r}_2; \\ E_{x}^{AB} &= -\iint \frac{w_A(\mathbf{r}_1)\rho^x(\mathbf{r}_1,\mathbf{r}_2)w_B(\mathbf{r}_2)}{|\mathbf{r}_1-\mathbf{r}_2|}d\mathbf{r}_1d\mathbf{r}_2, \end{aligned} \tag{1.128}$$

and correlation

$$E_c^{AA} = \frac{1}{2}\iint \frac{w_A(\mathbf{r}_1)\Gamma(\mathbf{r}_1,\mathbf{r}_2)w_A(\mathbf{r}_2)}{|\mathbf{r}_1-\mathbf{r}_2|}d\mathbf{r}_1 d\mathbf{r}_2;$$
$$E_c^{AB} = \iint \frac{w_A(\mathbf{r}_1)\Gamma(\mathbf{r}_1,\mathbf{r}_2)w_B(\mathbf{r}_2)}{|\mathbf{r}_1-\mathbf{r}_2|}d\mathbf{r}_1 d\mathbf{r}_2. \tag{1.129}$$

The repulsion between nuclei (Eq. 1.7) is the unique energy term that solely provides two-center terms, as the denominator of Eq. 1.130 cancels in the $\mathbf{R}_A = \mathbf{R}_B$ case

$$V_{NN}^{AB} = \sum_{A,B>A}^{N_{At}} \frac{Z^A Z^B}{|\mathbf{R}_A - \mathbf{R}_B|}. \tag{1.130}$$

With this, the general IQA decomposition of the total energy read as

$$\begin{aligned} E = &\sum_A T^A + \sum_A U^A + \sum_{A,B>A} U^{AB} + \sum_{A,B>A} V_{NN}^{AB} \\ &+ \sum_A E_{Coul}^{AA} + \sum_{A,B>A} E_{Coul}^{AB} + \sum_A E_x^{AA} + \sum_{A,B>A} E_x^{AB} + \sum_A E_c^{AA} + \sum_{A,B>A} E_c^{AB}. \end{aligned} \tag{1.131}$$

Note that to compute the energy terms for multi-reference (i.e. CASSCF/CI) wavefunctions it is required the use of the first- and second-order density matrices,[13] which are internally used but not readily available in most of the computational softwares. Considering the energy terms expressed as in Eqs. 1.125-1.129, the unique difference present in Hartree-Fock theory is that the correlation term is missing and the exchange density $\rho^x(\mathbf{r}_1,\mathbf{r}_2)$ can be directly expressed from the MOs as in Eqs. 1.41 and 1.42.

The story changes when one tries to decompose the KS-DFT energy. Compared to the HF expression, the exchange energy (two-electron) is substituted by the exchange-correlation energy, which essentially is a one-electron quantity (Eq. 1.46) as solely depends on the one-electron density and its derivatives. Thus, its natural real-space decomposition provides solely one-center (atomic) terms, which for chemical bonding analysis is clearly unsatisfactory. Moreover, the chemical bonding picture obtained from IQA-type analysis when using HF or KS-DFT (pure, or hybrid) will be completely different as for both HF and hybrid KS-DFT functionals there is a non-local HF-type exchange part (Eq. 1.47), which naturally provides both atomic and interatomic terms. Furthermore, the HF-like interatomic exchange between a pair of bonded atoms is negative/attractive, and responsible to describe the covalent contribution to the bonding. Thus, not considering it would make most of them positive (unphysical).

For these reasons, different approximations have been developed to recover the chemically meaningful $E_{xc}^{AB,DFT}$ terms. As first plausible solution, Tognetti *et al.* applied the HF-type exchange expression (E_x from Eq. 1.128) using the KS-MOs[49,50] for extracting both atomic and diatomic terms

$$\begin{aligned} E_{xc}^{DFT} \cong E_x^{HF-like} &= \sum_A E_x^{AA,HF-like} + \sum_{A,B>A} E_x^{AB,HF-like} \\ &= -\frac{1}{2}\sum_A \iint w_A(\mathbf{r}_1) w_A(\mathbf{r}_2) \rho^{x,KS}(\mathbf{r}_1,\mathbf{r}_2) r_{12}^{-1} d\mathbf{r}_1 d\mathbf{r}_2 \\ &- \sum_{A,B>A} \iint w_A(\mathbf{r}_1) w_B(\mathbf{r}_2) \rho^{x,KS}(\mathbf{r}_1,\mathbf{r}_2) r_{12}^{-1} d\mathbf{r}_1 d\mathbf{r}_2, \end{aligned} \tag{1.132}$$

presenting as main drawback that the sum of all components does not recover the total KS-DFT exchange-correlation energy (Eq. 1.124).

To the best of our knowledge, only the E_{xc}^{DFT} decomposition schemes introduced by Salvador and Mayer [48] and by Francisco *et al.* [51] ensure additivity

$$E_{xc}^{DFT} = \sum_{A} E_{xc}^{AA,DFT} + \sum_{A,B>A} E_{xc}^{AB,DFT}. \tag{1.133}$$

In 2007, Salvador and Mayer introduced a local function associated to each pair of atoms A and B which, upon integration, yields the corresponding real-space bond order. [48] Such function, namely the bond order density (BOD), $\beta_{AB}(\mathbf{r}_1)$, in the closed-shell single-determinant case reads as

$$\beta_{AB}(\mathbf{r}_1) = 2\sum_{i,j}^{nocc}[w_A(\mathbf{r}_1)S_{ij}^{B} + w_B(\mathbf{r}_1)S_{ij}^{A}]\phi_i^{*,KS}(\mathbf{r}_1)\phi_j^{KS}(\mathbf{r}_1). \tag{1.134}$$

Formally, the BOD represents the part of the one-electron density used to build the A-B interaction by means of the exchange. Thus, one could also exactly decompose the one-electron density into bonding and non-bonding counterparts at the single-determinant level. In their original work, Salvador and Mayer showed that the topology of $\beta_{AB}(\mathbf{r}_1)$ is very similar to that of the Hartree-Fock interatomic exchange energy density, exhibiting peaks at the atomic positions and, for bonded atom pairs, extending into the interatomic region. By using $\beta_{AB}(\mathbf{r}_1)$ (and its derivatives) instead of $\rho(\mathbf{r}_1)$ in the local exchange-correlation expression, the authors obtained an estimate of the diatomic local exchange

$$E_{xc}^{AB,DFT} = \int \epsilon^{xc}[\beta_{AB}(\mathbf{r}_1), \nabla\beta_{AB}(\mathbf{r}_1), ...]d\mathbf{r}_1. \tag{1.135}$$

Finally, the atomic exchange-correlation energy terms are obtained by substracting, for each atom A, half of the diatomic exchange-correlation energy contributions where atom A is involved to its exact one-center term obtained from the natural decomposition of Eq. 1.46 in the real-space (Eq. 1.68)

$$E_{xc}^{AA,DFT} = E_{xc}^{A,DFT} - \frac{1}{2}\sum_{B\neq A} E_{xc}^{AB,DFT}. \tag{1.136}$$

Such decomposition showed robust performance, obtaining almost perfect linear regressions for both atomic and diatomic terms when correlating the exchange-correlation energy terms obtained with a local functional (e.g. BLYP) against the HF-type ones obtained at the same geometry and KS MOs.

In 2016, Francisco *et al.* proposed an alternative strategy based on using the exact HF-exchange formula with the KS MOs, thus sharing Tognetti's phylosophy, but incorporating properly defined atomic scaling factors to ensure additivity. [51] For a hybrid functional, the total KS-DFT exchange-correlation energy, $E_{xc}^{hyb-DFT}$, can be written as

$$E_{xc}^{hyb-DFT} = \sum_{A} E_{xc}^{A,hyb-DFT} = \sum_{A}[E_{xc}^{A,DFT} + a_0 E_x^{A,HF-like}], \tag{1.137}$$

where

$$E_x^{A,HF-like} = -\frac{1}{4}\iint w_A(\mathbf{r}_1)\rho(\mathbf{r}_1;\mathbf{r}_2)\rho(\mathbf{r}_2;\mathbf{r}_1)r_{12}^{-1}d\mathbf{r}_1 d\mathbf{r}_2. \tag{1.138}$$

Here, the $E_x^{A,HF-like}$ component accounts for both atomic and interatomic contributions involving atom A

$$E_x^{A,HF-like} = E_x^{AA,HF-like} + \frac{1}{2}\sum_{B\neq A} E_x^{AB,HF-like}. \tag{1.139}$$

Then, the authors propose to scale both the atomic and diatomic terms by introducing the following atomic scaling factors

$$\lambda_A = \frac{E_{xc}^{A,hyb-DFT}}{E_x^{A,HF-like}}, \tag{1.140}$$

ensuring that add up to the total KS-DFT exchange-correlation energy simply expressed as

$$E_{xc}^{AB,hyb-DFT} = \frac{1}{2}[\lambda_A + \lambda_B]E_x^{AB,HF-like} \quad \forall A, B. \tag{1.141}$$

Its decomposition is not limited to hybrid functionals, pure functionals just present an $a_0 = 0$ value in Eq. 1.137 and thus $E_{xc}^{A,hyb-DFT} = E_{xc}^{A,DFT}$. However, this method make always use of the exact HF exchange expression to determine scaling factors and thus the one- and two-center exchange-correlation terms, independently of the functional nature.

To date, the KS-DFT IQA methodologies has been applied independently but proper comparison between them is still missing. Similarly happens with the EDA- and IQA-type energy decompositions, they both have been extensively applied in the literature to enlight about the nature of the chemical bond, characterizing both intra- and intermolecular interactions. This allowed to understand and even improve chemical reactivity, unveiling the chemical bonding picture of non-trivial systems and even suggesting a new types of bonds. However, tackling the chemical bonding description using *simultaneously* both energy decompositions is not common.

Some research groups have been trying to express some of the EDA descriptors in the IQA framework, and thus avoiding the use of artificial intermediate pseudostates. In this direction, in 2006 Pendas *et al.* compared the IQA behaviour to other energy decomposition schemes (e.g. EDA, NEDA and SAPT) for a series of hydrogen-bonded dimers.[156,157] The authors decomposed the interaction energy between the two monomers A and B (ΔE_{Int}) into the sum of classical electrostatics and exchange-correlation. They observed that the interaction was governed by exchange-correlation, showing thus the importance of the covalent picture. Moreover, the deformation energy of the proton acceptor moieties correlated well with the intermolecular charge transfer and classical electrostatic energy derived from IQA. Some years later, Pendas *et al.* also analyzed the concept of steric repulsion, arguing that in EDA the Pauli repulsion by nature depends on the fragment's reference states.[55] The authors decomposed the Hartree-Fock interaction energy into fragment's deformation and inter-fragment interactions, which further decompose into its classical electrostatics and exchange contributions, and showed that the Pauli repulsion is captured in the increase of the fragment's deformation energies of the intermediate (properly antisymmetrized) states. Moreover, the hyperconjugative effects in rotational barriers are captured by the inter-fragment exchange contribution, which is enhanced due to electron delocalization.

Recently, Racioppi *et al.* applied the opposite phylosophy and rearranged the EDA constributions to match IQA ones, instead of grouping IQA terms to recover EDA descriptors.[158] In their *pseudo*-IQA method, the Pauli, orbital interaction and electrostatic energies from EDA are regrouped into overall variations of the kinetic, classical electrostatic and exchange-correlation contributions. One can obtain the same terms

by considering the usual reference-state IQA, based on decomposing the binding energy between a pair of fragments A and B upon substraction of the IQA terms from the fully relaxed wavefunction of the system AB to the obtained for the isolated and geometrically unrelaxed fragments.

Chapter 2

General objectives

The main objective of the Thesis is the development and application of computational methodologies for chemical bonding analysis. In particular, the computational tools devoted to elucidate OSs from wavefunction analysis and the strategies which decompose the total energy of a molecular system into one- and two-center energy contributions. In this direction, we separated the main motivation of the Thesis in several more acute objectives, which will hereafter be generally described.

The use of centroids of LOs is a simple strategy to assign the electrons from each LO, and as consequence the OSs, in both solid state and molecular chemistry. To date, the electron assignment from each LO is mainly performed according to a distance criterion; the electrons are assigned to the atom which is closer to the LO centroid. Thus, it formally considers that all atoms are equal (in size), independently of the atom-type. Therefore, many problems may arise if the atom sizes are very different. Nonetheless, the closest-atom criterion is simple (by definition) and proved to be useful. However, it has also not been properly tested. For these reasons, our first aim is **to evaluate the performance of the closest-atom and an alternative (electronic) criterion to assign OSs from LOs using an extended set of systems of increasing complexity**.

An alternative to the use of centroids to assign the electrons from a LO, and as consequence the formal OSs, is by visual inspection or to couple orbital localization with another computational technique, i.e. population analysis. Most schemes perform appropriately when assigning the OSs of rather simple systems, but might fail when the complexity of the system increases. A plausible reason is the inhability to introduce the fragment definition priorly to perform the orbital localization. For this reason, our second aim is **to introduce a new fragment-based orbital localization procedure and explore its use to elucidate the fragment OSs**.

One of the state-of-the-art computational methods used to assign OSs is the EOS analysis. However, it presents an intrinsict limitation: its inability to characterize non-symmetric singlet diradical(oid)s from the analysis of the (proper) multireference wavefunction. Furthermore, within the unrestricted formulation, the EFOs for the alpha and beta parts of the density might differ considerable, even for the formally paired electrons, which prevents from the rationalization of the analysis in terms of electron pairs (see details in Section 1.4). This might be particularly problematic when spin-contamination takes place. Thus, the third aim is **to propose and alternative procedure to extract the EFOs, and the electron assignment**

within EOS, which surpass the aforementioned limitation and unify the procedure independently of the wavefunction used.

The decomposition of the total energy of a system into fragment and inter-fragment contributions is a widely used technique to study its chemical bonding. Within this topic, there are two main families of schemes, namely the EDA and IQA (see details in Section 1.5). Both have proved to be very useful, but very few works extracting chemical information from both *simultaneously* are present in the literature. In our opinion, exploring the performance of the EDA and IQA schemes when working together would be very appealing for the computational chemistry community. For this reason, the fourth objective is **to further decompose each of the EDA terms, i.e. electrostatics, Pauli repulsion and orbital interaction, into intra- and inter-fragment IQA contributions to enrich the conventional EDA approach with the IQA perspective**.

The Aquilles heel of the IQA-like schemes is the decomposition of the KS-DFT exchange-correlation energy into both one- and two-center contributions, as it naturally decomposes solely into one-center terms (see details in Section 1.5.2). Thus, the information regarding chemical bonds is lost. To date, there are only two reported approximations that achieve an exact one- and two-center decomposition, and a comparison between them is non-existent. Thus, the fifth objective is **to perform a quantitative comparison of the two IQA schemes that exactly decompose the total KS-DFT exchange-correlation energy into one- and two-center terms**. An exact IQA decomposition for both one- and two-center decomposition should involve the use of a genuine *two-electron* dependent KS-DFT exchange-correlation expression. Then, a sixth objective is **to mathematically derive a two-electron dependent expression for the KS-DFT exchange-correlation energy and use it within the IQA framework to naturally decompose this term into one- and two-center contributions**.

The application of the OS elucidation techniques, together with the local spin analysis (see details in Section 1.3.1) and other complementary chemical bonding tools, can be extremely useful to understand the interaction between central elements (being TMs or main-group elements) and their ligands, allowing to *ideally* explain their reactivity and properties (e.g. spectroscopic). One can argue that such tools are only useful to tag a bottle inside a laboratory, but the proper categorization of *any* system has been useful for the chemistry community along the years. To date, no proper comparison between state-of-the-art OSs elucidation techniques has been performed, being thus the seventh aim **to compare the chemical bonding picture obtained with EOS and LOBA, against the IUPAC IA or experimentally reported**. Finally, the last objective of the Thesis is **to make use of all the introduced chemical bonding tools to computationally characterize the chemical bonding picture of molecular systems which are of particular interest for both the experimental and computational chemistry community**.

Chapter 3

Methodology

3.1 Numerical integration in real-space

The numerical integration requires of the definition of a set of points, namely the grid, with a particular size and distribution along the real-space. Both the size and distribution of points used directly affects the accuracy of such integrations, being crucial for an accurate integration. It is well established that the larger the grid size, the more accurate the integration, but also the higher the computational cost. Thus, the use of an strategy that achieves high accuracy at an affordable computational cost is mandatory. In this Section, we discuss the basics about numerical integration for one- and two-electron functions as are used in, for example, the IQA energy decomposition schemes.

Let us consider a system constituted of a single atom. In this case, the integration of a one-electron function, $f(\mathbf{r})$, in the real-space is numerically achieved, up to some numerical error but with good accuracy, as

$$I = \int f(\mathbf{r}) d\mathbf{r} \approx \sum_{k}^{N_{Points}} f(\mathbf{r}_k) w_{grid}(\mathbf{r}_k), \tag{3.1}$$

where $w_{grid}(\mathbf{r}_k)$ is the integration weight from the quadrature (see below) of a given k point in the real-space and N_{Points} is the number of points of the integration grid. Thus, one needs to define the position of the points of the integration grid and its associated weights. For this aim, it is commonly used a spherical atom-centered grid, which involves a radial part defined on the range from 0 to ∞, and an angular part, fully covering the real-space. In APOST-3D, the radial distribution of points is obtained according to a Gaussian-Legendre quadrature,[159] coupled with the set of Lebedev-Laikov grids for the angular part.[160]

The Gaussian quadrature is an approximation to a defined integral of a single-coordinate function, $f(x)$, stated as a weighted sum of function values at specified points. In the Gauss-Legendre quadrature, the integration domain ranges from -1 to 1. For our purpose, it is required to transform the corresponding coordinates and its weight from [-1, 1] to [0, ∞), which can be achieved for instance as

$$I = \int_0^\infty f(r) dr \equiv \int_{-1}^{1} f(x) dx; \;\; r = r_0 \left(\frac{1+x}{1-x} \right) \;\; dr = \frac{2r_0}{(1-x)^2} dx. \tag{3.2}$$

The parameter r_0 represents the distance from the nucleus that contains half of the radial points. The

original integral (Eq. 3.2) can be thus rewritten as

$$I = \int_{-1}^{1} \left(\frac{2r_0}{(1-x)^2} \right) f\left(r_0 \left(\frac{1+x}{1-x} \right) \right) dx, \tag{3.3}$$

and approximately integrated within the [0, ∞) range as a weighted sum of the values of the function obtained at some pre-established points

$$I = \int_0^{\infty} f(r)dr \approx \sum_{l}^{N_{Rad}} f(r_l) w_{rad}(r_l), \tag{3.4}$$

where

$$f(r_l) = f\left(r_0 \left(\frac{1+x_l}{1-x_l} \right) \right); \;\; w_{rad}(r_l) = \left(\frac{2r_0}{(1-x_l)^2} \right) w_{rad}(x_l). \tag{3.5}$$

The point distribution is very relevant for the accuracy of the results. For instance, the points located far away from the grid center (atomic position) may hardly contribute to the numerical integration, being formally lost. It is important to use a radial distribution which maximizes the density of points relatively close to the grid center, sparse them in intermediate distances and almost vanishes at large distances. This can be controlled by the r_0 value. In the default integration setup, APOST-3D uses $r_0 = 0.5$ a.u.

The Lebedev-Laikov angular grid consists on a given set of points distributed on the surface of a sphere of radius unity, with their associated weights. To achieve a mapping on the three-dimensional space, this angular grid, formally in spherical coordinates, is first transformed to Cartesian coordinates and then combined with the aforementioned radial quadrature

$$I = \int f(\mathbf{r})d\mathbf{r} = \sum_{m}^{N_{Rad}} \sum_{i}^{N_{Ang}} f(\mathbf{r}_{mi}) w_{rad}(r_m) w_{ang}(\mathbf{r}_i), \tag{3.6}$$

where N_{Rad} and N_{Ang} corresponds to the number of radial and angular points, respectively, and $\mathbf{r}_{mi} = \{r_m, \mathbf{r}_i\}$. With this, the integration weight $w_{grid}(\mathbf{r}_k)$ from Eq. 3.1 is obtained as a product of the radial and angular weights (Eq. 3.6), $w_{grid}(\mathbf{r}_k) = w_{rad}(r_m) w_{ang}(\mathbf{r}_i)$.

In case of integrating a two-electron function, which formally invokes a 6D integral, one requires two sets of spherical grids; one integration set consisting on $N_{Points} = N_{Rad} \times N_{Ang}$ for each electron coordinate

$$I = \iint f(\mathbf{r}_1, \mathbf{r}_2) d\mathbf{r}_1 d\mathbf{r}_2 = \sum_{m,n}^{N_{Rad}} \sum_{i,j}^{N_{Ang}} f(\mathbf{r}_{mi}, \mathbf{r}_{nj}) w_{rad}(r_m) w_{ang}(\mathbf{r}_i) w_{rad}(r_n) w_{ang}(\mathbf{r}_j). \tag{3.7}$$

By considering $w_{grid}(\mathbf{r}_k) = w_{rad}(r_m) w_{ang}(\mathbf{r}_i)$ and $w_{grid}(\mathbf{r}_l) = w_{rad}(r_n) w_{ang}(\mathbf{r}_j)$, expression 3.7 is rewritten as

$$I = \iint f(\mathbf{r}_1, \mathbf{r}_2) d\mathbf{r}_1 d\mathbf{r}_2 = \sum_{k}^{N_{Points}} \sum_{l}^{N_{Points}} f(\mathbf{r}_k, \mathbf{r}_l) w_{grid}(\mathbf{r}_k) w_{grid}(\mathbf{r}_l), \tag{3.8}$$

requiring thus the use of N_{Points}^2 points to integrate for the atom.

For a poliatomic system, Becke proposed to evaluate the numerical integrals using a combination of atom-center center grids, giving rise to the so-called Becke multicenter scheme.[73] In particular, the one-electron

integrals are performed as

$$I = \int f(\mathbf{r}) d\mathbf{r} \approx \sum_{A}^{N_{At}} \sum_{k \in A}^{N_{Points}} w_A^{Becke}(\mathbf{r}_k) f(\mathbf{r}_k) w_{grid}(\mathbf{r}_k), \tag{3.9}$$

where $w_A^{Becke}(\mathbf{r}_k)$ is the Becke weight of the spherical grid of atom A at the point $\mathbf{r}_k$. Similarly, the two-electron integrals are evaluated including the Becke weight twice as

$$I = \iint f(\mathbf{r}_1, \mathbf{r}_2) d\mathbf{r}_1 d\mathbf{r}_2 \approx \sum_{A,B}^{N_{At}} \sum_{k \in A}^{N_{Points}} \sum_{l \in B}^{N_{Points}} w_A^{Becke} w_B^{Becke} f(\mathbf{r}_k, \mathbf{r}_l) w_{grid}(\mathbf{r}_k) w_{grid}(\mathbf{r}_l). \tag{3.10}$$

Notice that by Becke's scheme, the original multicenter integral is readily expressed as a sum of atom-center contributions

$$I = \int f(\mathbf{r}) d\mathbf{r} \approx \sum_{A}^{N_{At}} \sum_{k \in A}^{N_{Points}} w_A^{Becke}(\mathbf{r}_k) f(\mathbf{r}_k) w_{grid}(\mathbf{r}_k) = \sum_{A}^{N_{At}} I_A. \tag{3.11}$$

In practice, one may identify the atomic weight function in the integrand of Eq. 1.70 with the Becke weight above, and thus achieve the decomposition of I into atomic contributions, I_A, using the desired AIM as

$$I_A^{AIM} \cong \sum_{k \in A}^{N_{Points}} w_A^{AIM}(\mathbf{r}_k) f(\mathbf{r}_k) w_{grid}(\mathbf{r}_k), \tag{3.12}$$

using solely the grid points of atom A. Such technique is incorporated in other exiting software such as ChemmTools, under the term *local integration*.[161,162] In the case of two-electron integrations, this approach is mandatory, as for each atomic or diatomic term one must run over the square of the number of grid points

$$I_{AB}^{AIM} \approx \sum_{k \in A}^{N_{Points}} \sum_{l \in B}^{N_{Points}} w_A^{AIM}(\mathbf{r}_k) w_B^{AIM}(\mathbf{r}_l) f(\mathbf{r}_k, \mathbf{r}_l) w_{grid}(\mathbf{r}_k) w_{grid}(\mathbf{r}_l). \tag{3.13}$$

The Becke multicenter scheme proved to be very efficient (and accurate), being nowadays extensively used to compute properties or energies in the real-space, e.g. the KS-DFT exchange-correlation energy. In his original work, this scheme provided up to 5 figures accuracy for the one-electron density and electron-nuclei attraction of small diatomic and poliatomic systems, and with relatively small atomic grids.[73] In the IQA-type energy decomposition schemes, the two-electron dependent energy components (Eqs. 1.127-1.129) are numerically evaluated as in Eq. 3.13. In that case, the one-center two-electron integration must discard $N_{At} \times N_{Points}$ out of the $(N_{At} \times N_{Points})^2$ integration points as cancel the denominator from Eqs. 1.127-1.129. This directly impacts the accuracy of the numerical integration, lowering it (more error). For the two-center two-electron integration, the number of points to discard is very small because as the two sets of points are centered one in each atom, it is much more difficult that two points (one from each set) coincide in the same position.

In general, one can improve the accuracy of the numerical integration by (i) increasing the number of both radial and angular points or (ii) modifying the positions of the second electron grid points to maximize the number of points used in the integral evaluation. The first option brings associated a large increase of the computational cost, being not very appealing for large molecular systems. Alternatively, one can rotate

the coordinates of the grid points corresponding to the second electron, avoiding the overlap between points and thus maximizing the number of points used to integrate. One can rotate a set of grid points in both spherical or Cartesian coordinates. In the Cartesian coordinates convention, the position of the grid points is modified (without changing the value their the associated integration weights) by applying a rotation along one or two axis, achieved when using the appropriated rotational matrices. For example, in case of applying a rotation of α and β degrees along the z and y axis, respectively, the rotated coordinates $(x_{rot}, y_{rot}, z_{rot})$ respect to the original ones (x_0, y_0, z_0) read as

$$\begin{aligned} x_{rot} &= (x_0 \cos\alpha - y_0 \sin\alpha)\cos\beta - z_0 \sin\beta \\ y_{rot} &= x_0 \sin\alpha + y_0 \cos\alpha \\ z_{rot} &= (x_0 \cos\alpha - y_0 \sin\alpha)\sin\beta + z_0 \cos\beta. \end{aligned} \tag{3.14}$$

Some of us studied the effect of these rotations on the accuracy of the one- and two-center two-electron integrations by first using a simple analytical model that represents the two-electron repulsion found in molecular systems, and then for several small molecules.[163] The authors observed that the integrated two-center two-electron terms are three orders of magnitude more accurate that the one-center two-electron ones, when the atoms are distanced by more than 1.5 Bohr. Furthermore, a rotation angle that minimizes for *all* real systems studied the error on the one-center two-electron integrals was not found. Currently, the APOST-3D default setup uses $\alpha \approx 9.3$ and $\beta = 0$ degrees as rotation angles, which were the best performing coupled with atomic grids with 40 radial and 146 angular points.

3.2 Speeding up the decomposition of the exchange-correlation energy

As it was aforementioned, the bottleneck of the IQA methodologies is the decomposition of the two-electron dependent energy terms, Coulomb and exchange-correlation. Between them, the exchange-correlation is the most expensive, computationally, as not only required of *formally* 6D numerical integration but also 4 nested loops runs over the number of occupied MOs (see below). This last part is not present in the Coulomb energy term as it is written directly from the one-electron density (Eq. 1.127). Thus, one must apply strategies to speed-up or approximate (accurately) the decomposition of this term in order to make the IQA methodology suitable to compute systems larger than a few atoms. In the next subsections, we describe the two strategies used in the current thesis to faster the IQA decomposition of the exchange-correlation energy term.

3.2.1 Monadic diagonalization

In 2005, Pendas *et al.* introduced a computationally efficient method to evaluate the two-electron exchange-correlation integrals in the real-space, by using the monadic factorization of the RDM2 proposed in 1995 by Davidson,[164] which achieves full separation of the interelectronic components into *formally* one-electron terms.[165,166] The authors showed that the final computational cost is equivalent to integrate a single-determinant wavefunction with as many MOs as occupied functions in the correlated expansion.

In detail, for both single- and multi-determinant wavefunctions, the exchange-correlation energy is evaluated upon integration of the exchange-correlation density (Eq. 1.75)

$$E_{xc} = \frac{1}{2}\iint \rho^{xc}(\mathbf{r}_1,\mathbf{r}_2) r_{12}^{-1} d\mathbf{r}_1 d\mathbf{r}_2, \tag{3.15}$$

where r_{12}^{-1} is the two-electron operator (Eq. 1.6) and $\rho_{xc}(\mathbf{r}_1,\mathbf{r}_2)$ can be written in the MO basis as

$$\rho^{xc}(\mathbf{r}_1,\mathbf{r}_2) = \sum_{ijkl}^{N_{orb}} \lambda_{ijkl}\phi_i(\mathbf{r}_1)\phi_j(\mathbf{r}_1)\phi_k(\mathbf{r}_2)\phi_l(\mathbf{r}_2), \tag{3.16}$$

being, N_{orb} is the number of fully (or partially) occupied MOs. As the λ_{ijkl} matrix is symmetric in the ij and kl pairs, one can define a set of coefficients

$$\lambda'_{ijkl} = \lambda_{ijkl} + \lambda_{jikl}(1-\delta_{ij}) + \lambda_{ijlk}(1-\delta_{kl}) + \lambda_{jilk}(1-\delta_{ij})(1-\delta_{kl}), \tag{3.17}$$

where δ_{ij} is the Kronecker delta, and rewrite Eq. 3.16 much compactly as

$$\rho^{xc}(\mathbf{r}_1,\mathbf{r}_2) = \sum_{i\geq j}^{N_{orb}}\sum_{k\geq l}^{N_{orb}} \lambda'_{ijkl}\phi_i(\mathbf{r}_1)\phi_j(\mathbf{r}_1)\phi_k(\mathbf{r}_2)\phi_l(\mathbf{r}_2). \tag{3.18}$$

Finally, Eq. 3.18 is diagonalized using the basis of products of MOs, $\phi_i(\mathbf{r})\phi_j(\mathbf{r})$ where $i \geq j$, obtaining

$$\rho^{xc}(\mathbf{r}_1,\mathbf{r}_2) = \sum_{i\geq j}^{N_{orb}} \eta_{ij} f_{ij}(\mathbf{r}_1) f_{ij}(\mathbf{r}_2), \tag{3.19}$$

where the f_{ij} values are linear combinations of the MO products.

It can be easily seen that the exchange-correlation energy evaluation (Eq. 1.75), and thus its IQA decomposition, is computationally much more efficient when using the exchange-correlation density obtained with this procedure (Eq. 3.19) compared to the original one (Eq. 3.16). Let us mention that the aforementioned procedure does not limit the IQA decomposition to work with the exchange and correlation energy components together. One can apply the procedure independently for the exchange- and correlation-energy densities, being solely required to use the *exchange-* or *correlation-only* λ_{ijkl} matrix in Eq. 3.16.

3.2.2 Multipolar approach

In 2017, Francisco *et al.* showed that the interatomic exchange-correlation energy (E_{xc}^{AB}) can be exactly obtained from a multipolar expansion,[167] inspired by the interatomic decomposition of the Coulomb energy terms proposed by Popelier and coworkers for atom pairs with non-overlapping domains.[168–170] The aforementioned multipolar expansion is expressed as

$$E_{xc}^{AB} = \sum_{i,j\geq i}\eta_{ij}\sum_{l_1m_1}^{\infty}\sum_{l_2m_2}^{\infty} C_{l_1m_1,l_2m_2}(\hat{R})\left(\frac{\varrho_{l_1m_1}^{A,ij}\varrho_{l_2m_2}^{B,ij}}{R^{l_1+l_2+1}}\right), \tag{3.20}$$

where m_1 and m_2 run from $-l_1$ to l_1 and $-l_2$ to $-l_2$, respectively, the $C_{l_1m_1,l_2m_2}(\hat{R})$ coefficients are defined elsewhere (see appendix Ref.[167]), and $\varrho_{l_1m_1}^{A,ij}$ are the spherical atomic multipoles. The later are defined as

$$\varrho_{l_1 m_1}^{A,ij} = N_{l_1} \int w_A(\mathbf{r}_1) S_{l_1 m_1}(\hat{R}) f_{ij}(\mathbf{r}_1) d\mathbf{r}_1, \tag{3.21}$$

being $N_{l_1} = \sqrt{4\pi/(2l_1+1)}$ and $S_{l_1 m_1}(\hat{R})$ the real spherical harmonics (see also appendix Ref.[167]).

One can rewrite Eq. 3.20 from atomic monopoles, dipoles, quadrupoles and so forth, leading into an homologous expression to Popelier's *et al.* interatomic Coulomb energy terms (E_{Coul}^{AB}) but for the exchange-correlation. If one truncates the multipolar expansion, E_{xc}^{AB} is approximated, henceforth named multipolar approach. In the current implementation of the multipolar approach in the APOST-3D code, the expansion is trucated to $m_1 = m_2 = 2$ and $l_1 = l_2 = 2$. In this case, the approximate E_{xc}^{AB} term is obtained as the sum of the charge-charge ($E_{xc,cc}^{AB}$), charge-dipole ($E_{xc,cd}^{AB}$), dipole-dipole ($E_{xc,dd}^{AB}$), charge-quadrupole ($E_{xc,cq}^{AB}$), dipole-quadrupole ($E_{xc,dp}^{AB}$) and quadrupole-quadrupole ($E_{xc,qq}^{AB}$) energy components

$$E_{xc}^{AB} \approx E_{xc,cc}^{AB} + E_{xc,cd}^{AB} + E_{xc,dd}^{AB} + E_{xc,cq}^{AB} + E_{xc,dq}^{AB} + E_{xc,qq}^{AB}. \tag{3.22}$$

Using the ingredients from subsection 3.2.1, the charge-charge (cc) term is expressed as

$$E_{xc,cc}^{AB} = \sum_{i,j \geq i} \eta_{ij} \left(\frac{q^{A,ij} q^{B,ij}}{R} \right), \tag{3.23}$$

the charge-dipole (cd) as

$$E_{xc,cd}^{AB} = \sum_{i,j \geq i} \eta_{ij} \left(\frac{(\boldsymbol{\mu}^{A,ij} \cdot \mathbf{R}) q^{B,ij} - (\boldsymbol{\mu}^{B,ij} \cdot \mathbf{R}) q^{A,ij}}{R^3} \right), \tag{3.24}$$

and the dipole-dipole (dd) as

$$E_{xc,dd}^{AB} = \sum_{i,j \geq i} \eta_{ij} \left[\left(\frac{(\boldsymbol{\mu}^{A,ij} \cdot \boldsymbol{\mu}^{B,ij})}{R^3} \right) - \left(\frac{3(\boldsymbol{\mu}^{A,ij} \cdot \mathbf{R})(\boldsymbol{\mu}^{B,ij} \cdot \mathbf{R})}{R^5} \right) \right], \tag{3.25}$$

where $q^{A,ij} = \int w_A(\mathbf{r}_1) f_{ij}(\mathbf{r}_1) d\mathbf{r}_1$, $\boldsymbol{\mu}^{A,ij} = \mathbf{R} \int w_A(\mathbf{r}_1) f_{ij}(\mathbf{r}_1) d\mathbf{r}_1$, $\mathbf{R} = \mathbf{R}_B - \mathbf{R}_A$ and $R = |\mathbf{R}_B - \mathbf{R}_A|$.

For the remaining terms, the charge-quadrupole (cq) is expressed as

$$E_{xc,cq}^{AB} = \sum_{i,j \geq i} \eta_{ij} \left(\frac{(\mathbf{R} \cdot \boldsymbol{Q}^{A,ij} \cdot \mathbf{R}) q^{B,ij} + (\mathbf{R} \cdot \boldsymbol{Q}^{B,ij} \cdot \mathbf{R}) q^{A,ij}}{R^5} \right), \tag{3.26}$$

the dipole-quadrupole (dq) as

$$\begin{aligned} E_{xc,dq}^{AB} = \sum_{i,j \geq i} \eta_{ij} \Bigg[& \left(\frac{2\left((\mathbf{R} \cdot \boldsymbol{Q}^{A,ij} \cdot \boldsymbol{\mu}^{B,ij}) - (\mathbf{R} \cdot \boldsymbol{Q}^{B,ij} \cdot \boldsymbol{\mu}^{A,ij}) \right)}{R^5} \right) \\ & - \left(\frac{5\left((\boldsymbol{\mu}^{B,ij} \cdot \mathbf{R})(\mathbf{R} \cdot \boldsymbol{Q}^{A,ij} \cdot \mathbf{R}) - (\boldsymbol{\mu}^{A,ij} \cdot \mathbf{R})(\mathbf{R} \cdot \boldsymbol{Q}^{B,ij} \cdot \mathbf{R}) \right)}{R^7} \right) \Bigg], \end{aligned} \tag{3.27}$$

and the quadrupole-quadrupole (qq) as

$$E_{xc,qq}^{AB} = \sum_{i,j\geq i} \eta_{ij} \left[\left(\frac{2tr(\boldsymbol{Q}^{A,ij} \cdot \boldsymbol{Q}^{B,ij})}{3R^5} \right) - \left(\frac{60(\mathbf{R} \cdot \boldsymbol{Q}^{A,ij} \cdot \boldsymbol{Q}^{B,ij} \cdot \mathbf{R})}{9R^7} \right) + \left(\frac{35(\mathbf{R} \cdot \boldsymbol{Q}^{A,ij} \cdot \mathbf{R})(\mathbf{R} \cdot \boldsymbol{Q}^{B,ij} \cdot \mathbf{R})}{3R^9} \right) \right], \tag{3.28}$$

where the matrix elements of the quadrupole matrix read

$$Q_{\mu\nu}^{A,ij} = \int w_A(\mathbf{r}_1) f_{ij}(\mathbf{r}_1) \left(\frac{3}{2} R_\mu R_\nu - \frac{1}{2} ||\mathbf{R}||^2 \delta_{\mu\nu} \right) d\mathbf{r}_1, \quad \mu, \nu = x, y, z. \tag{3.29}$$

One can easily evaluate the accuracy of the multipolar approach to compute E_{xc}^{AB} depending on the terms included in the expansion. As an illustrative example, we compiled in Table 3.1 the errors obtained when evaluating E_{xc}^{AB} with the multipolar approach for the water dimer system at different intermolecular distances.

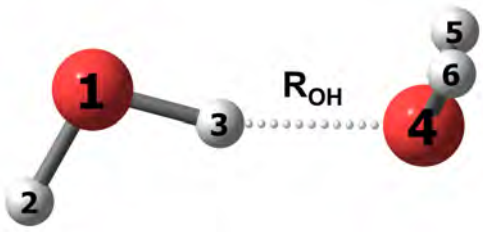

Figure 3.1: Molecular structure and atom tags of the illustrative water dimer.

Truncating the expansion to the quadrupole-quadrupole (qq) term provides satisfactory results when the bond orders are relatively low, and a clear improvement in general. Currently the APOST-3D code applies the multipolar approach to compute E_{xc}^{AB} when the bond order between the pair of atoms is lower than 0.05. This threshold can be modified depending on the accuracy desired on the two-center terms.

Table 3.1: Bond orders and errors (in kcal/mol) on the interatomic HF exchange energy obtained with the multipolar approach depending on the terms included. Unreported results produced at the HF/TZVP level with a a modified version of the APOST-3D code for the water dimer at the R_{OH} distances of 1.5Å (top) and 2.0Å (bottom) (see Figure 3.1) using the TFVC atomic definition.

Atom pair	Bond Order	E_x (a.u.)	Err. cc	Err. +cd+dd	Err. +cq+dq	Err. +qq
1 - 2	0.693	-0.215	15.18	9.80	-5.76	-0.52
1 - 3	0.429	-0.147	18.93	3.85	-4.79	0.46
1 - 4	0.159	-0.029	7.24	2.32	0.17	-0.21
1 - 5	0.002	0.000	0.02	0.01	0.00	0.00
2 - 3	0.004	-0.001	-0.10	0.01	-0.01	-0.01
2 - 4	0.004	0.000	0.01	0.00	0.00	0.00
2 - 5	0.000	0.000	0.00	0.00	0.00	0.00
3 - 4	0.125	-0.037	9.48	1.58	-1.19	-1.49
3 - 5	0.001	0.000	0.00	0.00	0.00	0.00
4 - 5	0.625	-0.195	14.83	9.87	-4.51	-0.15
5 - 6	0.006	-0.001	-0.18	0.02	-0.01	-0.01
1 - 2	0.678	-0.211	15.20	9.88	-5.50	-0.45
1 - 3	0.559	-0.180	17.39	6.03	-4.44	2.77
1 - 4	0.057	-0.008	2.12	0.73	0.12	0.04
1 - 5	0.000	0.000	0.00	0.00	0.00	0.00
2 - 3	0.006	-0.001	-0.16	0.02	-0.01	-0.01
2 - 4	0.001	0.000	0.01	0.00	0.00	0.00
2 - 5	0.000	0.000	0.00	0.00	0.00	0.00
3 - 4	0.071	-0.016	4.37	1.13	-0.09	-0.25
3 - 5	0.001	0.000	0.01	0.00	0.00	0.00
4 - 5	0.643	-0.200	14.97	9.85	-4.89	-0.24
5 - 6	0.007	-0.001	-0.20	0.03	-0.01	-0.01

3.3 General computational details

In this section, we summarize the computational methods, basis sets, softwares and some technicalities that has been used in the works included in the Thesis. For further details (i.e. spin-contamination corrections) from each work, and to find the corresponding references, we guide the reader to the section of computational details provided in each manuscript included within Chapters 4-6.

In Section 4.1, all calculations were performed with the Gaussian16 package.[171] The optimized geometries and wavefunctions were obtained at the B3LYP/cc-pVTZ level of theory, except for the sets of XH_n and TM carbenes, where the BP86/def2-TZVP combination of functional and basis set was used. The PM LOs were produced using the $IOp(4/9) = 20212$ keyword and the NLMOs with the NBO6 program.[172] The LO centroids position, steepest-ascent algorithm from the centroid to the corresponding attractor and EOS analysis were performed with the APOST-3D code,[173] using the TFVC[75] AIM definition and a 40 × 146 atom-centered grid for numerical integrations.

In Section 4.2, all calculations were performed with the Q-Chem 5 software.[174] The optimized geometries and wavefunctions were obtained at the ωB97X-V/def2-TZVP level of theory. The results of applying the OSLO algorithm were produced using the IAO-AutoSAD (analytically) and TFVC[75] (numerically) AIM definitions with the Q-Chem 5 and APOST-3D[173] softwares, respectively. All numerical integrations were performed using a 40 × 146 atom-centered grid.

In Section 4.3, all KS-DFT calculations were performed with the Gaussian16 package.[171] The ωB97x-D/def2-TZVP level of theory was used on-top of the reported geometries, in exception of the $[NaBH_3]^-$ system which both geometry and level of theory used are the reported ones. The multireference CASSCF wavefunctions were evaluated with the pySCF1.7 software,[175] including the chemically-meaningful orbitals in the active space. The number of orbitals and electrons included in the active spaces for each system are specified in the main text (Section 4.3). OSs were extracted with the APOST-3D code,[173] using the TFVC[75] AIM definition and a 40 × 146 atom-centered grid for numerical integrations.

In Section 5.1, all KS-DFT calculations were performed with the Gaussian16 package.[171] The optimized geometries and wavefunctions were obtained at the BP86-D3BJ/def2-TZVPP level of theory. To build all EDA states with Gaussian16, we evaluated the wavefunctions of each dimer and its isolated fragments at the optimized and dimer geometries. The pseudostate (see details in Section 5.1) electronic structure was reconstructed using the the isolated fragments' MOs at the dimer geometry. This step was performed with a modified version of APOST-3D,[173] providing its electronic structure information in a formatted checkpoint (.fchk) file. Transformation of the formatted into unformatted (.chk) checkpoint file was achieved by using the unfchk tool from Gaussian16. Finally, its corresponding total energy was evaluated by reading with Gaussian16 the MOs from the created .chk file and use them as starting guess but forcing to skip the SCF procedure (SCF = (MAXCYCLE = -1) keyword in Gaussian16). Finally, the symmetry = none keyword was included in these calculations to avoid any atomic basis set position difference. IQA decompositions were also performed with APOST-3D, using the TFVC AIM definition.[75] For the production results, a 150 × 974 atom-centered grid was used to evaluate the one-electron integrals and a a 150 × 590 atom-centered grid for the two-electron ones. In all cases, the newly introduced zero-error scheme was applied to obtain the one-center two-electron energy terms (Coulomb and HF-type exchange).

In Section 5.2, all calculations were performed with the Gaussian09 package.[176] The optimized geometries and wavefunctions were evaluated at the Hartree-Fock, and the BP86 and B3LYP KS-DFT levels of theory coupled with the cc-pVTZ full electron basis set. IQA decompositions were performed with the APOST-3D code,[173] using the TFVC[75] AIM definition and a 150 × 590 atom-centered grid for numerical integrations. In all cases, the newly introduced zero-error scheme was applied to obtain the one-center two-electron energy terms (Coulomb and HF-type exchange).

In Section 6.1, all calculations were performed with the Q-Chem 4 software.[177] The optimized geometries, wavefunctions and orbital localizations were obtained at the ωB97X-V/def2-TZVP level of theory. The LOBA results were produced using PM LOs in conjunction with the Löwdin[59] AIM definition for the atomic populations. EOS analysis was performed with the APOST-3D code,[173] using the TFVC[75] AIM definition and a 40 × 146 atom-centered grid for numerical integrations.

In Section 6.2, all calculations were performed with the Gaussian09 package.[176] The geometries were obtained at the BP86-D3BJ/TZVP level of theory, using the SDD pseudopotential for heavy atoms. Frequency calculations at the same level was performed to calculate the unscaled zero-point energies (ZPEs) as well as thermal corrections and entropy effects at 25 °C. On top of the optimized geometries, we performed single-point energy calculations at the M06/cc-pVTZ level, and solvent effects were estimated with the polarizable continuum model (PCM), using dichloromethane as solvent. The reported Gibbs free energies include

M06/cc-pVTZ SDD//BP86/TZVP SDD electronic energies with solvent effects obtained at the same level of theory, corrected with zero-point energies, thermal corrections and entropy effects evaluated at 25 °C at the BP86/TZVP SDD level. EOS analysis was performed with the APOST-3D code,[173] using the TFVC[75] AIM definition and a 40 × 146 atom-centered grid for numerical integrations.

In Section 6.3, all calculations were performed with the Gaussian16 package.[171] The optimized geometries and wavefunctions were obtained at the B3LYP-D3BJ/def2-TZVPP level of theory. Normal mode analysis was computed to confirm minima on the potential energy surface, and to extract the unscaled ZPE as well as thermal corrections and entropy effects using the standard statistical-mechanics relationships for an ideal gas. EOS analysis was performed with the APOST-3D code,[173] using the TFVC[75] AIM definition and a 40 × 146 atom-centered grid for numerical integrations.

In Section 6.4, all KS-DFT calculations were performed with the Gaussian16 package.[171] The geometries and electronic energies of all species were obtained using a series of KS-DFT functionals, namely BP86, B3LYP, PBE0, M06-2X, and ωB97x-D. The geometries were evaluated at the KS-DFT/def2-SVP level, and the electronic energies were extracted using the (larger) def2-TZVPP basis set, including dispersion corrections (D3BJ) when possible. For the singlet open-shell solutions, the spin-contaminated electronic energies were corrected using the (vertical) triplet spin-state solutions and applying the spin-contamination correction proposed by Yamaguchi.[178] On top of the B3LYP-D3(BJ)/def2-SVP geometries, we performed single-point multiconfigurational calculations at the CASSCF/cc-pVDZ level, and including within the active space the chemically relevant orbitals. In particular, the active space size consists on 10 electrons distributed within 10 active orbitals for the NHC-substituted compounds, or 10 electrons within 8 active orbitals for the cAAC-substituted compounds, or 4 electrons within 8 active orbitals for the NacNac-substituted ones. The CASSCF calculations were performed with the pySCF1.7 package.[175] For the smallest systems (Mg-NHC^{Me}, Be-NHC^{Me}, Mg-cAAC^{Me} and Be-cAAC^{Me}), we optimized their geometries at the SS-CASPT2/cc-pVDZ level, using the cc-pVDZ-jkfit auxiliary basis set using the same active spaces. The SS-CASPT2 calculations were carried out with the BAGEL program.[179] Atom/fragment charges, bond orders, EOS and local spin analysis was performed with the APOST-3D code,[173] using the TFVC[75] AIM definition and a 40 × 146 atom-centered grid for numerical integrations. EDA with the natural orbitals for chemical valence (NOCV) were instead obtained with ADF 2019.103,[180] using the B3LYP-D3(BJ)/TZ2P level of theory and including scalar relativistic effects with the zeroth-order regular approximation (ZORA).

We implemented the developed chemical bonding methodologies, together with the monadic diagonalization (Subsection 3.2.1) and multipolar approach (Subsection 3.2.2), within the inhouse developed APOST-3D code,[173] in exception of the OSLO algorithm that also was implemented within the Q-Chem 5 software.[174]

Chapter 4

On the development of methods to elucidate oxidation states

4.1 Can we safely obtain formal oxidation states from centroids of localized orbitals?

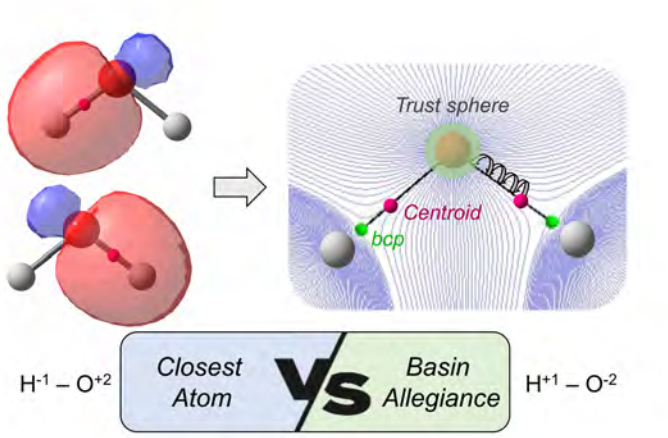

Published in: Gimferrer, M.; Comas-Vilà G.; Salvador, P. *Molecules* **2020**, 25, 234.

Abstract: The use of centroids of localized orbitals as a method to derive oxidation states (OS) from first-principles is critically analyzed. We explore the performance of the closest-atom distance criterion to assign electrons for a number of challenging systems, including high-valent transition metal compounds, π-adducts, and transition metal (TM) carbenes. Here, we also introduce a mixed approach that combines the position of the centroids with Bader's atomic basins as an alternative criterion for electron assignment. The closest-atom criterion performs reasonably well for the challenging systems, but wrongly considers O-H and N-H bonds as hydrides. The new criterion fixes this problem, but underperforms in the case of TM carbenes. Moreover, the OS assignment in dubious cases exhibit undesirable dependence on the particular choice for orbital localization.

molecules

MDPI

Article

Can We Safely Obtain Formal Oxidation States from Centroids of Localized Orbitals?

Martí Gimferrer, Gerard Comas-Vilà and Pedro Salvador *

Departament de Química and Institut de Química Computacional i Catàlisi, Universitat de Girona, Maria Aurèlia Capmany 69, 17003 Girona, Spain; mgimferrer18@gmail.com (M.G.); gerard.comas7@gmail.com (G.C.-V.)
* Correspondence: pedro.salvador@udg.edu; Tel.: +34-972418358

Academic Editors: Diego Andrada and Israel Fernández
Received: 5 December 2019; Accepted: 2 January 2020; Published: 6 January 2020

Abstract: The use of centroids of localized orbitals as a method to derive oxidation states (OS) from first-principles is critically analyzed. We explore the performance of the closest-atom distance criterion to assign electrons for a number of challenging systems, including high-valent transition metal compounds, π-adducts, and transition metal (TM) carbenes. Here, we also introduce a mixed approach that combines the position of the centroids with Bader's atomic basins as an alternative criterion for electron assignment. The closest-atom criterion performs reasonably well for the challenging systems, but wrongly considers O-H and N-H bonds as hydrides. The new criterion fixes this problem, but underperforms in the case of TM carbenes. Moreover, the OS assignment in dubious cases exhibit undesirable dependence on the particular choice for orbital localization.

Keywords: oxidation states; localized orbitals; metal carbenes; wavefunction analysis

1. Introduction

Heuristic concepts play a key role in chemical knowledge. By the time quantum mechanics was readily applicable to chemical systems, there was already a vast amount of chemical information that had been gathered and systematized over decades according to some constructs. It should not be a surprise that most of these chemical concepts are not observable in a strict quantum mechanical sense (hence, they have no few detractors claiming its inherent arbitrariness). Still, they have undoubtedly proven very useful for shedding light into chemical phenomena and more importantly, for achieving true predictions (i.e., without actually performing an experiment or even a computational exercise). Often, the problem of a chemical concept arises when it comes to its quantification as recently stressed by Grunenberg [1]. For instance, there are a myriad of aromaticity indicators or different realizations to compute bond orders that may sometimes lead to different interpretations emerging from the same input. There is, however, a concept of utmost relevance in chemistry, whose flaw was actually the lack of a well-established definition, namely the oxidation state (OS).

For years, the assignment of oxidation states was performed according to a set of "agreed upon" rules, but no explicit definition of the concept was given. Recently, the entry of OS on IUPAC's Gold Book has been modified to include a new generic definition following the recommendations of a task group lead by Prof. Karen [2,3]. The current OS definition reads "the atom's charge after ionic approximation of its heteronuclear bonds", while bonds between atoms of the same element must always be divided equally. In addition, back-of-the-envelope algorithms applicable to molecules and solids were provided. For instance, in the case of molecular systems, the so-called algorithm of assigning bonds starts by establishing the appropriate Lewis structure of the molecule. Then, the electron pairs between two bonded atoms are assigned to the more electronegative one according to Allen's scale [4], which represents the easiest application of the ionic approximation. Such a simple recipe works pretty well in most cases.

The current definition of OS is much more satisfactory than the previous set of agreed upon rules, and clearly represents an improvement. Moreover, a number of spectroscopic techniques and detailed information about the geometrical arrangement of the atoms are indirect experimental probes of the oxidation states (in the former case, referred as spectroscopic oxidation state). Yet, several recent works have exposed some intrinsic limitations of the ionic approximation [5,6]. Postils et al. [5] concluded that, in π-adducts, the local spin state of the π-system determines its formal charge, and concomitantly that of the TM. The cycloheptatryenil (C_7H_7) moiety can be found on his π-system as formally (+1) or (−3), fulfilling Hückel's rule, but also (−1) if it appears in triplet state, following instead Baird's rule. The case of transition metal (TM) carbenes is also illustrative [7]. Since carbon is more electronegative than the TM, the carbene moiety should keep all four electrons involved in the double-bond, reaching a formal charge of (−2). Thus, the straight application of IUPAC's rule naturally accounts for the nucleophilic Schrock-type carbenes. On the contrary, Fischer-type carbenes are typically depicted by a carbene unit keeping the σ electron pair and the TM keeping the π electron pair. Notice that such view cannot be reconciled with IUPAC's winner-takes-it-all rule, so that discerning Fischer or Schrock character from an OS perspective calls for approaches beyond IUPAC's ionic approximation.

Most of the ambiguities and caveats in IUPAC's scheme originate from the inability of atomic electronegativity scales to account for the different chemical environment of atoms within the molecule. On the other hand, the OS must be connected to the electron distribution around the atoms, which can be pretty well described with contemporary electronic structure methods. In our opinion, computational chemistry can and should have a major role in establishing oxidation states, particularly in those difficult cases where subtle details of the electronic structure are most relevant. While it is well-known that partial atomic charges do not match with OS (particularly for high-valent species), there is a generalized misconception that they still represent a sort of non-integer version of OS. One can still find vivid discussions in the literature on the basis of partial atomic charges or atomic spin populations computed one way or another [8–12].

When extracting chemical information from wavefunction analysis, one should clearly distinguish the function that is scrutinized from the method chosen to perform the analysis. The latter, in most analyses, refers to how atoms are identified within the molecule, which is essential in the assignation of the OS. In the so-called Hilbert-space analyses, the linear combination of atomic orbital approach to generate the molecular orbitals (LCAO-MO) framework is exploited to collect atomic contributions. When the density function is the one-electron density $\rho(\mathbf{r})$ and the atomic orbitals used are those of the underlying one-electron basis set, the well-known Mulliken [13] population analysis is recovered. Orthonormalized atomic orbitals such as those provided by Löwdin orthogonalization [14], Weinhold's natural orbitals [15], or Ruedenberg's quasiatomic orbitals [16] lead to more robust atomic populations (i.e., less dependent on the one-electron basis set choice). On the other hand, in real-space analyses the atoms are identified by a region of the three-dimensional physical space, that may be disjoint like in Bader's quantum theory of atoms in molecules (QTAIM) [17], or overlapping, like in the different flavors of Hirshfeld-type approaches [18]. Real-space analyses are very robust with respect to basis set but still bear the burden of arbitrariness. We do not consider one approach conceptually better than another. In fact, a link has been found between Hilbert-space and real-space analyses by means of a particular set of atomic orbitals, the so-called Mayer's effective atomic orbitals (eff-AOs) [19,20]. The recipe is simple: (i) Pick a real-space atomic definition such as Hirshfeld's approach, and obtain the corresponding numerical eff-AOs in that framework; (ii) Expand the original wave function in terms of these eff-AOs and perform a Mulliken-type analysis of the electron density. The original Hirshfeld's atomic populations will be exactly recovered [20,21]. Such a numerical exercise evidences that there is nothing fundamentally flawed with Mulliken's approach, it all depends on the underlying basis set used for the analysis. On the other hand, partial atomic charges account by definition for the average number of electrons associated to each atom, while by its actual definition the OS is not any average quantity. In our opinion, one does not need a more suitable or tailored atom-in-molecule definition for

population analysis when it comes to OS prediction with computational methods, but to figure out a scheme that overcomes population analysis and fits more faithfully with the concept of OS.

Oddly, little attention has been paid to the few computational schemes going beyond the use of conventional population analyses [22–29], while most of them render a very good mapping with the revised IUPAC definition of OS. These OS-oriented methods have in common the fact that they treat electrons individually (or by pairs, in the case of pure singlet states), and then apply one or another strategy to assign individual electrons to atoms, or directly to ligands/molecular fragments. For instance, Ramos-Cordoba et al. [29] introduced some years ago a scheme that is formally applicable on equal footing to any molecular system and wavefunction (e.g., singlet-determinant or correlated, using atomic basis functions or plane-waves). The so-called effective oxidation state (EOS) analysis relies on the abovementioned Mayer's effective orbitals and their occupation numbers, obtained for all fragments/ligands defined (EFOs). The spin-resolved EFOs are sorted by decreasing occupation number and then individual electrons are assigned to those EFOs with higher occupations, leading to an effective configuration of the atoms/ligands within the molecule, which directly determines their OS. Moreover, the difference between the occupation number of the last occupied and the first unoccupied EFOs is also a pointer of the reliability of the resulting analysis. They are used to derive the index *R*, that ranges from 50% (worst case scenario, with frontier EFOs degenerated in occupancy) to 100%. The larger its value the better the current electron distribution can be pictured into a discrete ionic model.

Alternatively, there are other approaches that are rooted in the use of localized orbitals [23,24,28]. It is well-known that for single-determinant wavefunctions one can perform unitary transformations to the canonical orbitals of the occupied space that leave the wavefunction unchanged (up to an unimportant phase factor), in such a way that the resulting orbitals appear more localized according to some criterion. Localization schemes are, of course, not unique. Boys [30], Edminston-Ruedenberg (ER) [31], Pipek-Mezey (PM) [32], and most recent improved formulations [27] produce localized orbitals by minimizing some atomic spread functional. A somewhat different strategy is used in the natural bond orbital (NBO) framework [14], aiming at sequentially finding one- and two-center localized orbitals that most closely represent the Lewis structure of the molecule. While the NBOs are not strictly doubly-occupied (i.e., do not span the occupied space), the exact doubly-occupancy can be restored leading to the so-called natural localized molecular orbitals (NLMOs) [33].

Thom et al. showed that combining orbital localization schemes with population analysis can lead to an efficient assignment of OS [23]. In their localized orbital bonding analysis (LOBA) scheme, the authors first apply an orbital localization (they seem to prefer ER but also use PM or even NBOs) and then perform a population analysis (Mulliken or Löwdin) on each individual localized orbital to determine in which atom the electron (pair) is localized above a given threshold. The LOBA scheme represents a nice computational mapping of IUPAC's algorithm of assigning bonds. The scheme proved to be quite robust, but little use has been made of it. Moreover, there are too many choices to be made (localization procedure, population scheme and cutoff threshold) in order to apply it.

Some of these degrees of freedom are eliminated in the strategy first put forward by Sit et al. [24] and later applied by Vidossich et al. [28]. Sit et al. used maximally localized Wannier functions (MLWFs) [34] as localized orbitals in the framework of plane-waves calculations and obtained the corresponding centroids (Wannier centers). Then, they simply used the position of the centroid to assign the associated electron (pair) to the closest atom. Since MLWFs reduce to the Boys localized orbitals of isolated molecules [34], the same scheme can be applied with computational codes using atomic basis sets. In that case, Vidossich et al. relied on PM localized orbitals, as they allow for σ and π separation.

Using centroids of localized orbitals to assign OS is very appealing because of its simplicity and, more importantly, because it represents a common framework that can be used indistinctly for molecules and in solid-state. Their use is also gaining recent attention. It has been shown that following the trajectory of the centroids along a chemical reaction allows to recover the curly arrow picture of

Robinson [35] from first principles [36–39]. Previous results indicated that they can be readily used to predict OS, but in our opinion this methodology has not yet been fully tested.

The aim of this work is to critically assess to which extent the centroids of localized orbitals combined with a distance criterion can be used as an all-purpose scheme to derive OS in molecular systems. We also introduce and test an alternative criterion to assign electrons to centers that makes use of Bader's topological atoms. atomic basins. We use both NLMO and PM for comparison in selected cases. The performance of these two approaches is compared with that of EOS analysis.

2. Results and Discussion

Let us first consider the series XH_n, where X = Li to Cl. The results obtained are gathered on Table 1. In this case, there is only one localized orbital whose centroid lies between centers X and H, which of course corresponds to a σ bond between X and H. The remaining localized orbitals correspond to core or lone pairs of X. The position of the centroid determines the ratio $C_X = (R_H - R_X)/(R_H + R_X)$ where R_H and R_X indicate the distance between the centroid and the corresponding center. Negative values of the ratio indicate a hydride character and positive values indicate proton. On the other hand, the ratio χ_X/χ_H of Allen's electronegativity values also discriminate hydride ($\chi_X/\chi_H < 1$) from proton ($\chi_X/\chi_H > 1$) character according to IUPAC's ionic approximation.

One can immediately see that the simplest closest-atom (CA) criterion to assign the electron pair leads in all cases to a formal (−1) charge on the H atom, the only exception being hydrogen fluoride. That is, C_X values are systematically negative. This result is clearly unsatisfactory, as the simplest H_2O would be described as a hydride. The same trends are observed using PM or NLMOs. The C_X values tend to increase (become less negative) along the period and decrease (more negative) along the group, suggesting a relationship with the relative electronegativities of the atoms. In Figure 1, we plot C_X values obtained with both localization schemes vs. the ratio χ_X/χ_H. The correlation is excellent ($r^2 = 0.97$), but most of the data points associated with proton character according to electronegative are predicted as hydride with the CA criterion. The excellent correlation does indicate that Allen's electronegativities could be used to correct for the relative atomic size when using the CA criterion.

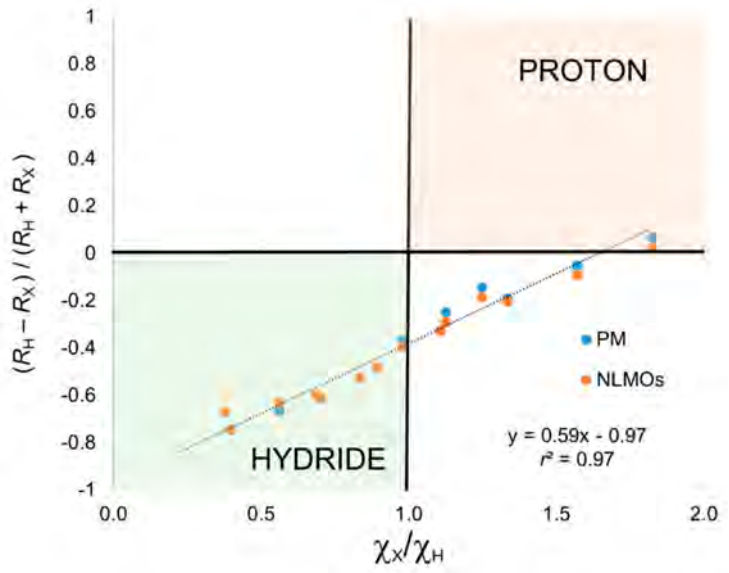

Figure 1. Centroid position (see text) versus electronegativity ratio for the XH_n set. OS assignment using closest-atom criterion.

Table 1. Structural and electronic parameters of the hydrides studied, including Allen's electronegativity (EN), bond distance, EFO occupancy, distance to the centroid (computed using the PM and NLMO localized orbitals) and distance to the bond critical point (R_{bcp}-H).

Molecule	Atom	χ_X/χ_H	EFO occ. λ_X	R_X (PM)	R_X (NLMO)	R_{bcp}-H
LiH	Li H	0.397	0.112 0.824	1.403 0.205	1.401 0.206	0.886
BeH_2	Be H	0.685	0.178 0.788	1.074 0.270	1.072 0.271	0.766
BH_3	B H	0.892	0.195 0.710	0.888 0.312	0.887 0.312	0.669
CH_4	C H	1.106	0.391 0.429	0.727 0.370	0.727 0.371	0.395
NH_3	N H	1.333	0.588 0.278	0.609 0.416	0.615 0.408	0.278
H_2O	O H	1.570	0.729 0.179	0.511 0.462	0.530 0.442	0.200
HF	F H	1.823	0.836 0.122	0.435 0.498	0.455 0.478	0.159
NaH	Na H	0.378	0.170 0.760	1.585 0.313	1.582 0.316	0.892
MgH_2	Mg H	0.562	0.233 0.760	1.427 0.287	1.397 0.318	0.833
AlH_3	Al H	0.701	0.249 0.746	1.284 0.309	1.281 0.312	0.792
SiH_4	Si H	0.833	0.234 0.713	1.139 0.353	1.136 0.356	0.758
PH_3	P H	0.980	0.183 0.653	0.977 0.454	0.998 0.433	0.720
H_2S	S H	1.126	0.427 0.439	0.845 0.508	0.871 0.482	0.479
HCl	Cl H	1.247	0.604 0.307	0.738 0.553	0.765 0.526	0.365

However, we believe that introducing electronegativity values in the model would eventually lead to the same problems observed when applying ionic approximation, namely all X-Y bonds would be treated in equal fashion, disregarding their chemical environment. At this point, we decided to explore a different avenue and abandon the CA criterion. Instead, we borrow a key ingredient of Bader's quantum theory of atoms in molecules (QTAIM), namely the atomic basin. Thus, rather than relying in the distance to a given center, we simply determine which atomic basin the centroid of the bond localized orbital belongs to. This alternative criterion would have some advantages. First of all, the chemical environment of the atoms will be automatically considered, as QTAIM basins are not determined by the nature of the atom but by the electron density, $\rho(\mathbf{r})$. Moreover, the relative size of the atomic basins is related to the ionicity of the bond. Secondly, in QTAIM, one should not refer to atoms but to attractors—local maxima of $\rho(\mathbf{r})$. There are systems, especially in condensed phase but also in molecules, where an attractor of $\rho(\mathbf{r})$ is found away from the nuclear positions. These so-called non-nuclear attractors (NNAs) are a necessary but not sufficient indicator of electride character [40], which could be confirmed by a location of a centroid in its basin (Care must be taken in the case of spurious NNAs, observed for instance in acetylene with some basis sets). Thus, associating the

centroid of the localized orbitals to attractor basins readily would incorporate the relative atomic size and environmental effects in the scheme, while introducing little additional arbitrariness.

This new criterion, henceforth basin-allegiance (BA), is incorporated as follows. First of all, we determine the atomic trust sphere for all atoms of the molecule, as described by Rodriguez et al. [41]. Any point inside a sphere is unambiguously assigned to the corresponding attractor. When a given centroid of localized orbital lies outside the spheres (usually associated to a bond localized orbital), the steepest-ascent path is followed until it reaches a trust sphere. We use both the gradient and the Hessian of the density with a reduced step in all points along the iterative process to ensure a faithful steepest-ascent path.

The results obtained using the BA criterion are also gathered in Table 1. Now, the hydrogen centers in H_2O, NH_3, H_2S, and HCl are predicted to have proton character as expected. In the case of H_2S the position of the centroid is extremely close to the bond critical point (*bcp*). It is worth mentioning that we previously observed that the shape of the atomic basins in H_2S can rather significantly depend on the level of theory used to compute $\rho(\mathbf{r})$. Thus, BA behaves essentially in agreement with the electronegativity ratio, with the exception of CH_4 for which OS have hardly any significance. To further illustrate this point, we depict in Figure 2 the distance of the centroid to the *bcp* versus the electronegativity ratio. In full analogy with Figure 1 for the CA criterion, negative values of the distance indicate that the centroid lies within the H attractor, whereas positive values indicate it belongs to the X atom basin. The correlation is again very good, and in this case all data points (except CH_4) lie in the right quadrants for hydride and proton character. Thus, introducing the BA criterion clearly improve the results for these systems while adding little extra complexity to the scheme.

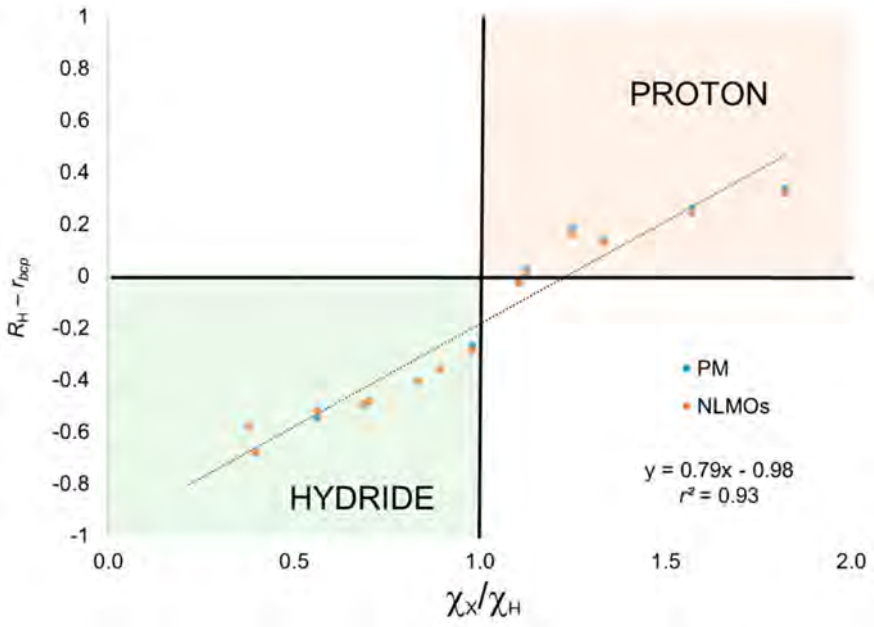

Figure 2. Centroid position relative to the bond critical point (see text) versus electronegativity ratio for the XH_n set. OS assignment using basin-allegiance criterion.

We have also applied EOS analysis to these systems for comparison. In this case, it is the occupation number (λ) of the EFOs of H and X that originate from the formal breaking of the H-X bond that lead to hydride ($\lambda_H > \lambda_X$) or proton ($\lambda_H < \lambda_X$) character. The ratio $(\lambda_H - \lambda_X)/(\lambda_H + \lambda_X)$ also correlates fairly well with χ_X/χ_H, as shown in Figure 3, but not as good as in the previous cases. One can easily see that EOS analysis is also able to discriminate hydride and proton character according to the electronegativity ratio, with the only exception of H_2S and again CH_4. The frontier EFOs are almost degenerate in these two examples, indicating a very unpolarized bond, and hence a very poor description of the electron distribution by any ionic model.

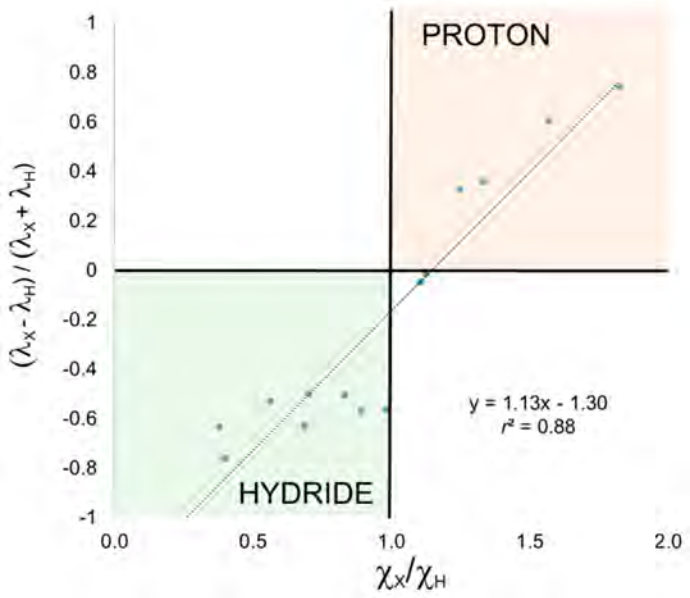

Figure 3. Relative occupation of frontier EFOs versus electronegativity ratio for the XH_n set and OS assignment using EOS analysis.

Recently, Postils et al. [5] applied EOS analysis to a set of over a hundred molecular systems. Most of them were included in the IUPAC reports for being either particularly challenging or ambiguous, but the set also included a number of additional examples including π-adducts, high-valent compounds and TM carbenes. The EOS method performed extremely well, even in really intricate bonding situations. In this work, we decided the analyze the performance of the method based upon orbital localization, using both the CA and the just introduced BA criteria for electron assignment, for some particularly relevant examples. When dealing with TM complexes or relatively large systems, it is usually of interest to determine the OS or formal charge of the ligands or molecular fragments as a whole. This is a key point in EOS analysis, where ligands/fragments are defined beforehand. When using centroids of localized orbitals this is not the case, as each individual atom accommodates a number of electrons according to one or another criterion. The formal charge or OS of a given ligand is simply obtained as the sum of the OS over all its atoms.

Let us consider first the rather simple $(CH_3)_3NO$ molecule. In order to fulfill the octet rule for N, a single bond between formal N(+) and O(−) is assumed as the dominant Lewis structure. Then, applying the ionic approximation one assign the two electrons of the σ N-O bond to the O atom, and all N-C bond electrons to the N atom, resulting in oxidation states of (−2) for O, (−1) for N and three CH_3 units being formally (+1). Both PM and NLMOs point towards the aforementioned Lewis structure, showing a single σ-type N-O localized orbital. No localized orbital corresponding to a N-O π bond is found and, instead, the O moiety bears two p-type lone-pairs. However, as sketched in Figure 4, the centroid of the σ orbital is closer to N than to O atom, and it lies within the atomic basin of N. Thus, for both CA and BA criteria the electron pair corresponding to the N-O σ bond should be assigned to N, leading to a final formal OS of (0) for O and (−3) for N. It is remarkable that the same alternative assignment was obtained using EOS analysis for the same level of theory, and even for a multireference wave function [5]. It appears that the actual electronic structure of this molecule is at odds with the straightforward application of the ionic approximation.

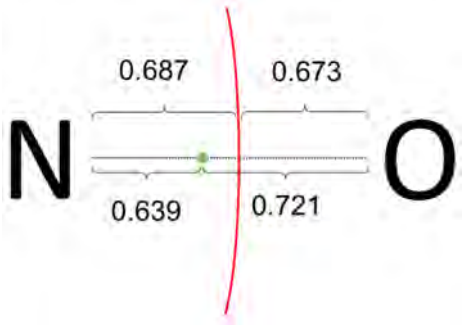

Figure 4. Pictorial representation of the zero-flux surface and position of the centroid of the NLMO σ N-O orbital for $(CH3)_3NO$. In the case of PM, the distances from the centroid to N and O are 0.660 and 0.692 (in Å).

We have also considered a series of highly-valent TM oxides, namely $Ti^{(IV)}O_2$, $Fe^{(VI)}O_4^{2-}$, $Re^{(VII)}O_4^{-}$, $Os^{(VIII)}O_4$, $Ir^{(IX)}O_4^{+}$, and $Pt^{(X)}O_4^{2+}$. EOS analysis performed very well for these systems [5], yielding OS in agreement with the formal values up to (+9) for Ir in IrO_4^{+} cation [42]. In the case of $Pt^{(X)}O_4^{2+}$, the occupation of the EFO on Pt was too large to be considered empty, so EOS analysis didn't yield the presumed (+10) oxidation state for this metastable cation [43]. Hence, it is interesting to test the performance of both CA and BA schemes. Since both PM and NLMOs were performing very similarly and we encounter some technical difficulties converging PM localized orbitals for such symmetric systems, we discuss only the results obtained with NLMOs. In all cases, the centroids of localized orbitals corresponding to π bonding between O and the TM were very close to the O atom, indicating almost lone-pair character. The electron pairs under dispute are those of the σ bonds between TM and O.

In Figure 5 we depict these localized orbitals together with the position of the centroid and the corresponding *bcp* of the density. It can be readily seen that, except for $Pt^{(X)}O_4^{2+}$ cation, the centroid of the σ localized orbital is located between the O atom and the *bcp*. It is closer to the O than to the TM, and therefore both CA and BA criteria yield the expected (−2) OS for the O atoms. This assignment becomes less and less clear cut when going to higher valent compounds. In the case of $Ir^{(IX)}O_4^{+}$ (Figure 5e), while the centroid is still much closer to O (0.931 Å) than to Ir (0.757 Å), it lies very close to the zero-flux surface, ca. 0.003 Å away from the *bcp*. Still, the centroid lies within the atomic basin of O, but one cannot rule out than with a different localization scheme or level of theory the BA assignation could be reversed.

In the case of $Pt^{(X)}O_4^{2+}$ cation, neither CA or BA criteria predict the presumed (+10) value. First of all, it is worth to point out that the NLMO procedure yielded three very similar Pt-O localized orbitals (Figure 5f) and a fourth one slightly different (Figure 5g). In the former, the centroids were still located closer to O (ca. 0.815 Å) than to Pt (0.894 Å), but already within the basin of Ir, as indicated by the position of the *bcp* in the Figure 5. Therefore, the CA and BA criteria differ in these bonds, yielding different OS assignations. Finally, the last NLMO associated to a Pt-O σ bond is even more polarized towards Pt and its centroid is closer to Pt (and well within Ir basin). All in all, the CA criterion assigns (+8) to Pt, with one the O atoms as (0). With the BA criterion, all O atoms are neutral (0), so Pt is assigned a rather unrealistic (+2) OS.

The OS assignment in π-adducts can be also problematic in some cases. In this case, the aromaticity of the π-ligand plays a key role, and usually determines the formal charge on the TM. For instance, the C_5H_5 moiety is considered as anionic with a formal charge of (−1), thus holding 6π electrons and becoming a Hückel aromatic cyclopentadienyl. In the case of C_7H_7 the situation is ambiguous, as both formal charges of (+1) and (−3), accommodating 6π and 10π electrons, are Hückel aromatic and therefore both are plausible. Moreover, Postils et al. recognized that when the π-ligand exhibited some local spin (e.g., triplet character), the OS assignment driven by aromaticity should be (−1), as in the

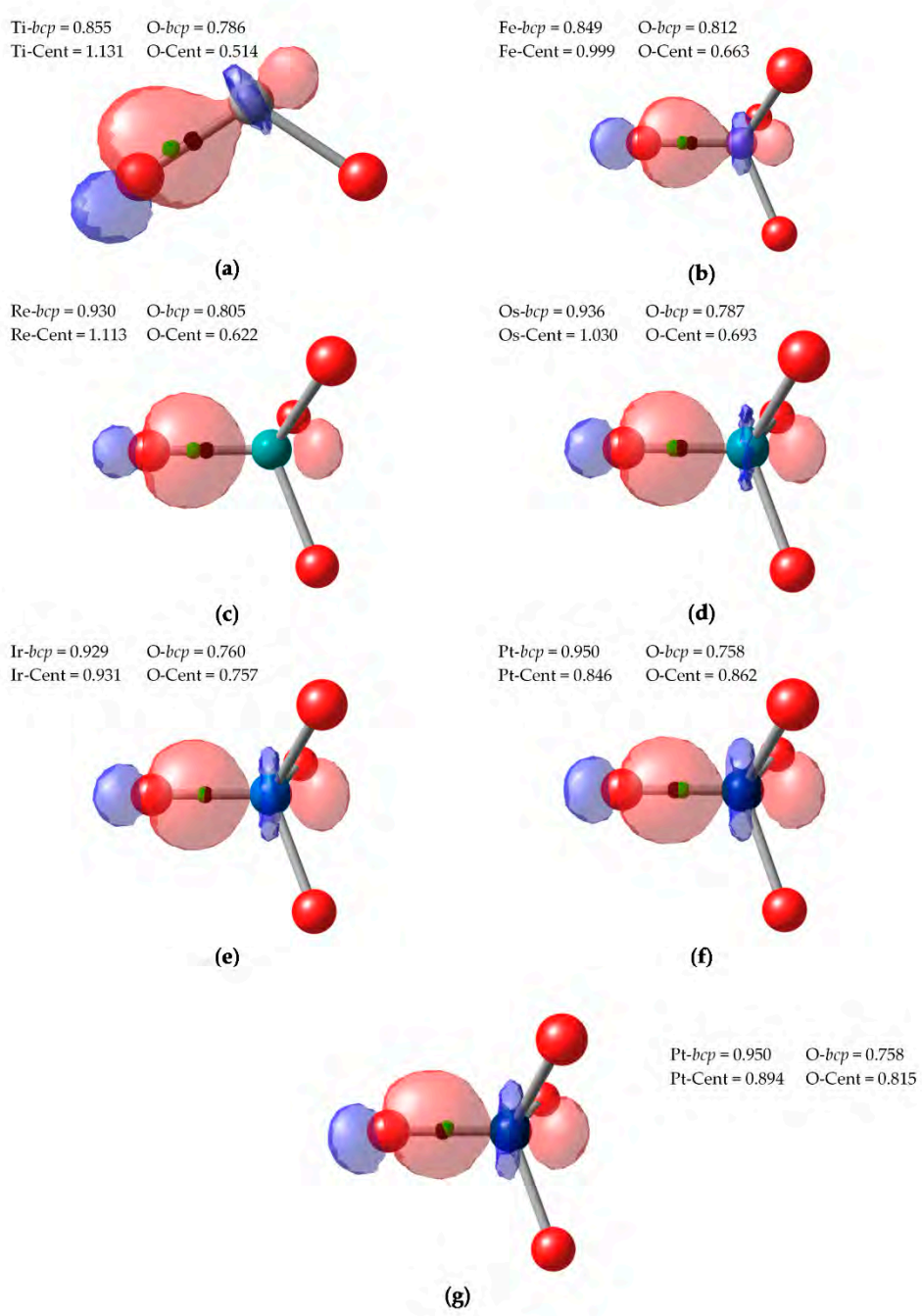

Figure 5. TM-O σ-type NLMO isocontour plot (0.1) for TiO_2 (**a**), FeO_4^{2-} (**b**), ReO_4^- (**c**), OsO_4 (**d**), IrO_4^+ (**e**) and PtO_4^{2+} (**f**,**g**). *bcp* and centroid represented by black and green dots, respectively. (distances in Å).

Let us see how the CA and BA schemes perform. We have carried out the analysis using NLMOs. for the three π-adducts $V(CO)_3(C_7H_7)$, $Mo(C_7H_7)(C_5H_5)$, and $Mn(C_7H_7)_2$. In the first case, there are four localized NLMOs that involve the π system of the ligand, as shown in Figure 6a. The centroids of the localized orbitals lie below the plane, as there is some contribution from the d-orbitals of the TM. In one of them, the contribution from the TM is so relevant that the centroid is pulled from the π-ligand (1.317 Å) on to the V center (0.957 Å), that keeps the electron pair applying both CA and BA criteria.

The remaining localized orbitals are associated to the ligand and the final OS assignment is neutral CO ligands, (−1) V and (+1) for the π-ligand. It is worth mentioning that, while (+1) is a plausible assignment for C_7H_7, this result differs from that obtained with EOS, leading to a (+3) V and a 10π aromatic (−3) C_7H_7 [5].

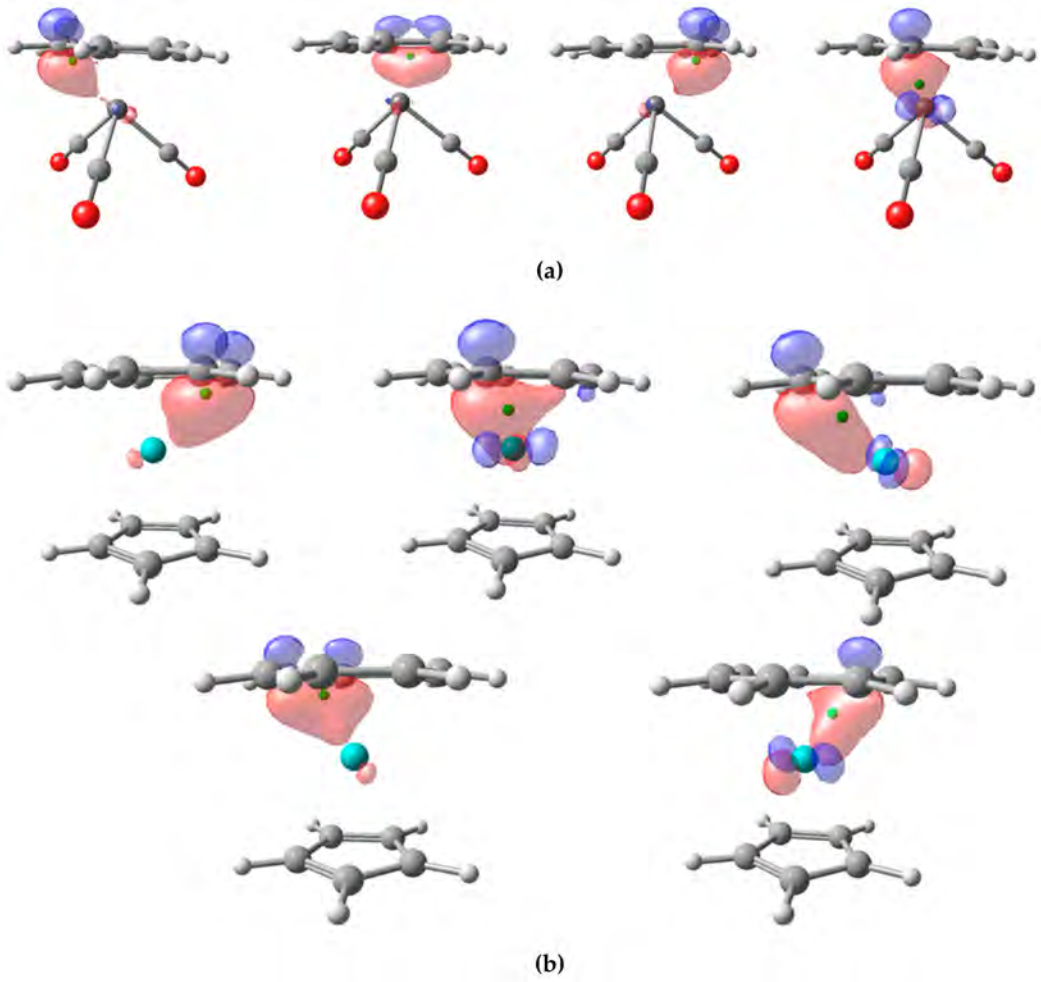

Figure 6. Isocontour plot (0.1) of NLMO localized on the C_7H_7 π-ligand for $V(CO)_3(C_7H_7)$ (**a**) and $Mo(C_7H_7)(C_5H_5)$ (**b**). Orbital centroid represented by green dots.

In $Mo(C_7H_7)(C_5H_5)$, the C_5H_5 moiety is readily considered as (−1) anionic for both CA and BA criteria, as could be anticipated. There are up to five localized orbitals with significant contribution from the C_7H_7 moiety, depicted in Figure 6b. Some of them exhibit significant contribution from the metal and their centroids appear way below the ring plane. The distances from the centroids to Mo center are 1.717Å, 1.712 Å, 1.264 Å, 1.248 Å, and 1.214 Å. In the last case (Figure 6b, bottom right), the distance between the centroid and the closest C atom of the ring is 1.080 Å, while the zero-flux surface is ca. 1.11Å from the C atom. Thus, all five centroids are closer to the C atoms of the π-ligand and into their atomic basins, leading to 10π electron C_7H_7 moiety with a formal OS of (−3), and consequently a Mo center with OS (+4). The same assignment is obtained with EOS analysis in this case [5].

The third test system is even more challenging. Here, two nonequivalent C_7H_7 rings are bound to a Mn atom. One of the C_7H_7 units exhibits noticeable deviation from planarity and its interaction with the TM could be described as η_3-type, as seen in Figure 7. The whole system is in a doublet state, but there is significant local spin on both the Mn and the ligands. Postils et al. found that, at this level of theory, the system is best described as two triplet C_7H_7 units antiferromagnetically coupled to a

high-spin d^5 Mn (+2) center. The EOS assignment of (−1) to the ligands was consistent with 8π Baird aromatic [44] rings in a triplet state (i.e., each ring bears three alpha and five beta π electrons) [5].

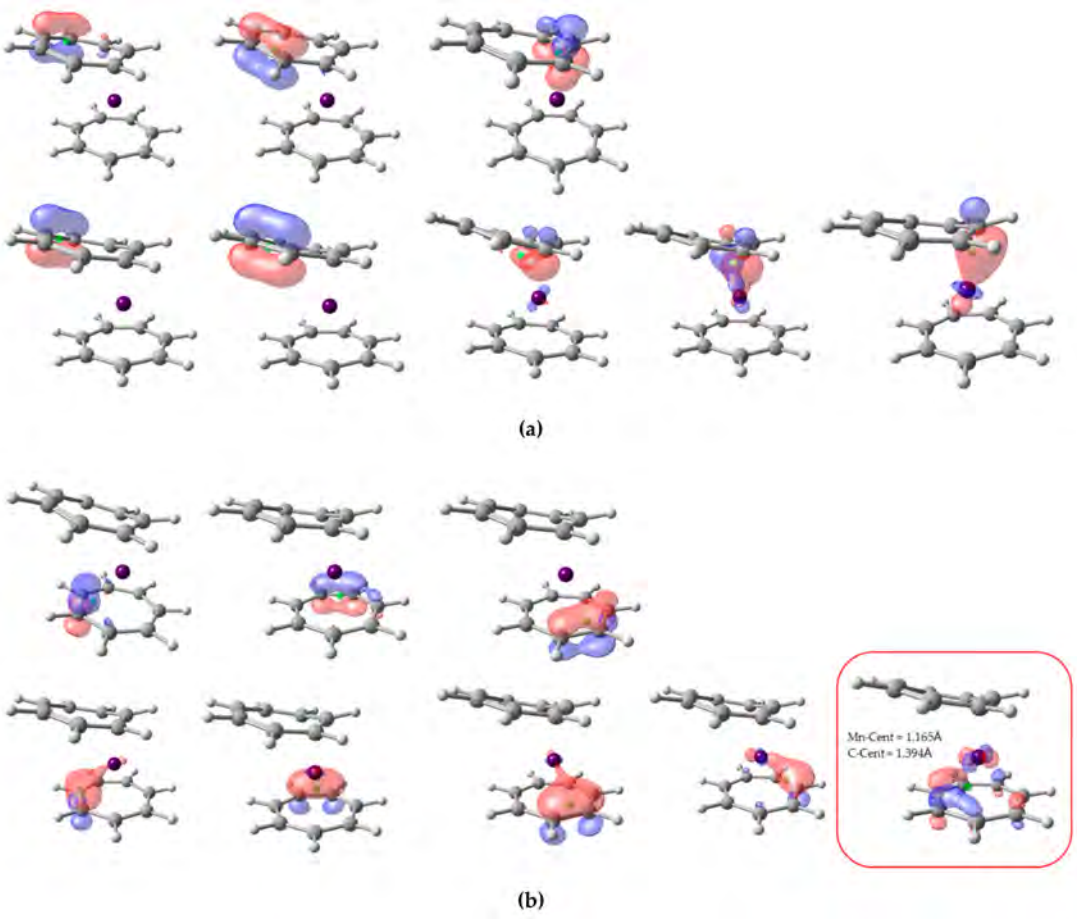

Figure 7. Isocontour plot (0.1) of NLMO localized on top (**a**) and bottom (**b**) π-ligands for $Mn(C_7H_7)_2$. In each case, top three orbitals correspond to alpha spin, and bottom five to beta spin. Orbital centroid represented by green dots.

The alpha and beta NLMOs involving the π-system of the ligands are sketched in Figure 7. For both ligands, there are three alpha and five beta orbitals. In the case of the top C_7H_7 ring (Figure 7a), all eight centroids lie much closer to the C atoms and also clearly within their atomic basins, so its OS is (+1), in line with the results of EOS analysis. However, in the bottom ring (actually the one that exhibits η_7-type coordination with the metal), the centroid of one beta NLMO is closer to the Mn (1.165 Å) than to the C (1.393 Å), and by virtue of the CA criterion is assigned to the metal. Careful inspection shows that the centroid is far from the C atoms but in fact very close to the plane containing the ligand (ca. 0.51 Å). So, considering the C_7H_7 ligand as a whole, the centroid could be associated to it. However, careful steepest-ascent path from the centroid leads to the basin of the Mn, so in this case both CA and BA criteria assign only seven π electrons to the second ligand, thus leading to a neutral OS and in consequence a (+1) Mn unit.

The last set of systems studied are the set of sixteen TM carbenes compiled by Occhipinti et al. [45] and depicted in Figure 8. The set includes four conventional W-based Fischer carbenes (1–4), five Schrock W- and Mo-based catalysts (5–9) and six Ru- and Os-based first- and second generation Grubbs catalysts (10–14) and precatalysts (15–16). We have applied both EOS analysis and CA and BA centroid-based schemes using PM and NLMOs. The key issue is to check the location of the centroids associated to the σ and π TM-carbene bonds (provided they are retrieved by the orbital localization procedure).

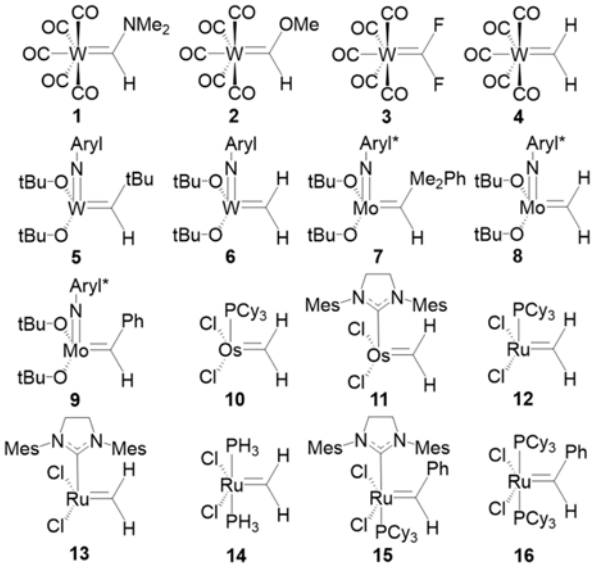

Figure 8. TM carbenes analyzed in this work. Abbreviation: Aryl = 2,6-diisopropylphenyl, Aryl* = 2,6-dimethylphenyl, Cy = cyclohexyl and Mes = mesityl.

In a Fischer carbene, the σ bond is expected to be polarized towards the carbene, while the π bond should have a large contribution from the TM, leading to a neutral (0) OS of the carbene unit. Again, it is worth remembering that such a picture cannot be derived from IUPAC's ionic approximation, which considers that all electrons of the bonds must be assigned to either one or another atom. This is the case one would expect for the more nucleophilic Schrock carbenes, with ionic character and a OS of (−2). On the other hand, Grubbs carbenes cannot be easily classified as Fischer or Schrock and, as matter of fact, Occhipinti et al. suggested that a new category of electrophilic Schrock carbenes [45].

The OS assignments for the set of TM carbenes are gathered on Table 2. The frontier EFOs and position of relevant orbital centroids and *bcp*s can be found in Supplementary Tables S4–S10. First of all, all three schemes assign the expected OS to the expectator ligands, namely neutral CO, NHC and phosphine ligands and anionic Cl (−1), tert-butoxide (−1) and phenylimido (−3) ligands (the OS of the TM is entirely determined by that of the ligands and will not be discussed). The only exception is for Grubbs catalyst 10 using NMLO combined with the BA criterion. Here, the σ bond of the phosphine ligand is assigned to the TM, leading to an unrealistic cationic (+2) phosphine.

According to EOS analysis, the OS of the carbene unit is either neutral (0) or anionic (−2) in all cases. The expected result is obtained for all TM carbenes predefined as Fischer or Schrock, with only one exception. In the case of Grubbs-type carbenes, the low *R* values, near 50% in some cases, indicate that the occupation number of the frontier EFOs on the TM and the carbene are almost degenerate, making the OS assignation uncertain. On the contrary, the OS assignment of the prototypical Schrock carbenes is clearer. In this case, the carbene unit keeps all four electrons of the bonds and becomes formally anionic (−2). These results can be easily visualized in Figure 9. Each molecule is represented by a point in the graph, and its position is determined by the difference of the occupation number of the σ (*x*-axis) and π (*y*-axis) EFOs of the TM and the carbene. Negative values indicate a larger occupation on the carbene.

Table 2. Formal OS for the carbene moiety (CR_1R_2) for the set of TM carbene compounds using centroids of localized orbitals (PM and NLMO) combined with CA and BA criteria and EOS analysis.

Molecule		CA		BA		EOS	*R* (%)
		PM	NLMO	PM	NLMO		
Fischer	1	0	0	0	0	0	67.8
	2	0	0	0	0	0	61.2
	3	0	0	0	0	0	59.2
	4	0	0	0	0	−2	56.9
Schrock	5	−2	−2	−2	−2	−2	72.0
	6	−2	−2	−2	−2	−2	74.1
	7	−2	−2	−2	−2	−2	64.1
	8	−2	−2	−2	0	−2	66.9
	9	−2	−2	−2	−2	−2	65.7
Grubbs	10	−2	+2	+2	+2 [a]	−2	51.5
	11	0	0	+2	+2	0	50.4
	12	0	+2	+2	+2	0	55.5
	13	0	+2	+2	+2	0	58.1
	14	0	+2	+2	+2	0	55.9
	15	0	0	+2	+2	0	62.4
	16	0	0	+2	+2	0	63.3

[a] Formal (+2) OS for the phosphine ligand was obtained.

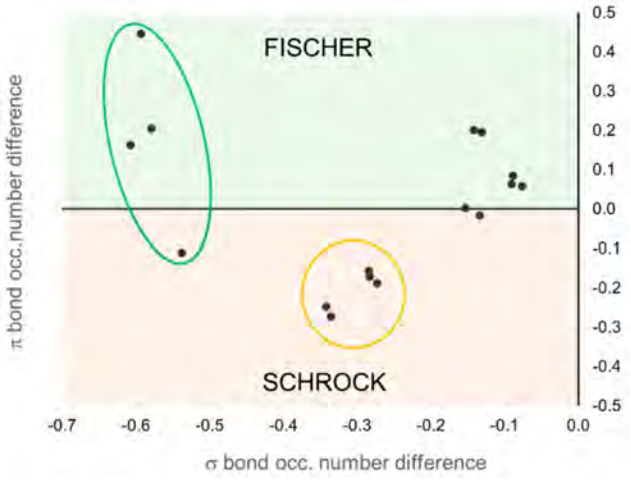

Figure 9. Classification of the TM carbenes according to the relative occupation number of the σ and π EFOs on the TM and the carbene moiety. Data points corresponding to 1–4 (green circle) and 5–9 (orange circle).

The occupation number of the EFOs associated to the σ bond is always larger for the carbene (negative values along *x*-axis), which keeps the σ electron pair. It is the relative occupation numbers of the EFOs associated to the π bonding that ultimately determines the OS. EFO occupation larger for the TM leads to positive values along the *y*-axis. This case corresponds to the typical picture of a Fischer carbene, with a neutral (0) OS. Negative values along the *y*-axis lead to the nucleophilic Schrock character. One can immediately see that the set of Grubbs carbenes are better described as Fisher carbenes (at least from the formal OS point of view), although some of them are right on the frontier. The first- and second-generation Grubbs precatalysts (molecules 15 and 16, respectively) are those with more pronounced Fisher character.

When using the centroids of localized orbitals, the relative occupation number of the EFOs can be replaced by appropriate distances (see Figure 10a) in order to obtain a graphical representation like that of Figure 9. When using the CA criterion, the σ and π bond distance indices used in Figure 10b

are given by the distance between the σ (red dot) and π (green dot) centroids to the midpoint of the TM-carbene bond. In the case of the BA criterion, the reference point becomes roughly the position of the *bcp*. Again, negative distances indicate that the electrons are assigned to the carbene moiety. For instance, Figure 10a illustrates the situation where both CA and BA criteria would be consistent with a Fischer-type neutral carbene. The green dot should be located to the right of the *bcp* in order for both approaches to predict a Schrock-type carbene. Having to consider two centroids at a time increases the risk of getting a different answer from CA and BA criteria, as is indeed the case.

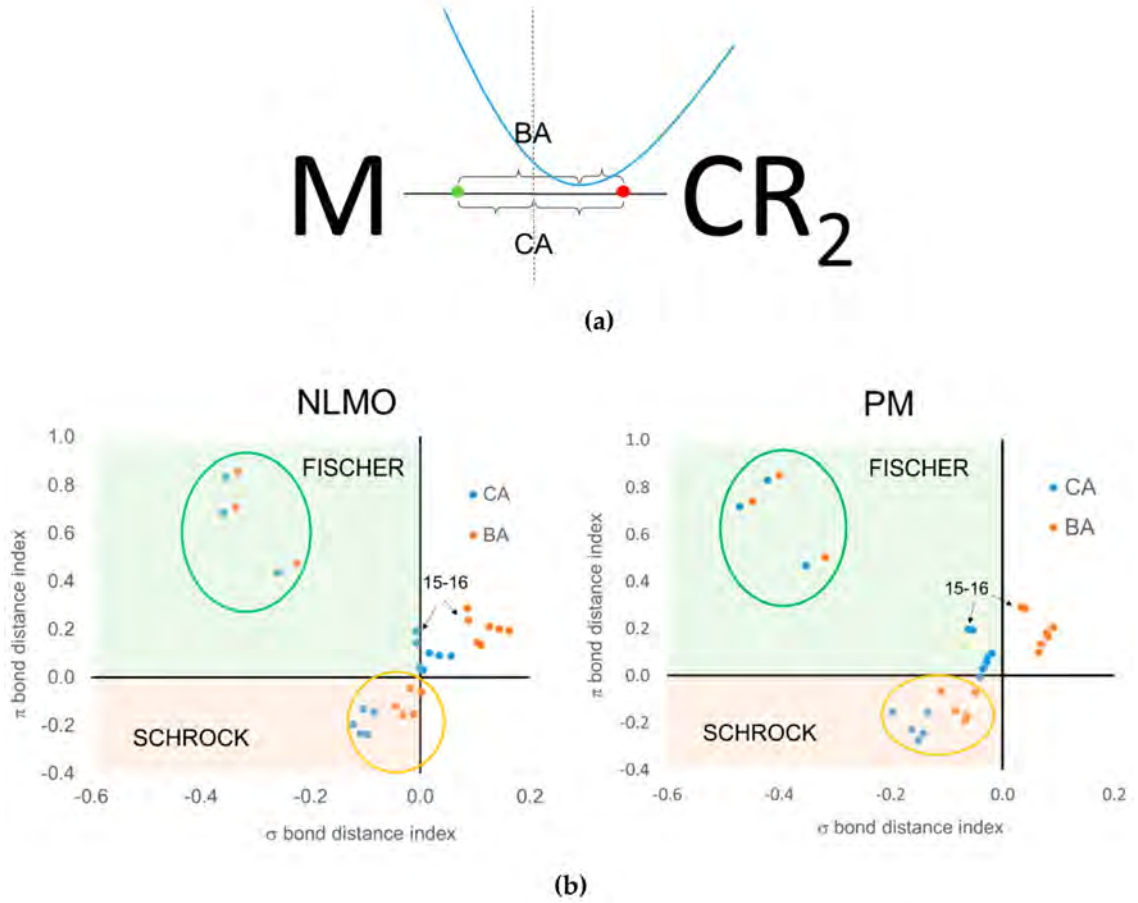

Figure 10. (**a**) Pictorial representation of a Fischer-type carbene, including the centroids of localized σ (red dot) and π (green dot) bond orbitals and relevant distances for CA (midpoint of the bond) and BA (*bcp*) criteria. (**b**) Classification of the TM carbenes according to the distance from the σ and π centroids to bond midpoint (CA) or *bcp* (BA). Data points corresponding to 1–4 (green circle) and 5–9 (orange circle).

Unfortunately, the results obtained using centroids of localized orbitals are not satisfactory for several reasons. First of all, one can see in Figure 10b that there are a number of data points corresponding to the Grubbs carbenes for which the σ bond distance index is positive, meaning that the σ electron pair is assigned to the TM rather than to the carbene. At the same time, the π bond distance index is also positive, leading to a hardly acceptable cationic (+2) carbene ligand. This wrong behavior is systematically observed when using the BA criterion, no matter the localized orbitals are PM or NLMO. The CA criterion does a better job for these systems, but the results are somewhat dependent on the orbital localization procedure used, particularly for Grubbs carbenes. With PM localization all data points can be associated to either Fischer or Schrock character, unlike with NLMOs. The behavior of both CA and BA criteria is nevertheless quite good for the prototypical Fischer and Schrock carbenes.

3. Materials and Methods

All calculations were performed with the Gaussian16 package (www.gaussian.com) [46]. Optimized structures and wave functions were determined at the B3LYP/cc-pVTZ level of theory, except for the sets of XH_n and TM carbenes, where BP86/def2-TZVP was used instead. PM localized orbitals were obtained using IOp(4/9) = 20212. NLMOs were produced using the NBO6 version [47]. The centroids of localized orbitals were determined by conventional multicenter numerical integration [48] using a 40 × 146 grid per atom with the in-house developed APOST-3D code [49]. The steepest-ascent algorithm from the centroid position to the corresponding attractor was implemented in APOST-3D. EOS analysis was also performed with APOST-3D, using the topological fuzzy Voronoi cells [50] real-space partitioning for the atomic definitions.

4. Conclusions

Finding robust schemes to assign OS from first principles is not a trivial task. The possibility of using centroids of localized orbitals is very attractive, as one could apply the same strategy for molecules and solids on equal footing. Our results, however, indicate that there is no straightforward general use of the centroids to obtain reliable OS. The simplest closest-atom criterion does a good job discriminating Fischer and Schrock carbenes and identifying high-valent species, but fails for the simplest case of H_2O. An alternative avenue introduced here for the first time consists on determining on which atomic basin each centroid is placed, and distribute the electrons among atoms/attractors accordingly. Such an approach would probably be able to identify electrides and fix the abovementioned hydride/proton issue. However, it does a poor job describing TM carbenes and some metal–ligand interactions. In addition, we have observed that the choice of orbital localization method can have a non-innocent role in the procedure. We have only partially explored the use of PM and NLMO schemes, and it would certainly be necessary to scrutinize more robust alternatives before turning down the use of centroids for OS assignation. In fact, for the present purpose, and in analogy to how EOS analysis is designed, one should probably incorporate the definition of fragments before applying the localization procedure, i.e., on the definition of the orbital spread functional. This work is beyond the scope of this paper. In the meantime, EOS analysis still represents a better approach to obtain OS from first principles.

Supplementary Materials: The following are available online, Oxidation state assignation of all evaluated species compiled in Tables S1 and S4. Structural and electronic parameters of the hydride species, and electronegativity ratios, relative distances and EFOs occupancies, compiled in Tables S2 and S3. Carbene σ and π EFO and relative EFO occupancies in Tables S5 and S6, structural parameters in Tables S7 and S8 and relative distances in Tables S9 and S10. Structural parameters for the π-adduct species depicted in Figures S1–S5.

Author Contributions: Writing—original draft preparation, P.S.; writing—review and editing, P.S. and M.G.; supervision, P.S.; software, P.S. and M.G.; data curation, M.G. and G.C.-V. All authors have read and agreed to the published version of the manuscript.

Funding: This research was funded by the Ministerio de Ciencia, Innovación y Universidades (MCIU), grant number PGC2018-098212-B-C22.

Acknowledgments: M.G. and G.C. thank the Generalitat de Catalunya and Fons Social Europeu for the predoctoral fellowship (2018 FI_B 01120 and 2020 FI_B 00180, respectively).

Conflicts of Interest: The authors declare no conflict of interest.

References

1. Grunenberg, J. Ill-defined chemical concepts: The problem of quantification. *Int. J. Quantum Chem.* **2017**, *117*, e25359. [CrossRef]
2. Karen, P.; McArdle, P.; Takats, J. Towards a comprehensive definition of oxidation state (IUPAC technical report). *Pure Appl. Chem.* **2014**, *86*, 1017–1081. [CrossRef]
3. Karen, P.; McArdle, P.; Takats, J. Comprehensive definition of oxidation state (IUPAC recommendations 2016). *Pure Appl. Chem.* **2016**, *88*, 831–839. [CrossRef]

4. Mann, J.B.; Meek, T.L.; Allen, L.C. Configuration energies of the main group elements. *J. Am. Chem. Soc.* **2000**, *122*, 2780–2783. [CrossRef]
5. Postils, V.; Delgado-Alonso, C.; Luis, J.M.; Salvador, P. An objective alternative to IUPACS's approach to assign oxidation states. *Angew. Chem. Int. Ed.* **2018**, *130*, 10685–10689. [CrossRef]
6. Monsch, G.; Klufers, P. $[Fe(H_2O)_{5(}NO)]^{2+}$, a "brown-ring" chromophore. *Angew. Chem. Int. Ed.* **2019**, *58*, 8566–8571. [CrossRef]
7. Gimferrer, M.; Salvador, P.; Poater, A. Computational monitoring of oxidation states in olefin metathesis. *Organometallics* **2019**, *38*, 4585–4592. [CrossRef]
8. Resta, R. Charge states in transition. *Nature* **2008**, *453*, 735. [CrossRef]
9. Raebiger, H.; Lanny, S.; Zunger, A. Charge self-regulation upon changing the oxidation state of transition metals in insulators. *Nature* **2008**, *453*, 763–766. [CrossRef]
10. Aullón, G.; Alvarez, S. Oxidation states, atomic charges and orbital populations in transition metal complexes. *Theo. Chem. Acc.* **2009**, *123*, 67–73. [CrossRef]
11. Walsh, A.; Sokol, A.A.; Buckeridge, J.; Scanlon, D.O.; Catlow, C.R.A. Electron counting in solids: Oxidation states, partial charges, and ionicity. *J. Phys. Chem. Lett.* **2017**, *8*, 2074–2075. [CrossRef] [PubMed]
12. Koch, D.; Manzhos, S. On the charge state of titanium in titanium dioxide. *J. Phys. Chem. Lett.* **2017**, *8*, 1593–1598. [CrossRef] [PubMed]
13. Mulliken, R.S. Electronic population analysis on LCAO-MO molecular wave functions. I. *J. Chem. Phys.* **1955**, *23*, 1833–1840. [CrossRef]
14. Lowdin, P.O. On the nonorthogonality problem connected with the use of atomic wave functions in the theory of molecules and crystals. *J. Chem. Phys.* **1950**, *18*, 365–375. [CrossRef]
15. Reed, A.E.; Weinstock, R.B.; Weinhold, F. Natural population analysis. *J. Chem. Phys.* **1985**, *83*, 735–746. [CrossRef]
16. Lu, W.C.; Wang, C.Z.; Schmidt, M.W.; Bytautas, L.; Ho, K.M.M.; Ruedenberg, K. Molecule intrinsic minimal basis sets. I. Exact resolution of ab initio optimized molecular orbitals in terms of deformed atomic minimal-basis orbitals. *J. Chem. Phys.* **2004**, *120*, 2629–2637. [CrossRef]
17. Bader, R.F.W. *Atoms in molecules: A quantum theory*; Oxford University Press: Oxford, UK, 1990.
18. Heidar-Zadeh, F.; Ayers, P.W.; Verstraelen, T.; Vinogradov, I.; Vohringer-Martinez, E.; Bultinck, P. Information-theoretic approaches to atoms-in-molecules: Hirshfeld family of partitioning schemes. *J. Phys. Chem. A* **2018**, *122*, 4219–4245. [CrossRef]
19. Mayer, I. Atomic orbitals from molecular wave functions: The effective minimal basis. *J. Phys. Chem.* **1996**, *100*, 6249–6257. [CrossRef]
20. Ramos-Cordoba, E.; Salvador, P.; Mayer, I. The atomic orbitals of the topological atom. *J. Chem. Phys.* **2013**, *138*, 214107. [CrossRef]
21. Mayer, I. Relation between the Hilbert space and "fuzzy atoms" analyses. *Chem. Phys. Lett.* **2013**, *585*, 198–200. [CrossRef]
22. Veremchuk, I.; Mori, T.; Prots, Y.; Schnelle, W.; Leithe-Jasper, A.; Kohout, M.; Grin, Y. Synthesis, chemical bonding and physical properties of *RE*RhB_4(*RE* = Y, Dy–Lu). *J. Solid State Chem.* **2008**, *181*, 1983–1991. [CrossRef]
23. Thom, A.J.W.; Sundstrom, E.J.; Head-Gordon, M. LOBA: A localized orbital bonding analysis to calculate oxidation states, with application to a model water oxidation catalyst. *Phys. Chem. Chem. Phys.* **2009**, *11*, 11297–11304. [CrossRef] [PubMed]
24. Sit, P.H.L.; Ziponi, F.; Chen, J.; Car, R.; Cohen, M.H.; Selloni, A. Oxidation state changes and electron flow in enzymatic catalysis and electrocatalysis through Wannier-function analysis. *Chem. Eur. J.* **2011**, *17*, 12136–12143. [CrossRef] [PubMed]
25. Sit, P.H.-L.; Car, R.; Cohen, M.H.; Selloni, A. Simple, unambiguous theoretical approach to oxidation state determination via first-principles calculations. *Inorg. Chem.* **2011**, *50*, 10259–10267. [CrossRef] [PubMed]
26. Jiang, L.; Levchenko, S.V.; Rappe, A.M. Rigorous definition of oxidation states of ions in solids. *Phys. Rev. Lett.* **2012**, *108*, 166403. [CrossRef] [PubMed]
27. Knizia, G. Intrinsic atomic orbitals: An unbiased bridge between quantum theory and chemical concepts. *J. Chem. Theory Comput.* **2013**, *9*, 4834–4843. [CrossRef] [PubMed]
28. Vidossich, P.; Lledos, A. The use of localised orbitals for the bonding and mechanistic analysis of organometallic compounds. *Dalton Trans.* **2014**, *43*, 11145–11151. [CrossRef]

29. Ramos-Cordoba, E.; Salvador, P. Oxidation states from wave function analysis. *J. Chem. Theory Comput.* **2015**, *11*, 1501–1508. [CrossRef]
30. Boys, S.F. Construction of some molecular orbitals to be approximately invariant for changes from one molecule to another. *Rev. Mod. Phys.* **1960**, *32*, 296–299. [CrossRef]
31. Edmiston, C.; Ruedenberg, K. Localized atomic and molecular orbitals. *Rev. Mod. Phys.* **1963**, *35*, 457–465. [CrossRef]
32. Pipek, J.; Mezey, P.G. A fast intrinsic localization procedure applicable for ab-initio and semiempirical linear combination of atomic orbital wave functions. *J. Chem. Phys.* **1989**, *90*, 4916–4926. [CrossRef]
33. Reed, A.E.; Weinhold, F. Natural localized molecular orbitals. *J. Chem. Phys.* **1985**, *83*, 1736–1740. [CrossRef]
34. Marzari, N.; Vanderbilt, D. Maximally localized generalized Wannier functions for composite energy bands. *Phys. Rev. B* **1997**, *56*, 12847–12865. [CrossRef]
35. Kermack, W.O.; Robinson, R. LI.—An explanation of the property of induced polarity of atoms and an interpretation of the theory of partial valencies on an electronic basis. *J. Chem. Soc. Trans.* **1922**, *121*, 427–440. [CrossRef]
36. Burke, L.A.; Leroy, G.; Sana, M. Theoretical study of the Diels-Alder reaction. *Theoret. Chim. Acta* **1975**, *40*, 313–321. [CrossRef]
37. Moyano, A.; Pericas, M.A.; Serratosa, F.; Valenti, E. A semiempirical (AM1, MNDO and MINDO/3) study on the thermolysis of 1-alkynyl ethers. Reaction analysis by correlation of localized molecular orbitals. *J. Org. Chem.* **1987**, *52*, 5532–5538. [CrossRef]
38. Knizia, G.; Klein, J.E.M.N. Electron flow in reaction mechanisms-revealed from first principles. *Angew. Chem. Int. Ed.* **2015**, *54*, 5518–5522. [CrossRef]
39. Sciortino, G.; Lledos, A.; Vidossich, P. Bonding rearrangements in organometallic reactions: From orbitals to curly arrows. *Dalton Trans.* **2019**, *48*, 15740–15752. [CrossRef]
40. Postils, V.; Garcia-Borràs, M.; Solà, M.; Luis, Josep, M.; Matito, E. On the existence and characterization of molecular electrides. *Chem. Commun.* **2015**, *51*, 4865–4868. [CrossRef]
41. Rodriguez, J.I.; Koster, A.M.; Ayers, P.W.; Santos-Valle, A.; Vela, A.; Merino, G. An efficient grid-based scheme to compute QTAIM atomic properties without explicit calculation of zero-flux surfaces. *J. Comput. Chem.* **2008**, *30*, 1082–1092. [CrossRef]
42. Wang, G.; Zhou, M.; Goettel, J.T.; Schrobilgen, G.J.; Su, J.; Li, J.; Schlöder, T.; Riedel, S. Identification of an iridium-containing compound with a formal oxidation state of IX. *Nature* **2014**, *514*, 475–477. [CrossRef] [PubMed]
43. Yu, H.S.; Truhlar, D.G. Oxidation state 10 exists. *Angew. Chem. Int. Ed.* **2016**, *55*, 9004–9006. [CrossRef] [PubMed]
44. Sung, Y.M.; Yoon, M.-C.; Lim, J.M.; Rath, H.; Naoda, K.; Osuka, A.; Kim, D. Reversal of Hückel (anti)aromaticity in the lowest triplet states of hexaphyrins and spectroscopic evidence of Baird's rule. *Nat. Chem.* **2015**, *7*, 418–422. [CrossRef] [PubMed]
45. Occhipinti, G.; Jensen, V.R. Nature of the transition metal-carbene bond in Grubbs olefin metathesis catalysts. *Organometallics* **2011**, *30*, 3522–3529. [CrossRef]
46. Frisch, M.J.; Trucks, G.W.; Schlegel, H.B.; Scuseria, G.E.; Robb, M.A.; Cheeseman, J.R.; Scalmani, G.; Barone, V.; Petersson, G.A.; Nakatsuji, H.; et al. *Gaussian 16, Revision, C.01*, Gaussian, Inc.: Wallingford, CT, USA, 2016.
47. Glendening, E.D.; Landis, C.R.; Weinhold, F. NBO 6.0: Natural bond orbital analysis program. *J. Comput. Chem.* **2013**, *34*, 1429–1437. [CrossRef]
48. Becke, A.D. A multicenter numerical integration scheme for polyatomic molecules. *J. Chem. Phys.* **1988**, *88*, 2547–2553. [CrossRef]
49. Salvador, P.; Ramos-Cordoba, E.; Gimferrer, M. *APOST-3D Program*; Universitat de Girona: Girona, Spain, 2012.
50. Salvador, P.; Ramos-Cordoba, E. An approximation to Bader's topological atom. *J. Chem. Phys.* **2013**, *139*, 071103. [CrossRef]

4.2 Oxidation state localized orbitals: a method for assigning oxidation states using optimally fragment-localized orbitals and a fragment orbital localization index

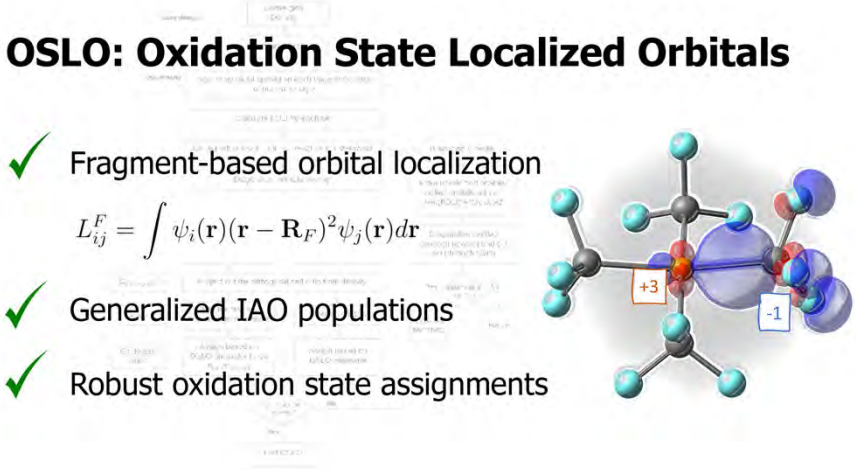

Published in: Gimferrer, M.; Aldossary, A.; Salvador, P.; Head-Gordon, M. *J. Chem. Theory Comput.* **2022**, 18, 1, 309-322.
Highlighted in: McCardle, K. *Nat. Comput. Sci.* **2022**, 2, 4.

Abstract: Oxidation states represent the ionic distribution of charge in a molecule and are significant in tracking redox reactions and understanding chemical bonding. While effective algorithms already exist based on formal Lewis structures as well as using localized orbitals, they exhibit differences in challenging cases where effects such as redox noninnocence are at play. Given a density functional theory (DFT) calculation with chosen total charge and spin multiplicity, this work reports a new approach to obtaining fragment-localized orbitals that is termed oxidation state localized orbitals (OSLO), together with an algorithm for assigning the oxidation state using the OSLOs and an associated fragment orbital localization index (FOLI). Evaluating the FOLI requires fragment populations, and for this purpose a new version of the intrinsic atomic orbital (IAO) scheme is introduced in which the IAOs are evaluated using a reference minimal basis formed from on-the-fly superposition of atomic density (IAO-AutoSAD) calculations in the target basis set and at the target level of theory. The OSLO algorithm is applied to a range of challenging cases including high valent metal oxide complexes, redox noninnocent NO and dithiolate transition metal complexes, a range of carbene-containing TM complexes, and other examples including the potentially inverted ligand field in $[Cu(CF_3)_4]^-$. Across this range of cases, OSLO produces generally satisfactory results. Furthermore, in borderline cases, the OSLOs and associated FOLI values provide direct evidence of the emergence of covalent interactions between fragments that nicely complements existing approaches.

JCTC Journal of Chemical Theory and Computation

pubs.acs.org/JCTC Article

Oxidation State Localized Orbitals: A Method for Assigning Oxidation States Using Optimally Fragment-Localized Orbitals and a Fragment Orbital Localization Index

Martí Gimferrer,[#] Abdulrahman Aldossary,[#] Pedro Salvador,[*] and Martin Head-Gordon[*]

Cite This: *J. Chem. Theory Comput.* 2022, 18, 309−322 Read Online

ACCESS | Metrics & More | Article Recommendations | Supporting Information

ABSTRACT: Oxidation states represent the ionic distribution of charge in a molecule and are significant in tracking redox reactions and understanding chemical bonding. While effective algorithms already exist based on formal Lewis structures as well as using localized orbitals, they exhibit differences in challenging cases where effects such as redox noninnocence are at play. Given a density functional theory (DFT) calculation with chosen total charge and spin multiplicity, this work reports a new approach to obtaining fragment-localized orbitals that is termed oxidation state localized orbitals (OSLO), together with an algorithm for assigning the oxidation state using the OSLOs and an associated fragment orbital localization index (FOLI). Evaluating the FOLI requires fragment populations, and for this purpose a new version of the intrinsic atomic orbital (IAO) scheme is introduced in which the IAOs are evaluated using a reference minimal basis formed from on-the-fly superposition of atomic density (IAO-AutoSAD) calculations in the target basis set and at the target level of theory. The OSLO algorithm is applied to a range of challenging cases including high valent metal oxide complexes, redox noninnocent NO and dithiolate transition metal complexes, a range of carbene-containing TM complexes, and other examples including the potentially inverted ligand field in $[Cu(CF_3)_4]^-$. Across this range of cases, OSLO produces generally satisfactory results. Furthermore, in borderline cases, the OSLOs and associated FOLI values provide direct evidence of the emergence of covalent interactions between fragments that nicely complements existing approaches.

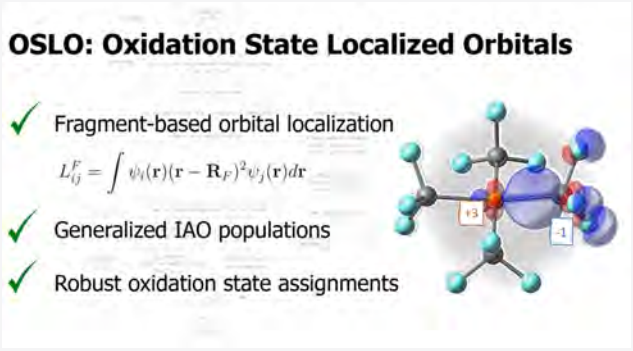

INTRODUCTION

The oxidation state (OS)[1] is a venerable concept reaching back to the early days of chemistry where the "oxydationsstufe" was introduced to rationalize the products obtained from reactions with oxygen. The electron-gathering tendency of oxygen is captured via its normal OS of −2 in compounds with ionic interactions, which is but one of the generally accepted counting rules to assign the OS. After a thorough revision of the concept, the IUPAC defines the OS of an atom as the charge of this atom after ionic approximation of its heteronuclear bonds.[2] They further recommend that this is accomplished by writing the Lewis structure of the compound of interest and partitioning the electron pairs such that each shared electron pair is given to the more electronegative of the two associated atoms.[3] The IUPAC procedure is simple and generally effective, and for these reasons should be the first resort in assigning OSs in new compounds of interest.

While the OS is a chemical concept of enduring value, it must be stressed that nevertheless, the OS of an atom is not itself a precisely defined observable. It *may* correlate with observables such as X-ray absorption spectral shifts, but this requires calibration. Ultimately, the validity of the OS depends on the extent of ionicity in the bonding. Thus, the OS becomes less well-defined as the chemical bonding approaches the covalent limit of electron pair sharing. Other situations such as ligand noninnocence[4] also can defeat normal OS conventions. Indeed the IUPAC report on OSs in chemistry states that there are "limits, beyond which OS ceases to be well-defined or becomes ambiguous". This situation is no different than other valuable chemical concepts such as aromaticity[5−7] and should not be viewed as a reason to discard the OS as something that cannot be measured. Instead, it is a reason to have tools that go beyond electron counting to assess the electron distribution in interesting and challenging borderline cases.

Electronic structure calculations directly yield the electron density and therefore offer an ideal starting point for probing the borderline cases. Thus, the assignment of OSs in molecular

Received: October 6, 2021
Published: December 20, 2021

systems has drawn continuing attention in recent years.[8−16] Beyond the electron density itself, there is particular interest in the development and application of specific schemes to extract OSs from electronic structure calculations, going beyond the (simple but clearly not satisfactory) use of partial atomic charges or atomic spin densities.[17−20] Most electronic structure approaches to OS assignment are predicated on assigning each electron pair (or individual electrons in case of open-shell systems) to one atom or ligand within the system based on some strategy that generalizes simple counting approaches such as the IUPAC definition. While we will concentrate on molecular systems in this work, it must be mentioned that precisely the same issue exists for oxidation state assignments in solid state materials.[21−23]

Some years ago, Ramos-Cordoba et al. introduced a general OS elucidation method applicable to any molecular system and wave function (single-determinant or correlated)[19] that relies on Mayer's effective fragment orbitals (EFOs) and their occupations.[24,25] The EFOs are obtained by diagonalization of the fragment's density matrix, according to some atom-in-molecule definition. For instance, in the case of QTAIM, they lie spatially within the fragment's boundary so they represent natural domain orbitals. The spin-resolved EFOs are obtained independently for each user-defined fragment (typically the transition metal (TM) and its ligands). They are sorted by decreasing occupation number, and electrons (or electron pairs for closed-shell systems) are assigned to them until one reaches the total number of electrons. The fragment OS is then obtained by subtraction from the corresponding nuclear charges. This effective oxidation states (EOS) analysis also provides a measure to quantify the extent to which the OS assignment is clear-cut, based on the difference in occupation between the last occupied and first unoccupied EFOs. EOS analysis has been successfully applied to a wide range of systems.[26] The method notably deviates from the IUPAC approach[2,3] because individual bonds are never explicitly considered. That permits EOS analysis to formally consider more than one Lewis structure at a time (i.e., treat multireference wave functions) on an equal footing.

Single-determinant wave functions are invariant to unitary transformations within the occupied molecular orbitals. While the canonical orbitals are typically delocalized (because they are appropriate for ionization), this invariance can be exploited to generate a set of localized orbitals (LO) based on some criterion.[27] This is directly possible within Kohn−Sham density functional theory (DFT), which is the dominant electronic structure approach.[28] The LO representation often produces orbitals that resemble the individual bonds in the dominant Lewis structure, and it is then natural to apply the ionic approximation to each LO individually, following the IUPAC definition more closely. However, since there is no unique way to define localization, there is a slew of different localization schemes to produce localized orbitals, namely, Boys[29] Pipek−Mezey (PM),[30] Edminston−Ruedenberg (ER),[31] or more recent realizations based on Cholesky decomposition of the density matrix[32] and the fourth moment[33] or Knizia's intrinsic bond orbitals (IBOs),[34] to name a few.

This avenue has been explored by a number of methods.[17,18,20] Thom et al.[17] first coupled orbital localization with population analysis in the localized orbitals bonding analysis (LOBA) to assign the electrons associated with each LO. The LOBA method starts with orbital localization by a chosen scheme and then obtains the atomic populations from each localized orbital. Using either PM or ER localization together with Löwdin population analysis produced quite robust results.[10,17] In the original paper, the OS assignment focused on the TM of the complex. A threshold of 60% in the atomic population was used to decide whether the electron pair is assigned to the TM or not. Recently, some of us[35] described an extension to the method, loosening the weight of the aforementioned threshold in the OS determination, to allow the possibility of covalent assignment (split between two atoms/fragments) and introducing a confidence measure for the assignment (either ionic or covalent) of each electron pair.

In that work,[35] we observed that for some of the most challenging systems such as TM-carbenes, the LOBA method struggled to reach the accepted OS. Careful inspection of the localized orbitals indicated that the first step of the procedure, namely, the orbital localization, was not always producing orbitals one could easily relate to a Lewis structure. The LOs often involve several atomic centers with appreciable contributions, which hinder the process of OS assignment. Moreover, using a different localization scheme could also lead to different OS assignments in some controversial cases. We concluded that a different orbital localization scheme, tailored for the purpose of OS assignment, was necessary to make progress in such cases.

A maximally robust procedure to assign OSs should rely on separating the localized orbitals into fragments, for which the degree of locality of core or valence orbitals *within* each fragment has no special relevance. Indeed there has been much development of specialized methods that aim to specifically localize orbitals onto fragments[36−44] rather than maximizing a global measure of localization. Such methods have considerable value in energy decomposition analysis of intermolecular interactions[45,46] as well as for fragment methods and embedding.[41,44,47] In our context there is a different need for fragment localization. For instance, if two fragments A and B, each formally bearing n_A and n_B electron pairs, are linked via a single bond with ionic character, then the OS should solely depend on a single localized orbital involving both A and B, leading either to A^+-B^- or A^--B^+. On the other hand, since standard system-optimal orbital localization schemes do not make a distinction between the contact atoms of the A−B bond and the remaining atoms of A and B, a potentially better localization of the critical A−B bonding orbital may be sacrificed for better overall localization of all $n_A + n_B$ orbitals.

In light of the above considerations, there are several new components that are presented here to enable assignment of OSs. First, we put forward a robust fragment-based orbital localization scheme. For a given fragment, the resulting oxidation state localized orbitals (OSLOs) comprise a full set of orbitals spanning the occupied space that are ordered by spatial locality in the fragment. Second, to further characterize each orbital, given a set of fragment populations, we introduce a fragment orbital localization index (FOLI) which measures the population of each OSLO on a per-fragment basis. Third, to obtain the fragment populations, a more robust Hilbert-space based population analysis based on Knizia's intrinsic atomic orbitals (IAOs)[34] is also introduced. Fourth, we use the above components to develop an iterative algorithm to best select a subset of the OSLOs for each fragment to span the full occupied space. The oxidation state of a given fragment is then determined by its number of assigned OSLOs relative to its total nuclear charge. Finally, with the new procedure in hand,

https://doi.org/10.1021/acs.jctc.1c01011
J. Chem. Theory Comput. 2022, 18, 309−322

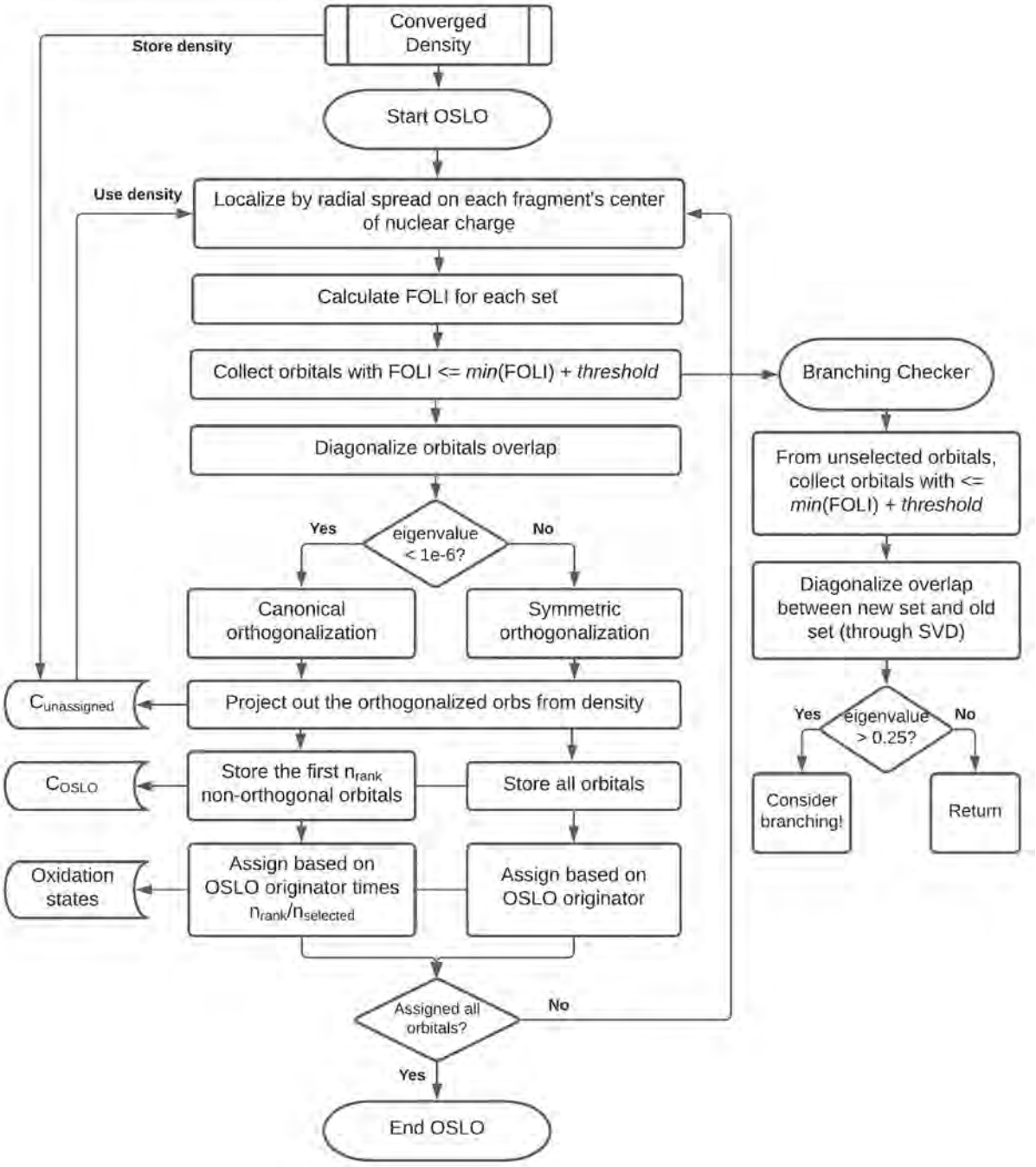

Figure 1. Flowchart of the iterative OSLO algorithm, where the most strongly fragment-localized orbitals (core and valence spectator orbitals) are projected out from the occupied space before the least fragment-localized orbitals that are most relevant to OS assignment are generated and inspected. This procedure has the desirable side-effect of improving the fragment-localization of orbitals that are not selected in later iterations.

we turn to exploration of a variety of interesting borderline cases, with focus on examples where LOBA was previously demonstrated to have some issues.[35]

METHODS

Oxidation States from Localized Orbitals (OSLO). Starting with a single-determinant wave function built of n_{occ} spin orbitals, the fragment localization procedure is based on minimizing the radial spread functional from a given reference point for fragment F, $\mathbf{R}_F$. For a TM atom, $\mathbf{R}_F$ will be the atomic position; for a ligand, $\mathbf{R}_F$ will be its center of charge. The minimization can be easily achieved in the molecular orbital (MO) basis by building a spread matrix, $\mathbf{L}^F$, with elements

$$L_{ij}^F = \int \psi_i(\mathbf{r})(\mathbf{r} - \mathbf{R}_F)^2 \psi_j(\mathbf{r})\, d\mathbf{r} \tag{1}$$

where ψ_i is the ith occupied MO. Equation 1 simplifies to

$$L_{ij}^F = \int \psi_i(\mathbf{r})\mathbf{r}^2\psi_j(\mathbf{r})\, d\mathbf{r} - 2\mathbf{R}_F \cdot \int \psi_i(\mathbf{r})\mathbf{r}\psi_j(\mathbf{r})\, d\mathbf{r} + \mathbf{R}_F{}^2\delta_{ij} \tag{2}$$

https://doi.org/10.1021/acs.jctc.1c01011
J. Chem. Theory Comput. 2022, 18, 309−322

where the first term contains the isotropic quadrupole moment matrix elements, the second term involves the dipole matrix elements, and the third term is merely a constant diagonal offset. The required matrix elements are readily available in many quantum chemistry software packages. Diagonalization of the matrix $\mathbf{L}^F$

$$\mathbf{L}^F\mathbf{U}^F = \mathbf{U}^F\mathbf{\Lambda}^F \tag{3}$$

yields eigenvalues $\lambda_i^F = \Lambda_{ii}^F$ and a corresponding set of n_{occ} localized orbitals centered around $\mathbf{R}_F$

$$\phi_i^{loc,F}(\mathbf{r}) = \sum_k U_{ki}^F \psi_k(\mathbf{r}) \tag{4}$$

with their (squared) spreads given by the λ_i^X values. When $\mathbf{R}_F$ corresponds to an atomic position, the localized orbitals obtained by this procedure reproduce the shell structure of the atom, with core orbitals having the smaller spread values.

The target is to define the OS of M user-defined fragments of a molecular system, such as the metal(s) and ligands of a TM complex. We localize around each fragment's center of nuclear charge and get n_{occ} OSLOs for each of them (Mn_{occ} altogether). Note that in cases like polydentate or hapto ligands, the ligand's centroid may be far from the ligand's nuclei or even coincide with that of the metal (e.g., TM−porphyrin compounds). Minimizing the spread function is simple, noniterative (no multiple minimum problem[48]), independent of any population assignment, and appealing. However, the OSLOs most strongly associated with a fragment cannot always be chosen based on the smallest spread. For instance, in the case of a TM center with some coordination sphere, OSLOs dominated by ligand contributions can exhibit lower orbital spreads than the most diffuse TM orbitals (e.g., a 4s-type orbital for a 3d metal). Similarly, when $\mathbf{R}_F$ is the center of a ligand, some compact ligand-centered OSLOs have a significant contribution from the neighboring TM center.

We therefore need a complementary measure to identify those OSLOs that are most localized on a fragment. Using Pipek's delocalization measure,[49] defined in terms of fragment populations, $N_F^i = \sum_{A\in F} n_A^i$, rather than atomic populations, n_A^i is a suitable starting point:

$$D_i = \left\{ \sum_F (N_F^i)^2 \right\}^{-1} \tag{5}$$

When an orbital is localized on a single fragment, then $D_i = 1$. If the ith orbital is perfectly delocalized across two fragments, F and F', then $N_F^i = N_{F'}^i = 1/2$ and $D_i = 2$, and so on.

Out of the OSLOs generated from fragment F with low delocalization measure, we are interested in those that are also highly localized on fragment F. For this purpose, we introduce the fragment orbital localization index (FOLI)

$$D_i^F = \sqrt{\frac{D_i}{N_F^i}} \tag{6}$$

The FOLI, D_i^F, is 1 when orbital i is perfectly localized on that fragment ($D_i = N_F^i = 1$). The FOLI $D_i^F \to 2$ when the orbital is perfectly delocalized over two fragments ($D_i = 2, N_F^i = N_{F'}^i = 0.5$). The FOLI gradually increases for OSLOs that are more delocalized and less centered on fragment F. Note that while a FOLI value of $D_i^F = 1$ means perfect fragment localization, higher FOLI values can result from different instances of delocalization. For example, a FOLI value of 2 can also arise from three fragments with $D_i = 2.339$ via $N_F = 0.584$, $N_{F'} = N_{F''} = 0.208$.

How should one select the n most fragment-localized OSLOs from among the redundant set of $M \cdot n$ candidates? One could select the n_{occ} OSLOs with the smallest FOLI values and assign them to their parent fragments. However, we have observed that this procedure sometimes leads to linear dependencies among the selected OSLOs. We instead prefer the iterative scheme depicted in Figure 1. On the first iteration, the best localized orbital (in the sense of smallest FOLI value) is selected and projected out from the occupied space for the next iteration. The second iteration begins by constructing a new set of $M \cdot (n_{occ} - 1)$ localized orbitals, followed by selecting and removing the best localized orbital. Iterations continue until a total of n_{occ} optimal fragment-localized orbitals are selected. In the case of an unrestricted Slater determinant, the procedure is carried out for the α and β occupied spaces separately, and individual α and β OSLOs are thus produced and assigned to each fragment.

The basic algorithm is modified by introducing a tolerance (typically 10^{-3}) associated with the lowest FOLI values so that all OSLOs with D_i^F values within the tolerance are selected in a given iteration. These orbitals are symmetrically orthogonalized and then projected out from the occupied space for the next iteration. This strategy avoids the problem that for symmetric systems, projecting out individual localized orbitals may result in a symmetry-broken density-matrix for the next iteration.

There are a number of aspects of the procedure that are worth discussing in some detail. The localized orbitals obtained in the first few iterations are basically the atomic core orbitals of the fragment's atoms. As the iterative process advances, on-fragment localized valence orbitals are produced. They correspond to orbitals not particularly involved in the bonding between fragments, i.e., spectator orbitals. In the later iterations, the least-fragment localized valence orbitals are eventually selected. They correspond to bonds (or dative bonds) between fragments (e.g., TM-ligand orbitals). A nice side effect of the iterative procedure is that, by first removing the more fragment-localized orbitals from the occupied space, the relevant across-fragment orbitals are better localized on fragments (i.e., their FOLI values are *smaller* than those obtained in the first iteration using the whole occupied space). The final result thus depends to some extent on the order in which OSLOs are selected.

In borderline cases (where the FOLI-based selection is a close call), this may affect the OS assignment. The algorithm allows the user to explore alternative outcomes in borderline cases by flagging when the OSLO selection procedure could *branch* into 2 (or more) paths. Consider a simple case with a single bond between fragments F and G. At some point in the iterative procedure, the corresponding bond localized orbital centered on F will be produced. At the same time, a similar bond localized orbital will be produced in the OSLOs associated with fragment G. The one with the smaller FOLI value is selected and projected out from the remaining occupied space. In the following iteration, this bond orbital will be absent from the new set of OSLOs obtained for both fragment F and G. If the $F-G$ bond is very nonpolar (rare in TM complexes), the D_i^F and D_i^G values would be very similar, and one can argue that instead choosing the OSLO associated with G would produce a plausible alternative solution to selecting the one associated with F.

https://doi.org/10.1021/acs.jctc.1c01011
J. Chem. Theory Comput. 2022, 18, 309−322

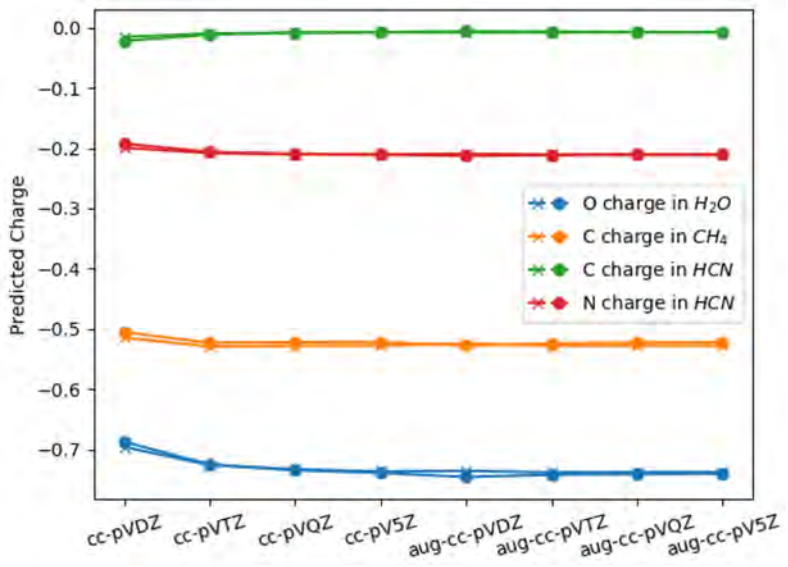

Figure 2. IAO atomic charges for H_2O, CH_4, and HCN where the crosses are charges from calculations using the AutoSAD reference minimal basis, while the circles used the MinAO basis.[34] All calculations are done with Hartree−Fock wave functions, and it is evident that the two sets of results are nearly indistinguishable.

Our iterative algorithm automatically detects these (borderline) cases as follows. At each iteration, linear dependencies are checked between the OSLO that is selected and that with the second smallest FOLI value that is not selected (there may be multiple selected and nonselected localized orbitals if their FOLI values are within the tolerance). If near linear dependencies are indeed found *and* the difference in D_i^F values is small enough, our algorithm will print a diagnostic message. This allows the user to rerun the calculation, toggling a branching flag that selects the OSLO with the somewhat larger FOLI value and proceed to obtain a second distinct solution.

To turn to the OS assignment, we recall that each of the selected localized orbitals was generated from a fragment center with a low FOLI value. This makes it natural to assign the fragments' oxidation states based on the originator fragment. That is the procedure followed in the results reported here and represents a "winner-takes-all" approach to the OS, similar to the IUPAC rules. However, once the optimal set of orthogonal fragment-localized orbitals are obtained, each orbital's allegiance may be reassigned according to the fragments' populations, either in a "winner-takes-all" fashion again or alternatively by allowing covalent assignments in nonpolar cases, as described elsewhere.[35]

An atomic partitioning scheme is necessary to evaluate the FOLI values. In this work, we use two very different partitioning approaches to demonstrate that different reasonable choices in fact work very similarly. First, we use the so-called topological fuzzy Voronoi cells (TFVC) atomic definition,[50] a real-space scheme that is used in the effective oxidation states (EOS) approach.[19] Second, we introduce a Hilbert-space based procedure based on Knizia's intrinsic atomic orbitals (IAOs),[34] where the reference minimal basis is obtained on-the-fly at the chosen level of theory. This IAO-AutoSAD procedure is described below.

IAO-AutoSAD Reference Minimal Basis. Hilbert-space methods to assign atomic or fragment populations so that the results do not artificially depend on the underlying AO basis set often rely on using a minimal basis to *exactly* span the occupied space.[51−53] Among many such possibilities, intrinsic atomic orbitals (IAOs) are perhaps the simplest and have been shown to be robust for population analysis.[34,44,54] The basic idea of IAOs is to rely on a projection onto a reference minimal basis to facilitate atom-tagging.

Starting from a converged SCF solution, one projects the occupied MO coefficients, $\mathbf{C}_{\mathrm{occ}}$, into the small reference minimal basis set and back to the big one as follows:

$$\tilde{\mathbf{C}}_{\mathrm{occ}} = \mathrm{ortho}(\mathbf{R}_{\mathrm{ls}}\mathbf{R}_{\mathrm{sl}}\mathbf{C}_{\mathrm{occ}}) \tag{7}$$

$\mathbf{R}_{\mathrm{sl}} = \mathbf{s}^{-1}\mathbf{S}_{\mathrm{sl}}$ projects from the big basis into the small basis, given that $\mathbf{S}$ and $\mathbf{s}$ are the overlap matrices in the large and small basis sets, and $\mathbf{S}_{\mathrm{sl}}$ is the matrix of overlaps between functions in the small and large basis sets. In the same notation, $\mathbf{R}_{\mathrm{ls}} = \mathbf{S}^{-1}\mathbf{S}_{\mathrm{ls}}$ projects from the small basis into the big basis. After symmetric orthogonalization to restore orthonormality, the so-called depolarized orbitals are gathered in the matrix $\tilde{\mathbf{C}}_{\mathrm{occ}}$.

The rectangular transformation matrix, $\mathbf{A}$, from the large basis, $\{\omega_\mu\}$, to the minimal IAO basis, $\chi_\alpha^{\mathrm{IAO}} = \sum_\mu \omega_\mu A_{\mu\alpha}$, is produced by the following double projection step:

$$\mathbf{A}_{\mathrm{ls}} = \mathrm{ortho}(\mathbf{PS}\tilde{\mathbf{P}}\mathbf{S}_{\mathrm{ls}} + \mathbf{QS}\tilde{\mathbf{Q}})\mathbf{S}_{\mathrm{ls}}) \tag{8}$$

$\mathbf{P} = \mathbf{C}_{\mathrm{occ}}\mathbf{C}_{\mathrm{occ}}^{\dagger}$ and $\tilde{\mathbf{P}} = \tilde{\mathbf{C}}_{\mathrm{occ}}\,\tilde{\mathbf{C}}_{\mathrm{occ}}^{\dagger}$ are the density matrices (i.e., occupied projectors) associated with the original occupied MOs and the depolarized occupied MOs, respectively. Their orthogonal complements are $\mathbf{Q} = \mathbf{S}^{-1} - \mathbf{P}$ and $\tilde{\mathbf{Q}} = \mathbf{S}^{-1} - \tilde{\mathbf{P}}$. Once the orthogonal IAOs are available, the IAO atomic population of atom B is obtained as

$$N_B = \sum_{\beta\in B} (\mathbf{P}^{\mathrm{IAO}})_{\beta\beta} = \sum_{\beta\in B} (\mathbf{A}^{\dagger}\mathbf{SPSA})_{\beta\beta} \tag{9}$$

The reference minimal basis originally used[34] for construction of the IAOs is the so-called "MinAO" set, which is the standard cc-pVTZ AO basis manually truncated to a minimal basis. When the molecular calculation uses effective core potentials (ECPs), "MinAO-PP" was employed, which is cc-pVTZ-PP truncated to a minimal basis (i.e., excluding core AOs). However, this reference minimal basis fails to be valid

https://doi.org/10.1021/acs.jctc.1c01011
J. Chem. Theory Comput. 2022, 18, 309−322

Table 1. Summary of the OSLO Results for the Molecular Systems Studied, Obtained with the IAO-AutoSAD and TFVC (in Parentheses) Population Analyses[a]

complex	M OS	L OS	Δ-FOLI	last FOLI
$[TiO_2]$	+4 (+4)	−2 (−2)	3.453 (3.367)	1.321 (1.372)
$[VO_4]^{3-}$	+5 (+5)	−2 (−2)	1.548 (1.748)	1.466 (1.461)
$[FeO_4]^{2-}$	+6 (+6)	−2 (−2)	1.598 (1.682)	1.569 (1.623)
$[ReO_4]^{-}$	+7 (+7)	−2 (−2)	1.806 (1.829)	1.470 (1.480)
$[OsO_4]$	+8 (+8)	−2 (−2)	1.415 (1.363)	1.592 (1.609)
$[IrO_4]^{+}$	+9 (+9)	−2 (−2)	1.529 (1.084)	1.705 (1.742)
$[PtO_4]^{2+}$[b]	+10 (+10)	−2 (−2)	1.023 (0.707)	1.859 (1.904)
$FeCp_2$	+2 (+2)	−1 (−1)	1.800 (2.343)	1.313 (1.437)
Zn(**porphyrin**)	+2 (+2)	−2 (−2)	0.958 (1.470)	1.509 (1.319)
$[Ni(S_2C_2Me_2)_2]^0$	+2 (+2)	−1 (−1)	0.000 (0.000)	2.000 (2.245)
$[Ni(S_2C_2Me_2)_2]^{1-}$ α	+2 (+3)	−1.5 (−2)	0.603 (0.913)	1.634 (1.656)
$[Ni(S_2C_2Me_2)_2]^{1-}$ β			0.000 (0.110)	2.000 (1.901)
$[Ni(S_2C_2Me_2)_2]^{2-}$	+2 (+2)	−2 (−2)	1.085 (1.374)	1.482 (1.509)
$[Cu(CF_3)_4]^{1-}$	+3 (+3)	−1 (−1)	0.373 (0.728)	1.516 (1.531)
$[Cu(CF_3)_4]^{2-}$ α	+2 (+2)	−1 (−1)	4.823 (4.845)	1.075 (1.152)
$[Cu(CF_3)_4]^{2-}$ β		−1 (−1)	2.528 (2.867)	1.267 (1.270)
$[Cu(CF_3)_4]^{3-}$	+1 (+1)	−1 (−1)	4.383 (4.581)	1.084 (1.145)
$Rh(SO_2)Cl(PH_3)_2$ (L-type)	+1 (+1)	0 (0)	1.421 (1.209)	1.402 (1.509)
$Rh(SO_2)Cl(CO)(PH_3)_2$ (Z-type)	+1 (+1)	0 (0)	1.064 (1.688)	1.606 (1.516)
$Ru(SO_2)Cl(NO)(PH_3)_2$ (π-type)[c]	0 (0)	0 (0)	0.514 (0.339)	2.432 (2.550)
$[Fe(CN)_5NO]^{2-}$	+2 (+2)	+1 (+1)	0.981 (0.802)	1.573 (1.827)
$[Fe(CN)_5NO]^{3-}$ α	+2 (+2)	0 (0)	0.839 (0.674)	1.688 (1.987)
$[Fe(CN)_5NO]^{3-}$ β			2.638 (2.162)	1.375 (1.436)
$(CO)_5W{=}CHN(CH_3)_2$ (**1**) (Fischer)	0 (0)	0 (0)	3.069 (2.205)	1.920 (3.196)
$(CO)_5W{=}CHOCH_3$ (**2**) (Fischer)	0 (0)	0 (0)	1.860 (1.148)	2.037 (3.311)
$(CO)_5W{=}CF_2$ (**3**) (Fischer)	0 (0)	0 (0)	1.567 (0.893)	2.017 (3.232)
$(CO)_5W{=}CH_2$ (**4**) (Fischer)	0 (+2)	0 (−2)	0.612 (0.194)	2.279 (3.142)
$NAr(OtBu)_2W{=}CHtBu$ (**5**) (Schrock)	+6 (+6)	−2 (−2)	0.283 (0.659)	1.924 (1.933)
$NAr(OtBu)_2W{=}CH_2$ (**6**) (Schrock)	+6 (+6)	−2 (−2)	0.455 (0.806)	1.845 (1.908)
$NAr^1(OtBu)_2Mo{=}CHCMe_2Ph$ (**7**) (Schrock)	+6 (+6)	−2 (−2)	0.253 (0.565)	1.916 (1.917)
$NAr^1(OtBu)_2Mo{=}CH_2$ (**8**) (Schrock)	+6 (+6)	−2 (−2)	0.203 (0.487)	1.956 (2.018)
$NAr^1(OtBu)_2Mo{=}CHPh$ (**9**) (Schrock)	+6 (+6)	−2 (−2)	0.153 (0.430)	1.986 (2.042)
$PCy_3Cl_2Os{=}CH_2$ (**10**) (Grubbs)	+2 (+4)	0 (−2)	0.048 (0.044)	2.089 (2.278)
$H_2IMesCl_2Os{=}CH_2$ (**11**) (Grubbs)	+4 (+4)	−2 (−2)	0.192 (0.259)	2.375 (2.709)
$PCy_3Cl_2Ru{=}CH_2$ (**12**) (Grubbs)	+2 (+2)	0 (0)	0.222 (0.150)	1.964 (2.199)
$H_2IMesCl_2Ru{=}CH_2$ (**13**) (Grubbs)	+2 (+2)	0 (0)	0.276 (0.306)	2.013 (2.149)
$(PH_3)_2Cl_2Ru{=}CH_2$ (**14**) (Grubbs)	+2 (+2)	0 (0)	0.241 (0.090)	1.961 (2.153)

[a]OS for TM and selected ligand (L) in bold. tBu = *tert*-butyl, Cp = cyclopentadienyl, Ar = 2,6-diisopropylphenyl, Ar^1 = 2,6-dimethylphenyl, Cy = cyclohexyl, IMes = 1,3-Dimesitylimidazol-2-ylidene. [b]IAO-AutoSAD alternative solution. [c]TFVC results using a tolerance value of 10^{-4}.

for ECPs of other sizes (i.e., larger or smaller core). These limitations that result from the MinAO reference minimal basis are particularly relevant when dealing with transition metals and heavier elements.

A universally applicable reference minimal basis is made on-the-fly from appropriate free atom density matrices obtained with the same functional and basis sets as the molecular calculation. This is done using Q-Chem's[55] so-called AutoSAD functionality, which is normally employed to construct superposition of atomic density (SAD) initial guesses for DFT calculations at the target level of theory. Sphericalization is necessary to ensure proper shell structure in the reference minimal basis, since many atoms have partly occupied degenerate orbitals. For simplicity as well as to avoid ambiguity, we use the ground state of the neutral atom, although for some atoms, a case can be made for using different spin or charge states. For open shell atoms, the unrestricted SCF equations are solved, and the resulting α and β density matrices are spin-averaged as well as sphericalized.

The IAO-AutoSAD procedure first solves the following generalized eigenvalue problem separately for each free atom, A:

$$\mathbf{P}^A\mathbf{c}_\alpha^A = \mathbf{S}^A\mathbf{c}_\alpha^A\lambda_\alpha \tag{10}$$

Each matrix is defined in the full basis of the free atom (rank n_A), and $\mathbf{P}^A$ is the sphericalized and spin-averaged density matrix. The reference minimal basis set (MBS) on atom A is defined by choosing m_A orbitals, corresponding to the fully and fractionally occupied atomic orbitals (with $\lambda_\alpha \geq \frac{1}{14}$, such that the f shell is selected even for a cerium atom with a single f electron). The set of selected column vectors $\{\mathbf{c}_\alpha^A\}$ defines an $n_A \times m_A$ transformation to the MBS, $\mathbf{C}_{\mathrm{MBS}}^A$. The reference minimal basis has rank $M = \sum_A m_A$ with functions defined by the direct sum of the atomic transformations:

$$\mathbf{T} = \bigoplus_A \mathbf{C}_{\mathrm{MBS}}^A \tag{11}$$

https://doi.org/10.1021/acs.jctc.1c01011
J. Chem. Theory Comput. 2022, 18, 309−322

Given the $N \times M$ transformation from the AO basis to the reference minimal basis, $\mathbf{T}$, all quantities needed to evaluate the IAOs with this MBS are available. For instance, referring back to eqs 7 and 8, we see that $\mathbf{s} = \mathbf{T}^{\dagger}\mathbf{S}\mathbf{T}$ and $\mathbf{S}_{sl} = \mathbf{T}^{\dagger}\mathbf{S}$.

One must be aware that IAO orbitals and atomic charges do depend on the underlying choice of the reference minimal basis. Fortunately, our IAO-AutoSAD procedure shows results that are generally very similar to using MinAO for problems where the latter can be applied (i.e., no pseudopotentials). Some examples are shown in Figure 2, for a wide range of AO basis sets. This is encouraging and sets the stage for the results we report for the OSLO procedure in the following section. However, IAO charges do exhibit some dependence on the reference minimal basis. For instance, the O atomic charge in H_2O changes by $0.25e^-$ when using STO-3G as the reference minimal basis instead of MinAO or AutoSAD. For IAO-AutoSAD applied to transition metals, the choice of atomic state also has an impact. These issues may deserve further study in the future, as IAOs become more widely used.

Implementation and Computational Details. We have completed two independent implementations of the OSLO method, which serves as validation that both are correct and also provides the opportunity to employ two different approaches to evaluate the fragment populations. Adopting the IAO-AutoSAD Hilbert-space approach to charges described above, one of our implementations of the OSLO method is within the Q-Chem program[55] and consequently uses OSLO fragment populations and FOLI values that are obtained analytically. Our second implementation uses the topological fuzzy Voronoi cells (TFVC) real-space atomic definition,[50] within the APOST-3D[56] package. The numerical evaluation of the TFVC charges used the atom-centered Becke multicenter quadrature scheme[57] with 40 × 146 grid points (per atom).

Geometry optimizations were performed by using the ωB97X-V density functional[58] with the def2-TZVP basis set (all electron for light atoms (through Kr) and with def2-ECP for heavier atoms).[59] The ωB97X-V functional performs very well for both main group[28,60] and transition metal compounds.[61,62] Vibrational frequency calculations, to confirm minima on the potential energy surface, were computed at the same level of theory. Wave functions, energies, and orbital localizations were also evaluated at the same level. All DFT calculations were performed with the Q-Chem package,[55] while the OSLO analysis was performed with both the Hilbert- and real-space implementations described above.

RESULTS AND DISCUSSION

We evaluate the performance of the OSLO approach for a number of challenging systems, including high-valent oxides, TMs with noninnocent ligands, sulfur dioxide adducts with different bonding patterns, a Zn-based porphyrinic system, and TM carbenes of different types (Schrock, Fischer, and Grubbs first and second generation). We apply both IAO-AutoSAD and TFVC atomic population schemes to test the robustness of the OSLO procedure to the definition of fragment charges. The full set of results obtained are summarized in Table 1. The OS of the TM and the relevant ligand are reported, together with the FOLI values of the last selected OSLO, which is the least localized one (i.e., largest FOLI value among all selected OSLOs). In fact, once $n_{occ} - 1$ localized orbitals have been projected out from the density matrix, there is only one (localized) orbital left. This last OSLO is associated with the fragment with the smallest FOLI value.

In many cases the last FOLI value is close to its smallest value of 1, indicating very good orbital localization and, consequently, a clear-cut OS assignment. In cases where the last FOLI value is larger than 1, it is very instructive to examine the Δ-FOLI value (the difference between the smallest and second smallest FOLI values) to see how clear-cut the OS assignment is, the larger the better. Cases with Δ-FOLI > 1 suggest clear-cut ionic character. Overall, the formal OS assignments using both fragment charge schemes agree in almost all cases (30 out of 33). The very few discordant cases have associated Δ-FOLI values below 0.2, which is probably smaller than can be meaningfully associated with application of the ionic approximation (this will be discussed more later).

We will discuss a few of the more clear-cut cases only briefly. For the high-valent oxides ranging from TiO_2 to IrO_4^+, the OS obtained with OSLO are in full agreement with LOBA, EOS, and also with IUPAC's ionic approximation.[35] Clear-cut formal oxo (O^{2-}) ligands are obtained in all cases, resulting in an OS as high as Ir (+9).

The PtO_4^{2+} system deserves particular attention. We treat the case of the spin-restricted solution, which is stable in orbital space, and leads to the optimized T_d geometry. There are lower energy spin-polarized solutions, but we do not consider them here. The valence MO diagram can be found elsewhere;[63] there are eight π and four σ-type doubly occupied MOs. In a T_d environment, the 5d orbitals of Pt split into E and T_2 symmetries, while the 6s orbital is A_1. The four symmetry-equivalent O atoms lead to σ- and π-type symmetry-adapted orbitals, with symmetries $\Gamma_\sigma = A_1 + T_2$ and $\Gamma_\pi = E + T_1 + T_2$. Toward the end of the iterative procedure, the E type OSLOs on Pt are very close in FOLI with the eight Γ_π of the O centers, due to the significant covalent character of the Pt−O bonds. When using TFVC, the FOLI value of O atoms (1.67) is smaller than that of Pt's E OSLOs (1.84), so they are selected and projected out of the P matrix for the next iteration. Since there is only one set of E orbitals in the occupied space, the aforementioned E-type OSLOs on Pt are now absent, and the OSLOs with smaller FOLI value become those corresponding to the Γ_σ of the O centers, leading to a fairly clear Pt (+10) assignment (see Table 1).

When using IAO-AutoSAD, however, at the same step of the process the situation is reversed. The FOLI value of the Pt E OSLOs is smaller (1.50) than that of the eight Γ_π (1.69). When the former are selected and projected out from the *P*-matrix, the eight π-type OSLOs of the O centers become rank deficient for the next iterations. This leads to two undesirable outcomes. First, the localized orbitals on the O are mixed-up by the canonical orthogonalization process. Second, a last OSLO of A_1 symmetry delocalized over the four O centers remains left in the last iteration, leading to a huge FOLI value (4.63) and a split of the electron pair among the four equivalent O centers. By applying the branching option on the IAO-AutoSAD calculation, the Pt (+10) picture obtained with TFVC is recovered, with a similar Δ-FOLI value. Selecting OSLOs with a higher FOLI value at a given step of the iterative process ends up providing a final solution where the *sum* of the FOLI values of the selected OSLOs is smaller (36.34 vs 33.22).

The Zn-porphyrin system is potentially challenging for OSLO because, due to its symmetry, the center of charge of the porphyrin ligand *exactly* coincides with the position of the Zn nucleus. Nevertheless, as a result of using the FOLI values,

https://doi.org/10.1021/acs.jctc.1c01011
J. Chem. Theory Comput. 2022, 18, 309−322

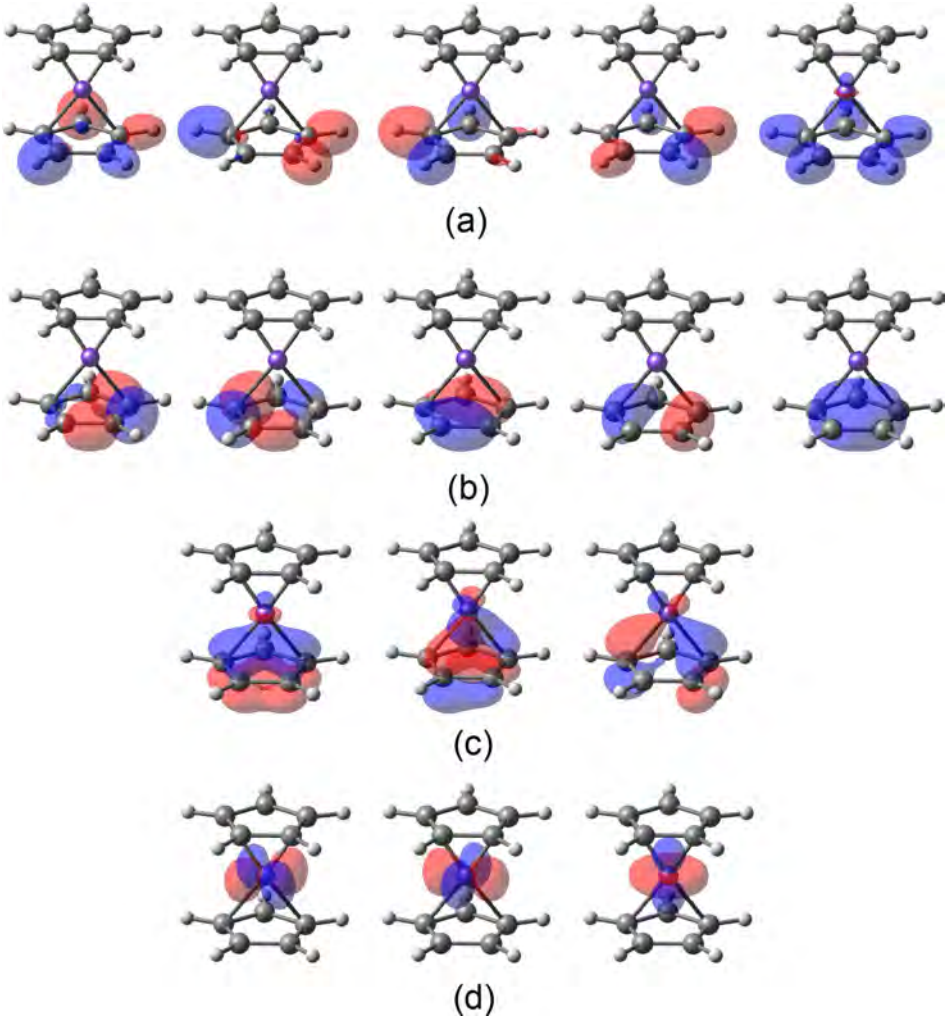

Figure 3. Valence OSLOs for the $FeCp_2$ complex as produced by the algorithm shown in Figure 1. The lower cyclopentadienyl ligand's σ_{C-H} OSLOs are shown in panel a, its σ_{C-C} OSLOs are shown in panel b, and its π OSLOs in panel c. The 3d-type OSLOs on Fe are shown in panel d. The isosurface value is 0.075 au.

the OSLO procedure performs smoothly, yielding the expected Zn (+2) OS with a Δ-FOLI value close to or even larger (TFVC) than 1. The OSLO results for the nitroprusside anion ($[Fe(CN)_5NO]^{2-}$) and its reduced form are also very clear, leading to a formal Fe (+2) species and a ligand-based reduction, in line with the well-known noninnocent nature of the nitrosyl ligand. The IAO-AutoSAD population yields larger Δ-FOLI values as compared to TFVC.

Ferrocene (see Figure 3) is a nice example because it shows the utility of the OSLOs themselves. The cyclopentadienyl anion OSLOs are shown in panels a−c, and the fragment localized π orbitals are particularly pleasing because they resemble the delocalized π orbitals of the isolated anion. In other words, this shows the advantage of *fragment* localization over *global* localization (see also the recent treatment via intrinsic fragment orbitals[44]). The three occupied Fe (3d) orbitals emerge as expected, and the OS assignment is very clear based on the small FOLI value of the last orbital as well as the large Δ-FOLI gap.

The redox series of nickel diothiolate complexes, $[Ni(S_2C_2Me_2)_2]^{n-}$ with n = 0, 1, 2, is particularly interesting. The n = 0 complex is a closed shell singlet. Figure 4 gathers the most relevant OSLOs and the corresponding FOLI values. For Ni, four well-localized d-type orbitals (Figure 4a) are obtained, leading to a Ni (+2) OS. Then, for each thiolate ligand, one finds two S lone pairs and two σ-type orbitals associated with the two S−Ni σ bonds (see Figure 4b). Since each thiolate is a fragment, these two sets of orbitals are not localized into individual S lone pair and S−Ni bonds but form two in-phase (+,+) and out-of-phase (+,−) localized orbitals within the fragment. The σ (+,−) OSLO exhibits a relatively large FOLI value (∼1.7), indicating some partial contribution from the Ni center. The σ (+,+) orbital shows a minor Ni contribution, leading to a smaller FOLI value (∼1.3). In addition, each thiolate exhibits a well localized π-type orbital on the two sp^2 carbon atoms, with FOLI ∼1. The last OSLO, in Figure 4b (bottom right), corresponds to a π-type orbital delocalized over the two thiolate ligands, consistent with the FOLI value (∼2). Moreover, the Δ-FOLI value is *exactly* zero for both population schemes. This indicates a formal split of the electron pair between the two ligands (in other words, a covalent assignment), leading to two thiolate (−1) moieties to accompany the Ni (+2) center. We can envisage similar situations with the OSLO procedure when dealing with mixed-valence compounds. Visual inspection of the critical localized

https://doi.org/10.1021/acs.jctc.1c01011
J. Chem. Theory Comput. 2022, 18, 309−322

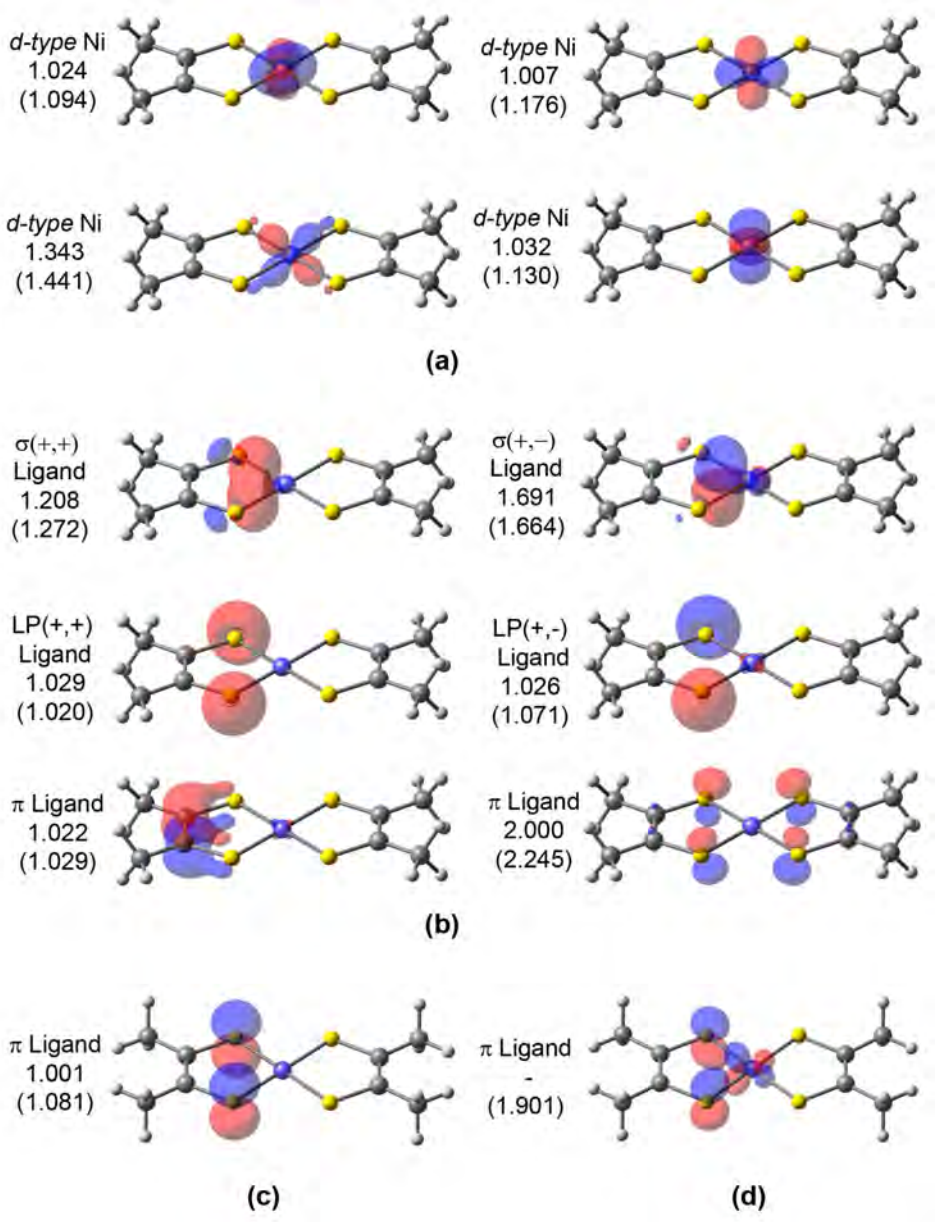

Figure 4. Valence LOs of the $[Ni(S_2C_2Me_2)_2]^0$ system with IAO-AutoSAD and TFVC (in parentheses) FOLI values. d-Type orbitals on Ni (a), ligand's σ, lone pair (LP), and π orbitals (b). Last localized ligand π orbital for $[Ni(S_2C_2Me_2)_2]^{2-}$ (c). Last localized ligand π orbital from the beta density of $[Ni(S_2C_2Me_2)_2]^{-}$ using TFVC (d). The isosurface value is 0.075 au.

orbital(s) will confirm or deny mixed valence or covalent character suggested by very small Δ-FOLI values.

The two-electron reduction of $[Ni(S_2C_2Me_2)_2]$ leads to the $S = 0$ closed-shell species $[Ni(S_2C_2Me_2)_2]^{2-}$. The OSLO procedure yields essentially the same valence localized orbitals as in the previously discussed oxidized form (i.e., four d-type localized orbitals on Ni, two lone pairs, and two σ type S−Ni orbitals), except that the last delocalized orbital is replaced by two well-localized π-type orbitals, one on each thiolate ligand, as shown in Figure 4c. The Δ-FOLI value is larger than 1, clearly pointing to ligand-based reduction, and in turn, Ni (+2) and two thiolate (−2) moieties.

One-electron reduction to $[Ni(S_2C_2Me_2)_2]^{1-}$ is more tricky. The system is an open-shell doublet ($S = \frac{1}{2}$), and the α and β parts are treated separately. The α part is rather clear-cut, yielding similar localized orbitals as in the fully reduced $n = 2$ species, with Δ-FOLI > 0.6. For the β part, using IAO-AutoSAD populations leads to localized orbitals comparable to those of the oxidized form ($n = 0$): four d orbitals on Ni and a last π orbital delocalized over the two thiolate moieties, with FOLI ∼2 and Δ-FOLI = 0. These OLSOs suggest a mixed-valence situation with Ni (+2) and two partially reduced thiolates (−1.5), from equal sharing of the last beta electron between the thiolates. This result, as well as those for the closed-shell species, agrees with the experimental evidence[64,65] and with the EOS scheme.[35]

However, the results for the β part of the $S = \frac{1}{2}$ species are somewhat different when using TFVC populations. In the iterative process, two equivalent π-type orbitals centered on each thiolate with significant contribution from the Ni center

https://doi.org/10.1021/acs.jctc.1c01011
J. Chem. Theory Comput. 2022, 18, 309−322

(see Figure 4d) are selected over the d-type orbital centered on Ni (which also exhibits significant mixing with the ligands). The FOLI values are 1.901 and 2.011, respectively, indicating a large degree of delocalization of these last orbitals. As a consequence, the picture obtained is a Ni (+3) with two fully reduced thiolate (−2) ligands, with a Δ-FOLI value of merely 0.11. This very small Δ-FOLI value argues for equal sharing of the last electron pair.

In Naumann's ion,[66] $[Cu(CF_3)_4]^-$, Cu OS and the role of the CF_3 ligands have been debated for more than 25 years.[67−72] Based on the DFT frontier molecular orbitals, Snyder considered that the metal center is best described as Cu (+1) (i.e., d^{10}), instead of a d^8 Cu (+3) as would follow if all CF_3 ligands were formally anionic (−1).[67] According to Snyder, the anion features an "inverted" ligand field,[72] where the lowest unoccupied molecular orbital (LUMO) exhibits dominant ligand character. This assignment has been questioned by others, who support the latter, more conventional, view of four CF_3^- ligands.[68,69] Most recently, the Lancaster group have put forward further experimental and computational arguments in favor of d^{10}.[70,71] Other arguments supporting the Cu (+1) and Cu (+3) picture have also been given.[72]

These conflicting views are rooted in the relatively nonpolar character of the Cu−C bond. In recent work, some of us showed that both the LOBA and EOS schemes give OS assignments consistent with a formal Cu (+3) species.[35] While the LOBA results were rather clear, the $R(\%)$ = 51.7 value of the EOS assignment indicated a very close call. The OSLO procedure (with either population analysis) points toward formal anionic CF_3 (−1) ligands and hence a Cu (+3) species, as shown in Table 1. One can identify four well-localized d-type orbitals centered on Cu (Figure 5a), while the σ-type interaction between Cu and each CF_3 is captured by four equivalent ligand-centered orbitals with non-negligible contribution from the Cu (Figure 5b). Notice also the mixing of p-type orbitals from the F atoms of the CF_3 moiety. These localized orbitals provide a much clearer picture as compared to those obtained with PM localization for the same wave function.[35] Encouragingly, the FOLI values of the last orbitals are virtually the same with both atomic population schemes (∼1.5). The Δ-FOLI value for the assignment is somewhat smaller using IAO-AutoSAD (0.373) as compared to TFVC (0.728), but the same picture emerges in both cases. Finally, OSLO results for the one- and two-electron reduction of $[Cu(CF_3)_4]^-$ indicate that both processes are metal based, as expected given the Cu (+3) assignment of the anion.

In TM carbenes, a double bond is formed between the TM and the carbene. The σ bond is understood as originating from σ-donation of a sp^2 lone pair on the carbon atom to the TM. The nature of the π-type interaction is much more system-dependent, leading to two well-established situations. In the so-called Fischer carbenes, the π electrons formally sit on the TM d-type orbital, which back-donates to a formally neutral carbene moiety. In Schrock-type carbenes, the π electrons are formally associated with the carbene moiety, which becomes anionic (−2). Previous experience indicated that the OS assignment in TM-carbene complexes is challenging. Often, EOS analysis yields low $R(\%)$ values rather close to 50, driven by nearly equal populations of the π-type EFOs on the TM and the carbene moiety. With LOBA, Pipek−Mezey localized orbitals do not readily correspond with the σ and π bonds.[35] We studied a set of 14 TM carbenes.[73] The set includes four

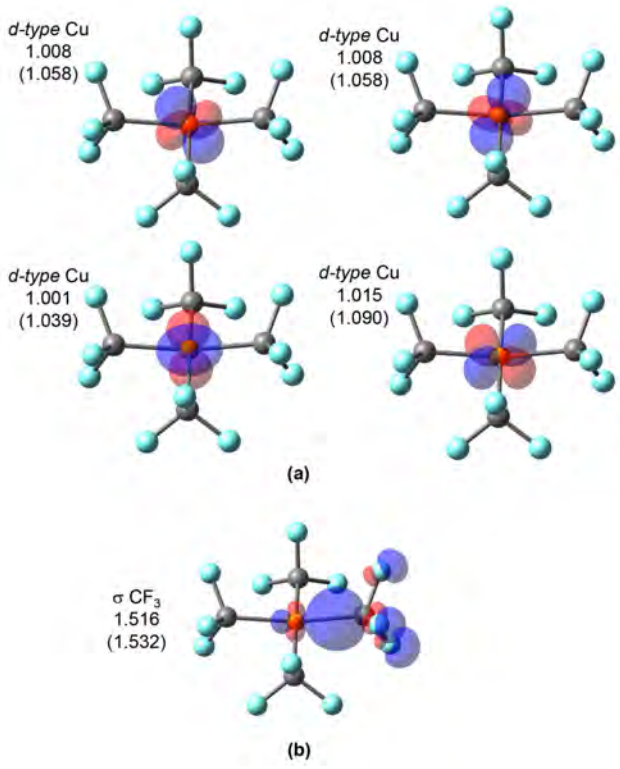

Figure 5. Selected LOs of $[Cu(CF_3)_4]^-$ with IAO-AutoSAD and TFVC (in parentheses) FOLI values for Cu (a) and the CF_3 ligand (b). The relatively nonpolar character of the σ Cu-CF_3 interaction is clearly evident. However, the FOLI value (∼1.5) as well as visual inspection indicates that this orbital has greater CF_3^- character than Cu (3d) character so that in a winner-take-all assignment, the ligands emerge as CF_3^- and the metal adopts a Cu (+3) OS. The isosurface value for the plots is 0.075 au.

conventional W-based Fischer carbenes (**1**−**4**), five Schrock W- and Mo-based catalysts (**5**−**9**), and five Ru- and Os-based first and second generation Grubbs catalysts (**10**−**14**).

Referring again to Table 1, the OSLO procedure combined with IAO-AutoSAD populations correctly identifies all prototypical Fischer and Schrock carbenes, while all Grubbs catalysts but **11** are pictured as formal neutral Fisher-type carbenes. Notice the Δ-FOLI values are mostly below 0.3 (especially for nominal Schrock and Grubbs carbenes), with FOLI values around 2.0, indicating significant delocalization of the last orbital. Such values could support a covalent division of charge and, at the very least, call for inspection of the relevant σ-type and π-type TM-carbene OSLOs. To this end, Figure 6 shows two examples of OSLOs involving the TM and the carbene unit. The FOLI values of the σ-type bonds (left) are noticeably smaller than those of the π-type bonds (right), which exhibit a very similar contribution from both fragments. Yet, one can see that the OSLO procedure produces nice, chemically interpretable localized orbitals for the σ and π bonding.

For the two cases shown in Figure 6, the IAO-AutoSAD and TFVC fragment charges lead to different OS assignments, despite yielding almost identical sets of localized orbitals. The σ-type OSLO belongs to the carbene, with FOLI values of ∼1.5 and ∼1.8 for the Fischer-type $(CO)_5W{=}\mathbf{CH}_2$ complex (**4**) and the Grubbs-type $PCy_3Cl_2Os{=}\mathbf{CH}_2$ complex (**10**), respectively. The π-type OSLO is the origin of the discrepancy.

https://doi.org/10.1021/acs.jctc.1c01011
J. Chem. Theory Comput. 2022, 18, 309−322

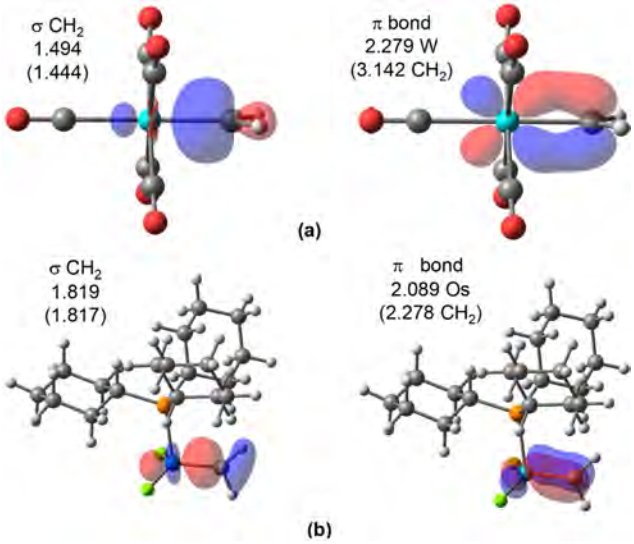

Figure 6. σ and π TM-carbene OSLOs for (a) the Fischer-type $(CO)_5W{=}\mathbf{CH_2}$ complex (species **4**) and (b) the Grubbs-type $PCy_3Cl_2Os{=}\mathbf{CH_2}$ complex (species **10**). The FOLI values for each orbital are shown using IAO-AutoSAD (with the corresponding TFVC values in parentheses). The large FOLI values (>2) for the π-type TM−carbene interaction as well as visual inspection show the shared electron character of this interaction. The isosurface value is 0.075.

Since this is the last selected orbital in the OSLO procedure, its allegiance is based on the FOLI values for each fragment. In the case of **10**, TFVC provides FOLI values of 2.28 for the carbene and 2.32 for the TM, while for IAO-AutoSAD the values are 2.14 and 2.09, respectively. Consequently, ionic assignment leads to a neutral CH_2 according to IAO-AutoSAD and to an anionic CH_2 (−2) according to TFVC. Notice that Δ-FOLI values are below 0.05 in both cases, the smallest seen in this study. The genuinely covalent nature of this π bond precludes meaningful classification of this system as Fischer or Schrock: instead the electron pair is shared.

On the other hand, the different OS assignment for **4** is rather unexpected, as both population methods produce virtually the same set of OSLOs. With IAO-AutoSAD, **4** is quite clearly a neutral Fischer-type carbene with a Δ-FOLI value of 0.61. However, when using TFVC, the assignment is not only reversed, with a small Δ-FOLI (0.19), but also the FOLI values of the last π-type OSLO are significantly higher (3.14 and 3.34 for the carbene and TM metal, respectively). The fragment TFVC populations on the carbene and the W atom are 0.76 e^- and 0.66 e^-, respectively. Hence, the remaining 0.58 e^- belongs to the spectator CO ligands, which explains the large FOLI value obtained. By contrast, with IAO-AutoSAD, the population of the carbene and W are 0.64 and 1.03 e^-, so the electron pair is more clearly on W (although covalent character is visually evident in Figure 6).

As a last example, let us consider the species described in IUPAC's technical report illustrating three different bonding modes of the SO_2 ligand.[2,3] Karen showed that when acting as a Z-type ligand (i.e., as a Lewis acid), the electronegative-acceptor caveat had to be applied to the ionic approximation so that the SO_2 ligand remains neutral. With EOS analysis, the expected neutral SO_2 ligand was recovered in all three cases.[26] The OSLO results of Table 1 also clearly identify a neutral SO_2 moiety for both the L-type and Z-type configurations, with large Δ-FOLI values of over 1.0. In the case of the π-type bonding configuration, the SO_2 is once again clearly identified as neutral, but there is a close-call situation involving Ru and a noninnocent nitrosyl ligand trans to the SO_2, which calls for visual inspection of the OSLOs. The last three OSLOs (from IAO-AutoSAD results) belong to Ru, with FOLI values of 1.44, 1.88 and 2.43 and are depicted in Figure 7. The admixture of

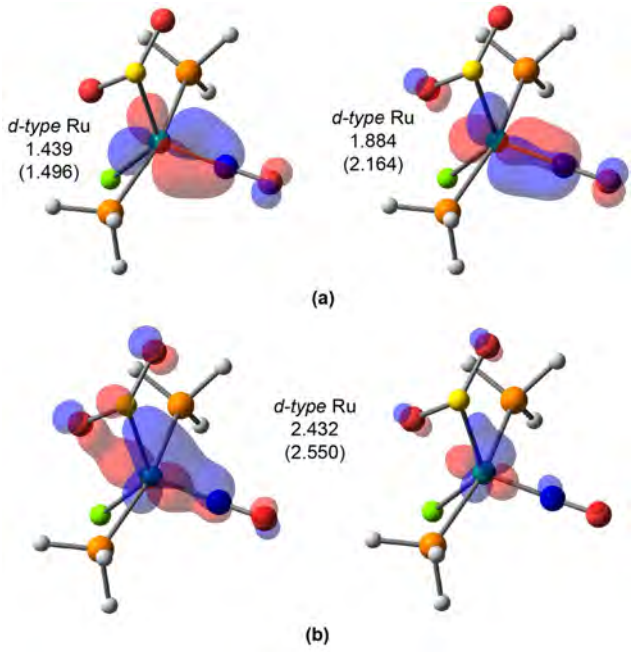

Figure 7. Selected Ru-centered OSLOs for $Ru(SO_2)Cl(NO)(PH_3)_2$ (π-type), with IAO-AutoSAD and TFVC (in parentheses) FOLI values. The isosurface is 0.075 au for panel a, which shows the third and second last OSLOs to be selected. In panel b, which shows the last OSLO selected, there are also significant ligand contributions as evident from the larger FOLI value and visual inspection of the orbital isosurface of 0.075 au (left), which can be clarified by choosing a larger value of 0.125 au for the isosurface (right).

contributions from the SO_2 and NO ligands is indeed significant for the last OLSO (Figure 7b), but the Δ-FOLI value of 0.51 suggests that an ionic assignment to Ru remains justified. Overall, this results in a Ru (0), SO_2 (0), and NO (+1) OS assignment.

When using TFVC populations with the default tolerance of 10^{-2}, the last two localized orbitals, one centered on Ru and another on NO, have FOLI values within the tolerance and are therefore selected together in the last step of the iterative procedure, leading to a different OS assignment. However, the linear-dependency check indicates significant overlap between these two orbitals. As a consequence, their shape substantially changes after orthogonalization, leading to a pair of localized orbitals very similar to those of Figure 7. In this case, being a nonsymmetric system, a tighter tolerance of 10^{-4} affords the selection of the last orbitals in the iterative process one by one, readily producing the same results obtained with IAO-AutoSAD.

CONCLUSIONS

The purpose of this work was to report a new oxidation state localized orbital (OSLO) scheme that performs orbital localization based on *molecular fragments* after a DFT

https://doi.org/10.1021/acs.jctc.1c01011
J. Chem. Theory Comput. 2022, 18, 309−322

calculation with a chosen total charge and spin state. The user should select a fragmentation of the target complex, such as separation into one (or more) metal centers and individual ligands. After an iterative process to select the most strongly fragment-localized OSLOs, each molecular fragment is associated with a set of localized orbitals derived from a simple orbital spread criterion. This association, in turn, determines the fragment's formal charge or oxidation state (OS) in a natural manner.

We introduced a new index, namely, the fragment orbital localization index (FOLI), to quantify the degree of locality of each OSLO (or any input orbital) on each fragment. As examples, the lowest possible FOLI value of 1 corresponds to complete localization on that fragment, while perfect delocalization between two fragments yields a FOLI value of 2. Evaluation of FOLIs requires fragment populations. Two distinct population schemes have been tested for this purpose, namely, a real-space approach (TFVC) and a new version of the intrinsic atomic orbitals (IAO-AutoSAD) that uses on-the-fly evaluation of the reference minimal basis based on superposition of atomic densities (SAD).

The OSLO iterative procedure selects the orbital with lowest FOLI value on each iteration, so that the last OSLO produced has the largest FOLI value (and is least strongly fragment-localized) among the whole set. The Δ-FOLI value for the last localized orbital measures the gap with the second smallest FOLI value among the fragments. Δ-FOLI measures the reliability of the OS assignment, such that a Δ-FOLI value larger than 0.5 usually indicates a clear OS assignment. Smaller values suggest increasingly covalent character in the least localized OSLO.

Numerical tests of the new scheme shows that the OSLOs are in much better agreement with the expected Lewis structure than those obtained with other *global* localization schemes such as Pipek−Mezey (apart from straightforward cases). As a result, previously identified limitations of the localized orbital bonding analysis (LOBA) procedure for OS assignment that originate in the use of global orbital localization methods are overcome with the OSLO approach. Transition metal carbenes are one such class of examples.

The OSLOs themselves carry significant chemical information, and their visualization helps to clarify borderline OS assignments. One such example discussed here is the $Cu(CF_3)_4^-$ anion, where the OSLO corresponding to the σ (Cu−CF_3) interaction exhibits some covalent character but supports a conventional d^8 Cu configuration rather than d^{10}. Another example is the Grubbs catalyst, $PCy_3Cl_2Os{=}CH_2$, where the OSLO corresponding to the Os−carbene π bond is almost perfectly covalent, thus rendering the conventional Fischer and Schrock classifications inapplicable.

We find the IAO-AutoSAD population scheme performs well in combination with OSLO, outperforming the TFVC scheme that is conventionally used in the framework of effective oxidation state (EOS) analysis. IAO-AutoSAD represents a promising all-round general, fast, analytical, basis-set independent Hilbert-space based atomic population scheme.

■ ASSOCIATED CONTENT

Supporting Information

The Supporting Information is available free of charge at https://pubs.acs.org/doi/10.1021/acs.jctc.1c01011.

xyz files for all inputs needed to reproduce the calculations reported herein (XYZ)

■ AUTHOR INFORMATION

Corresponding Authors

Pedro Salvador − *Institut de Química Computacional i Catàlsi and Departament de Química, Universitat de Girona, 17003 Girona, Catalonia, Spain;* orcid.org/0000-0003-1823-7295; Email: pedro.salvador@udg.edu

Martin Head-Gordon − *Pitzer Center for Theoretical Chemistry, Department of Chemistry, University of California, Berkeley, California 94720, United States;* orcid.org/0000-0002-4309-6669; Email: mhg@cchem.berkeley.edu

Authors

Martí Gimferrer − *Institut de Química Computacional i Catàlsi and Departament de Química, Universitat de Girona, 17003 Girona, Catalonia, Spain;* orcid.org/0000-0001-5222-2201

Abdulrahman Aldossary − *Pitzer Center for Theoretical Chemistry, Department of Chemistry, University of California, Berkeley, California 94720, United States*

Complete contact information is available at: https://pubs.acs.org/10.1021/acs.jctc.1c01011

Author Contributions

#M.G. and A.A. made equal contributions.

Notes

The authors declare the following competing financial interest(s): One of the authors (M.H.-G.) is a part-owner of Q-Chem Inc., whose software was extended with the method described here and used for calculations reported herein.

■ ACKNOWLEDGMENTS

M.G. thanks the Generalitat de Catalunya and Fons Social Europeu for the predoctoral fellowship (Grant 2018 FI_B 01 120). P.S. was supported by the Ministerio de Ciencia, Innovacion y Universidades (MCIU), Grant PGC2018-098 212-B-C22. A.A. and M.H.-G. acknowledge support from the U.S. National Science Foundation through Grant No. CHE-1955 643 and additional support from CALSOLV.

■ REFERENCES

(1) Karen, P. Oxidation State, A Long-Standing Issue! *Angew. Chem., Int. Ed.* **2015**, *54*, 4716−4726.

(2) Karen, P.; McArdle, P.; Takats, J. Toward a comprehensive definition of oxidation state (IUPAC Technical Report). *Pure Appl. Chem.* **2014**, *86*, 1017−1081.

(3) Karen, P.; McArdle, P.; Takats, J. Comprehensive definition of oxidation state (IUPAC Recommendations 2016). *Pure Appl. Chem.* **2016**, *88*, 831−839.

(4) Lyaskovskyy, V.; de Bruin, B. Redox non-innocent ligands: versatile new tools to control catalytic reactions. *ACS Catal.* **2012**, *2*, 270−279.

(5) Minkin, V. I.; Glukhovtsev, M. N.; Simkin, B. Y. *Aromaticity and Antiaromaticity*; John Wiley & Sons, Inc., 1994.

(6) Balaban, A. T.; Oniciu, D. C.; Katritzky, A. R. Aromaticity as a cornerstone of heterocyclic chemistry. *Chem. Rev.* **2004**, *104*, 2777−2812.

(7) Boldyrev, A. I.; Wang, L.-S. Beyond organic chemistry: aromaticity in atomic clusters. *Phys. Chem. Chem. Phys.* **2016**, *18*, 11589−11605.

(8) Heitkemper, T.; Sarcevic, J.; Sindlinger, C. P. A Neutral Silicon(II) Half-Sandwich Compound. *J. Am. Chem. Soc.* **2020**, *142*, 21304−21309.
(9) Min, X.; Popov, I. A.; Pan, F.-X.; Li, L.-J.; Matito, E.; Sun, Z.-M.; Wang, L.-S.; Boldyrev, A. I. All-Metal Antiaromaticity in Sb4-Type Lanthanocene Anions. *Angew. Chem., Int. Ed.* **2016**, *55*, 5531−5535.
(10) Panetier, J. A.; Letko, C. S.; Tilley, T. D.; Head-Gordon, M. Computational Characterization of Redox Non-Innocence in Cobalt-Bis(Diaryldithiolene)-Catalyzed Proton Reduction. *J. Chem. Theory Comput.* **2016**, *12*, 223−230.
(11) Raebiger, H.; Lany, S.; Zunger, A. Charge self-regulation upon changing the oxidation state of transition metals in insulators. *Nature* **2008**, *453*, 763−766.
(12) Resta, R. Charge states in transition. *Nature* **2008**, *453*, 735−735a.
(13) Steen, J. S.; Knizia, G.; Klein, J. E. M. N. σ-Noninnocence: Masked Phenyl-Cation Transfer at Formal NiIV. *Angew. Chem., Int. Ed.* **2019**, *58*, 13133−13139.
(14) Walsh, A.; Sokol, A. A.; Buckeridge, J.; Scanlon, D. O.; Catlow, C. R. A. Electron Counting in Solids: Oxidation States, Partial Charges, and Ionicity. *J. Phys. Chem. Lett.* **2017**, *8*, 2074−2075.
(15) Ampßler, T.; Monsch, G.; Popp, J.; Riggenmann, T.; Salvador, P.; Schröder, D.; Klüfers, P. Not Guilty on Every Count: The "Non-Innocent" Nitrosyl Ligand in the Framework of IUPAC's Oxidation-State Formalism. *Angew. Chem., Int. Ed.* **2020**, *59*, 12381−12386.
(16) Wang, G.; Zhou, M.; Goettel, J. T.; Schrobilgen, G. J.; Su, J.; Li, J.; Schlöder, T.; Riedel, S. Identification of an iridium-containing compound with a formal oxidation state of IX. *Nature* **2014**, *514*, 475−477.
(17) Thom, A. J. W.; Sundstrom, E. J.; Head-Gordon, M. LOBA: a localized orbital bonding analysis to calculate oxidation states, with application to a model water oxidation catalyst. *Phys. Chem. Chem. Phys.* **2009**, *11*, 11297−11304.
(18) Sit, P. H.-L.; Zipoli, F.; Chen, J.; Car, R.; Cohen, M. H.; Selloni, A. Oxidation State Changes and Electron Flow in Enzymatic Catalysis and Electrocatalysis through Wannier-Function Analysis. *Chem. - Eur. J.* **2011**, *17*, 12136−12143.
(19) Ramos-Cordoba, E.; Postils, V.; Salvador, P. Oxidation States from Wave Function Analysis. *J. Chem. Theory Comput.* **2015**, *11*, 1501−1508.
(20) Gimferrer, M.; Comas-Vilà, G.; Salvador, P. Can We Safely Obtain Formal Oxidation States from Centroids of Localized Orbitals? *Molecules* **2020**, *25*, 234.
(21) Catlow, C. R. A.; Stoneham, A. M. Ionicity in solids. *J. Phys. C: Solid State Phys.* **1983**, *16*, 4321.
(22) Jiang, L.; Levchenko, S. V.; Rappe, A. M. Rigorous definition of oxidation states of ions in solids. *Phys. Rev. Lett.* **2012**, *108*, 166−403.
(23) Walsh, A.; Sokol, A. A.; Buckeridge, J.; Scanlon, D. O.; Catlow, C. R. A. Oxidation states and ionicity. *Nat. Mater.* **2018**, *17*, 958−964.
(24) Mayer, I. Relation between the Hilbert space and "fuzzy atoms" analyses. *Chem. Phys. Lett.* **2013**, *585*, 198−200.
(25) Ramos-Cordoba, E.; Salvador, P.; Mayer, I. The atomic orbitals of the topological atom. *J. Chem. Phys.* **2013**, *138*, 214107.
(26) Postils, V.; Delgado-Alonso, C.; Luis, J. M.; Salvador, P. An Objective Alternative to IUPAC's Approach To Assign Oxidation States. *Angew. Chem., Int. Ed.* **2018**, *57*, 10525−10529.
(27) Høyvik, I.-M.; Jørgensen, P. Characterization and generation of local occupied and virtual Hartree−Fock orbitals. *Chem. Rev.* **2016**, *116*, 3306−3327.
(28) Mardirossian, N.; Head-Gordon, M. Thirty years of density functional theory in computational chemistry: an overview and extensive assessment of 200 density functionals. *Mol. Phys.* **2017**, *115*, 2315−2372.
(29) Boys, S. F. Construction of Some Molecular Orbitals to Be Approximately Invariant for Changes from One Molecule to Another. *Rev. Mod. Phys.* **1960**, *32*, 296−299.
(30) Edmiston, C.; Ruedenberg, K. Localized Atomic and Molecular Orbitals. *Rev. Mod. Phys.* **1963**, *35*, 457−464.
(31) Pipek, J.; Mezey, P. G. A fast intrinsic localization procedure applicable for ab initio and semiempirical linear combination of atomic orbital wave functions. *J. Chem. Phys.* **1989**, *90*, 4916−4926.
(32) Aquilante, F.; Bondo Pedersen, T.; Sánchez de Merás, A.; Koch, H. Fast noniterative orbital localization for large molecules. *J. Chem. Phys.* **2006**, *125*, 174101.
(33) Høyvik, I.-M.; Jansik, B.; Jørgensen, P. Orbital localization using fourth central moment minimization. *J. Chem. Phys.* **2012**, *137*, 224114.
(34) Knizia, G. Intrinsic Atomic Orbitals: An Unbiased Bridge between Quantum Theory and Chemical Concepts. *J. Chem. Theory Comput.* **2013**, *9*, 4834−4843.
(35) Gimferrer, M.; Van der Mynsbrugge, J.; Bell, A. T.; Salvador, P.; Head-Gordon, M. Facing the Challenges of Borderline Oxidation State Assignments Using State-of-the-Art Computational Methods. *Inorg. Chem.* **2020**, *59*, 15410−15420.
(36) Stoll, H.; Wagenblast, G.; Preuss, H. On the use of local basis-sets for localized molecular-orbitals. *Theor. Chim. Acta* **1980**, *57*, 169−178.
(37) Raimondi, M.; Famulari, A.; Specchio, R.; Sironi, M.; Moroni, F.; Gianinetti, E. Ab initio non-orthogonal approaches to the computation of weak interactions and of localised molecular orbitals for QM/MM procedures. *J. Mol. Struct.: THEOCHEM* **2001**, *573*, 25−42.
(38) Nagata, T.; Takahashi, O.; Saito, K.; Iwata, S. Basis set superposition error free self-consistent field method for molecular interaction in multi-component systems: Projection operator formalism. *J. Chem. Phys.* **2001**, *115*, 3553−3560.
(39) Khaliullin, R. Z.; Head-Gordon, M.; Bell, A. T. An efficient self-consistent field method for large systems of weakly interacting components. *J. Chem. Phys.* **2006**, *124*, 204105.
(40) Sax, A. F. Localization of molecular orbitals on fragments. *J. Comput. Chem.* **2012**, *33*, 1495−1510.
(41) de Silva, P.; Giebułtowski, M.; Korchowiec, J. Fast orbital localization scheme in molecular fragments resolution. *Phys. Chem. Chem. Phys.* **2012**, *14*, 546−552.
(42) Horn, P. R.; Sundstrom, E. J.; Baker, T. A.; Head-Gordon, M. Unrestricted absolutely localized molecular orbitals for energy decomposition analysis: Theory and applications to intermolecular interactions involving radicals. *J. Chem. Phys.* **2013**, *138*, 134119.
(43) Li, Z.; Li, H.; Suo, B.; Liu, W. Localization of molecular orbitals: from fragments to molecule. *Acc. Chem. Res.* **2014**, *47*, 2758−2767.
(44) Senjean, B.; Sen, S.; Repisky, M.; Knizia, G.; Visscher, L. Generalization of Intrinsic Orbitals to Kramers-Paired Quaternion Spinors, Molecular Fragments, and Valence Virtual Spinors. *J. Chem. Theory Comput.* **2021**, *17*, 1337−1354.
(45) Mo, Y.; Bao, P.; Gao, J. Energy decomposition analysis based on a block-localized wavefunction and multistate density functional theory. *Phys. Chem. Chem. Phys.* **2011**, *13*, 6760−6775.
(46) Mao, Y.; Loipersberger, M.; Horn, P. R.; Das, A.; Demerdash, O.; Levine, D. S.; Prasad Veccham, S.; Head-Gordon, T.; Head-Gordon, M. From Intermolecular Interaction Energies and Observable Shifts to Component Contributions and Back Again: A Tale of Variational Energy Decomposition Analysis. *Annu. Rev. Phys. Chem.* **2021**, *72*, 641−666.
(47) Giovannini, T.; Koch, H. Energy-based molecular orbital localization in a specific spatial region. *J. Chem. Theory Comput.* **2021**, *17*, 139−150.
(48) Subotnik, J. E.; Sodt, A.; Head-Gordon, M. Localized orbital theory and ammonia triborane. *Phys. Chem. Chem. Phys.* **2007**, *9*, 5522−5530.
(49) Pipek, J. Localization measure and maximum delocalization in molecular systems. *Int. J. Quantum Chem.* **1989**, *36*, 487−501.
(50) Salvador, P.; Ramos-Cordoba, E. Communication: An approximation to Bader's topological atom. *J. Chem. Phys.* **2013**, *139*, 071103.

https://doi.org/10.1021/acs.jctc.1c01011
J. Chem. Theory Comput. 2022, 18, 309−322

(51) Lee, M. S.; Head-Gordon, M. Extracting polarized atomic orbitals from molecular orbital calculations. *Int. J. Quantum Chem.* **2000**, *76*, 169−184.
(52) Lu, W. C.; Wang, C. Z.; Schmidt, M. W.; Bytautas, L.; Ho, K. M.; Ruedenberg, K. Molecule intrinsic minimal basis sets. I. Exact resolution of ab initio optimized molecular orbitals in terms of deformed atomic minimal-basis orbitals. *J. Chem. Phys.* **2004**, *120*, 2629−2637.
(53) Laikov, D. N. Intrinsic minimal atomic basis representation of molecular electronic wavefunctions. *Int. J. Quantum Chem.* **2011**, *111*, 2851−2867.
(54) Janowski, T. Near equivalence of intrinsic atomic orbitals and quasiatomic orbitals. *J. Chem. Theory Comput.* **2014**, *10*, 3085−3091.
(55) Epifanovsky, E.; Gilbert, A. T.; Feng, X.; Lee, J.; Mao, Y.; Mardirossian, N.; Pokhilko, P.; White, A. F.; Coons, M. P.; Dempwolff, A. L.; et al. Software for the frontiers of quantum chemistry: An overview of developments in the Q-Chem 5 package. *J. Chem. Phys.* **2021**, *155*, 084801.
(56) Salvador, P.; Ramos-Cordoba, E.; Gimferrer, M. *APOST-3D*; Institute of Computational Chemistry and Catalysis, University of Girona: Girona, Spain, 2019.
(57) Becke, A. D. A multicenter numerical integration scheme for polyatomic molecules. *J. Chem. Phys.* **1988**, *88*, 2547−2553.
(58) Mardirossian, N.; Head-Gordon, M. ωB97X-V: A 10-parameter, range-separated hybrid, generalized gradient approximation density functional with nonlocal correlation, designed by a survival-of-the-fittest strategy. *Phys. Chem. Chem. Phys.* **2014**, *16*, 9904−9924.
(59) Weigend, F.; Ahlrichs, R. Balanced basis sets of split valence, triple zeta valence and quadruple zeta valence quality for H to Rn: Design and assessment of accuracy. *Phys. Chem. Chem. Phys.* **2005**, *7*, 3297−3305.
(60) Goerigk, L.; Hansen, A.; Bauer, C.; Ehrlich, S.; Najibi, A.; Grimme, S. A look at the density functional theory zoo with the advanced GMTKN55 database for general main group thermochemistry, kinetics and noncovalent interactions. *Phys. Chem. Chem. Phys.* **2017**, *19*, 32184−32215.
(61) Dohm, S.; Hansen, A.; Steinmetz, M.; Grimme, S.; Checinski, M. P. Comprehensive thermochemical benchmark set of realistic closed-shell metal organic reactions. *J. Chem. Theory Comput.* **2018**, *14*, 2596−2608.
(62) Chan, B.; Gill, P. M.; Kimura, M. Assessment of DFT methods for transition metals with the TMC151 compilation of data sets and comparison with accuracies for main-group chemistry. *J. Chem. Theory Comput.* **2019**, *15*, 3610−3622.
(63) Hu, S.-X.; Li, W.-L.; Lu, J.-B.; Bao, J. L.; Yu, H. S.; Truhlar, D. G.; Gibson, J. K.; Marçalo, J.; Zhou, M.; Riedel, S.; Schwarz, W. H. E.; Li, J. On the Upper Limits of Oxidation States in Chemistry. *Angew. Chem., Int. Ed.* **2018**, *57*, 3242−3245.
(64) Davison, A.; Edelstein, N.; Holm, R. H.; Maki, A. H. The Preparation and Characterization of Four-Coordinate Complexes Related by Electron-Transfer Reactions. *Inorg. Chem.* **1963**, *2*, 1227−1232.
(65) Lim, B. S.; Fomitchev, D. V.; Holm, R. H. Nickel Dithiolenes Revisited: Structures and Electron Distribution from Density Functional Theory for the Three-Member Electron-Transfer Series $[Ni(S_2C_2Me_2)_2]^{0,1-,2-}$. *Inorg. Chem.* **2001**, *40*, 4257−4262.
(66) Naumann, D.; Roy, T.; Tebbe, K.-F.; Crump, W. Synthesis and Structure of Surprisingly Stable Tetrakis(trifluoromethyl)cuprate(III) Salts. *Angew. Chem. Int. Ed.* **1993**, *32*, 1482−1483.
(67) Snyder, J. P. Elusiveness of Cu^{III} Complexation; Preference for Trifluoromethyl Oxidation in the Formation of $[Cu^{I}(CF_3)_4]^-$ Salts. *Angew. Chem., Int. Ed. Engl.* **1995**, *34*, 80−81.
(68) Kaupp, M.; von Schnering, H. G. Formal Oxidation State versus Partial Charge-A Comment. *Angew. Chem., Int. Ed. Engl.* **1995**, *34*, 986−986a.
(69) Aullón, G.; Alvarez, S. Oxidation states, atomic charges and orbital populations in transition metal complexes. *Theor. Chem. Acc.* **2009**, *123*, 67−73.
(70) Walroth, R. C.; Lukens, J. T.; MacMillan, S. N.; Finkelstein, K. D.; Lancaster, K. M. Spectroscopic Evidence for a $3d^{10}$ Ground State Electronic Configuration and Ligand Field Inversion in $[Cu(CF_3)_4]^{1--}$. *J. Am. Chem. Soc.* **2016**, *138*, 1922−1931.
(71) DiMucci, I. M.; Lukens, J. T.; Chatterjee, S.; Carsch, K. M.; Titus, C. J.; Lee, S. J.; Nordlund, D.; Betley, T. A.; MacMillan, S. N.; Lancaster, K. M. The Myth of d^8 Copper(III). *J. Am. Chem. Soc.* **2019**, *141*, 18508−18520.
(72) Hoffmann, R.; Alvarez, S.; Mealli, C.; Falceto, A.; Cahill, T. J.; Zeng, T.; Manca, G. From Widely Accepted Concepts in Coordination Chemistry to Inverted Ligand Fields. *Chem. Rev.* **2016**, *116*, 8173−8192.
(73) Occhipinti, G.; Jensen, V. R. Nature of the transition metal-carbene bond in Grubbs olefin metathesis catalysts. *Organometallics* **2011**, *30*, 3522−3529.

https://doi.org/10.1021/acs.jctc.1c01011
J. Chem. Theory Comput. 2022, 18, 309−322

4.3 Towards a unified treatment of spin-polarization in wavefunction analysis

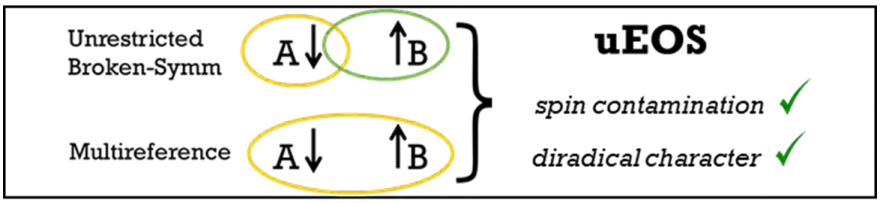

Gimferrer, M.; Salvador, P. **2023**, *Submitted* (manuscript under revision).

Abstract: Current wavefunction analysis techniques treat the alpha and beta electrons separately, in particular those designed to extract oxidation states (OS). With this strategy the classical electron pair picture can be sometimes blurred by spin contamination or spin polarization. We propose a change of paradigm by replacing the alpha and beta electron densities by paired and unpaired densities, in particular in the framework of the effective oxidation states (EOS). The new approach, hencefort uEOS, yields exactly the same results as EOS for restricted single-determinant WF in singlet state, but affords a unified treatment of spin-polarization. That is, treats on equal footing broken-symmetry and truly correlated wavefunctions, providing rationale for the formal homolytic split of the electron pair in the OS assignment of spin polarized or diradicaloid systems.

RESEARCH ARTICLE

Towards a unified treatment of spin-polarization in wavefunction analysis

Martí Gimferrer[a] and Pedro Salvador*[a]

This paper is dedicated to the memory of Professor Joseph J. Danneberg (1941-2023), brilliant scientist and dear friend, who passed away on 6 January 2023.

[a] MSc. M. Gimferrer and Dr. P. Salvador
Institut de Química Computacional i Catàlisi, Departament de Química
University of Girona
Maria Aurèlia Capmany i Farnés 69, 17003, Girona, Catalonia, Spain
E-mail: pedro.salvador@udg.edu

Supporting information for this article is given via a link at the end of the document.

Abstract: Current wavefunction analysis techniques treat the alpha and beta electrons separately, in particular those designed to extract oxidation states (OS). With this strategy the classical electron pair picture can be sometimes blurred by spin contamination or spin polarization. We propose a change of paradigm by replacing the alpha and beta electron densities by paired and unpaired densities, in particular in the framework of the effective oxidation states (EOS). The new approach, henceforth uEOS, yields exactly the same results as EOS for restricted single-determinant WF in singlet state, but affords a unified treatment of spin-polarization. That is, treats on equal footing broken-symmetry and truly correlated wavefunctions, providing rationale for the formal homolytic split of the electron pair in the OS assignment of spin polarized or diradicaloid systems.

Introduction

After two centuries, the oxidation state (OS) has survived as chemical concept of utmost significance in different areas of Chemistry. When it comes to chemical bonding, OSs are essential for electron counting.[1] Wavefunction (WF) analysis techniques specially devoted to extract OS explicitly avoid considering atomic average quantities such as partial atomic charges or spin densities, which are far from a non-integer version of the atom's OS.[2] Instead, the key of success of these approaches is that the electrons pairs are treated individually, much more in line with current IUPAC's definition.[3] Then, one or another strategy is used to assign each electron pair to a given atom or molecular fragment (ligand). For instance, in the localized orbital bonding analysis (LOBA) the molecular orbitals are first localized and then population analysis is applied on each of them to determine whether the electron pair is assigned to the transition metal (TM) center or not.[4] Recently, we developed a scheme (OSLO) to obtain optimal fragment-localized orbitals that also results in OS assignation for single-determinant wavefunctions[5] Alternatively, in the scheme first introduced by Sit,[6] the position of the centroid of each localized orbital is used, following either a simple geometric or a more involved criterion,[7] to assign the electron pair to the TM or to a ligand.

Among these rather recent approaches, only the so-called effective oxidation state (EOS) analysis was developed with the aim of being applied on equal footing for single-determinant or correlated WFs.[8] This is so because EOS does not rely on molecular localized orbitals but on the occupation of Mayer's effective fragment orbitals (EFOs),[9] i.e. the natural orbitals of the net's fragment density. In the case of atomic fragments (the original effective atomic orbitals), the EFOs recover the notion of minimal basis (i.e. atomic hybrids for core/lone pair and valence orbitals). When applied to molecular fragments (e.g. ligands), the EFOs resemble the molecular orbitals of the free fragment, polarized by the environment and exhibiting fractional occupations, even for the virtual space.[10] The EFOs are simply obtained by diagonalization of the $\mathbf{PS}^{A}$ matrix, where **P** is the first-order density matrix and $\mathbf{S}^{A}$ is the fragment's net overlap matrix, both in an atomic orbital basis (see the supporting information for technical details). Since the **P** matrix is readily available for most electronic structure methods, EOS analysis is of most general applicability. The scheme also requires an underlying atom-in-molecule (AIM) scheme that ultimately defines the shape of the $\mathbf{S}^{A}$ matrices. The AIM schemes that better capture the partial ionic character of the bonds, both Hilbert-space or real-space, perform better in the context of OS.[8]

In the original EOS scheme (see the supporting information for further details), the alpha and beta EFOs are obtained for each molecular fragment and then are sorted by decreasing occupation number. Electrons are given to those with higher occupancies until the total number of alpha and beta electrons have been assigned.[8] Then, the last occupied (LO) and the first unoccupied (FU) EFOs (belonging to different fragments) make up the frontier EFOs. From their non-integer occupations for each spin case (λ) one can define a reliability index

$$R_{\sigma}(\%) = 100\, min(1, \lambda^{\sigma}_{LO} - \lambda^{\sigma}_{FU} + 1/2) \wedge R(\%) = min(R_{\alpha}, R_{\beta}) \quad (1)$$

that quantifies how close the actual electron distribution is to the formal ionic picture given by the OS. When the difference in occupation of the frontier EFOs exceeds half electron the OS assignment is considered as undisputable (R (%) = 100). Two (or

more) frontier EFOs from different fragments being degenerate in occupation number represents the worst-case scenario, leading to two different equally plausible OS distributions and *R* (%) = 50. Moreover, EOS analysis does more than the mere OS assignation, which could be regarded as immaterial beyond the realm of chemical concepts and categorization. The shape of the EFOs is also a valuable tool to visualize where individual electrons of each metal/ligand are assigned. They also afford the separate quantification of σ-donation, π-donation and π-backdonation of ligands from ground-state properties (i.e. without any additional fragment reference calculation),[10] or the quantification of Lewis acid/base character.[11]

Current methods designed for OS assignation have in common that, in the case of open-shell systems, the alpha and beta electrons are treated separately, either by diagonalizing the spin-resolved $\mathbf{P}^{\alpha}$ and $\mathbf{P}^{\beta}$ matrices in the case of EOS analysis or by obtaining the corresponding localized orbitals of each spin channel separately. Thus, when formally distributing the electrons over the molecular fragments, the number of both alpha and beta electrons is conserved, as it should. However, this strategy precludes the coveted straightforward interpretation into genuine chemical terms, namely electron pairs. Dealing with separate alpha and beta EFOs or localized orbitals with unequal shapes (in particular with spin contaminated WFs) is clearly not satisfactory. Indeed, albeit in a different context, the so-called quasi-restricted orbitals have also been introduced for similar reasons.[12]

In a single-determinant restricted-open-shell description, an easy way out is to deal first with the doubly-occupied space to assign electron pairs, and then the singly-occupied space to assign the remaining (alpha) electrons. But single-determinant description of open-shell systems typically involves unrestricted molecular orbitals, where the spatial distribution of the alpha and beta electrons differs. For instance, a recent study showed strong spin-polarization in the Fe-NO π-type interaction of a high spin *S* = 3/2 complex, which accumulated α-density on the metal and β-density on the nitrosyl ligand.[13] The authors pinpointed conceptual difficulties reconciling IUPAC's ionic approximation of electron pairs with the α/β separation in such spin polarized bonds. In their study the authors used both Kohn-Sham Density Functional Theory (KS-DFT) and Complete Active Space Self-Consistent Field (CASSCF) methods, and applied EOS analysis leading to quite consistent results. However, if the molecular system had been in the singlet state the situation could have been different.

Unrestricted KS-DFT methods can readily capture spin-polarization in singlet states by recurring to the so-called broken symmetry approach (BS-DFT).[14] BS-DFT calculations are routinely used when studying magnetic interactions in e.g. dinuclear TM compounds as a way to describe their antiferromagnetic states.[14a, 14b] BS-DFT can also describe diradicals, an extreme case of spin polarization. All these cases result in a spurious non-zero spin density for singlet states. On the contrary, when turning to a proper description of these singlet states, namely a multireference WF, there is no spin density. In this case, the spin polarization is introduced by populating the antibonding orbitals, while keeping the restricted framework. Consequently, the alpha and beta parts of the density are *exactly* equivalent (as it should be for a singlet state), so the fate of the alpha electrons and beta electrons resulting from any analysis should be the same.

For instance, let us consider an A-B system with marked diradical character. With the less theoretically sound BS-DFT description, the spin-density will clearly indicate the spin polarization, and allocate e.g. the alpha electron on A and the beta electron on B. EOS analysis does not rely on the spin density but will also lead to the same result, because of the separate treatment of both spin channels. The same situation is expected for other localization-based OS approaches like LOBA or OSLO. However, if the same system is properly described with a multireference WF, the application of EOS would not yield a formal homolytic split of the electron pair, no matter how large the diradical character is. This supposes a more serious conceptual concern for the aforementioned schemes for OS elucidation.

On the other hand, the density of effectively unpaired electrons introduced by Takatsuka as

$$u(\mathbf{r}) = 2\rho(\mathbf{r}) - \int \rho(\mathbf{r},\mathbf{r}')\rho(\mathbf{r}',\mathbf{r})d\mathbf{r}' \quad , \qquad (2)$$

accounts for the deviation of the first-order density matrix, $\rho(\mathbf{r},\mathbf{r}')$, from idempotency.[15] Such unpaired density plays the role of the spin density, $\rho_s(\mathbf{r})$, when the latter vanishes. For that reason it has been recently used as ingredient in density functional theory for multiconfigurational WFs.[16] It was also utilized by Mayer in his improved bond order formulation, in place of the exchange density of the alpha and beta electrons (i.e. explicit use of $\mathbf{P}^{\alpha}$ and $\mathbf{P}^{\beta}$ matrices).[17] In fact, it can be readily seen that in the case of a restricted open-shell WF, $u(\mathbf{r}) \equiv \rho_s(\mathbf{r})$. In a more general case, $u(\mathbf{r})$ is conveniently expressed in terms of the natural orbitals of the first-order density matrix and their occupation numbers as[15]

$$u(\mathbf{r}) = \sum_i n_i(2-n_i)\phi_i^*(\mathbf{r})\phi_i(\mathbf{r}). \qquad (3)$$

Contrary to the spin density, $u(\mathbf{r})$ is positive definite so that it accounts for local excess of either alpha or beta electrons. Integrated over the whole space gives the number of effectively unpaired electrons (N_d),[18] used in the past to quantify diradical character.[15] The effectively paired density can be simply obtained by subtracting $u(\mathbf{r})$ from the total first-order density

$$\rho_p(\mathbf{r}) = \rho(\mathbf{r}) - u(\mathbf{r}). \qquad (5)$$

The main idea of this work is to obtain the EFOs and their occupations from the paired and unpaired densities, and use them into the EOS scheme, instead of those from the alpha and beta densities, as it is commonly used. We will show that the new approach, henceforth uEOS, fixes the problems described above while keeping the essential ingredients of the EOS scheme for OS assignation. In fact, uEOS and EOS produce *exactly* the same results for restricted single-determinant WF in singlet state. The new scheme can be applied on equal footing for any single-determinant or correlated WFs, thus affording a unified treatment of spin-polarization.

Results and Discussion

Let us start by considering the dissociation of singlet LiH, described with a full configuration interaction WF. The evolution of the occupation number of the EFOs for Li and H from the paired and unpaired density along the dissociation profile are shown in Figure 1 (top). They both correspond to polarized 2s and 1s effective orbitals, respectively (there is an additional 1s-type EFO on Li from the paired density, not shown). Notice that the occupations of the paired EFOs have been halved, to allow a better comparison between the relevance of the paired and unpaired densities.

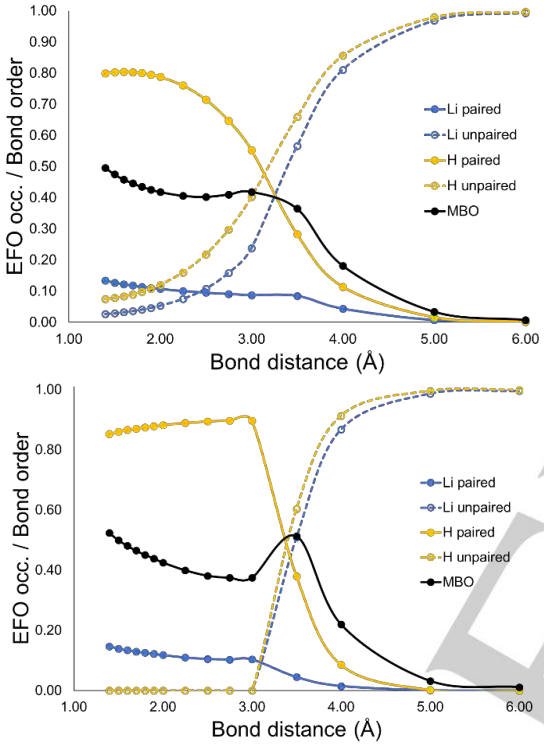

Figure 1. Occupation number of the EFOs and Mayer bond orders (MBO) along the Li-H bond dissociation. FCI (top) and BS-DFT (bottom).

At large interatomic distances the unpaired density clearly dominates. The occupation of both EFOs (dashed curve) is close to 1, clearly pointing towards a homolytic Li· + H· situation, with the unpaired electrons on each atom coupled as a singlet. As the atoms get closer, the occupation of the unpaired EFOs monotonically decrease, while the occupation of the EFOs from the paired density increase, particularly that of the H moiety (solid lines). At ca. 3 Å, the dominating paired and unpaired curves cross, very close to the maximum of the covalent bond order (black curve).[19] At shorter distances, the occupation of the unpaired EFOs is very small, and also that of the Li 2s EFO from the paired density, clearly indicating that the formal heterolytic assignment of the electron pair as Li(+1) + H(-1) is preferred. Table S1 and Figure S1 of the supporting material shows the deviation of the actual occupation numbers of the EFOs from those of the ideal formal homolytic and heterolytic situations. The best picture at each point is that with lower deviation, and the worst scenario from a formal point of view is precisely at the crossing point near 3.2 Å, where the uncertainty of the fate of the two electrons is maximal. The deviation of the preferred heterolytic assignment of the electrons at equilibrium distance is not zero, due to the partial covalent character of the LiH bond. Figure 1 (bottom) gathers the same type of analysis performed from a KS-DFT density obtained with the ωB97XD functional. The picture is qualitatively similar, even though the structure of the underlying WF is completely different. At short interatomic distances one has a closed-shell solution, and the unpaired density vanishes. The occupation of the paired EFOs clearly indicates the hydride character of the species. Again, at around 3.2 Å, a BS solution is found and the occupation of the paired EFOs drastically drop, in favor of the unpaired counterpart. It also coincides with a maximum of the covalent bond order. At long distances the unpaired density fully dominates, and each atom bear one electron, the spin which is revealed by the sign of the respective atomic spin densities.

This type of paired/unpaired information can be readily incorporated into a general scheme for OS assignation from WF, namely uEOS analysis. In the same way as conventional EOS, one starts by defining the molecular fragments (i.e. metals and ligands). Then, the EFOs are obtained for each fragment using the paired and unpaired densities. For that, one just needs to diagonalize $\mathbf{P}^{p}\mathbf{S}^{A}$ and $\mathbf{P}^{u}\mathbf{S}^{A}$, where $\mathbf{P}^{p}$ and $\mathbf{P}^{u}$ are the matrix representation of the paired and unpaired densities in the AO basis, respectively. The EFOs are then sorted by decreasing occupation number and electron pairs are assigned to those EFOs from the paired density with higher occupation, and individual electrons (usually of unknown spin) are assigned to EFOs of the unpaired density. However, while in EOS analysis the number of alpha and beta electrons is predefined, in uEOS the total (integer) number of paired and unpaired electrons is in general not known and must be inferred by comparing the occupations of the respective EFOs.

Let us discuss in detail the different situations one may encounter for a molecular system holding N electrons, depending on the nature of the WF. In the case of a restricted single-determinant WF, the unpaired density trivially vanishes, so $\mathbf{P}^{u} = 0$. Accordingly, the uEOS procedure is applied using solely the total **P** matrix, from which $N/2$ pairs of electrons are assigned to the most populated EFOs, just like the original EOS scheme. This leads naturally to the formal heterolytic cleavage of the bonds, in agreement with the winner-takes-it-all principle of the ionic approximation.[3]

In the restricted open-shell case, since $u(\mathbf{r}) = \rho_s(\mathbf{r})$, the unpaired density holds exactly $N_\alpha - N_\beta$ electrons. As the number of unpaired electrons is known, the number of electron pairs is also predetermined. The uEOS procedure is performed independently for the unpaired density (where $N_\alpha - N_\beta$ electrons are individually assigned to fragments), and for the paired density (where N_β pairs of electrons are distributed among fragments). However, for open-shell systems the use of unrestricted single-determinant WFs is much more common. In that case, the unpaired density no longer coincides with the spin density due to spin contamination and therefore $\int u(\boldsymbol{r})\, d\boldsymbol{r} \geq n_\alpha - n_\beta$. Consequently, the total (integer) number of unpaired electrons is no longer predetermined.

We will illustrate the new procedure by considering the complex $[Fe(CN)_5NO]^{3-}$ in its S = 1/2 ground-state. The occupation number of the relevant EFOs of the paired and unpaired densities for the restricted open-shell and unrestricted WFs are compiled in Table 1. Notice that the occupations of the paired EFOs have been halved throughout this manuscript. In the restricted case, a doublet leads to exactly one unpaired electron. The occupation number of the unpaired EFOs are 0.143, 0.816 and 0.010 for Fe, NO and each CN fragment, respectively. The unpaired electron is thus clearly assigned to the NO moiety. Afterwards, the uEOS procedure is safely applied to the paired density and the remaining N_β pairs of electrons are assigned. The last electron pair is assigned to a 3d hybrid EFO on Fe, with an occupation of 0.690. The first unoccupied EFO sits on the NO moiety, with an occupation of 0.233. The procedure finally results in a formal d^6 Fe(+2), NO(0) and CN(-1) picture. As far as the reliability of the uEOS assignation is concerned, one can simply replace in Eq. 1 the frontier occupations of the alpha and beta parts by those of the paired and unpaired densities. This results in a clear cut assignation, with R_p (%) = 95.7 and R_u (%) = 100.

Table 1. Occupation numbers of selected paired and unpaired EFOs for the $[Fe(CN)_5NO]^{3-}$ anion with restricted open-shell and unrestricted WFs.

Fe			NO			CN		
Rest.		Unrest.	Rest.		Unrest.	Rest.		Unrest.
paired								
3d	**0.851**	**0.854**	π	**0.994**	**0.993**	π	**0.989**	**0.989**
3d	**0.770**	**0.755**	π	**0.993**	**0.992**	π	**0.988**	**0.988**
3d	**0.690**	**0.602**	3σ	**0.880**	**0.876**	3σ	**0.790**	**0.788**
3d	0.282	0.287	π*	0.233	0.210	π*	0.050	0.049
4s	0.254	0.253	π*	0.151	0.138	π*	0.044	0.041
Unpaired								
0.143		0.175	π*	**0.816**	**0.813**	0.010		0.012
		0.115			0.120			0.004
		0.031			0.004			

The occupation numbers obtained with the unrestricted WF are quite similar to the restricted ones, even though the spin contamination is significant ($\langle S^2 \rangle$ = 0.93). Noticeably, the spin contamination induces a number of additional EFOs of the unpaired density with small but non-zero occupation. If one assumes that there is only one unpaired electron, the occupation number of the last possible electron pair is 0.602, much larger than the second highest occupation from the unpaired density (0.175). This indicates that the assumption is valid and hence the OS assignation coincides with that of the RO-DFT case, with R_p (%) = 89.2 and R_u (%) = 100.

The conventional EOS analysis of the unrestricted WF also leads to the same OS assignation by considering the alpha and beta electrons separately, albeit with lower reliability index (R_α (%) = 62.3 and R_β (%) = 99.6). The shape of the relevant EFOs is shown in Figure 2. Here, the spin polarization induces a significant mismatch not only on the occupation but also on the shape of the alpha and beta EFOs (top). The 3σ and π* EFOs of the alpha part are mixed so that it is not clear the nature of the EFO holding the unpaired alpha electron.

With uEOS, however, the picture obtained is much easier to interpret in terms of electron pairs. A single set of either singly or doubly occupied EFOs is obtained (Figure 2, bottom). The two π* EFOs of the NO moiety are clearly identified in the paired part, together with the matching 3d EFOs on Fe that account for the Fe-NO bonds, polarized towards the Fe, as indicated by the respective occupation numbers. In the unpaired density, the only EFO significantly populated (0.813) is a clear π* on the NO moiety, similar to the (unoccupied) EFO of the paired part with occupation 0.138, altogether pointing to a rather clear neutral NO moiety. It is also interesting to note that the shape of the paired and unpaired EFOs is strikingly similar, differing only by the occupation numbers. This appears to be a common feature of all systems studied thus far.

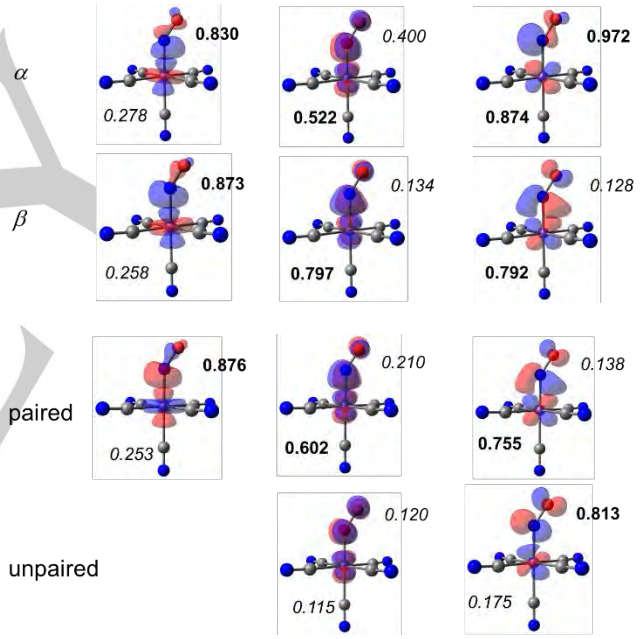

Figure 2. Alpha/beta (top) vs paired/unpaired (bottom) EFOs for the $[Fe(CN)_5NO]^{3-}$ anion from an unrestricted WF, including occupation numbers of occupied (bold) and unoccupied (italic) EFOs.

One may foresee situations where more than N_α - N_β EFOs of the unpaired density have occupation numbers larger than (half) the occupation of the N_β pairs from the paired density. In the new scheme uEOS this is an indication that one (or more) formal electron pairs must be homolytically split, leading to a larger number of formally unpaired electrons than those expected from N_α - N_β. This is indeed the case polynuclear compounds exhibiting magnetic interactions, complexes having one or more redox-active ligands that can be found in different OS,[20] or mixed-valence compounds in general.

Let us analyze in some detail the simple complex $Ni(S_2C_2Me_2)_2$ in singlet state, described at closed-shell DFT, BS-DFT and CASSCF(2,2) levels of theory. The uEOS analysis of the closed-shell WF assigns 13 electron pairs to the metal for a Ni(+2), but ultimately leads to the undesired situation where two EFOs of the paired density (one on each thiolate ligand, see Figure 3 top) are degenerate in occupation (0.531), and there is only one electron pair left to assign. In the past, we had assumed a formal homolytic split of the electron pair on the basis of the degeneracy of the frontier EFOs. However, any asymmetry of the ligands would break that degeneracy and forbid the formal homolytic split, unless artificially introduced.

On the other hand, the BS-DFT WF has significant diradical character ($<S^2>$ = 0.63). The immediate effect is a decrease of the occupation number of the (previously) last paired EFO on each ligand, down to 0.250. At the same time, a very similar EFO from the unpaired density on each ligand raises its occupation to 0.554 (see Figure 3 bottom-left). The uEOS procedure automatically assigns one unpaired electron to each ligand without any additional external input.

The picture is even clearer at the CASSCF(2,2) level. The occupation of the paired frontier EFO of the closed-shell WF (2 × 0.531) appears roughly decomposed in the uEOS CASSCF treatment into an unpaired (0.725) and a paired (2 × 0.132) contribution (see Figure 3). Thus, uEOS naturally affords the homolytic split that had to be externally imposed in the closed-shell case.

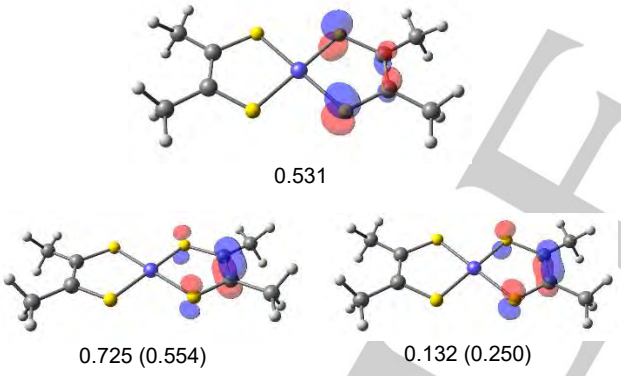

Figure 3. Frontier EFO of the thiolate ligand in $[Ni(S_2C_2Me_2)_2]$. (top) paired EFO from a closed-shell WF; unpaired (bottom-left) and paired (bottom-right) EFO from a CASSCF(2,2) WF. Occupations from the BS-DFT WF in parenthesis.

The complexes $[Fe_2S_2(SCH_3)_4]^{2-/3-}$ are synthetic bimetallic rhomboidal iron-sulfur clusters present in metalloproteins like ferredoxins. In the oxidized form, two high-spin Fe(+3) are antiferromagnetically coupled to a S = 0 state. In the asymmetric reduced form one has a high-spin Fe(+3) and a high-spin Fe(+2) coupled as an overall S = 1/2 doublet state. These model have been long studied in the past,[21] mostly at the BS-DFT level, but also with remarkable exceptions from WF theory.[21b, 21c]

The electronic distribution of the BS-DFT description of both the oxidized and reduced forms is rather straightforward (see Table S4 and Figures S2 and S3). However, the singlet ground-state of the oxidized form described by a CASSCF(10,10) WF, with vanishing spin density, is not so simple. Here is where the new uEOS scheme clearly supersedes conventional EOS analysis and in fact any other method for OS assignation. The analysis of the paired density reveals only nine highly occupied EFOs on each iron center, corresponding to the 1s2s2p3s3p shells. The occupation of the first paired EFO of the d-shell is only 0.169. At the same time, the unpaired density yields five d-type EFOs on each iron center with very large occupations (> 0.8), thus clearly pointing towards a high-spin antiferromagnetically coupled state. The local spin[22] value of the iron centers is 7.37, close to the ideal $<S^2>$ = 8.75 for a high-spin sextet, in line with this interpretation.

Upon one-electron reduction of the system, uEOS yields now for one of the iron centers, one d-type EFO from the paired density with high occupation (0.958), accompanied by four highly occupied d-type EFOs from the unpaired density (0.961-0.934). The other iron center exhibits again five highly occupied d-type EFOs from the unpaired density (0.955-0.864) and very low occupation of the d-shell from the paired density. This clearly leads to the asymmetric Fe(+2)/Fe(+3) assignment, with R(%) = 100. On the other hand, the occupation number of the unpaired EFOs on the ligands is smaller than 0.1 in all cases, making them clear sulfide and thiolate formal species.

Another paradigmatic example that has drawn some attention is the $[Fe(CO)_3NO]^-$ anion, studied in detail by several authors.[23] By combining spectroscopic features with theoretical considerations Klein *et al.* concluded that the most appropriate picture was a neutral Fe center with an anionic NO(-1) ligand, who exhibits two π-type and no σ-type bonds with the metal.[23d] Conventional EOS analysis of the closed-shell KS-DFT description struggles with this system, partly due to its C_{3v} symmetry. At the point of the procedure when there are two pairs of electrons left to assign, the NO ligand still has available two degenerate π* EFOs with an occupation extremely close to that of a pair of degenerate d-type EFOs on the Fe, already indicating a strong covalent character of the Fe-NO bonds. Since the homolytic splitting is not allowed (unless a pseudo-degeneracy occurs in the frontier EFOs), one necessarily ends with either formal Fe(-2)/NO(+1), if the last four electrons are formally assigned to the d-type EFOs of Fe, or Fe(+2)/NO(-3) if these four electrons are assigned to the π* EFOs of the NO ligand. Switching from a closed-shell KS-DFT description to a multireference WF does not make a significant difference with conventional EOS, for the reasons explained above. With uEOS, however, if the unpaired density becomes dominant, the homolytic splitting of the two electron pairs can still be achieved, leading to the Fe(0)/NO(-1) picture suggested by Klein *et al.*[23d] This is exactly what happens when analyzing the CASSCF(4,4) WF used by Klein *et al* (see Table S3 for further details). First, the total number of effectively unpaired electrons, N_D, is 1.50 (0.71 on both Fe and NO), indicating significant static correlation (see also Table S3). The frontier EFOs of the paired and unpaired densities are strikingly similar in shape (see Figure 4), and correspond to the aforementioned d-type on Fe and π*-type on NO. The symmetry of the EFOs on each moiety also indicate that these are involved in two π-bonds. The key aspect for OS assignation are the corresponding occupation numbers obtained from the unpaired (0.337 and 0.342) and paired (0.321 and 0.301) densities. The larger value of the former calls for the

formal homolytic splitting of the two Fe-NO bonds, and the consideration of the anion as a double diradicaloid.

It is interesting to assess the effect of increasing the active space, by using e.g. a CASSCF(10,10) WF. First off, the number of effectively unpaired electrons increases up to N_D = 2.15. However, the occupation number of the relevant frontier unpaired EFOs actually *decreases* to 0.269 and 0.245 for Fe and NO, respectively. The increase in N_D originates from a number of additional EFOs on Fe with smaller but non-negligible occupation, a signature of the additional correlation introduced by enlarging the active space. At the same time, the occupation of the EFOs from the paired density increases to 0.381 and 0.330 for Fe and NO, respectively. The picture originating from the uEOS procedure is now closer to a formal Fe(-2)/NO(+1) closed-shell scenario. Further increasing the active space to (10,14) leads to an intermediate situation between the (4,4) and (10,10) description, with still dominant character of the paired density (see Figure 4). This seems to indicate that using small active spaces tends to overestimate the static correlation of the Fe-NO bonds. The diradicaloid character of the molecule decreases using a (10,14) active space according to uEOS analysis, while at the same time, the number of effectively unpaired electrons increases up to 1.22 for Fe and 0.63 for NO (see supporting material). This shows again that relying on average quantities can be misleading when it comes to settle the fate of individual electrons.

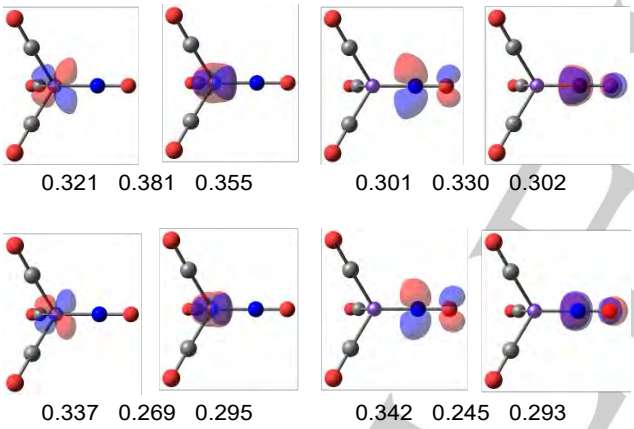

Figure 4. Frontier EFO of the Fe (left) and NO (right) fragments of $[Fe(CO)_3NO]^-$ anion. (top) paired and (bottom) unpaired EFOs from a CASSCF(4,4), CASSCF(10,10) and CASSCF(10,14) WFs.

The OS assignment of a family of di-coordinated compounds ML_2 (M = Be, Mg) with ligands of cyclic (alkyl)(amino) carbene (cAAC) and N-heterocyclic carbene (NHC) type has been recently discussed. The synthetic $Be(cAAC^{Dip})_2$ complex (Dip = 2,6-diisopropylphenyl), was originally described as zero valent Be(0) compound bound by two donor-acceptor interactions between the ligands and the central atom, with the concomitant 2s → 2p promotion of the valence electrons of Be. We have recently shown that the singlet diradicaloid L(-1)→Be(+2)←L(-1) situation better represents this compound, due to the extremely low population of the 2p orbital of Be and the static correlation effects that make some closed-shell KS-DFT WFs unstable.[24] In our previous work we considered both BS-DFT and CASSCF(10,8) WFs to describe the complex and applied EOS analysis. In the case of the restricted KS or CASSCF WFs, the occupation of the 2p π-type EFO on Be is extremely low. The frontier EFOs are two degenerate (in occupation) π-type EFOs on each cAAC ligand, that forced the homolytic splitting of the 3c-2e π bond. However, similarly to the $[Ni(S_2C_2Me_2)_2]$ complex, this OS assignation was performed in an *ad hoc* manner on the basis of the degeneracy of the frontier EFOs due to symmetry.

The new uEOS scheme affords the same OS assignation but in a clearer and more robust way. The relevant EFOs of the paired and unpaired density are shown on Figure 5. At this point of the uEOS procedure there is only one electron pair left to assign. One can see that the occupation of the EFOs of the paired density on all fragments is very small, while a π-type EFO from the unpaired density on each cAAC ligand has the largest occupation of all (0.531). The uEOS scheme thus clearly points towards the aforementioned diradicaloid Be(+2) picture. Notice the irrelevant role of the Be atom, with both paired and unpaired occupations far too small to consider a Be(0) situation.

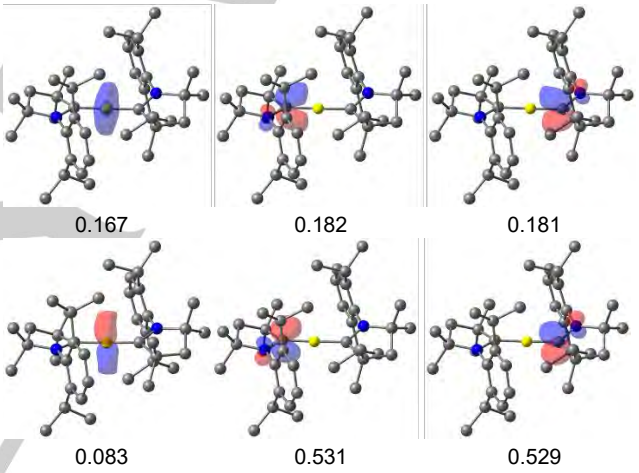

Figure 5. Frontier EFOs of the Be (left) and cAAC (middle and right) fragments of $Be(cAAC^{Dip})_2$. (top) paired EFOs and (bottom) unpaired EFOs from a CASSCF(10,8) WF. Hydrogen atoms omitted for clarity.

As a final illustrative example we will discuss the situation of the $[NaBH_3]^-$ anion, which has generated strong debate in the recent literature about the nature of the Na-B bond.[25] The ground state is singlet, but the closed-shell WF is not stable. The lowest energy solution at the single-determinant level is a broken-symmetry open-shell singlet. The corresponding $\langle S^2 \rangle$ values are strongly dependent on the choice of the DFT functional, and in particular to the admixture of exact exchange. Consequently, the results obtained applying the uEOS procedure are also functional-dependent to some extent, as shown in Tables S5 and S6.

The CASSCF(8,8) wavefunction, a much more appropriate description, exhibits diradicaloid character, due to the significant population of the σ* Na-B bond orbital.[25b] If the diradical character is large enough, the appropriate picture from a OS perspective should be Na(0)/BH_3(-1), in agreement with a formal homolytic cleavage of the Na-B bond. The shape and occupancies of the relevant frontier EFOs obtained with uEOS scheme on the CASSCF(8,8) WF are depicted in Figure 6.

At the point of the uEOS procedure when there is only one electron pair to assign, the occupation of the available unpaired EFO on Na (0.508) and BH_3 (0.459) is much larger than that of the corresponding paired EFOs (0.316 and 0.189, respectively). Consequently, uEOS results in the aforementioned formal homolytic split of the electron pair of the Na-B bond.

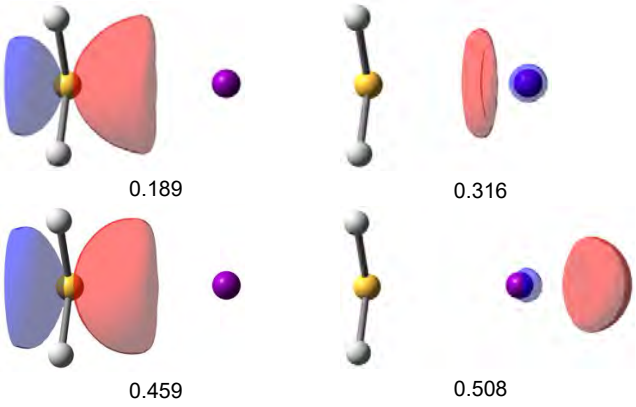

Figure 6. Frontier EFO of the BH_3 (left) and Na (right) fragments of $[NaBH_3]^-$ anion. (top) paired EFOs and (bottom) unpaired EFOs from a CASSCF(8,8) WF.

Remarkably, the shape of the singly occupied unpaired EFOs (Figure 6, bottom) is in striking agreement with the valence active orbitals of the covalent valence-bond WF (i.e. Figure 2 left of Ref. [25c]). The unpaired EFOs thus provide a picture fully consistent with the one put forward by Radenkovic *et al.*[25c]: a dominant diradical character but at the same time an enhanced electrostatic interaction induced by the charge-separation on the two fragments. It does not support the interpretation of Pino-Rios *et al.*,[25d] who considered both unpaired electrons on a formal Na(-1) fragment.

Conclusion

We have shown that analyzing the effectively paired and unpaired densities, rather than the spin-separated alpha and beta electron densities, leads to much more consistent OS assignation in systems exhibiting strong static correlation and spin-polarization. The new scheme applied in the framework of EOS analysis not only accounts for the formal homolytic splitting of electron pairs in singlet diradical(oid) species, but it also affords a better picture of spin-contaminated unrestricted wavefunctions in terms of electron pairs. Similar strategies based on the paired and unpaired densities could be also incorporated in other schemes for OS assignation based on orbital localization, or in more general wavefunction analysis tools deriving from the first-order density matrix.

Acknowledgements

This work was supported by the Ministerio de Ciencia, Innovación y Universidades (MCIU), Grant PGC2018-098212-B-C22. M.G. thanks the Generalitat de Catalunya and Fons Social Europeu for the predoctoral fellowship (2018 FI_B 01120).

Keywords: Oxidation states • Chemical bonding • Redox-active compounds • Diradicaloids • Wavefunction analysis

References

[1] J. E. Carpenter, F. Weinhold, *Journal of Molecular Structure: THEOCHEM* **1988**, *169*, 41-62.

[2] (a) R. Resta, *Nature* **2008**, *453*, 735-735; (b) H. Raebiger, S. Lany, A. Zunger, *Nature* **2008**, *453*, 763-766; (c) A. Walsh, A. A. Sokol, J. Buckeridge, D. O. Scanlon, C. R. A. Catlow, *The Journal of Physical Chemistry Letters* **2017**, *8*, 2074-2075; (d) A. Walsh, A. A. Sokol, J. Buckeridge, D. O. Scanlon, C. R. A. Catlow, *Nature Materials* **2018**, *17*, 958-964.

[3] (a) P. Karen, P. McArdle, J. Takats, *Pure and Applied Chemistry* **2014**, *86*, 1017-1081; (b) P. Karen, P. McArdle, J. Takats, *Pure and Applied Chemistry* **2016**, *88*, 831-839.

[4] A. J. W. Thom, E. J. Sundstrom, M. Head-Gordon, *Physical Chemistry Chemical Physics* **2009**, *11*, 11297-11304.

[5] M. Gimferrer, A. Aldossary, P. Salvador, M. Head-Gordon, *Journal of Chemical Theory and Computation* **2022**, *18*, 309-322.

[6] P. H.-L. Sit, F. Zipoli, J. Chen, R. Car, M. H. Cohen, A. Selloni, *Chemistry – A European Journal* **2011**, *17*, 12136-12143.

[7] (a) P. Vidossich, A. Lledós, *Dalton Transactions* **2014**, *43*, 11145-11151; (b) M. Gimferrer, G. Comas-Vilà, P. Salvador, *Molecules* **2020**, *25*, 234.

[8] E. Ramos-Cordoba, V. Postils, P. Salvador, *Journal of Chemical Theory and Computation* **2015**, *11*, 1501-1508.

[9] (a) E. Ramos-Cordoba, P. Salvador, I. Mayer, *The Journal of Chemical Physics* **2013**, *138*, 214107; (b) I. Mayer, *The Journal of Physical Chemistry* **1996**, *100*, 6249-6257.

[10] G. Comas-Vilà, P. Salvador, under preparation, **2023**.

[11] M. Gimferrer, S. Danés, D. M. Andrada, P. Salvador, *Inorganic Chemistry* **2021**, *60*, 17657-17668.

[12] F. Neese, *Journal of the American Chemical Society* **2006**, *128*, 10213-10222.

[13] G. Monsch, P. Klüfers, *Angewandte Chemie International Edition* **2019**, *58*, 8566-8571.

[14] (a) J. G. Norman, P. B. Ryan, L. Noodleman, *Journal of the American Chemical Society* **1980**, *102*, 4279-4282; (b) L. Noodleman, *The Journal of Chemical Physics* **1981**, *74*, 5737-5743; (c) L. Noodleman, D. A. Case, in *Advances in Inorganic Chemistry, Vol. 38* (Ed.: R. Cammack), Academic Press, **1992**, pp. 423-470.

[15] K. Takatsuka, T. Fueno, K. Yamaguchi, *Theoretica chimica acta* **1978**, *48*, 175-183.

[16] D. Zhang, M. R. Hermes, L. Gagliardi, D. G. Truhlar, *Journal of Chemical Theory and Computation* **2021**, *17*, 2775-2782.

[17] I. Mayer, *Chemical Physics Letters* **2012**, *544*, 83-86.

[18] R. M. Lobayan, R. C. Bochicchio, L. Lain, A. Torre, *The Journal of Chemical Physics* **2005**, *123*, 144116.

[19] M. Rodríguez-Mayorga, E. Ramos-Cordoba, P. Salvador, M. Solà, E. Matito, *Molecular Physics* **2015**, *114*, 1345-1355.

[20] miller.

[21] (a) L. Noodleman, C. Y. Peng, D. A. Case, J. M. Mouesca, *Coordination Chemistry Reviews* **1995**, *144*, 199-244; (b) D. Presti, S. J. Stoneburner, D. G. Truhlar, L. Gagliardi, *The Journal of Physical Chemistry C* **2019**, *123*, 11899-11907; (c) S. Sharma, K. Sivalingam, F. Neese, G. K.-L. Chan, *Nature Chemistry* **2014**, *6*, 927-933; (d) E. Ruiz, J. Cano, S. Alvarez, P. Alemany, *Journal of Computational Chemistry* **1999**, *20*, 1391-1400; (e) O. Hübner, J. Sauer, *Physical Chemistry Chemical Physics* **2002**, *4*, 5234-5243; (f) O. Hübner, J. Sauer, *The Journal of Chemical Physics* **2001**, *116*, 617-628; (g) M. Shoji, K. Koizumi, T. Taniguchi, Y. Kitagawa, S. Yamanaka, M. Okumura, K.

Yamaguchi, *International Journal of Quantum Chemistry* **2007**, *107*, 116-133.

[22] E. Ramos-Cordoba, E. Matito, I. Mayer, P. Salvador, *Journal of Chemical Theory and Computation* **2012**, *8*, 1270-1279.

[23] (a) W. Hieber, K. Beutner, *Zeitschrift für Naturforschung B* **1960**, *15*, 323-324; (b) B. Plietker, A. Dieskau, *European Journal of Organic Chemistry* **2009**, *2009*, 775-787; (c) M. Gruden, M. Zlatar, *Theoretical Chemistry Accounts* **2020**, *139*, 126; (d) J. E. M. N. Klein, B. Miehlich, M. S. Holzwarth, M. Bauer, M. Milek, M. M. Khusniyarov, G. Knizia, H.-J. Werner, B. Plietker, *Angewandte Chemie International Edition* **2014**, *53*, 1790-1794.

[24] (a) M. Gimferrer, S. Danés, E. Vos, C. B. Yildiz, I. Corral, A. Jana, P. Salvador, D. M. Andrada, *Chemical Science* **2022**, *13*, 6583-6591; (b) M. Gimferrer, S. Danés, E. Vos, C. B. Yildiz, I. Corral, A. Jana, P. Salvador, D. M. Andrada, *Chemical Science* **2023**, *14*, 384-392.

[25] (a) C. Foroutan-Nejad, *Angewandte Chemie International Edition* **2020**, *59*, 20900-20903; (b) P. Salvador, E. Vos, I. Corral, D. M. Andrada, *Angewandte Chemie International Edition* **2021**, *60*, 1498-1502; (c) S. Radenković, S. S. Shaik, B. Braïda, *Angewandte Chemie International Edition* **2021**, *60*, 12723-12726; (d) R. Pino-Rios, D. Inostroza, W. Tiznado, *Angewandte Chemie International Edition* **2021**, *60*, 12747-12753.

Chapter 5

On the development of energy decomposition schemes

5.1 Merging the energy decomposition analysis and the interacting quantum atoms approaches

Gimferrer, M.; Danés, S.; Andrada, D. M.; Salvador, P. **2023**, *Submitted* (manuscript under revision).

Abstract: The Energy decomposition analysis (EDA) has established itself as one of most widely used approaches for the decomposition of the interaction energy into chemically sound components. The inherent requirement of reference states for EDA (and its dependence on their nature) has been a matter of recent debate. Alternative molecular energy decomposition schemes that decompose the total energy into atomic and diatomic contributions, such as the Interacting Quantum Atoms (IQA), offer an interesting alternative, since no external references are required and also the intra and intermolecular interactions are treated on equal footing. It has been argued that they possess limited predictive power. Despite a number of efforts to reconcile the chemical picture obtained by both methodologies, none has been particularly devoted to actually combine them. In this work we present the IQA decomposition of the individual terms arising from the EDA in the context of intermolecular interactions, henceforth EDA-IQA. The method is applied to a molecular set covering a wide range of interaction types, including hydrogen bonding, charge-dipole, π-π and halogen interactions. We find that the electrostatic energy from EDA, entirely seen as intermolecular, leads to meaningful and non-negligible intra-fragment contributions upon IQA decomposition, originated from charge penetration. EDA-IQA also affords the decomposition of the Pauli repulsion term into intra- and inter-fragment contributions. The intra-fragment term is destabilizing, particularly for the moieties that are net acceptors of charge, while the inter-fragment Pauli term is actually stabilizing. In the case of the orbital interaction term, the sign and magnitude of the intra-fragment contribution at equilibrium geometries is largely driven by the amount of charge transfer, while the inter-fragment contribution is clearly stabilizing. EDA-IQA terms show a smooth behaviour along the intermolecular dissociation path of selected systems. The new EDA-IQA methodology provides a richer energy decomposition scheme that aims at bridging the gap between the two main distinct real-space and Hilbert-space methodologies.

Merging the Energy Decomposition Analysis with the Interacting Quantum Atoms Approach

Martí Gimferrer,[a] *Sergi Danés,*[a,b] *Diego M. Andrada,*[b] *Pedro Salvador.*[a,*]

a) Institut de Química Computacional i Catàlisi i Departament de Química, Universitat de Girona, c/ Maria Aurèlia Capmany i Farnés 69, 17003, Girona, Catalonia, Spain.

b) Faculty of Natural Sciences and Technology, Department of Chemistry, Saarland University, 66123 Saarbrücken, Federal Republic of Germany.

ABSTRACT

The Energy decomposition analysis (EDA) has established itself as one of most widely used approaches for the decomposition of the interaction energy into chemically sound components. The inherent requirement of reference states for EDA (and its dependence on their nature) has been a matter of recent debate. Alternative molecular energy decomposition schemes that decompose the total energy into atomic and diatomic contributions, such as the Interacting Quantum Atoms (IQA), offer an interesting alternative, since no external reference are required and also the intra- and intermolecular interactions are treated on equal footing. It has been argued that they possess limited predictive power. Despite a number of efforts to reconcile the chemical picture obtained

by both methodologies, none has been particularly devoted to actually *combine* them. In this work we present the IQA decomposition of the individual terms arising from the EDA in the context of intermolecular interactions, henceforth EDA-IQA. The method is applied to a molecular set covering a wide range of interaction types, including hydrogen bonding, charge-dipole, π–π and halogen interactions. We find that the electrostatic energy from EDA, entirely seen as intermolecular, leads to meaningful and non-negligible intra-fragment contributions upon IQA decomposition, originated from charge penetration. EDA-IQA also affords the decomposition of the Pauli repulsion term into intra- and inter-fragment contributions. The intra-fragment term is destabilizing, particularly for the moieties that are net acceptors of charge, while the inter-fragment Pauli term is actually stabilizing. In the case of the orbital interaction term, the sign and magnitude of the intra-fragment contribution at equilibrium geometries is largely driven by the amount of charge transfer, while the inter-fragment contribution is clearly stabilizing. EDA-IQA terms show a smooth behaviour along the intermolecular dissociation path of selected systems. The new EDA-IQA methodology provides a richer energy decomposition scheme that aims at bridging the gap between the two main distinct real-space and Hilbert-space methodologies.

INTRODUCTION

Understanding and accurately assessing intra- and intermolecular interactions is one of the main challenges in chemistry, representing the key to the rational design of molecular systems. Unravelling the physical origin of a particular chemical interaction/bond is often inaccessible directly from experiments. Computationally, however, there is no exact quantum-mechanical operator that directly describes the *chemical bond* and thus different approaches have been developed over the years.

A number of methods focus on the analysis of the electron density in a system (AB) by comparing it with that from the composing fragments (A and B). The concept of deformation density[1] is invoked in some analyses, such as Voronoi deformation density (VDD) charges[2] or charge displacement analysis.[3,4] The electron density of the AB system is also the main ingredient of the Quantum Theory of Atoms in Molecules[5] (QTAIM), from whose topological analysis leads to a plethora of descriptors that can be used to categorize different types of intra- and intermolecular interactions.

An alternative is wavefunction analysis tools that operate directly on the energetics of bond formation and intermolecular interactions, in particular those schemes that decompose the molecular (or formation) energy into chemically meaningful terms. One of the most widely used is the Ziegler-Rauk Energy Decomposition Analysis (EDA),[6] derived from the pioneering work of Kitaura and Morokuma[7].

Let us consider the formal formation of molecule *AB* (henceforth complex) from fragments *A* and *B*. The overall stabilization energy (without basis set superposition error correction) reads as

$$\Delta E_{stab} = E(AB^{AB}) - E(A^{A}) - E(B^{B}), \tag{1}$$

where $E(X^{Y})$ refers to the energy of the subsystem X at the optimized geometry of Y. Thus, ΔE_{stab} is the energy of formation of the system from the isolated fragments in their ground states.

In the EDA formalism, ΔE_{stab} (Eq. 1) is decomposed as follows

$$\Delta E_{stab} = \Delta E_{\mathrm{int}}[A^{0}, B^{0}] + \Delta E_{prep}[A^{0}, B^{0}], \tag{2}$$

being ΔE_{int} and ΔE_{prep} the so-called interaction and preparation energy terms, respectively, which are defined as

$$\Delta E_{\mathrm{int}}[A^{0}, B^{0}] = E(AB^{AB}) - E(A^{0,AB}) - E(B^{0,AB}) \tag{3}$$

$$\Delta E_{prep}[A^0, B^0] = E(A^{0,AB}) - E(A^A) + E(B^{0,AB}) - E(B^B) \equiv \Delta E_{prep,A} + \Delta E_{prep,B}\,. \quad (4)$$

Here, $E(A^{0,AB})$ represents the energy of fragment A computed at the optimized geometry of the complex (superindex *AB*) with a given electronic configuration (A^0), which may not correspond to that of the ground state for the isolated fragment. Defined as such, the preparation energy accounts for *both* the geometrical distortion of the fragments upon formation of the complex and the *promotion* energy from the electronic ground state to the chosen electronic configurations A^0 and B^0. One often refers to strain energy when it only involves the geometrical deformation. Furthermore, it is necessarily positive (repulsive) because $E(A^A)$ and $E(B^B)$ are, *by definition*, the ground state energies of the isolated fragments from both the electronic and geometric perspective. Instead, ΔE_{int} will be negative (attractive) if the interaction between the fragments A and B while forming complex AB is favorable. Importantly, both the interaction and preparation energies depend on the choice for the states A^0 and B^0 as indicated in Eqs. 3 and 4, being crucial its appropriate selection (see below for further details).

By introducing additional intermediate (pseudo)states build up at the optimized geometry of the complex, the interaction energy is further decomposed. Firstly, one considers a *pseudostate* of complex AB formed by the superposition of the undeformed (frozen) densities associated to the fragments in states A^0 and B^0 , namely ($A^0 \cup B^0$), with its associated electronic energy $E(A^0 \cup B^0)$. We refer to ($A^0 \cup B^0$) as a *pseudostate* because it does not have a well-defined antisymmetric wavefunction associated to it.[6, 8] The energy difference with respect to the deformed fragments read as

$$\Delta\widetilde{E}^0(A^0 \cup B^0) = E(A^0 \cup B^0) - E(A^0) - E(B^0), \quad (5)$$

which can be further expressed as

$$\Delta\widetilde{E}^0(A^0 \cup B^0) = \Delta E_{elec}[A^0, B^0] + \Delta\widetilde{E}^0_{XC}[A^0, B^0], \quad (6)$$

where the AB superindex has been omitted for clarity. The term $\Delta E_{elec}[A^0,B^0]$ accounts for the electrostatic interaction of the frozen electron density of fragment A with the nuclei of fragment B and vice versa (attractive), the Coulombic repulsion of the frozen electron densities of A and B and the nuclear repulsion between A and B.

$$\Delta E_{elec}[A^0,B^0] = -\sum_{i\in B}\int \rho_{A^0}(\boldsymbol{r})\frac{Z_i}{|\boldsymbol{r}-\boldsymbol{R}_i|}d\boldsymbol{r} - \sum_{i\in A}\int \rho_{B^0}(\boldsymbol{r})\frac{Z_i}{|\boldsymbol{r}-\boldsymbol{R}_i|}d\boldsymbol{r} + \\ + \int\int \rho_{A^0}(\boldsymbol{r}_1)\,\rho_{B^0}(\boldsymbol{r}_2)\boldsymbol{r}_{12}^{-1}d\boldsymbol{r}_1 d\boldsymbol{r}_2 + \sum_{\substack{i\in A\\ j\in B}}\frac{Z_i Z_j}{|\boldsymbol{R}_i-\boldsymbol{R}_j|}. \tag{7}$$

Equation 7 may be also rewritten as

$$\Delta E_{elec}[A^0,B^0] = -\int \rho_{A^0}(\boldsymbol{r})V_B(\boldsymbol{r})d\boldsymbol{r} - \int \rho_{B^0}(\boldsymbol{r})V_A(\boldsymbol{r})d\boldsymbol{r} + \left(\sum_{\substack{i\in A\\ j\in B}}\frac{Z_i Z_j}{|\boldsymbol{R}_i-\boldsymbol{R}_j|} - \int\int \rho_{A^0}(\boldsymbol{r}_1)\,\rho_{B^0}(\boldsymbol{r}_2)\boldsymbol{r}_{12}^{-1}d\boldsymbol{r}_1 d\boldsymbol{r}_2\right), \tag{8}$$

where the molecular electrostatic potential (MEP) of fragment A in state A^0, $V_A(\boldsymbol{r})$, reads as

$$V_A(\boldsymbol{r}) = \sum_{i\in A}\frac{Z_i}{|\boldsymbol{r}-\boldsymbol{R}_i|} - \int \frac{\rho_{A^0}(\boldsymbol{r}_2)}{|\boldsymbol{r}-\boldsymbol{r}_2|}d\boldsymbol{r}_2. \tag{9}$$

The potential originated from charge clouds is smaller than the one from point charges (nuclei) so that for neutral species the MEP of the fragments afford a favorable interaction that, at chemically relevant distances, overcomes the nuclear repulsion term.[9] In Kohn-Sham density functional theory (KS-DFT) there is an additional contribution from the exchange-correlation functional,[8, 9] which is absent in wavefunction theory.

In a subsequent step, an intermediate state (A^0B^0) is formed by Löwdin orthogonalizing the occupied molecular orbitals (MOs) of the states (A^0) and (B^0), in order to build a proper antisymmetrized wavefunction. Orthogonalization is required as MOs belonging to different fragments were not orthogonal (in principle one could build a Slater determinant with non-

orthogonal MOs but then the expectation value of the energy takes a much complicated form). The Löwdin orthogonalization procedure does not induce charge transfer between the fragments, as the Hilbert-space based electron numbers of the interacting fragments are conserved. This will not be the case when applying a real-space analysis, as will be discussed later.

The energy difference between this intermediate step and that of the previous *pseudostate* reads as

$$\Delta\widetilde{E}_{Pauli}[A^0, B^0] = E(A^0B^0) - E(A^0 \cup B^0), \tag{10}$$

which upon combination of Eqs. 6 and 10 leads to the so-called Pauli repulsion term (ΔE_{Pauli}) [8]

$$\Delta E_{Pauli}[A^0, B^0] = \Delta\widetilde{E}_{Pauli}[A^0, B^0] + \Delta\widetilde{E}^0_{XC}[A^0, B^0]. \tag{11}$$

Hence, the sum $\Delta E_{Pauli}[A^0, B^0] + \Delta E_{elec}[A^0, B^0]$ accounts for the energy change when going from the prepared fragments to the *true* intermediate state with orthogonalized but unrelaxed MOs, and it is a well-defined quantity in the sense that involves properly antisymmetrized states

$$\Delta E_{Pauli}[A^0, B^0] + \Delta E_{elec}[A^0, B^0] = E(A^0B^0) - E(A^0) - E(B^0). \tag{12}$$

It is worth to note that $\Delta\widetilde{E}^0(A^0 \cup B^0)$ is never considered, as the $\Delta\widetilde{E}^0_{XC}[A^0, B^0]$ term is not evaluated explicitly. Once the electrostatic contribution is calculated using Eq. 7 or 8, the Pauli repulsion term is readily obtained from Eq. 12.

In the last step, the MOs of the complex are allowed to relax to the *ground state* of the complex. The energy lowering accompanying this process leads to the so-called orbital interaction term (ΔE_{Orb}), that is necessarily negative (any intermediate state must be higher in energy than the ground state)

$$\Delta E_{orb}[A^0, B^0] = E(AB) - E(A^0B^0). \tag{13}$$

All the steps along the EDA process are illustrated in Scheme 1.

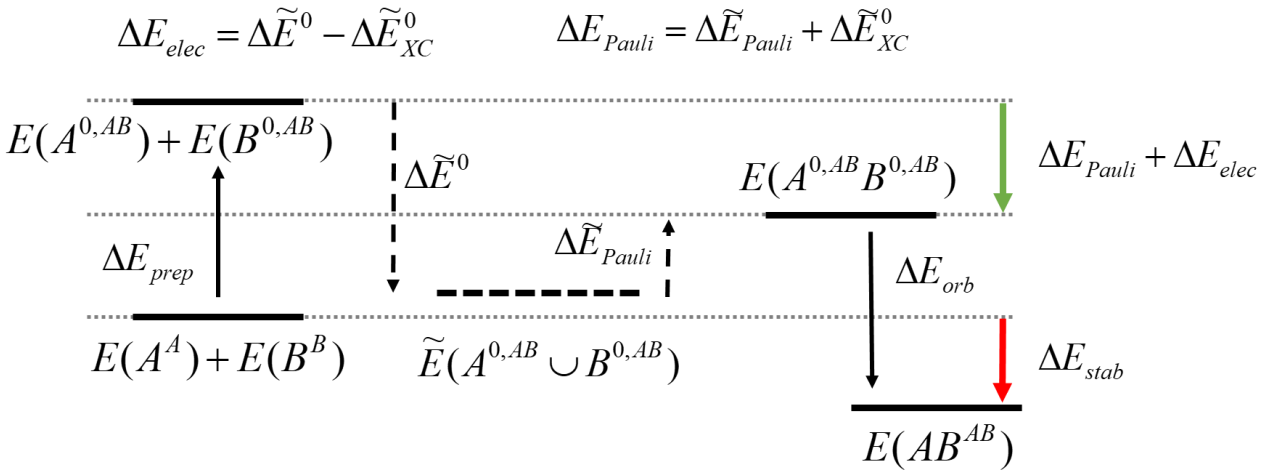

Scheme 1. Energy components of the EDA process with the corresponding intermediate states and pseudo-states for the formation of complex *AB* from the isolated fragments *A* and *B*. $E(X^{Y})$ refers to the energy of subsystem X at the optimized geometry of Y

Localized orbitals can also be introduced in this type energy decomposition schemes. In the Absolutely Localized Molecular Orbitals EDA[10-13] (ALMO-EDA), the interaction energy is further decomposed into a frozen-density, polarization and charge-transfer terms by making use of (variationaly optimized) block-localized orbitals, and explicitly avoiding any reference to intermediate pseudo-states. Natural EDA[14] (NEDA) makes use of the well-known Natural Bond Orbitals (NBO).[15-18] In the Symmetry Adapted Pertubation Theory (SAPT) schemes the interaction energy is perturbationally computed, thus avoiding the supermolecular approach, and decomposed into physically meaningful terms.[19] For further details about these EDA-like methodologies we guide the reader to references [20] and [21].

On the other hand, the total energy of any molecular system can also be decomposed into intra- and inter-atomic contributions. Such decomposition does not require external references or predefined fragments, and treat intra and intermolecular interactions (covalent and non-covalent)

on equal footing. Grouping the one- and two-center terms into intra-fragment and inter-fragment contributions is only optional, but helpful in the case of dealing with intermolecular interactions between well-defined subsystems. In Mayer's Chemical Hamiltonian Approach (CHA), atomic projector operators were used to decompose the Hamiltonian into one- and two-center terms.[22] Further developments in the Hilbert-space ultimately lead to the Chemical Energy Component Analysis (CECA).[23] Considering instead a decomposition of the real-space, the one- and two-electron contributions to the total energy readily afford one- and two-center terms that exactly decompose (up to numerical accuracy) the molecular energy. Such methodologies rely on the identification of the atom within the molecule (AIM). Salvador and Mayer first decomposed the Hartree-Fock energy in the framework of QTAIM,[19] paving the way for the nowadays known as the Interacting Quantum Atoms (IQA) approaches.[24-26,27-31]

In real-space analysis, a given quantity, F_1, expressed in terms of a one-electron density function, $f(\boldsymbol{r}_1)$, is readily decomposed into one-center (atomic or fragment) contributions

$$F_1 \equiv \int f(\boldsymbol{r}_1) d\boldsymbol{r}_1 = \sum_A \int_{\Omega_A} f(\boldsymbol{r}_1) d\boldsymbol{r}_1 = \sum_A F_1^A \,, \tag{14}$$

by integrating over the respective domains. Similarly, two-electron quantities decompose into both one- and two-center components

$$F_2 \equiv \iint f(\boldsymbol{r}_1, \boldsymbol{r}_2) d\boldsymbol{r}_1 d\boldsymbol{r}_2 = \sum_A \int_{\Omega_A}\int_{\Omega_A} f(\boldsymbol{r}_1, \boldsymbol{r}_2) d\boldsymbol{r}_1 d\boldsymbol{r}_2 + \sum_{A,B\neq A} \int_{\Omega_A}\int_{\Omega_B} f(\boldsymbol{r}_1, \boldsymbol{r}_2) d\boldsymbol{r}_1 d\boldsymbol{r}_2 = \sum_A F_2^A + \sum_{A,B\neq A} F_2^{AB} \,. \tag{15}$$

It is worth noting that real-space analysis is not restricted to non-overlapping disjoint domains such as those of QTAIM, where each atom is identified by its nucleus and its atomic basin. The AIM may be more generally represented by continuous atomic weight functions $w_A(\mathbf{r}) \geq 0$ fulfilling $\Sigma_A w_A(\boldsymbol{r}) = 1$ so that the integration of molecular density functions over the atomic

domains are effectively replaced by integrations over the whole real-space of atomic/diatomic effective density functions

$$\int_{\Omega_A} f(\boldsymbol{r})d\boldsymbol{r} \Rightarrow \int w_A(\boldsymbol{r}) f(\boldsymbol{r})d\boldsymbol{r} \equiv \int f_A(\boldsymbol{r})d\boldsymbol{r} \tag{16}$$

$$\int_{\Omega_B}\int_{\Omega_A} f(\boldsymbol{r}_1,\boldsymbol{r}_2)d\boldsymbol{r}_1 d\boldsymbol{r}_2 \Rightarrow \int w_A(\boldsymbol{r}_1) f(\boldsymbol{r}_1,\boldsymbol{r}_2) w_B(\boldsymbol{r}_2)d\boldsymbol{r}_1 d\boldsymbol{r}_2 \equiv \int f_{AB}(\boldsymbol{r}_1,\boldsymbol{r}_2)d\boldsymbol{r}_1 d\boldsymbol{r}_2 .$$

Such atomic weight functions can be derived from a variety of Hirshfeld-type approaches[32] or even mathematical constructs borrowing elements of QTAIM theory.[33] Whether the AIM are allowed to overlap or not might be to some extent matter of taste. Using one or another AIM only has an effect on the actual numerical values obtained for the terms obtained by the IQA decomposition, but not on their definition and physical meaning.

Since the Born-Oppenheimer energy is entirely written in terms of one- and two-electron energy density functions, IQA naturally affords the decomposition of the molecular energy of a complex AB into atomic and diatomic contributions as

$$E(AB) = \sum_i \varepsilon_i + \sum_{i,j<i} \varepsilon_{ij}, \tag{17}$$

where the ε_i and ε_{ij} terms account for the static net atomic and pairwise atomic interaction energies, respectively. The atomic and diatomic terms can be further grouped according to the composing fragments A and B, so that the total energy of the complex can be simply expressed as

$$E(AB) = \varepsilon_A + \varepsilon_B + \varepsilon_{AB}, \tag{18}$$

where

$$\begin{aligned} \varepsilon_A &= \sum_{i\in A} \varepsilon_i + \sum_{i,j\in A} \varepsilon_{ij} \\ \varepsilon_{AB} &= \sum_{\substack{i\in A \wedge j\in B \\ i\in B \wedge j\in A}} \varepsilon_{ij}, \end{aligned} \tag{19}$$

and

$$\varepsilon_A = T_A + V_{AA}^{en} + V_{AA}^{ee}$$
$$\varepsilon_{AB} = V_{AB}^{en} + V_{AB}^{ne} + V_{AB}^{nn} + V_{AB}^{ee}. \quad (20)$$

Each of the intra- and inter-fragment energy term is built upon the physical components of the electronic energy, i.e. kinetic, electron nuclear attraction, nuclear repulsion and electronic repulsion. The latter may be further decomposed into the usual Coulomb, exchange and correlation contributions. One peculiarity of the IQA-type approaches is that the actual formulation depends upon the particular electronic structure method that is used to compute the molecular energies in the first place. Appropriate formulations have been developed for Hartree-Fock[34,24,26] and correlated methods (including CASSCF and CI,[27] MP2[35,28] and Coupled Cluster[29,36,30]). Non-perturbative approaches explicitly require the second order reduced density matrix, which is not available in most electronic structure codes. Curiously, the KS-DFT case is the most problematic one because of the exchange-correlation energy nature. Within wavefunction theory framework, the exchange energy is expressed as a two-electron non-local contribution, that naturally decomposes into both one- and two-center terms. The later are essential to account for the stability of the diatomic bonding interactions.[21] In KS-DFT, the exchange-correlation energy is essentially written in terms of the exchange energy density as

$$V_{xc} = \int \varepsilon_{xc}[\rho(r_1), \nabla\rho(r_1)...]\ dr_1, \quad (21)$$

so that the straightforward real-space decomposition only affords one-center (atomic) terms Different approaches have been introduced to (approximately) recover the chemically meaningful diatomic components from V_{xc}.[25, 31]

Both EDA and IQA methodologies independently have been extensively used in the literature to gain deeper insight into the nature of the chemical bond and to characterize intra- and

intermolecular interactions, allowing to understand and improve chemical reactivity, shelling light to the chemical-bonding picture of non-trivial systems and even most recently suggesting a new type of bond.[37-42]

Recent efforts have been made trying to express some of the EDA-derived descriptors in the framework of real-space analysis, i.e. without recurring to any artificial intermediate (pseudo)states. In this direction, in 2006 Pendas *et al.* compared the behavior of IQA to that of other decomposition schemes (e.g. EDA, NEDA and SAPT) for a series of hydrogen-bonded dimers.[43, 44] The authors decomposed the interaction energy between the two monomers A and B (E_{int}^{AB}) into the sum of classical electrostatics (V_{cl}^{AB}) and exchange-correlation (V_{xc}^{AB}) contributions. They observed that the interaction was governed by the exchange-correlation, thus highlighting the importance of the covalent picture. On the other hand, the deformation energy of the proton acceptor moieties correlated well with the intermolecular charge transfer and classical electrostatic energy derived from IQA. Furthermore, by making use of the fragment's promolecular, polarized (by locating point charges) and fully relaxed densities, they observed that in weakly-bonded (almost non-overlapping) systems the quantities defined by other energy decomposition schemes, i.e. SAPT, KM, EDA and specially NEDA, can be obtained to a good approximation from the inter-fragment (AB) IQA terms. For instance, the electrostatic energy from NEDA was found to be roughly equivalent to the total inter-fragment interaction from IQA.[44]

Pendas *et al.* also critically analyzed the concept of steric repulsion from an IQA perspective.[45] The authors argued that Pauli repulsion is inherently dependent on the fragment's reference states in EDA. They applied IQA to decompose the Hartree-Fock interaction energy into fragment's deformation and inter-fragment interactions

$$\Delta E_{\text{int}} = E_{def} + \sum_{A>B} \varepsilon_{AB} = \sum_{A} \left(\varepsilon_{A,self} - \varepsilon_{A,self}^{0} \right) + \sum_{A>B} V_{cl}^{AB} + V_{xc}^{AB} , \tag{22}$$

where the latter is further decomposed into its classical electrostatic and exchange-(correlation) contributions. The authors concluded that the Pauli repulsion is readily captured in the increase of the fragment's deformation energies of the intermediate (properly antisymmetrized) states. In the case of rotational barriers, the hyperconjugative effects are captured by the inter-fragment exchange contribution, enhanced due to electron delocalization. All in all, they show a certain degree of correspondence between EDA or NBO descriptors and those steaming from IQA.

More recently, Racioppi *et al.* walked a reverse path. Instead of recovering EDA descriptors from IQA, they rearranged the EDA contributions to match those of IQA analysis.[46] In particular, in their pseudo-IQA energy decomposition the EDA contributions of Pauli repulsion, orbital interaction and electrostatic to the interaction energy are regrouped into overall variations of the kinetic, classical electrostatic and exchange-correlation contributions

$$\Delta E_{\text{int}} \equiv \Delta E_{bind}^{EDA} = \Delta E_{Kin} + \Delta E_{cl} + \Delta E_{xc}. \tag{23}$$

The same terms can be obtained by considering the usual reference-state IQA, which is based on decomposing the binding energy between two fragments A and B (ΔE_{bind}^{IQA}) by subtracting the IQA terms from the fully relaxed complex's state from those obtained for the isolated fragments at the complex geometry. The authors showed excellent agreement between the like terms of both schemes in illustrative hydrogen bond and donor-acceptor interactions.[46]

In this work we pursue a different path, namely to enrich the conventional EDA approach by applying a fragment-based IQA decomposition to *each of the EDA terms* of the interaction energy. Thus, in the EDA-IQA scheme we introduce here, the electrostatic, Pauli repulsion and orbital interaction energy terms are further decomposed into intra- and inter-fragment contributions.

THEORY

Let us consider again the formation of the complex *AB* from fragments *A* and *B*. The application of Eqs. 14-16 to the complex's final ground state (AB) readily affords the real-space decomposition of the interaction energy into intra- and inter-fragment terms, namely

$$\Delta E_{\text{int}} = \Delta\varepsilon_{\text{int},A} + \Delta\varepsilon_{\text{int},B} + \Delta\varepsilon_{\text{int},AB}, \tag{24}$$

where

$$\begin{aligned} \Delta\varepsilon_{\text{int},A} &= \varepsilon_A(AB) - E_A(A^0) \\ \Delta\varepsilon_{\text{int},B} &= \varepsilon_B(AB) - E_B(B^0) \\ \Delta\varepsilon_{\text{int},AB} &= \varepsilon_{AB}(AB). \end{aligned} \tag{25}$$

For clarity, in the previous equation and henceforth we omit the explicit dependence of the EDA term on the reference states (A^0 and B^0). The $\Delta\varepsilon_{\text{int,A}}$ and $\Delta\varepsilon_{\text{int,B}}$ account for the energy gain/loss by the fragments when going from their isolated reference state to their *effective* state within the final complex. It is worth to note that in the context of real-space analysis, these contributions do not only originate from changes in the MOs upon complex formation, but also by the fact that the fragments share the physical space once the complex is formed (in intermolecular interactions the second effect should be dominant). In Ref. [44] the authors refer to these terms as fragment's electronic deformation energies. We will adopt here this nomenclature, so that $\Delta\varepsilon_{\text{int,A}} \equiv \Delta\varepsilon_{\text{def.el,A}}$ and $\Delta\varepsilon_{\text{int,B}} \equiv \Delta\varepsilon_{\text{def.el,B}}$.

On the other hand, the term $\Delta\varepsilon_{\text{int,AB}}$ describes the energy gain upon complex formation that can be purely ascribed to inter-fragment interactions. The net interaction energy is thus seen as a balance between the prize the fragments must pay to share the physical space and be electronically prepared, and the gain originating from the new interactions that were absent before the complex's formation.

In a similar fashion, by applying again Eqs. 14-16 to the complex's intermediate state (A^0B^0) one can also obtain an analogous decomposition of the orbital interaction EDA term, namely

$$\Delta E_{orb} = \Delta\varepsilon_{orb,A} + \Delta\varepsilon_{orb,B} + \Delta\varepsilon_{orb,AB}, \tag{26}$$

where

$$\begin{aligned}
\Delta\varepsilon_{orb,A} &= \varepsilon_A(AB) - \varepsilon_A(A^0B^0) \\
\Delta\varepsilon_{orb,B} &= \varepsilon_B(AB) - \varepsilon_B(A^0B^0) \\
\Delta\varepsilon_{orb,AB} &= \varepsilon_{AB}(AB) - \varepsilon_{AB}(A^0B^0).
\end{aligned} \tag{27}$$

The intra-fragment terms account for the net energy gain/loss upon relaxing the wavefunction from the intermediate state to the ground state of the AB complex. This relaxation comes with a change in the electron density. If the underlying AIM definition depends upon this scalar (e.g. QTAIM, TFVC or iterative Hirshfeld approaches), these terms contain also a contribution from the change on the boundaries of physical space going from AB to A^0B^0. The latter could be removed by using the *same* AIM definition for states AB and A^0B^0. In the QTAIM context that means integrating the density functions of state A^0B^0 on the atomic basins obtained from the AB state. In the case of overlapping AIM schemes, it implies using the same atomic weight functions throughout. Such strategies have been already used in the context of QTAIM and fuzzy atoms in similar contexts.[44,47,48] In the present case, since it is actually impossible by construction to use the same AIM definition for the complex and the isolated fragments, we opt for using the AIM definition derived from each state.

The IQA decomposition of state (A^0B^0) readily affords an analogous decomposition of $\Delta E_{\text{Pauli}} + \Delta E_{\text{elec}}$, by taking the isolated fragment states A^0 and B^0 as reference. On the other hand, since each term in ΔE_{elec} involves the electron density and/or potential from different fragments (see Eq. 7), one may argue that this term is entirely of intermolecular nature. In that case, ΔE_{elec} would contribute solely to the inter-fragment term, and consequently one would have the following decomposition for ΔE_{Pauli} :

$$\begin{aligned}\Delta\varepsilon_{Pauli,A} &= \varepsilon_A(A^0B^0) - E_A(A^0)\\ \Delta\varepsilon_{Pauli,B} &= \varepsilon_B(A^0B^0) - E_B(B^0)\\ \Delta\varepsilon_{Pauli,AB} &= \varepsilon_{AB}(A^0B^0) - \Delta E_{elec}.\end{aligned} \tag{28}$$

However, such scheme is not satisfactory neither numerically nor conceptually. The main concern is that $\Delta\varepsilon_{Pauli,AB}$ thus defined mixes up real-space and Hilbert-space quantities, while in this case they behave quite differently. Indeed, as mentioned above, there is no net charge-transfer between fragments *A* and *B* when building the intermediate state A^0B^0 according to Hilbert-space analysis (e.g. Mulliken and Löwdin populations add up to the number of electrons of each fragment). This is not the case when performing a real-space analysis (using disjoint or fuzzy domains), again because the fragments within the complex share the physical space:

$$\int_{\Omega_A} \rho_{A^0}(\boldsymbol{r})d\boldsymbol{r} \neq N_{A^0} \quad \wedge \int_{\Omega_B} \rho_{B^0}(\boldsymbol{r})d\boldsymbol{r} \neq N_{B^0}\,. \tag{29}$$

Hence, the frozen density of isolated fragment *A* when brought to the complex's geometry does not entirely *belong* to fragment *A*, and similarly for fragment *B*. This influences the numerical values obtained using Eq. 27 and, for consistency, this effect should be also taken into account when applying the real-space analysis to the other EDA terms, and in particular to ΔE_{elec}. One should essentially ignore the original allegiance of the fragment's frozen densities and treat the integrand in the exactly same manner as one does it with the electron-nuclear and the Coulombic contributions to the energy in the conventional IQA scheme, namely

$$\begin{aligned}\Delta\varepsilon_{elec,A} &= -\int_{\Omega_A} \rho_{B^0}(\boldsymbol{r})\left[\sum_{i\in A}\frac{Z_i}{|\boldsymbol{r}-\boldsymbol{R}_i|} - \int_{\Omega_A}\frac{\rho_{A^0}(\boldsymbol{r}_2)}{|\boldsymbol{r}-\boldsymbol{r}_2|}d\boldsymbol{r}_2\right]d\boldsymbol{r} = -\int_{\Omega_A}\rho_{B^0}(\boldsymbol{r})V_{A^0}^{net}(\boldsymbol{r})\,d\boldsymbol{r}\\ \Delta\varepsilon_{elec,B} &= -\int_{\Omega_B} \rho_{A^0}(\boldsymbol{r})\left[\sum_{i\in B}\frac{Z_i}{|\boldsymbol{r}-\boldsymbol{R}_i|} - \int_{\Omega_B}\frac{\rho_{B^0}(\boldsymbol{r}_2)}{|\boldsymbol{r}-\boldsymbol{r}_2|}d\boldsymbol{r}_2\right]d\boldsymbol{r} = -\int_{\Omega_B}\rho_{A^0}(\boldsymbol{r})V_{B^0}^{net}(\boldsymbol{r})\,d\boldsymbol{r}\,.\end{aligned} \tag{30}$$

Here, we introduce the fragment's *net* electrostatic potentials $V_{\text{A}}^{\text{net}}(\boldsymbol{r})$ and $V_{\text{B}}^{\text{net}}(\boldsymbol{r})$. They are different from the electrostatic potentials $V_{\text{A}}(\boldsymbol{r})$ and $V_{\text{B}}(\boldsymbol{r})$ of Eq. 9, because in the electronic term

the integration is carried out within the fragment's domain. Since only part of the fragment density is used, $V_A^{net}(\boldsymbol{r}) > V_A(\boldsymbol{r})$. Figure 1 depicts the topology of the net electrostatic potentials and fragment's densities along the inter-fragment distance for NaCl and water dimer. In the vicinity of the nuclei, the electrostatic potential is large and positive, as the electronic part cannot compensate for the nuclear term. At longer distances from the nucleus, the net potential slowly decays to zero. However, in the case of a strong acceptor or an anionic fragment, since there is an excess of electron charge compared to the nuclear one, the net potential becomes *negative,* and tends to zero from below (see light orange curves in Figure 1). This effect is much more pronounced when the donor of charge is anionic (Cl^- vs H_2O). On the other hand, there is a fraction of electron density of *B* that penetrates into *A* (i.e. $w_A(\boldsymbol{r})\rho_B^0(\boldsymbol{r})$) and vice versa. They correspond to the dark orange and dark blue curves in Figure 1. As expected, the density of the donor of charge penetrates more and *deeper* into the acceptor region than the other way around. The interaction of that density from *B* with the net potential of the acceptor *A* results in the electrostatic contribution assigned to *A*, $\Delta\varepsilon_{elec,A}$. It corresponds to the integration of the grey curve in Figure 1b. This term is negative for the acceptor (notice the negative sign on the r.h.s. of Eq. 30) and can be significant if the density of the donor is able to penetrate deep into the acceptor's domain. However, in the case of the donor, the net potential can be negative in the region where it interacts with the density penetrating from the acceptor *A*, so it might result in a (small) positive $\Delta\varepsilon_{elec,B}$ contribution, as shown by the yellow curve in Figure 1b in the case of Cl^-. Of note, these contributions are expected to be somewhat larger when using overlapping atomic domains as compared to disjoint ones such as QTAIM. The shadowed area indicated in Figure 1b roughly indicates the contribution that would not be included in that case.

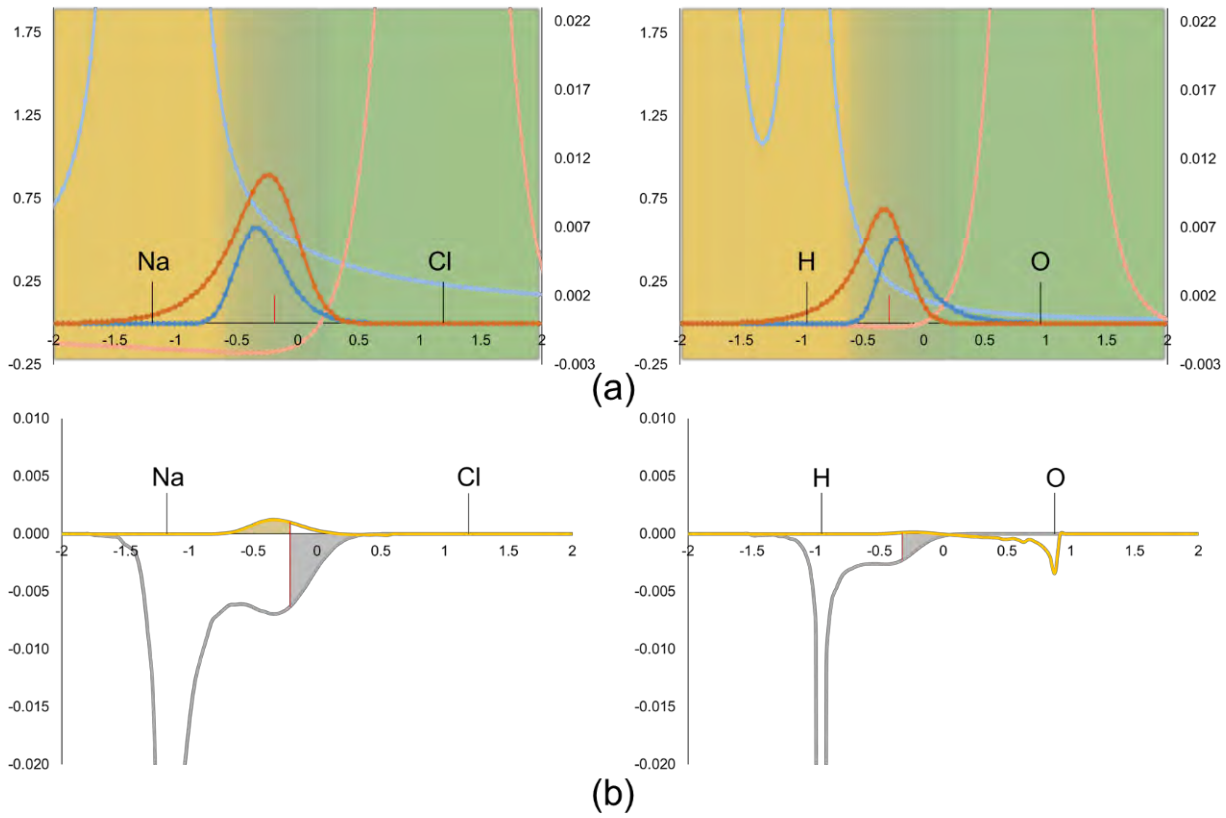

Figure 1. Potential and electron density profiles for NaCl and water dimer along the Na-Cl and the intermolecular H···O bonds, respectively. (a) Topology of $V_{A^0}^{net}(\boldsymbol{r})$ (light blue), $V_{B^0}^{net}(\boldsymbol{r})$ (light orange), $w_B(\boldsymbol{r})\rho_{A^0}(\boldsymbol{r})$ (dark blue) and $w_A(\boldsymbol{r})\rho_{B^0}(\boldsymbol{r})$ (dark orange). (b) Topology of $-w_A(\boldsymbol{r})\rho_{B^0}(\boldsymbol{r})V_{A^0}^{net}(\boldsymbol{r})$ (grey) and $-w_B(\boldsymbol{r})\rho_{A^0}(\boldsymbol{r})V_{B^0}^{net}(\boldsymbol{r})$ (yellow). Atomic (fuzzy) domains depicted as surface, yellow for *A* and green for *B*. Bond critical point depicted as red vertical line. Geometries and wavefunctions evaluated at the BP86/def2-TZVPP level of theory. Fragment definition: $A = Na^+$, $B = Cl^-$ (NaCl) and A = HO-H, $B = OH_2$ ($H_2O\cdots H_2O$).

In the case of the inter-fragment contribution one obtains

$$\Delta\varepsilon_{elec,AB} = -\int_{\Omega_A} \rho_{A^0}(\boldsymbol{r}) \sum_{i\in B} \frac{Z_i}{|\boldsymbol{r}-\boldsymbol{R}_i|} d\boldsymbol{r} + \int_{\Omega_A} \rho_{A^0}(\boldsymbol{r}_1) \int_{\Omega_B} \rho_{B^0}(\boldsymbol{r}_2) r_{12}^{-1} d\boldsymbol{r}_2 d\boldsymbol{r}_1 -$$
$$-\int_{\Omega_B} \rho_{B^0}(\boldsymbol{r}) \sum_{i\in A} \frac{Z_i}{|\boldsymbol{r}-\boldsymbol{R}_i|} d\boldsymbol{r} + \int_{\Omega_B} \rho_{A^0}(\boldsymbol{r}_1) \int_{\Omega_A} \rho_{B^0}(\boldsymbol{r}_2) r_{12}^{-1} d\boldsymbol{r}_2 d\boldsymbol{r}_1 + \sum_{\substack{i\in A \\ j\in B}} \frac{Z_i Z_j}{|\boldsymbol{R}_i - \boldsymbol{R}_j|} \quad (31)$$

$$\Delta\varepsilon_{elec,AB} = -\int_{\Omega_A} \rho_{A^0}(\boldsymbol{r}) V_{B^0}^{net}(\boldsymbol{r}) d\boldsymbol{r} - \int_{\Omega_B} \rho_{B^0}(\boldsymbol{r}) V_{A^0}^{net}(\boldsymbol{r}) d\boldsymbol{r} + \sum_{\substack{i\in A \\ j\in B}} \frac{Z_i Z_j}{|\boldsymbol{R}_i - \boldsymbol{R}_j|}.$$

The numerical value of this contribution will account to which extent the net potential of fragment *A* penetrates into fragment *B* and vice versa, compensated by the point charge nuclear repulsions. As we will see, this term can be positive of negative. In any case, one can readily see that

$$\Delta E_{elec} = \Delta\varepsilon_{elec,A} + \Delta\varepsilon_{elec,B} + \Delta\varepsilon_{elec,AB}\,. \quad (32)$$

It is fair to note that Jiménez-Grávalos and Suárez recently achieved a similar decomposition of the electrostatic interaction in the QTAIM framework for a different purpose.[49] They did not explicitly considered fragment's electrostatic potentials, but it can be seen that their $E_{ele}^{A}(\rho_A^0, \rho_B^0)$ and $E_{ele}^{B}(\rho_A^0, \rho_B^0)$ terms correspond to our $\Delta\varepsilon_{elec,A}$ and $\Delta\varepsilon_{elec,B}$, respectively. Jiménez-Grávalos and Suárez further decompose the inter-fragment electrostatic contribution into a dominant term $E_{ele}^{AB}(\rho_A^0, \rho_B^0)$ that tends to the overall ΔE_{elec} at long distances, and a residual one $E_{ele}^{BA}(\rho_A^0, \rho_B^0)$ which, together with the intra-fragment contributions, accounts for the charge-penetration energy. We shall see that $\Delta\varepsilon_{elec,AB}$ from Eq. 31 also converges smoothly to ΔE_{elec} at long inter-fragment distances, so for the present purpose we do not consider such additional decomposition.

Subtracting the contributions of Eq. 32 from those originating from the IQA decomposition of $\Delta E_{\text{Pauli}} + \Delta E_{\text{elec}}$ finally yield the appropriate real-space decomposition of the Pauli repulsion term

$$\begin{aligned}
\Delta\varepsilon_{Pauli,A} &= \varepsilon_A(A^0B^0) - E_A(A^0) - \Delta\varepsilon_{elec,A} \\
\Delta\varepsilon_{Pauli,B} &= \varepsilon_B(A^0B^0) - E_B(B^0) - \Delta\varepsilon_{elec,B} \\
\Delta\varepsilon_{Pauli,AB} &= \varepsilon_{AB}(A^0B^0) - \Delta\varepsilon_{elec,AB},
\end{aligned} \tag{33}$$

Fulfilling again the sum rule

$$\Delta E_{Pauli} = \Delta\varepsilon_{Pauli,A} + \Delta\varepsilon_{Pauli,B} + \Delta\varepsilon_{Pauli,AB}. \tag{34}$$

The final EDA picture is completed by the inclusion of the preparation energies from Eq. 4 and, if required, a dispersion correction. In the case of the semiempirical dipole-dipole model of Grimme, the dispersion correction is added to the interaction energy and has no influence in the intermediate steps, being trivially decomposed by construction as

$$\begin{aligned}
\Delta E_{disp} &= E_{disp}(A^A) - E_{disp}(A^{AB}) + E_{disp}(B^B) - E_{disp}(B^{AB}) + E_{disp}(AB^{AB}) \\
&\equiv \Delta E_{disp,A} + \Delta E_{disp,B} + \Delta E_{disp,AB}.
\end{aligned} \tag{35}$$

This will not be the case if one uses more sophisticated density-dependent dispersion corrections such as VV10.[50] Finally, the basis set superposition error (BSSE) correction can be estimated *a posteriori* via the counterpoise formula[51, 52], which is also additive

$$\Delta E_{BSSE} = E(A^A) - E(A^{AB}) + E(B^B) - E(B^{AB}) \equiv \Delta E_{BSSE,A} + \Delta E_{BSSE,B}. \tag{36}$$

Summarizing, the present approach affords a real-space fully additive decomposition into intra- (A or B) and inter-fragment (AB) contributions of all terms occurring in the EDA scheme

$$\Delta E_{stab,A} = \underbrace{\Delta\varepsilon_{elec,A} + \Delta\varepsilon_{Pauli,A} + \Delta\varepsilon_{orb,A}}_{\Delta\varepsilon_{def.el,A}} + \Delta E_{prep,A} + \Delta E_{disp,A} + \Delta E_{BSSE,A} \tag{37}$$

$$\Delta E_{stab,AB} = \underbrace{\Delta\varepsilon_{elec,AB} + \Delta\varepsilon_{Pauli,AB} + \Delta\varepsilon_{orb,AB}}_{\Delta\varepsilon_{\mathrm{int},AB}} + \Delta E_{disp,AB}.$$

COMPUTATIONAL DETAILS

All KS-DFT calculations were performed with the Gaussian16 A03 software[53], using the gradient corrected BP86 functional from Becke and Perdew[54, 55], including dispersion correction to the electronic energy by means of Grimme D3[56] with Becke-Johnson (BJ) damping function[57], and the Ahlrichs def2-TZVPP full electron basis set.[58] Geometry optimizations were performed without symmetry constrains for all systems. Stationary points were characterized by computing analytical Hessians, obtaining zero imaginary frequencies in all cases (minima).

To construct all EDA states, the wavefunctions of the dimer and the isolated fragments at the optimized and dimer geometries were evaluated with Gaussian16. The pseudo-state ($A^0 \cup B^0$) electronic structure was constructed using the MOs of the isolated fragments at the dimer geometry. This step was performed with the local program APOST-3D,[59] providing its electronic structure information in a formatted checkpoint (.fchk). Transformation of the formatted into unformatted (.chk) checkpoint file was realized with the *unfchk* tool from Gaussian. Finally, its associated total energy was extracted using the created .chk file as starting guess and forcing to skip the SCF procedure (e.g. SCF = (MAXCYCLE = -1) keyword in Gaussian16). In these calculations the symmetry use was fully disabled to prevent any atomic basis set position difference.

Energy decomposition calculations were also performed with the APOST-3D code using the Topological Fuzzy Voronoi Cells (TFVC) atomic definition.[33] For the production results, one-electron numerical integrals were realized using 150 radial (Gauss-Legendre quadrature[60]) and 974

angular Lebedev-Laikov[61] grid points per atom, while two-electron numerical integrals have been performed using 150 radial and 590 angular grid mesh. Numerical error minimization of the one-center two-electron contributions was performed using the zero-error strategy (ZES).[62]

RESULTS AND DISCUSSION

We have considered the set of intermolecular complexes from Ref. 20, that essentially includes hydrogen bonded species, cation-dipole, cation-π, halogen-π and π-π interactions between dimers. In addition, we have also considered several anion-π complexes from Quiñonero et al.[63] Except for the π-π interactions, one can identify electron donor and acceptor moieties, which entails certain charge-transfer upon complex formation. We will henceforth refer to fragment *A* as the net acceptor of charge and fragment *B* as the donor of charge.

Let us start by analyzing the electrostatic contribution of EDA. Table 1 gathers the IQA decomposition of the electrostatic contributions for the whole set of systems at equilibrium. Note how cation-π and anion-π interactions result in similar values of ΔE_{elec}, but their IQA decomposition reveals a completely different mechanism. In the former, the cation is largely stabilized (large and negative $\Delta\mathcal{E}_{\text{elec,A}}$ values) upon complex formation because of its interaction with the frozen density of the donor. This is largely compensated by a positive inter-fragment electrostatic term $\Delta\mathcal{E}_{\text{elec,AB}}$, that becomes more repulsive as the equilibrium inter-fragment distance shortens from K^+ to Li^+. In the case of anion-π interactions, the $\Delta\mathcal{E}_{\text{elec},B}$ contribution is positive, in line with the situation of Cl^- in NaCl previously depicted in Figure 1, and the inter-fragment term is positive. In dispersion bound systems, both the overall electrostatic and their IQA components are very small, and in most cases within numerical accuracy. In the hydrogen bonded and cation-

dipole systems, one can not see a clear trend neither for the intra-fragment contributions (in almost all cases negative) nor for the $\Delta\mathcal{E}_{\mathrm{elec,AB}}$ values.

Table 1. Fragment (IQA) decomposition of the ΔE_{elec} term from EDA of the systems studied. All the energies are given in kcal/mol. DMA = dimethylacetamide.

A=Acceptor	B=Donor	$\int_{\Omega_A}\rho_{B^0}(\boldsymbol{r})\,d\boldsymbol{r}$	$\int_{\Omega_B}\rho_{A^0}(\boldsymbol{r})\,d\boldsymbol{r}$	$\Delta\mathcal{E}_{\mathrm{elec,A}}$	$\Delta\mathcal{E}_{\mathrm{elec,B}}$	$\Delta\mathcal{E}_{\mathrm{elec,AB}}$	ΔE_{elec}
H_2O	H_2O	0.050	0.043	-6.1	-0.6	-2.2	-8.9
H_2O	MeOH	0.055	0.050	-6.8	-0.9	-1.6	-9.4
MeOH	MeOH	0.058	0.052	-7.2	-1.1	-1.3	-9.7
H_2O	NH_3	0.080	0.045	-10.2	-0.4	-2.3	-12.9
NH_4^+	H_2O	0.077	0.060	-26.7	-2.3	1.9	-27.2
Li^+	H_2O	0.062	0.012	-26.7	0.1	-7.3	-33.9
Na^+	H_2O	0.051	0.022	-17.5	0.2	-8.1	-25.4
K^+	H_2O	0.039	0.042	-11.0	0.6	-8.5	-19.0
NH_4^+	C_4H_4S	0.139	0.041	-32.9	-2.5	22.0	-13.4
NH_4^+	C_6H_6	0.122	0.044	-29.3	-1.9	17.4	-13.8
NH_4^+	C_4H_4O	0.108	0.041	-27.1	-2.3	17.2	-12.1
NH_4^+	C_4H_4NH	0.124	0.046	-32.6	-2.4	15.8	-19.2
Li^+	C_6H_6	0.069	0.014	-28.7	-0.3	12.7	-16.4
Na^+	C_6H_6	0.042	0.021	-13.2	-0.1	0.0	-13.3
K^+	C_6H_6	0.047	0.049	-12.8	-0.2	1.4	-11.5
C_6H_6	C_6H_6	0.080	0.080	-1.8	-1.8	1.2	-2.4
C_5H_5N	C_6H_6	0.082	0.078	-2.5	-1.8	1.3	-3.0
$C_4H_4N_2$	C_6H_6	0.083	0.078	-3.4	-1.7	2.0	-3.1
DMA	C_6H_6	0.089	0.073	-3.8	-1.7	1.5	-4.0
C_6H_6	C_6H_6 (T)	0.054	0.044	-1.9	-0.9	0.9	-1.9
C_6H_6	C_6H_5F	0.021	0.015	0.0	0.1	0.5	0.7
C_6H_6	C_6H_5Cl	0.028	0.060	-0.9	0.1	0.3	-0.5
C_6H_6	C_6H_5Br	0.099	0.074	-1.2	-0.1	0.2	-1.1
C_6F_6	F^-	0.145	0.046	-6.1	13.2	-21.8	-14.7
C_6F_6	Cl^-	0.187	0.038	-6.5	5.6	-10.3	-11.2
C_6F_6	Br^-	0.099	0.074	-8.0	3.7	-7.2	-11.5

To shed light into the origin of these numerical values we have also considered the evolution of ΔE_{elec} as well as its IQA-decomposed terms along the dissociation pathway of representative intermolecular complexes. The results are depicted in Figure 2. As it is well-known, when the frozen densities of the two fragments are brought at the complex's optimized geometry, ΔE_{elec} is favorable[9] and the shorter the inter-fragment distance, the more negative the total ΔE_{elec} contribution. The real-space decomposition of ΔE_{elec} yields further insight on this interaction. As previously discussed, the intra-fragment contributions originate from the net electrostatic potential of one fragment interacting with the density of the other fragment that is able to penetrate into its domain. These terms are strongly attractive, particularly in the case of the acceptor *A* (blue curves in Figure 2), as the more $\rho_B^0(\mathbf{r})$ is able to penetrate into the Ω_A domain, the more negative the $\Delta\varepsilon_{elec,A}$ contribution becomes. Thus, $\Delta\varepsilon_{elec,A}$ is enhanced as the interacting fragments come closer in all cases. Furthermore, this contribution is much larger for cationic acceptor species than for neutral ones (notice the different scales in the examples of Figure 2).

In the case of $\Delta\varepsilon_{elec,B}$ (donor of charge), the trend is similar but the magnitude is much smaller, as the amount of density from the acceptor *A* able to penetrate into the donor is much reduced. In the case of a donor interacting with a hard cation like Li^+, this term is essentially zero at all interatomic distances (see $Li^+\cdots H_2O$ and $Li^+\cdots C_6H_6$ curves in Figure 2). However, when the donor is anionic, the trend for $\Delta\varepsilon_{elec,B}$ is completely reversed. Since $N_B^0 > Z_B$ its *net* electrostatic potential on Ω_B can be negative, and thus any $\rho_A^0(\mathbf{r})$ able to penetrate into Ω_B leads to *positive* $\Delta\varepsilon_{elec,B}$ values. This effect is clearly seen in the $C_6F_6\cdots F^-$ case of Figure 2.

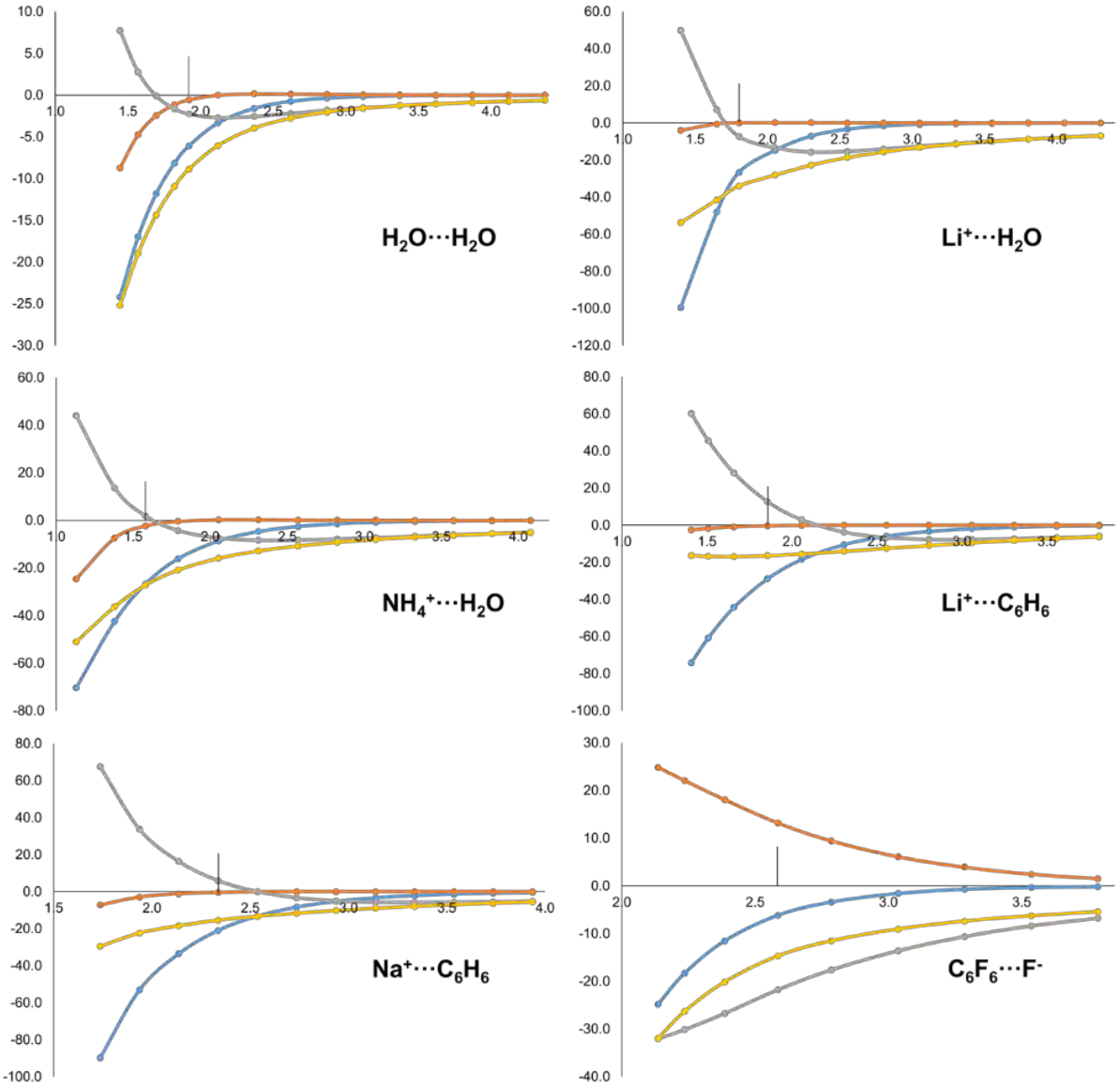

Figure 2. Energy evolution (in kcal/mol, y-axis) of ΔE_{elec} (yellow) and its IQA-decomposed terms, i.e. $\Delta\varepsilon_{elec,A}$ (blue), $\Delta\varepsilon_{elec,B}$ (orange) and $\Delta\varepsilon_{elec,AB}$ (grey), along the dissociation pathway (in Å, x-axis) of $H_2O\cdots H_2O$, $Li^+\cdots H_2O$, $NH_4^+\cdots H_2O$, $Li^+\cdots C_6H_6$, $Na^+\cdots C_6H_6$ and $C_6F_6\cdots F^-$ molecular systems. Equilibrium distance marked with a vertical line.

The usefulness of the IQA decomposition of ΔE_{elec} is most clearly seen in the case of $Li^+\cdots C_6H_6$. As shown in Figure 2, the yellow curve is surprisingly flat, and even becomes *less attractive* at very short distances, totally at odds with the expected behavior. Yet, the overall picture of the intra- and inter-fragment contributions for this system is strikingly similar to that of $Li^+\cdots H_2O$ or $Na^+\cdots C_6H_6$. Close inspection to Figure 2 indicates that the behavior of ΔE_{elec} in $Li^+\cdots C_6H_6$ can be explained by an insufficient enhancement of the intra-fragment contribution of Li^+ at short distances.

It is worth to note that both $\Delta\mathcal{E}_{elec,A}$ and $\Delta\mathcal{E}_{elec,B}$ tend asymptotically to zero as the inter-fragment distance increases. This is the expected behavior since at large distances the fragments are essentially in their reference state. Consequently, the inter-fragment $\Delta\mathcal{E}_{elec,AB}$ contribution tends to the overall ΔE_{elec} value. As the distance decreases, however, $\Delta\mathcal{E}_{elec,AB}$ becomes less favorable and even repulsive at very short distances. Thus, the $\Delta\mathcal{E}_{elec,AB}$ value for a given complex *at* equilibrium geometry may be slightly positive (e.g. $Li^+\cdots C_6H_6$) or negative ($Li^+\cdots H_2O$), but the behavior of the components is analogous in both cases.

Still, the $\Delta\mathcal{E}_{elec,AB}$ contribution at equilibrium distance is very sensitive to the nature of fragments *A* and *B*. When both *A* and *B* are neutral, the electron-nuclear attraction compensate the nuclear-nuclear repulsion and the $\Delta\mathcal{E}_{elec,AB}$ values are very small (ca. ± 2 kcal/mol). However, when the donor *B* is anionic the picture is reversed and at equilibrium $\Delta\mathcal{E}_{elec,AB}$ is negative. The case of $C_6F_6\cdots F^-$ behaves opposite to the other systems (i.e. it becomes more negative as the inter-fragment distance decreases). The second term on the r.h.s. of Eq. 31 is key to explain this behavior. Since *B* is an anion, $\rho_B^0(\mathbf{r})$ holds an excess of electrons with respect to Z_B. In addition, the net potential of *A* in Ω_B is governed by the nuclear contribution (hence positive). In that

scenario, the closer the fragments, the larger the potential and consequently, even if part of $\rho_B^0(\mathbf{r})$ smears into Ω_A, the more dominant the negative term becomes.

Let us proceed by analyzing the Pauli repulsion EDA term, ΔE_{Pauli}, whose contribution originates from the intermediate state A^0B^0. Bickelhaupt and Baerends showed that the antisymmetrization of the frozen fragment densities to build A^0B^0 induces an electron density flow from the intermolecular region to the atomic regions.[9] By decomposing ΔE_{Pauli} into kinetic (ΔT^0) and potential (ΔV_{Pauli}) terms, they showed that the contraction effect translates into an increase of the kinetic energy, and a concomitant decrease (more negative) of the potential energy. The latter is due to the fact that more density is accumulated at regions (e.g. close to nuclei) where the Coulombic potential is larger.

The IQA decomposition of ΔE_{Pauli} recovers this picture from a real-space perspective. By definition, kinetic energy contributions only have intra-fragment character upon IQA decomposition and, consequently, they are captured by the $\Delta\mathcal{E}_{\text{Pauli,A}}$ and $\Delta\mathcal{E}_{\text{Pauli,B}}$ terms. The kinetic energy increase is so dominant that these terms are expected to be positive and increase along the shortening of the inter-fragment distance. This is exactly the behavior depicted in Figure 3. Furthermore, the corresponding values at equilibrium distance (Table 2) indicate positive contributions for both the donor and the acceptor fragments with very few exceptions.

On the other hand, the $\Delta\mathcal{E}_{\text{Pauli,AB}}$ contributions are large and negative in all cases, and also become more favorable at shorter distances. The origin of this behavior is that, according to Eq. 33, this term does not explicitly contain energy differences between the intermediate and isolated fragment's states, as there is no inter-fragment term associate to the latter. Deeper analysis indicates that the classical part of the potential energy differences cancels (particularly in the

neutral complexes), so the inter-fragment exchange-correlation contribution becomes the dominant term.

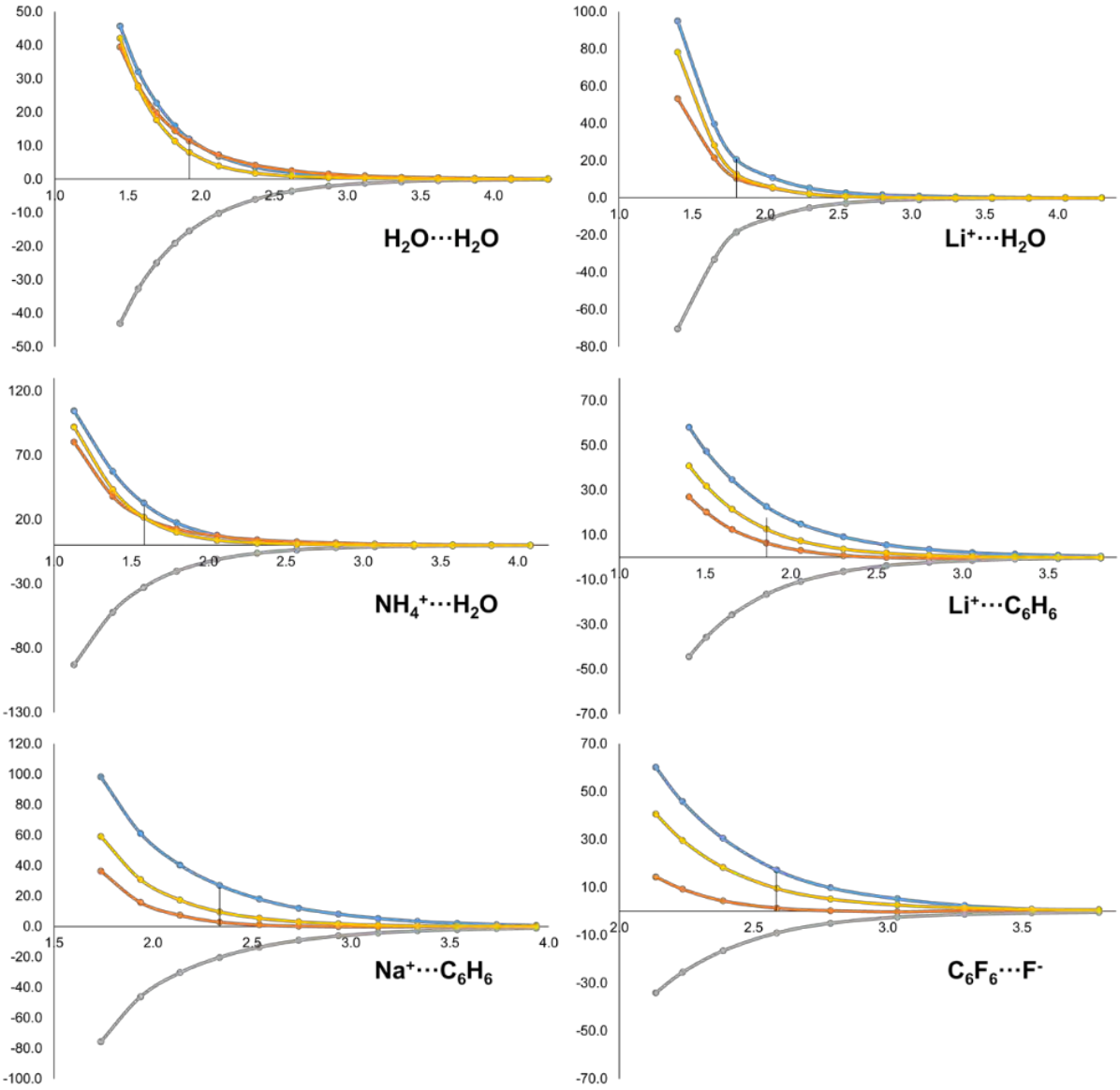

Figure 3. Energy evolution (in kcal/mol, y-axis) of ΔE_{Pauli} (yellow) and its IQA-decomposed terms, i.e. $\Delta\varepsilon_{\text{Pauli,A}}$ (blue), $\Delta\varepsilon_{\text{Pauli,B}}$ (orange) and $\Delta\varepsilon_{\text{Pauli,AB}}$ (grey), along the dissociation pathway (in Å, x-axis) of $H_2O\cdots H_2O$, $Li^+\cdots H_2O$, $NH_4^+\cdots H_2O$, $Li^+\cdots C_6H_6$, $Na^+\cdots C_6H_6$ and $C_6F_6\cdots F^-$ molecular systems. Equilibrium distance marked with a vertical line.

Notice that the aforementioned contraction effect also increases (makes it more negative) the overall exchange-correlation energy of A^0B^0 with respect to that of A^0 and B^0. The dominant exchange contribution is governed by the density close to the nuclei, by virtue of its $\rho(\boldsymbol{r})^{4/3}$ dependence. It might appear counterintuitive that a depletion of charge in the inter-atomic region leads nevertheless to a negative inter-fragment exchange-correlation. As pointed out by Salvador and Mayer, neither the bond order nor the Hartree-Fock exchange energy components are directly related to overlap populations, but to part of the density localized on the atoms that leads to a correlation between the fluctuations of the atomic populations, even in the absence of overlap.[25] Indeed, inter-atomic exchange energy contribution in the Salvador-Mayer KS-DFT IQA formulation originates on the bond order density between a pair of atoms, which is actually *large* in the vicinity of the nuclei.[25] An even simpler explanation is that part of the exchange-correlation energy of the A^0B^0 state is assigned to inter-fragment character by the IQA decomposition, while, once again, there is no inter-fragment contribution from the isolated fragments to compensate for it, as shown in Eq. 33.

The net result (see Table 2) is that the $\Delta\mathcal{E}_{\text{Pauli,AB}}$ contributions are systematically large and negative. On the contrary, the intra-fragment $\Delta\mathcal{E}_{\text{Pauli,A}}$ and $\Delta\mathcal{E}_{\text{Pauli,B}}$ terms are positive, mimicking the behavior of ΔT^0, but bearing not just kinetic but also intra-fragment electrostatic and exchange-correlation contributions. Beyond the overall trend, it is not easy to compare the values of the inter- and intra-fragment contributions from one system to another, especially among different interaction types. Again, even though the behavior of the IQA components is analogous for all interaction types, the actual numerical values are largely dictated by the respective equilibrium distances.

Table 2. Fragment (IQA) decomposition of the ΔE_{Pauli} term from EDA of the systems studied. All the energies are given in kcal/mol. DMA = dimethylacetamide.

A=Acceptor	B=Donor	$\Delta\varepsilon_{\text{Pauli,A}}$	$\Delta\varepsilon_{\text{Pauli,B}}$	$\Delta\varepsilon_{\text{Pauli,AB}}$	ΔE_{Pauli}
H_2O	H_2O	12.0	11.5	-15.5	8.0
H_2O	MeOH	14.2	12.5	-17.2	9.5
MeOH	MeOH	14.3	14.0	-18.0	10.2
H_2O	NH_3	15.6	15.1	-18.5	12.2
NH_4^+	H_2O	32.8	21.7	-32.7	21.8
Li^+	H_2O	20.6	10.5	-18.4	12.6
Na^+	H_2O	22.4	5.6	-19.7	8.3
K^+	H_2O	27.7	1.3	-22.2	6.7
NH_4^+	C_4H_4S	16.2	26.4	-27.2	15.4
NH_4^+	C_6H_6	17.5	23.6	-26.5	14.6
NH_4^+	C_4H_4O	17.0	22.3	-24.8	14.4
NH_4^+	C_4H_4NH	21.9	24.6	-27.7	18.8
Li^+	C_6H_6	22.7	6.5	-16.5	12.7
Na^+	C_6H_6	18.0	1.1	-13.5	5.6
K^+	C_6H_6	30.5	-1.8	-21.7	7.0
C_6H_6	C_6H_6	10.5	10.5	-13.9	7.1
C_5H_5N	C_6H_6	11.8	10.0	-14.4	7.4
$C_4H_4N_2$	C_6H_6	12.4	9.6	-14.9	7.1
DMA	C_6H_6	11.5	12.0	-16.3	7.2
C_6H_6	C_6H_6 (T)	5.8	7.8	-9.6	4.1
C_6H_6	C_6H_5F	2.1	2.5	-3.5	1.2
C_6H_6	C_6H_5Cl	13.8	-2.0	-9.2	2.7
C_6H_6	C_6H_5Br	18.0	-2.9	-11.8	3.3
C_6F_6	F^-	17.2	1.4	-9.0	9.6
C_6F_6	Cl^-	6.3	7.0	-5.1	8.3
C_6F_6	Br^-	3.8	11.0	-5.5	9.2

The orbital interaction from EDA, ΔE_{orb}, originates from the relaxation of the MOs of the complex's intermediate state A^0B^0 to the final complex's *AB* ground state. It is by definition a

negative contribution (if the final state of *AB* is the ground state), that compensates for the repulsive Pauli term. At short intermolecular distances the intermediate state A^0B^0 is higher in energy, so that the relaxation energy to the state *AB* becomes more negative. This behavior can be observed in Figure 4 (yellow curve) for all systems. The orbital relaxation induces an increase of electron density in the inter-atomic (and thus intermolecular) region, making the inter-fragment exchange-correlation contributions of the *AB* ground state *larger* (in absolute value) compared to the ones from the intermediate state A^0B^0. This is captured by the $\Delta\varepsilon_{\mathrm{orb,AB}}$ term (grey curve in Figure 4), that closely follows the trend of the global ΔE_{orb} value, with the exception of the $C_6F_6\cdots F^-$ system but for reasons that will be disclosed later. The trends observed for the intra-fragment terms (blue and orange curves) vary according to the nature of the donor and acceptor moieties. The intra-fragment contribution of the electron donor, $\Delta\varepsilon_{\mathrm{orb,B}}$, vanishes at long distances but as the fragments approach it becomes destabilizing. At distances much shorter than the equilibrium the term becomes less repulsive and can even be stabilizing in the case of the water dimer. On the contrary, the intra-fragment contribution for the acceptor, $\Delta\varepsilon_{\mathrm{orb,A}}$, is very small (particularly at equilibrium distances) but usually stabilizing along the dissociation profile.

The decomposition of ΔE_{orb} at the equilibrium geometries can be found in Table 3. It is well-known that the ΔE_{orb} contribution accounts for both polarization and charge-transfer effects from the intermediate to the final state. It is precisely the amount of charge-transfer that largely dominates these intra-fragment contributions to ΔE_{orb}. The more charge is transferred to the acceptor *A* going from the intermediate A^0B^0 state to the final state, the more stabilizing the $\Delta\varepsilon_{\mathrm{orb,A}}$ contribution, as shown in Figure S1 of the Supporting Material. In the case of the donor moieties the correlation is not as good, but the contributions follow the same trend: the more charge is transferred to the acceptor, the more destabilizing the $\Delta\varepsilon_{\mathrm{orb,B}}$ values are.

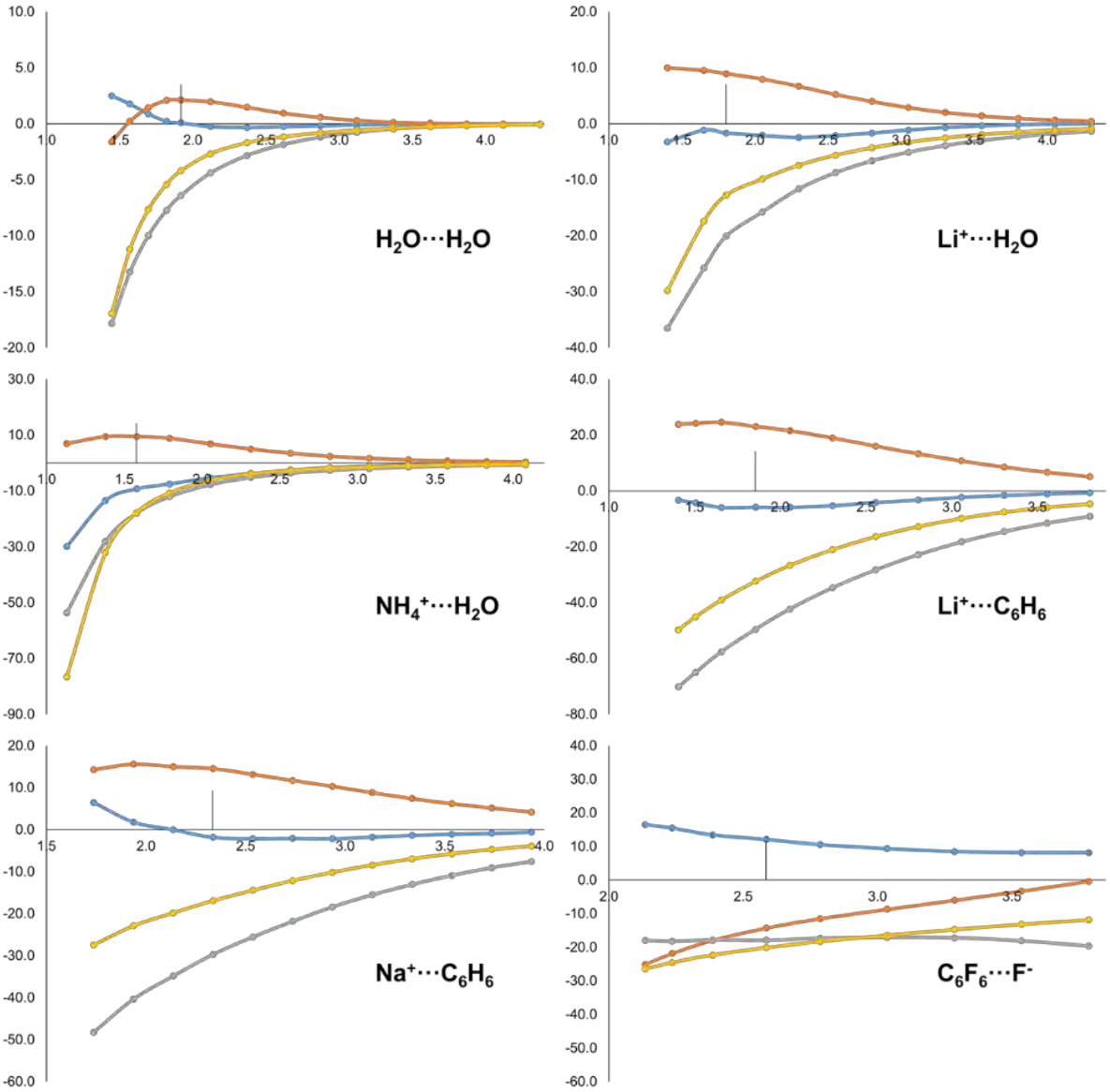

Figure 4. Energy evolution (in kcal/mol, y-axis) of ΔE_{orb} (yellow) and its IQA-decomposed terms, i.e. $\Delta\varepsilon_{orb,A}$ (blue), $\Delta\varepsilon_{orb,B}$ (orange) and $\Delta\varepsilon_{orb,AB}$ (grey), along the dissociation pathway (in Å, x-axis) of $H_2O\cdots H_2O$, $Li^+\cdots H_2O$, $NH_4^+\cdots H_2O$, $Li^+\cdots C_6H_6$, $Na^+\cdots C_6H_6$ and $C_6F_6\cdots F^-$ molecular systems. Equilibrium distance marked with a vertical line.

Remarkably, the anion-π systems exhibit a completely opposite trend. The anion donates charge upon interaction, yet the $\Delta\varepsilon_{orb,B}$ contribution is stabilizing. It is in fact along the whole dissociation

profile, as shown in Figure 4. At the same time, the acceptor gains charge but its $\Delta\varepsilon_{orb,A}$ contribution is destabilizing. One can also notice in Figure 4 the wrong asymptotics of the intra- and inter-fragment contributions for $C_6F_6\cdots F^-$ at long distances. This is in fact a clear fingerprint of delocalization error in the KS density, coming from the BP86 functional. First, the dissociation profile could not be further extended at longer distances due to sever SCF convergence problems but, most importantly, the partial charge on F^- actually *increases* from a value of -0.841 at 3.79Å distance to -0.865 at equilibrium distance, which might explain the aforementioned opposite trend of these systems. It is beyond the scope of the present work to examine the dependence of the decomposed terms on the underlying density functional approximation, but it appears the chosen level of theory is not particularly appropriate to describe these anion-π interactions.

Of course, since the present EDA-IQA decomposition is fully additive, one can obtain the intra- and inter-fragment decomposition of the total interaction energy, ΔE_{int}, by adding the corresponding electrostatic, Pauli repulsion and orbital interaction terms (and dispersion, if included). Numerically, this is not necessary as one can simply perform a conventional IQA decomposition of the final *AB* state of the complex and subtract the isolated fragment's energies of A^0 and B^0 to obtain the intra-fragment or deformation contributions.

Table 3. Fragment (IQA) decomposition of the ΔE_{orb} term from EDA of the systems studied. All the energies are given in kcal/mol. DMA = dimethylacetamide.

A=Acceptor	B=Donor	$\Delta\varepsilon_{orb,A}$	$\Delta\varepsilon_{orb,B}$	$\Delta\varepsilon_{orb,AB}$	ΔE_{orb}
H_2O	H_2O	0.1	2.1	-6.4	-4.2
H_2O	MeOH	0.5	2.1	-7.8	-5.3
MeOH	MeOH	0.3	2.1	-8.0	-5.6
H_2O	NH_3	-0.2	2.5	-8.5	-6.1
NH_4^+	H_2O	-9.3	9.4	-17.9	-17.7
Li^+	H_2O	-1.6	8.9	-20.0	-12.7
Na^+	H_2O	-0.7	5.6	-11.4	-6.5
K^+	H_2O	-1.5	4.4	-7.9	-5.0
NH_4^+	C_4H_4S	-16.4	21.4	-23.9	-18.9
NH_4^+	C_6H_6	-14.7	17.2	-20.1	-17.6
NH_4^+	C_4H_4O	-15.2	16.5	-19.1	-17.7
NH_4^+	C_4H_4NH	-18.1	18.0	-21.8	-22.0
Li^+	C_6H_6	-5.8	23.1	-49.6	-32.3
Na^+	C_6H_6	-2.1	13.2	-25.5	-14.4
K^+	C_6H_6	-2.0	9.9	-18.8	-10.9
C_6H_6	C_6H_6	0.4	0.4	-2.1	-1.3
C_5H_5N	C_6H_6	0.2	0.8	-2.5	-1.5
$C_4H_4N_2$	C_6H_6	-0.1	1.4	-3.0	-1.7
DMA	C_6H_6	0.2	1.2	-3.4	-2.0
C_6H_6	C_6H_6 (T)	-0.1	0.8	-1.8	-1.2
C_6H_6	C_6H_5F	0.0	0.0	-0.5	-0.4
C_6H_6	C_6H_5Cl	0.0	0.5	-1.2	-0.7
C_6H_6	C_6H_5Br	0.1	0.6	-1.5	-0.8
C_6F_6	F^-	12.0	-14.2	-17.9	-20.1
C_6F_6	Cl^-	4.4	-4.2	-10.7	-10.5
C_6F_6	Br^-	2.3	-1.2	-9.1	-8.0

For completeness, the IQA decomposition of ΔE_{int} along the dissociation profile of the representative systems is shown in Figure 5, while the corresponding values at equilibrium geometries are gathered on Table 4. Similarly to the orbital interaction contribution, the electronic deformation energies ($\Delta\varepsilon_{def.el,A}$ and $\Delta\varepsilon_{def.el,B}$) at equilibrium are governed by the amount of charge transfer, in this case between the final state and the that of the isolated free fragments. Note that this charge-transfer is different from the one accounted for in the orbital interaction term because, in real-space analysis, there is already some charge-transfer when forming the intermediate A^0B^0 state. Since the charge transfer from the isolated fragments to the final state is larger, the electronic deformation energies on Table 4 are larger (in absolute value) as well. The correlation between the electronic deformation energies of both the donor and acceptor moieties and the respective amount of charge-transfer is excellent ($r^2 = 0.95$, see Figure S2 of the SI). However, the correlation curve does not cross the (0,0) point but slightly above. That is, even though the acceptor *A* can eventually gain a small amount of charge (e.g. 0.05e for Na^+ in $Na^+\cdots C_6H_6$), the corresponding electronic deformation energy is still slightly positive (+2.7 kcal/mol), due to the accompanying polarization of the fragment's density within the complex. Finally, as usual in the conventional IQA analysis, the $\Delta\mathcal{E}_{int,AB}$ contributions are largely stabilizing along the dissociation profile and also at equilibrium, even for the dispersion-bound complexes (notice that the interaction energies in Table 4 do not contain the dispersion correction). There is also a decent correlation ($r^2 = 0.82$, see Figure S3 of the SI) between the $\Delta\mathcal{E}_{int,AB}$ and ΔE_{int} values at equilibrium, even considering the unreliable anion-π complexes.

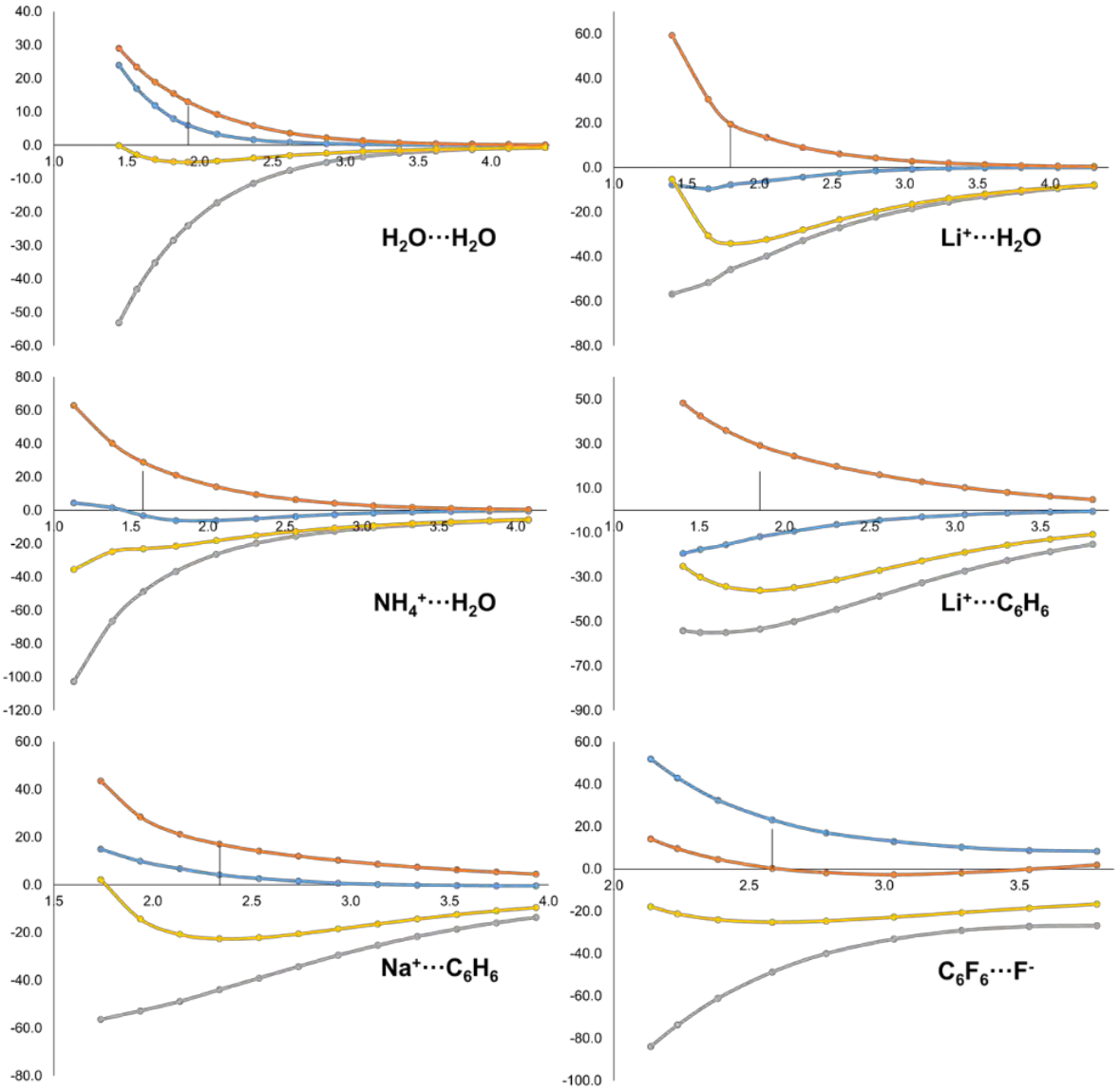

Figure 5. Energy evolution (in kcal/mol, y-axis) of ΔE_{int} (yellow) and its IQA-decomposed terms, i.e. $\Delta\varepsilon_{def.el,A}$ (blue) and $\Delta\varepsilon_{def.el,A}$ (orange) and $\Delta\varepsilon_{int,AB}$ (grey), along the dissociation pathway (in Å, x-axis) of $H_2O\cdots H_2O$, $Li^+\cdots H_2O$, $NH_4^+\cdots H_2O$, $Li^+\cdots C_6H_6$, $Na^+\cdots C_6H_6$ and $C_6F_6\cdots F^-$ molecular systems. Equilibrium distance marked with a vertical line.

Table 4. Fragment (IQA) decomposition of the ΔE_{int} term from EDA of the systems studied. All the energies are given in kcal/mol. DMA = dimethylacetamide.

A=Acceptor	B=Donor	$\Delta\varepsilon_{def.el,A}$	$\Delta\varepsilon_{def.el,A}$	$\Delta\varepsilon_{int,AB}$	ΔE_{int}
H_2O	H_2O	6.0	13.1	-24.1	-5.0
H_2O	MeOH	7.8	13.7	-26.7	-5.2
MeOH	MeOH	7.3	15.0	-27.4	-5.1
H_2O	NH_3	5.2	17.2	-29.3	-6.8
NH_4^+	H_2O	-3.2	28.8	-48.8	-23.1
Li^+	H_2O	-7.7	19.5	-45.8	-34.0
Na^+	H_2O	4.2	11.5	-39.2	-23.6
K^+	H_2O	15.1	6.3	-38.6	-17.2
NH_4^+	C_4H_4S	-33.1	45.4	-29.2	-16.9
NH_4^+	C_6H_6	-26.5	38.8	-29.2	-16.8
NH_4^+	C_4H_4O	-25.2	36.5	-26.7	-15.4
NH_4^+	C_4H_4NH	-28.8	40.2	-33.7	-22.4
Li^+	C_6H_6	-11.9	29.2	-53.4	-36.1
Na^+	C_6H_6	2.7	14.2	-39.1	-22.2
K^+	C_6H_6	15.8	7.8	-39.1	-15.5
C_6H_6	C_6H_6	9.1	9.1	-14.8	7.0
C_5H_5N	C_6H_6	9.4	9.0	-15.6	7.2
$C_4H_4N_2$	C_6H_6	8.9	9.4	-16.0	7.3
DMA	C_6H_6	7.9	11.5	-18.2	6.7
C_6H_6	C_6H_6 (T)	3.8	7.7	-10.5	3.7
C_6H_6	C_6H_5F	2.1	2.7	-3.4	1.4
C_6H_6	C_6H_5Cl	12.9	-1.4	-10.1	1.4
C_6H_6	C_6H_5Br	16.8	-2.4	-13.1	1.3
C_6F_6	F^-	23.1	0.3	-48.7	-25.2
C_6F_6	Cl^-	4.2	8.4	-26.1	-13.5
C_6F_6	Br^-	-1.9	13.5	-21.9	-10.2

CONCLUSIONS

The IQA decomposition of the individual terms arising from the EDA, namely electrostatic, Pauli repulsion and orbital interaction, has been implemented. The performance of the EDA-IQA approach has been illustrated for a set of complexes, covering different types of intermolecular interactions. In this context of intermolecular interactions, the atomic and diatomic contributions obtained for each EDA term have been conveniently grouped into intra-fragment and inter-fragment terms. Through the lens of real-space analysis such as IQA, the electrostatic interaction from EDA can no longer be seen as intermolecular in nature, but also results into meaningful and non-negligible intra-fragment contributions, because the interacting fragments share the physical space once the complex is formed. The EDA-IQA decomposition of the Pauli repulsion shows destabilizing intra-fragment contributions, particularly in the case of fragments that are net acceptors of charge. On the contrary, the inter-fragment Pauli contribution is strongly stabilizing. The intra- and inter-fragment ΔE_{Pauli} contributions closely mimic the behavior of the classical decomposition of Pauli repulsion into kinetic and potential terms, respectively. In the case of the orbital interaction term, the sign and magnitude of the intra-fragment contribution at equilibrium geometries is largely driven by the amount of charge transfer: the net acceptors of charge stabilize and the donor moieties destabilize. The proper asymptotics of all EDA-IQA terms is also confirmed along the intermolecular dissociation path of selected molecular complexes. In this work we have focused in intermolecular interactions but the EDA-IQA methodology is of general applicability. It might be useful for instance to gain deeper insight into the effect (or reliability) of choosing one or another fragmentation pattern for chemical bonding analysis with conventional EDA. This work is in progress in our laboratory.

ASSOCIATED CONTENT

Supporting Information.

The supporting information contains the correlations between the intra-fragment orbital interaction and interaction energy components (IQA), with the fragment charge differences associated to their associated states (Figures S1 and S2, respectively), the correlation between the total interaction energy (EDA) and its inter-fragment (IQA) component (Figure S3), fragment charges (TFVC) for each of the states of the EDA process (Table S1) and fragment charge differences (TFVC) associated to each EDA energy term (Table S2).

The following files are available free of charge:

Coordinates of the studied systems (XYZ format)

AUTHOR INFORMATION

Corresponding Author

* Pedro Salvador. Email: pedro.salvador@udg.edu

Funding Sources

ACKNOWLEDGMENT

M.G. Thanks the Fons Social Europeu and the Generalitat de Catalunya for the predoctoral fellowship (Grant 2018 FI_B 01120). P.S and M.G. were supported by the Ministerio de Ciencia, Innovacion y Universidades (MCIU) Grant PGC2018-098212-B-C22. S.D and D.M.A. thanks the European Research Council (EU805113).

REFERENCES

1. Coppens, P.; Hall, M. B., *Electron distributions and the chemical bond*. New York : Plenum Press: New York, 1982.
2. Fonseca Guerra, C.; Handgraaf, J.-W.; Baerends, E. J.; Bickelhaupt, F. M., Voronoi deformation density (VDD) charges: Assessment of the Mulliken, Bader, Hirshfeld, Weinhold, and VDD methods for charge analysis. *Journal of Computational Chemistry* **2004,** *25* (2), 189-210.
3. Belpassi, L.; Infante, I.; Tarantelli, F.; Visscher, L., The Chemical Bond between Au(I) and the Noble Gases. Comparative Study of NgAuF and NgAu+ (Ng = Ar, Kr, Xe) by Density Functional and Coupled Cluster Methods. *Journal of the American Chemical Society* **2008,** *130* (3), 1048-1060.
4. Cappelletti, D.; Ronca, E.; Belpassi, L.; Tarantelli, F.; Pirani, F., Revealing Charge-Transfer Effects in Gas-Phase Water Chemistry. *Accounts of Chemical Research* **2012,** *45* (9), 1571-1580.
5. Bader, R. F. W., A quantum theory of molecular structure and its applications. *Chemical Reviews* **1991,** *91* (5), 893-928.
6. Ziegler, T.; Rauk, A., On the calculation of bonding energies by the Hartree Fock Slater method. *Theoretica chimica acta* **1977,** *46* (1), 1-10.
7. Kitaura, K.; Morokuma, K., A new energy decomposition scheme for molecular interactions within the Hartree-Fock approximation. *International Journal of Quantum Chemistry* **1976,** *10* (2), 325-340.
8. Mitoraj, M. P.; Michalak, A.; Ziegler, T., A Combined Charge and Energy Decomposition Scheme for Bond Analysis. *Journal of Chemical Theory and Computation* **2009,** *5* (4), 962-975.
9. Bickelhaupt, F. M.; Baerends, E. J., Kohn-Sham Density Functional Theory: Predicting and Understanding Chemistry. In *Reviews in Computational Chemistry*, 2000; pp 1-86.
10. Khaliullin, R. Z.; Head-Gordon, M.; Bell, A. T., An efficient self-consistent field method for large systems of weakly interacting components. *The Journal of Chemical Physics* **2006,** *124* (20), 204105.
11. Khaliullin, R. Z.; Cobar, E. A.; Lochan, R. C.; Bell, A. T.; Head-Gordon, M., Unravelling the Origin of Intermolecular Interactions Using Absolutely Localized Molecular Orbitals. *The Journal of Physical Chemistry A* **2007,** *111* (36), 8753-8765.
12. Horn, P. R.; Head-Gordon, M., Polarization contributions to intermolecular interactions revisited with fragment electric-field response functions. *The Journal of Chemical Physics* **2015,** *143* (11), 114111.
13. Levine, D. S.; Horn, P. R.; Mao, Y.; Head-Gordon, M., Variational Energy Decomposition Analysis of Chemical Bonding. 1. Spin-Pure Analysis of Single Bonds. *Journal of Chemical Theory and Computation* **2016,** *12* (10), 4812-4820.
14. Schenter, G. K.; Glendening, E. D., Natural Energy Decomposition Analysis: The Linear Response Electrical Self Energy. *The Journal of Physical Chemistry* **1996,** *100* (43), 17152-17156.
15. Foster, J. P.; Weinhold, F., Natural hybrid orbitals. *Journal of the American Chemical Society* **1980,** *102* (24), 7211-7218.
16. Reed, A. E.; Weinhold, F., Natural bond orbital analysis of near-Hartree–Fock water dimer. *The Journal of Chemical Physics* **1983,** *78* (6), 4066-4073.
17. Reed, A. E.; Weinhold, F.; Curtiss, L. A.; Pochatko, D. J., Natural bond orbital analysis of molecular interactions: Theoretical studies of binary complexes of HF, H2O, NH3, N2, O2, F2,

CO, and CO2 with HF, H2O, and NH3. *The Journal of Chemical Physics* **1986,** *84* (10), 5687-5705.
18. Reed, A. E.; Curtiss, L. A.; Weinhold, F., Intermolecular interactions from a natural bond orbital, donor-acceptor viewpoint. *Chemical Reviews* **1988,** *88* (6), 899-926.
19. Jeziorski, B.; Moszynski, R.; Szalewicz, K., Perturbation Theory Approach to Intermolecular Potential Energy Surfaces of van der Waals Complexes. *Chemical Reviews* **1994,** *94* (7), 1887-1930.
20. Phipps, M. J. S.; Fox, T.; Tautermann, C. S.; Skylaris, C.-K., Energy decomposition analysis approaches and their evaluation on prototypical protein–drug interaction patterns. *Chemical Society Reviews* **2015,** *44* (10), 3177-3211.
21. Andrés, J.; Ayers, P. W.; Boto, R. A.; Carbó-Dorca, R.; Chermette, H.; Cioslowski, J.; Contreras-García, J.; Cooper, D. L.; Frenking, G.; Gatti, C.; Heidar-Zadeh, F.; Joubert, L.; Martín Pendás, Á.; Matito, E.; Mayer, I.; Misquitta, A. J.; Mo, Y.; Pilmé, J.; Popelier, P. L. A.; Rahm, M.; Ramos-Cordoba, E.; Salvador, P.; Schwarz, W. H. E.; Shahbazian, S.; Silvi, B.; Solà, M.; Szalewicz, K.; Tognetti, V.; Weinhold, F.; Zins, É.-L., Nine questions on energy decomposition analysis. *Journal of Computational Chemistry* **2019,** *40* (26), 2248-2283.
22. Mayer, I., Towards a "Chemical" Hamiltonian. *International Journal of Quantum Chemistry* **1983,** *23* (2), 341-363.
23. Mayer, I., A chemical energy component analysis. *Chemical Physics Letters* **2000,** *332* (3), 381-388.
24. Salvador, P.; Duran, M.; Mayer, I., One- and two-center energy components in the atoms in molecules theory. *The Journal of Chemical Physics* **2001,** *115* (3), 1153-1157.
25. Salvador, P.; Mayer, I., One- and two-center physical space partitioning of the energy in the density functional theory. *The Journal of Chemical Physics* **2007,** *126* (23), 234113.
26. Salvador, P.; Mayer, I., Energy partitioning for "fuzzy" atoms. *The Journal of Chemical Physics* **2004,** *120* (11), 5046-5052.
27. Blanco, M. A.; Martín Pendás, A.; Francisco, E., Interacting Quantum Atoms: A Correlated Energy Decomposition Scheme Based on the Quantum Theory of Atoms in Molecules. *Journal of Chemical Theory and Computation* **2005,** *1* (6), 1096-1109.
28. Casals-Sainz, J. L.; Guevara-Vela, J. M.; Francisco, E.; Rocha-Rinza, T.; Martín Pendás, Á., Efficient implementation of the interacting quantum atoms energy partition of the second-order Møller–Plesset energy. *Journal of Computational Chemistry* **2020,** *41* (13), 1234-1241.
29. Chávez-Calvillo, R.; García-Revilla, M.; Francisco, E.; Martín Pendás, Á.; Rocha-Rinza, T., Dynamical correlation within the Interacting Quantum Atoms method through coupled cluster theory. *Computational and Theoretical Chemistry* **2015,** *1053*, 90-95.
30. Fernández-Alarcón, A.; Casals-Sainz, J. L.; Guevara-Vela, J. M.; Costales, A.; Francisco, E.; Martín Pendás, Á.; Rocha-Rinza, T., Partition of electronic excitation energies: the IQA/EOM-CCSD method. *Physical Chemistry Chemical Physics* **2019,** *21* (25), 13428-13439.
31. Francisco, E.; Casals-Sainz, J. L.; Rocha-Rinza, T.; Martín Pendás, A., Partitioning the DFT exchange-correlation energy in line with the interacting quantum atoms approach. *Theoretical Chemistry Accounts* **2016,** *135* (7), 170.
32. Bultinck, P.; Van Alsenoy, C.; Ayers, P. W.; Carbó-Dorca, R., Critical analysis and extension of the Hirshfeld atoms in molecules. *The Journal of Chemical Physics* **2007,** *126* (14), 144111.
33. Salvador, P.; Ramos-Cordoba, E., Communication: An approximation to Bader's topological atom. *The Journal of Chemical Physics* **2013,** *139* (7), 071103.

34. Mayer, I.; Hamza, A., Energy decomposition in the topological theory of atoms in molecules and in the linear combination of atomic orbitals formalism: a note. *Theoretical Chemistry Accounts* **2001,** *105* (4), 360-364.
35. Tognetti, V.; Silva, A. F.; Vincent, M. A.; Joubert, L.; Popelier, P. L. A., Decomposition of Møller–Plesset Energies within the Quantum Theory of Atoms-in-Molecules. *The Journal of Physical Chemistry A* **2018,** *122* (38), 7748-7756.
36. Holguín-Gallego, F. J.; Chávez-Calvillo, R.; García-Revilla, M.; Francisco, E.; Pendás, Á. M.; Rocha-Rinza, T., Electron correlation in the interacting quantum atoms partition via coupled-cluster lagrangian densities. *Journal of Computational Chemistry* **2016,** *37* (19), 1753-1765.
37. Hermann, M.; Frenking, G., Carbones as Ligands in Novel Main-Group Compounds E[C(NHC)2]2 (E=Be, B+, C2+, N3+, Mg, Al+, Si2+, P3+): A Theoretical Study. *Chemistry – A European Journal* **2017,** *23* (14), 3347-3356.
38. Frenking, G.; Hermann, M.; Andrada, D. M.; Holzmann, N., Donor–acceptor bonding in novel low-coordinated compounds of boron and group-14 atoms C–Sn. *Chemical Society Reviews* **2016,** *45* (4), 1129-1144.
39. Takagi, N.; Shimizu, T.; Frenking, G., Divalent Silicon(0) Compounds. *Chemistry – A European Journal* **2009,** *15* (14), 3448-3456.
40. Frenking, G.; Solà, M.; Vyboishchikov, S. F., Chemical bonding in transition metal carbene complexes. *Journal of Organometallic Chemistry* **2005,** *690* (24), 6178-6204.
41. Vyboishchikov, S. F.; Frenking, G., Structure and Bonding of Low-Valent (Fischer-Type) and High-Valent (Schrock-Type) Transition Metal Carbene Complexes. *Chemistry – A European Journal* **1998,** *4* (8), 1428-1438.
42. Foroutan-Nejad, C., The Na···B Bond in NaBH3−: A Different Type of Bond. *Angewandte Chemie International Edition* **2020,** *59* (47), 20900-20903.
43. Martín Pendás, A.; Francisco, E.; Blanco, M. A., Binding Energies of First Row Diatomics in the Light of the Interacting Quantum Atoms Approach. *The Journal of Physical Chemistry A* **2006,** *110* (47), 12864-12869.
44. Martín Pendás, A.; Blanco, M. A.; Francisco, E., The nature of the hydrogen bond: A synthesis from the interacting quantum atoms picture. *The Journal of Chemical Physics* **2006,** *125* (18), 184112.
45. Pendás, A. M.; Blanco, M. A.; Francisco, E., Steric repulsions, rotation barriers, and stereoelectronic effects: A real space perspective. *Journal of Computational Chemistry* **2009,** *30* (1), 98-109.
46. Racioppi, S.; Sironi, A.; Macchi, P., On generalized partition methods for interaction energies. *Physical Chemistry Chemical Physics* **2020,** *22* (42), 24291-24298.
47. Montilla, M.; Luis, J. M.; Salvador, P., Origin-Independent Decomposition of the Static Polarizability. *Journal of Chemical Theory and Computation* **2021,** *17* (2), 1098-1105.
48. Bultinck, P.; Fias, S.; Van Alsenoy, C.; Ayers, P. W.; Carbó-Dorca, R., Critical thoughts on computing atom condensed Fukui functions. *The Journal of Chemical Physics* **2007,** *127* (3), 034102.
49. Jiménez-Grávalos, F.; Suárez, D., A Quantum Chemical Topology Picture of Intermolecular Electrostatic Interactions and Charge Penetration Energy. *Journal of Chemical Theory and Computation* **2021,** *17* (8), 4981-4995.
50. Vydrov, O. A.; Van Voorhis, T., Nonlocal van der Waals density functional: The simpler the better. *The Journal of Chemical Physics* **2010,** *133* (24), 244103.

51. Boys, S. F.; Bernardi, F., The calculation of small molecular interactions by the differences of separate total energies. Some procedures with reduced errors. *Molecular Physics* **1970,** *19* (4), 553-566.
52. Simon, S.; Duran, M.; Dannenberg, J. J., How does basis set superposition error change the potential surfaces for hydrogen-bonded dimers? *The Journal of Chemical Physics* **1996,** *105* (24), 11024-11031.
53. Frisch, M. J.; Trucks, G. W.; Schlegel, H. B.; Scuseria, G. E.; Robb, M. A.; Cheeseman, J. R.; Scalmani, G.; Barone, V.; Petersson, G. A.; Nakatsuji, H.; Li, X.; Caricato, M.; Marenich, A. V.; Bloino, J.; Janesko, B. G.; Gomperts, R.; Mennucci, B.; Hratchian, H. P.; Ortiz, J. V.; Izmaylov, A. F.; Sonnenberg, J. L.; Williams; Ding, F.; Lipparini, F.; Egidi, F.; Goings, J.; Peng, B.; Petrone, A.; Henderson, T.; Ranasinghe, D.; Zakrzewski, V. G.; Gao, J.; Rega, N.; Zheng, G.; Liang, W.; Hada, M.; Ehara, M.; Toyota, K.; Fukuda, R.; Hasegawa, J.; Ishida, M.; Nakajima, T.; Honda, Y.; Kitao, O.; Nakai, H.; Vreven, T.; Throssell, K.; Montgomery Jr., J. A.; Peralta, J. E.; Ogliaro, F.; Bearpark, M. J.; Heyd, J. J.; Brothers, E. N.; Kudin, K. N.; Staroverov, V. N.; Keith, T. A.; Kobayashi, R.; Normand, J.; Raghavachari, K.; Rendell, A. P.; Burant, J. C.; Iyengar, S. S.; Tomasi, J.; Cossi, M.; Millam, J. M.; Klene, M.; Adamo, C.; Cammi, R.; Ochterski, J. W.; Martin, R. L.; Morokuma, K.; Farkas, O.; Foresman, J. B.; Fox, D. J. *Gaussian 16 Rev. A.03*, Wallingford, CT, 2016.
54. Becke, A. D., Density-functional exchange-energy approximation with correct asymptotic behavior. *Physical Review A* **1988,** *38* (6), 3098-3100.
55. Perdew, J. P., Density-functional approximation for the correlation energy of the inhomogeneous electron gas. *Physical Review B* **1986,** *33* (12), 8822-8824.
56. Grimme, S., Density functional theory with London dispersion corrections. *WIREs Computational Molecular Science* **2011,** *1* (2), 211-228.
57. Grimme, S.; Ehrlich, S.; Goerigk, L., Effect of the damping function in dispersion corrected density functional theory. *Journal of Computational Chemistry* **2011,** *32* (7), 1456-1465.
58. Weigend, F.; Ahlrichs, R., Balanced basis sets of split valence, triple zeta valence and quadruple zeta valence quality for H to Rn: Design and assessment of accuracy. *Physical Chemistry Chemical Physics* **2005,** *7* (18), 3297-3305.
59. Salvador, P.; Ramos-Cordoba, E.; Gimferrer, M.; Montilla, M., APOST-3D Program. *Universitat de Girona: Girona, Spain* **2020**.
60. Stroud, A. H. S. D., Gaussian quadrature formulas. **1966**.
61. Lebedev, V. I.; Laikov, D. N., A QUADRATURE FORMULA FOR THE SPHERE OF THE 131ST ALGEBRAIC ORDER OF ACCURACY. *Doklady Mathematics* **1999,** *59*, 477-481.
62. Gimferrer, M.; Salvador, P., Exact Decompositions of the Total KS-DFT Exchange-Correlation Energy into One- and Two-Center Terms. *Submitted*.
63. Quiñonero, D.; Garau, C.; Rotger, C.; Frontera, A.; Ballester, P.; Costa, A.; Deyà, P. M., Anion–π Interactions: Do They Exist? *Angewandte Chemie International Edition* **2002,** *41* (18), 3389-3392.

5.2 Exact decompositions of the total KS-DFT exchange-correlation energy into one- and two-center terms

Gimferrer, M.; Salvador, P. **2023**, *Submitted* (manuscript under revision).

Abstract: In the so-called Interacting Quantum Atoms (IQA) approach, the molecular energy is numerically decomposed as a sum of atomic and diatomic contributions. While proper formulations have been put forward for both Hartree-Fock and postHartree-Fock wavefunctions, this is not the case for Kohn-Sham density functional theory (KS-DFT). In this work, we critically analyze the performance of two fully additive approaches for the IQA decomposition of the KS-DFT energy, namely the one from Francisco *et al.*, that uses atomic scaling factors (F-IQA), and that from Salvador and Mayer, based upon the bond order density (SM-IQA). Atomic and diatomic exchange-correlation (xc) energy components are obtained for a molecular test set comprising different bond types and multiplicities and along the reaction coordinate of a Diels-Alder reaction. Both methodologies behave similarly for all systems considered. In general, the SM-IQA diatomic xc components are less negative than the Hartree-Fock ones, which is in good agreement with the known effect of electron correlation upon (most) covalent bonds. In addition, a new general scheme to minimize the numerical error of the sum of two-electron energy contributions (i.e. Coulomb and exact exchange) in the framework of overlapping atoms is described in detail.

Exact Decompositions of the Total KS-DFT Exchange-Correlation Energy into One- and Two-Center Terms

Martí Gimferrer[1] and Pedro Salvador[1]

Institut de Química Computacional i Catàlisi and Departament de Química, Universitat de Girona, Maria Aurèlia Capmany 69, 17003 Girona, Catalonia, Spain

(*Electronic mail: pedro.salvador@udg.edu)

(*Electronic mail: marti.gimferrer@udg.edu)

(Dated: 17 January 2023)

In the so-called Interacting Quantum Atoms (IQA) approach, the molecular energy is numerically decomposed as a sum of atomic and diatomic contributions. While proper formulations have been put forward for both Hartree-Fock and post-Hartree-Fock wavefunctions, this is not the case for Kohn-Sham density functional theory (KS-DFT). In this work, we critically analyze the performance of two fully additive approaches for the IQA decomposition of the KS-DFT energy, namely the one from Francisco *et al.*, that uses atomic scaling factors (F-IQA), and that from Salvador and Mayer, based upon the bond order density (SM-IQA). Atomic and diatomic exchange-correlation (xc) energy components are obtained for a molecular test set comprising different bond types and multiplicities and along the reaction coordinate of a Diels-Alder reaction. Both methodologies behave similarly for all systems considered. In general, the SM-IQA diatomic xc components are less negative than the Hartree-Fock ones, which is in good agreement with the known effect of electron correlation upon (most) covalent bonds. In addition, a new general scheme to minimize the numerical error of the sum of two-electron energy contributions (i.e. Coulomb and exact exchange) in the framework of overlapping atoms is described in detail.

INTRODUCTION

Molecular energy decomposition schemes are routinely used to shed light into a wide variety of chemical phenomena.[1–9] With these approaches the total energy of a quantum system, either a molecule or a complex, is decomposed into different contributions. In the case of the so-called interacting quantum atoms (IQA) approaches, the total energy is exactly (up to numerical integration error) decomposed into one- and two-center contributions.[10] The centers can be the individual atoms composing the system or groups of atoms, permitting the identification of energetic interactions between functional groups in the case of a molecular system, or individual monomers in a complex. This type of molecular energy decomposition schemes relies on the identification of the atom within the molecule (AIM), which in the case of IQA is typically chosen to be that from the quantum theory of atoms in molecules (QTAIM).[11] It is important to stress that the real-space decomposition of properties such as the energy is not restricted to that particular atomic model. An atom A within the molecule may be more generally identified by continuous atomic weight functions $w_A(\mathbf{r}) \leq 0$ centered in the nucleus of the atom. Such atomic weight functions can be derived from a variety of approaches, including a number of Hirshfeld-type variants[12–14] or schemes that borrow elements of QTAIM model such as the topological fuzzy Voronoi cells (TFVC) approach.[15]

In real-space analysis, any one-electron density function, namely $f(\mathbf{r})$, naturally decomposes into one-center contributions either upon integration on their respective domains or introducing the respective atomic weight function, $w_A(\mathbf{r})$, as follows

$$\begin{aligned} F_1 = \int f(\mathbf{r})d\mathbf{r} &= \sum_A \int_{\Omega_A} f(\mathbf{r})d\mathbf{r} \\ &= \sum_A \int w_A(\mathbf{r})f(\mathbf{r})d\mathbf{r} = \sum_A F_1^A. \end{aligned} \tag{1}$$

Note that one may consider $w_A(\mathbf{r})f(\mathbf{r})$ as the atomic *effective* density function of the property F_1, which upon integration over the whole space yields the corresponding average atomic contribution. Similarly, two-electron density functions, namely $f(\mathbf{r}_1,\mathbf{r}_2)$, naturally yield both one- and two-center terms

$$F_2 = \iint f(\mathbf{r}_1,\mathbf{r}_2)d\mathbf{r}_1 d\mathbf{r}_2 = \sum_{A,B} F_2^{AB}, \tag{2}$$

where

$$\begin{aligned} F_2^{AA} &= \iint w_A(\mathbf{r}_1)w_A(\mathbf{r}_2)f(\mathbf{r}_1,\mathbf{r}_2)d\mathbf{r}_1 d\mathbf{r}_2 \\ F_2^{AB} &= \iint w_A(\mathbf{r}_1)w_B(\mathbf{r}_2)f(\mathbf{r}_1,\mathbf{r}_2)d\mathbf{r}_1 d\mathbf{r}_2. \end{aligned} \tag{3}$$

Since the total energy can be expressed in terms of one- and two-electron density functions, it quite naturally decomposes into one- (atomic) and two-center (diatomic) contributions by applying equations above. However, contrary to electron distribution analyses (e.g. atomic populations, bond orders or local spins), the formulation of the molecular energy decomposition scheme depends upon how the total energy is obtained for each particular electronic structure method. Popelier *et al.* first considered two-electron integrations over different QTAIM domains.[16] Salvador *et al.* introduced the IQA scheme for the Hartree-Fock energy both for QTAIM and fuzzy-atom AIMs.[17,18] Later, Blanco *et al.* extended

it to correlated wavefunctions[19] (e.g. CISD or CASSCF) and introduced an efficient numerical quadrature algorithm for the two-center integrations.[20,21] More recently, proper formulations for MP2[22,23] and CCSD[24–26] energies have also been successfully introduced. Curiously enough, the extension of the method to Kohn-Sham density functional theory (KS-DFT) has proven to be the most challenging, being the origin of the problem the local contribution of the exchange-correlation functional.

In the Hartree-Fock model, the non-local exchange energy (henceforth exact exchange) is expressed for the simplest case of a restricted closed-shell single-determinant wavefunction as

$$\begin{aligned} E_x^{HF} &= -\frac{1}{4}\iint \rho(\mathbf{r}_1;\mathbf{r}_2)\rho(\mathbf{r}_2;\mathbf{r}_1) r_{12}^{-1} d\mathbf{r}_1 d\mathbf{r}_2 \\ &= -\sum_{i,j}^{N_{occ}} \int \phi_i^*(\mathbf{r}_1)\phi_j^*(\mathbf{r}_2)\phi_i(\mathbf{r}_2)\phi_j(\mathbf{r}_1) r_{12}^{-1} d\mathbf{r}_1 d\mathbf{r}_2 \\ &= \iint \rho_x(\mathbf{r}_1;\mathbf{r}_2) r_{12}^{-1} d\mathbf{r}_1 d\mathbf{r}_2, \end{aligned} \quad (4)$$

where we have introduced the spinless non-local HF-exchange density, $\rho_x(\mathbf{r}_1;\mathbf{r}_2)$.

Upon introduction of the atomic weight functions, the exact exchange can be trivially decomposed into one-center

$$E_x^{AA,HF} = \iint w_A(\mathbf{r}_1)\rho_x(\mathbf{r}_1;\mathbf{r}_2) w_A(\mathbf{r}_2) r_{12}^{-1} d\mathbf{r}_1 d\mathbf{r}_2, \quad (5)$$

and two-center contributions

$$E_x^{AB,HF} = 2\iint w_A(\mathbf{r}_1)\rho_x(\mathbf{r}_1;\mathbf{r}_2) w_B(\mathbf{r}_2) r_{12}^{-1} d\mathbf{r}_1 d\mathbf{r}_2, \quad (6)$$

which are fully additive (up to the numerical accuracy of the numerical integrations)

$$E_x^{HF} = \sum_A E_x^{AA;HF} + \sum_{A,B>A} E_x^{AB;HF}. \quad (7)$$

On the other hand, in KS-DFT the exchange-correlation energy is expressed through the exchange-correlation functional, which in turn is typically expressed as an additive contribution of the exchange and the correlation functionals. The exchange-correlation energy can be written in the most general form as

$$E_{xc}^{DFT} = a_0 E_x^{nl,HF} + E_x^{local} + a_c E_c^{nl} + E_c^{local}. \quad (8)$$

The first term is the non-local exchange, which has the form of Eq. 4 but using the Kohn-Sham molecular orbitals (KS-MOs). It is modulated by the parameter a_0, ranging from zero (pure local exchange) to 1 (HF-like). The correlation part also can be expressed through non-local and local contributions. In double-hybrid functionals, the former borrows the form of the Moller-Plesset second-order energy correction formula, again using the KS-MOs. In the case of range-separated functionals, the non-local and local parts of the exchange functional are modified according to the range-separation parameter, but the essence of the two contributions is kept.

Going back to Eq. 4, the second and fourth term correspond to the local exchange and correlation energy, respectively. Their particular form depends on the one-electron density and its derivatives. Usually, both terms are grouped, E_{xc}^{local}, and evaluated upon integration of the corresponding exchange-correlation energy functional ε^{xc}

$$E_{xc}^{local} = \int \varepsilon^{xc}[\rho(\mathbf{r}_1), \nabla\rho(\mathbf{r}_1), \ldots] d\mathbf{r}_1 = \sum_A E_{xc}^{A,local}. \quad (9)$$

According to Eq. 1, E_{xc}^{local} naturally decomposes into one-center (atomic) contributions. This fact has been recently used by some of us to develop an origin-independent decomposition of the electronic polarizability into atomic/fragment contributions.[27] However, for chemical bonding analysis this situation is clearly unsatisfactory. First of all, since the HF-like non-local part of E_{xc}^{DFT} does decompose into both one- and two-center terms, an IQA-type analysis would render a completely different picture of the atomic and diatomic interactions within the molecule when using a pure KS-DFT functional as compared to Hartree-Fock (with KS-DFT hybrids somewhat in between). Moreover, it has been repeatedly shown that the HF-like inter-atomic exchange contribution between bonded atoms is attractive, and essentially responsible for the bonding. Ignoring this term would make most IQA inter-atomic energies of bonded atoms positive.

A first and plausible solution to the problem was introduced by Tognetti *et al.*, where the authors applied the exact-exchange expression for the atomic and inter-atomic terms but with the KS-MOs obtained by the given functional.[28,29] Thus, introducing the approximated Kohn-Sham exchange density

$$\rho_x^{KS}(\mathbf{r}_1;\mathbf{r}_2) = -\sum_{i,j}^{N_{occ}} \phi_i^{KS,*}(\mathbf{r}_1)\phi_j^{KS,*}(\mathbf{r}_2)\phi_i^{KS}(\mathbf{r}_2)\phi_j^{KS}(\mathbf{r}_1), \quad (10)$$

and performing the decomposition analogously to the Hartree-Fock energy

$$\begin{aligned} E_{xc}^{DFT} \cong E_x^{HF-like} &= \sum_A E_x^{AA,HF-like} + \sum_{A,B>A} E_x^{AB,HF-like} \\ &= -\frac{1}{2}\sum_A \iint w_A(\mathbf{r}_1) w_A(\mathbf{r}_2) \rho_x^{KS}(\mathbf{r}_1,\mathbf{r}_2) r_{12}^{-1} d\mathbf{r}_1 d\mathbf{r}_2 \\ &\quad - \sum_{A,B>A} \iint w_A(\mathbf{r}_1) w_B(\mathbf{r}_2) \rho_x^{KS}(\mathbf{r}_1,\mathbf{r}_2) r_{12}^{-1} d\mathbf{r}_1 d\mathbf{r}_2. \end{aligned} \quad (11)$$

An obvious drawback of this strategy is that the total KS-DFT exchange-correlation energy is not recovered by the sum of all atomic and inter-atomic terms, i.e. the decomposition is not fully additive.

To date, only the strategies devised by Salvador and Mayer[30] and by Francisco *et al.*[31] ensure the proper additiv-

ity (Eq. 12) of E_{xc}^{DFT} upon decomposition into one- and two-center terms, namely

$$E_{xc}^{DFT} = \sum_{A} E_{xc}^{AA,DFT} + \sum_{A,B>A} E_{xc}^{AB,DFT}. \quad (12)$$

In 2007, Salvador and Mayer (henceforth SM-IQA) introduced a bond order density (BOD), i.e. a local function associated to each atomic pair A and B which, upon integration, yields the corresponding real-space bond order.[30] For the simplest case of a closed-shell single-determinant wavefunction, the BOD $\beta_{AB}(\mathbf{r}_1)$ reads as

$$\beta_{AB}(\mathbf{r}_1) = 2\sum_{i,j}^{N_{occ}} \left[w_A(\mathbf{r}_1) S_{ij}^{B} + w_B(\mathbf{r}_1) S_{ij}^{A} \right] \phi_i^{*,KS}(\mathbf{r}_1) \phi_j^{KS}(\mathbf{r}_1), \quad (13)$$

where S_{ij}^{A} corresponds to the atomic overlap matrix elements in the MO basis

$$S_{ij}^{A} = \int w_A(\mathbf{r}_1) \phi_i^{*,KS}(\mathbf{r}_1) \phi_j^{KS}(\mathbf{r}_1) d\mathbf{r}_1. \quad (14)$$

The BOD represents the part of the one-electron density used to build the A-B interaction through the exchange. As such, it also affords an exact decomposition of the single-determinant molecular first-order density into bonding and non-bonding counterparts. Salvador and Mayer showed that the topology of $\beta_{AB}(\mathbf{r}_1)$ is very similar to that of the Hartree-Fock inter-atomic exchange energy density. In particular, the BOD exhibits peaks at the atomic positions and also extends into the inter-atomic region (for bonded atoms) resembling a bonding MO. Then, in a rather heuristic manner, the authors obtained an estimate of the inter-atomic local exchange energy, $E_{xc}^{AB,local}$, using $\beta_{AB}(\mathbf{r}_1)$ (and its derivatives) instead of $\rho(\mathbf{r}_1)$ in the local exchange-correlation expression:

$$E_{xc}^{AB,local} = \int \varepsilon^{xc} \left[\beta_{AB}(\mathbf{r}_1), \nabla\beta_{AB}(\mathbf{r}_1), \ldots \right] d\mathbf{r}_1. \quad (15)$$

The atomic (A = B) exchange contributions were defined such that the sum rule in Eq. 12 is conserved. The authors used the readily available (exact) one-center terms obtained from the decomposition of the exchange-correlation energy of Eq. 9, $E_{xc}^{A,local}$, and subtracted half of the inter-atomic exchange energy terms where the center A is involved, namely

$$E_{xc}^{AA,local} = E_{xc}^{A,local} - \frac{1}{2}\sum_{B\neq A} E_{xc}^{AB,local}. \quad (16)$$

This strategy performed extremely well from a numerical point of view. Both the atomic and diatomic exchange energy components obtained with a local exchange functional (e.g. from a BLYP calculation) exhibited almost perfect correlation with the values obtained with the exact exchange formula (using the same KS-MOs and geometries).[30]

In 2016, Francisco *et al.* introduced an alternative strategy (henceforth F-IQA) to decompose the KS-DFT exchange-correlation energy fulfilling Eq. 12.[31] The idea was again to use the exact exchange formula using the KS-MOs, but incorporating properly defined atomic scaling factors to ensure additivity.

For a hybrid functional, the total KS-DFT exchange-correlation energy can be written as

$$E_{xc}^{DFT} = \sum_{A} E_{xc}^{A,DFT} = \sum_{A} \left[E_{xc}^{A,local} + a_0 E_{x}^{A,HF-like} \right], \quad (17)$$

where

$$E_{x}^{A,HF-like} = -\frac{1}{4} \iint w_A(\mathbf{r}_1) \rho_x^{KS}(\mathbf{r}_1,\mathbf{r}_2) r_{12}^{-1} d\mathbf{r}_1 d\mathbf{r}_2. \quad (18)$$

By introducing the following atomic scaling factors

$$\lambda_A = \frac{E_{xc}^{A,DFT}}{E_{x}^{A,HF-like}}, \quad (19)$$

properly scaled atomic and inter-atomic contributions that add up to the total KS-DFT exchange-correlation energy are simply expressed as

$$E_{xc}^{AB,DFT} = \frac{1}{2}\left[\lambda_A + \lambda_B\right] E_{x}^{AB,HF-like} \;\; \forall \;\; A,B. \quad (20)$$

Hence, in the F-IQA method, the exact HF-exchange expression is always used to determine the atomic and inter-atomic exchange-correlation energies, even in the case of purely local KS-DFT functionals.

The main purpose of this work is to assess the performance of the aforementioned KS-DFT IQA schemes. The atomic and inter-atomic exchange-correlation terms obtained for a molecular set using a local (GGA) functional, a hybrid (GGA) functional and Hartree-Fock are compared. In addition, we also describe in detail a numerical procedure to improve the accuracy of the decomposition of the two-electron energy terms, which are the bottleneck of the IQA approaches. We show that, in the context of overlapping atomic definitions, it is possible that the sum of all atomic and diatomic contributions to the two-electron energy (i.e. Coulomb and exact exchange if needed) exactly reproduce the analytical molecular value. We refer to this strategy as the (two-electron) zero-error scheme (ZES).

RESULTS AND DISCUSSION

A. A two-electron zero-error scheme

The two-electron contributions to the molecular energy, namely Coulomb, Hartree-Fock exchange and correlation, in the case of wavefunction methods, are both the bottleneck and the major source of numerical error in the IQA energy decomposition schemes. They formally scale N^6, being N the number of grid points, albeit efficient algorithms achieving N^4 scaling have also been introduced in the QTAIM framework.[19] In general, the numerical integration of one- or

two-electron density functions over disjoint (e.g. QTAIM) atomic domains is more challenging than for fuzzy-atom (e.g. TFVC) domains. In the latter case, the atomic weight functions (Eq. 1) tailor the molecular density functions. Then, the integrals are formally carried out over the entire space, for which conventional and well-tested numerical integration schemes can be safely applied. Among them, the multicenter integration scheme introduced by Becke, which merges atom-centered spherical grids, is by far the most widely used.[32]

In the first realization of the Hartree-Fock IQA decomposition in the general framework of fuzzy atoms, the numerical two-electron integrations required to decompose the Coulomb and exchange energy terms were carried out by using two sets of atom-centered grid points, associated to the electron coordinates of electron 1 ($\mathbf{r}_1$) and 2 ($\mathbf{r}_2$).[18] It was shown that, because of the r_{12}^{-1} operator in the denominator, if exactly the same grid was used for both electron coordinates, all points where $\mathbf{r}_1 = \mathbf{r}_2$ (in fact, N grid points) had to be discarded to avoid the singularity. Thus, the overall accuracy of the integration is compromised, i.e. the sum of the one- and two-center terms compared to the corresponding molecular (analytical) value. In order to avoid this situation, the authors used two identical grids for both electrons but one of them rotated along the ϕ angle of the spherical coordinates to obtain the one-center terms. In this manner, sufficiently good accuracy was achieved using atom-centered grids consisting on 40 radial and 146 angular points. For the angular mesh, the grid associated to electron 2 was rotated 0.229 rad along ϕ.

We have observed that appropriate rotation angles depend mostly on the size of the angular grid. Also, in a preliminary analysis, we explored the possibility of introducing a second rotation (with respect to the θ angle) to the grid for electron 2. No significant improvement was observed for a small set of molecular systems as compared to that obtained with a single rotation. Another observation was that the two-center two-electron terms are contributing to the numerical error several orders of magnitude less than the one-center ones, while being rather unaffected by the rotation of the second grid.[33]

Yet, the most relevant observation is depicted in Figure 1. Here, the integration error in the two-electron B3LYP/cc-pVTZ energy of N_2 is shown with respect to the rotation angle of the second grid. The error is just defined as the difference between the sum of all one- and two-center contributions of the molecular two-electron energy and the exact (analytical) value, V_{ee}. One can see that, if the atomic grid provided is sufficiently large, there is always a rotation angle for which the overall two-electron integration error vanishes. Thus, a 30×74 (radial and angular points, respectively) atomic grid is clearly insufficient, and with the optimum rotation angle the error is still of ca. 15 kcal/mol. However, using a 40×146 atomic grid the integration error first crosses the zero-error at around 0.18 rad and then again at 0.217 rad, close to the default rotation angle used in Ref.[18]. By using larger atomic grids the zero-error line is crossed at smaller rotation angles.

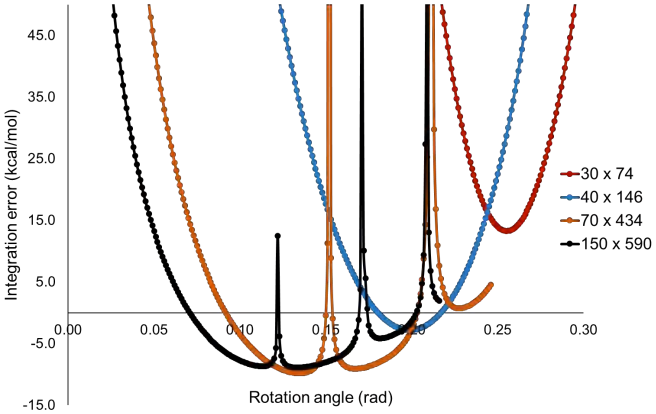

FIG. 1. Two-electron integration error (kcal/mol) versus angular rotation of the electron 2 grid for N_2 at the B3LYP/cc-pVTZ level of theory.

In addition, several poles are observed in the curves due to near singularities in r_{12}^{-1}. Noteworthy, using sufficiently large atomic grids such as 70×434 or 150×590, the shape of the curves is strikingly similar irrespective of the molecule. That is, the rotation angle that produces a zero-error in the two-electron energy lies within an extremely narrow range. This is illustrated in Figure 2, where a 150×590 atomic grid for a set of ten small molecules was used. With this, we observed that the optimum rotation angle is within the 0.169-0.170 (in rad) range in all cases.

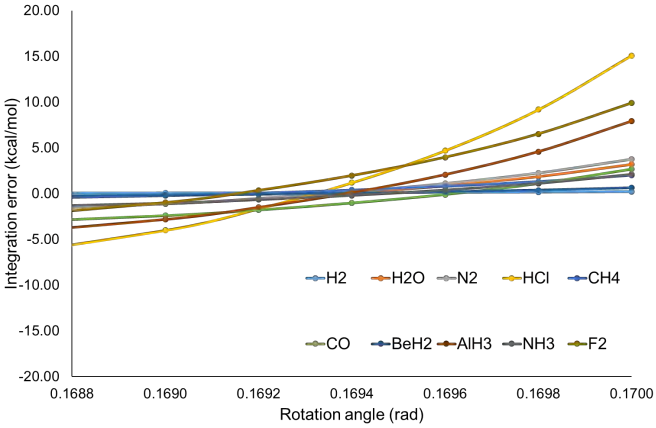

FIG. 2. Two-electron integration error (kcal/mol) versus angular rotation of the electron 2 grid for a set of small molecules at the B3LYP/cc-pVTZ level of theory.

With these findings in mind, we propose a rather simple strategy to minimize the two-electron integration error in IQA schemes with overlapping atomic domains, solely requiring V_{ee}, i.e. the exact two-electron energy of the molecular system. In the Hartree-Fock case, it comprises the Coulomb and exact-exchange terms. In correlated wavefunction methods, an additional correlation contribution coming from the cumulant of the second-order reduced density matrix (RDM2)

is also included. In KS-DFT, it contains the Coulomb and the amount of exact-exchange that is actually used in the exchange functional definition. The strategy proceed as follows. In a first step, the total two-electron energy is decomposed into one and two-center terms, as usual in the IQA framework, with an associated (numerical) integration error of

$$\delta V_{ee}^{(1)} = \sum_A E^{(1),A} + \sum_{A,B>A} E^{AB} - V_{ee}, \tag{21}$$

where an appropriate rotation of the grid for $\mathbf{r}_2$ has been applied to compute the one-center terms. For instance, using a 150×590 atomic grid, a rotation of 0.169 rad performs very well (vide infra). Then, the process is repeated using a second rotation angle, but now *only* the one-center terms are recomputed. This leads to another estimation of the two-electron energy, using the two-center terms evaluated in the previous step

$$\delta V_{ee}^{(2)} = \sum_A E^{(2),A} + \sum_{A,B>A} E^{AB} - V_{ee}. \tag{22}$$

We proceed by introducing a damping between both estimates to impose the error on the two-electron energy to be zero

$$(1-\gamma)\delta V_{ee}^{(1)} + \gamma \delta V_{ee}^{(2)} = 0. \tag{23}$$

Substituting Eqs. 21 and 22 into 23 and rearranging, we obtain the following expression for the damping parameter γ

$$\gamma = \frac{\delta V_{ee}^{(1)}}{\sum_A \left(E^{(1),A} - E^{(2),A}\right)}, \tag{24}$$

and the corrected one-center terms

$$E^A \equiv E^{(1),A} + \gamma\left(E^{(2),A} - E^{(1),A}\right). \tag{25}$$

It can be readily seen that the one- and two-center terms thus defined *exactly* reproduce the total two-electron energy.

Ideally, the applied rotation angles in steps 1 and 2 should be previously optimized to provide small deviations with respect to the exact two-electron energy and, most importantly, of opposite sign. In that case, the γ value lies within the [0,1] range and an actual damping (interpolation) is performed between the two estimates of V_{ee}. As such, a linear behaviour of V_{ee} with the rotation angle of the second grid is implicitly assumed. As mentioned before, we have found that a combination of 150×590 atomic grids and a rotation of 0.169 rad typically overestimates V_{ee} by 1-5 kcal/mol, while using a rotation of 0.170 rad in the second step leads to a somewhat larger underestimation of V_{ee}. In Table I we gathered the integration errors in V_{ee} for a set of 31 molecules obtained at B3LYP/cc-pVTZ level of theory (for further details see Computational Details section). It can be seen that the two-electron integration errors in step 1 are already rather small and negative, with the only exception of H_2 for which the error is merely 0.1 kcal/mol. For most applications these errors might be acceptable. The errors associated to the second step are somewhat larger but positive in all cases, so that the γ values that afford the exact decomposition are within 0 and 1.

TABLE I. Two-electron energy integration error for the first and second rotation (in kcal/mol) and optimal γ values at B3LYP/cc-pVTZ level of theory.

System	$\delta V_{ee}^{(1)}$	$\delta V_{ee}^{(2)}$	γ
C_2H_2	0.0	3.7	0.996
C_2H_4	-0.6	3.2	0.835
C_6H_6	-0.4	11.8	0.965
C_2H_6	-0.9	3.3	0.777
$HCONH_2$	-1.8	7.8	0.812
HCNO	-2.0	6.2	0.757
B_2H_6	-0.5	2.3	0.824
CO	-2.4	2.7	0.524
CO_2	-3.6	5.5	0.604
SO_2	-6.5	17.1	0.725
SO_3	-6.0	22.5	0.790
H_2	0.1	0.2	**1.619**
N_2	-1.1	3.8	0.769
NO^+	-2.6	2.8	0.515
CN^-	-2.0	2.3	0.533
LiF	-1.7	3.8	0.697
F_2	-1.0	9.9	0.909
LiH	-0.2	0.3	0.677
BeH_2	-0.2	0.6	0.779
BH_3	-0.2	1.2	0.838
CH_4	-0.2	2.0	0.903
NH_3	-1.0	2.2	0.686
H_2O	-1.1	3.2	0.745
HF	-1.5	3.8	0.724
NaH	-2.0	5.7	0.735
MgH_2	-2.6	6.5	0.713
AlH_3	-2.8	7.9	0.736
SiH_4	-2.7	9.7	0.780
PH_3	-3.8	10.2	0.727
H_2S	-3.8	12.8	0.771
HCl	-4.0	15.1	0.791

It is important to stress that with such (two-electron) zero-error scheme the two-center terms are evaluated only once, in the first step. We have observed that their value is rather unaffected by a rotation of the second grid and exhibit integration errors 2-3 orders of magnitude smaller than those of the one-center terms.[33] This is because there are no near singularities caused by small r_{12}^{-1} values and also because their contribution to the total two-electron energy is much smaller than that of the one-center terms, specially if heavy atoms are involved. Thus, it is only the much larger one-center terms that are slightly modulated to yield an overall exact decomposition of the two-electron energy.

Of course, the zero-error scheme could also be applied independently to each of the contributions to V_{ee}, namely Coulomb and exact-exchange (and correlation in case of correlated wavefunction methods), provided their exact value is known beforehand. However, we find that the behaviour of V_{ee} in the vicinity of the optimum rotation angles is very similar for HF, B3LYP and BP86, as illustrated by Figure 3. Since

the overall errors are very small anyway it is more efficient to apply the zero-error scheme only once to reproduce the exact V_{ee}.

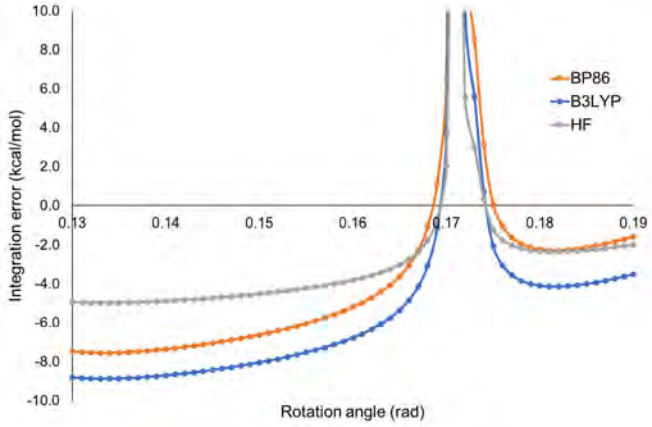

FIG. 3. Two-electron integration error (kcal/mol) versus angular rotation of the second grid for N_2 at different levels of theory.

In this vein, Table S1 of the Supporting material gathers the γ values for the molecular test set at the HF, B3LYP and BP86 levels of theory. The integration errors have been omitted for clarity, being all of them lower than 0.5 kcal/mol (in absolute value), as proceeding from the one-electron integrations. For the later, the same 150×590 atomic grid was used, being the main source of numerical error the atomic kinetic energy contributions due to the oscillatory character of the kinetic energy density near the nuclei. The C_6H_6 molecule is the worst case, with errors of up to 0.4 kcal/mol. Of course, the one-electron grid can still be further improved to decrease the residual integration error if necessary. More importantly, using the aforementioned 0.169 and 0.170 rad rotation angles for the two steps of the two-electron zero-error scheme resulted in the desired interpolation in almost all cases, disregarding whether V_{ee} contains any exact-exchange contribution.

Summarizing this section, the two-electron zero-error scheme smoothly worked for the molecular systems tested, obtaining most of the γ values within the [0,1] range using a system-independent fixed setup. In very few cases the corrected two-electron energy terms were obtained by extrapolation, but with γ values still close to 1. Alternatively, in the case the γ value would be far off the [0,1] range, one could consider performing second grid rotations iteratively until the desired numerical conditions are fulfilled. It is worth to mention that the robustness of the zero-error scheme had already been put into stringent test. Some of us recently showed that the elements of the α tensor can be expressed through the second derivative of a zero-th order field-dependent energy, so that an energy decomposition of the latter readily affords the decomposition of α.[27] Using very large atomic grids for the one-electron energy terms and the zero-error scheme for the two-electron part was absolutely critical to obtain numerically converged atomic contributions to α. Overall, the zero-error scheme appears to be a promising strategy for obtaining accurate IQA energy decomposition terms for large molecular systems while keeping an affordable computational cost.

B. IQA decompositions of the exchange-correlation energy

The atomic and inter-atomic exchange-correlation energy terms obtained using the aforementioned F-IQA and SM-IQA schemes for the molecular set (see Computational details) are compiled in Tables II-IV. We have considered the systems described at the HF, B3LYP and BP86 levels of theory, at their own geometry optimized structures. We focus exclusively on the exchange-correlation (xc) terms, as the remaining ones are exactly the same with both KS-DFT IQA approaches. Regarding the one-center xc terms, we discuss separately the results for the hydrogen atoms, as in our previous study we observed significant differences between HF and pure KS-DFT due to the absence of core electrons.[30] Also, the atomic xc energies for H are of the same order or magnitude as the inter-atomic xc terms of bonded atoms, while the corresponding values for heavier atoms are one or two orders of magnitude larger.

Let us start with the analysis of the inter-atomic xc components, with up to 43 values compiled in Table II. The first observation is that all xc (exchange-only in case of HF) inter-atomic contributions of chemically bonded atoms are negative, as it is well known for IQA decompositions. Their magnitude (in absolute value) is deeply connected with the covalent bond order, so that bonds with higher multiplicitly tend to exhibit larger (more negative) inter-atomic xc contributions. Thus, the larger values are obtained for N_2, NO^+ and the C-C triple bond in C_2H_2.

The inter-atomic xc terms obtained with B3LYP and BP86 functionals correlate extremely well with the HF values, using either the F-IQA and SM-IQA formulations, as shown in Figure S1 of the Supporting material (worst case exhibits R^2 = 0.98). It is more interesting to focus on how the contributions differ from each other in each case. With the F-IQA formulation, the inter-atomic xc components for B3LYP are systematically more negative than the HF ones with only two exceptions (F_2 and H_2S). In both cases, this discrepancy can be attributed to significant differences in the wavefunction itself (F_2 is poorly described at HF level and the shape of the atomic boundaries in H_2S was already found to change significantly from one method to another[15]). This observation is a direct consequence of the scaling factors used in Eq. 20. The total xc energy in B3LYP contains both exchange and correlation contributions, whereas in HF it only contains exchange. Since the total xc value is more negative, the scaling factors are greater than 1 and hence all terms (both atomic and inter-atomic) become more negative. Going to BP86 the picture is very similar. In fact, the mean unsigned deviation (MUD) between the BP86 and B3LYP xc components is merely 2.2 kcal/mol, whereas the respective MUD values with respect to HF are 14.5 kcal/mol and 14.2 kcal/mol, respectively.

With the SM-IQA formulation the trends are different.

Most of the B3LYP inter-atomic xc contributions (32 out of 43) are less negative than the HF ones. The differences are significant in the C-C and C-H bonds of the alkane series. However, the opposite trend is observed mainly for the systems with large (in absolute value) inter-atomic xc contributions, namely triple bonds like in acetylene, CO, N_2 or NO^+ (see Figure S1). Similarly to F-IQA, the MUD between BP86 and B3LYP SM-IQA values is very small (3.5 kcal/mol).

It is worth to note that the general effect of electron correlation in wavefunction theory is precisely the weakening of the covalent bonds. This is readily observed in equilibrium geometries, where bond lengths tend to increase upon inclusion of electron correlation. It is also well-known that electronic bonding indicators such as bond orders also decrease. For instance, the bond order in N_2 goes from 3.04 at the HF level to 2.83 for a CISD WF using Ángyán-Mayer formulation, which only involves the first-order density matrix (i.e. the exchange density). Including the contribution from the cumulant of the second-order reduced density matrix (the so-called delocalization index[34]), further decreases the value to 2.20.[35] In the seminal work of Blanco *et al.* about the IQA approach for correlated wavefunctions, the authors showed that the IQA decomposition of the cumulant of the RDM2 (electron correlation contribution) results in positive inter-atomic contributions for systems like H_2, N_2 or the O-H bond in H_2O. Popelier *et al.* performed a more systematic study of the role of electron correlation in the IQA-MP2 decomposition.[36] The authors found that the inter-atomic correlation energy contributions are usually positive for covalent bonds. Also, the stronger the bond the larger the inter-atomic correlation contribution. Exception to the rule where hydrides and weak interactions, exhibiting much smaller and negative contributions. Of course, the total electron correlation energy contribution is negative, so the atomic correlation terms are large and negative to compensate.[37] In the F-IQA formulation this effect should be captured by the the scaling factors. As shown on Table III, the atomic xc energies from both B3LYP and BP86 are systematically more negative than the HF ones, which means that the net effect of correlation is as anticipated. Table IV gathers the atomic xc energies for hydrogen atoms, which are much smaller than for 2nd and 3rd period atoms (in fact, they are of the same order of magnitude as the inter-atomic terms for bonded atoms). The differences between the HF and F-IQA values are very small. Except in the aforementioned case of H_2S, where the shape of the atomic domains changes significantly going from HF to a DFT density, the MUD between between the HF and F-IQA atomic contributions for H atoms is merely 7-8 kcal/mol. More importantly, the atomic xc values with BP86 are less negative than the HF values in several cases. In contrast, with the SM-IQA formulation the atomic xc contributions are systematically more negative than the HF ones; in the case of the H atoms by ca. 20 kcal/mol on average. This means that the observed trends of the atomic correlation contributions in IQA-MP2[37] are better captured by the SM-IQA formulation, at least for the set of studied systems.

It is fair to note that the numbers discussed so far have been obtained at the corresponding stationary points on the potential energy surface of the given level of theory. Thus, several factors influence the observed differences between HF and BP86 or B3LYP one- and two-center xc contributions, namely the way the total exchange (correlation) energy is expressed, the shape of the MOs and the geometry. To explore the latter effect we have studied in more detail F_2, for which a deviation from the general trend was observed (i.e. the F-IQA inter-atomic xc values are less negative, and the SM-IQA values are more negative, than the HF ones). In Figure 4 we show the evolution of the inter-atomic xc values with the inter-atomic distance for HF, BP86 and B3LYP wavefunctions. Notice that the HF optimized geometry (1.328 Å) is significantly shorter than the experimental value (1.412 Å), while BP86 slightly overestimates the distance. The inter-atomic xc energies for KS-DFT using either F-IQA or SM-IQA formulations are more negative than the HF ones for all inter-atomic distances. An important observation is that the differences between all schemes is roughly constant along the (rather short) inter-atomic distance profile, while the shorter the inter-atomic distance, the more negative the inter-atomic xc value. Consequently, the IQA-DFT xc values at their equilibrium distances may lie above the HF values at the compressed HF equilibrium distance, even if the IQA-DFT xc values are systematically more negative than the HF along the profile. What makes the bond in F_2 different from the other cases is that the SM-IQA values lie well below the F-IQA ones. A plausible explanation might be the unexpectedly large value of the bond order, around 1.4 for the considered distances).

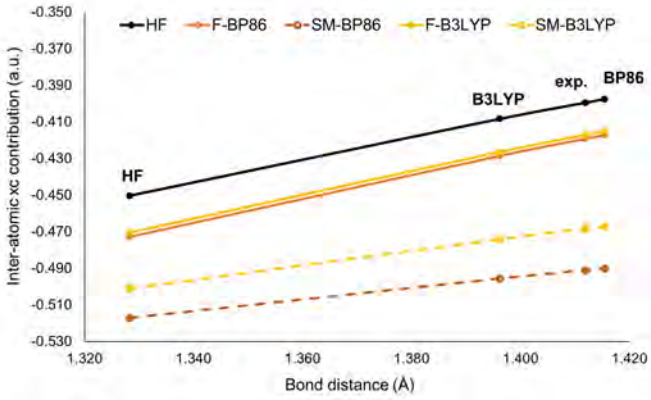

FIG. 4. Inter-atomic xc values along the F-F inter-atomic distance in F_2 for HF and IQA-DFT methods.

As a final illustrative example we applied the IQA decomposition along the energy profile (i.e. intrinsic reaction coordinate obtained at each level of theory) of the Diels-Alder reaction between 1,3-butadiene and ethylene. As shown in Figure S2, Hartree-Fock largely overestimates the barrier height, whereas pure GGA BP86 functional underestimates it. Hybrid functionals like B3LYP do a particularly good job in this case, predicting a barrier height close to the experimental es-

TABLE II. Total inter-atomic exchange-correlation energies (a.u.) from the test set calculated with HF and the BP86 and B3LYP KS-DFT functionals. a) F-IQA and b) SM-IQA.

Bond	Mol.	E_{HF}	E^a_{BP86}	E^a_{B3LYP}	E^b_{BP86}	E^b_{B3LYP}
C-C	C_2H_2	-0.813	-0.819	-0.829	-0.814	-0.822
C-H	C_2H_2	-0.305	-0.316	-0.320	-0.276	-0.282
C-C	C_2H_4	-0.544	-0.557	-0.561	-0.511	-0.519
C-H	C_2H_4	-0.306	-0.313	-0.317	-0.270	-0.277
C-C	C_6H_6	-0.437	-0.446	-0.450	-0.370	-0.384
C-H	C_6H_6	-0.307	-0.313	-0.317	-0.268	-0.277
C-C	C_2H_6	-0.300	-0.315	-0.314	-0.259	-0.262
C-H	C_2H_6	-0.296	-0.306	-0.309	-0.262	-0.269
C-H	$HCONH_2$	-0.273	-0.279	-0.283	-0.234	-0.242
C-O	$HCONH_2$	-0.392	-0.444	-0.439	-0.380	-0.386
C-N	$HCONH_2$	-0.288	-0.345	-0.339	-0.272	-0.276
N-H	$HCONH_2$	-0.252	-0.276	-0.277	-0.243	-0.245
N-H	$HCONH_2$	-0.259	-0.282	-0.283	-0.248	-0.251
H-C	HCNO	-0.288	-0.307	-0.309	-0.264	-0.269
C-N	HCNO	-0.654	-0.644	-0.655	-0.586	-0.607
N-O	HCNO	-0.647	-0.674	-0.673	-0.611	-0.619
B-B	B_2H_6	-0.009	-0.016	-0.015	-0.010	-0.009
B-H_b	B_2H_6	-0.080	-0.102	-0.099	-0.061	-0.065
B-H	B_2H_6	-0.139	-0.166	-0.164	-0.121	-0.123
C-O	CO	-0.549	-0.608	-0.603	-0.597	-0.590
C-O	CO_2	-0.449	-0.496	-0.493	-0.422	-0.430
S-O	SO_2	-0.426	-0.458	-0.454	-0.394	-0.392
S-O	SO_3	-0.372	-0.398	-0.395	-0.315	-0.320
H-H	H_2	-0.268	-0.282	-0.284	-0.266	-0.271
N-N	N_2	-1.007	-1.009	-1.020	-1.073	-1.069
N-O	NO^+	-0.817	-0.885	-0.880	-0.941	-0.916
C-N	CN^-	-0.658	-0.709	-0.709	-0.701	-0.701
Li-F	LiF	-0.083	-0.097	-0.098	-0.078	-0.080
F-F	F_2	-0.450	-0.417	-0.426	-0.490	-0.474
Li-H	LiH	-0.075	-0.087	-0.088	-0.073	-0.075
Be-H	BeH_2	-0.118	-0.132	-0.132	-0.107	-0.108
B-H	BH_3	-0.154	-0.185	-0.182	-0.140	-0.143
C-H	CH_4	-0.296	-0.307	-0.310	-0.264	-0.271
N-H	NH_3	-0.279	-0.299	-0.300	-0.269	-0.272
O-H	H_2O	-0.194	-0.236	-0.230	-0.216	-0.209
H-F	HF	-0.137	-0.172	-0.165	-0.158	-0.149
Na-H	NaH	-0.087	-0.108	-0.108	-0.100	-0.100
Mg-H	MgH_2	-0.110	-0.126	-0.125	-0.105	-0.105
Al-H	AlH_3	-0.123	-0.140	-0.138	-0.108	-0.108
Si-H	SiH_4	-0.140	-0.160	-0.158	-0.118	-0.117
P-H	PH_3	-0.210	-0.234	-0.231	-0.185	-0.183
S-H	H_2S	-0.346	-0.325	-0.330	-0.294	-0.294
H-Cl	HCl	-0.291	-0.307	-0.309	-0.286	-0.282

TABLE III. Atomic exchange-correlation energies (in a.u.) calculated with HF and the BP86 and B3LYP KS-DFT functionals (hydrogen atoms excluded). a) F-IQA and b) SM-IQA.

Atom	Mol.	E_{HF}	E^a_{BP86}	E^a_{B3LYP}	E^b_{BP86}	E^b_{B3LYP}
C	C_2H_2	-4.627	-4.837	-4.835	-4.857	-4.856
C	C_2H_4	-4.547	-4.782	-4.772	-4.847	-4.832
C	C_6H_6	-4.558	-4.782	-4.776	-4.883	-4.865
C	C_2H_6	-4.463	-4.728	-4.710	-4.821	-4.795
C	$HCONH_2$	-3.985	-4.233	-4.216	-4.320	-4.292
O	$HCONH_2$	-8.476	-8.740	-8.764	-8.771	-8.793
N	$HCONH_2$	-6.766	-6.900	-6.932	-6.969	-6.996
C	HCNO	-4.259	-4.495	-4.481	-4.517	-4.505
N	HCNO	-6.323	-6.540	-6.550	-6.601	-6.601
O	HCNO	-7.985	-8.322	-8.328	-8.326	-8.337
B	B_2H_6	-3.023	-3.151	-3.153	-3.234	-3.225
C	CO	-4.361	-4.547	-4.549	-4.551	-4.555
O	CO	-8.450	-8.720	-8.742	-8.727	-8.750
C	CO_2	-3.825	-4.030	-4.018	-4.102	-4.079
O	CO_2	-8.462	-8.724	-8.746	-8.746	-8.768
S	SO_2	-23.653	-24.301	-24.261	-24.360	-24.317
O	SO_2	-8.508	-8.777	-8.805	-8.796	-8.829
S	SO_3	-23.149	-23.806	-23.752	-23.922	-23.857
O	SO_3	-8.503	-8.764	-8.792	-8.794	-8.826
N	N_2	-6.074	-6.342	-6.342	-6.310	-6.318
N	NO^+	-5.436	-5.761	-5.733	-5.732	-5.715
O	NO^+	-8.178	-8.350	-8.386	-8.322	-8.368
C	CN^-	-4.428	-4.654	-4.654	-4.657	-4.657
N	CN^-	-6.849	-7.077	-7.097	-7.082	-7.102
Li	LiF	-1.650	-1.681	-1.697	-1.691	-1.706
F	LiF	-10.270	-10.623	-10.640	-10.633	-10.650
F	F_2	-9.784	-10.168	-10.170	-10.132	-10.146
Li	LiH	-1.665	-1.700	-1.715	-1.705	-1.720
Be	BeH_2	-2.340	-2.393	-2.410	-2.415	-2.431
B	BH_3	-3.044	-3.168	-3.173	-3.229	-3.228
C	CH_4	-4.458	-4.735	-4.711	-4.814	-4.782
N	NH_3	-6.570	-6.784	-6.797	-6.823	-6.834
O	H_2O	-8.515	-8.749	-8.782	-8.765	-8.799
F	HF	-10.295	-10.627	-10.650	-10.631	-10.656
Na	NaH	-13.913	-14.283	-14.303	-14.284	-14.304
Mg	MgH_2	-15.730	-16.121	-16.140	-16.137	-16.156
Al	AlH_3	-17.553	-17.992	-18.002	-18.033	-18.042
Si	SiH_4	-19.403	-19.892	-19.888	-19.968	-19.960
P	PH_3	-21.690	-22.311	-22.281	-22.373	-22.343
S	H_2S	-24.233	-25.291	-25.241	-25.312	-25.268
Cl	HCl	-27.491	-28.177	-28.156	-28.182	-28.165

timate of 27.5 kcal/mol.[38] In any case, this reaction profile poses a good example where the three methods considered in this work exhibit quantitative different behaviour. To what extent these differences are translated into the one- and two-center terms from the respective IQA analyses is shown in Figure 5. The IQA terms were grouped according to the two molecular fragments along the profile, namely the dienophile (F_1) and the diene (F_2). Hence, the total energy is decomposed into the two fragment's deformation energies and the inter-fragment F_1-F_2 interaction.

In line with the picture obtained with other schemes like the activation strain model,[39–41] the fragment deformation energy dominates the energy profile starting from the reactant complex. The inter-fragment interaction is always negative and monotonically increases (in absolute value) until the formation of products (where the fragments are covalently bound). Comparing the behaviour of both IQA-DFT formulations, Figure 5 shows that the differences between the HF and DFT values are much smaller in the F-IQA scheme. In most of the points along the profile, specially at the beginning, the energy components follow the energy ordering observed for the underlying methods (HF > B3LYP > BP86). After the transition state is reached, the curves corresponding to the different methods cross, specially for the deformation energies. With the SM-IQA scheme the difference between the HF and both DFT methods is more notorious (perhaps

TABLE IV. Atomic exchange-correlation energies (in a.u.) calculated with HF and the BP86 and B3LYP KS-DFT functionals (hydrogen atoms only). a) F-IQA and b) SM-IQA.

Atom	Mol.	E_{HF}	E^{a}_{BP86}	E^{a}_{B3LYP}	E^{b}_{BP86}	E^{b}_{B3LYP}
H	C_2H_2	-0.160	-0.169	-0.173	-0.191	-0.194
H	C_2H_4	-0.212	-0.210	-0.216	-0.235	-0.240
H	C_6H_6	-0.214	-0.211	-0.219	-0.238	-0.245
H	C_2H_6	-0.233	-0.223	-0.231	-0.252	-0.258
H_b	B_2H_6	-0.443	-0.435	-0.445	-0.514	-0.510
H	B_2H_6	-0.431	-0.420	-0.432	-0.463	-0.469
H_C	$HCONH_2$	-0.214	-0.211	-0.216	-0.238	-0.242
H_N	$HCONH_2$	-0.071	-0.090	-0.088	-0.108	-0.106
H_N	$HCONH_2$	-0.075	-0.093	-0.091	-0.111	-0.109
H	HCNO	-0.131	-0.149	-0.150	-0.172	-0.172
H	LiH	-0.405	-0.432	-0.435	-0.440	-0.443
H	BeH_2	-0.435	-0.450	-0.457	-0.464	-0.470
H	BH_3	-0.444	-0.433	-0.444	-0.467	-0.474
H	CH_4	-0.225	-0.217	-0.225	-0.245	-0.251
H	NH_3	-0.093	-0.110	-0.109	-0.127	-0.126
H	H_2O	-0.036	-0.054	-0.051	-0.066	-0.063
H	HF	-0.017	-0.027	-0.024	-0.035	-0.034
H	NaH	-0.363	-0.377	-0.378	-0.383	-0.385
H	MgH_2	-0.391	-0.407	-0.413	-0.419	-0.424
H	AlH_3	-0.420	-0.428	-0.437	-0.448	-0.455
H	SiH_4	-0.428	-0.428	-0.439	-0.461	-0.469
H	PH_3	-0.418	-0.401	-0.415	-0.444	-0.454
H	H_2S	-0.379	-0.230	-0.245	-0.253	-0.270
H	HCl	-0.116	-0.131	-0.132	-0.147	-0.151
H	H_2	-0.197	-0.209	-0.210	-0.217	-0.217

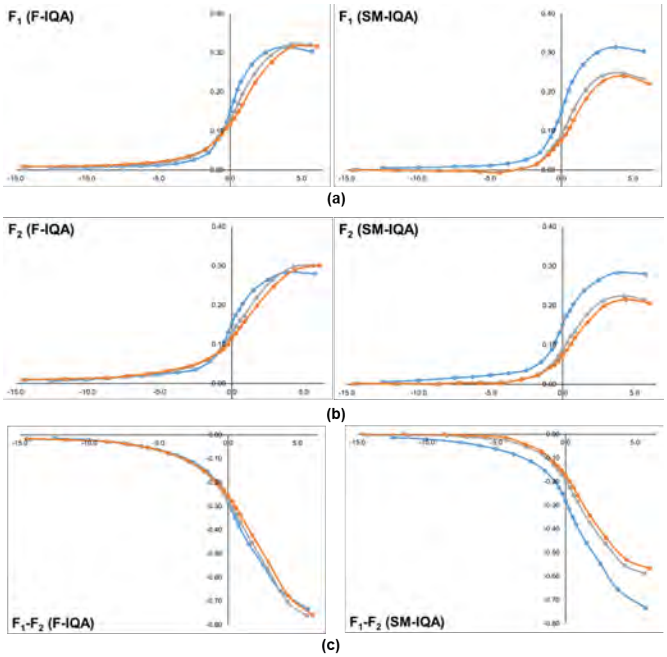

FIG. 5. Fragment deformation energies (a and b) and inter-fragment energy values (c) in a.u. along the reaction coordinate of the Diels-Alder reaction obtained at the HF (blue), B3LYP (grey) and BP86 (orange) levels of theory.

somewhat exaggerated taking into account the relatively small overall energy differences between the methods in Figure S2). In this case, the same ordering of energies is maintained along the whole energy profile for both deformation and inter-fragment interaction energies.

CONCLUSIONS

A new scheme to eliminate the numerical error of the sum of two-electron energy contributions (i.e. Coulomb and exact exchange) has been introduced. It is readily applicable in the framework of overlapping atoms such as TFVC or Hirshfeld approaches. Such two-electron zero-error scheme provided robust numerical integrations for both equilibrium structures and along the potential energy surface.

A critical comparison of the performance of two fully additive approaches for the IQA decomposition of the KS-DFT energy (F-IQA and SM-IQA) has also been performed for a wide molecular test set and along the reaction coordinate of a Diels-Alder reaction. The atomic and diatomic exchange-correlation energy components obtained with both approaches are in very good agreement and also exhibit excellent correlation with the Hartree-Fock results. As a general trend, the SM-IQA diatomic xc components tend to be less negative than the Hartree-Fock ones, in accordance with the known effect of electron correlation on covalent bonds.

COMPUTATIONAL DETAILS

All *ab-initio* calculations have been performed using the Gaussian09 package[42] at the Hartree-Fock (HF) and at the BP86[43,44] and B3LYP[45,46] Kohn-Sham DFT levels of theory coupled with the cc-pVTZ full electron basis set.[47] Molecular (equilibrium) structures have been obtained for each level of theory and confirmed by vibrational frequency analysis (no negative frequencies).

Real-space energy decompositions have been performed with the APOST-3D program[48], using the Topological Fuzzy Voronoi Cells atomic definition[15] for both the F-[31] and SM-IQA[30] approximations of the inter-atomic exchange-correlation energy term. For the production results, both one- and two-electron numerical integrals were evaluated using 150 radial and 590 angular points distributed according to Lebedev-Laikov.[49] The zero-error scheme was applied in all cases for the two-electron energy contributions.

The test set of 31 molecules consists of carbon and sulphur oxides, particularly SO_2, SO_3, CO and CO_2; the hydrocarbon series of C_2H_6, C_6H_6, C_2H_4 and C_2H_2, a set of 2nd and 3r row hydrides with general formula XH_n, where X goes from Li to Cl and other neutral and charged inter-atomic molecules exhibiting different bond multiplicities, e.g. CN^-, N_2 or F_2.

Geometries and wavefunctions of the prototypical Diels-Alder reaction between 1,3-butadiene and ethylene were obtained at the HF, BP86 and B3LYP levels by means of IRC calculations starting from the optimized transition states. IRC

step numbers were increased to ensure convergence to both reactants and products at each level of theory. The Hessian matrix was recomputed at each step of the IRC to ensure smooth potential energy curves.

DATA AVAILABILITY STATEMENT

The data that support the findings of this study are available within the article [and its supplementary material]. Extra data is available upon request to the authors.

CONFLICTS OF INTEREST

There are no conflicts to declare.

ACKNOWLEDGMENTS

Financial support has been furnished by the Ministerio de Ciencia, Innovación y Universidades (MCIU), grant number PGC2018-098212-B-C22. M.G acknowledges the Generalitat de Catalunya and Fons Social Europeu for the predoctoral fellowship (2018 FI_B 01120).

REFERENCES

[1] K. Eskandari and C. Van Alsenoy, "Hydrogen–hydrogen interaction in planar biphenyl: A theoretical study based on the interacting quantum atoms and hirshfeld atomic energy partitioning methods," Journal of Computational Chemistry **35**, 1883–1889 (2014).

[2] T. D. Kühne and R. Z. Khaliullin, "Nature of the asymmetry in the hydrogen-bond networks of hexagonal ice and liquid water," Journal of the American Chemical Society **136**, 3395–3399 (2014).

[3] D. S. Levine and M. Head-Gordon, "Clarifying the quantum mechanical origin of the covalent chemical bond," Nature Communications **11**, 4893 (2020).

[4] D. S. Levine, P. R. Horn, Y. Mao, and M. Head-Gordon, "Variational energy decomposition analysis of chemical bonding. 1. spin-pure analysis of single bonds," Journal of Chemical Theory and Computation **12**, 4812–4820 (2016).

[5] Y. Mao, M. Loipersberger, P. R. Horn, A. Das, O. Demerdash, D. S. Levine, S. Prasad Veccham, T. Head-Gordon, and M. Head-Gordon, "From intermolecular interaction energies and observable shifts to component contributions and back again: A tale of variational energy decomposition analysis," Annual Review of Physical Chemistry **72**, 641–666 (2021).

[6] A. Martín Pendás, M. A. Blanco, and E. Francisco, "The nature of the hydrogen bond: A synthesis from the interacting quantum atoms picture," The Journal of Chemical Physics **125**, 184112 (2006).

[7] A. Martín Pendás, E. Francisco, and M. A. Blanco, "Binding energies of first row diatomics in the light of the interacting quantum atoms approach," The Journal of Physical Chemistry A **110**, 12864–12869 (2006).

[8] J. C. R. Thacker and P. L. A. Popelier, "Fluorine gauche effect explained by electrostatic polarization instead of hyperconjugation: An interacting quantum atoms (iqa) and relative energy gradient (reg) study," The Journal of Physical Chemistry A **122**, 1439–1450 (2018).

[9] L. Zhao, M. Hermann, W. H. E. Schwarz, and G. Frenking, "The lewis electron-pair bonding model: modern energy decomposition analysis," Nature Reviews Chemistry **3**, 48–63 (2019).

[10] J. M. Guevara-Vela, E. Francisco, T. Rocha-Rinza, and A. Martín Pendás, "Interacting quantum atoms-a review," Molecules **25** (2020), 10.3390/molecules25174028.

[11] R. F. W. Bader, "A quantum theory of molecular structure and its applications," Chemical Reviews **91**, 893–928 (1991).

[12] F. L. Hirshfeld, "Bonded-atom fragments for describing molecular charge densities," Theoretica chimica acta **44**, 129–138 (1977).

[13] P. Bultinck, C. Van Alsenoy, P. W. Ayers, and R. Carbó-Dorca, "Critical analysis and extension of the hirshfeld atoms in molecules," The Journal of Chemical Physics **126**, 144111 (2007).

[14] F. Heidar-Zadeh, P. W. Ayers, T. Verstraelen, I. Vinogradov, E. Vöhringer-Martinez, and P. Bultinck, "Information-theoretic approaches to atoms-in-molecules: Hirshfeld family of partitioning schemes," The Journal of Physical Chemistry A **122**, 4219–4245 (2018).

[15] P. Salvador and E. Ramos-Cordoba, "Communication: An approximation to bader's topological atom," The Journal of Chemical Physics **139**, 071103 (2013).

[16] P. L. A. Popelier and D. S. Kosov, "Atom–atom partitioning of intramolecular and intermolecular coulomb energy," The Journal of Chemical Physics **114**, 6539–6547 (2001).

[17] P. Salvador, M. Duran, and I. Mayer, "One- and two-center energy components in the atoms in molecules theory," The Journal of Chemical Physics **115**, 1153–1157 (2001).

[18] P. Salvador and I. Mayer, "Energy partitioning for "fuzzy" atoms," The Journal of Chemical Physics **120**, 5046–5052 (2004).

[19] M. A. Blanco, A. Martín Pendás, and E. Francisco, "Interacting quantum atoms: A correlated energy decomposition scheme based on the quantum theory of atoms in molecules," Journal of Chemical Theory and Computation **1**, 1096–1109 (2005).

[20] A. M. Pendás, M. A. Blanco, and E. Francisco, "Two-electron integrations in the quantum theory of atoms in molecules," The Journal of Chemical Physics **120**, 4581–4592 (2004).

[21] A. M. Pendás, E. Francisco, and M. A. Blanco, "Two-electron integrations in the quantum theory of atoms in molecules with correlated wave functions," Journal of Computational Chemistry **26**, 344–351 (2005).

[22] V. Tognetti, A. F. Silva, M. A. Vincent, L. Joubert, and P. L. A. Popelier, "Decomposition of møller–plesset energies within the quantum theory of atoms-in-molecules," The Journal of Physical Chemistry A **122**, 7748–7756 (2018).

[23] J. L. Casals-Sainz, J. M. Guevara-Vela, E. Francisco, T. Rocha-Rinza, and A. Martín Pendás, "Efficient implementation of the interacting quantum atoms energy partition of the second-order møller–plesset energy," Journal of Computational Chemistry **41**, 1234–1241 (2020).

[24] R. Chávez-Calvillo, M. García-Revilla, E. Francisco, A. Martín Pendás, and T. Rocha-Rinza, "Dynamical correlation within the interacting quantum atoms method through coupled cluster theory," Computational and Theoretical Chemistry **1053**, 90–95 (2015).

[25] F. J. Holguín-Gallego, R. Chávez-Calvillo, M. García-Revilla, E. Francisco, A. M. Pendás, and T. Rocha-Rinza, "Electron correlation in the interacting quantum atoms partition via coupled-cluster lagrangian densities," Journal of Computational Chemistry **37**, 1753–1765 (2016).

[26] A. Fernández-Alarcón, J. L. Casals-Sainz, J. M. Guevara-Vela, A. Costales, E. Francisco, A. Martín Pendás, and T. Rocha-Rinza, "Partition of electronic excitation energies: the iqa/eom-ccsd method," Physical Chemistry Chemical Physics **21**, 13428–13439 (2019).

[27] M. Montilla, J. M. Luis, and P. Salvador, "Origin-independent decomposition of the static polarizability," Journal of Chemical Theory and Computation **17**, 1098–1105 (2021).

[28] V. Tognetti and L. Joubert, "On the physical role of exchange in the formation of an intramolecular bond path between two electronegative atoms," The Journal of Chemical Physics **138**, 024102 (2013).

[29] V. Tognetti and L. Joubert, "Density functional theory and bader's atoms-in-molecules theory: towards a vivid dialogue," Physical Chemistry Chemical Physics **16**, 14539–14550 (2014).

[30] P. Salvador and I. Mayer, "One- and two-center physical space partitioning of the energy in the density functional theory," The Journal of Chemical Physics **126**, 234113 (2007).

[31] E. Francisco, J. L. Casals-Sainz, T. Rocha-Rinza, and A. Martín Pendás, "Partitioning the dft exchange-correlation energy in line with the interacting quantum atoms approach," Theoretical Chemistry Accounts **135**, 170

(2016).
[32]A. D. Becke, "A multicenter numerical integration scheme for polyatomic molecules," The Journal of Chemical Physics **88**, 2547–2553 (1988).
[33]M. Gimferrer Andrés, *Towards an accurate Kohn-Sham Density Functional Theory Molecular Energy Decomposition scheme*, Bachellor's thesis, Universitat de Girona, Departament de Química (2016).
[34]X. Fradera, M. A. Austen, and R. F. W. Bader, "The lewis model and beyond," The Journal of Physical Chemistry A **103**, 304–314 (1999).
[35]E. Matito, M. Solà, P. Salvador, and M. Duran, "Electron sharing indexes at the correlated level. application to aromaticity calculations," Faraday Discuss. **135**, 325–345 (2007).
[36]J. L. McDonagh, A. F. Silva, M. A. Vincent, and P. L. A. Popelier, "Quantifying electron correlation of the chemical bond," The Journal of Physical Chemistry Letters **8**, 1937–1942 (2017), pMID: 28402120, https://doi.org/10.1021/acs.jpclett.7b00535.
[37]A. F. Silva and P. L. A. Popelier, "Mp2-iqa: upscaling the analysis of topologically partitioned electron correlation," Journal of Molecular Modelling **24**, 201–211 (2018).
[38]D. Rowley and H. Steiner, "Kinetics of diene reactions at high temperatures," Discuss. Faraday Soc. **10**, 198–213 (1951).
[39]L. P. Wolters and F. M. Bickelhaupt, "The activation strain model and molecular orbital theory," WIREs Computational Molecular Science **5**, 324–343 (2015).
[40]X. Sun, T. M. Soini, J. Poater, T. A. Hamlin, and F. M. Bickelhaupt, "Pyfrag 2019—automating the exploration and analysis of reaction mechanisms," Journal of Computational Chemistry **40**, 2227–2233 (2019).
[41]J. L. Casals-Sainz, E. Francisco, and A. Martín Pendás, "The activation strain model in the light of real space energy partitions," Zeitschrift für anorganische und allgemeine Chemie **646**, 1062–1072 (2020).
[42]M. J. Frisch, G. W. Trucks, H. B. Schlegel, G. E. Scuseria, M. A. Robb, J. R. Cheeseman, G. Scalmani, V. Barone, B. Mennucci, G. A. Petersson, H. Nakatsuji, M. Caricato, X. Li, H. P. Hratchian, A. F. Izmaylov, J. Bloino, G. Zheng, J. L. Sonnenberg, M. Hada, M. Ehara, K. Toyota, R. Fukuda, J. Hasegawa, M. Ishida, T. Nakajima, Y. Honda, O. Kitao, H. Nakai, T. Vreven, J. A. Montgomery, Jr., J. E. Peralta, F. Ogliaro, M. Bearpark, J. J. Heyd, E. Brothers, K. N. Kudin, V. N. Staroverov, R. Kobayashi, J. Normand, K. Raghavachari, A. Rendell, J. C. Burant, S. S. Iyengar, J. Tomasi, M. Cossi, N. Rega, J. M. Millam, M. Klene, J. E. Knox, J. B. Cross, V. Bakken, C. Adamo, J. Jaramillo, R. Gomperts, R. E. Stratmann, O. Yazyev, A. J. Austin, R. Cammi, C. Pomelli, J. W. Ochterski, R. L. Martin, K. Morokuma, V. G. Zakrzewski, G. A. Voth, P. Salvador, J. J. Dannenberg, S. Dapprich, A. D. Daniels, O. Farkas, J. B. Foresman, J. V. Ortiz, J. Cioslowski, and D. J. Fox, "Gaussian09 Revision E.01," (2009), gaussian Inc. Wallingford CT.
[43]A. D. Becke, "Density-functional exchange-energy approximation with correct asymptotic behavior," Physical Review A **38**, 3098–3100 (1988).
[44]J. P. Perdew, "Density-functional approximation for the correlation energy of the inhomogeneous electron gas," Physical Review B **33**, 8822–8824 (1986).
[45]A. D. Becke, "Density-functional thermochemistry. iii. the role of exact exchange," The Journal of Chemical Physics **98**, 5648–5652 (1993).
[46]C. Lee, W. Yang, and R. G. Parr, "Development of the colle-salvetti correlation-energy formula into a functional of the electron density," Physical Review B **37**, 785–789 (1988).
[47]T. H. Dunning, "Gaussian basis sets for use in correlated molecular calculations. i. the atoms boron through neon and hydrogen," The Journal of Chemical Physics **90**, 1007–1023 (1989).
[48]P. Salvador, E. Ramos-Cordoba, and M. Gimferrer, "Apost-3d," (2019), institute of Computational Chemistry and Catalysis, University of Girona: Girona.
[49]V. I. Lebedev and D. N. Laikov, "A quadrature formula for the sphere of the 131st algebraic order of accuracy," Doklady Mathematics **59**, 477–481 (1999).

Chapter 6

Applying computational tools for chemical bonding characterization

6.1 Facing the challenges of borderline oxidation state assignments using state-of-the-art computational methods

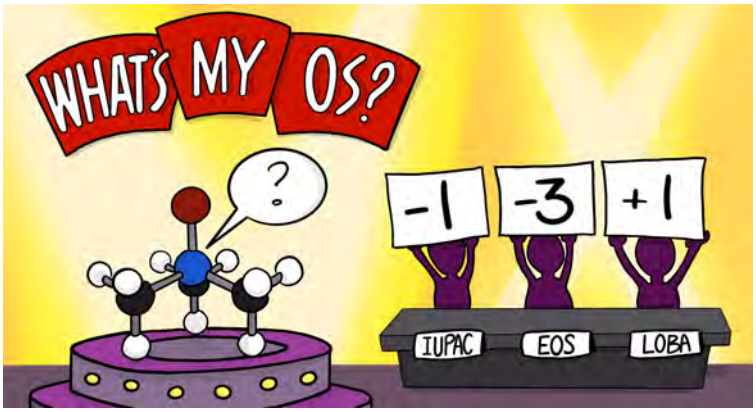

Published in: Gimferrer, M.; Van der Mynsbrugge, J.; Bell, A. T.; Salvador, P.; Head-Gordon, M. *Inorg. Chem.* **2020**, 59, 20, 15410-15420.

Abstract: The oxidation state (OS) of metals and ligands in inorganic complexes may be defined by carefully curated rules, such as from IUPAC, or by computational procedures such as the effective oxidation state (EOS) or localized orbital bonding analysis (LOBA). Such definitions typically agree for systems with simple ionic bonding and innocent ligands but may disagree as the boundary between ionic and covalent bonds is approached, or as the role of ligand noninnocence becomes nontrivial, or high oxidation states of metals are supported by heavy dative bonding, and so on. This work systematically compares IUPAC, EOS, and LOBA across a series of complexes where OS assignment is challenging. These systems include high-valent transition metal oxides, transition metal complexes with noninnocent ligands such as dithiolate and nitrosyl, metal sulfur dioxide adducts, and two transition metal carbene complexes. The differences in OS assignment by the three methods are carefully discussed, demonstrating the synergy between EOS and

LOBA. In addition, a clarity index for LOBA OS assignments is introduced that provides an indication of whether or not its predictions are close to the ionic–covalent boundary.

Inorganic Chemistry

pubs.acs.org/IC Article

Facing the Challenges of Borderline Oxidation State Assignments Using State-of-the-Art Computational Methods

Martí Gimferrer, Jeroen Van der Mynsbrugge, Alexis T. Bell, Pedro Salvador, and Martin Head-Gordon*

Cite This: *Inorg. Chem.* 2020, 59, 15410−15420 Read Online

ACCESS | Metrics & More | Article Recommendations | Supporting Information

ABSTRACT: The oxidation state (OS) of metals and ligands in inorganic complexes may be defined by carefully curated rules, such as from IUPAC, or by computational procedures such as the effective oxidation state (EOS) or localized orbital bonding analysis (LOBA). Such definitions typically agree for systems with simple ionic bonding and innocent ligands but may disagree as the boundary between ionic and covalent bonds is approached, or as the role of ligand noninnocence becomes nontrivial, or high oxidation states of metals are supported by heavy dative bonding, and so on. This work systematically compares IUPAC, EOS, and LOBA across a series of complexes where OS assignment is challenging. These systems include high-valent transition metal oxides, transition metal complexes with noninnocent ligands such as dithiolate and nitrosyl, metal sulfur dioxide adducts, and two transition metal carbene complexes. The differences in OS assignment by the three methods are carefully discussed, demonstrating the synergy between EOS and LOBA. In addition, a clarity index for LOBA OS assignments is introduced that provides an indication of whether or not its predictions are close to the ionic−covalent boundary.

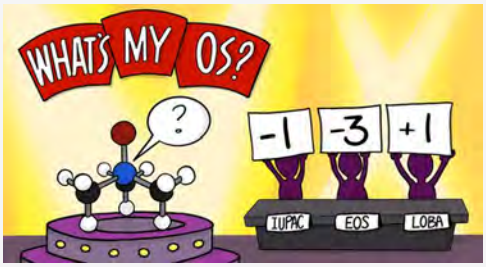

INTRODUCTION

One of the most fundamental chemical concepts is the oxidation state (OS), which is widely used for the rationalization, characterization, categorization, and prediction of reactivity of inorganic compounds. However, despite being universally taught and used, a well-established definition for this concept is still lacking. Informally, the oxidation state of an element (typically a metal) in a compound is the net charge that results from an ionic division of electrons and electron pairs between the selected element and the remainder of the molecule.

For years, the OS assignment was performed following a set of agreed upon rules, but without having an explicit definition of the concept. Recently, a new generic definition of OS has been entered into IUPAC's Gold Book, which reads as the *atom's charge after ionic approximation of its heteronuclear bonds.*[1,2] For homonuclear bonds, its electrons must always be divided equally, independently of the chemical environment. For assigning OS in molecular systems, the IUPAC algorithm starts by establishing the appropriate Lewis structure of the molecule. Then, each electron pair between bonded atoms is assigned to the more electronegative one, representing the simplest application of the ionic approximation. The atomic electronegativities are evaluated according to Allen's scale.[3]

The new OS definition represents a large improvement compared with the previous set of rules. However, some limitations have already been exposed.[4,5] One example is the case of the transition metal (TM) carbenes.[6] In these systems, the carbene unit exhibits a double bond with the metal center. Because the carbene carbon atom is more electronegative than the metal, the four electrons of the C═M double bond should be assigned to the carbon atom, leading to a formal C (−2). Thus, following IUPAC's rule, all carbene systems are assigned as Schrock-type. However, other carbene types exist, for instance the Fischer-type, which presents a neutral carbene moiety. One way to account for this OS assignment is to consider the σ-type bond polarized toward the C and the π-type to the metal center, giving two electrons to each moiety. This view cannot be reconciled with IUPAC's winner-takes-it-all rule, so classifying a carbene as Fischer-type requires approaches beyond IUPAC's ionic approximation. Another example is the nitrosyl-containing compounds.[7] In this case the nitrosyl−metal bonding relies on three interactions: one formal M ← NO^+ sigma donor bond of virtually pure ligand character that the ionic approximation assigns to the NO and two M−π^*(NO) bonds whose character may vary between the limiting M ← NO^- and M → NO^+ scenarios. These two interactions are highly covalent, resulting in ambiguous OS assignments.[8] Furthermore, the NO^0 picture is not supported by the ionic approximation.

Arguably, the most important limitation of IUPAC's algorithm is the inability of the atomic electronegativity scale

Received: August 12, 2020
Published: October 8, 2020

https://dx.doi.org/10.1021/acs.inorgchem.0c02405
Inorg. Chem. 2020, 59, 15410−15420

to account for differences in the local chemical environment. A plausible solution is to define atom types, as commonly used in force fields for molecular dynamics, with associated electronegativity values. However, the complexity of the algorithm will increase rapidly, lowering its practical utility. From our perspective, the OS must be connected to the electron distribution around the atoms. Today, modern electronic structure methods can accurately describe the electron density, which makes computational chemistry a natural candidate to aid in elucidating oxidation states.

A common misconception is that atomic charges from population analysis are a noninteger form of the OS. While one can still find atomic charges being used in the literature for OS assignment,[9−11] more appropriate computational methods for OS assignment treat electrons by pairs (in the case of pure singlet states) or individually (for open-shell systems). Then, each scheme applies one or another strategy to assign the electrons to atoms/fragments.

Some approaches are based on the use of localized occupied orbitals,[12−15] although the localization procedure is of course not unique. For single-determinant wave functions, one can perform unitary transformations on the occupied canonical orbitals, obtaining different localized orbitals without changing the wave function or energy. If a molecule is well-described by a single Lewis structure, we would expect the localized orbitals to fall into three categories: fully localized and atomic core orbitals, bonding orbitals that are shared between a pair of atoms (perhaps not equally, depending on their electronegativity difference), and nonbonding orbitals which are again completely atom-localized (e.g., lone pairs). However, more complex bonding patterns, like delocalized electrons shared between more than two atoms, can be encountered.

Within this family of methods, Thom et al. proposed the localized orbitals bonding analysis (LOBA), based on combining orbital localization with atomic population analysis to extract the OS from transition metal complexes.[12] Concretely, first the electronic structure of the complex is obtained at a single-determinant level. Then, the occupied molecular orbitals (MOs) from the system are localized following the desired localization procedure, e.g., Pipek−Mezey[16] or Edminston−Ruedenberg.[17] Afterward, atomic population analysis, e.g., Mulliken-,[18] Löwdin-,[19] or Hirshfeld-type,[20] for each localized orbital is performed. Finally, the integer number of electrons from the orbital (two in the case of closed-shell and one for open-shell wave functions) is assigned to the selected atom if its population surpasses a given threshold. To date, the method aims to evaluate the OS of metals within transition metal complexes, and the threshold is set at 60%. If an orbital exhibits a population lower than 60%, its electrons are strictly assigned to the rest of the molecular system. Thus, LOBA directly provides the OS of the heavy (or selected) atoms within the complex. To assign the OS of the fragments, it is necessary to evaluate the shape of the localized orbitals and their atomic populations.

Similar strategies have been developed by Sit et al.[13] and later applied by Vidossich et al.[14] Sit et al. used maximally localized Wannier functions[21] as localized orbitals and obtained the corresponding centroids. Then, they used the position of the centroids to assign the electron pairs to the closest atom (closest-atom strategy). Vidossich et al. applied the same strategy, relying instead on the Pipek−Mezey (PM) localized orbitals. Recently, an extension to this procedure was explored by some of us,[15] whereby the 3D-space was partitioned into atomic domains, and the electron pair from each localized orbital is assigned to the atomic basin where the orbital centroid is situated (basin-allegiance strategy). Even though the latter scheme performed better, it still failed on the TM carbenes.

Alternatively, Ramos-Cordoba et al. introduced the effective oxidation state (EOS) analysis, which is formally applicable to any molecular system and wave function.[22] The scheme relies on Mayer's effective fragment orbitals (EFOs) obtained for each fragment/atom defined and their occupation number (λ).[23,24] Once the spin-resolved EFOs are obtained, they are sorted by decreasing occupation number, and individual electrons are assigned to them until reaching the total system number of electrons. This procedure leads to an effective configuration of the ligands/atom within the molecule and, as a consequence, its OS. Furthermore, the difference between occupation numbers from the last occupied (LO) and first unoccupied (FU) EFOs is used to evaluate the reliability of the assignment. The larger this difference, the better the current electron distribution can be pictured as a discrete ionic model. This reliability index, R (%) = min(R_α, R_β), is defined for each spin case σ as

$$R_\sigma(\%) = 100 \cdot \min(1,\ \max(0,\ \lambda^\sigma_{\mathrm{LO}} - \lambda^\sigma_{\mathrm{FU}} + 1/2)) \qquad (1)$$

By definition, if the difference between occupation numbers of the frontier EFOs is larger than half an electron, the OS assignment is considered as undisputable (R (%) = 100). The worst-case scenario is in case that two or more frontier EFOs from different fragments present the same occupancy. In this case, two different equally plausible OS distributions are present with R (%) = 50. Reliability index values lower than 50 are only possible if the electrons have not been assigned following the *aufbau* principle. Such assignments can be used to quantify to which extent the molecular system conforms to a given set of predefined OSs.

Both EOS and LOBA methodologies have been successfully applied by several authors to a broad range of chemical systems, proving their usefulness.[25−27] However, to date, there has been no comparison between the two schemes. Such a comparison with reference assignments (IUPAC, experimental characterization and/or previous assignments using alternative strategies) allows us not only to evaluate the synergy between both but also to critically evaluate the reference OS.

In this work, we first reformulate the use of population analysis within the LOBA scheme by including the definition of an index which quantifies the clarity in our OS assignments. Herein, we support the idea of assigning the electrons of localized orbitals ionically when the atomic populations are truly unbalanced, as observed by clarity index values larger than e.g. 70. The remaining electrons to assign require consideration of the localized orbital shape, based on chemical intuition. Thus, we remove the dependencies on population analysis method used (Mulliken, Löwdin, or Hirshfeld, among others) and rigidity of using a single population value as threshold, increasing the robustness of the method. Second, we computationally assign using both schemes the OS of 20 molecular systems of varying chemical nature and complexity, including high-valence transition metal oxides, transition metal complexes with noninnocent ligands, metal sulfur dioxide adducts, and transition metal carbene complexes. The majority of these systems have been already characterized by means of EOS by using the X-ray geometries when available.[4,6] Here, we

https://dx.doi.org/10.1021/acs.inorgchem.0c02405
Inorg. Chem. 2020, 59, 15410−15420

re-evaluate the EOS results using the wB97X-V/def2-TZVP optimized geometries for robustness of the production results.

RESULTS AND DISCUSSION

Reliability Index for the LOBA Method. As mentioned above, LOBA requires the use of a population analysis threshold to assign the electrons from a localized orbital to either the metal center or the rest of the molecular system. Prior studies have shown that setting the population threshold to 60% yields satisfactory performance for the systems tested.[12,26] However, the chosen systems typically had well-defined OS. By contrast, when facing compounds with nontrivial bonding situations, the number of electrons from localized orbitals with atomic populations close to the borderline 50−70% region increases. In this regime, there may be scope for different interpretations from the same computational result, since a small geometric change can interconvert two different OS by crossing the LOBA threshold.

To quantify the extent to which LOBA OS assignments are clear-cut, we introduce a new clarity index, CI_a. First, we define the following quantity, x, from the population analysis performed for every localized orbital

$$x = \frac{\mathrm{abs}(\lambda_M - \lambda_X)}{\lambda_M + \lambda_X} \quad (2)$$

where λ_M corresponds to the atomic population of the selected atom (e.g., the metal center, for the case of transition metal complexes) and λ_X is the population of the rest of the molecular system. With this definition, the parameter x is bounded within the [0, 1] range, independently of the wave function being closed or open shell. As limits, the $x = 1$ case is when the orbital population is completely on either the selected atom M or on the rest of the molecular system X, while $x = 0$ corresponds to the $\lambda_M = \lambda_X$ scenario.

Next, we define a parameter P, which corresponds to a threshold for ionicity, to separate the assignment of the electrons of a given localized orbital into two ranges depending on the x value obtained (Figure 1): covalent ($0 < x < P$) and ionic ($P < x < 1$). In the ionic range, the electrons in the localized orbital are entirely assigned to M if $(\lambda_M - \lambda_X) > 0$ or to the rest of the molecular system X if $(\lambda_M - \lambda_X) < 0$. In the covalent (or shared-pair) range, the electrons in the orbital are split equally between the two moieties.

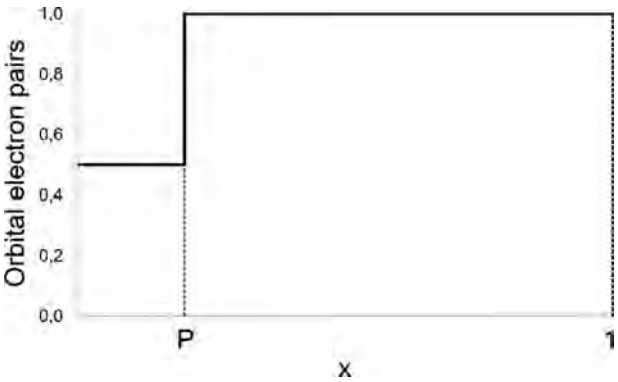

Figure 1. Plot of the assignment of the electrons in a localized orbital for $x \in [0, 1]$, where x is defined by eq 1. The covalent regime is $0 < x < P$ while the ionic regime is $P < x < 1$.

Finally, to quantify the extent to which the assignment is clear, we introduce a second parameter, W, which corresponds to the width for switching the electronic assignment from ionic to covalent. Using x and the parameters P and W, we define the new clarity index, CI_a, where a = i for ionic and a = c for covalent assignments, in three ranges: $CI_c = 100$ for $x \in [0, P - W]$, $CI_i = 100$ for $x \in [P + W, 1]$, and $CI_a = CI_a(x)$ within the $x \in [P - W, P + W]$ interval. With all conditions set, a plausible form for $CI_a(x)$ is

$$CI_a(x) = 100 \cos^2\left(\pi\left(\frac{P + W - x}{2W}\right)\right) \quad (3)$$

which is a smooth, continuous function with a symmetrical shape (Figure 2) and a rather simple mathematical expression.

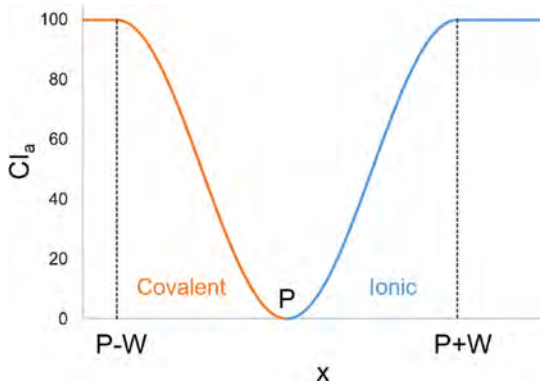

Figure 2. $CI_a(x)$ index representation.

Herein, we use $P = 0.2$ and $W = 0.1$. This P choice corresponds to the x value for the original population threshold (60%), while the selected W value is based on the population threshold calibration calculations performed in ref 12; it matches the region which minimizes the error on the OS assignment.

By definition, a CI_a value is obtained for each localized orbital, reflecting the clarity in the assignment of the electron(s) from that orbital. Evidently, the least clearly assigned electrons in the molecular system will determine how conclusive the final OS assignment will be. For this reason, we ultimately select the lowest CI_a value as the most conservative indicator of our overall OS assignment clarity.

Illustrative Examples. To evaluate the strengths and weaknesses of the EOS and LOBA methods, we have considered a series of compounds that present challenges when it comes to making OS assignments. The selected compounds include high-valent transition metal oxides, transition metal complexes with noninnocent ligands (thiolate, nitrosyl, and (presumably) trifluoromethyl), transition metal sulfur dioxide adducts, and transition metal carbene complexes. We discuss in detail the OS assignments obtained from both the EOS and LOBA methods and compare them with reference values (typically given by IUPAC's ionic approximation). We also evaluate the performance of the newly introduced LOBA clarity index CI_a.[1,2]

Trimethylamine N-Oxide. Before discussing various transition metal complexes, let us first discuss the relatively simple molecule trimethylamine *N*-oxide, $(CH_3)_3NO$. The dominant Lewis structure for this system presents a single bond between formal N (+) and O (−), as N fulfills the octet rule. Applying

https://dx.doi.org/10.1021/acs.inorgchem.0c02405
Inorg. Chem. 2020, 59, 15410−15420

IUPAC's ionic approximation, all electrons (by pairs, as $(CH_3)_3NO$ is a closed-shell system) from the σ N−C bonds are assigned to N, while the ones from the N−O bond are assigned to the oxygen. Such an electron assignment leads to formal oxidation states of (−1) for N, (−2) for O, and (+1) for the three CH_3 moieties.

From the EOS perspective, we obtained the OS assignment of N (−3), O (0), and each CH_3 (+1) with R (%) = 55.7. The same result was previously reported,[4] with small differences in R (%) because of the different level of theory and geometry used here versus in ref 4. We quantified the weight of IUPAC's N (−1) and O (−2) assignment by not following the *aufbau* principle on the electron assignment, resulting in R (%) = 44.3.

When analyzing the shape of the PM localized orbitals, no localized orbital corresponding to a π-type N−O bond is found, but two lone pairs localized on O are present. This points to the aforementioned Lewis structure. In this direction, some of us assigned its OS using the position of the centroids of the localized orbitals. They obtained the EOS assignment from both the closest-atom and basin-allegiance strategies.[15] This result is in contradiction with the IUPAC assignment, and further analysis is warranted.

We performed LOBA calculations and depict the shape of selected PM localized orbitals, together with their Löwdin population analysis and CI_a values in Figure 3. Each localized

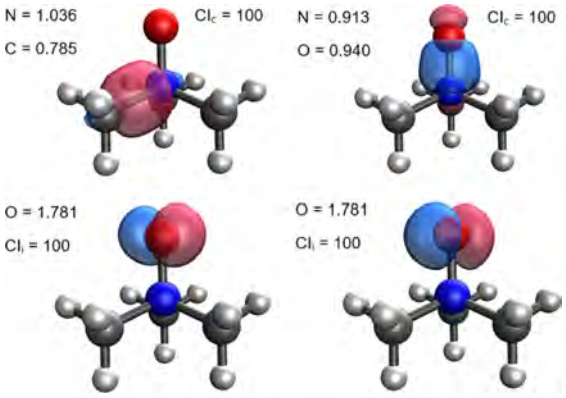

Figure 3. Selected valence PM localized orbitals for the $(CH_3)_3NO$ molecular system, together with Löwdin population and CI_a values. The isocontour value is selected for clarity as 0.3 au.

orbital accounts for an electron pair as the system is closed-shell. Visual inspection shows two lone pairs localized on O and localized σ(NO) and σ(CN) bond orbitals. Evaluating the orbital shape, both localized σ orbitals are characterized as shared-pair, resulting in assigning one electron to each atom involved (per orbital). Such an assignment leads to N (+1), O (−1), and each CH_3 (0). When evaluating the reliability of our assignments, we obtain the covalent assignment for both σ(N−C) and σ(N−O) orbitals with CI_c = 100. This assignment is different from both the IUPAC and EOS results. The LOBA σ(N−O) assignment can only be supported by EOS in the case of occupation degeneracy of the frontier EFOs. In this situation, one electron is assigned into each EFO, mimicking the covalent (shared-pair) assignment. Thus, the closer the frontier EFOs occupancies, the more shared-pair "character". However, EOS clearly assigned each CH_3 moiety as (+1).

High-Valent Transition Metal Oxides. Our first group of transition metal complexes consists of a series of high-valent transition metal oxides, including TiO_2, FeO_4^{2-}, ReO_4^-, OsO_4, IrO_4^+, and PtO_4^{2+}.[28,29] According to the IUPAC's ionic approximation, such species present a rich variety of metal oxidation states ranging from (+4) to (+10). Prior studies showed very good performance for this systems by EOS, as compared to OS assignments following IUPAC's rules, resulting in formal OS values up to (+9) for Ir in IrO_4^+.[4] In the case of PtO_4^{2+}, the Pt atom presented several d-type EFOs with occupations too large to be considered empty, compared to those of the O atoms, and the EOS scheme assigned Pt (+2) with R (%) = 50.8. By contrast, at the current level of theory, EOS achieves the (+6) OS assignment for Pt, again with a very small R (%) = 50.3 value. This method dependency makes the system a matter of interest, particularly as we have previously demonstrated the robustness of the EOS method for an extensive combination of functionals and basis sets.[6] Considering the ωB97X-V/def2-TZVP description at the geometry reported in ref 4 leads to a Pt (+2) assignment, with R (%) = 52.8. Thus, disagreement on the assignment is mostly caused by geometrical differences. Nevertheless, it appears that the use of more sophisticated long-range corrected DFT functionals such as ωB97X-V, which include a density-dependent dispersion correction, may increase the ionic character of each bond by lowering the delocalization error. The more ionic the bonds, the more oxidized is the character of the metal center.

In Figure 4 we depict the valence PM orbitals corresponding to one σ(M−O) bond for each complex. By symmetry, the

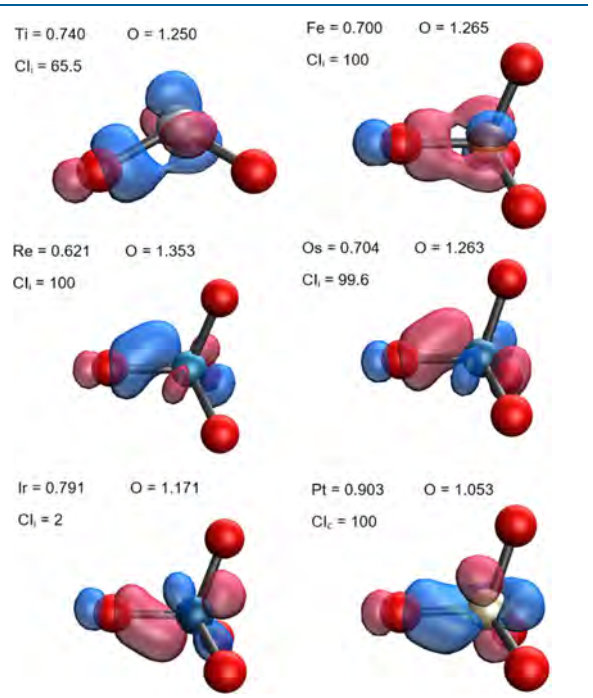

Figure 4. Selected valence PM localized orbitals for TiO_2, FeO_4^{2-}, ReO_4^-, OsO_4, IrO_4^+, and PtO_4^{2+} molecular systems, together with Löwdin population and CI_a values. The isocontour value is 0.3 au.

orbital picture and population analysis are equal for all σ(M−O) bonds. Differences between atomic populations become less clear when going to higher valent compounds, not only from LOBA but also from the R (%) values close to 50 from EOS. The electron pair from the σ(M−O) bonds is assigned to

https://dx.doi.org/10.1021/acs.inorgchem.0c02405
Inorg. Chem. 2020, 59, 15410−15420

the O atom for all systems, as the atomic populations differences are large enough, except for PtO_4^{2+}. In PtO_4^{2+}, population analysis and localized orbital shape support a covalent assignment for the Pt−O pairs. Thus, as by symmetry there are four electron pairs in this situation, assigning one electron to each moiety leads to a formal OS for Pt (+6) and each O (−1). Covalent assignment is confirmed, with CI_c = 100. Interestingly, the OS assignment for the Ir-based oxide is at the frontier between covalent and ionic assignment, being ionic with a pyrrhic CI_i = 2. The Ir and Pt systems show the way in which extremely high formal IUPAC oxidation states play out via the orbital shape.

Transition Metal Complexes with Noninnocent Ligands. Next, we consider OS assignments for different families of transition metal complexes with noninnocent ligands such as thiolate, nitrosyl, and trifluoromethyl. Our first set of noninnocent ligand complexes consists of the redox series of nickel dithiolates $[Ni(S_2C_2Me_2)_2]^{n-}$, with n = 0, 1, and 2.[30] From experiments and DFT calculations, Lim et al. characterize the dianionic species as a Ni (+2) metal center with two closed-shell thiolate (−2) ligands. Furthermore, the one-electron oxidations on this species are ligand based, such that the Ni OS remains constant throughout the redox process.[31] Particularly, for n = 1, the reference OS for the thiolate ligands can be either −1/−2 (asymmetric assignment) or −1.5/−1.5 (mixed valence). Finally, the neutral species presents two formally (−1) thiolate ligands.

EOS analysis matches the reference OS with R (%) values of 55.7, 65.7, and 82.4 for the 0, 1, and 2 species, respectively. The most interesting case is the lower R value neutral species. Here, as the system is closed-shell, the only manner by which the (−1) OS solution can be obtained is if the two last occupied EFOs are degenerate in occupancy and are located one on each ligand, thus splitting the electron pair between both fragments. Wave function stability analysis confirmed that the ground state solution is closed-shell. We obtained the described scenario, with two degenerate EFOs (occupancy 0.51), one from each ligand, and a Ni EFO (occupancy 0.45). An alternative, though unfaithful, assignment is a Ni (0) center with two neutral ligands, resulting in a R (%) value of 44.3.

LOBA also assigns the Ni center as (+2) with CI_i = 100, as the Ni atom presents four d-type localized orbitals, two fewer electrons than a formal Ni (0). With regard to the ligands, we obtain two formal (−1) dithiolates. Obtaining this solution from localized orbitals is more complicated than from EOS, as a single doubly occupied orbital must be delocalized between the two ligands. In particular, that orbital must present atomic populations that are split between four atoms (at least). We depict the aforementioned orbital in Figure 5, observing a shared-pair character and thus leading to the (−1) OS for each ligand. However, the localized orbital is not truly symmetric between fragments, giving some weight to the asymmetric (0)/(−2) assignment. Using the sum of carbon populations in the right fragment against the total, the asymmetric assignment is obtained with CI_i = 18.1. As the complementary localized orbital can be obtained by an alternative combination of MOs, the asymmetric assignment in this case is caused by the difficulty to localize the orbital, resulting in a broken symmetry representation of a symmetric bonding situation.

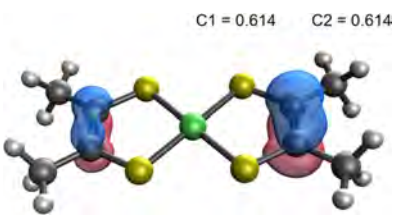

Figure 5. PM localized orbital between both noninnocent ligands of the $[Ni(S_2C_2Me_2)_2]^0$ system, together with the Löwdin population. The isocontour value is 0.15 au.

For n = 2, LOBA shows a similar orbital pattern and the same Ni OS assignment. Instead of one localized orbital split between both ligands (as in Figure 5), we find a fully localized one for each ligand. Thus, we obtain two formal (−2) ligands. Finally, in the n = 1 case the ground state multiplicity is a doublet. Consequently, alpha and beta localized orbitals are treated independently. It is worth mentioning that at the present level of theory the spin density is almost perfectly shared among the Ni and each of the ligands (0.34, 0.33, and 0.33, respectively). In the LOBA approach, the σ Ni−S bond electrons are assigned to S by both population analysis and orbital shape (Figure 6). The Ni center presents 4α and 3β d

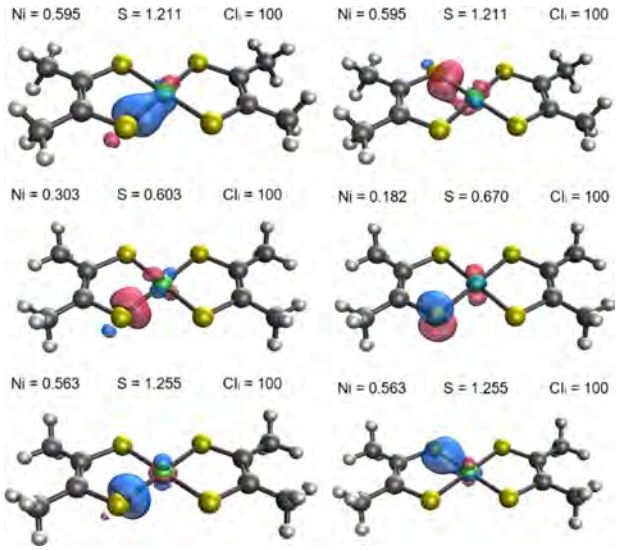

Figure 6. Selected PM localized orbitals for $[Ni(S_2C_2Me_2)_2]^{n-}$ molecular systems, n = 0 (top), 1 (middle; alpha, left, and beta, right), and 2 (bottom), together with Löwdin population and CI_a values. The isocontour value is 0.3 au.

localized orbitals, leading to a formal Ni (+3) species with CI_i = 100. Such an assignment opposes both the reference results and the EOS values, as LOBA instead hints at a metal-based oxidation instead of ligand-based. It is important to note that obtaining a nonsymmetric (or mixed-valence) OS assignment from a geometrically symmetric system is a challenge for any methodology. In the EOS case, there are two degenerate EFOs, one per thiolate ligand, and only one electron left to assign. Thus, the splitting of the last electron leads to the −1.5/−1.5 (mixed-valence) result. Alternatively, one may consider two equivalent resonance structures with OS of −2/−1 and −1/−2 for the ligands. For this set of systems, limitations of the LOBA scheme are observed, but these limitations derive from challenges in orbital localization and not from the OS assignment procedure or the CI_a index definition.

https://dx.doi.org/10.1021/acs.inorgchem.0c02405
Inorg. Chem. 2020, 59, 15410−15420

As a second set of transition metal complexes with noninnocent ligands, we considered the redox couple of nitroprusside anions $[Fe(CN)_5(NO)]^{n-}$,[32] where n = 2, 3. NO is a simple noninnocent ligand that can present three different oxidation states, −1, 0, or +1, depending on its interaction with the metal center. For its OS assignment, IUPAC's statement is clear: *the MNO segment should be linear for NO$^+$ but bent for NO$^-$*.[7] For n = 2, the geometry of the complex indicates a linear FeNO segment. Thus, according to IUPAC's rule, the NO is formally (+1). Then, from the ionic approximation each CN ligand is (−1), leading to a formal Fe (+2) OS. Applying the same rules, the bent geometry of the FeNO linkage in the n = 3 system is characteristic of NO (−1). However, the last system is properly characterized as neutral NO, which leads to a formal Fe (+2).[32]

EOS analysis reproduced the reference OS for both species with R (%) = 81.0 and 74.0. From LOBA, for both n = 2 and 3, the σ(Fe−C) localized orbitals are ionically assigned to the CN moiety with CI_i = 100, thus leading to the CN (−1) OS assignment. In the n = 2 system, the two localized orbitals from the Fe−N interaction (Figure 7) are assigned to the iron

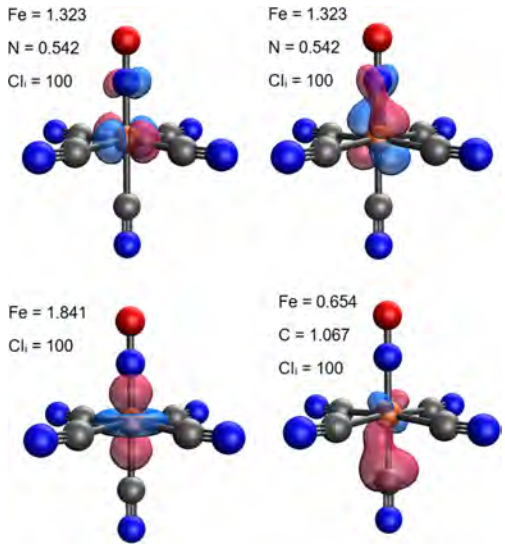

Figure 7. Selected valence PM localized orbitals for $[Fe(CN)_5(NO)]^{2-}$ molecular system, together with its Löwdin population and CI_a values. The isocontour value is 0.30 au.

center with a clear CI_i = 100. This together with a Fe-centered d-type localized orbital leads to the formal Fe (+2) OS. As a consequence, the NO moiety is then characterized as (+1).

For n = 3, with spin unrestricted localized orbitals depicted in Figure 8, the Fe exhibits 2α and 3β d-type orbitals, which, together with the nontrivial assignment of the Fe−N interaction to the iron (CI_i = 28.7 (alpha)), lead to the (+2) OS for Fe. As a consequence, the NO ligand is characterized as neutral. These results are in perfect agreement with both reference values and EOS analysis.

A final set of systems within this category are the copper trifluoromethyl complexes $[Cu(CF_3)_4]^{n-}$, with n = 1, 2, and 3. For n = 1, Snyder characterized computationally the metal center as a formal Cu (+1), leading to one CF_3 (+1), one (−1), and two formally (−0.5).[33] Several authors argued against this assignment, pointing instead to a formally Cu (+3) species.[34,35] Recent experimental evidence seems to point

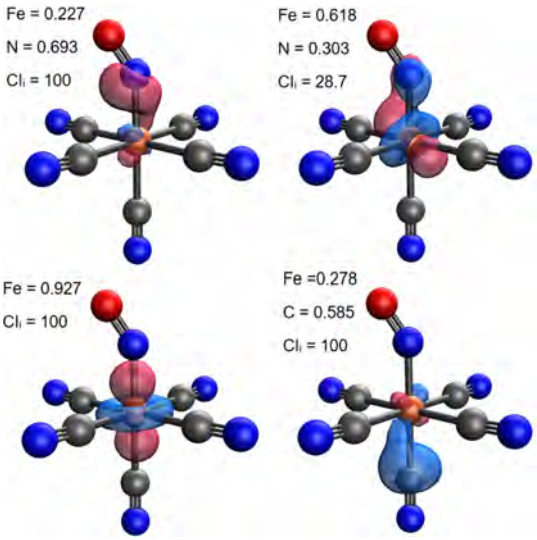

Figure 8. Selected valence PM localized orbitals for $[Fe(CN)_5(NO)]^{3-}$ molecular systems (alpha spin), together with Löwdin population and CI_a values. The isocontour value is 0.30 au.

toward a Cu (+1) metal center,[36,37] casting doubts on the mere existence of any Cu (+3) species. At any rate, the OS assignment of this system has proved challenging because of the significant covalency of the Cu−C bonds. One can even find studies where authors opt for different interpretations/assignments within the same work.[38] According to the ionic approximation, each CF_3 ligand should present the (−1) OS in all species, leading to Cu (+3) for the n = 1 system, which is successively reduced to Cu (+1) for n = 3.

EOS analysis assigns the OS of Cu in the n = 1 species (+3) with R (%) = 51.7, which is at odds with a recent combined experimental−computational interpretation.[36] It is particularly striking to notice that the authors used virtually the same level of theory as in this work but arrived at different conclusions. On the other hand, the low R value obtained is indeed indicative of the high covalency of the Cu−C bond. An alternative assignment consists of assigning two electrons from the four pseudo-degenerate LO EFOs, each one located on a CF_3 moiety, to Cu. This leads to a formal Cu (+1) and four CF_3 (−1/2) with R (%) = 48.3, supporting in some sense Snyder's original proposal and highlighting the delicate balance in assigning the OSs. For the reduced species, metal-based reduction is observed, leading to unambiguous EOS assignments of Cu (+2) and Cu (+1) with R (%) = 78.5 and 100 for n = 2 and 3, respectively.

According to LOBA, with selected localized orbitals depicted in Figure 9, the n = 1 system is clearly characterized as a Cu (+3) species with high clarity (CI_a = 100). The electron pair from each σ(Cu−C) bond is assigned to the CF_3 moiety, each of which is formally (−1). This, together with the four d-type localized orbitals sitting on the Cu atom, provides a clear Cu (+3) assignment. For n = 3, we obtained the same assignment for the σ(Cu−C) localized orbitals, but now five d-type localized orbitals from Cu are occupied, leading to Cu (+1) with four CF_3 (−1) ligands. In the n = 2 system, the α and β electrons from σ(Cu−C) localized orbitals are assigned to the CF_3 moiety, leading once again to a formal CF_3 (−1). Five α and four β localized orbitals are localized on Cu, giving the formal (+2) OS with CI_i = 100.

https://dx.doi.org/10.1021/acs.inorgchem.0c02405
Inorg. Chem. 2020, 59, 15410−15420

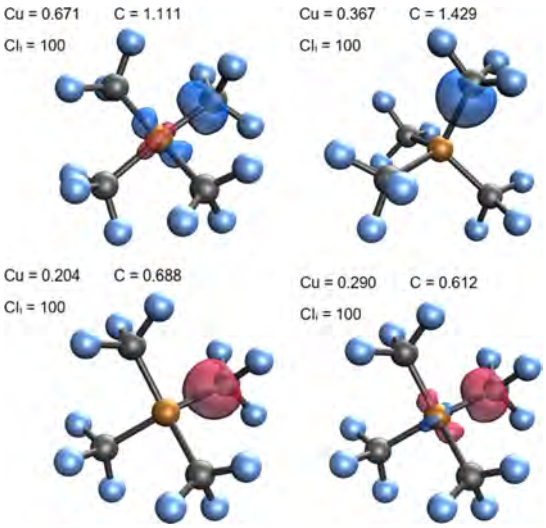

Figure 9. Selected valence PM localized orbitals for $[Cu(CF_3)_4]^{n-}$ molecular systems, n = 1 (top left), 3 (top right), and 2 (middle; alpha, left, and beta, right), together with Löwdin population and CI_a values. The isocontour value is 0.30 au.

In summary, both EOS and LOBA analysis characterize the $[Cu(CF_3)_4]^-$ system as a Cu (+3)-based species and the subsequent reductions as metal-based. For n = 1, the EOS assignment is less clear than for the LOBA, which unambiguously assigned the Cu (+3) species. Clear assignments are obtained for the reduced species by using both schemes.

Metal Sulfur Dioxide Adducts. Another family of compounds we investigated are transition metal adducts with sulfur dioxide as a ligand. SO_2 presents the ability to coordinate in three different manners (Z-, L-, and π-type). According to IUPAC, L-type ligands act as Lewis bases, donating the two electrons to the metal center to form a dative bond. Then, the ionic approximation assigns the electron pair to the S atom by electronegativity difference, leading to a neutral SO_2. For the Z-type, the ligand acts as a Lewis acid, and the metal atom sacrifices the electron pair for dative bond formation. Crude ionic approximation should lead to a formal SO_2 (−2) ligand, which is at odds with the experimental observables. Thus, an exception to the ionic approximation is introduced to address such situations, which thereby leads to the expected neutral SO_2. Knowing when the exception should be invoked is perhaps challenging.

To explore the role of SO_2 as a ligand, we selected the $Rh(SO_2)Cl(CO)(PH_3)_2$ (Z-type), $Rh(SO_2)Cl(PH_3)_2$ (L-type), and $Ru(SO_2)Cl(NO)(PH_3)_2$ (π-type) systems to assign the OS of the metal and the SO_2 ligands. Selected PM orbitals for these systems are depicted in Figures 10, 11, and 12, respectively.

For the Z-type ligand case of $Rh(SO_2)Cl(CO)(PH_3)_2$ (Figure 10), LOBA provides clear Rh (+1) and SO_2 (0) assignments, with CI_i = 100. Furthermore, there is no localized orbital which, from population analysis, involves both Rh and S from SO_2. Rh presents four doubly occupied d-type localized orbitals, while SO_2 obtains the 24 electrons required for being a neutral ligand. Clear-cut assignments are also obtained for all PH_3, CO, and Cl σ-like localized orbitals, which leads to these normally innocent ligands being formally (0), (0), and (−1), respectively, as expected.

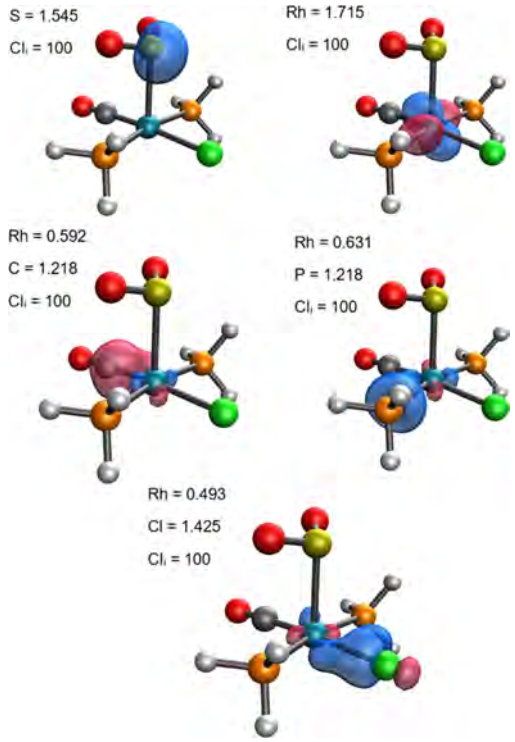

Figure 10. Selected valence PM localized orbitals for Z-type Rh-based compound, $Rh(SO_2)Cl(CO)(PH_3)_2$, together with Löwdin population and CI_a values. The isocontour value is 0.30 au.

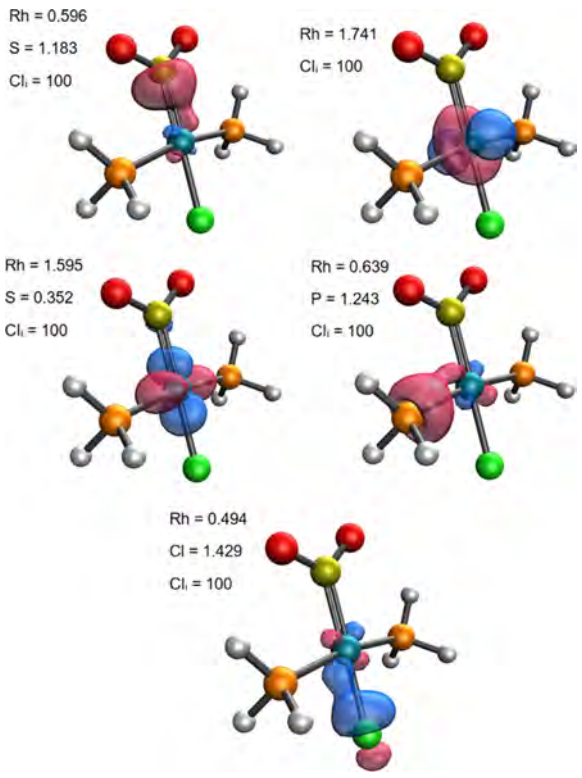

Figure 11. Selected valence PM localized orbitals for L-type Rh-based compound, $Rh(SO_2)Cl(PH_3)_2$, together with Löwdin population and CI_a value. The isocontour value is 0.30 au.

https://dx.doi.org/10.1021/acs.inorgchem.0c02405
Inorg. Chem. 2020, 59, 15410−15420

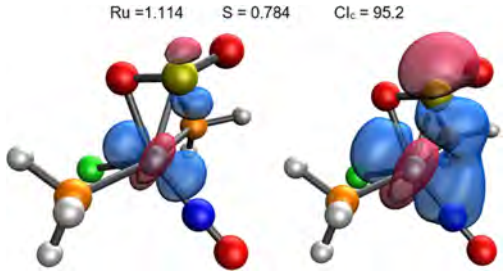

Figure 12. A selected valence PM localized orbital for the π-type Ru-based compound, $Ru(SO_2)Cl(NO)(PH_3)_2$, together with Löwdin population and CI_a value. Two isocontour values are used: 0.30 au (left) and 0.10 au (right).

For the L-type ligand case of $Rh(SO_2)Cl(PH_3)_2$ (Figure 11), Rh presents three d-type localized orbitals and one resulting from the combination of a σ-type orbital from S and a d-type from Rh, leading to the formal (+1) OS with CI_i = 100. The SO_2 ligand is characterized as neutral, which is in nice agreement with the reference values. The PH_3 and Cl ligands present the same conventional bonding situation as for the Z-type ligand.

Finally, a more complicated bonding situation is observed for the π-type case of $Ru(SO_2)Cl(NO)(PH_3)_2$. Starting from the SO_2 ligand, a nonbonding orbital between the Ru and S atoms is obtained (Figure 12), which is characterized as a shared pair with CI_c = 95.2. Decreasing the isocontour value for this orbital, a weak σ-type interaction between the S of SO_2 and the N of NO ligand is unveiled. Even though the localized orbital is shared between three atoms, it is mainly localized between the Ru and S, so that the NO is not involved in this particular electron assignment process.

The localized orbital from the Ru−O interaction (Figure 13) is ionically assigned to the O of SO_2 with CI_i = 100, meaning that SO_2 is assigned as (−1). With regard to the NO ligand, the π(Ru−N) localized orbital is characterized as a shared pair with CI_c = 100, leading to a neutral NO moiety. Because the Cl

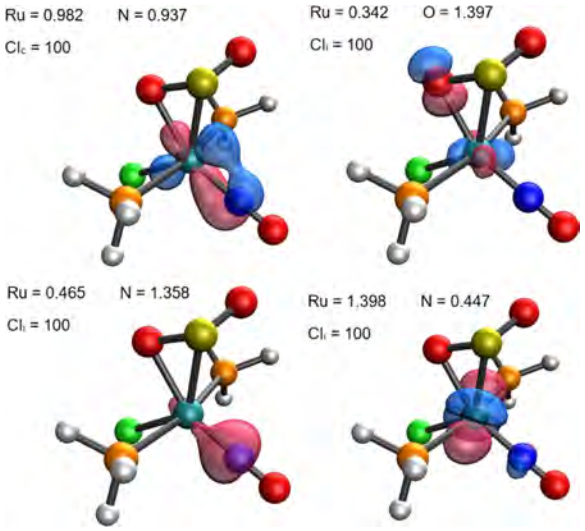

Figure 13. Selected valence PM localized orbitals for π-type Ru-based compound, $Ru(SO_2)Cl(NO)(PH_3)_2$, together with Löwdin population and CI_a values. The isocontour value is 0.30 au.

and PH_3 ligands present their typical (−1) and (0) OS, respectively, the Ru center OS is (+2).

EOS analysis matched the reference OS for the SO_2 moiety with R (%) = 85.2, 84.0, and 50.3 for the L-, Z-, and π-type, respectively. EOS is in agreement also with the LOBA assignments for the L- and Z-type compounds. In the π-type case, EOS also indicates a covalent assignment for the σ(Ru−N) localized orbital, as the frontier EFOs between both fragments are almost degenerate in occupation number, leading to a formal NO (0) ligand. Contrary to LOBA, a clear SO_2 (0) assignment, and consequently Ru (+1), has been obtained for the π-type species by EOS.

Transition Metal Carbene Complexes. The last two evaluated compounds are within the transition metal carbene family. In particular, we examine the Schrock-type compound, $Mo(=CH_2)(NC_8H_{10})(OtBu)_2$, and the Fischer-type complex, $W(=CF_2)(CO)_5$. As mentioned above, IUPAC's ionic approximation fails on elucidating the carbene moiety OS in the Fischer-type carbenes, assigning a formal (−2) OS instead of the accepted value of (0).

EOS analysis properly characterized the carbene moiety as (−2) for the Schrock-type compound with R (%) = 63.0 and as neutral for the Fischer-type species with R (%) = 96.6.

We depict the selected PM orbitals from the Fischer-type carbene, $W(=CF_2)(CO)_5$, in Figure 14. There are two

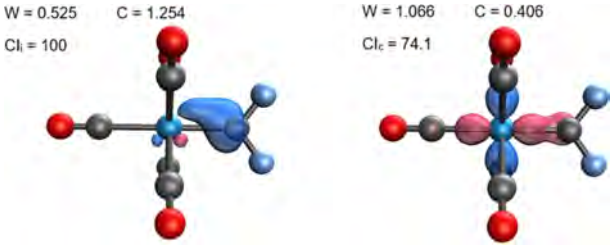

Figure 14. Selected valence PM localized orbital for $W(=CF_2)(CO)_5$, together with Löwdin population and CI_a values. The isocontour value is 0.30 au.

localized orbitals which describe the W=C bond. From LOBA, an ionic assignment with CI_i = 100 is obtained for the first, while the second has a covalent assignment with CI_c = 74.1. These assignments lead to the carbene moiety having (−1) formal OS, instead of the expected (0).

For the Schrock-type complex, $Mo(=CH_2)(NC_8H_{10})(OtBu)_2$, we depict the two localized orbitals that describe the Mo=C bond in Figure 15. Both orbitals are associated with a covalent assignment, with CI_c = 33.1 and 91.4. This

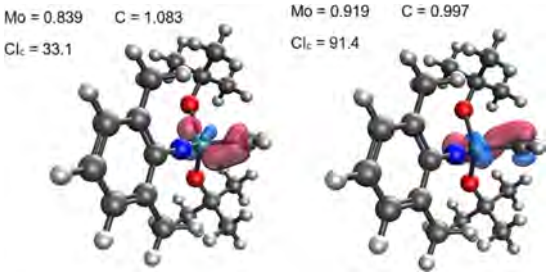

Figure 15. Selected valence PM localized orbital for $Mo(=CH_2)(NC_8H_{10})(OtBu)_2$, together with its Löwdin population and CI_a values. The isocontour value is 0.30 au.

https://dx.doi.org/10.1021/acs.inorgchem.0c02405
Inorg. Chem. 2020, 59, 15410−15420

results in a carbene unit with a formal OS of (0), which was the expected for a Fischer-type carbene. Here, the assignment of the four electrons from the Mo=C bond to the carbene moiety was expected.

EOS showed better performance for the carbene systems than LOBA. For the latter, these systems showed its primary challenge: the nonuniqueness of the localization procedure and the difficulty to obtain cleanly localized orbitals. Thus, more robust procedures need to be tested/developed before discarding the LOBA utility for this particular type of compound.

CONCLUSIONS

In this work, we have examined the application of effective oxidation state (EOS) analysis and localized orbital bonding analysis (LOBA) to a series of compounds that present challenges in oxidation state (OS) assignment. Table 1 summarizes the results obtained with both approaches for all systems considered. The OS is a chemically useful concept that, much like aromaticity, does not have a unique definition. Ultimately, all approaches that aim to assign an integer OS will become ambiguous in regimes where the results approach the boundaries associated with a given assignment. This aspect is reflected in the very useful reliability index (R) of the EOS procedure. Here we have introduced a clarity index to quantify the extent to which a LOBA OS is clear. The CI_a index approaches 100 away from the ionic/covalent boundary and approaches 0 as the boundary is approached from above or below.

Table 1. OS Assignments of the Atom/Ligand Indicated in Bold by EOS and LOBA[a]

molecule	EOS	LOBA	IUPAC/ other
$(CH_3)_3$**NO**[b]	−3 (55.7)	+1 (100)	−1
TiO_2	+4 (92.6)	+4 (65.5)	+4
FeO_4^{2-}	+6 (68.9)	+6 (100)	+6
ReO_4^-	+7 (90.8)	+7 (100)	+7
OsO_4	+8 (76.1)	+8 (99.6)	+8
IrO_4^+	+9 (60.2)	+9 (2)	+9
PtO_4^{2+}	+6 (50.3)	+6 (100)	+10
[**Ni**$(S_2C_2Me_2)_2]^0$	+2 (55.7)	+2 (100)	+2
[**Ni**$(S_2C_2Me_2)_2]^{1-}$	+2 (65.7)	+3 (100)	+2
[**Ni**$(S_2C_2Me_2)_2]^{2-}$	+2 (82.4)	+2 (100)	+2
[Fe$(CN)_5$(**NO**)$]^{2-}$	+1 (80.9)	+1 (100)	+1
[Fe$(CN)_5$(**NO**)$]^{3-}$	0 (74.0)	0 (28.7)	0
[**Cu**$(CF_3)_4]^{1-}$	+3 (51.7)	+3 (100)	+1/+3
[**Cu**$(CF_3)_4]^{2-}$	+2 (78.5)	+2 (100)	+2
[**Cu**$(CF_3)_4]^{3-}$	+1 (100)	+1 (100)	+1
Rh(**S**O_2)Cl$(CO)(PH_3)_2$ (Z-type)	0 (84.0)	0 (100)	0
Rh(**S**O_2)Cl$(PH_3)_2$ (L-type)[c]	0 (85.2)	0 (100)	0
Ru(**S**O_2)Cl$(NO)(PH_3)_2$ (π-type)	0 (50.3)	−1 (95.2)	0
Mo(**C**H_2)$(OtBu)_2(NC_8H_{10})$ (Schrock-type)	−2 (63.0)	0 (33.1)	−2
W(**C**F_2)$(CO)_5$ (Fischer-type)	0 (96.6)	−1 (74.1)	−2/0

[a]The values of R and CI indices are in parentheses. [b]OS of the O atom: 0 (EOS), −1 (LOBA), and −2 (IUPAC). [c]OS of Ru atom: + 1 (EOS), + 2 (LOBA), and 0 (IUPAC).

We observed how both EOS and LOBA methods operate synergistically for assigning OS. In the EOS approach, covalent assignments are rare, as there is no EFO occupancy difference range where the assignment is considered shared pair. In contrast, the LOBA scheme opens a range of population analysis differences (and orbital shape evaluation), where the covalent assignment presents some weight. This is illustrated by the ostensibly simple molecule $(CH_3)_3NO$, for which IUPAC, EOS, and LOBA arrive at different results. Close inspection of the localized orbitals reveals that the LOBA assignment of CH_3 (0), N (+1), and O (−1) relies strongly on covalent character in the bonding, which is not available in EOS.

For the high-valence transition metal oxides culminating with IrO_4^+ and PtO_4^{2+} which have IUPAC oxidation states of (+9) and (+10), the latter assignment is neither supported by EOS nor LOBA. LOBA illustrates how delicate these high oxidation states are. With each M−O bond equivalent, LOBA predicts Ir (+9) with low clarity (i.e., O (−2)) and Pt (+6) with higher clarity (i.e., O (−1)) as these systems traverse the ionic/covalent threshold.

Other challenging systems such as a Schrock and a Fisher transition metal carbene complexes show impressive successes for EOS and results that do not match conventional wisdom for LOBA. Relatively low CI_a values provide a warning that one should carefully inspect the orbitals to assess the LOBA results.

The primary challenge for the LOBA approach is the nonuniqueness of the localization procedure, and the fact that the orbitals in some systems do not localize cleanly. If the final goal is to properly scrutinize the OS of both the ligands and the TM, one should probably incorporate the definition of fragments already when performing the orbital localization, for instance by using fragment populations instead of atomic ones in the localization functional.

Overall, our results cannot be taken as an overall endorsement of any single approach to defining an OS, be it IUPAC, EOS, or LOBA. All these methods will typically agree in straightforward cases (which we have avoided here). In the less straightforward cases, comparing the assignments of all three methods is instructive as a guide to three complementary, and often convergent ways to characterize complex bonding in the simplest possible way. When they differ, it is typically a signature of some interesting complexity or, otherwise, a limitation of one of the approaches.

COMPUTATIONAL DETAILS

Geometry optimizations were performed by using the ωB97X-V density functional[39] coupled with the def2-TZVP basis set (all electron for light atoms and with def2-ECP pseudopotential for heavy atoms).[40] Vibrational frequency calculations, to confirm minima on the potential energy surface, were computed at the same level of theory. Wave functions, orbital localization, and energies were also evaluated at the same level. All calculations were performed with the Q-Chem package.[41]

Localized orbitals bonding analysis (LOBA) calculations were performed with the Q-Chem software, employing the Pipek−Mezey[16] localization procedure, which maximize the locality of Mulliken populations, in conjunction with Löwdin population analysis for each localized orbital, one by one.[19]

Spin-resolved effective fragment orbitals (EFOs) and effective oxidation states (EOS) analysis have been obtained with the APOST-3D program,[42] using the Topological Fuzzy Voronoi Cells (TFVC) 3D-space partitioning method[43] and a 40 × 146 atomic grid for numerical integrations.

https://dx.doi.org/10.1021/acs.inorgchem.0c02405
Inorg. Chem. 2020, 59, 15410−15420

■ ASSOCIATED CONTENT

Supporting Information

The Supporting Information is available free of charge at https://pubs.acs.org/doi/10.1021/acs.inorgchem.0c02405.

Cartesian coordinates of all optimized species (XYZ)

■ AUTHOR INFORMATION

Corresponding Author

Martin Head-Gordon − *Department of Chemistry, University of California, Berkeley, Berkeley, California 94720, United States; Chemical Sciences Division, Lawrence Berkeley National Laboratory, Berkeley, California 94720, United States;* orcid.org/0000-0002-4309-6669; Email: mhg@cchem.berkeley.edu

Authors

Martí Gimferrer − *Institut de Química Computacional i Catàlisi and Departament de Química, Universitat de Girona, 17003 Girona, Catalonia, Spain;* orcid.org/0000-0001-5222-2201

Jeroen Van der Mynsbrugge − *Department of Chemical and Biomolecular Engineering, University of California, Berkeley, Berkeley, California 94720, United States;* orcid.org/0000-0003-3852-4726

Alexis T. Bell − *Department of Chemical and Biomolecular Engineering, University of California, Berkeley, Berkeley, California 94720, United States;* orcid.org/0000-0002-5738-4645

Pedro Salvador − *Institut de Química Computacional i Catàlisi and Departament de Química, Universitat de Girona, 17003 Girona, Catalonia, Spain;* orcid.org/0000-0003-1823-7295

Complete contact information is available at: https://pubs.acs.org/10.1021/acs.inorgchem.0c02405

Notes

The authors declare the following competing financial interest(s): M.H.-G. is a part-owner of Q-Chem Inc., whose software was used for part of this research.

■ ACKNOWLEDGMENTS

M.G. thanks the Generalitat de Catalunya and Fons Social Europeu for the predoctoral fellowship (2018 FI_B 01120). P.S. was supported by the Ministerio de Ciencia, Innovación y Universidades (MCIU), Grant PGC2018-098212-B-C22, and J.V.d.M. was supported by the U.S. Department of Energy's Office of Energy Efficiency and Renewable Energy (EERE) under the Vehicle Technologies Program Award DE-EE0008213. A.T.B. and M.H.G. were supported by the U.S. Department of Energy, Office of Science, Office of Advanced Scientific Computing Research, Scientific Discovery through Advanced Computing (SciDAC) program.

■ REFERENCES

(1) Karen, P.; McArdle, P.; Takats, J. Toward a comprehensive definition of oxidation state (IUPAC Technical Report). *Pure Appl. Chem.* **2014**, *86* (6), 1017−1081.

(2) Karen, P.; McArdle, P.; Takats, J. Comprehensive definition of oxidation state (IUPAC Recommendations 2016). *Pure Appl. Chem.* **2016**, *88* (8), 831−839.

(3) Mann, J. B.; Meek, T. L.; Allen, L. C. Configuration energies of the main group elements. *J. Am. Chem. Soc.* **2000**, *122*, 2780−2783.

(4) Postils, V.; Delgado-Alonso, C.; Luis, J. M.; Salvador, P. An objective alternative to IUPAC's approach to assign oxidation states. *Angew. Chem.* **2018**, *130*, 10685−10689.

(5) Monsch, G.; Klufers, P. $[Fe(H_2O)_5(NO)]^{2+}$, a "brown-ring" chromophore. *Angew. Chem., Int. Ed.* **2019**, *58*, 8566−8571.

(6) Gimferrer, M.; Salvador, P.; Poater, A. Computational monitoring of oxidation states in olefin metathesis. *Organometallics* **2019**, *38*, 4585−4592.

(7) Ampßler, T.; Monsch, G.; Popp, J.; Riggenmann, T.; Salvador, P.; Schröder, D.; Klüfers, P. Not guilty on every count: the "non-innocent" nitrosyl ligand in the framework of IUPAC's oxidation-state formalism. *Angew. Chem., Int. Ed.* **2020**, *59*, 12381−12386.

(8) McCleverty, J. A. Chemistry of nitric oxide relevant to biology. *Chem. Rev.* **2004**, *104*, 403−418.

(9) Resta, R. Charge states in transition. *Nature* **2008**, *453*, 735.

(10) Raebiger, H.; Lany, S.; Zunger, A. Charge self-regulation upon changing the oxidation state of transition metals in insulators. *Nature* **2008**, *453*, 763−766.

(11) Walsh, A.; Sokol, A. A.; Buckeridge, J.; Scanlon, D. O.; Catlow, C. R. A. Electron counting in solids: Oxidation states, partial charges, and ionicity. *J. Phys. Chem. Lett.* **2017**, *8*, 2074−2075.

(12) Thom, A. J. W.; Sundstrom, E. J.; Head-Gordon, M. LOBA: A localized orbital bonding analysis to calculate oxidation states, with application to a model water oxidation catalyst. *Phys. Chem. Chem. Phys.* **2009**, *11*, 11297−11304.

(13) Sit, P. H.-L.; Zipoli, F.; Chen, J.; Car, R.; Cohen, M. H.; Selloni, A. Oxidation state changes and electron flow in enzymatic catalysis and electrocatalysis through Wannier-function analysis. *Chem. - Eur. J.* **2011**, *17*, 12136−12143.

(14) Vidossich, P.; Lledos, A. The use of localised orbitals for the bonding and mechanistic analysis of organometallic compounds. *Dalton Trans.* **2014**, *43*, 11145−11151.

(15) Gimferrer, M.; Comas-Vila, G.; Salvador, P. Can we safely obtain formal oxidation states from centroids of localized orbitals? *Molecules* **2020**, *25*, 234.

(16) Pipek, J.; Mezey, P. G. A fast intrinsic localization procedure applicable for ab-initio and semiempirical linear combination of atomic orbital wave functions. *J. Chem. Phys.* **1989**, *90*, 4916−4926.

(17) Edmiston, C.; Ruedenberg, K. Localized atomic and molecular orbitals. *Rev. Mod. Phys.* **1963**, *35*, 457−465.

(18) Mulliken, R. S. Electronic population analysis on LCAO-MO molecular wave functions. I. *J. Chem. Phys.* **1955**, *23*, 1833−1840.

(19) Löwdin, P. O. On the nonorthogonality problem connected with the use of atomic wave functions in the theory of molecules and crystals. *J. Chem. Phys.* **1950**, *18*, 365−375.

(20) Heidar-Zadeh, F.; Ayers, P. W.; Verstraelen, T.; Vinogradov, I.; Vohringer-Martinez, E.; Bultinck, P. Information-theoretic approaches to atoms-in-molecules: Hirshfeld family of partitioning schemes. *J. Phys. Chem. A* **2018**, *122*, 4219−4245.

(21) Marzari, N.; Vanderbilt, D. Maximally localized generalized Wannier functions for composite energy bands. *Phys. Rev. B: Condens. Matter Mater. Phys.* **1997**, *56*, 12847−12865.

(22) Ramos-Cordoba, E.; Postils, V.; Salvador, P. Oxidation states from wave function analysis. *J. Chem. Theory Comput.* **2015**, *11*, 1501−1508.

(23) Mayer, I. Atomic orbitals from molecular wave functions: The effective minimal basis. *J. Phys. Chem.* **1996**, *100*, 6249−6257.

(24) Ramos-Cordoba, E.; Salvador, P.; Mayer, I. The atomic orbitals of the topological atom. *J. Chem. Phys.* **2013**, *138*, 214107.

(25) Min, X.; Popov, I. A.; Pan, F.-X.; Li, L.-J.; Matito, E.; Sun, Z.-M.; Wang, L.-S.; Boldyrev, A. I. All-metal antiaromaticity in Sb4-type lanthanocene anions. *Angew. Chem., Int. Ed.* **2016**, *55*, 5531−5535.

(26) Panetier, J. A.; Letko, C. S.; Tilley, D.; Head-Gordon, M. Computational characterization of redox non-innocence in cobalt-bis(diaryldithiolene)-catalyzed proton reduction. *J. Chem. Theory Comput.* **2016**, *12*, 223−230.

(27) Steen, J. S.; Knizia, G.; Klein, J. E. M. N. σ-Noninnocence: Masked phenyl-cation transfer at formal Ni^{IV}. *Angew. Chem., Int. Ed.* **2019**, *58*, 13133−13139.

(28) Scrocco, M. X-ray photoelectron spectra of Ti4+ in TiO_2. Evidence of band structure. *Chem. Phys. Lett.* **1979**, *61*, 453−456.
(29) Yu, H. S.; Truhlar, D. G. Oxidation state 10 exists. *Angew. Chem., Int. Ed.* **2016**, *55*, 9004−9006.
(30) Davison, A.; Edelstein, N.; Holm, R. H.; Maki, A. H. The preparation and characterization of four-coordinate complexes related by electron-transfer reactions. *Inorg. Chem.* **1963**, *2*, 1227−1232.
(31) Lim, B. S.; Fomitchev, D. V.; Holm, R. H. Nickel dithiolenes revisited: structures and electron distribution from density functional theory for the three-member electron-transfer series $[Ni(S_2C_2Me_2)_2]^{0,1-,2-}$. *Inorg. Chem.* **2001**, *40*, 4257−4262.
(32) Karen, P. Oxidation state, a long-standing issue! *Angew. Chem., Int. Ed.* **2015**, *54*, 4716−4726.
(33) Snyder, J. P. Elusiveness of CuIII complexation; preference for trifluoromethyl oxidation in the formation of $[Cu^{I}(CF_3)_4]^-$ salts. *Angew. Chem., Int. Ed. Engl.* **1995**, *34*, 80−81.
(34) Kaupp, M.; von Schnering, H. G. Formal oxidation state versus partial charge - A comment. *Angew. Chem., Int. Ed. Engl.* **1995**, *34*, 986.
(35) Aullón, G.; Alvarez, S. Oxidation states, atomic charges and orbital populations in transition metal complexes. *Theor. Chem. Acc.* **2009**, *123*, 67−73.
(36) Walroth, R. C.; Lukens, J. T.; MacMillan, S. N.; Finkelstein, K. D.; Lancaster, K. M. Spectroscopic evidence for a $3d^{10}$ ground state electronic configuration and ligand field inversion in $[Cu(CF_3)_4]^{1-}$. *J. Am. Chem. Soc.* **2016**, *138*, 1922−1931.
(37) DiMucci, I. M.; Lukens, J. T.; Chatterjee, S.; Carsch, K. M.; Titus, C. J.; Lee, S. J.; Nordlund, D.; Betley, T. A.; MacMillan, S. M.; Lancaster, K. M. The myth of d^8 copper(III). *J. Am. Chem. Soc.* **2019**, *141*, 18508−18520.
(38) Hoffmann, R.; Alvarez, S.; Mealli, C.; Falceto, A.; Cahill, T. J., III; Zeng, T.; Manca, G. From widely accepted concepts in coordination chemistry to inverted ligand fields. *Chem. Rev.* **2016**, *116*, 8173−8192.
(39) Mardirossian, N.; Head-Gordon, M. ωB97X-V: A 10-parameter, range-separated hybrid, generalized gradient approximation density functional with nonlocal correlation, designed by a survival-of-the-fittest strategy. *Phys. Chem. Chem. Phys.* **2014**, *16*, 9904−9924.
(40) Weigend, W.; Ahlrichs, R. Balanced basis sets of split valence, triple zeta valence and quadruple zeta valence quality for H to Rn: Design and assessment of accuracy. *Phys. Chem. Chem. Phys.* **2005**, *7*, 3297.
(41) Shao, Y.; Gan, Z.; Epifanovsky, E.; Gilbert, A. T. B.; Wormit, M.; Kussmann, J.; Lange, A. W.; Behn, A.; Deng, J.; Feng, X.; Ghosh, D.; Goldey, M.; Horn, P. R.; Jacobson, L. D.; Kaliman, I.; Khaliullin, R. Z.; Kuś, T.; Landau, A.; Liu, J.; Proynov, E. I.; Rhee, Y. M.; Richard, R. M.; Rohrdanz, M. A.; Steele, R. P.; Sundstrom, E. J.; Woodcock, H. L.; Zimmerman, P. M.; Zuev, D.; Albrecht, B.; Alguire, E.; Austin, B.; Beran, G. J. O.; Bernard, Y. A.; Berquist, E.; Brandhorst, K.; Bravaya, K. B.; Brown, S. T.; Casanova, D.; Chang, C.-M.; Chen, Y.; Chien, S. H.; Closser, K. D.; Crittenden, D. L.; Diedenhofen, M.; DiStasio, R. A.; Do, H.; Dutoi, A. D.; Edgar, R. G.; Fatehi, S.; Fusti-Molnar, L.; Ghysels, A.; Golubeva-Zadorozhnaya, A.; Gomes, J.; Hanson-Heine, M. W. D.; Harbach, P. H. P.; Hauser, A. W.; Hohenstein, E. G.; Holden, Z. C.; Jagau, T.-C.; Ji, H.; Kaduk, B.; Khistyaev, K.; Kim, J.; Kim, J.; King, R. A.; Klunzinger, P.; Kosenkov, D.; Kowalczyk, T.; Krauter, C. M.; Lao, K. U.; Laurent, A. D.; Lawler, K. V.; Levchenko, S. V.; Lin, C. Y.; Liu, F.; Livshits, E.; Lochan, R. C.; Luenser, A.; Manohar, P.; Manzer, S. F.; Mao, S.-P.; Mardirossian, N.; Marenich, A. V.; Maurer, S. A.; Mayhall, N. J.; Neuscamman, E.; Oana, C. M.; Olivares-Amaya, R.; O'Neill, D. P.; Parkhill, J. A.; Perrine, T. M.; Peverati, R.; Prociuk, A.; Rehn, D. R.; Rosta, E.; Russ, N. J.; Sharada, S. M.; Sharma, S.; Small, D. W.; Sodt, A.; Stein, T.; Stück, D.; Su, Y.-C.; Thom, A. J. W.; Tsuchimochi, T.; Vanovschi, V.; Vogt, L.; Vydrov, O.; Wang, T.; Watson, M. A.; Wenzel, J.; White, A.; Williams, C. F.; Yang, J.; Yeganeh, S.; Yost, S. R.; You, Z.-Q.; Zhang, I. Y.; Zhang, X.; Zhao, Y.; Brooks, B. R.; Chan, G. K. L.; Chipman, D. M.; Cramer, C. J.; Goddard, W. A.; Gordon, M. S.; Hehre, W. J.; Klamt, A.; Schaefer, H. F.; Schmidt, M. W.; Sherrill, C. D.; Truhlar, D. G.; Warshel, A.; Xu, X.; Aspuru-Guzik, A.; Baer, R.; Bell, A. T.; Besley, N. A.; Chai, J.-D.; Dreuw, A.; Dunietz, B. D.; Furlani, T. R.; Gwaltney, S. R.; Hsu, C.-P.; Jung, Y.; Kong, J.; Lambrecht, D. S.; Liang, W.; Ochsenfeld, C.; Rassolov, V. A.; Slipchenko, L. V.; Subotnik, J. E.; Van Voorhis, T.; Herbert, J. M.; Krylov, A. I.; Gill, P. M. W.; Head-Gordon, M. Advances in molecular quantum chemistry contained in the Q-Chem 4 program package. *Mol. Phys.* **2015**, *113*, 184.
(42) Salvador, P.; Ramos-Cordoba, E.; Gimferrer, M. *APOST-3D Program*; Universitat de Girona: Girona, Spain, 2019.
(43) Salvador, P.; Ramos-Cordoba, E. An approximation to Bader's topological atom. *J. Chem. Phys.* **2013**, *139*, 071103.

https://dx.doi.org/10.1021/acs.inorgchem.0c02405
Inorg. Chem. 2020, 59, 15410−15420

6.2 Computational monitoring of oxidation states in olefin metathesis

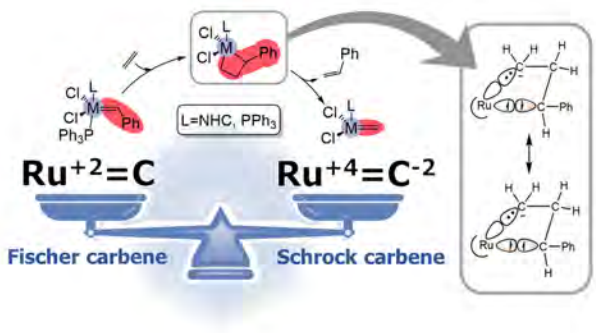

Published in: Gimferrer, M.; Salvador, P.; Poater, A. *Organometallics* **2019**, 38, 24, 4585-4592.

Abstract: Ruthenium-based catalysts play a pivotal role in the formation of carbon–carbon double bonds in olefin metathesis. The reaction mechanism always involves the formation of a four-membered metallacycle where the Ru centers should exhibit a formal +4 oxidation state. The steric and electronic properties of the so-called spectator N-heterocyclic carbene (NHC) ligand of Ru-benzylidene complexes are, presumably, responsible for the ability/inability of the metal center to achieve the necessary formal oxidation state for the catalytic process run on, and hence should be an essential ingredient in the design of efficient catalysts. In the present study we make use of density functional theory (DFT) calculations combined with the so-called effective oxidation state (EOS) analysis to examine the evolution of the metal oxidation state along the reaction mechanism. In particular, we tackle the Ru^{2+} versus Ru^{4+} debate in Grubbs catalysts, deepening into details about the different nature of the intermediates of the reaction pathway. We also analyze the picture of (cheaper and cleaner) iron- and osmium-based catalysts. Moreover, the nature and occupancy number of the frontier effective fragment orbitals of the ligands sheds light into the subtle electronic differences between first- and second-generation Grubbs catalysts that nevertheless do not affect the assignment of oxidation states.

ORGANOMETALLICS
Article
Cite This: Organometallics 2019, 38, 4585−4592
pubs.acs.org/Organometallics

Computational Monitoring of Oxidation States in Olefin Metathesis

Martí Gimferrer, Pedro Salvador,* and Albert Poater*

Institut de Química Computacional i Catàlisi and Departament de Química, Universitat de Girona, Campus Montilivi, 17003 Girona, Catalonia, Spain

Supporting Information

ABSTRACT: Ruthenium-based catalysts play a pivotal role in the formation of carbon−carbon double bonds in olefin metathesis. The reaction mechanism always involves the formation of a four-membered metallacycle where the Ru centers should exhibit a formal +4 oxidation state. The steric and electronic properties of the so-called spectator *N*-heterocyclic carbene (NHC) ligand of Ru-benzylidene complexes are, presumably, responsible for the ability/inability of the metal center to achieve the necessary formal oxidation state for the catalytic process run on, and hence should be an essential ingredient in the design of efficient catalysts. In the present study we make use of density functional theory (DFT) calculations combined with the so-called effective oxidation state (EOS) analysis to examine the evolution of the metal oxidation state along the reaction mechanism. In particular, we tackle the Ru^{2+} versus Ru^{4+} debate in Grubbs catalysts, deepening into details about the different nature of the intermediates of the reaction pathway. We also analyze the picture of (cheaper and cleaner) iron- and osmium-based catalysts. Moreover, the nature and occupation number of the frontier effective fragment orbitals of the ligands sheds light into the subtle electronic differences between first- and second-generation Grubbs catalysts that nevertheless do not affect the assignment of oxidation states.

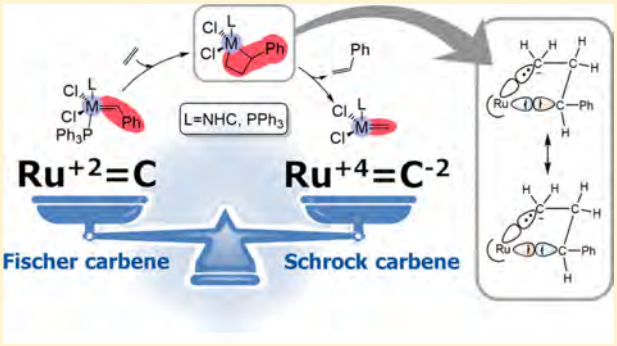

INTRODUCTION

Transition metal (TM) catalyzed olefin metathesis has proved a powerful tool for transforming carbon−carbon double bonds,[1] with remarkable performance in cross-metathesis through the Shell higher olefin process (SHOP) method and in polymerization by ring-opening metathesis polymerization (ROMP).[2] Among all TM catalysts, the development of ruthenium-based ones, pioneered by Grubbs et al.,[3] has led to numerous applications in organic synthesis. For this reason, there is a strong interest in understanding how these catalysts work (see Scheme 1).[4]

Indeed, we have a very good picture of many mechanistic details, both from the experimental[5] and theoretical[6] point of view. The generally accepted mechanism incorporates the pioneer work of Chauvin, who considered a four-membered metallacycle as the central intermediate,[7] as depicted in Scheme 1. Here, one can distinguish the first-generation (L = phosphine) and second-generation (L = *N*-heterocyclic carbene (NHC)) olefin metathesis Grubbs catalysts.

Going into specific details in the olefin metathesis reaction, first Chen and Grubbs[8] had predicted that the hindered rotation around the Ru−P bond in the metallacycle is the cause of the slower reactivity for the first-generation catalysts. Cavallo[9] and Nolan reported that this order of binding energy appears due to the stronger trans influence provided by the NHC ligand.[10] The σ-donation and π-acceptor properties of the phosphine and the NHC ligands have been computationally analyzed by Carbó and Poblet,[11] Cavallo,[12] Eisenstein,[13] and Frenking,[14] among others.[15] These properties have been also probed electrochemically by Plenio.[16] The transition states for the second-generation catalysts exhibit higher energy barriers to close and then open the metallacycle because of the stronger σ-donating carbene capacity of the NHC ligand that consequently was supposed to stabilize the +4 oxidation state (OS) of the Ru moiety in the metallacycle.[17] This

Scheme 1. Accepted Mechanism for Ruthenium-Based Olefin Metathesis Catalysis[a]

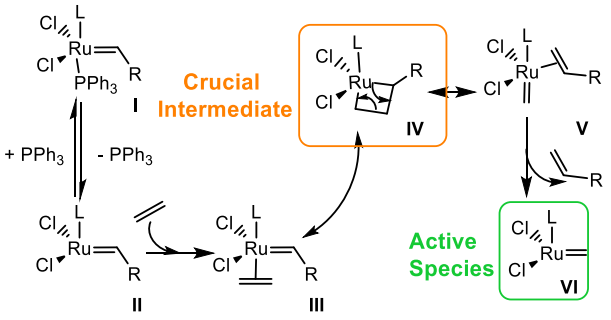

[a]R = H, Ph; L = phosphine or NHC.[7]

Received: August 29, 2019
Published: December 4, 2019

DOI: 10.1021/acs.organomet.9b00591
Organometallics 2019, 38, 4585−4592

hypothesis was also latter proposed in the case of the *P*-heterocyclic carbenes (PHC).[18] On the contrary, Kennepohl[19] found that the σ-donation ability of NHC ligand was lower than that of phosphine. Electronically speaking, the TM holds 16 electrons throughout the catalytic cycle, except for a loss of 2 electrons in intermediate **II**. In 2005, Harvey[17] showed that the rate-limiting step for metathesis of ruthenium bisphosphine and diaminocarbene/phosphine catalysts $[L_2RuCl_2(=CH_2)]$, where L = PCy_3 or NHC, is either the ring-closing of alkene complex **III**, to form a ruthenacyclobutane, or the ring-opening of the latter to form isomeric alkene complex **V**. Again, the higher efficiency of the diaminocarbene based catalysts[8,20] was attributed to the stabilization of the formal +4 OS of the ruthenium center in the metallacycle[17] and a larger phosphine dissociation energy for the bisphosphine catalyst.[21]

Apart from the metallacycle, the formal characterization of TM carbene species **II**, **III**, and **V** has also lead to some controversy.[22−24] TM carbenes are usually divided into two classes, namely, Fischer and Schrock. Both the nature of the TM and its chemical environment (π-donor/-acceptor ligands) and the substituents on the carbene ligand are responsible for the Fischer (electrophilic) or Schrock (nucleophilic) character.[25,26] The Ru=C moiety is often interpreted as a Fischer-type carbene, leading to a formal oxidation state of +2 for the Ru (that corresponds to a d^6 configuration),[26] whereas the ylidene ligand (either $=CH_2$ or =CHPh) is considered neutral. In the case of Grubbs catalysts, this distinction is not too clear, as the alkyl groups of the ylidene ligands should furnish Schrock character to the carbene.[27] Occhipinti et al. found that Grubbs catalysts share some features of the Schrock carbenes and even suggested a new subcategory of "electrophilic Schrock carbenes" for the Grubbs catalysts.[24] The formal classification of these TM carbenes could be regarded as immaterial except for the implications it may have in the assignment of the formal OS of the TM moiety.

The oxidation state is a heuristic concept that plays a key role in chemical knowledge when it comes to rationalization, systematization, or classification of chemical phenomena, which however has been lacking a proper, clear-cut definition for many years. Consequently, vivid debates and controversy can be found in the literature concerning OS assignments, mainly in TM metal complexes with intricate bonding situations. Last year, the oxidation state was given a refined generic definition by the IUPAC, namely, the atom's charge after ionic approximation of its heteronuclear bonds.[28] Practical algorithms were also provided, that essentially start with the molecule's Lewis structure, followed by a subsequent assignment of the bond electrons to the most electronegative atom, in a winner-takes-all fashion. As a corollary, bonds between atoms of the same element are always divided equally.

While the current definition of OS represents a clear improvement over the previous set of agreed upon rules, there have been recent works that pinpoint the limitations of the so-called ionic approximation. Monsch et al.[29] have most recently challenged the concept of oxidation state with an in-depth analysis of the bonding situation in the apparently simple $[Fe(H_2O)_5(NO)]^{2+}$ cation. Postils et al.[30] have shown that rather than the nature of the free atoms it is their chemical environment that bears the chemical information that ultimately can lead to proper a OS assignment. The authors also highlighted inherent difficulties of the ionic approximation when applied to TM carbenes, which is most relevant for the present work. The fact that the *same* compound (Grubbs first-generation catalyst, with CAS number 172222−30−9) still appears with different nomenclatures in the Sigma-Aldrich catalog (labeled as either Ru(II) or Ru(IV)) nicely illustrates the issue.

In TM carbenes, a carbene unit exhibits a double bond with the metal center. Since carbon is more electronegative than the TM, the carbene moiety should keep all four electrons involved in the double-bond, reaching a formal charge of (−2). Hence, following IUPAC's rule the carbene fragment in TM carbenes is readily considered anionic, accounting for Schrock-type carbenes and in line with their nucleophilic character. Notably, while the bonding in Schrock carbenes is often discussed in terms of a covalent interaction involving triplet carbene and metal moieties, such alleged formal bond origin may not necessarily be reflected on the corresponding OS, as in the ionic approximation only the final allegiance of the bond electrons must be considered, not their origin.[28]

In contrast, the carbene fragment is assumed formally neutral in Fisher-type carbenes. One way to account for this OS assignment is to consider the σ bond polarized toward the carbene and the π bond polarized toward the TM, each moiety keeping two electrons. This view, which is usually pictured in textbooks, cannot be reconciled with IUPAC's rule that all electrons of the bonds between two atoms are assigned to the most electronegative one. Thus, discriminating TM carbenes (Fischer or Schrock) from an OS perspective necessarily requires approaches that go beyond IUPAC's ionic approximation. At this point, computational chemistry methods can come to the rescue, but establishing oxidation states from first-principles is not a trivial task.

Unfortunately, the fact that oxidation states are written as a charge (albeit an imaginary one) has contributed to the misbelief that partial atomic charges represent a sort of noninteger version of oxidation states. Atomic spin populations, used by many authors to assign OS to TM centers, also represent averaged electron populations and moreover are clearly futile for pure singlet state species. However, by treating electrons individually, computational chemistry tools are able to derive oxidation states from first principles. For instance, Ramos-Cordoba[31] introduced a scheme that is formally applicable on equal footing to any molecular system and wave function. The so-called effective oxidation state (EOS) analysis relies on Mayer's effective orbitals (EFOs) and their occupation numbers, obtained for all atoms or fragments/ligands defined. The spin-resolved EFOs are sorted by decreasing occupation number and then individual electrons are assigned to those EFOs with higher occupations, leading to an effective configuration of the atoms/ligands within the molecule, which directly determines their OS. Moreover, the difference between the occupation number (λ) of the last occupied (LO) and the first unoccupied (FU) EFOs is also a pointer of the reliability of the resulting analysis. The larger this difference, the better the current electron distribution can be pictured into a discrete ionic model. So, together with the OS, the EOS analysis yields an associated reliability index, $R = \min(R_\alpha, R_\beta)$, defined for each spin case σ as

$$R_\sigma\ (\%) = 100 \cdot \min(1, \max(0, \lambda^\sigma_{LO} - \lambda^\sigma_{FU} + \frac{1}{2})) \quad (1)$$

When the difference between the occupation number of the frontier EFOs exceeds half an electron, the overall assignment of OS is considered as undisputable, and the R index reaches 100%. The worst-case scenario is when two or more frontier

DOI: 10.1021/acs.organomet.9b00591
Organometallics 2019, 38, 4585−4592

EFOs sitting on different fragments exhibit the same occupation number. In that case, the EOS analysis provides two different equally plausible OS distributions with R = 50%. Note that R can take values formally from 0 to 100%, where values below 50% indicate that the assignment of the electrons has not followed an aufbau principle according to the occupation numbers of the EFOs. This alternative approach can be used to quantify to which extent the molecular system conforms with a given set of oxidation states.

The EOS method has been successfully applied by several authors[29,32] to a broad spectrum of chemical systems, proving its usefulness. The aim of this work is to tackle from the oxidation state perspective the key steps of the olefin metathesis reaction mechanism, characterizing the TM carbene intermediates trying to go beyond the classical Fischer versus Schrock dichotomy and actually quantifying the presumed Ru(IV) character of the four-member metallacycle.[33] For this purpose, we have applied the EOS scheme to monitor oxidation state changes of the involved species along the olefin metathesis reaction pathway using DFT calculations. The key role[34] of the nature of the TM is scrutinized by *in silico* replacing ruthenium by the potentially active osmium and the cheap (but ineffective) iron. The subtle electronic differences between first- and second-generation Grubb's catalysts are also analyzed in the light of the frontier EFOs of the ligands.

RESULTS AND DISCUSSION

For all Ru and Os complexes, a singlet (low-spin) configuration has been considered throughout the reaction pathway (test calculations on the triplet and the quintet states found lie at higher energy than the singlet ones), except for iron. In the case of Fe complexes, despite the strong field character of the ligands,[35] its natural tendency to show high-spin configurations prompted us to analyze also triplet and quintet states for all species involved,[36] being the initial precatalyst **I** triplet and the 14e species quintuplet.

The Gibbs free energy results (M06/cc-pVTZ ∼ sdd//BP86/TZVP ∼ sdd) obtained for the catalytic olefin metathesis cycle, using the first- and second-generation Grubbs catalysts and ethylene as substrate, are compiled in Figure 1. As it was aforementioned, the mechanism involving Ru and Os follows the same pathway, maintaining the singlet ground state.

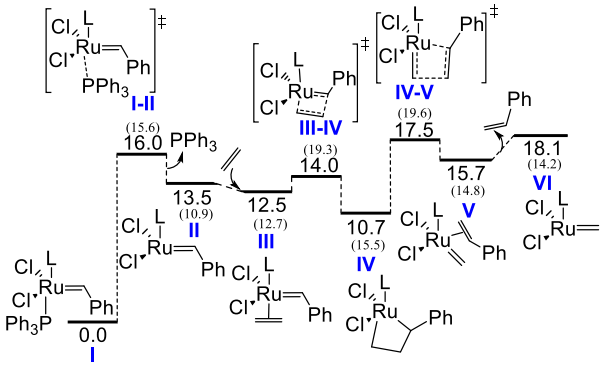

Figure 1. Gibbs free energies (kcal/mol) for the first catalytic olefin metathesis cycle of the second-generation Grubbs catalyst, L = SIMes with ethylene as substrate. The values for the first-generation Grubbs catalyst are given in parentheses; L = PPh_3. SIMes = 1,3-bis(2,4,6-trimethylphenyl)-4,5-dihydroimidazol-2-ylidene.

Significant differences are observed in the case of Fe, for which 14-electron intermediates **II** and **VI** exhibit a quintet state, and coordination intermediates **III** and **V** are absent.

Energetically, it is worth mentioning that metallacycle **IV** is 1.7 kcal/mol more stable than **I** for osmium, whereas this difference amounts to 31.1 kcal/mol for iron (see the structural differences in Figure 2),[37] an energy wall difficult to surpass

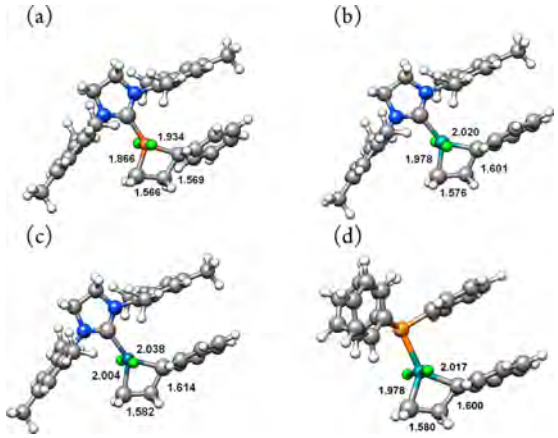

Figure 2. Metallacycle **IV** for the second-generation Grubbs olefin metathesis catalysts with (a) iron, (b) ruthenium, and (c) osmium as metal center (main distances in Å) and (d) the first-generation ruthenium one.

which would make the iron-based catalyst less active, as stated previously.[36,38] The upper barrier is the opening of the metallacycle, i.e., transition state **IV**−**V**, even the release of the styrene subproduct via the transition state **V**−**VI** has also been considered since it is in competition, but with an extremely low negative frequency associated with this transition state (see the Supporting Information).[39]

The oxidation states of the TM center and ligands, as well as the R index of the assignment along the pathway are gathered in Table 1. It is worth mentioning that in all cases the EOS analysis predicts phosphine ligands as neutral (0), chlorine ligands as anionic (−1), and in the case of second-generation Grubbs catalyst, the NHC ligand as neutral (0). Visual inspection of the frontier EFOs associated with this fragment shows that the last occupied has clear σ character toward the TM and a high occupation (>0.60), while the first unoccupied one has π character, with an occupation of just ca. 0.15. Upon EOS analysis, the σ-type hybrid on the NHC is considered occupied and the π hybrid is considered empty. The small occupation of the π EFO on NHC indicates a residual π contribution to the NHC−TM bond, which is mainly of σ type. As a comparison, the occupation of the frontier π EFO of the other carbenes (either $=CH_2$ or $=CHPh$) is ca. 0.4. Hence, the NHC−TM unit does not quite fit the textbook picture of a Fischer carbene with a double bond between the TM and the carbene. As a matter of fact, it is usually depicted in chemical structures with a single bond. This is also the picture derived from the ligand's EFOs and EOS analysis.

In all cases studied, the EOS analysis assigns the last electron pair to a d-type hybrid on the TM, whereas the unoccupied EFO with the highest occupation lies on the ($=CHR_1$) carbene moiety (see Table 1). That is, the OS of the TM is (+2), with an increasing character of (+4) as the R value decreases. A direct trend when going from Fe to Os can be

DOI: 10.1021/acs.organomet.9b00591
Organometallics 2019, 38, 4585−4592

Table 1. Oxidation States and Reliability Index along the Olefin Metathesis Reaction Pathway for Catalyst $MCl_2(L)(R_2)(=CHR_1)$[a]

						first-gen. Grubbs	second-gen. Grubbs		
	R_1	R_2	OS [M]	OS R_1	OS R_2	R_{Ru} (%)	R_{Fe} (%)	R_{Ru} (%)	R_{Os} (%)
I	Ph	PPh_3	+2	0	0	62.3	65.9	64.3	63.8
I–II	Ph	PPh_3	+2	0	0	59.2	64.4	61.3	62.0
II	Ph		+2	0		59.0	50.0	60.5	57.1
III	Ph	Et	+2	0	0	62.0		63.7	63.5
III–IV	Ph	Et	+2	0	0	68.5	65.4	68.7	63.4
IV	$PhCH_2CH_2$		+2	0		53.1	54.7	50.8	44.1
IV–V	H	Ph CH_2	+2	0	0	66.8	68.0	66.8	60.6
V	H	Ph CH_2	+2	0	0	58.7		67.0	57.1
VI	H		+2	0	0	55.0	50.0	58.1	51.4

[a]M = Fe, Ru, and Os; L = SIMes, PPh_3.

established, which highlights the noninnocent role of the TM in the mechanism. We observe that the *R* values for intermediate **IV** decrease from Fe- to Os-based catalysts. Actually, for intermediate **IV**, *R* values are close to 50%, providing equally the M^{+4}/L^{-2} and M^{+2}/L^0 combinations of OS. In the case of the Os-based, the preference for the M^{+2}/L^0 is less favored. The latter combination is predominant along the reaction pathway but sharing with a low contribution of M^{+4}/L^{-2}, since no *R* of any intermediate is over 65%, except for intermediates Fe-**I** and Ru-**V**, for which *R* is 65.9 and 67.0%, respectively. The general trend is that the +4 OS on the metal is more favored for osmium than iron, with ruthenium in between. For intermediate **II**, iron breaks this trend, which might be due to the fact that the ground state switches from singlet to triplet. We have explored a possible relationship between the *R* values or the occupation of the frontier's EFOs or the TM/ligand and the relative stability of the species along the reaction path, but we could not find a significant correlation.

To deepen into the origin of the *R* values, the EFOs from the EOS analysis were analyzed using first simple intermediate **II**, to evaluate its formal double bond with the ═CHPh carbene ligand, and then metallacycle **IV**. In **II**, the formal oxidation state on the Ru atom is +2 with *R* = 60.5%. Thus, according to EOS the TM carbene is in line with a Fischer type carbene, where as frontier EFOs reveal in Figure 3, the electrons of the σ-bond are associated with the carbene moiety whereas the electrons of the π-bond are held by the Ru. More precisely, the LO EFO (with occupation number 0.522) corresponds to a σ-type orbital localized on the carbon atom of the carbene moiety. One can see a clear correspondence with the FU EFO (with occupation number 0.417), which corresponds to a d-type orbital on the Ru atom associated with the σ bond with the carbene (the sum of the occupation numbers does not have to be exactly 1). Moreover, there is an additional π-type EFO on the C atom of the carbene with a much lower occupation number (0.395), which is considered unoccupied in the EOS process. If this EFO was occupied, then the carbene would be formally dianionic (−2) and hence Schrock-type. This is clearly not the case.

In intermediate **IV**, the Ru atom is part of the four-membered metallacycle, while conserving its spectator ligands. According to the EOS analysis, there are again two Cl (−1) ligands and a formal neutral NHC moiety. Thus, the formal OS of the whole metallacycle is +2. In this case, there are three EFOs with very similar occupation numbers, and there are two pairs of electrons left to be assigned. These EFOs are depicted in Figure 3b. Two of them are sitting on the $(CH_2)_2CHPh$ moiety and correspond to π-type hybrids on each of the C

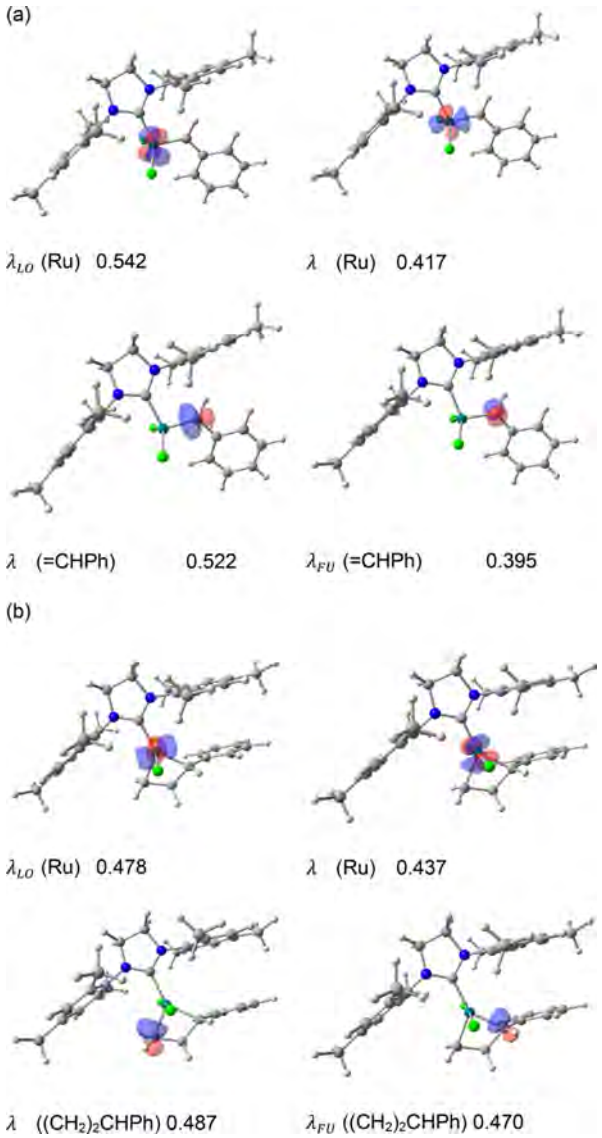

Figure 3. EFOs of intermediates (a) **II** and (b) **IV** for second-generation Grubbs olefin metathesis catalysts with ruthenium as a metal (occupancies in electrons).

DOI: 10.1021/acs.organomet.9b00591
Organometallics 2019, 38, 4585−4592

atoms that are forming σ-type bonds with the TM, with occupation numbers 0.487 and 0.470, respectively. If the two pairs of σ electrons of the Ru−C bonds are assigned to the C atom, then these EFOs must be occupied, and the $(CH_2)_2CHPh$ moiety will have a formal charge of (−2). Consequently, we will have a formal Ru(+4). There is, however, an EFO of d-type on the Ru atom with an occupation number in between that of these two EFOs (0.478), which avoids such a clear-cut assignment. There is also another d-type hybrid on the Ru but with an occupation number significantly smaller (0.437).

In the strict application of the EOS scheme, the EFO with occupation number 0.470 is unoccupied, and the last electron pair goes to the d-type orbital on the Ru with occupation 0.478. That leads to a formal Ru(+2) and neutral $(CH_2)_3CHPh$ moiety. Nonetheless, the occupation numbers of the frontier EFOs are so close (pseudodegenerate in occupation) that the alternate assignment (namely Ru(+4) and $(CH_2)_3CHPh$ (−2)) is just as plausible as the former. In fact, there are two pairs of electrons that can be considered to be almost equally distributed among three pseudodegenerate EFOs. From the nine possible different distributions of these four electrons among six orbitals, only one leads to a formal Ru(+4); therefore, the picture obtained from EOS analysis is probably closer to a formal Ru(+2) than a fully oxidized Ru(+4). Another argument against the Ru(+4) assignment comes from considering the $(CH_2)_2CHPh$ moiety frozen at the geometry of the complex and isolated in different electronic states. Considering a neutral charge, the ground state is singlet diradicaloid (triplet diradical is almost degenerate) and lies 21 kcal/mol below the closed-shell solution. The doubly anionic state (−2) lies +65.7 kcal/mol above the energy of the neutral diradical state. The lowest energy, however, corresponds to the (−1) charge, with a doublet state that lies 24 kcal/mol below the singlet diradical state. In this case, the additional electron is located on the terminal CH_2 unit, on a MO that essentially coincides with the above-mentioned EFO with 0.487 occupation.

So, from an energetic perspective (of the $(CH_2)_2CHPh$ unit), the most favorable charge is −1, which is right in between the formal (0) and (−2) OS. That means Ru could also be regarded as a (+3) formal OS without unpaired electrons, by considering the two resonant structures on Scheme 2.

The robustness of the EOS approach has been tested by using different functionals to obtain the electron distribution namely GGA (BP86), hybrid-GGA (B3LYP), and meta-hybrid GGA (M06-2X) functionals, combined with different basis sets such as SVP, TZVP and cc-pVTZ (see the Supporting Information). The results obtained for the EOS analysis were very consistent in all cases. For instance, for the Ru-based metallacycle **IV**, the *R* values obtained were 50.8% for SVP and 51.0% for cc-pVTZ basis sets, whereas the value was 50.0% (SVP, TZVP and cc-pVTZ) for B3LYP. Increasing the Hartree−Fock (HF) exchange contribution, from 0% for BP86 to 60% of M06-2X, M06-2X confirmed again that the EOS analysis is extremely robust, obtaining *R* values of 51.0% (SVP), 51.1% (TZVP), and 51.3% (cc-pVTZ), despite the overestimation of the Ru(+2) configuration that the HF-type exchange might induce.[40,41] Of course, empirical dispersion correction does not affect the results (as long as it does not affect the density).[42] Apart from the similarity in results by all tested functionals here, the BP86 functional was used based on the multiplicity complexity of iron and the wonderful performance for ruthenium-based catalysts, demonstrated recently in agreement with Piers et al. results.[43]

Finally, direct comparison of first- and second-generation Ru-based Grubbs catalysts indicates no changes on the OS, and only a minor effect is observed on the *R* values that are slightly smaller for the first-generation species. The only exception is metallacycle intermediate **IV** previously discussed, which has somewhat more Ru(IV) character in the case of the second-generation catalyst. Energetically, the metallacycle **IV** for the first-generation is 4.8 kcal/mol more kinetically demanding, and the closure and opening transition states are 5.3 and 2.1 kcal/mol, respectively. Thus, a higher Ru(IV) character might explain the better performance of the second-generation Grubbs olefin metathesis catalysts, in agreement with Harvey.[17]

We note that Kennepohl[19] compared XAS spectra for both families of catalysts and found that the charge on the metal was larger (more positive) for NHC-bound complex than for the analogous bisphosphine one, but the difference was smaller than that expected for oxidation state changes. They also concluded that the σ-donation of PCy_3 ligand was larger than that of NHC and the opposite trend for their π-acceptor capacity, thereby explaining the difference in partial atomic charge on the Ru ion.

We find that the experimental behavior is explained for all species involved in the reaction mechanism.[24] The real-space partial atomic charge on Ru is systematically more positive by ca. +0.2 for second-generation catalysts (Mulliken charges of Ru are predicted negative). Moreover, the extent of σ-donation and π-backdonation can also be compared by looking at the occupation of the frontier EFOs of the respective ligands (see the Supporting Information). The occupation of the σ-type hybrid is systematically larger for the NHC ligand (0.67 vs 0.63, on average), indicating that it is keeping a larger share of the electron pair associated to the σ bond with the metal, i.e., it is donating *less* σ density. Similarly, the occupation of the π-type EFO (which is considered unoccupied by EOS analysis) is systematically larger for NHC (0.13 vs 0.07, on average), indicating its better π-acceptor character.

Concomitantly, the occupation of the d-type hybrid of the Ru involved in the aforementioned σ bond is systematically smaller for the NHC-bound complexes. In all cases, it is the fourth highest occupied d orbital, with occupations of ca. 0.40 on average. The EOS analysis always renders this EFO as unoccupied (otherwise a Ru(0) would be obtained), and this nicely explains why these differences in electronic effects (including Ru partial charge) cannot affect the oxidation state, as seen experimentally.[24]

Scheme 2. Schematic Representation of the Bonding Situation in Intermediate IV Leading to a formal Ru(+3) OS

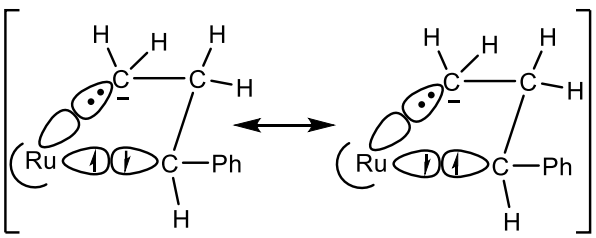

DOI: 10.1021/acs.organomet.9b00591
Organometallics 2019, 38, 4585−4592

CONCLUSIONS

In conclusion, we observed that the metallic center of metallacycle species **IV** presents half character M^{+4} and M^{+2}, whereas for the rest of the reaction pathway the latter oxidation state is mainly preferred. This is in agreement with the trend proposed in the past by theoreticians.[8] Even though accordingly to the IUPAC's rules the Ru=CHR$_1$ bond is formally described as a (+4) metal moiety and (−2) anionic carbene (corresponding to a Schrock-type carbene), our results indicate that the (+4) OS character on the metal is only relevant for metallacycle **IV**. Actually, the (+2) OS is preferred and better describes the nature of the metal within the molecule. The higher Ru(IV) character of the second-generation Grubbs catalysts might be responsible for their better catalytic performance respect to the first-generation ones. We also show how the occupation number of the EFOs explain the neutral character of the NHC ligand, the electronic differences between first- and second-generation Grubbs catalysts in terms of σ-donation and π-backdonation effects, and the reason OS of the Ru center is unaffected. Moreover, an alternative bonding picture for the metallacycle **IV** involving a formal Ru(III) species is also suggested, in the light of electronic and energetic evidence.

COMPUTATIONAL DETAILS

DFT calculations were performed with the Gausian 09 set of programs,[44] using the BP86 functional of Becke and Perdew,[45,46] checking the Grimme D3BJ[42] correction term to the electronic energy. We described the electronic configuration of the molecular systems with the triple-ζ basis set of Weigend and Ahlrichs for all atoms (TZVP keyword in Gaussian),[47] except for the metals for which the quasirelativistic Stuttgart/Dresden effective core potential, with an associated valence basis set contracted (standard SDD keywords in Gaussian 09) was used.[48] We performed the geometry optimizations without symmetry constraints, and analytical frequency calculations were carried out to characterize the located stationary points. These frequencies were used to calculate unscaled zero-point energies (ZPEs) as well as thermal corrections and entropy effects at 25 °C. Single-point energy calculations were performed on the optimized geometries with the M06 functional[40] and the cc-pVTZ basis set for the main atoms.[49] The same functional and basis set were used to estimate solvent effects with the PCM model,[50] using dichloromethane as the solvent. The reported Gibbs energies in this work include M06/cc-pVTZ ∼ sdd//BP86/TZVP ∼ sdd electronic energies with solvent effects obtained at the same level of theory, corrected with zero-point energies, thermal corrections and entropy effects evaluated at 25 °C with the BP86/TZVP ∼ sdd method.

EOS analysis was performed with the in-house program APOST-3D,[31] using the Topological Fuzzy Voronoi Cells (TFVC) real-space partitioning for the atomic definitions.[51]

ASSOCIATED CONTENT

Supporting Information

The Supporting Information is available free of charge at https://pubs.acs.org/doi/10.1021/acs.organomet.9b00591.

XYZ coordinates and energies of all computed species (XYZ)

Benchmark results from the EOS analysis (PDF)

AUTHOR INFORMATION

Corresponding Authors

*E-mail: albert.poater@udg.edu (A.P.)
*E-mail: pedro.salvador@udg.edu (P.S.).

ORCID

Martí Gimferrer: 0000-0001-5222-2201
Pedro Salvador: 0000-0003-1823-7295
Albert Poater: 0000-0002-8997-2599

Notes

The authors declare no competing financial interest.

ACKNOWLEDGMENTS

A.P. is a Serra Húnter fellow. A.P. and P.S. thank the Spanish MICINN for projects PGC2018-097722-B-I00 and PGC2018-098212-B-C22 and the EU for a FEDER fund (UNGI08-4E-003). M.G. thanks the Generalitat de Catalunya and Fons Social Europeu for the predoctoral fellowship (2018 FI_B 01120). We thank Prof. Cavallo for helpful comments and one of the reviewers for calling our attention to the different nomenclature used in Sigma-Aldrich catalog for the Grubbs catalyst.

REFERENCES

(1) Grubbs, R. H. *Handbook of Olefin Metathesis*; Wiley-VCH: Weinheim, Germany, 2003.

(2) Rosebrugh, L. E.; Ahmed, T. S.; Marx, V. M.; Hartung, J.; Liu, P.; Lopez, J. G.; Houk, K. N.; Grubbs, R. H. Probing Stereoselectivity in Ring-Opening Metathesis Polymerization Mediated by Cyclometalated Ruthenium-Based Catalysts: A Combined Experimental and Computational Study. *J. Am. Chem. Soc.* **2016**, *138*, 1394−1405.

(3) (a) Samojłowicz, C.; Bieniek, M.; Grela, K. *Chem. Rev.* **2009**, *109*, 3708−3742. (b) Vougioukalakis, G. C.; Grubbs, R. H. Ruthenium-Based Olefin Metathesis Catalysts Bearing N-Heterocyclic Carbene Ligands. *Chem. Rev.* **2010**, *110*, 1746−1787.

(4) Luo, S.-X.; Engle, K. M.; Dong, X.; Hejl, A.; Takase, M. K.; Henling, L. M.; Liu, P.; Houk, K. N.; Grubbs, R. H. An Initiation Kinetics Prediction Model Enables Rational Design of Ruthenium Olefin Metathesis Catalysts Bearing Modified Chelating Benzylidenes. *ACS Catal.* **2018**, *8*, 4600−4611.

(5) (a) Romero, P. E.; Piers, W. E. Direct Observation of a 14-Electron Ruthenacyclobutane Relevant to Olefin Metathesis. *J. Am. Chem. Soc.* **2005**, *127*, 5032−5033. (b) van der Eide, E. F.; Romero, P. E.; Piers, W. E. Generation and Spectroscopic Characterization of Ruthenacyclobutane and Ruthenium Olefin Carbene Intermediates Relevant to Ring Closing Metathesis Catalysis. *J. Am. Chem. Soc.* **2008**, *130*, 4485−4491. (d) Grubbs, R. H.; Burk, P. L.; Carr, D. D. Mechanism of the Olefin Metathesis Reaction. *J. Am. Chem. Soc.* **1975**, *97*, 3265−3267.

(6) (a) Urbina-Blanco, C. A.; Poater, A.; Lebl, T.; Manzini, S.; Slawin, A. M. Z.; Cavallo, L.; Nolan, S. P. The Activation Mechanism of Ru−Indenylidene Complexes in Olefin Metathesis. *J. Am. Chem. Soc.* **2013**, *135*, 7073−7079. (b) Correa, A.; Cavallo, L. The Elusive Mechanism of Olefin Metathesis Promoted by (NHC)Ru-Based Catalysts: A Trade between Steric, Electronic, and Solvent Effects. *J. Am. Chem. Soc.* **2006**, *128*, 13352−13353. (c) Engle, K. M.; Lu, G.; Luo, S. X.; Henling, L. M.; Takase, M. K.; Liu, P.; Houk, K. N.; Grubbs, R. H. Origins of Initiation Rate Differences in Ruthenium Olefin Metathesis Catalysts Containing Chelating Benzylidenes. *J. Am. Chem. Soc.* **2015**, *137*, 5782−5792. (d) Poater, A.; Ragone, F.; Correa, A.; Cavallo, L. Comparison of Different Ruthenium-alkylidene Bonds in the Activation Step with N-heterocyclic carbene Ru-catalysts for Olefins Metathesis. *Dalton Trans.* **2011**, *40*, 11066−11069. (e) Leitgeb, A.; Abbas, M.; Fischer, R. C.; Poater, A.; Cavallo, L.; Slugovc, C. A Latent Ruthenium Based Olefin Metathesis Catalyst with a Sterically Demanding NHC Ligand (Pre)catalysts. *Catal. Sci. Technol.* **2012**, *2*, 1640−1643. (f) Wappel, J.; Fischer, R. C.; Cavallo, L.; Slugovc, C.; Poater, A. Simple Activation by Acid of Latent Ru-NHC-based Metathesis Initiators Bearing 8-quinolinolate Co-ligands. *Beilstein J. Org. Chem.* **2016**, *12*, 154−165. (g) Yang, H.-C.; Huang, Y.-C.; Lan, Y.-K.; Luh, T.-Y.; Zhao, Y.; Truhlar, D. G. Carbene Rotamer

DOI: 10.1021/acs.organomet.9b00591
Organometallics 2019, 38, 4585−4592

Switching Explains the Reverse Trans Effect in Forming the Grubbs Second-Generation Olefin Metathesis Catalyst. *Organometallics* **2011**, *30*, 4196−4200.
(7) Hérisson, P. J.-L.; Chauvin, Y. Catalyse de Transformation des Oléfines par les Complexes du Tungstène. II. Télomérisation des Oléfines Cycliques en Présence d'Oléfines Acycliques. *Makromol. Chem.* **1971**, *141*, 161−176.
(8) (a) Adlhart, C.; Chen, P. Ligand Rotation Distinguishes First- and Second-Generation Ruthenium Metathesis Catalysts. *Angew. Chem., Int. Ed.* **2002**, *41*, 4484−4487. (b) Adlhart, C.; Chen, P. Mechanism and Activity of Ruthenium Olefin Metathesis Catalysts: The Role of Ligands and Substrates from a Theoretical Perspective. *J. Am. Chem. Soc.* **2004**, *126*, 3496−3510. (c) Sanford, M. S.; Love, J. A.; Grubbs, R. H. Mechanism and Activity of Ruthenium Olefin Metathesis Catalysts. *J. Am. Chem. Soc.* **2001**, *123*, 6543−6554.
(9) (a) Cavallo, L. Mechanism of Ruthenium-Catalyzed Olefin Metathesis Reactions from a Theoretical Perspective. *J. Am. Chem. Soc.* **2002**, *124*, 8965−8973. (b) Falivene, L.; Cavallo, L. Theoretical NMR Spectroscopy of N-heterocyclic Carbenes and their Metal Complexes. *Coord. Chem. Rev.* **2017**, *344*, 101−114.
(10) Sajith, P. K.; Suresh, C. H. Bond Dissociation Energies of Ligands in Square Planar Pd(II) and Pt(II) Complexes: An Assessment Using Trans Influence. *J. Organomet. Chem.* **2011**, *696*, 2086−2092.
(11) Antonova, N. S.; Carbó, J. J.; Poblet, J. M. Quantifying the Donor−Acceptor Properties of Phosphine and N-Heterocyclic Carbene Ligands in Grubbs' Catalysts Using a Modified EDA Procedure Based on Orbital Deletion. *Organometallics* **2009**, *28*, 4283−4287.
(12) Credendino, R.; Falivene, L.; Cavallo, L. π-Face Donation from the Aromatic N-Substituent of N-Heterocyclic Carbene Ligands to Metal and Its Role in Catalysis. *J. Am. Chem. Soc.* **2012**, *134*, 8127−8135.
(13) Halbert, S.; Copéret, C.; Raynaud, C.; Eisenstein, O. Elucidating the Link between NMR Chemical Shifts and Electronic Structure in d^0 Olefin Metathesis Catalysts. *J. Am. Chem. Soc.* **2016**, *138*, 2261−2272.
(14) (a) Chen, W.-C.; Shih, W.-C.; Jurca, T.; Zhao, L.-L.; Andrada, D. M.; Peng, C.-J.; Chang, C.-C.; Liu, S.-K.; Wang, Y.-P.; Wen, Y.-S.; Yap, G. P. A.; Hsu, C.-P.; Frenking, G.; Ong, T. G. Carbodicarbenes: Unexpected π-Accepting Ability during Reactivity with Small Molecules. *J. Am. Chem. Soc.* **2017**, *139*, 12830−12836. (b) Andrada, D. M.; Holzmann, N.; Hamadi, T.; Frenking, G. Direct Estimate of the Internal π-donation to the Carbene Centre within N-heterocyclic Carbenes and Related Molecules. *Beilstein J. Org. Chem.* **2015**, *11*, 2727−2736. (c) Jerabek, P.; Roesky, H. W.; Bertrand, G.; Frenking, G. Coinage Metals Binding as Main Group Elements: Structure and Bonding of the Carbene Complexes $[TM(cAAC)_2]$ and $[TM(cAAC)_2]^+$ (TM = Cu, Ag, Au). *J. Am. Chem. Soc.* **2014**, *136*, 17123−17135. (d) Tonner, R.; Frenking, G. Tolman's Electronic Parameters for Divalent Carbon(0) Compounds. *Organometallics* **2009**, *28*, 3901−3905. (e) Krapp, A.; Pandey, K. K.; Frenking, G. Transition Metal-Carbon Complexes. A Theoretical Study. *J. Am. Chem. Soc.* **2007**, *129*, 7596−7610.
(15) (a) Vummaleti, S. V. C.; Nelson, D. J.; Poater, A.; Gómez-Suarez, A.; Cordes, D. B.; Slawin, A. M. Z.; Nolan, S. P.; Cavallo, L. What Can NMR Spectroscopy of Selenoureas and Phosphinidenes Teach us About the π-Accepting Abilities of N-Heterocyclic Carbenes? *Chem. Sci.* **2015**, *6*, 1895−1904. (b) Jacobsen, H.; Correa, A.; Poater, A.; Costabile, C.; Cavallo, L. Understanding the M (NHC) (NHC = N-Heterocyclic Carbene) Bond. *Coord. Chem. Rev.* **2009**, *253*, 687−703. (c) Martin, D.; Melaimi, M.; Soleilhavoup, M.; Bertrand, G. A Brief Survey of Our Contribution to Stable Carbene Chemistry. *Organometallics* **2011**, *30*, 5304−5313.
(16) (a) Süßner, M.; Plenio, H. π-Face Donor Properties of N-heterocyclic carbenes. *Chem. Commun.* **2005**, 5417−5419. (b) Sashuk, V.; Peeck, L. H.; Plenio, H. $[(NHC)(NHC_{ewg})RuCl_2(CHPh)]$ Complexes with Modified NHC_{ewg} Ligands for Efficient Ring-Closing Metathesis Leading to Tetrasubstituted Olefins. *Chem. - Eur. J.* **2010**, *16*, 3983−3993. (c) Peeck, L. H.; Savka, R. D.; Plenio, H. Fast Olefin Metathesis at Low Catalyst Loading. *Chem. - Eur. J.* **2012**, *18*, 12845−12853.
(17) Tsipis, A. C.; Orpen, A. G.; Harvey, J. N. Substituent Effects and the Mechanism of Alkene Metathesis Catalyzed by Ruthenium Dichloride Catalysts. *Dalton Trans.* **2005**, 2849−2858.
(18) Jacobsen, H. P-Heterocyclic Carbenes as Potential Ligands in the Design of New Metathesis Catalysts. A Computational Study. *Dalton Trans.* **2006**, 2214−2224.
(19) Getty, K.; Delgado-Jaime, M. U.; Kennepohl, P. An Electronic Rationale for Observed Initiation Rates in Ruthenium-Mediated Olefin Metathesis: Charge Donation in Phosphine and N-Heterocyclic Carbene Ligands. *J. Am. Chem. Soc.* **2007**, *129*, 15774−15776.
(20) Poater, A.; Cavallo, L. A Comprehensive Study of Olefin Metathesis Catalyzed by Ru-Based Catalysts. *Beilstein J. Org. Chem.* **2015**, *11*, 1767−1780.
(21) Minenkov, Y.; Occhipinti, G.; Heyndrickx, W.; Jensen, V. R. The Nature of the Barrier to Phosphane Dissociation from Grubbs Olefin Metathesis Catalysts. *Eur. J. Inorg. Chem.* **2012**, *2012*, 1507−1516.
(22) (a) Frenking, G.; Solà, M.; Vyboishchikov, S. F. Chemical Bonding in Transition Metal Carbene Complexes. *J. Organomet. Chem.* **2005**, *690*, 6178−6204. (b) Vyboishchikov, S. F.; Frenking, G. Chemical Bonding in Transition Metal Carbene Complexes. *Chem. - Eur. J.* **1998**, *4*, 1428−1438.
(23) (a) du Toit, J.-I.; van Sittert, C. G. C. E.; Vosloo, H. C. M. Towards a Better Understanding of Alkene Metathesis: Elucidating the Properties of the Major Metal Carbene Catalyst Types. *Monatsh. Chem.* **2015**, *146*, 1115−1129. (b) Santamaria, J.; Aguilar, E. Beyond Fischer and Schrock Carbenes: Non-Heteroatom-Stabilized Group 6 Metal Carbene Complexes − a General Overview. *Org. Chem. Front.* **2016**, *3*, 1561−1588. (c) Esteruelas, M. A.; Gonzalez, A. I.; Lopez, A. M.; Onate, E. An Osmium-Carbene Complex with Fischer−Schrock Ambivalent Behavior. *Organometallics* **2003**, *22*, 414−425. (d) Whited, M. T.; Grubbs, R. H. Late Metal Carbene Complexes Generated by Multiple C−H Activations: Examining the Continuum of M═C Bond Reactivity. *Acc. Chem. Res.* **2009**, *42*, 1607−1616.
(24) Occhipinti, G.; Jensen, V. R. Nature of the Transition Metal−Carbene Bond in Grubbs Olefin Metathesis Catalysts. *Organometallics* **2011**, *30*, 3522−3529.
(25) Louie, J.; Grubbs, R. H. Metathesis of Electron-Rich Olefins: Structure and Reactivity of Electron-Rich Carbene Complexes. *Organometallics* **2002**, *21*, 2153−2164.
(26) (a) Wu, Z.; Nguyen, S.-B. T.; Grubbs, R. H.; Ziller, J. W. Reactions of Ruthenium Carbenes of the Type $(PPh_3)_2(X)_2Ru{:}CH{-}CH{:}CPh_2$ (X = Cl and CF3COO) with Strained Acyclic Olefins and Functionalized Olefins. *J. Am. Chem. Soc.* **1995**, *117*, 5503−5511. (b) Katayama, H.; Nagao, M.; Ozawa, F. Convenient Route to Fischer-Type Carbene Ruthenium Complexes: Highly Selective Catalysts for Ring Opening/Cross-Metathesis of Norbornene Derivatives. *Organometallics* **2003**, *22*, 586−593.
(27) Schrock, R. R.; Hoveyda, A. H. Molybdenum and Tungsten Imido Alkylidene Complexes as Efficient Olefin-Metathesis Catalysts. *Angew. Chem., Int. Ed.* **2003**, *42*, 4592−4633.
(28) Karen, P.; McArdle, P.; Takats, J. Comprehensive Definition of Oxidation State (IUPAC Recommendations 2016). *Pure Appl. Chem.* **2016**, *88*, 831−839.
(29) Monsch, G.; Klüfers, P. $[Fe(H_2O)_5(NO)]^{2+}$, the "Brown-Ring" Chromophore. *Angew. Chem., Int. Ed.* **2019**, *58*, 8566−8571.
(30) Postils, V.; Delgado-Alonso, C.; Luis, J. M.; Salvador, P. An Objective Alternative to IUPAC's Approach To Assign Oxidation States. *Angew. Chem., Int. Ed.* **2018**, *57*, 10525−10529.
(31) Ramos-Cordoba, E.; Postils, V.; Salvador, P. Oxidation States from Wave Function Analysis. *J. Chem. Theory Comput.* **2015**, *11*, 1501−1508.
(32) (a) Klein, J. E. M. N.; Havenith, R. W. A.; Knizia, G. The Pentagonal-Pyramidal Hexamethylbenzene Dication: Many Shades of Coordination Chemistry at Carbon. *Chem. - Eur. J.* **2018**, *24*, 12340−12345. (b) Castiñeira Reis, M.; Marín-Luna, M.; Silva López, C.;

DOI: 10.1021/acs.organomet.9b00591
Organometallics 2019, 38, 4585−4592

Faza, O. N. $[MoO_2]^{2+}$-Mediated Oxygen Atom Transfer via an Unusual Lewis Acid Mechanism. *Inorg. Chem.* **2017**, *56*, 10570−10575. (c) Poater, J.; Gimferrer, M.; Poater, A. Covalent and Ionic Capacity of MOFs To Sorb Small Gas Molecules. *Inorg. Chem.* **2018**, *57*, 6981−6990. (d) Min, X.; Popov, I. A.; Pan, F.-X.; Li, L.-J.; Matito, E.; Sun, Z.-M.; Wang, L.-S.; Boldyrev, A. I. All-Metal Antiaromaticity in Sb_4-Type Lanthanocene Anions. *Angew. Chem., Int. Ed.* **2016**, *55*, 5531−5535. (e) Skara, G.; Gimferrer, M.; De Proft, F.; Salvador, P.; Pinter, B. Scrutinizing the Noninnocence of Quinone Ligands in Ruthenium Complexes: Insights from Structural, Electronic, Energy, and Effective Oxidation State Analyses. *Inorg. Chem.* **2016**, *55*, 2185−2199. (f) Steen, J. S.; Knizia, G.; Klein, J. E. M. N. σ-Noninnocence: Masked Phenyl-Cation Transfer at Formal Ni^{IV}. *Angew. Chem., Int. Ed.* **2019**, *58*, 13133−13139.

(33) Wenzel, A. G.; Grubbs, R. H. Ruthenium Metallacycles Derived from 14-Electron Complexes. New Insights into Olefin Metathesis Intermediates. *J. Am. Chem. Soc.* **2006**, *128*, 16048−16049.

(34) Vasiliu, M.; Arduengo, A. J., III; Dixon, D. A. Role of Electronegative Substituents on the Bond Energies in the Grubbs Metathesis Catalysts for M = Fe, Ru, Os. *J. Phys. Chem. C* **2014**, *118*, 13563−13577.

(35) Watson, L. A.; Ozerov, O. V.; Pink, M.; Caulton, K. G. Four-Coordinate, Planar Ru(II). A Triplet State as a Response to a 14-Valence Electron Configuration. *J. Am. Chem. Soc.* **2003**, *125*, 8426−8427.

(36) (a) Poater, A.; Chaitanya Vummaleti, S. V.; Pump, E.; Cavallo, L. Comparing Ru and Fe-Catalyzed Olefin Metathesis. *Dalton Trans.* **2014**, *43*, 11216−11220. (b) Poater, A.; Pump, E.; Vummaleti, S. V. C.; Cavallo, L. The Activation Mechanism of Fe-Based Olefin Metathesis Catalysts. *Chem. Phys. Lett.* **2014**, *610*−*611*, 29−32.

(37) At M06/cc-pVTZ ∼ sdd//BP86/TZVP ∼ sdd level to deal with the spin states of iron accurately, bearing the ruthenium as a reference, metallacycle **IV**, with respect to precatalyst **I**, is 1.0 kcal/mol more stable for osmium, whereas it is 13.6 kcal/mol more stable for iron.

(38) De Brito Sá, E.; Rodríguez-Santiago, L.; Sodupe, M.; Solans-Monfort, X. Toward Olefin Metathesis with Iron Carbene Complexes: Benefits of Tridentate σ-Donating Ligands. *Organometallics* **2016**, *35*, 3914−3923.

(39) (a) Vummaleti, S. V. C.; Cavallo, L.; Poater, A. The Driving Force Role of Ruthenacyclobutanes. *Theor. Chem. Acc.* **2015**, *134*, 22−27. (b) Nuñez-Zarur, F.; Solans-Monfort, X.; Rodríguez-Santiago, L.; Sodupe, M. Differences in the Activation Processes of Phosphine-Containing and Grubbs−Hoveyda-Type Alkene Metathesis Catalysts. *Organometallics* **2012**, *31*, 4203−4215.

(40) Zhao, Y.; Truhlar, D. G. The M06 Suite of Density Functionals for Main Group Thermochemistry, Thermochemical Kinetics, Noncovalent Interactions, Excited States, and Transition Elements: Two New Functionals and Systematic Testing of Four M06-Class Functionals and 12 Other Functionals. *Theor. Chem. Acc.* **2008**, *120*, 215−241.

(41) Zhao, Y.; Truhlar, D. G. A New Local Density Functional for Main-Group Thermochemistry, Transition Metal Bonding, Thermochemical Kinetics, and Noncovalent Interactions. *J. Chem. Phys.* **2006**, *125*, 194101.

(42) (a) Grimme, S.; Antony, J.; Ehrlich, S.; Krieg, H. A Consistent and Accurate Ab Initio Parametrization of Density Functional Dispersion Correction (DFT-D) for the 94 Elements H-Pu. *J. Chem. Phys.* **2010**, *132*, 154104. (b) Grimme, S.; Ehrlich, S.; Goerigk, L. A Thorough Benchmark of Density Functional Methods for General Main Group Thermochemistry, Kinetics, and Noncovalent Interactions. *J. Comput. Chem.* **2011**, *32*, 1456−1465.

(43) (a) van der Eide, E. F.; Piers, W. E. Mechanistic Insights into the Ruthenium-Catalysed Diene Ring-Closing Metathesis Reaction. *Nat. Chem.* **2010**, *2*, 571−576. (b) Poater, A.; Pump, E.; Vummaleti, S. V. C.; Cavallo, L. The Right Computational Recipe for Olefin Metathesis with Ru-based Catalysts: the Whole Mechanism of Ring-Closing Olefin Metathesis. *J. Chem. Theory Comput.* **2014**, *10*, 4442−4448.

(44) Frisch, M. J.; Trucks, G. W.; Schlegel, H. B.; Scuseria, G. E.; Robb, M. A.; Cheeseman, J. R.; Scalmani, G.; Barone, V.; Mennucci, B.; Petersson, G. A.; Nakatsuji, H.; Caricato, M.; Li, X.; Hratchian, H. P.; Izmaylov, A. F.; Bloino, J.; Zheng, G.; Sonnenberg, J. L.; Hada, M.; Ehara, M.; Toyota, K.; Fukuda, R.; Hasegawa, J.; Ishida, M.; Nakajima, T.; Honda, Y.; Kitao, O.; Nakai, H.; Vreven, T.; Montgomery, J. A., Jr.; Peralta, J. E.; Ogliaro, F.; Bearpark, M.; Heyd, J. J.; Brothers, E.; Kudin, K. N.; Staroverov, V. N.; Kobayashi, R.; Normand, J.; Raghavachari, K.; Rendell, A.; Burant, J. C.; Iyengar, S. S.; Tomasi, J.; Cossi, M.; Rega, N.; Millam, J. M.; Klene, M.; Knox, J. E.; Cross, J. B.; Bakken, V.; Adamo, C.; Jaramillo, J.; Gomperts, R.; Stratmann, R. E.; Yazyev, O.; Austin, A. J.; Cammi, R.; Pomelli, C.; Ochterski, J. W.; Martin, R. L.; Morokuma, K.; Zakrzewski, V. G.; Voth, G. A.; Salvador, P.; Dannenberg, J. J.; Dapprich, S.; Daniels, A. D.; Farkas, O.; Foresman, J. B.; Ortiz, J. V.; Cioslowski, J.; Fox, D. J. *Gaussian 09*, revision E.01; Gaussian, Inc.: Wallingford, CT, 2009.

(45) Becke, A. Density-Functional Exchange-Energy Approximation with Correct Asymptotic Behaviour. *Phys. Rev. A: At., Mol., Opt. Phys.* **1988**, *38*, 3098−3100.

(46) (a) Perdew, J. P. Density-Functional Approximation for the Correlation Energy of the Inhomogeneous Electron Gas. *Phys. Rev. B: Condens. Matter Mater. Phys.* **1986**, *33*, 8822−8824. (b) Perdew, J. P. Erratum: Density-Functional Approximation for the Correlation Energy of the Inhomogeneous Electron Gas. *Phys. Rev. B: Condens. Matter Mater. Phys.* **1986**, *34*, 7406−7406.

(47) Weigend, F.; Ahlrichs, R. Balanced Basis Sets of Split Valence, Triple Zeta Valence and Quadruple Zeta Valence Quality for H to Rn: Design and Assessment of Accuracy. *Phys. Chem. Chem. Phys.* **2005**, *7*, 3297−3305.

(48) (a) Häussermann, U.; Dolg, M.; Stoll, H.; Preuss, H.; Schwerdtfeger, P.; Pitzer, R. M. Accuracy of Energy-Adjusted Quasirelativistic ab initio Pseudopotentials. *Mol. Phys.* **1993**, *78*, 1211−1224. (b) Küchle, W.; Dolg, M.; Stoll, H.; Preuss, H. Energy-Adjusted Pseudopotentials for the Actinides. Parameter Sets and Test Calculations for Thorium and Thorium Monoxide. *J. Chem. Phys.* **1994**, *100*, 7535−7542. (c) Leininger, T.; Nicklass, A.; Stoll, H.; Dolg, M.; Schwerdtfeger, P. The accuracy of the pseudopotential approximation. II. A Comparison of Various Core Sizes for Indium Pseudopotentials in Calculations for Spectroscopic Constants of InH, InF, and InCl. *J. Chem. Phys.* **1996**, *105*, 1052−1059.

(49) Kendall, R. A.; Dunning, T. H., Jr.; Harrison, R. J. Electron affinities of the First-Row Atoms Revisited. Systematic Basis Sets and Wave Functions. *J. Chem. Phys.* **1992**, *96*, 6796−6806.

(50) (a) Barone, V.; Cossi, M. Quantum Calculation of Molecular Energies and Energy Gradients in Solution by a Conductor Solvent Model. *J. Phys. Chem. A* **1998**, *102*, 1995−2001. (b) Tomasi, J.; Persico, M. Molecular Interactions in Solution: An Overview of Methods Based on Continuous Distributions of the Solvent. *Chem. Rev.* **1994**, *94*, 2027−2094.

(51) Salvador, P.; Ramos-Cordoba, E. *J. Chem. Phys.* **2013**, *139*, 071103.

DOI: 10.1021/acs.organomet.9b00591
Organometallics 2019, 38, 4585−4592

6.3 Unveiling the electronic structure of the Bi(+1)/Bi(+3) redox couple on NCN and NNN pincer complexes

Published in: Gimferrer, M.; Danés, S.; Andrada, D. M.; Salvador, P. *Inorg. Chem.* **2021**, 60, 23, 17657-17668.

Abstract: Low-valent group 15 compounds stabilized by pincer ligands have gained particular interest, given their direct access to fine-tune their reactivity by the coordination pattern. Recently, bismuth has been employed in a variety of catalytic transformations by taking advantage of the (+1/+3) redox couple. In this work, we present a detailed quantum–chemical study on the electronic structure of bismuth pincer complexes from two different families, namely, bis(ketimine)phenyl (NCN) and triamide bismuthinidene (NNN). The use of the so-called effective oxidation state analysis allows the unambiguous assignation of the bismuth oxidation state. In contrast to previous studies, our calculations suggest a Bi(+1) assignation for NCN pincer ligands, while Bi(+3) character is found for NNN pincer complexes. Notably, regardless of its oxidation state, the central bismuth atom disposes of up to two lone pairs for coordinating Lewis acids, as indicated by very high first and second proton affinity values. Besides, the Bi–NNN systems can also accommodate two Lewis base ligands, indicating also ambiphilic behavior. The effective fragment orbital analysis of Bi and the ligand allows monitoring of the intricate electron flow of these processes, revealing the noninnocent nature of the NNN ligand, in contrast with the NCN one. By the dissection of the electron density into effective fragment orbitals, we are able to quantify and rationalize the Lewis base/acid character.

Inorganic Chemistry

pubs.acs.org/IC

Article

Unveiling the Electronic Structure of the Bi(+1)/Bi(+3) Redox Couple on NCN and NNN Pincer Complexes

Martí Gimferrer, Sergi Danés, Diego M. Andrada,* and Pedro Salvador*

Cite This: *Inorg. Chem.* 2021, 60, 17657−17668

Read Online

ACCESS | Metrics & More | Article Recommendations | Supporting Information

ABSTRACT: Low-valent group 15 compounds stabilized by pincer ligands have gained particular interest, given their direct access to fine-tune their reactivity by the coordination pattern. Recently, bismuth has been employed in a variety of catalytic transformations by taking advantage of the (+1/+3) redox couple. In this work, we present a detailed quantum−chemical study on the electronic structure of bismuth pincer complexes from two different families, namely, bis(ketimine)phenyl (NCN) and triamide bismuthinidene (NNN). The use of the so-called effective oxidation state analysis allows the unambiguous assignation of the bismuth oxidation state. In contrast to previous studies, our calculations suggest a Bi(+1) assignation for NCN pincer ligands, while Bi(+3) character is found for NNN pincer complexes. Notably, regardless of its oxidation state, the central bismuth atom disposes of up to two lone pairs for coordinating Lewis acids, as indicated by very high first and second proton affinity values. Besides, the Bi−NNN systems can also accommodate two Lewis base ligands, indicating also ambiphilic behavior. The effective fragment orbital analysis of Bi and the ligand allows monitoring of the intricate electron flow of these processes, revealing the noninnocent nature of the NNN ligand, in contrast with the NCN one. By the dissection of the electron density into effective fragment orbitals, we are able to quantify and rationalize the Lewis base/acid character.

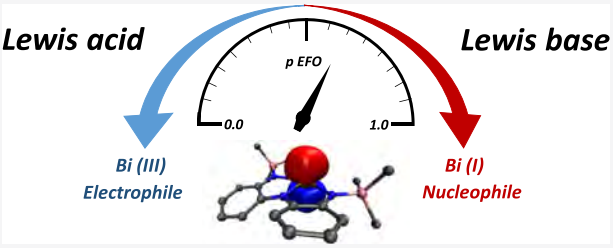

INTRODUCTION

In recent years, there has been an increasing interest in using heavier main group elements as a potential replacement of transition metals (TMs) in catalytic reactions.[1−3] The work on heavier group 15 elements, "pnictogen(Pn)-based" species P, As, Sb, and Bi, has showcased their capability to participate as catalysts in a number of reaction transformations.[4−8]

It has been recognized that the activity sharply depends on the nature of the ligand and the pnictogen center since special combinations allow to fine-tune the geometry and the oxidation state of the central pnictogen atom. Thus, a number of complexes with different rigidities, steric protection, and pnictogen centers have been experimentally accomplished.[9−11] Bismuth has brought plenty of possibilities given its ability to adopt all oxidized and reduced states from +5 to −3.[12,13] Bi-based complexes can act as catalysts in a wide variety of chemical reactions, namely, in the activation of challenging bonds,[6,8] CO_2 fixation,[14,15] or as precursors in materials science,[16,17] among others. For a recent review on bismuth catalysis, see ref 18.

Efforts are justified as nontoxic bismuth has potential applications in medicinal chemistry, in contrast to its lighter congeners (P, As, and Sb).[19−21] The utilization of tridentate rigid meridional pincer ligands has been the key to engineering the energetic levels of frontier orbitals, encompassing similar chemical bonding and reactivity patterns to transition metals and, in some cases, exhibiting unprecedented reactivity.[1] The pyramidal C_{3v} coordination mode has a lone pair in an a_1 orbital, while the e degenerated orbitals are located high in energy, resulting in typical Lewis base behavior (Figure 1A).

Pincer ligands enforce a C_{2v} coordination mode (T-shape), where the lone pair becomes an empty p-orbital (b_1), and one of the e antibonding orbitals reduces its energy, becoming a_1 lone pair in the plane of the ligand. As a result, the HOMO−LUMO gap is considerably reduced, resembling the electronic situation of a transition metal. Such a bonding situation engages reactivity as a Lewis base or acid.

Notably, the use of pincer ligands with π-conjugated systems gives another channel to tailor the reactivity via conjugation with the empty p-orbital interaction (Figure 1B). The p-orbital (b_1) of the bismuth atom can interact with b_1-orbitals of the pincer ligand on the π-system. The resulting π-bonding orbital can be located either at the bismuth or at the ligand, depending on the relative energy level of the constituting fragments, leading to an oxidation state of +1 or +3, respectively.

Received: July 25, 2021
Published: November 12, 2021

https://doi.org/10.1021/acs.inorgchem.1c02252
Inorg. Chem. 2021, 60, 17657−17668

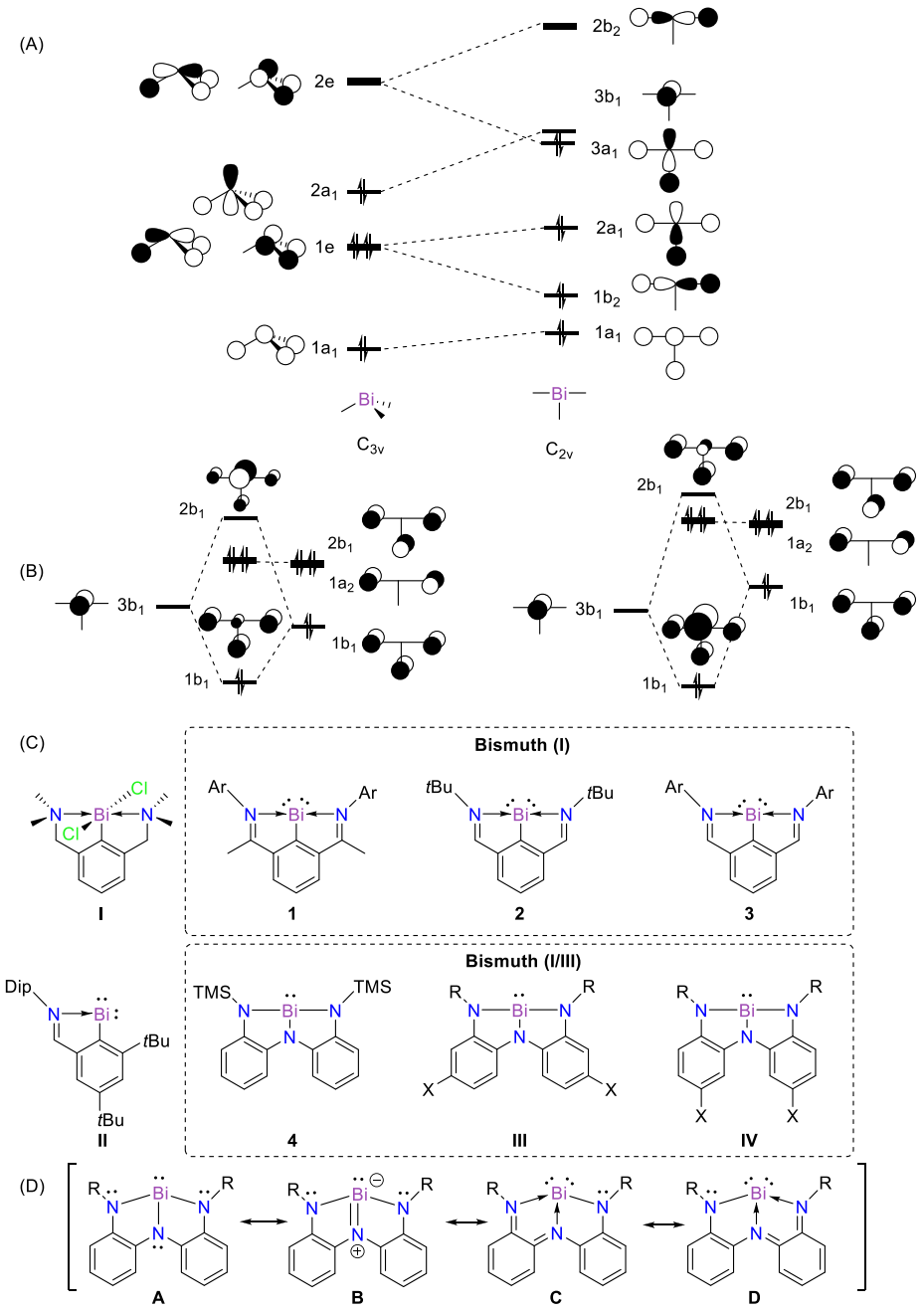

Figure 1. (A) Qualitative frontier molecular orbital diagram of BiH_3 in C_{3v} and C_{2v} symmetries. (B) Molecular orbital diagram of interaction between bismuth and the conjugated pincer; weak (left) and strong (right) π-donors. (C) Bi-based complexes: **I** (ref 22), **II** (ref 23) **1** Ar = 2,6-$Me_2C_6H_3$ (ref 24) **2**, **3** Ar = 4-$Me_2NC_6H_4$ (refs 23, 25), **4** (ref 26), **III**, and **IV** (ref 27). Dip = 1,3-diisopropylphenyl; TMS = trimethylsilyl; tBu = *tert*-butyl. (D) Possible resonance structures.

Soran et al. described the synthesis of organobismuth(+3) dihalide containing (NCN)-pincer ligand **I**.[22] The complexes presented a T-shaped $CBiCl_2$ core stabilized by two intramolecular dative N → Bi bonds. After that, Simon et al. characterized the first examples of a monomeric bismuthinidene **1**.[24] The use of 2,6-bis(ketimine)phenyl ligand ensured steric protection of the orbitals at central bismuth. Similar ligands were later used by Vránová et al. to access **2** and **3** via reduction of the corresponding chelated bismuth chlorides.[23,25] They demonstrated that the reduction outcomes are influenced by the strength of the N → Bi interaction. This led to the rational design of unprecedented two-coordinated bismuthinidene **II**.[23]

The presence of the bismuth lone pair has been proven by the ability to coordinate various transition-metal carbonyl moieties.[24] Recently, Cornella et al. demonstrated the capacity of bismuth compounds to be engaged in catalytic redox transformations by making use of the oxidation states +1 and +3. Thus, complex **2** resulted useful for the transfer hydrogenation of azoarenes and nitroarenes with ammonia-borane as a transfer agent.[5] Mechanistic investigations suggested a Bi(+3) hydride as the key intermediate. The

https://doi.org/10.1021/acs.inorgchem.1c02252
Inorg. Chem. 2021, 60, 17657−17668

same group showed that N_2O activation is facilitated by low-valent bismuth complexes through the formation of a Bi(+3) = O intermediate.[28]

The first example of a planar geometry for bismuth triamides **4** has been recently described by Kindervater et al.[26] The term "redox-confused" was coined for this compound, as it has significant Bi(+1) character but also exhibits reactivity similar to Bi(+3) electrophiles. The coordination of either pyridine *N*-oxide or $W(CO)_5$ revealed either a vacant or a filled $6p_z$-orbital at the Bi atom. Noteworthily, the assignation of **4** as a Bi(+1) species was based on previous NCN-coordinated compounds. Nonetheless, its preparation uses a Bi(+3) precursor to yield **4** without external reduction agents. This chemical behavior points toward rather ambiguous oxidation state (OS) labeling. Marczenko et al. studied the periodic trends in the structure, bonding, and reactivity of E-NNN species, where E = P, As, Sb, and Bi(**4**).[29] Their experimental and computational findings suggested a major tendency to adopt planar geometries the heavier the central atom (i.e. going down the group), which carries an evident increase in the acidity. In a subsequent study, Marczenko et al.[27] computationally explored the fine tuning of the Lewis acidity character by substitution on the aryl ring. Introducing electron-withdrawing groups such as $-CF_3$ (**5**) induced stronger Lewis acid character, while electron-donating groups such as $-OCH_3$ (**6**) lead to lower acidity, compared to **4** (see Scheme 1).

Scheme 1. Molecular Systems of Bismuth Pincer Complexes Considered in This Study

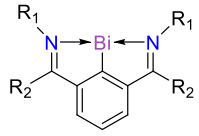

Bi-NCN

R_1= 2,6-$Me_2C_6H_3$; R_2 = Me (**1**)
R_1= *t*Bu ; R_2 = H (**2**)
R_1= 4-$Me_2NC_6H_4$; R_2= H (**3**)

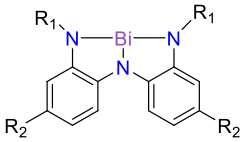

Bi-NNN

R_1= TMS ; R_2 = H (**4**)
R_1= CF_3 ; R_2= CF_3 (**5**)
R_1= Me ; R_2= OMe (**6**)

A redox couple involving closed-shell species in combination with the absence of unpaired electrons/spin density makes the oxidation state (OS) assignation particularly difficult with traditional approaches.[30,31] The OS is inherently connected to the electron distribution around the atom. Several schemes based on computational methods have been recently developed to assist in the task of OS assignation in dubious cases. Rather than relying on average quantities such as partial atomic charges or spin populations, these schemes assign individual (or pairs of) electrons to the atoms or fragments/ligands of the compound. Many of these approaches take advantage of the use of localized orbitals.[32−36] We have recently developed an automated method so-called effective oxidation state (EOS) analysis.[36] This method is based on Mayer's spin-resolved effective fragment orbitals (EFOs)[37,38] and their occupations (λ) to perform the OS assignation. The EFOs are the eigenvectors of the net fragment overlap matrix, and the corresponding eigenvalues represent the occupation numbers. Thus, the EFOs are the orbitals of the fragment's net density and, as such, they are normalized within the fragment boundary. They are obtained for each atom/fragment separately. In EOS assignation, rather than rounding the occupation to the nearest integer, the total number of α and β electrons are assigned to those EFOs with higher occupation numbers. Thus, no occupation threshold is introduced. This procedure leads to an effective configuration of each atom or fragment and hence its OS. The difference in the occupation between the last occupied (λ_{LO}) and first unoccupied (λ_{FU}) EFO indicates to which extent the electron distribution can be pictured as a discrete ionic model. In addition, a reliability index, R (%) = min (R_α, R_β), of the OS distribution can be defined for each spin case σ (α or β) as

$$R_\sigma(\%) = 100 \cdot \min(1, \max(0, \lambda^\sigma_{LO} - \lambda^\sigma_{FU} + 1/2)) \quad (1)$$

The OS assignment is considered as undisputable (R (%) = 100) when the difference in occupation of the frontier EFOs exceeds half-electron. The worst-case scenario occurs when two or more frontier EFOs from different fragments present the same occupation. In this case, two different equally plausible OS distributions would be present with R (%) = 50. Experience indicates that undisputable OS assignments are usually obtained for textbook examples of TM compounds,

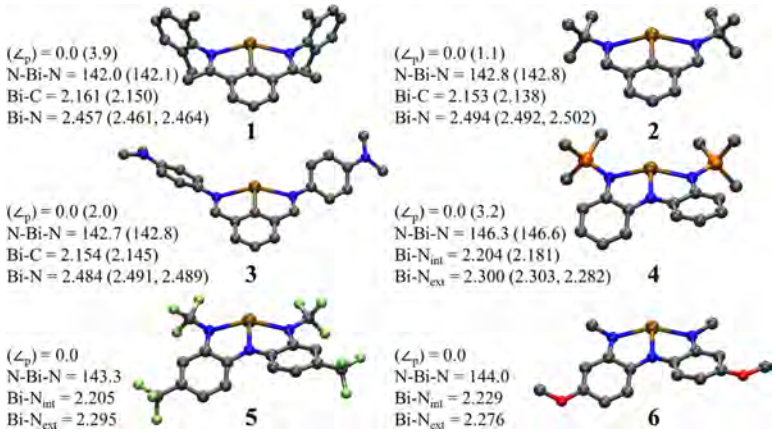

Figure 2. Optimized Bi-pincer complexes with selected bond distances (in Å) and bond angles (in deg) at B3LYP-D3(BJ)/def2-TZVPP, experimental data (in parentheses) from refs 23, 24 and 26. The pyramidalization angle ($\angle_p$) has been taken as the dihedral angle N−C−N−Bi and N−N−N−Bi. Hydrogen atoms were omitted for clarity.

https://doi.org/10.1021/acs.inorgchem.1c02252
Inorg. Chem. 2021, 60, 17657−17668

while R (%) values of around 65−70 are expected for systems with more intricate electronic structures.[39] The presence of noninnocent or redox-active ligands such as nitrosyl may lead to close-call situations with R (%) < 60 between NO(+)/NO(−) due to the high covalent character of the sigma metal−nitrosyl bond.[40] Similar high covalent character was also observed for the Ru−C bonds along the catalytic cycle of Ru-based olefin metathesis.[41]

EOS analysis has already been successfully applied to a wide variety of systems.[39,40,42−44] Most of the systems studied so far involved transition-metal compounds, but the EOS method is of general applicability. Herein, we extend the EOS scope into main group chemistry using this tool to tackle the intriguing Bi(+1/+3) redox couple. The systems considered in this work include monomeric bis(ketimine)phenyl (Bi−NCN) and triamide bismuthinidene (Bi−NNN), given their rather challenging and ambiguous bonding picture. Thus, the description by different resonance structures (Figure 1D) may lead to either oxidation state +1 or +3, which can be reduced to the question: does bismuth possess one or two lone pairs? To gain insight into the electronic structure of these complexes, we examined the oxidation state involving a series of structural variations where the size of the flanking groups R_1 is increased, and the electronic nature of the π-conjugated system is tuned by donor or electron-withdrawing groups. Beyond the mere assignation of a formal OS, the visualization of the frontier EFOs unambiguously shed light on the intricate electronic structure of these compounds. Besides, EOS analysis provides reliable and robust quantification of the Lewis acid/base character from ground-state properties, without recurring to intermediate states.

RESULTS AND DISCUSSION

Figure 2 shows the calculated optimized geometries at the B3LYP-D3(BJ)/def2-TZVPP level of theory for the studied bismuth complexes outlined in Scheme 1. The equilibrium geometries are in very good agreement with the experimental ones, when available, or with previous computational studies.[23,24] NCN-based systems **1**−**3** present a planar central moiety with a general C_{2v} symmetry. The pyramidalization angles of bismuth ($\angle_p$), taken as the dihedral angles N−C−N−Bi, are 0.0° for all computed species, while the experimentally determined are lower than 4.0° (see Figure 2).

The computed Bi−C bond lengths slightly vary throughout the series, i.e., 2.161 Å (**1**), 2.153 Å (**2**), and 2.154 Å (**3**), lying within the expected bond length of a Bi−C (2.26 Å) single and Bi=C (2.08 Å) double bond.[45] In the case of Bi−N, the bond lengths range from 2.457 Å (**1**) to 2.494 Å (**2**), which are longer than the expected bond length of a Bi−N (2.22 Å) single bond,[45] pointing to a N → Bi donor−acceptor interaction as suggested elsewhere.[20] The reported average experimental bond lengths are 2.150 Å (**1**), 2.138 Å (**2**), and 2.145 Å (**3**) for Bi−C and 2.463 Å (**1**), 2.496 Å (**2**), and 2.490 Å (**3**) for Bi−N. Although the crystal structures are not completely symmetric, there is a very good agreement with the computed ones.

The coordination of the NNN ligand in **4**−**6** is essentially planar, but the H···H repulsion between the aryl moieties induces a tilt of about 30°. This effect lowers the symmetry of the systems from C_{2v} to C_2.[26] The experimental average Bi−N_{ext} distance in **4** (2.292 Å) is in agreement with our DFT-optimized value of 2.300 Å. These values are also longer than the expected distance of a Bi−N single bond but shorter than in **1**−**3** complexes. Besides, the central Bi−N_{int} displays a shorter bond length (2.201/2.181 Å), suggesting a single bond with a weak double bond character. Such structural changes could imply a different oxidation state according to the ligand nature.

Thus, we have applied EOS analysis (see the Computational Details section for further technical details) to determine the oxidation state of bismuth. All calculations have been performed at the B3LYP-D3(BJ)/def2-TZVPP level of theory. First, since EOS had been mostly applied to TM systems, we have tested the method against a chemically diverse set of 19 Bi-based systems. The OS assignations are very clear in almost all cases (R% > 75) and in perfect agreement with the expected OS (see Table S7). The only significant exception is a dibismuthene species, for which the rather low R (%) = 58 value emerges from the essentially unpolarized covalent nature of the Bi−Bi bond. Table 1 gathers the predicted OS of systems **1**−**6**, where the fragments are the Bi atom and the pincer ligands. The occupations of the relevant EFOs for the Bi atom and the pincer ligand are also included, together with the reliability index R (%).

Table 1. Frontier EFO Occupations (in au) of Bi and Pincer Ligand (NCN or NNN) and the Assigned Oxidation States of 1−6 Complexes

	6s Bi	$6p_z$ Bi	π L	OS Bi	OS L	R (%)
1	0.93	0.59	0.41	+1	−1	68.6
2	0.93	0.59	0.41	+1	−1	68.1
3	0.93	0.60	0.40	+1	−1	69.6
4	0.91	0.43	0.57	+3	−3	65.0
5	0.92	0.39	0.61	+3	−3	71.5
6	0.91	0.48	0.52	+3	−3	58.4

Let us first consider the relatively simple Bi−NCN system **2** from Vránová et al.[23] EOS analysis gives a picture of Bi(+1) and NCN(−1) with R (%) = 68.1. Such values suggest a rather clear OS assignation at the level of theory used. The inspection of the shape and occupation number of the EFOs adds valuable information about the OS assignation process. The most relevant EFOs are depicted in Figure 3. Since the EFOs maintain the $\sigma-\pi$ separation, the respective electron distributions separately can be easily visualized. The ligand exhibits three EFOs with σ character toward the Bi center with gross occupations of 0.97, 0.86, and 0.70, respectively. The corresponding orbitals on the Bi atom are formally unoccupied with gross occupations of 0.03 (not shown), 0.14, and 0.30. Thus, with the EFOs' partitioning, the ligand is considered to have three σ lone pairs, which are coordinating a bismuth atom via dative bonds. The smaller the occupation of the lone pair, the larger the σ-donation from the ligand to the Bi center. The fact that the EFO with a smaller occupation is at the C atom of the ring is in line with the better σ-donating ability of C- than N-ligands.

Concerning the π-bonding, the NCN ligand exhibits five π-type EFOs with an occupation above 0.99, which essentially describe the five π occupied molecular orbitals of the free anionic ligand (see Figure S1 in the Supporting Information). There is an additional π-type EFO that essentially corresponds to the LUMO of the free anionic ligand (Figure 3). It exhibits a gross occupation of 0.41, smaller than that of the p-type orbital on Bi (0.59). Consequently, the EOS analysis considers the latter as formally occupied, which results in a Bi(+1)

https://doi.org/10.1021/acs.inorgchem.1c02252
Inorg. Chem. 2021, 60, 17657−17668

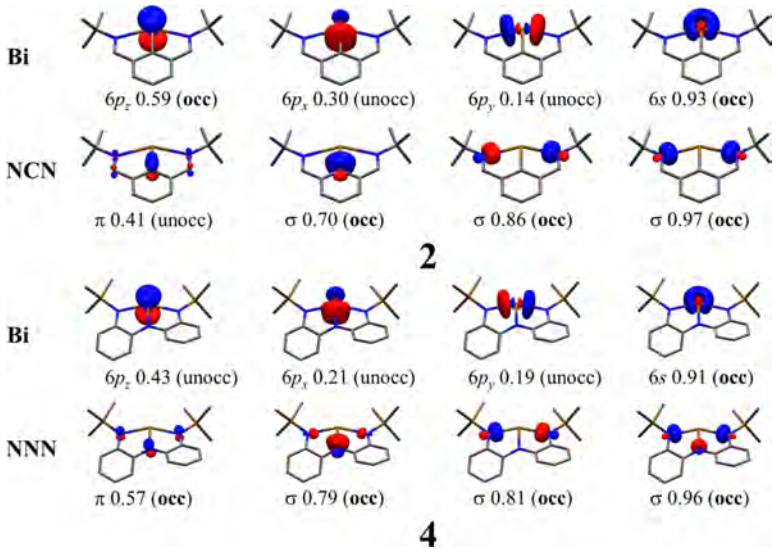

Figure 3. Effective fragment orbitals (EFOs) at the B3LYP-D3(BJ)/def2-TZVPP level of theory for **2** and **4** complexes. The orbital symmetry, gross occupation, and EOS analysis: occupied (occ) and unoccupied (unocc). The isocontour is 0.1 au. Hydrogen atoms are omitted for clarity.

assignation. Its partial Bi(+3) character originates in π-bonding due to the non-negligible occupation of the ligand's frontier π-type EFO. Replacing the *t*Bu group of **2** with phenyl derivatives in **1** and **3** has a negligible effect on the EFOs and their occupations, as shown in the Supporting Information (Figures S2 and S3). All of these systems are consistently described as Bi(+1) species.

The consistent NCN(−1) formal charge assignation should not be surprising considering the nature of the ligand. From the isolated ligand perspective, the more plausible formal charge is the one that maintains the aromaticity of the six-membered ring and that corresponds to the (−1) charge. In the hypothetical case, the ligand would gain an electron pair upon fragmentation, the fragment would become formally (−3), but these extra electrons will be located at the π-system, breaking its Hückel aromaticity.[46−48] The same aromaticity breaking would happen if the ligand would transfer electrons to the metal (see below).

The triamide NNN ligand of compounds **4**−**6** presents an intriguing situation. There are two plausible anionic states for the NNN ligand, which are associated with the Lewis structures depicted in Figure 1D. In the case of bismuth with an oxidation state of +3, the ligand would carry (−3) of the total charge, with each of the three N-coordinating atoms exhibiting two lone pairs (with σ and π symmetries). In addition, each of the phenyl rings formally bears six π-electrons, as outlined in Figure 1D (**A**). With oxidation state +1, the total charge on the ligand is (−1). This situation is best represented by two resonant Lewis structures, where only one of the coordinating N atoms bears two lone pairs and the remaining N atoms have one lone pair with N → Bi interaction (Figure 1D (**C** and **D**)). The former N atoms are conjugated with the aromatic rings and as a consequence their aromatic character decreases. Nonetheless, there are up to 16 π-electrons that can delocalize among the phenyl rings, which could make the NNN(−1) state plausible.

Notably, EOS analysis for **4** indicates a Bi(+3) center and a formal NNN(−3) ligand with *R* (%) = 65.0, in contrast with a former OS assignment.[26] The corresponding frontier EFOs are depicted in Figure 3. The shape of the EFOs is very similar to those obtained for the NCN-coordinated system **2**. The σ interaction is split, with the occupations of the ligand-centered EFOs being much higher (0.79, 0.81, 0.96) than those of the 6p-type hybrids on Bi (0.21, 0.19, and 0.04). The higher electronegativity of N (with respect to C) makes the ligand a weaker σ donor, so the $6p_x$ occupation of Bi is 0.21 rather than 0.30 as in **2**. The π system shows EFOs analogous to the Bi−NCN system, but here, the occupation of the $6p_z$ EFO on Bi (0.43) is smaller than that of the frontier π EFO on the ligand (0.57), which formally keeps the electron pair. There are eight additional π-type EFOs occupied in the ligand, thus leading to the NNN (−3) formal charge and consequently the Bi(+3) assignation (Figure S4).

As mentioned above, Marczenko et al. have explored the substituent effect on the NNN ligand.[26] We consider here two extreme systems, **5** and **6**, where $-CF_3$ and $-OCH_3$ substituents, respectively, induce opposite effects on the Lewis acid character of the Bi center. A higher Lewis acid character of Bi should be accompanied by a decrease of its $6p_z$ occupation and hence a more marked Bi(+3) character. We have performed EOS analysis on both systems and the occupation of the $6p_z$ EFO on Bi decreases from 0.43 for **4** to 0.39 for **5** and increases up to 0.48 for **6**. An opposite trend is observed for the occupation of the ligand's frontier π EFO.

Note that the assignation of the oxidation state within the EOS approach relies mainly on the dissection of the π-orbital occupation (Figure 3, first column). In most of the cases, the relative occupation of the π frontier EFOs on bismuth and pincer ligand is quite similar. The extreme case is compound **6**, where the occupations are 0.48 for Bi and 0.52 for the NNN fragment, which is translated in a rather small value of the *R* (%) index (54.8). Despite these small differences, the EOS analysis assigns the electron pairs to the ligand, leading into a formal Bi(+3). Note, however, that for the oxidation state assignation of Bi(+1), the occupation dissection is not completely different from the one observed in **1**, where the occupation of the $6p_z$-orbital at bismuth is 0.59.

The closed-call OS situation in these systems prompted us to further test the robustness of the assignments. On the one hand, we have studied both basis set and DFT functional

https://doi.org/10.1021/acs.inorgchem.1c02252
Inorg. Chem. 2021, 60, 17657−17668

Table 2. NBO Results for 1−6 Complexes: C/N−Bi Wiberg Bond Order, NBO Occupations, Orbital Contributions, and Population of Bi's $6p_z$ from the Orbital Contributions of the Bonding and Antibonding $\pi_{C/N-Bi}$ NBOs

	$WBI_{C/N-Bi}$	Pop. $6p_z$ Bi	$\sigma_{C/N-Bi}$	$\sigma^*_{C/N-Bi}$	$\pi_{C/N-Bi}$	$\pi^*_{C/N-Bi}$
1	1.09	1.43	1.95, Bi(30%)−C(70%)	0.05, Bi(70%)−C(30%)	1.83, Bi(67%)−C(33%)	0.62, Bi(33%)−C(67%)
2	1.11	1.40	1.95, Bi(30%)−C(70%)	0.05, Bi(70%)−C(30%)	1.82, Bi(65%)−C(35%)	0.62, Bi(35%)−C(65%)
3	1.12	1.40	1.95, Bi(31%)−C(69%)	0.05, Bi(69%)−C(31%)	1.82, Bi(65%)−C(35%)	0.61, Bi(35%)−C(65%)
4[a]	0.68	1.00	1.95, Bi(16%)−N(84%)	0.13, Bi(84%)−N(16%)	1.78, Bi(27%)−N(73%)	0.71, Bi(73%)−N(27%)
5[a]	0.70	0.89	1.95, Bi(16%)−N(84%)	0.11, Bi(84%)−N(16%)	1.78, Bi(24%)−N(76%)	0.62, Bi(76%)−N(24%)
6[a]	0.67	1.12	1.95, Bi(16%)−N(84%)	0.16, Bi(84%)−N(16%)	1.80, Bi(32%)−N(68%)	0.80, Bi(68%)−N(32%)

[a]Enforced Lewis structure with lower non-Lewis density % value.

Table 3. First and Second Proton Affinities (PAs)[a] and Bond Dissociation Energies Including ZPE Corrections of 1−6 with One and Two $W(CO)_5$ and $HNMe_2$ (D_0)[b,c,d,e]

	n = 1							n = 2						
system	PA/D_0	6s Bi	$6p_z$ Bi	π L	OS Bi	OS L	R (%)	PA/D_0	6s Bi	$6p_z$ Bi	π L	OS Bi	OS L	R (%)
1-$(H^+)_n$	244.2	0.92	0.34	<0.05	+3	−1	75.8	103.1	0.69	0.33	<0.05	+3	−1	50.0
1-$(W(CO)_5)_n$	48.1	0.92	0.53	0.20	+1	−1	71.0	33.2	0.87	0.55	0.13	+1	−1	78.3
2-$(H^+)_n$	243.3	0.92	0.35	<0.05	+3	−1	75.4	94.4	0.69	0.33	<0.05	+3	−1	50.0
2-$(W(CO)_5)_n$	52.0	0.92	0.54	0.19	+1	−1	73.4	37.1	0.88	0.53	0.10	+1	−1	77.7
3-$(H^+)_n$	249.6	0.92	0.36	<0.05	+3	−1	75.5	114.5	0.70	0.34	<0.05	+3	+1	53.6
3-$(W(CO)_5)_n$	53.4	0.92	0.55	0.18	+1	−1	74.1	44.1	0.87	0.52	0.10	+1	−1	76.5
4-$(H^+)_n$	220.4	0.90	0.34	<0.05	+3	−1	75.9	98.4	0.68	0.33	<0.05	+3	−1	71.6
4-$(W(CO)_5)_n$	38.7	0.90	0.48	0.31	+1	−1	65.6	34.5	0.88	0.51	0.18	+1	−1	80.2
4-$(HNMe_2)_n$	12.1	0.90	0.28	0.74	+3	−3	97.4	16.4	0.88	0.18	0.87	+3	−3	100
5-$(H^+)_n$	188.0	0.91	0.36	<0.05	+3	−1	73.7	62.5	0.69	0.34	<0.05	+3	−1	67.6
5-$(W(CO)_5)_n$	27.8	0.91	0.46	0.38	+1	−1	56.1	30.7	0.88	0.51	0.20	+1	−1	77.0
5-$(HNMe_2)_n$	20.4	0.91	0.23	0.85	+3	−3	100	21.2	0.88	0.18	0.91	+3	−3	100
6-$(H^+)_n$	229.1	0.90	0.35	<0.05	+3	−1	76.4	100.5	0.69	0.33	<0.05	+3	−1	72.8
6-$(W(CO)_5)_n$	41.9	0.90	0.51	0.25	+1	−1	73.0	39.7	0.86	0.52	0.13	+1	−1	76.7
6-$(HNMe_2)_n$	8.0	0.90	0.36	0.63	+3	−3	77.3	11.3	0.88	0.21	0.83	+3	−3	100

[a]The proton affinities are defined as $PA_1 = \Delta H(\mathbf{1-6}) + \Delta H(H^+) - \Delta H(\mathbf{1-6}\text{-}(H^+))$ and $PA_2 = \Delta H(\mathbf{1-6}\text{-}(H^+)) + \Delta H(H^+) - \Delta H(\mathbf{1-6}\text{-}(H^+)_2)$ as described in ref 54. Proton enthalpy +1.5 kcal/mol. [b]Frontier EFOs occupations (in au) of Bi and the pincer ligand (NCN or NNN) and assigned oxidation states. [c]All calculations were performed at the B3LYP-D3(BJ)/def2-TZVPP level of theory. [d]All energies are in kcal/mol. [e]Three pseudodegenerated EFOs (in occupation), one from the NCN pincer ligand and two from H atoms (one each).

dependence of the EOS results for prototypical systems **2** and **4**. The results are gathered in Table S5 of the ESI. We obtain the same OS assignations in all cases, with very small differences in the frontier EFO occupations among the different DFT functionals tested.

On the other hand, we have compared the EOS picture against the one provided by the natural bond orbital method,[49−51] which has been applied in former studies.[23,26] Table 2 summarizes the contributions of the most relevant localized orbitals involving Bi. More details about the shape and contribution of the NBOs are collected in Tables S8−S17 of the SI.

The orbital localization leads in all cases to a 6s-type bismuth lone pair with an occupation of ca. 2 electrons, as described by Vránová et al.[23] In systems **1−3**, the σ-type interaction between Bi and the pincer ligand is represented by one lone pair on each N atom and a two-electron Bi−C bond polarized toward the ligand's C atom. In addition, we obtain a bonding Bi−C π-bond polarized toward Bi with an occupation of ca. 1.8, and the corresponding antibonding NBO with the reversed bond polarization and an occupation of ca. 0.60. This clear Bi(+1) picture is in perfect agreement with our EOS results.

It is worth pointing out that our results for **3** differ from those obtained by Vránová et al. for the same system,[23] where instead of a Bi−C π-bond they obtain a fully localized $6p_z$ orbital on Bi with an occupation of 1.35. By enforcing in the NBO analysis[52,53] to include a Bi $6p_z$ lone pair into the Lewis structure, we essentially recovered Vránová results (see Table S14), leading to a non-Lewis density value (2.35%) somewhat larger than that of the default calculation (2.19%). Both pictures reconcile by quantifying the population of the Bi $6p_z$ natural atomic orbital from the bonding and antibonding Bi−C π-bonds, as gathered in Table 2. Nonetheless, in our opinion, the two-electron bonding/antibonding NBO description permits a much closer connection with IUPAC's winner-takes-all principle (in line with the LOBA[32] approach for OS assignation).

The $6p_z$ lone-pair picture also emerged by default for system **4** with an occupation as low as 1.0 (Table S11), in perfect agreement with the results reported by Kindervater et al.[26] However, the default NBO analysis of complexes **5−6** lead instead to a pair of bonding and antibonding Bi−N π-bonds clearly polarized toward the ligand's atom and to some minor differences in the σ-bonding involving Bi (lone-pair vs strongly polarized bond, see Tables S12 and S13).

According to Marczenko et al.[27] and to EOS analysis, one would expect the Bi(+3) character of **4** to lie somewhat in between **5** and **6**. This is precisely what could be inferred from the population of the calculated Bi $6p_z$ orbital in Table 2. Moreover, the WBI_{N-Bi} values for **4−6** are very similar (the same as among **1−3**), which does not seem to indicate that a

https://doi.org/10.1021/acs.inorgchem.1c02252
Inorg. Chem. 2021, 60, 17657−17668

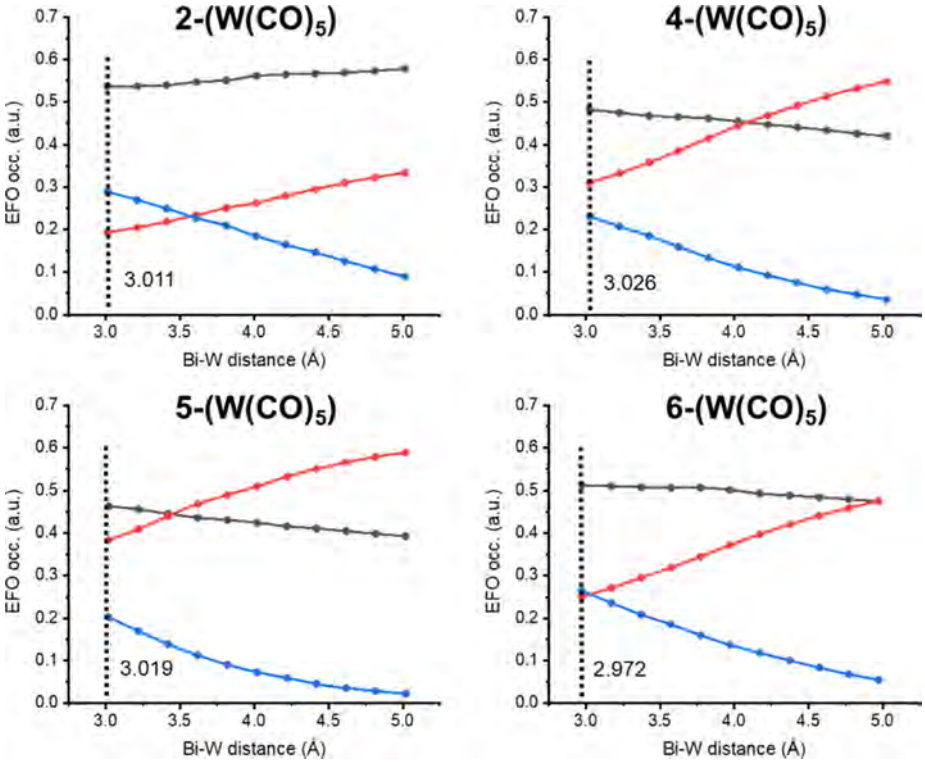

Figure 4. Gross EFO occupations along the Bi−W bond distance for species **2**-($W(CO)_5$), **4**-($W(CO)_5$), **5**-($W(CO)_5$), and **6**-($W(CO)_5$). Bi $6p_z$ (grey line), NCN/NNN π-type (red line) and W σ-type (blue line).

significantly different picture is expected for **4**, **5**, and **6**. We then opted for an enforced NBO analysis for **4**−**6** leading to a picture analogous to that obtained for **1**−**3**, that is, including a pair of bonding and antibonding Bi−N π-bonds and the two lone pairs on the N centers. To our surprise, the non-Lewis density values were smaller than those obtained by the default calculations in all cases (see Tables S15−S17).

So, it appears that different formal pictures (not necessarily associated with the lowest non-Lewis density value) can be obtained with NBO analysis by default, which hinders the comparison of the bonding situation among Bi−NCN and Bi−NNN systems. Considering the same NBO solution for all systems (which is also the one with lower non-Lewis density values) clearly confirms that the Bi−C π-bond polarity in **1**−**3** (toward Bi) is completely reversed in the case of **4**−**6** (toward N), in full agreement with EOS. A clear advantage of EOS analysis for these systems is that it readily permits a straight comparison of the electronic structure of all systems on equal footing, independently of the dominant Lewis structure.

To further corroborate the relationship between the occupation of the EFOs and the Lewis base properties, we have computed the first and the second proton affinities for compounds **1**−**6**. Previous studies have shown that the first and second proton affinities (PAs) are sensitive probes for the presence of chemically available lone pairs of a molecule.[55−59] Thus, the values provide information about the location and the ability of the lone pairs to coordinate Lewis acids.

Table 3 gathers the calculated PAs of **1**−**6** at the B3LYP-D3(BJ)/def2-TZVPP level of theory. The first PAs of all compounds, but **5**, are higher than 220 kcal/mol, which suggests a highly basic nature. Note that the calculated PA values follow the trend of the occupation of the $6p_z$ EFOs of the Bi atom. The highest PA is for **3** (249.6 kcal/mol) with a $6p_z$ occupation of 0.60. At the other extreme, compounds **5** has a PA (188 kcal/mol) and an occupation of 0.39. The first PA also closely follows the trends of the 6s and $6p_z$ natural atomic orbital (NAO) energies, in line with the findings of Chval et al.[60] for donor−acceptor adducts driven by electrostatic interactions.

Applying EOS analysis on compounds **1**−**6**-(H^+) shows a clear picture with Bi(+3), NCN/NNN(−1), and H(−1) assignation. Such situation results from the different electronegativity of H and Bi, which implies formal oxidation of the Bi center to Bi(+3), while the H moiety is pictured as a hydride (−1). Bi(+3)-hydride **2**-(H^+) was postulated as an intermediate in the catalytic dehydrogenation of ammonia-borane with **2**. This species was detected by high-resolution mass spectrometry (MS), but all attempts for its isolation were unsuccessful.[5] Noteworthily, regardless of the formal nature of the Bi center (+1 in **1**−**3** and +3 in **4**−**6**), we observe in all cases a full decay of the π-EFO occupation (<0.05) of the ligand upon hydride formation. In **1**−**3**, Bi is electronically rich enough and readily provides the electron pair to form the hydride, thereby formally oxidizing to +3. In **4**−**6**, it is mainly the NNN ligand that provides the electrons to form the hydride.

Table 3 also gathers the calculated values for the second PA of the molecules, which are particularly important for testing the coordinating ability of the second lone pair and hence the Bi(+1) character. The values are relatively high (ca. 100 kcal/mol) and comparable to those reported for divalent ylidone E(0) compounds.[55−59] The reported values for the elusive Pb(0) species are 273.8 and 114.9 kcal/mol for the first and second proton affinities, respectively.[55] The correlation with

https://doi.org/10.1021/acs.inorgchem.1c02252
Inorg. Chem. 2021, 60, 17657−17668

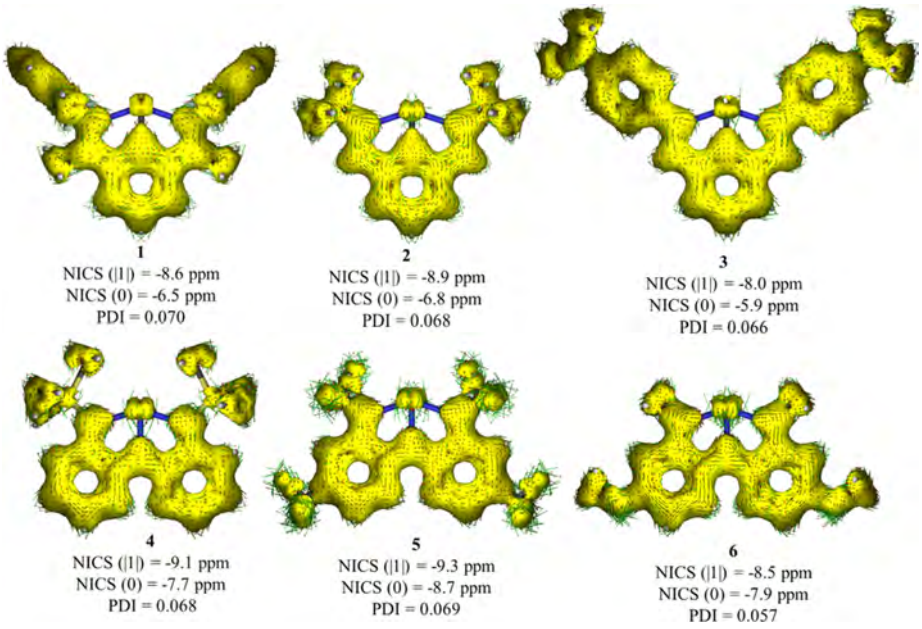

Figure 5. AICD plot of **1**−**6** at B3LYP-D3(BJ)/def2-TZVPP isosurface values (0.03 au) together with NICS (in ppm) and PDI values of the phenyl rings. For AICD, clockwise and counterclockwise circulations suggest diatropicity and paratropicity, respectively. Computed reference values (benzene): NICS (|1|) = −10.1 ppm, NICS (0) = −8.2 ppm, PDI = 0.098.

the Bi's $6p_z$ occupation of the deprotonated species is not as good as for the first PA. In fact, the second PA should probe the second available lone pair on Bi, which corresponds to a 6s-type EFO exhibiting a large and constant occupation of ca. 0.90 for all species. This explains why the second PA is rather constant among the systems studied, no matter their formal OS is Bi(+1) or Bi(+3). Species **5** is the only exception, for which both the first and second PAs are somewhat smaller than for the rest of the systems, in line with its weakest Lewis basic character. Noteworthily, the energies of the 6s and $6p_z$ NAO of the monoprotonated species do follow closely the trend of the second PA.

Our calculations suggest that both formal Bi(+1) and Bi(+3) are able to coordinate two strongly polarizing Lewis acids. The second protonation is likely to be experimentally unachievable, considering that already the single Bi(+3)-hydride has not yet been isolated. EOS analysis of these species also indicate only partial hydride character of the H moieties, as Bi remains with the formal OS of (+3) in all cases.

We also considered the adducts with the electron-deficient $W(CO)_5$ species (**1**−**6**-($\mathbf{W(CO)_5}$)).[23] The successful synthesis of tungsten complexes is typically used as an experimental signature of Bi(+1) character, where the available $6p_z$ electrons of Bi are used to form a dative Bi → W bond. Hence, upon reaction with the $W(CO)_5$ Lewis acid, the Bi center should formally remain Bi(+1). Indeed, the results of the EOS analysis are in full agreement with these considerations. For instance, for **2**-($\mathbf{W(CO)_5}$) EOS gives a clear Bi(+1), NCN(−1) and $W(CO)_5$(0) assignment, with R (%) = 73.4. The OS assignation is driven by newly formed bond, as the σ interaction between Bi and NCN ligand remains essentially unchanged (see most relevant EFOs in Figure S5). However, when bonded to the $W(CO)_5$ unit, the occupation of the $6p_z$ EFO on Bi slightly decreases from 0.59 (**2**) to 0.54e (**2**-$\mathbf{W(CO)_5}$). Also, the occupation of the frontier π EFO on the ligand drops from 0.41 (**2**) to 0.19 (**2**-$\mathbf{W(CO)_5}$). These electrons are used to populate the otherwise empty σ-type EFO on the $W(CO)_5$ moiety (0.29). Still, the large occupation of the $6p_z$ EFO of Bi indicates its predominant Bi(+1) character. The π-density of the NCN ligand is significantly altered, but still the ligands act formally as a spectator in both species.

The aforementioned OS assignation of species **4**−**6** implies that the $6p_z$ lone pair on Bi is formally absent, so they could potentially exhibit different reactivity toward Lewis acid and protonation than **1**−**3**. However, adduct **4**-$\mathbf{W(CO)_5}$ was observed and characterized by MS and NMR spectroscopy,[28] which could be in an apparent contradiction to the Bi(+3) assignment.

Notably, the dissociation energies of the adducts **1**−**6** exhibit again an excellent correlation with the Bi $6p_z$ occupation of the precursor, no matter the formal OS of the Bi center. Thus, the smaller the occupation, the smaller the D_0 value, in line with a more pronounced Bi(+3) character.

For further illustration, Figure 4 depicts the gross occupation evolution of the relevant EFOs along the Bi−NCN/N···$W(CO)_5$ dissociation profile. For **2**-($\mathbf{W(CO)_5}$), when the metal approaches Bi, the σ-EFO of the $W(CO)_5$ moiety pointing toward Bi steadily increases its occupation from essentially zero (5.0 Å) to ca. 0.2 in equilibrium (3.011 Å). This accounts for the modest donation from Bi to W. The small value is consistent with a dative picture of the Bi−W bond. However, the occupation of Bi's $6p_z$ EFO remains rather constant along the profile (gray curve) and hence the Bi(+1) character is kept. On the contrary, it is the occupation of the ligand's π EFO (red curve in Figure 4) that steadily decreases as the Lewis acid $W(CO)_5$ approaches.

The same mechanism occurs in **4**−**6**-($\mathbf{W(CO)_5}$) adducts. However, since in **4**−**6** the NNN ligand has a formal (−3) charge, the adduct formation implies formal oxidation of the ligand and reduction to Bi(+1). Figure 4 shows the π EFO occupation of NNN (red curve) steadily decreasing from its

https://doi.org/10.1021/acs.inorgchem.1c02252
Inorg. Chem. 2021, 60, 17657−17668

large value for the isolated Bi−NNN species (5.0 Å) to a value below that of Bi's $6p_z$ (gray curve) upon adduct formation. The crossing point corresponds to the formal change of OS from Bi(+3) to Bi(+1) and the corresponding oxidation of NNN. The occupation of the $6p_z$ EFO of Bi slightly increases upon adduct formation, but the electron pair of the new Bi → W bond essentially comes from the ligand's π system, which again explains the fact that these adducts are stable regardless of the formal OS of the Bi center of the precursor. The location of the crossing point in Figure 4 is in line with Lewis basic character of the latter. Thus, the formal change of OS upon coordination occurs close to equilibrium distance for the least Lewis basic species **5** (3.3 Å), followed by **4** (4.0 Å) and **6** (5.0 Å). Note that coordination to a second $W(CO)_5$ is thermodynamically plausible, despite no experimental evidence has been reported. The data in Table 3 clearly indicates that with the second $W(CO)_5$ unit the occupation of the π EFO of the ligand further halves, while that of Bi's $6p_z$ EFO remains essentially constant.

We have also considered the coordination of species **4**−**6** with one and two units of dimethylamine ($HNMe_2$). The low D_0 values obtained suggest a rather labile Lewis pair. The release $HNMe_2$ has been experimentally observed by Kindervater et al. for the preparation of **4** from **4-(HNMe$_2$)$_2$**.[26] The authors argued that the deamination leads to a reduction of the original Bi(+3) center to Bi(+1) by concomitant oxidation of the pincer ligand that would provide the electron pair, but according to our calculation, no change on the oxidation state is observed. EOS analysis of the mono- and diaminated species points to an undisputed Bi(+3) NNN(−3) character, especially for the diaminated ones. The occupation of the π EFO of the NNN ligand steadily increases going from **4** (0.57) to **4-(HNMe$_2$)** (0.74) and to **4-(HNMe$_2$)$_2$** (0.87), indicating that it is the π system of the ligand that collects the excess electrons coming from the σ-donating amines. Such substantial change in occupation is concomitant with a structural deformation of NNN that points toward a certain dearomatization of the phenyl rings upon deamination, as noted by Kindervater et al.[26] Comparing the results for species **4**−**6**, we observe a decrease of the D_0 values with the occupation of the $6p_z$ EFO on Bi, supporting the relationship between the EFO occupations with the Lewis acid/base character.

Finally, Vránová et al.[25] studied the aromaticity of **2** by means of the magnetic indicator nucleus-independent chemical shift (NICS(−1), NICS(0), and NICS(+1)), finding that the phenyl ring was clearly aromatic. To assess the π-conjugation and magnetic properties of **1**−**6**, we performed anisotropy of induced current density (AICD),[61] NICS,[62] and the electronic para-delocalization index (PDI)[63,64] analyses (see the Computational Details section). Figure 5 shows the results on the aromaticity indexes for compounds **1**−**6**. We find NICS rather inconvenient for these systems that involve rather bulky ligands that can alter their numerical values, especially for the nonplanar systems. Moreover, except for the very symmetric species, the value of NICS (1, −1) depends upon the direction from the geometric center of the ring (see Supporting Information Table S6). Therefore, we report the average of the two options as NICS (|1|). On the contrary, a much simpler electronic descriptor such as PDI can better capture the subtle changes in aromaticity.

Comparing the aromaticity indices obtained with reference values for benzene, one can clearly identify the analyzed rings as aromatic. The PDI values for species **1**−**3** are very similar, in line with the almost constant occupation of ca. 0.40 of the π-type EFO of the respective ligand. More significant changes are observed upon adduct formation or protonation. For instance, the PDI values for **2-(W(CO)$_5$)** and **2-(H$^+$)** species increase up to 0.077 and 0.083, respectively (see SI Table S6). At the same time, the occupation of the π-type EFO **in 2-(W(CO)$_5$)** and **2-(H+)** decreases to 0.19 and <0.05, respectively. Thus, the smaller the occupation of the ligand frontier π EFO, the more the NCN(−1) character and, consequently, the larger the aromaticity of the ring.

A similar trend is observed for species **4**−**6**. In this case, however, the larger the occupation of the ligand frontier π EFO, the more the NNN(−3) character and the larger the aromaticity. The PDI value of the rings in **6** is as low as 0.057, in line with the smaller π EFO occupation (0.52) and its larger share of partial NNN(−1) character. Also, protonation and adduct formation induce a decrease of the ligand's π EFO occupation (and a formal reduction of the ligand), which contrary to **1**−**3** leads to a decrease of the aromaticity.

CONCLUSIONS

The intriguing Bi(+1)/Bi(+3) redox couple on pincer complexes represents a challenging example for traditional oxidation state assignation based on the reactivity pattern. We have shown that the effective fragment orbitals and the effective oxidation states analysis affords a scrutiny of the electronic structure of the complexes from ground-state properties, i.e., without recurring to reference states. The application of this method on bismuthinidene bis(ketimine)-phenyl (NCN) and triamide bismuthinidene (NNN) pincer complexes results in a different oxidation state for the central bismuth atom, being Bi(+1) and Bi(+3), respectively. However, regardless of the formal oxidation state, all complexes are able to react with a series of Lewis bases and acids. The ambiphilic behavior of these complexes is a direct consequence of the strong π-conjugation between the bismuth atom and the pincer ligand. Interestingly, such reactivity can be quantitatively assessed by Bi's $6p_z$ effective fragment orbital occupation.

COMPUTATIONAL DETAILS

All geometry optimizations were performed using the B3LYP density functional[65,66] in combination with the def2-TZVPP basis set for H, C, N, O, F, and Si atoms.[67] For bismuth, a def2-TZVPP basis was combined with the def-ECP pseudopotential.[68] Normal mode analyses were computed to confirm minima on the potential energy surface and to calculate unscaled zero-point energies (ZPEs) as well as thermal corrections and entropy effects using the standard statistical−mechanical relationships for an ideal gas.[69] All DFT calculations were performed with the Gaussian16 package,[70] including in all cases the empirical dispersion correction of Grimme (D3),[71] together with the Becke−Johnson (BJ) damping function.[72]

Spin-resolved effective fragment orbitals (EFOs) and subsequent EOS analyses have been performed with the APOST-3D program.[73] The topological fuzzy Voronoi cells (TFVC)[74] atomic definition, a fuzzy-atom efficient and robust real-space alternative to QTAIM, has been used. The sum of the occupations of the EFOs of each fragment equals the fragment's *net* population. Gross occupations adding up to the total fragment population[36,37] have been used throughout.

https://doi.org/10.1021/acs.inorgchem.1c02252
Inorg. Chem. 2021, 60, 17657−17668

Aromaticity has been evaluated by means of the (magnetic) nuclear-independent chemical shift (NICS)[63] and the (electronic) para-delocalization index (PDI).[64] NICS values correspond to the negative value of the absolute shielding computed at the geometric ring center (NICS(0)) or at a distance above and below it and perpendicular to the ring plane. An extensively used distance value is 1 Å above (NICS(1)) and below (NICS(−1)). The larger (and negative) the value, the more aromatic the ring. The PDI is defined as the average of the bond order between atoms in the para position of the ring. Thus, it can only be applied to evaluate the aromaticity of six-membered rings. Large and positive values are obtained for aromatic rings. The NICS results have been obtained using the gauge-including atomic orbital method (GIAO)[75,76] from Gaussian16, while the PDI values were obtained with APOST-3D.

■ ASSOCIATED CONTENT

Supporting Information

The Supporting Information is available free of charge at https://pubs.acs.org/doi/10.1021/acs.inorgchem.1c02252.

Graphical representation of the relevant EFOs and their occupation for all species (Figures S1−S9), numerical data associated with Figure 4 (Tables S1−S4), benchmark of EOS analysis for **2** and **4** with several KS-DFT functionals (Table S5), aromaticity indicators for species **1**−**6** (Table S6), EOS analysis benchmark of Bi-based compounds (Table S7), and NBO analysis for species **1**−**6** (Tables S8−S17) (PDF)

Cartesian coordinates of all optimized species (XYZ)

■ AUTHOR INFORMATION

Corresponding Authors

Diego M. Andrada − *Faculty of Natural Sciences and Technology, Department of Chemistry, Saarland University, 66123 Saarbrücken, Federal Republic of Germany;* orcid.org/0000-0003-2515-7859; Email: pedro.salvador@udg.edu

Pedro Salvador − *Institut de Química Computacional i Catàlisi and Departament de Química, Universitat de Girona, 17003 Girona, Catalonia, Spain;* orcid.org/0000-0003-1823-7295; Email: diego.andrada@uni-saarland.de

Authors

Martí Gimferrer − *Institut de Química Computacional i Catàlisi and Departament de Química, Universitat de Girona, 17003 Girona, Catalonia, Spain;* orcid.org/0000-0001-5222-2201

Sergi Danés − *Institut de Química Computacional i Catàlisi and Departament de Química, Universitat de Girona, 17003 Girona, Catalonia, Spain; Faculty of Natural Sciences and Technology, Department of Chemistry, Saarland University, 66123 Saarbrücken, Federal Republic of Germany*

Complete contact information is available at: https://pubs.acs.org/10.1021/acs.inorgchem.1c02252

Notes

The authors declare no competing financial interest.

■ ACKNOWLEDGMENTS

M.G. thanks the Generalitat de Catalunya and Fons Social Europeu for the predoctoral fellowship (2018 FI_B 01120). S.D. and DMA thank ERC StG (EU805113). P.S. and M.G. were supported by the Ministerio de Ciencia, Innovación y Universidades (MCIU), grant number PGC2018-098212-B-C22. The work has been performed under Project HPC-EUROPA3 (INFRAIA-2016-1-730897), with the support of the EC Research Innovation Action under the H2020 Programme; in particular, M.G. gratefully acknowledges the support of DMA and the computing resources and technical support provided by HLRS Stuttgart.

■ REFERENCES

(1) Abbenseth, J.; Goicoechea, J. M. Recent developments in the chemistry of non-trigonal pnictogen pincer compounds: from bonding to catalysis. *Chem. Sci.* **2020**, *11*, 9728−9740.

(2) Lipshultz, J. M.; Li, G.; Radosevich, A. T. Main Group Redox Catalysis of Organopnictogens: Vertical Periodic Trends and Emerging Opportunities in Group 15. *J. Am. Chem. Soc.* **2021**, *143*, 1699−1721.

(3) Mohan, R. Green bismuth. *Nat. Chem.* **2010**, *2*, 336.

(4) Kundu, S. Pincer-Type Ligand-Assisted Catalysis and Small-Molecule Activation by non-VSEPR Main-Group Compounds. *Chem. Asian J.* **2020**, *15*, 3209−3224.

(5) Wang, F.; Planas, O.; Cornella, J. Bi(I)-Catalyzed Transfer-Hydrogenation with Ammonia-Borane. *J. Am. Chem. Soc.* **2019**, *141*, 4235−4240.

(6) Planas, O.; Wang, F.; Leutzsch, M.; Cornella, J. Fluorination of arylboronic esters enabled by bismuth redox catalysis. *Science* **2020**, *367*, 313−317.

(7) Singha, S.; Buchsteiner, M.; Bistoni, G.; Goddard, R.; Fürstner, A. A New Ligand Design Based on London Dispersion Empowers Chiral Bismuth−Rhodium Paddlewheel Catalysts. *J. Am. Chem. Soc.* **2021**, *143*, 5666−5673.

(8) Janssen-Müller, D.; Oestreich, M. Transition-Metal-Like Catalysis with a Main-Group Element: Bismuth-Catalyzed C−F Coupling of Aryl Boronic Esters. *Angew. Chem., Int. Ed.* **2020**, *59*, 8328−8330.

(9) Arduengo, A. J.; Stewart, C. A.; Davidson, F.; Dixon, D. A.; Becker, J. Y.; Culley, S. A.; Mizen, M. B. The synthesis, structure, and chemistry of 10-*Pn*-3 systems: tricoordinate hypervalent pnicogen compounds. *J. Am. Chem. Soc.* **1987**, *109*, 627−647.

(10) Ellis, B. D.; Macdonald, C. L. B. Stable compounds containing heavier group 15 elements in the +1 oxidation state. *Coord. Chem. Rev.* **2007**, *251*, 936−973.

(11) Dostál, L. Quest for stable or masked pnictinidenes: Emerging and exciting class of group 15 compounds. *Coord. Chem. Rev.* **2017**, *353*, 142−158.

(12) Walley, J. E.; Warring, L. S.; Wang, G. C.; Dickie, D. A.; Pan, S.; Frenking, G.; Gilliard, R. J. Carbodicarbene Bismaalkene Cations: Unravelling the Complexities of Carbene versus Carbone in Heavy Pnictogen Chemistry. *Angew. Chem., Int. Ed.* **2021**, *60*, 6682−6690.

(13) Planas, O.; Peciukenas, V.; Cornella, J. Bismuth-Catalyzed Oxidative Coupling of Arylboronic Acids with Triflate and Nonaflate Salts. *J. Am. Chem. Soc.* **2020**, *142*, 11382−11387.

(14) Yin, S.-F.; Maruyama, J.; Yamashita, T.; Shimada, S. Efficient Fixation of Carbon Dioxide by Hypervalent Organobismuth Oxide, Hydroxide, and Alkoxide. *Angew. Chem., Int. Ed.* **2008**, *47*, 6590−6593.

(15) Yin, S.-F.; Shimada, S. Synthesis and structure of bismuth compounds bearing a sulfur-bridged bis(phenolato) ligand and their catalytic application to the solvent-free synthesis of propylene carbonate from CO_2 and propylene oxide. *Chem. Commun.* **2009**, 1136−1138.

(16) Suzuki, H.; Matano, Y.*Organobismuth Chemistry*; Suzuki, H.; Matano, Y., Eds.; Elsevier Science: Amsterdam, 2001.

(17) Schulz, S. The chemistry of Group 13/15 compounds (III−V compounds) with the higher homologues of Group 15, Sb and Bi. *Coord. Chem. Rev.* **2001**, *215*, 1−37.
(18) Lichtenberg, C. Molecular bismuth(III) monocations: structure, bonding, reactivity, and catalysis. *Chem. Commun.* **2021**, *57*, 4483−4495.
(19) Briand, G. G.; Burford, N. Bismuth Compounds and Preparations with Biological or Medicinal Relevance. *Chem. Rev.* **1999**, *99*, 2601−2658.
(20) Sadler, P. J.; Li, H.; Sun, H. Coordination chemistry of metals in medicine: target sites for bismuth. *Coord. Chem. Rev.* **1999**, *185*−*186*, 689−709.
(21) Tiekink, E. R. T. Antimony and bismuth compounds in oncology. *Crit. Rev. Oncol./Hematol.* **2002**, *42*, 217−224.
(22) Soran, A. P.; Silvestru, C.; Breunig, H. J.; Balázs, G.; Green, J. C. Organobismuth(III) Dihalides with T-Shaped Geometry Stabilized by Intramolecular N→Bi Interactions and Related Diorganobismuth-(III) Halides. *Organometallics* **2007**, *26*, 1196−1203.
(23) Vránová, I.; Alonso, M.; Lo, R.; Sedlák, R.; Jambor, R.; Růžička, A.; Proft, F. D.; Hobza, P.; Dostál, L. From Dibismuthenes to Three- and Two-Coordinated Bismuthinidenes by Fine Ligand Tuning: Evidence for Aromatic BiC3N Rings through a Combined Experimental and Theoretical Study. *Chem. − Eur. J.* **2015**, *21*, 16917−16928.
(24) Šimon, P.; de Proft, F.; Jambor, R.; Růžička, A.; Dostál, L. Monomeric Organoantimony(I) and Organobismuth(I) Compounds Stabilized by an NCN Chelating Ligand: Syntheses and Structures. *Angew. Chem., Int. Ed.* **2010**, *49*, 5468−5471.
(25) Vránová, I.; Kremláček, V.; Erben, M.; Turek, J.; Jambor, R.; Růžička, A.; Alonso, M.; Dostál, L. A comparative study of the structure and bonding in heavier pnictinidene complexes [(ArE)M-(CO)n] (E = As, Sb and Bi; M = Cr, Mo, W and Fe). *Dalton Trans.* **2017**, *46*, 3556−3568.
(26) Kindervater, M. B.; Marczenko, K. M.; Werner-Zwanziger, U.; Chitnis, S. S. A Redox-Confused Bismuth(I/III) Triamide with a T-Shaped Planar Ground State. *Angew. Chem., Int. Ed.* **2019**, *58*, 7850−7855.
(27) Marczenko, K. M.; Jee, S.; Chitnis, S. S. High Lewis Acidity at Planar, Trivalent, and Neutral Bismuth Centers. *Organometallics* **2020**, *39*, 4287−4296.
(28) Pang, Y.; Leutzsch, M.; Nöthling, N.; Cornella, J. Catalytic Activation of N_2O at a Low-Valent Bismuth Redox Platform. *J. Am. Chem. Soc.* **2020**, *142*, 19473−19479.
(29) Marczenko, K. M.; Zurakowski, J. A.; Kindervater, M. B.; Jee, S.; Hynes, T.; Roberts, N.; Park, S.; Werner-Zwanziger, U.; Lumsden, M.; Langelaan, D. N.; Chitnis, S. S. Periodicity in Structure, Bonding, and Reactivity for p-Block Complexes of a Geometry Constraining Triamide Ligand. *Chem. − Eur. J.* **2019**, *25*, 16414−16424.
(30) Karen, P.; McArdle, P.; Takats, J. Toward a comprehensive definition of oxidation state (IUPAC Technical Report). *Pure Appl. Chem.* **2014**, *86*, 1017−1081.
(31) Karen, P.; McArdle, P.; Takats, J. Comprehensive definition of oxidation state (IUPAC Recommendations 2016). *Pure Appl. Chem.* **2016**, *88*, 831−839.
(32) Thom, A. J. W.; Sundstrom, E. J.; Head-Gordon, M. LOBA: a localized orbital bonding analysis to calculate oxidation states, with application to a model water oxidation catalyst. *Phys. Chem. Chem. Phys.* **2009**, *11*, 11297−11304.
(33) Sit, P. H.-L.; Zipoli, F.; Chen, J.; Car, R.; Cohen, M. H.; Selloni, A. Oxidation State Changes and Electron Flow in Enzymatic Catalysis and Electrocatalysis through Wannier-Function Analysis. *Chem.−Eur. J.* **2011**, *17*, 12136−12143.
(34) Vidossich, P.; Lledós, A. The use of localised orbitals for the bonding and mechanistic analysis of organometallic compounds. *Dalton Trans.* **2014**, *43*, 11145−11151.
(35) Gimferrer, M.; Comas-Vilà, G.; Salvador, P. Can We Safely Obtain Formal Oxidation States from Centroids of Localized Orbitals? *Molecules* **2020**, *25*, 234.
(36) Ramos-Cordoba, E.; Postils, V.; Salvador, P. Oxidation States from Wave Function Analysis. *J. Chem. Theory Comput.* **2015**, *11*, 1501−1508.
(37) Mayer, I. Atomic Orbitals from Molecular Wave Functions: The Effective Minimal Basis. *J. Phys. Chem. A* **1996**, *100*, 6249−6257.
(38) Ramos-Cordoba, E.; Salvador, P.; Mayer, I. The atomic orbitals of the topological atom. *J. Chem. Phys.* **2013**, *138*, No. 214107.
(39) Postils, V.; Delgado-Alonso, C.; Luis, J. M.; Salvador, P. An Objective Alternative to IUPAC's Approach To Assign Oxidation States. *Angew. Chem., Int. Ed.* **2018**, *57*, 10525−10529.
(40) Ampßler, T.; Monsch, G.; Popp, J.; Riggenmann, T.; Salvador, P.; Schröder, D.; Klüfers, P. Not Guilty on Every Count: The "Non-Innocent" Nitrosyl Ligand in the Framework of IUPAC's Oxidation-State Formalism. *Angew. Chem., Int. Ed.* **2020**, *59*, 12381−12386.
(41) Gimferrer, M.; Salvador, P.; Poater, A. Computational Monitoring of Oxidation States in Olefin Metathesis. *Organometallics* **2019**, *38*, 4585−4592.
(42) Min, X.; Popov, I. A.; Pan, F.-X.; Li, L.-J.; Matito, E.; Sun, Z.-M.; Wang, L.-S.; Boldyrev, A. I. All-Metal Antiaromaticity in Sb4-Type Lanthanocene Anions. *Angew. Chem., Int. Ed.* **2016**, *55*, 5531−5535.
(43) Steen, J. S.; Knizia, G.; Klein, J. E. M. N. σ-Noninnocence: Masked Phenyl-Cation Transfer at Formal Ni^{IV}. *Angew. Chem., Int. Ed.* **2019**, *58*, 13133−13139.
(44) Klein, J. E. M. N.; Havenith, R. W. A.; Knizia, G. The Pentagonal-Pyramidal Hexamethylbenzene Dication: Many Shades of Coordination Chemistry at Carbon. *Chem. − Eur. J.* **2018**, *24*, 12340−12345.
(45) Pyykkö, P. Additive Covalent Radii for Single-, Double-, and Triple-Bonded Molecules and Tetrahedrally Bonded Crystals: A Summary. *J. Phys. Chem. A* **2015**, *119*, 2326−2337.
(46) Hückel, E. Quantentheoretische beiträge zum benzolproblem I. Die elektronenkonfiguration des benzols und verwandter verbindungen. *Z. Phys.* **1931**, *70*, 104−186.
(47) Hückel, E. Quanstentheoretische Beiträge zum Benzolproblem. *Z. Phys.* **1931**, *72*, 310−337.
(48) Hückel, E. Quantentheoretische beiträge zum problem der aromatischen und ungesättigten verbindungen. III. *Z. Phys.* **1932**, *76*, 628−648.
(49) Glendening, E. D.; Badenhoop, J. K.; Weinhold, F. Natural resonance theory: III. Chemical applications. *J. Comp. Chem.* **1998**, *19*, 628−646.
(50) Glendening, E. D.; Weinhold, F. Natural Resonance Theory: II. Natural bond order and valency. *J. Comp. Chem.* **1998**, *19*, 610−627.
(51) Glendening, E. D.; Weinhold, F. Natural resonance theory: I. General formalism. *J. Comp. Chem.* **1998**, *19*, 593−609.
(52) Sergeieva, T.; Mandal, D.; Andrada, D. M. Chemical Bonding in Silicon Carbonyl Complexes. *Chem. − Eur. J.* **2021**, *27*, 10601−10609.
(53) Fernández, I.; Holzmann, N.; Frenking, G. The Valence Orbitals of the Alkaline-Earth Atoms. *Chem. − Eur. J.* **2020**, *26*, 14194−14210.
(54) Hunter, E. P.; Lias, S. G.; Rooney, C. M.; Winstead, J. L.; Liebman, J. F. "Thermochemical mimicry" of phenyl and vinyl groups: can it be extended to charged species? *Int. J. Mass Spectrom.* **1998**, *179*−*180*, 261−266.
(55) Takagi, N.; Frenking, G. Divalent Pb(0) compounds. *Theor. Chem. Acc.* **2011**, *129*, 615−623.
(56) Takagi, N.; Shimizu, T.; Frenking, G. Divalent E(0) compounds (E = Si-Sn). *Chem. − Eur. J.* **2009**, *15*, 8593−8604.
(57) Takagi, N.; Shimizu, T.; Frenking, G. Divalent silicon(0) compounds. *Chem. − Eur. J.* **2009**, *15*, 3448−3456.
(58) Takagi, N.; Tonner, R.; Frenking, G. Carbodiphosphorane analogues $E(PPh_3)_2$ with E=C-Pb: A theoretical study with implications for ligand design. *Chem. − Eur. J.* **2012**, *18*, 1772−1780.
(59) Klein, S.; Tonner, R.; Frenking, G. Carbodicarbenes and related divalent carbon(0) compounds. *Chem. − Eur. J.* **2010**, *16*, 10160−10170.

https://doi.org/10.1021/acs.inorgchem.1c02252
Inorg. Chem. 2021, 60, 17657−17668

(60) Chval, Z.; Dvořáčková, O.; Chvalová, D.; Burda, J. V. Square-Planar Pt(II) and Ir(I) Complexes as the Lewis Bases: Donor−Acceptor Adducts with Group 13 Trihalides and Trihydrides. *Inorg. Chem.* **2019**, *58*, 3616−3626.
(61) Geuenich, D.; Hess, K.; Kohler, F.; Herges, R. Anisotropy of the induced current density (ACID), a general method to quantify and visualize electronic delocalization. *Chem. Rev.* **2005**, *105*, 3758−3772.
(62) Chen, Z.; Wannere, C. S.; Corminboeuf, C.; Puchta, R.; Schleyer, P. v. R. Nucleus-Independent Chemical Shifts (NICS) as an Aromaticity Criterion. *Chem. Rev.* **2005**, *105*, 3842−3888.
(63) Schleyer, P. v. R.; Maerker, C.; Dransfeld, A.; Jiao, H.; van Eikema Hommes, N. J. R. Nucleus-Independent Chemical Shifts: A Simple and Efficient Aromaticity Probe. *J. Am. Chem. Soc.* **1996**, *118*, 6317−6318.
(64) Poater, J.; Fradera, X.; Duran, M.; Solà, M. The Delocalization Index as an Electronic Aromaticity Criterion: Application to a Series of Planar Polycyclic Aromatic Hydrocarbons. *Chem. − Eur. J.* **2003**, *9*, 400−406.
(65) Becke, A. D. Density-functional thermochemistry. III. The role of exact exchange. *J. Chem. Phys.* **1993**, *98*, 5648−5652.
(66) Lee, C.; Yang, W.; Parr, R. G. Development of the Colle-Salvetti correlation-energy formula into a functional of the electron density. *Phys. Rev. B* **1988**, *37*, 785−789.
(67) Weigend, F.; Ahlrichs, R. Balanced basis sets of split valence, triple zeta valence and quadruple zeta valence quality for H to Rn: Design and assessment of accuracy. *Phys. Chem. Chem. Phys.* **2005**, *7*, 3297−3305.
(68) Metz, B.; Stoll, H.; Dolg, M. Small-core multiconfiguration-Dirac−Hartree−Fock-adjusted pseudopotentials for post-d main group elements: Application to PbH and PbO. *J. Chem. Phys.* **2000**, *113*, 2563−2569.
(69) Atkins, P. W.; De Paula, J. *Physical Chemistry*, 8th ed.; Oxford University Press: New York, 2006.
(70) Frisch, M. J.; Trucks, G. W.; Schlegel, H. B.; Scuseria, G. E.; Robb, M. A.; Cheeseman, J. R.; Scalmani, G.; Barone, V.; Petersson, G. A.; Nakatsuji, H.; Li, X.; Caricato, M.; Marenich, A. V.; Bloino, J.; Janesko, B. G.; Gomperts, R.; Mennucci, B.; Hratchian, H. P.; Ortiz, J. V.; Izmaylov, A. F.; Sonnenberg, J. L.; Williams-Young, D.; Ding, F.; Lipparini, F.; Egidi, F.; Goings, J.; Peng, B.; Petrone, A.; Henderson, T.; Ranasinghe, D.; Zakrzewski, V. G.; Gao, J.; Rega, N.; Zheng, G.; Liang, W.; Hada, M.; Ehara, M.; Toyota, K.; Fukuda, R.; Hasegawa, J.; Ishida, M.; Nakajima, T.; Honda, Y.; Kitao, O.; Nakai, H.; Vreven, T.; Throssell, K.; J A Montgomery, J.; Peralta, J. E.; Ogliaro, F.; Bearpark, M. J.; Heyd, J. J.; Brothers, E. N.; Kudin, K. N.; Staroverov, V. N.; Keith, T. A.; Kobayashi, R.; Normand, J.; Raghavachari, K.; Rendell, A. P.; Burant, J. C.; Iyengar, S. S.; Tomasi, J.; Cossi, M.; Millam, J. M.; Klene, M.; Adamo, C.; Cammi, R.; Ochterski, J. W.; Martin, R. L.; Morokuma, K.; Farkas, O.; Foresman, J. B.; Fox, D. J. *Gaussian 16*, revision C.01; Gaussian, Inc.: Wallingford, CT, 2019.
(71) Grimme, S. Density functional theory with London dispersion corrections. *Wiley Interdiscip. Rev.: Comput. Mol. Sci.* **2011**, *1*, 211−228.
(72) Grimme, S.; Ehrlich, S.; Goerigk, L. Effect of the Damping Function in Dispersion Corrected Density Functional Theory. *J. Comput. Chem.* **2011**, *32*, 1456−1465.
(73) Salvador, P.; Ramos-Cordoba, E.; Gimferrer, M.; Montilla, M. *APOST-3D Program*; Universitat de Girona: Girona, Spain, 2020.
(74) Salvador, P.; Ramos-Córdoba, E. An approximation to Bader's topological atom. *J. Chem. Phys.* **2013**, *139*, No. 071103.
(75) Ditchfield, R. Self-consistent perturbation theory of diamagnetism. *Mol. Phys.* **1974**, *27*, 789−807.
(76) Wolinski, K.; Hinton, J. F.; Pulay, P. Efficient implementation of the gauge-independent atomic orbital method for NMR chemical shift calculations. *J. Am. Chem. Soc.* **1990**, *112*, 8251−8260.

https://doi.org/10.1021/acs.inorgchem.1c02252
Inorg. Chem. 2021, 60, 17657−17668

6.4 The oxidation state in low-valent beryllium and magnesium compounds

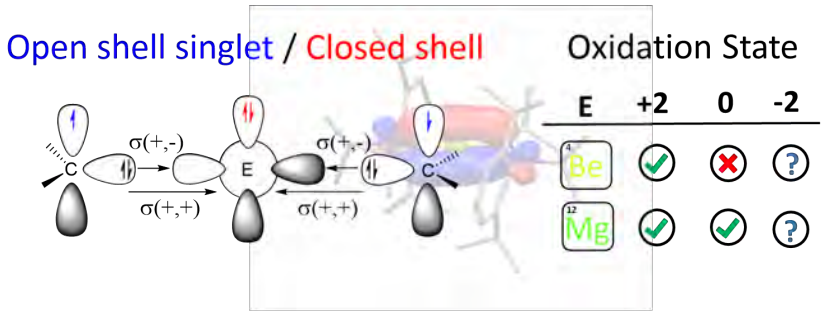

Published in: Gimferrer, M.; Danés, S.; Vos, E.; Yildiz, C. B.; Corral, I.; Jana, A.; Salvador, P.; Andrada, D. M. *Chem. Sci.* **2022**, 13, 6583-6591.

Abstract: Low-valent group 2 (E = Be and Mg) stabilized compounds have been long synthetically pursued. Here we discuss the electronic structure of a series of Lewis base-stabilized Be and Mg compounds. Despite the accepted zero(0) oxidation state nature of the group 2 elements of some recent experimentally accomplished species, the analysis of multireference wavefunctions provides compelling evidence for a strong diradical character with an oxidation state of +2. Thus, we elaborate on the distinction between a description as a donor–acceptor interaction L(0) $\leftrightarrows$ E(0) $\leftrightarrows$ L(0) and the internally oxidized situation, better interpreted as a diradical L(-1) $\rightarrow$ E(+2) $\leftarrow$ L(-1) species. The experimentally accomplished examples rely on the strengthened bonds by increasing the π-acidity of the ligand; avoiding this interaction could lead to an unprecedented low-oxidation state.

Chemical Science

ROYAL SOCIETY OF CHEMISTRY

EDGE ARTICLE

View Article Online
View Journal | View Issue

Cite this: *Chem. Sci.*, 2022, **13**, 6583

All publication charges for this article have been paid for by the Royal Society of Chemistry

Received 9th March 2022
Accepted 7th May 2022

DOI: 10.1039/d2sc01401g

rsc.li/chemical-science

The oxidation state in low-valent beryllium and magnesium compounds†

Martí Gimferrer, ‡[a] Sergi Danés,‡[ab] Eva Vos,[c] Cem B. Yildiz, [d] Inés Corral, *[c] Anukul Jana, *[e] Pedro Salvador *[a] and Diego M. Andrada *[b]

Low-valent group 2 (E = Be and Mg) stabilized compounds have been long synthetically pursued. Here we discuss the electronic structure of a series of Lewis base-stabilized Be and Mg compounds. Despite the accepted zero(0) oxidation state nature of the group 2 elements of some recent experimentally accomplished species, the analysis of multireference wavefunctions provides compelling evidence for a strong diradical character with an oxidation state of +2. Thus, we elaborate on the distinction between a description as a donor–acceptor interaction L(0) ⇆ E(0) ⇄ L(0) and the internally oxidized situation, better interpreted as a diradical L(−1) → E(+2) ← L(−1) species. The experimentally accomplished examples rely on the strengthened bonds by increasing the π-acidity of the ligand; avoiding this interaction could lead to an unprecedented low-oxidation state.

Introduction

The scope of the concept of oxidation states in main group compounds has remarkably expanded in the last two decades.[1–3] Stable singlet carbenes featuring non-oxidative electron-pair donation such as *N*-heterocyclic carbenes (NHCs)[4] and cyclic(alkyl)(amino) carbenes (cAACs)[5,6] have been crucial to preparatively access unique low oxidation states. For the description of chemical bonding, donor–acceptor interactions have been invoked, traditionally connected to transition metals.[7] Thus, the formal electron deficiency of the central atom is alleviated by σ-donation from the ligand, which is counterbalanced by a somewhat weaker π-backdonation.[7,8] While the chemistry of low-valent p-block compounds has substantially benefitted from this coordinative bonding concept, the s-block chemistry has lagged behind.[1]

The Group 2 chemistry has been long dominated by the +2 oxidation state, given the strong propensity of these elements to lose the valence electrons. Significant progress in the obtention of species with different oxidation states has been reported by Jones and co-workers on the Mg(+1) dimer compound **I** (Scheme 1), containing Mg^{I}–Mg^{I} bonds stabilized by guanidinate or β-diketiminate (NacNac) ligands.[9] Over the years, the Jones compound has evolved from curiosity into a highly selective reducing agent.[9,10] Although species with a Be^{I}–Be^{I} single bond have been computationally predicted, stable molecules featuring this bonding motif remain unrealized so far.[11–14] Zero-valent Be(0) or Mg(0) compounds **II** were also elusive until recently. In 2016, Braunschweig and co-workers reported the seminal isolation of dicoordinated neutral Be(0)(cAAC)$_2$ complexes **III**.[15] The unusual bonding situation has been rationalized in terms of donor–acceptor interactions between cAAC ligands acting as σ-donors to empty s-type orbitals of a Be(0) atom, which would have available p-type electrons to furnish a significantly strong π-backdonation towards the ligands, cAAC ← Be → cAAC (Scheme 1B).

This bonding scheme provides access to a stable beryllium radical cation **V** and a neutral species **VI**, with beryllium in the formal oxidation state of +1.[16,17] Attempts to prepare the Mg(0) congener were unsuccessful, leading instead to the ligand activation product **IV**.[18] The reaction outcome has been ascribed to the formation of the highly reactive Mg(0)(cAAC)$_2$ species, followed by ligand rearrangement. Only recently, large charge transfer has been recognized from Mg to the cAAC ligands.[19]

The quest for Mg(0) compound has been recently fulfilled by Harder and co-workers, using an extraordinarily bulky ligand (BDI* = HC{C(*t*Bu)N[2,6-(3-pentyl)-phenyl]}$_2$) to stabilize the Mg(+2) precursor.[20] The reduction with sodium powder furnished a Mg(0) compound {[(BDI*)Mg^{-}][Na^{+}]}$_2$, which upon heating yielded a three-magnesium atom cluster **VII** (recall Scheme 1). Notably, the bonding situation of the latter differs from that of the previous species, as the stability is driven by two

[a]*Institut de Química Computacional i Catàlisi, Departament de Química, Universitat de Girona, c/M. Aurelia Capmany 69, 17003, Girona, Spain. E-mail: pedro.salvador@udg.edu*

[b]*General and Inorganic Chemistry Department, University of Saarland, Campus C4.1, 66123 Saarbruecken, Germany. E-mail: diego.andrada@uni-saarland.de*

[c]*Departamento de Química, Universidad Autónoma de Madrid, c/Francisco Tomás y Valiente 7, 28049 Cantoblanco Madrid, Spain. E-mail: ines.corral@uam.es*

[d]*Department of Medicinal and Aromatic Plants, Aksaray University, Hacilar harmani 2, 68100 Aksaray, Turkey*

[e]*Tata Institute of Fundamental Research Hyderabad, Gopanpally, Hyderabad-500046, Telangana, India. E-mail: ajana@tifrh.res.in*

† Electronic supplementary information (ESI) available. See https://doi.org/10.1039/d2sc01401g

‡ These authors contributed equally to this work.

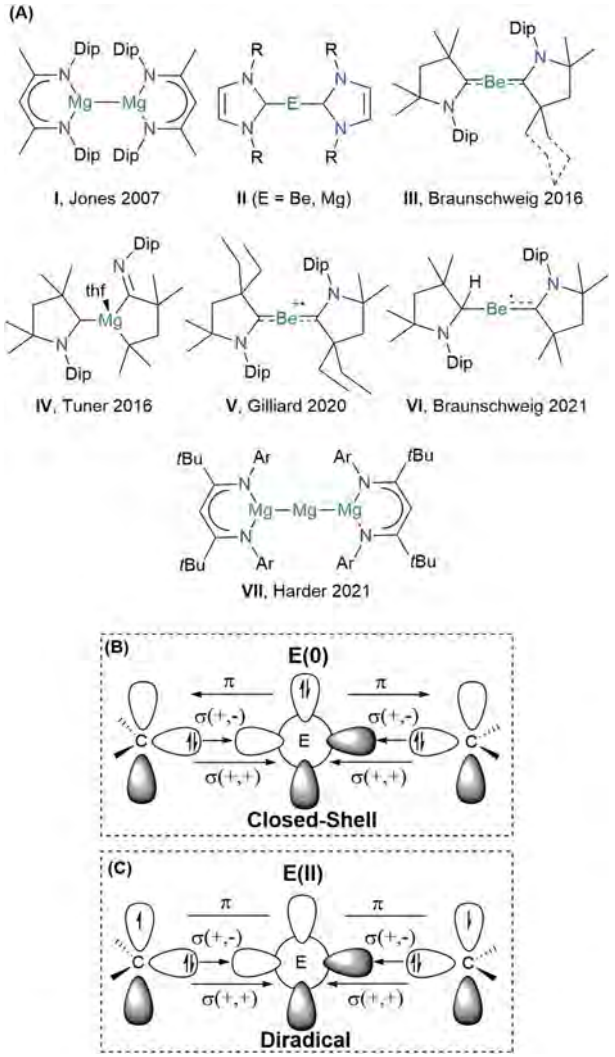

Scheme 1 (A) Schematic view of the s-block low-valent main group compounds experimentally achieved: Dip = 2,6-di*iso*propyl-phenyl; R = H, methyl, phenyl; Ar = 2,6-(3-pentyl)-phenyl. Schematic view of the orbital interactions in $E(0)L_2$ (L = NHC and cAAC): (B) donor–acceptor interaction in the singlet closed-shell electronic state, and (C) electron-sharing interaction in the open-shell singlet electronic state (diradical). Notation "+,+" and "+,−" stand for the in-phase and out-of-phase combination of lone-pair orbitals.

Mg–Mg electron-sharing bonds rather than a donor–acceptor interaction.[21]

The oxidation state assessment of these species is connected to the molecular orbital theory picture.[22] The donor–acceptor interaction in a closed-shell singlet configuration, similar to that in the Dewar–Chatt–Duncanson (DCD) model, assumes an electronic structure preorganization of E(0) from the ground state ^1S (ns^2np^0) into the doubly excited singlet state ^1D (ns^0np^2) to interact with the σ-donor/π-acceptor ligands (Scheme 1B). Within this description, applying the ionic approximation to the σ- and π-type bonds could indeed lead to the zero oxidation state picture of the alkali earth metal. Note, however, that Be ($X_P = 1.57$) and Mg ($X_P = 1.31$) are much less electronegative than C ($X_P = 2.55$).[23] Moreover, while the energy for such electron promotion is accessible for transition metals, the experimental gas-phase values for Be and Mg are as high as 178.3 and 399.9 kcal mol^{-1}, respectively.[24] A plausible alternative scenario can be postulated, whereupon bonding of the ligands, the metal centre oxidizes, and its electron pair ends up at the ligands, forming a diradical(oid) species (Scheme 1C). The interaction between the unpaired electrons would be significant in a closed-shell description, leading to the three-centre two-electron system (3c-2e). However, a broken-symmetry solution would suggest a diradical(oid) species, where the paring between the electrons is lower than optimal. A relatively small singlet–triplet gap (ΔE_{S-T}) is a key indicator for observing the diradical character.[25]

However, distinguishing between these two pictures using single-reference methods is not straightforward, if not impossible, as the incomplete description of the spin polarization can mislead the wavefunction analysis.[26] Previous investigations have pointed out the multi-reference character of related systems such as germanium $Ge(cAAC)_2$ and zinc $Zn(cAAC)_2$ counterparts.[27,28] Herein, we pinpoint the subtle features of prominent low-valent Be- and Mg-based compounds through quantum chemistry calculations.

Results and discussion

As an outset, we included NHC and cAAC ligands where the flanking groups have different stereoelectronic properties, *i.e.* methyl (Me) and 2,6-di*iso*propyl-phenyl (Dip). Both the singlet and triplet states of the systems were optimized at the B3LYP level of theory. Broken symmetry (BS) solutions, such as the open-shell singlet (OSS), lower in energy were found for the systems stabilized by cAAC ligands. In fact, the closed-shell B3LYP solution for **Be-cAAC^{Dip}** is not stable. Thus, the ground state is singlet in all cases, either closed-shell or open-shell. The relative energies of the singlet and triplet states at the B3LYP-D3(BJ)/def2-TZVPP level are relatively close, ranging from 7.9 to 2.6 kcal mol^{-1} for Be-NHC^{Dip} and Be-cAAC^{Me}, respectively and from 13.3 to 2.4 kcal mol^{-1} for Mg-NHC^{Dip} and Mg-cAAC^{Me}, respectively. The triplet state in **Mg-cAAC^{Dip}** lies 9.1 kcal mol^{-1} below the closed-shell singlet, but the ground state is of OSS nature. Similar observations have been obtained with different functionals (Tables S1–S3†).

Fig. 1 displays the ground-state geometries of the studied compounds, together with their dissociation energies (D_0) and singlet/triplet energy differences, and Table 1 shows the numerical values of their main geometrical parameters. The Be–C bond lengths vary slightly with the nature of the ligand, *i.e.* from 1.634 to 1.648 Å, in good agreement with previous studies.[11–15,19] These values fall in the expected bond lengths of single and double bonds (1.77 and 1.57 Å, respectively).[29] Moreover, the bond angles are almost collinear for all cases 167.4–179.9°, favouring a strong delocalization on the C–Be–C π-system. On the other hand, the Mg–C bond lengths are shorter than those reported by Couchman *et al.* for $Mg_2(NHC)_2$ and $Mg_2(NHC)_4$ systems.[12] Note, however, that the computed values are, in fact, longer than expected for a single bond Mg–C (2.14 Å). Only in the case of the **Mg-cAAC^{Dip}** compound, the

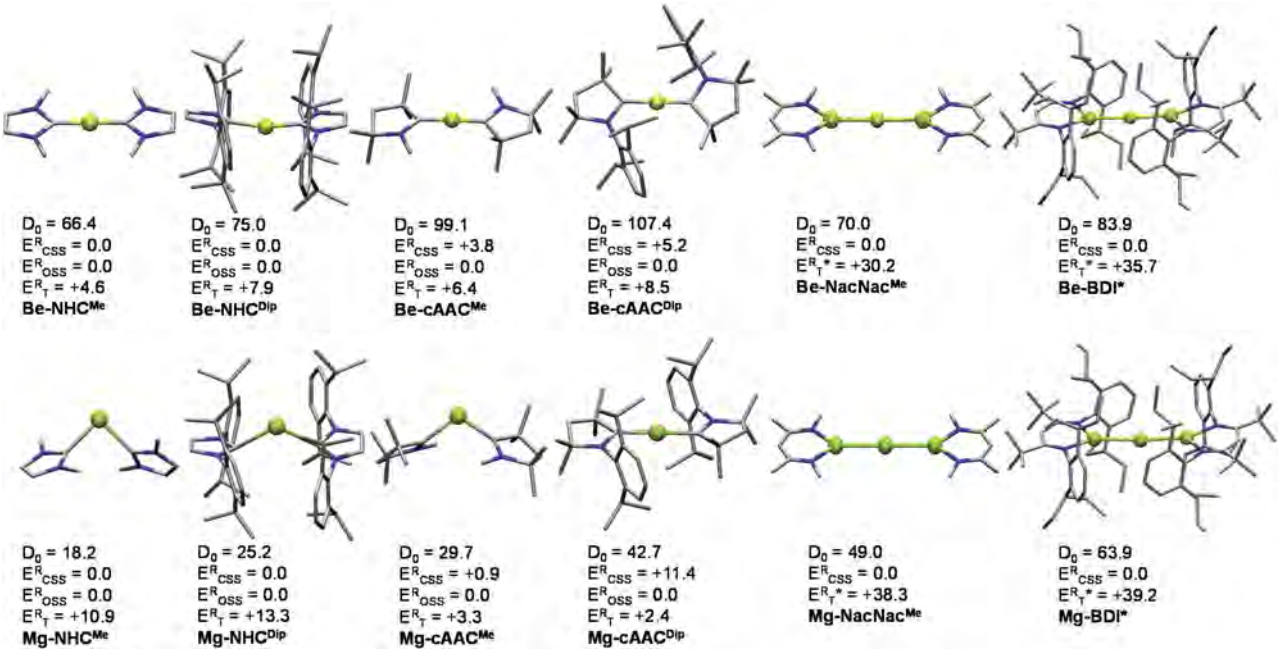

Fig. 1 Optimized ground state geometries (B3LYP-D3(BJ)/def2-SVP), dissociation energies (D_0) (B3LYP-D3(BJ)/def2-TZVPP//B3LYP-D3(BJ)/def2-SVP) considering the $EL_2 \rightarrow E(0) + 2L(0)$ dissociation, relative electronic energy for the closed shell singlet (E^R_{CSS}), open-shell singlet (E^R_{OSS}) and triplet (E^R_T) at the B3LYP/def2-TZVPP level. *Vertical E_T values. Energies are in kcal mol^{-1}. Hydrogen atoms were omitted for clarity.

Table 1 Geometrical parameters (B3LYP), adiabatic singlet-triplet gap (ΔE_{S-T}), partial atomic charges, Q(E), (E = Mg or Be), E-C/Mg bond orders (BO_{E-L}),[a] fragment and inter-fragment local spin ($\langle S^2\rangle_f$ and $\langle S^2\rangle_{f-f'}$), EOS results and global reliability index (R[%]) of the studied compounds in their ground-state at the CASSCF/cc-pVDZ//B3LYP-D3(BJ)/def2-SVP level

E–L_2 system	Ground state	ΔE_{S-T}	d_{E-L} [Å]	BA_{L-E-L} [°]	Q(E)	BO_{E-L}	$\langle S^2\rangle_E$	$\langle S^2\rangle_L$	$\langle S^2\rangle_{L1-L2}$	Be/Mg OS	L OS	R (%)
Be–H[c]	CSS	145.7	1.331	180.0	1.39	0.52	0.04	0.02	0.00	+2	−1	100
Be-NHC^{Me}	CSS	5.3	1.639	179.9	1.10	0.56	0.06	0.14	−0.11	+2	−1	74.0
Be-NHC^{Dip}	CSS	8.0	1.648	167.4	1.12	0.54	0.08	0.22	−0.18	+2	−1	73.8
Be-$cAAC^{Me}$	OSS	8.3	1.634	176.4	1.17	0.56	0.07	0.30	−0.26	+2	−1	77.8
Be-$cAAC^{Dip}$	OSS	8.6	1.644	177.8	1.19	0.54	0.08	0.39	−0.35	+2	−1	78.9
Be-$NacNac^{Mec}$	CSS	26.2	2.541	180.0	−0.90	0.61	0.07	0.06	−0.02	−2	+1	86.7
Be-BDI*[bc]	CSS	35.7	2.489	177.9	−0.42	0.51	—	—	—	−2	+1	73.0
Mg–H[c]	CSS	123.5	1.699	180.0	1.32	0.58	0.05	0.03	−0.01	+2	−1	100
Mg-NHC^{Me}	CSS	9.9	2.300	90.1	0.25	0.27	0.10	0.07	−0.02	0	0	100
Mg-NHC^{Dip}	CSS	23.3	2.347	119.3	0.61	0.25	0.09	0.07	−0.02	0	0	82.7
Mg-$cAAC^{Me}$	OSS	5.3	2.174	107.8	0.60	0.35	0.12	0.10	−0.04	0	0	80.0
Mg-$cAAC^{Dip}$	OSS	1.0	2.040	178.9	1.34	0.45	0.08	0.68	−0.64	+2	−1	82.4
Mg-$NacNac^{Mec}$	CSS	33.6	2.917	180.0	0.06	0.76	0.12	0.10	−0.02	0	0	59.0
Mg-BDI*[bc]	CSS	39.2	2.800	175.4	0.37	0.52	—	—	—	0	0	59.9

[a] Improved definition of bond orders for correlated wavefunctions from ref. 40. [b] Evaluated at the B3LYP-D3(BJ)/def2-SVP level. [c] Vertical singlet–triplet gap.

coordination distance is within the single and double bond (1.99 Å).[29] The series of Mg shows an appreciable coordination change, as **Mg-$cAAC^{Dip}$** exhibits an almost collinear C–Mg–C angle of 178.9°, while the others possess a rather acute angle (from 90.1° to 119.3°). These structural features have already been described for the $Ga^+(NHC^{Dip})_2$ analogue.[30] Similarly, the tilted coordination mode of MgL_2 (L = NHC^{Me}, NHC^{Dip} and $cAAC^{Me}$) can be rationalized with a different bonding situation. Here, the two electrons of Mg are not promoted from the s orbital to the p orbital; instead the ligands donate into the p-orbital of Mg, with a backdonation from the occupied s-orbital into the carbene empty orbitals takes place.

Fig. 1 also summarizes the calculated homolytic dissociation energies (D_0) from the ground state EL_2 into E(0) (^{1}S ground state) and two neutral ligands ($EL_2 \rightarrow E(0) + 2L(0)$). The consistency at different levels of theory is presented in Tables

S5–S7 in the ESI.† The D_0 values indicate that the Mg–NHC^{Me} complex (18.2 kcal mol^{-1}) is much less stable than the Be–NHC^{Me} analogue (66.4 kcal mol^{-1}). The **Be-cAAC^{Dip}** is the most stable of the series (107.4 kcal mol^{-1}) and is about 60 kcal mol^{-1} more strongly bonded than **Mg-cAAC^{Dip}** (42.7 kcal mol^{-1}). Comparing the homolytic with the heterolytic bond dissociation energies ($EL_2 \rightarrow E(+2) + 2L(-1)$, Table S5†), the ionic fragments are much less favoured than the neutral ones in all cases, in agreement with the donor–acceptor picture shown in Scheme 1B. Note that this holds true for **Mg-cAAC^{Dip}** even when the OSS solution lies 11.4 kcal mol^{-1} below the closed-shell one.

Further insight into the bonding situation is often obtained by means of EDA[31,32] calculations in conjunction with the NOCV (Natural Orbitals for Chemical Valence) method on the ground state (often BS) KS-DFT descriptions.[33–35] Details about the method and recent examples have been reported elsewhere,[36] with a discussion of the nature of the energy components.[37,38] The method allows the preselection of the electronic structure description outlined as donor–acceptor with E(0) (Scheme 1B) or diradical(oid) with E(+2) (Scheme 1C), using fragment reference states. The best representation is assumed to be the one that provides the lowest orbital relaxation, measured by using the lowest absolute orbital term values. To illustrate this, we have computed the EDAs for the **Be-cAAC^{Dip}** and **Mg-cAAC^{Dip}** systems. The values are summarized in Table S8.† The principal bonding picture that emerges from EDA analysis would feature E(0) with two neutral cAAC ligands. The orbital energy terms are −231.4 and −193.0 kcal mol^{-1}, for **Be-cAAC^{Dip}** and **Mg-cAAC^{Dip}**, respectively. Compared with the E(+2) situation, the orbital relaxation leads to higher orbital interactions, −443.8 and −289.8 kcal mol^{-1}, for **Be-cAAC^{Dip}** and **Mg-cAAC^{Dip}**, respectively.

Such energy-based assignation is in contrast with the valence state derived from the effective oxidation state analysis (*vide infra*), and also from that previously suggested by Ponec *et al.*[39] Both pictures can be reconciled by focusing on the electron flow associated with the orbital interactions rather than focusing on the energy costs. Indeed, the EDA-NOCV approach provides this information as the eigenvalues of the deformation densities. In the π interaction channel, using Be(0) in the ^{1}D reference state (Fig. S40†), 0.75α and 0.74β electrons are transferred from the starting electron pair of the Be p_z orbital to the π-type symmetry ligand orbital. On the contrary, using the Be(+2) reference (Fig. S41†), the electron flow from the ligands to the empty Be p_z orbital is just 0.20α and 0.22β electrons. Note that the final result is similar in both cases: one ends with 0.49e and the other with 0.42e on the Be p_z orbital. However, the latter fragmentation leads to an overall smaller electron flow. Thus, one may argue that the reference state for which a smaller electron flow among fragments is found, is the most appropriate reference state. However, this is in contrast with the accepted criterion of choosing the reference states according to the minimum deformation energy required to form a molecule.[2,13,41] Hence the dichotomy is: should we use the energy or density criterion? one should recall that in the (revised) definition of the oxidation state from the IUPAC there is no mention of energetics, but it is essentially an electron counting problem based on "winner-takes-it-all" principle.[42]

Then, why does a smaller electron flow associated with the Be p_z orbital have a more significant energy cost? The reason can be inferred again from the NOCV analysis. While the aforementioned electron flow to the Be p_z empty orbital is just 0.20α and 0.22β electrons, the total electron displacement of this channel is *ca.* 1.8*e*. Therefore, over 75% of the electron flow is associated with the internal reorganization of the fragment density, which certainly has an important energetic impact, but has no influence on the oxidation state.

This conundrum adds up to another related issue of EDA that some of us have recently exposed: EDA cannot distinguish an electron-sharing interaction from a spin-polarized one (diradicaloid).[26] This problem pops out whenever the closed-shell solution is unstable, which is precisely the case for most systems considered here. For all these reasons, we do not consider the combination of KS-DFT and the energy-based EDA criterion as a reliable approach to ascertain the proper valence state of Be and Mg in these systems.

Alternatively, we resort to multireference CASSCF wave functions to tackle the electronic structure of these systems. This permits to consider the bonding situation for all systems on equal footing (*i.e.*, including those with CSS and OSS ground-states according to KS-DFT methods). The results obtained for all species for their KS-DFT optimized structures are shown in Table 1. Notably, CASSCF wave functions on SS-CASPT2 optimized geometries for the smallest systems E-NHC^{Me} and E-cAAC^{Me} show no significant differences from CASSCF wave functions calculated on DFT geometries, validating the CASSCF//DFT approach used for the largest compounds (see details in the ESI†). The ΔE_{S-T} values obtained at CASSCF and CASPT2 levels of theory are in rather good agreement with those obtained with the B3LYP method (see Fig. 1). However, for Be–NHC^{Me}, CASPT2 predicts the triplet state to be more stable than the singlet state, by −1.3 kcal mol^{-1}, while DFT and CASSCF estimate the triplet state about 5 kcal mol^{-1} above the singlet.

The CASSCF natural orbitals (NOs) and their occupations in EL_2 complexes already hint about the bonding situation (Figures S1–S24). These complexes with an acute bond angle present the HONO (Highest Occupied Natural Orbital) and LUNO (Lowest Unoccupied Natural Orbital) localized at the E atom with marked s-type and p-type character, respectively; in agreement with its low partial charge (*vide infra*). Instead, the frontier NOs of the linear complexes resemble the allyl π-system. Thus, the HONO is described as a π-system with in-phase combination π-(+,+,+), while the LUNO is the out-of-phase combination of the extremes π*-(+,•,−) of the C–E–C p-type orbital lobes. The NO corresponding to the π-(+,−,+) combination has negligible occupation. Fig. 2 depicts the orbitals of **Be-cAAC^{Dip}** and **Mg-cAAC^{Dip}** species. The occupancies reveal that the HONO has significantly less than two π-electrons, namely 1.62e (**Be-cAAC^{Dip}**) and 1.21e (**Mg-cAAC^{Dip}**). Note that Mg has a weak contribution in the HONO as a consequence of the poor overlap, which also justifies the geometry change throughout the series. In addition, the LUNO carries a significant occupation, *i.e.* 0.38e (**Be-cAAC^{Dip}**) and

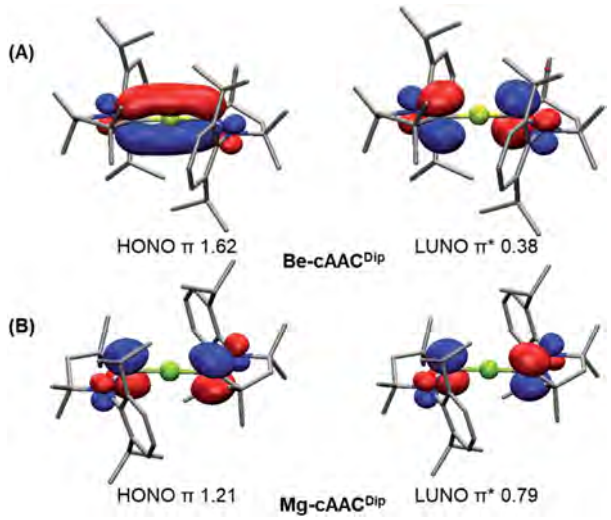

Fig. 2 Frontier natural orbitals and occupancies for the **Be-cAAC^{Dip}** (A) and **Mg-cAAC^{Dip}** (B) systems at CASSCF/cc-pVDZ//B3LYP-D3(BJ)/def2-SVP. Isocontour value of 0.05. Hydrogen atoms were omitted for clarity.

0.79e (**Mg-cAAC^{Dip}**). The LUNO occupation varies in the range of 0.13e to 0.38e in the series of BeL_2.

Different population analyses lead to contradictory results for the partial charge of the E centre (see Tables S9 and S10†). Classical Mulliken or Löwdin schemes yield a quite substantial negative charge on E, which is rather odd considering that they are less electronegative than the C atom. On the contrary, NPA and real-space methods such as QTAIM or TFVC lead to positive charges on E, over +1*e* in the case of Be. These results confirm our above hypothesis that π electrons are much more localized at the ligands than the metal centre. Note that the more π-acidic the character of the ligand, the higher the (positive) partial charge on E. As a consequence, the complexes can also exhibit a different degree of diradical character.

On the other hand, the E–C bond orders (BO) for the NHC- and cAAC-substituted systems indicate the binding degree of the ligand to the central element. In particular, the obtained BO values range from 0.25 (Mg-NHC^{Dip}) to 0.56 (Be-cAAC^{Me}). These values are well complemented with the corresponding dissociation energies (especially for the Mg-based compounds) and also with the occupation of the HONO (the more it deviates from 2, the smaller the BO).

Noteworthily, Ponec *et al.* also analysed a small collinear model Be-cAAC system in light of the domain-averaged Fermi Hole (DAFH) analysis at the CASSCF level of theory.[39] By dissecting the σ and π bonding between the fragments, they found evidence for a 3c-2e π bond involving both ligands and Be, with contributions of 0.95e from each ligand and 0.14e from Be. That is, the contribution of Be to the π bonding is residual, which puts into question the alleged Be(0) valence state of these systems according to the authors.

In this context, the cAAC-substituted compounds could be better interpreted as diradical(oid)s species. The global diradical(oid) character is typically quantified from the occupation numbers of the NOs.[43,44] However, in some systems several NOs with significant occupations are involved, so the usual underlying 2c-2e model is insufficient to describe the diradical character.

Instead, we have used the local spin analysis (LSA), which quantifies the presence of local spin on atoms/fragments and their couplings from correlated wavefunctions even in the singlet state (*i.e.* with no spin density) (see Table 1). In LSA, the $\langle S^2\rangle$ value is dissected in atomic and diatomic contributions, which can be further grouped into fragment contributions (*i.e.* Mg/Be atom and each of the two ligands).[45] For the NHC-coordinated systems, both the $\langle S^2\rangle_{NHC}$ and $\langle S^2\rangle_E$ values are below 0.15 in all cases except Be-NHC^{Dip} ($\langle S^2\rangle_{NHC} = 0.22$). Interestingly, in the cAAC-based compounds the $\langle S^2\rangle_{cAAC}$ values increase from 0.10 (Mg-cAAC^{Me}) to 0.68 (**Mg-cAAC^{Dip}**), and from 0.30 (Be-cAAC^{Me}) to 0.39 (**Be-cAAC^{Dip}**). The $\langle S^2\rangle_E$ values also remain below 0.12 in all cases, ruling out the presence of unpaired electrons in the central atom. The bonding picture thus points towards two antiferromagnetically coupled unpaired spins, each one located at the π-system of the cAAC ligand. This coupling is supported by the $\langle S^2\rangle_{cAAC\text{-}cAAC}$ values (see the ESI† for details), being −0.64 (very close to the ideal value −0.75, see the ESI†) for **Mg-cAAC^{Dip}**. In the case of the experimentally known **Be-cAAC^{Dip}**, the $\langle S^2\rangle_{cAAC}$ and $\langle S^2\rangle_{cAAC\text{-}cAAC}$ values are 0.39 and −0.35, respectively, indicating the marked diradical character. In the diradical(oid) scenario, the valence state of the E atom would be E(+2).

A more unambiguous look at the formal valence state or OS of the E centre and the ligands is given by the effective oxidation state (EOS) analysis,[46] a wavefunction analysis tool specifically devised for this purpose. EOS analysis relies on Mayer's effective fragment orbitals (EFOs) and their occupations, obtained in this case for the E atom and each of the two ligands.[47,48] The EFOs are sorted by decreasing occupation number and individual electrons (electron pairs for closed-shell systems) are assigned to them until the total number of electrons is reached. The last occupied and first unoccupied orbitals form the frontier EFOs, and from their relative occupations a reliability index (*R*) can be derived, measuring to which extent the formal OS model matches the actual electron distribution (for further details see the ESI†).

The results of EOS analysis applied to the ground-state CASSCF wavefunctions are also shown in Table 1. For comparison, we have included BeH_2 (Be–H) and MgH_2 (Mg–H) as genuine E(+2) species. The real-space TFVC atomic definition was used throughout. In the case of near collinear systems (C–E–C angle >160°), the OS of the central E is +2, in line with the discussion above and also in agreement with the study by Ponec *et al.*[39] Fig. 3 illustrates the situation. The last occupied EFOs of **Be-cAAC^{Dip}** and **Mg-cAAC^{Dip}** correspond to π-type orbitals located on the cAAC ligands with occupancies of 0.435 and 0.467, respectively. When frontier EFOs are degenerated in occupation, EOS analysis advocates for homolytic assignation of the last electron pair, leading to the formal picture shown in Scheme 1C. In any case, the occupation of the last unoccupied EFO on E is so small (see Fig. 3) that the E(+2) assignation is unambiguous.

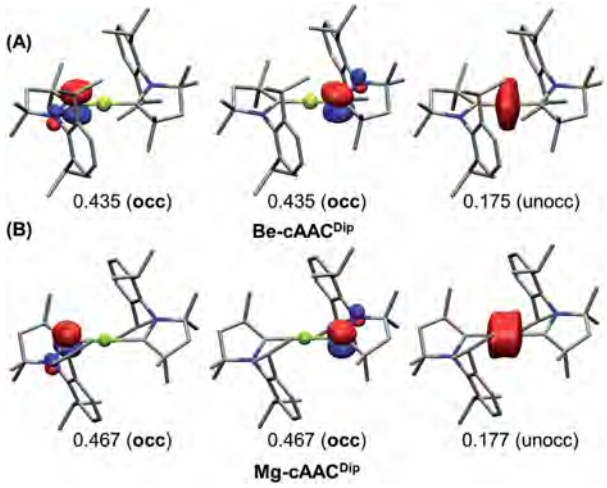

Fig. 3 Frontier EFOs with their corresponding gross occupancies for the Be-cAAC^{Dip} (A) and Mg-cAAC^{Dip} (B) systems (singlet spin state) obtained at the CASSCF/cc-pVDZ//B3LYP-D3(BJ)/def2-SVP level. Isocontour value: 0.1. Hydrogen atoms were omitted for clarity.

On the contrary, in the bent Mg system, the EOS scheme clearly points towards a genuine Mg(0) compound, even for a system like Mg-cAAC^{Me} with incipient diradical character.

It is fair to note that EOS analysis can be applied using different underlying atomic definitions, which can impact the occupations of the EFOs and therefore the OS assignation itself. Indeed, using EOS in the framework of Mulliken or Löwdin analyses leads to Be(0) assignment in Be–NHC^{Me} and Be-cAAC^{Me} systems (see Table S9†). However, more reliable NAO or QTAIM schemes yield essentially the same results as those reported in Table 1. Still, the EOS procedure is shown to be much more robust than the partial atomic charges. Note, for instance, the unambiguous Mg(0) picture obtained for Mg–NHC^{Me} or Mg-cAAC^{Me} systems across all atomic definitions, while the partial atomic charge in Mg varies from −0.75e to +0.60e. We have also applied EOS on the B3LYP ground-state description of these systems (see Table S10†). Other than the particular case of Be–NHC^{Me} in combination with Löwdin analysis, which again yields Be(0), the OS assignation is fully consistent with that derived from CASSCF wavefunctions.

So far we have consistently shown that the equilibrium structures of some of these systems exhibit diradical character and are best described as E(+2). The dissociation energies, however, clearly point towards the homolytic dissociation into E(0) + 2L(0) (see Fig. 1). This situation is reminiscent of the simplest LiH diatomic molecule, where at the equilibrium bond distance the best description is Li(+1)/H(−1) but the dissociation is homolytic.

We have thus monitored the OS of representative EL_2 species along the symmetric E–L dissociation profile. Fig. 4 and 5 show the gross occupation of the frontier EFOs of E and L with the increase of the E–L distance. In the case of Be–NHC^{Me}, the coordination is essentially collinear at equilibrium. Therefore, the EFO occupation of the ligand is higher than that of Be, leading to a Be(+2) picture. As the Be–C distance increases, the

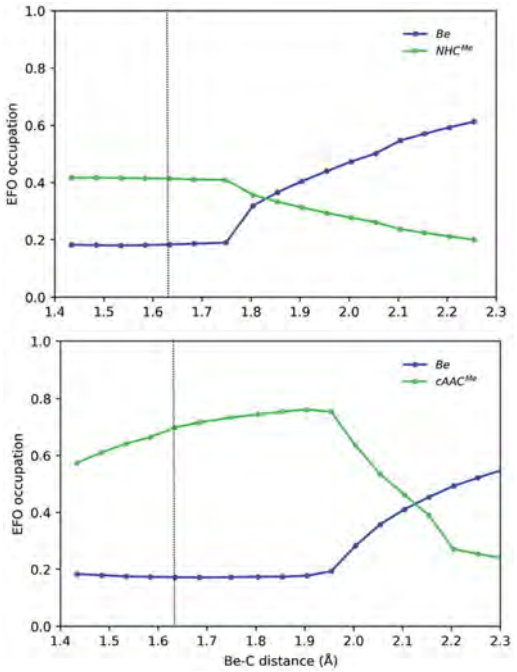

Fig. 4 Gross occupations of the frontier EFOs for Be-NHC^{Me} (top) and Be-cAAC^{Me} (bottom) along the Be–C distance at the B3LYP-D3(BJ)/def2-TZVPP//B3LYP-D3(BJ)/def2-SVP level of theory. The dotted line indicates the equilibrium structure.

occupation of the ligand's EFO gradually decreases, while that of Be increases. The lowest energy dissociation profile proceeds first in a collinear configuration until a Be–C distance of *ca* 1.7

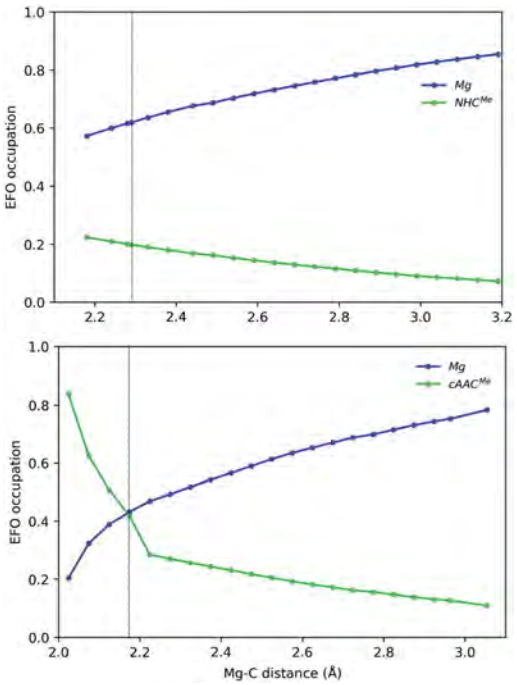

Fig. 5 Gross occupations of the frontier EFOs for Mg-NHC^{Me} (top) and Mg-cAAC^{Me} (bottom) along the Mg–C distance at the B3LYP-D3(BJ)/def2-TZVPP//B3LYP-D3(BJ)/def2-SVP level of theory. The dotted line indicates the equilibrium structure.

Å, when the C–Be–C angle bends so that the Be atom dissociates perpendicularly to the interatomic C–C axis. From this point on, the occupation of Be 2s-type EFO rapidly increases and the change of formal OS from Be(+2) to Be(0) occurs at a Be–C distance of *ca.* 1.85 Å.

In Be-cAAC^{Me}, the BS solution is lower in energy at the equilibrium geometry. The spin polarization is mostly notorious on the ligands' frontier EFOs, which have α and β occupations much larger than those of the Be centre. The dissociation starts in a collinear fashion. The diradical character increases with the Be–C distance, reaching its maximum ($<S^2> = 0.60$) at *ca.* 1.95 Å, thus resulting in a much marked Be(+2) character. Beyond this point, the C–Be–C angle bends so that once again the Be atom dissociates perpendicularly to the interatomic C–C axis. In the process the diradical character rapidly decreases, inducing a charge transfer from the ligands to Be's 2s-type EFO until the formal OS changes at around 2.1 Å, where the open-shell solution merges into the closed-shell one. This again shows that a stable angular geometry is a key to achieving genuine low valent species.

In the case of the Mg-based species, the equilibrium structure already points towards a Mg(0) species, so that the increase of the Mg–C distance further increases monotonically the gap in the EFO occupations in favour of the Mg moiety in closed-shell dissociation profiles (see Fig. 5). Coincidentally, in Mg-cAAC^{Me}, the ground state is still of OSS nature after spin-contamination correction, and the occupations of Mg and cAAC frontier EFOs are almost equal. When using the CASSCF wavefunction at this geometry, the situation is more clear, resulting in an Mg(0) description with $R(\%) = 80$ as shown in Table 1.

Since the OS of the central E atom is clearly influenced by the C–E–C angle, we also analysed the EOS performance along the C–E–C bond angle for Be-cAAC^{Me} and Mg-cAAC^{Me} species at the B3LYP level of theory (Fig. 6). The occupation of the frontier EFO on E monotonically increases as the C–E–C angle deviates from collinearity. In the case of Be, the EFO occupation remains always below 0.3 and that of the ligand remains always larger, even for closed C–Be–C angles (up to *ca.* 130°) where the CS solution prevails. However, in the case of Mg-cAAC^{Me} one can observe a crossing point at around 110° where the occupation of the Mg EFO becomes large enough to yield a Mg(0) picture. This occurs even before the closed-shell regime is reached, and in line with the CASSCF results.

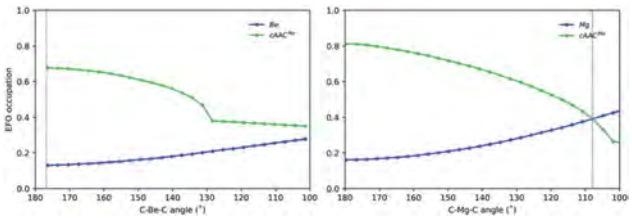

Fig. 6 Gross occupations of the frontier EFOs for Be-cAAC^{Me} and Mg-cAAC^{Me} along the C–E–C angle at the B3LYP-D3(BJ)/def2-TZVPP//B3LYP-D3(BJ)/def2-SVP level of theory. The dotted line indicates the equilibrium structure.

At this point we can safely state that the +2 oxidation state is a consequence of the strong electron π-accepting properties of the ligands. It is interesting to contrast this analysis with the strong σ-donor and weak π-acceptor monoanionic β-diketiminate magnesium ligands. Optimizing the experimentally accomplished Mg-BDI* leads to an almost collinear structure with an Mg–Mg–Mg angle of 175.4°. Structures resulting from reducing the steric encumber hold the same structural features with a bond angle of 180°. However, the bond lengths are sharply increased from 2.800 Å (Mg-BDI*) to 2.917 Å (Mg-NacNac). No open-shell singlet solutions were found for these compounds, and large vertical singlet–triplet gaps were obtained at both DFT and CASSCF levels (>25 kcal mol^{-1}). As expected, the ligand interaction with the central element is explained by the σ-type natural orbital (NO) with an occupancy close to 1.90 (see Fig. S17 and S19†). The p- and π*-type natural orbitals present occupancies lower than 0.1, a fingerprint of dynamic correlation. In the triplet state, one electron from the σ-type NO needs to be transferred to a π-type NO from the central element. Besides, the bond dissociation energies 49.0 and 63.9 kcal mol^{-1} suggest stable compounds for NacNac and BDI* derivatives, respectively, in agreement with the large Mg–Mg BOs (0.76 and 0.52). Note that Mg-BDI* has a lower BO despite the higher dissociation energy, due to the dispersion interaction between the ligands. In line with these findings, EOS analysis also yields a relatively straightforward Mg(0) assignation (see Table S4 and Fig. S38†).

This concept can be used to take beryllium to even lower oxidation states. Be-NacNac and Be-BDI* are predicted to be stable towards the dissociation, with 70.0 and 83.9 kcal mol^{-1}, respectively. The description of the electronic structures shows no appreciable diradical character, with singlet–triplet gaps of 30.2 and 35.7 kcal mol^{-1}. Given the higher electronegativity of Be with respect to Mg, the partial charges at Be are strongly negative −0.90 and −0.42 au. Formally, these molecules bear a beryllium atom with an oxidation state of −2, which is further corroborated by EOS analysis (see Table S4 and Fig. S39†).

Conclusions

In summary, we re-examine the features of the structure, chemical bonding, and stability of the low-valent group 2 compounds. In contrast to the accepted understanding, beryllium still remains in the +2 oxidation state territory. The strong σ-donor stabilized approach produces an internal electronic rearrangement furnishing diradical(oid) species with two unpaired electrons on the ligands. Magnesium analogues might present oxidation state zero when the ligands are not too π-acidic, but the chemical bond is too weak to consider these molecules thermally stable. Nonetheless, the effective oxidation state analysis suggests that the strongly Mg-based ligands are key to accessing genuine low-valent compounds. Our study does not only give more insight into the peculiar features of the molecules considered, but also suggest a promising novel type of beryllium −2 oxidation state. The presented results indicate that many more are yet to come to the fore from these combinations.

Data availability

Data available in article ESI.†

Author contributions

M. G., S. D., E. V., and C. Y. performed the calculations. A. J., I. C., P. S., and D. M. A. acquired funding and contributed methodologies. M. G., S. D. P. S., and D. M. A. prepared the manuscript and the ESI.† All authors contributed to the interpretation of the computed data and the writing and editing of the manuscript.

Conflicts of interest

There are no conflicts to declare.

Acknowledgements

The work at University of Saarland has been supported by the ERC StG (EU805113). MG thanks the Generalitat de Catalunya and Fons Social Europeu for the predoctoral fellowship (2018 FI_B 01120). PS and MG were supported by the Ministerio de Ciencia, Innovación y Universidades (MCIU), grant number PGC2018-098212 B-C22. IC and EV thank the Ramón y Cajal program (Grant: RYC-2016-20489), a FPU grant and the MCIU project PGC2018-094644 B-C21. The Red Española de Supercomputación and the Centro de Computación Científica UAM are also acknowledged. AJ acknowledges generous support of the Department of Atomic Energy, Government of India, under Project Identification No. RTI 4007, CSIR (01(2863)/16/EMR-II), India and SERB (CRG/2019/003415), India. The authors thank Prof. Dr David Scheschkewitz for his kind support.

References

1 V. Nesterov, D. Reiter, P. Bag, P. Frisch, R. Holzner, A. Porzelt and S. Inoue, *Chem. Rev.*, 2018, **118**, 9678–9842.
2 L. L. Zhao, M. Hermann, N. Holzmann and G. Frenking, *Coord. Chem. Rev.*, 2017, **344**, 163–204.
3 G. Frenking, M. Hermann, D. M. Andrada and N. Holzmann, *Chem. Soc. Rev.*, 2016, **45**, 1129–1144.
4 M. N. Hopkinson, C. Richter, M. Schedler and F. Glorius, *Nature*, 2014, **510**, 485–496.
5 M. Melaimi, M. Soleilhavoup and G. Bertrand, *Angew. Chem., Int. Ed.*, 2010, **49**, 8810–8849.
6 M. Melaimi, R. Jazzar, M. Soleilhavoup and G. Bertrand, *Angew. Chem., Int. Ed.*, 2017, **56**, 10046–10068.
7 A. Dyker and G. Bertrand, *Nat. Chem.*, 2009, **1**, 265–266.
8 L. L. Zhao, S. Pan, N. Holzmann, P. Schwerdtfeger and G. Frenking, *Chem. Rev.*, 2019, **119**, 8781–8845.
9 S. P. Green, C. Jones and A. Stasch, *Science*, 2007, **318**, 1754–1757.
10 C. Jones, *Nat. Rev. Chem.*, 2017, **1**, 0059.
11 S. De and P. Parameswaran, *Dalton Trans.*, 2013, **42**, 4650–4656.
12 S. A. Couchman, N. Holzmann, G. Frenking, D. J. D. Wilson and J. L. Dutton, *Dalton Trans.*, 2013, **42**, 11375–11384.
13 M. Hermann and G. Frenking, *Chem. –Eur. J.*, 2017, **23**, 3347–3356.
14 R. Saha, S. Pan, G. Merino and P. K. Chattaraj, *Angew. Chem., Int. Ed.*, 2019, **58**, 8372–8377.
15 M. Arrowsmith, H. Braunschweig, M. A. Celik, T. Dellermann, R. D. Dewhurst, W. C. Ewing, K. Hammond, T. Kramer, I. Krummenacher, J. Mies, K. Radacki and J. K. Schuster, *Nat. Chem.*, 2016, **8**, 890–894.
16 G. Wang, J. E. Walley, D. A. Dickie, S. Pan, G. Frenking and R. J. Gilliard, *J. Am. Chem. Soc.*, 2020, **142**, 4560–4564.
17 C. Czernetzki, M. Arrowsmith, F. Fantuzzi, A. Gärtner, T. Tröster, I. Krummenacher, F. Schorr and H. Braunschweig, *Angew. Chem., Int. Ed.*, 2021, **60**, 20776–20780.
18 Z. R. Turner, *Chem. –Eur. J.*, 2016, **22**, 11461–11468.
19 D. Jędrzkiewicz, J. Mai, J. Langer, Z. Mathe, N. Patel, S. DeBeer and S. Harder, *Angew. Chem., Int. Ed.*, 2022, **61**, e202200511.
20 B. Rösch, T. X. Gentner, J. Eyselein, J. Langer, H. Elsen and S. Harder, *Nature*, 2021, **592**, 717–721.
21 B. Rösch and S. Harder, *Chem. Commun.*, 2021, **57**, 9354–9365.
22 J. L. Dutton and G. Frenking, *Angew. Chem., Int. Ed.*, 2016, **55**, 13380–13382.
23 J. Emsley, *The elements*, Clarendon Press ; Oxford University Press, Oxford; New York, 1998.
24 C. E. Moore and H. N. Russell, *J. Res. Natl. Bur. Stand.*, 1952, **48**, 61–67.
25 F. Breher, *Coord. Chem. Rev.*, 2007, **251**, 1007–1043.
26 P. Salvador, E. Vos, I. Corral and D. M. Andrada, *Angew. Chem., Int. Ed.*, 2021, **60**, 1498–1502.
27 A. P. Singh, P. P. Samuel, H. W. Roesky, M. C. Schwarzer, G. Frenking, N. S. Sidhu and B. Dittrich, *J. Am. Chem. Soc.*, 2013, **135**, 7324–7329.
28 Y. Li, K. C. Mondal, H. W. Roesky, H. Zhu, P. Stollberg, R. Herbst-Irmer, D. Stalke and D. M. Andrada, *J. Am. Chem. Soc.*, 2013, **135**, 12422–12428.
29 P. Pyykko, *J. Chem. Phys. A*, 2015, **119**, 2326–2337.
30 A. Higelin, S. Keller, C. Gohringer, C. Jones and I. Krossing, *Angew. Chem., Int. Ed.*, 2013, **52**, 4941–4944.
31 K. Morokuma, *J. Chem. Phys.*, 1971, **55**, 1236–1244.
32 T. Ziegler and A. Rauk, *Inorg. Chem.*, 1979, **18**, 1755–1759.
33 M. Mitoraj and A. Michalak, *Organometallics*, 2007, **26**, 6576–6580.
34 A. Michalak, M. Mitoraj and T. Ziegler, *J. Chem. Phys. A*, 2008, **112**, 1933–1939.
35 M. P. Mitoraj, A. Michalak and T. Ziegler, *J. Chem. Theory Comput.*, 2009, **5**, 962–975.
36 L. L. Zhao, M. von Hopffgarten, D. M. Andrada and G. Frenking, *Wiley Interdiscip. Rev.: Comput. Mol. Sci.*, 2018, **8**, e13450.
37 J. Poater, D. M. Andrada, M. Solà and C. Foroutan-Nejad, *Phys. Chem. Chem. Phys.*, 2022, **24**, 2344–2348.
38 D. M. Andrada and C. Foroutan-Nejad, *Phys. Chem. Chem. Phys.*, 2020, **22**, 22459–22464.

39 R. Ponec and D. L. Cooper, *Struct. Chem.*, 2017, **28**, 1033–1043.
40 I. Mayer, *Chem. Phys. Lett.*, 2012, **544**, 83–86.
41 D. C. Georgiou, L. Zhao, D. J. D. Wilson, G. Frenking and J. L. Dutton, *Chem. –Eur. J.*, 2017, **23**, 2926–2934.
42 P. Karen, P. McArdle and J. Takats, *Pure Appl. Chem.*, 2014, **86**, 1017–1081.
43 V. Bachler, G. Olbrich, F. Neese and K. Wieghardt, *Inorg. Chem.*, 2002, **41**, 4179–4193.
44 D. Herebian, E. Bothe, F. Neese, T. Weyhermuller and K. Wieghardt, *J. Am. Chem. Soc.*, 2003, **125**, 9116–9128.
45 E. Ramos-Cordoba, E. Matito, I. Mayer and P. Salvador, *J. Chem. Theory Comput.*, 2012, **8**, 1270–1279.
46 E. Ramos-Cordoba, V. Postils and P. Salvador, *J. Chem. Theory Comput.*, 2015, **11**, 1501–1508.
47 I. Mayer, *Chem. Phys. Lett.*, 2013, **585**, 198–200.
48 E. Ramos-Cordoba, P. Salvador and I. Mayer, *J. Chem. Phys.*, 2013, **138**, 214107.

Chapter 7

Results and discussion

In this chapter, we provide a general perspective from the research works presented in Chapters 4-6. To reduce redundancy, the most important results of each topic will be summarized, together with non-reported (or compiled in the supplementary material) data and personal perspectives.

7.1 On the development of methods to elucidate oxidation states

7.1.1 Assigning oxidation states from centroids of localized orbitals

The use of centroids of LOs to assign OSs is very appealing due to its simplicity and, more importantly, because it represents a common framework which can be used for molecular systems and in solid-state, indistinctly. In the last years, the interest about their use by the chemistry community increased, as for example one can recovers Robinson's curly arrow picture[135] from first principles just by following the trajectory of the centroids along a chemical reaction. Previous results indicated that they can also be used to elucidate OSs, by simply assigning the electrons from each LMO to the closest-atom. Such simple assignment criterion has proved to be useful (see Section 1.4) but, in our opinion, it has not been fully tested yet. With these precedents in hand, the aims of this project were:

1) To critically assess to which extend the centroids of LOs coupled with a distance criterion can be used to elucidate OSs in molecular systems.

2) To introduce a new (electronic) criterion to assign the electrons from each LMO but using its centroid position and the Bader atomic basins.

To accomplish these goals, we explored the performance of the closest-atom (distance) criterion for assigning electrons for a variety of systems of increasing complexity, including hydrides, high-valent TM compounds, π-adducts and TM carbenes, among others. Then, we introduced an approach that combines the centroids position with the Bader atomic basins as alternative criterion for the electron assignment. Finally, we evaluated the performance of both approaches by comparing the resulting OSs with the obtained by means of the EOS analysis.

Starting with the rather simple XH_n series, where X goes from Li to Cl, the chemical bonding of these systems is mainly explained by the σ LMO between X and H. Thus, its centroid lies between both X and H centers, and its position determines the $C_X = (R_H - R_X)/(R_H + R_X)$ ratio where R_H and R_X are the distances between the centroid and the corresponding centers. The sign of C_X is indicative of the character of the H atom, being hydride for $C_X < 0$ and proton for $C_X > 0$. Considering the IUPAC IA coupled with the Allen electronegativity scale, the ratio χ_X/χ_H also discriminate hydride ($\chi_X/\chi_H < 1$) from proton ($\chi_X/\chi_H > 1$) character. From the results obtained (Table 7.1), one can see that the closest-atom (CA) criterion characterizes in all cases, in exception of HF, the H atom as hydride. Such characterization is clearly unsatisfactory as the simplest H atom from H_2O is formally described as hydride, when it is well established its proton character.

A relationship between the C_X values and the relative atomic electronegativities is present, becoming C_X less negative (increase) along the period and more negative (decrease) along the group. For consistency, we evaluated how changing the orbital localization procedure affects the quality of the results, obtaining the same trends by using both PM or NLMOs.

Table 7.1: Structural and electronic parameters of the hydrides studied including: Allen's electronegativity (EN), X-H bond distance, EFO occupancy, distance to the centroid (computed using both PM and NLMO LOs) and distance to the bond critical point (R_{bcp-H}).

Molecule	Atom	χ_X/χ_H	EFO occ. λ_X	R_X (PM)	R_X (NLMO)	R_{bcp-H}
LiH	Li	0.397	0.112	1.403	1.401	0.886
	H		0.824	0.205	0.206	
BeH_2	Be	0.685	0.178	1.074	1.072	0.766
	H		0.788	0.270	0.271	
BH_3	B	0.892	0.195	0.888	0.887	0.669
	H		0.710	0.312	0.312	
CH_4	C	1.106	0.391	0.727	0.727	0.395
	H		0.429	0.370	0.371	
NH_3	N	1.333	0.588	0.609	0.615	0.278
	H		0.278	0.416	0.408	
H_2O	O	1.570	0.729	0.511	0.530	0.200
	H		0.179	0.462	0.442	
HF	F	1.823	0.836	0.435	0.455	0.159
	H		0.122	0.498	0.478	
NaH	Na	0.378	0.170	1.585	1.582	0.892
	H		0.760	0.313	0.316	
MgH_2	Mg	0.562	0.233	1.427	1.397	0.833
	H		0.760	0.287	0.318	
AlH_3	Al	0.701	0.249	1.284	1.281	0.792
	H		0.746	0.309	0.312	
SiH_4	Si	0.833	0.234	1.139	1.136	0.758
	H		0.713	0.353	0.356	
PH_3	P	0.980	0.183	0.977	0.998	0.720
	H		0.653	0.454	0.433	
H_2S	S	1.126	0.427	0.845	0.871	0.479
	H		0.439	0.508	0.482	
HCl	Cl	1.247	0.604	0.738	0.765	0.365
	H		0.307	0.553	0.526	

We found an excellent correlation ($R^2 = 0.97$) between the C_X values and the χ_X/χ_H ratio obtained with both orbital localization procedures. However, most of the data points to be associated with proton

character, according to the atomic electronegativities, are characterized as hydride by using the CA criterion (Figure 7.1a). These results hint that the Allen electronegativities might be used to correct the relative atomic size when assigning the LMO electrons according to the CA criterion. Nonetheless, in our opinion introducing *fixed* electronegativity values in the model will lead to the same intrinsic problems of the IUPAC IA; the differences between atoms of the same type arising from a different chemical environment are not considered. As solution, we propose to determine which atomic basin the centroid belongs to, and abandon the CA criterion. This alternative criterion present some advantages, being the most relevant one that the chemical environment of the atoms is automatically considered, as the basins are determined by the topology of the electron density, $\rho(\mathbf{r}_1)$. This new criterion, namely the basin-allegiance (BA), has been implemented as follows. First, we determine for all atoms in the system their associated atomic trust spheres, as described by Rodríguez *et al.*[181] Then, the LMO electrons are assigned to the corresponding atom if the centroid resides inside the trust sphere. In case that the centroid lies outside any trust sphere, which is common for bonding LOs, the steepest-ascent path is followed until reaching a trust sphere. For this aim, we use both the gradient and the Hessian of the density with a reduced step in all points along the iterative procedure, ensuring thus a faithful steepest-ascent path. The results obtained using the BA criterion are also compiled in Table 7.1. Using the new criterion, one can see that the H atoms from H_2O, NH_3, HCl and H_2S are characterized as protons, as expected. Then, the BA is behaving as the electronegativity ratio, in exception of CH_4 for which the OS assignment is not trivial due to the high covalency of the C-H bond. For further insight, we depicted in Figure 7.1b the distance from the centroid to the bond critical point (bcp) against the electronegativity ratio. Analogously to Figure 7.1a, positive distance values are obtained when the centroid is inside the X atom basin, whereas negative values indicate that the centroid lies inside the H atom basin. Once again, the correlation is excellent ($R^2 = 0.93$), being all points (again CH_4 is the exception) lying in the right quadrants for proton and hydride character. Therefore, the results obtained with the BA criterion are more satisfactory compared to the CA one, at least for these systems, while the addition of complexity is minor.

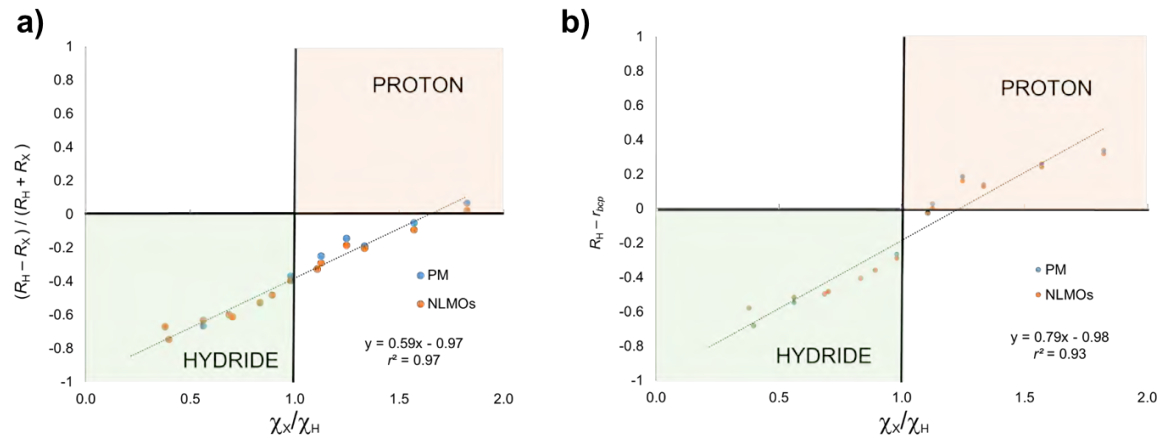

Figure 7.1: Correlations for the XH_2 set of systems between (a) the centroid position versus electronegativity ratio (OS assignment using the CA criterion) and (b) centroid position relative to the bcp against electronegativity ratio (OS assignment using the BA criterion).

To critically analyze the performance of both CA and BA criteria to assign OSs from centroids of LOs, we selected a variety of relevant examples including TM carbenes, π-adducts and high-valent TM oxides, to name a few. Starting for the rather simple $(CH_3)_3NO$ system, it is assumed that its dominant Lewis

structure is a single bond between a formal N(+1) and O(-1) in order to fulfill the octet rule of N. By applying the IUPAC IA, the electron pair of the σ N-O bond is assigned to the O atom, and all N-C bond electrons to N. These results in formal OSs of -2 for O, -1 for N and +1 for the three CH_3 units. The LOs from both PM and NLMO procedures points towards the aforementioned Lewis structure, showing a single σ N-O LO. We did not found a LMO corresponding to a π N-O bond and, instead, the O moiety presents two p-type lone pairs. Evaluating the centroid position (Figure 7.2) of the σ N-O LO, it is closer to the N atom than to O, and it lies within the atomic basin of N. As consequence, both CA and BA criteria assign the electron pair to N, leading to the formal OS of -3 for N and 0 for O. Such assignment is also obtained by EOS at the same level of theory and when using a multireference wavefunction, being at odds with the straightforward application of the IUPAC IA.[42]

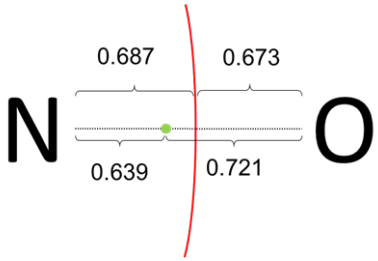

Figure 7.2: Pictorial representation of the zero-flux surface and centroid position of the σ-type N-O NLMO for $(CH_3)_3NO$. For PM, the distances from the centroid to N and O are 0.660 and 0.692 (in Å), respectively.

Moving to TM-based compounds, we first considered a series of high-valent TM oxides, including TiO_2, FeO_4^{2-}, ReO_4^-, OsO_4, IrO_4^+, and PtO_4^{2+}, in which the TM OS ranges from +4 (Fe) to presumably +10 (Pt). Previously, EOS has already been applied to these systems, yielding OSs in agreement with the formal values up to Ir(+9) in $Ir^{(+9)}O_4^+$.[42,182] For the metastable PtO_4^{2+} cation,[183] the occupancy of the d-type EFO from Pt is too large to be considered empty, not leading into its presumed +10 OS. This makes these systems interesting to evaluate the performance of both CA and BA strategies. Herein, we will solely discuss the results obtained from NLMOs, as both both PM and NLMOs presented very similar performance and some technical issues have been encountered to converge the PM LOs for such symmetric systems. In all cases, the centroids of the LOs involved in the π TM-O bond are very close to the O atom, indicating almost lone pair character. Thus, the electron pairs under dispute are the ones from the σ TM-O bond. We depicted in Figure 7.3 the aforementioned LO, together with the position of its centroid and the corresponding bcp.

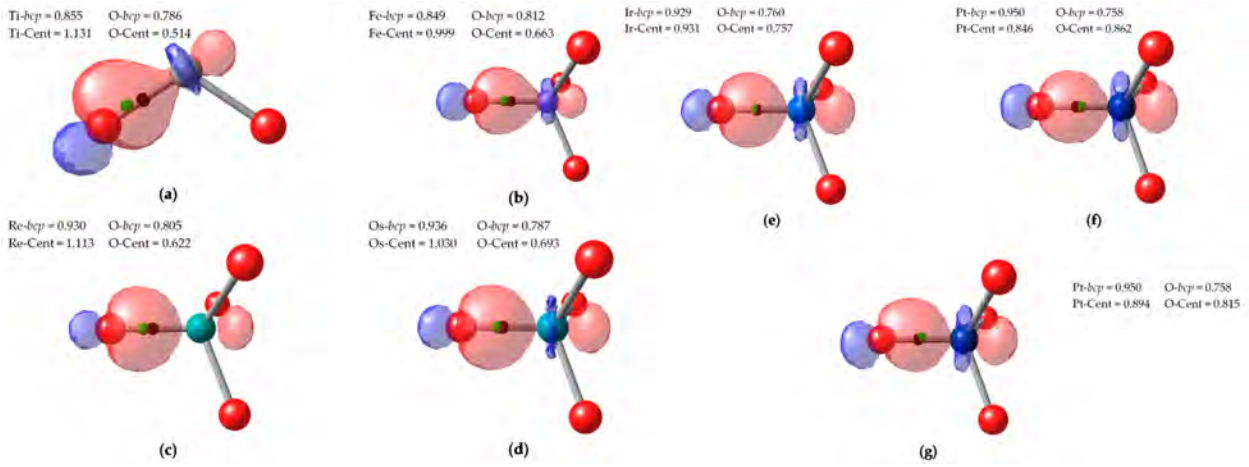

Figure 7.3: σ-type TM-O NLMO for TiO_2 (a), FeO_4^{2-} (b), ReO_4^- (c), OsO_4 (d), IrO_4^+ (e) and PtO_4^{2+} (f, g). Centroid and bcp represented by green and black, respectively. Selected isocontour value of 0.1 a.u., distances in Å.

In exception of the Pt-based system, the centroid of the σ TM-O LMO is located between the bcp and the O atom. As it is closer to O than to the TM, both BA and CA strategies assign the electron pair to the O atom, being each O in the formal -2 OS. However, the assignment becomes less clear-cut when going to higher-valent complexes. In fact, the IrO_4^+ system present the centroid of the σ Ir-O LMO very close to the bcp, being still within the O atomic basin. Thus, one cannot rule out that a different orbital localization scheme (or level of theory) reverse the BA assignment. For PtO_4^{2+}, both CA and BA criteria do not predict the presumed +10 OS. The NLMO procedure provided three very similar Pt-O LOs (Figure 7.3f) and a fourth one slightly different (Figure 7.3g). In the first, the centroids are located closer to O than to Pt (0.815 and 0.894 Å, respectively), but still within Pt basin (see bcp position in the Figure). The BA and CA criteria differ on the assignment of the electron pair from each one of these bonds, and thus leading into different OS assignments. The last NLMO is more polarized towards Pt and thus its centroid is also closer to Pt (and within Pt basin). As result, the CA criterion assigns the +8 OS to Pt with one the O atoms neutral, while the BA criterion assigns all O atoms as neutral and the Pt in the rather unrealistic +2 OS.

Lastly, we studied a collection of TM carbenes (Figure 7.4) compiled by Occhipinti *et al.*[110] which includes: four conventional W-based Fischer-type carbenes (**1-4**), five Schrock Mo- and W-based catalysts (**5-9**) and six Os- and Ru- based first- and second-generation Grubbs-type carbenes (**10-14**), together with the precatalysts (**15-16**).

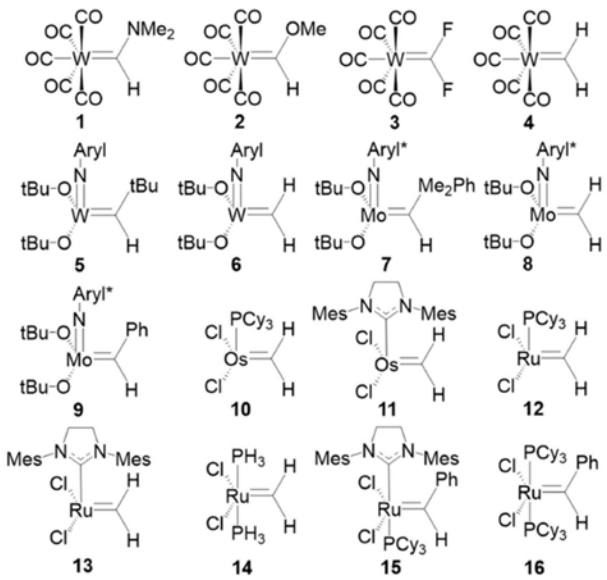

Figure 7.4: Set of TM carbenes studied. Abbreviations: Aryl = 2,6-diisopropylphenyl, Aryl* = 2,6-dimethylphenyl, Cy = cyclohexyl and Mes = mesityl.

For these systems, the most relevant interaction is the associated with the σ and π TM-carbene bonds, thus we will solely focus on the centroids of these two particular LOs. As it was aforementioned (Section 1.4), in a Fischer-type carbene the σ TM-C bond is expected to be polarized towards the C atom of the carbene unit, while the π TM-C bond to the TM, leading into a formally neutral carbene unit. It is worth remembering that this chemical bonding picture can not be recovered from IUPAC's IA as assigns the two electron pairs to the carbene unit (C more electronegative than TM). This scenario is the expected for a Schrock-type carbene, with a formally -2 carbene unit. Grubbs-type carbenes are not easily classifiable into the Firscher- or Schrock-type categories. In fact, Occhipinti *et al.* suggested for them a new category, namely the electrophilic Schrock carbenes.[110] The resulting OSs from applying both CA and BA criteria (using both NLMO and PM LOs) and the EOS analysis are compiled in Table 7.2.

Table 7.2: Oxidation states of the carbene unit (=CR_1R_2) from EOS analysis, together with its reliability index R(%), and from centroids of LOs (PM and NLMO). Electrons from LOs assigned according to the CA (a) and BA (b) criteria.

Molecule	EOS	R(%)	PM[a]	NLMO[a]	PM[b]	NLMO[b]
1	0	67.8	0	0	0	0
2	0	61.2	0	0	0	0
3	0	59.2	0	0	0	0
4	-2	56.9	0	0	0	0
5	-2	72.0	-2	-2	-2	-2
6	-2	74.1	-2	-2	-2	-2
7	-2	64.1	-2	-2	-2	-2
8	-2	66.9	-2	-2	-2	0
9	-2	65.7	-2	-2	-2	-2
10	-2	51.5	-2	2	2	2
11	0	50.4	0	0	2	2
12	0	55.5	0	2	2	2
13	0	58.1	0	2	2	2
14	0	55.9	0	2	2	2
15	0	62.4	0	0	2	2
16	0	63.3	0	0	2	2

EOS analysis characterized in all cases the carbene unit as neutral (0) or anionic (-2). Moreover, the expected carbene-type classification is obtained for the predefined as Fischer- or Schrock-type carbenes, in exception of **4**. The Grubbs-type carbenes are better described as Fischer-type, at least from the formal OS perspective. However, the assignment is rather uncertain, as indicated by the R(%) values close to 50. Such scenario is present when the frontier EFOs are almost degenerated in occupancy, meaning that the system is described by two *almost* equally plausible chemical bonding pictures.

When applying the CA criterion, the σ and π TM-C bond distance indices used (Figure 7.5b) are given by the distance between the σ (red dot) and π (green dot) centroids to the midpoint of the TM-carbene bond. When applying the BA criterion the bcp position is used, instead, as reference point. In both cases, a negative value on a given axis indicates that the electron pair from the corresponding LMO is assigned to the carbene unit.

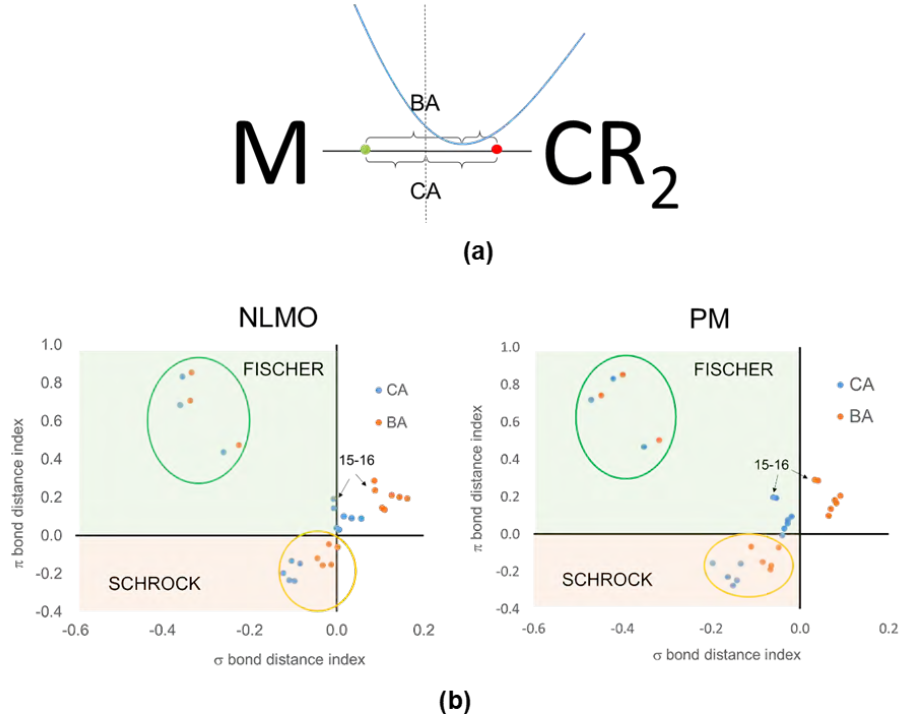

Figure 7.5: (a) Pictorial representation of a prototypical Fischer-type carbene including: centroids of both σ (red dot) and π (green dot) TM-C bond LOs, with the relevant distances for CA (midpoint of the bond) and BA (bcp) criteria. (b) Classification of the TM carbenes according to the distance from the σ and π centroids to bond midpoint (CA) or bcp (BA). Data points corresponding to **1-4** (green circle) and **5-9** (orange circle).

Unfortunately, the use of centroids of LOs to assign OS provided unsatisfactory results for several reasons. First, there are a number of data points corresponding to the Grubbs-type carbenes for which the σ bond distance index is positive (Figure 7.5b). This means that the σ TM-C electron pair is formally assigned to the TM instead of to the carbene. Simultaneously, the π TM-C bond distance index is also positive. As consequence, the carbene unit presents the hardly acceptable +2 OS. The same (wrong) scenario is systematically observed when using the BA criterion, and independently of the localization procedure. The use of the CA criterion presents better results for these systems, even they somewhat depend on the LOs used. Nonetheless, both CA and BA criteria behave quite good for the prototypical Schrock- and Fischer-type carbenes.

Concluding this section, the search of robust schemes to assign OSs using the LOs centroids is not a trivial task. In this work, we critically assessed the use of centroids of LOs as one can apply the same strategy on equal footing for both solids and molecular systems. However, our results indicated that there is no general (and straightforward) use of them to reliably elucidate OSs. The simplest CA criterion performs rather well for discriminating Fischer- and Schrock-type carbenes and identifying high-valent species, but fails for the simplest H_2O case. We introduced and evaluated the performance of the BA criterion, solving many issues presented by CA, but performing worse in describing TM carbenes. Furthermore, the choice of orbital localization procedure might have an impact on the resulting OSs. All our conclusions are extracted by using the centroids from PM and NLMO localized molecular orbitals, and we accept that before discarting the use of centroids for assigning OSs it would be necessary to scrutinize more (and more robust) orbital

localization procedures. In fact, to assign OSs one should probably incorporate the definition of fragments before applying the localization procedure, i.e. on the definition of the orbital spread functional. This avenue is explored in Section 4.2.

7.1.2 Defining a new fragment-based orbital localization procedure for oxidation states purposes

One of the main conclusions from Sections 4.1 and 6.1 is that robust orbital localization procedures are required for OSs purposes and, more importantly, that include the fragment definition *when* localizing the orbitals. Indeed, development on specialized schemes which aim to specifically localize orbitals into fragments rather than maximizing a *global* criterion exist, but for other purposes.[67,140,184–190] In particular, such methods have relevant value in energy decomposition schemes for intermolecular interactions,[191,192] as well as for embedding and fragment methods.[67,188,193] Fragment localization for OS purposes presents different needs. Take for instance two fragments A and B that are connected by a single bond with ionic character, and each formally contains n_{A} and n_{B} electron pairs. In such scenario, the OS should solely depend on a single LMO involving both fragments A and B, leading either to A^{-}-B^{+} or A^{+}-B^{-}. Moreover, standard orbital localization procedures do not distinct between the contact atoms of the A-B bond of the remaining atoms of A and B. Thus, a better localization of the critical A-B bonding orbital may be sacrificed for achieving a better *overall* localization of the $n_{\mathrm{A}}+n_{\mathrm{B}}$ orbitals. With this, the main objectives of this second project were:

1) To introduce a new fragment-orbital localization procedure, together with an associated index that quantifies how much localized within each fragment each orbitals is, to ensure maximizing the *intra*-fragment localization.

2) To propose an algorithm for assigning OSs using the aforementioned fragment-localized orbitals.

To accomplish these goals, we explored a new approach to obtain fragment-localized orbitals, termed oxidation state localized orbitals (OSLO), together with an algorithm for assigning the OSs using the OSLOs and an associated fragment orbital localization index (FOLI). Technically, the OSLOs comprise a full set of localized molecular orbitals spanning the occupied space, ordered by spatial locality in the fragment. Further characterization of each orbital is performed by the FOLI, which measures the population of each OSLO on a per-fragment basis. These fragment populations (for each orbital) are obtained using the highly robust real-space TFVC scheme and also a newly introduced (and more robust) version of the Hilbert-space IAO scheme (see details in Sections 1.2.2 and 1.2.1 for TFVC and IAO, respectively), in which the IAOs are evaluated using a reference minimal basis formed from on-the-fly superposition of atomic density (IAO-AutoSAD) calculations at the target level of theory. The fragment OS is determined by the number of assigned OSLOs relative to its total nuclear charge. Finally, the performance of the OSLO algorithm was critically evaluated using a range of challenging systems, including high-valent TM oxides, TM complexes with redox non-innocent ligands (i.e. NO and thiolate), the potentially inverted ligand field in $[\mathrm{Cu}(\mathrm{CF}_3)_4]^{-}$ and a variety of carbene-containing TM compounds, among others.

Starting for the fragment localization procedure, we based it on minimizing the radial spread functional from a given reference point for fragment F, $\mathbf{R}_F$. In case of the fragment being an atom, $\mathbf{R}_F$ corresponds

to the atomic position and, for a ligand, $\mathbf{R}_F$ is its center of charge. The minimization can be easily achieved in the MO basis by building a spread matrix, $\mathbf{L}^F$, with elements

$$L_{ij}^F = \int \psi_i(\mathbf{r})(\mathbf{r} - \mathbf{R}_F)^2 \psi_j(\mathbf{r}) d\mathbf{r}. \tag{7.1}$$

Upon diagonalization of the $\mathbf{L}^F$ matrix

$$\mathbf{L}^F \mathbf{U}^F = \mathbf{U}^F \mathbf{\Lambda}^F, \tag{7.2}$$

one obtains the eigenvalues $\lambda_i^F = \Lambda_{ii}^F$ (squared-spreads) and a corresponding set of N_{occ} LOs centered around $\mathbf{R}_F$

$$\phi_i^{loc,F}(\mathbf{r}) = \sum_k U_{ki}^F \psi_k(\mathbf{r}). \tag{7.3}$$

When the fragment is a single atom, such as the TM from an inorganic compound, the resulting LOs reproduce the shell structure of the atom, with core orbitals presenting the smaller spreads.

Our target is to define the OS of M user-defined fragments from a given molecular system, such as the ligands and metal(s) of a TM complex. For this aim, we first localize around each fragment's center of charge and get N_{occ} OSLOs for each of them ($M \times N_{occ}$ in total).

The definition of the centroid of the ligand may arise doubts. Let us mention that for small ligands such as CO, H_2O or CH_3 it does not make a big difference whether we use the position of the contact atom or some centroid (center of mass or charge). However, for hapto or polydentate ligands, where there is more than one contact atom with the TM (e.g. ferrocene), using the center of charge is probably the less arbitrary and reasonable choice. Note that in these cases the ligand centroid may be far from any ligand's nuclei, or even coincide with that of the metal center (e.g. TM-porphyrin).

The minimization of the spread function is very appealing because it is (mathematically) simple, non-iterative and independent of the AIM definition. However, the OSLOs which are most strongly associated with a fragment can not be chosen based on the smallest spread. For instance, let us consider the case of a single TM with some coordination sphere. In such scenario, OSLOs dominated by ligand contributions can exhibit lower spread values than the most diffuse TM orbitals (e.g. a 4p-type orbital for a third-row TM). Similarly, when $\mathbf{R}_F$ is the center of a ligand hapto-coordinated to the TM, some compact ligand-centered OSLOs have a significant contribution from the neighboring TM center.

Since $M \times N_{occ}$ LOs are redundantly produced (i.e. N_{occ} for each of the M fragments), selecting the N_{occ} OSLOs that are most strongly localized on fragments is required. As it was aforementioned, these are not simply the ones exhibiting lower spread values. Then, we require a complementary measure to identify the OSLOs that are most localized on a fragment. For this aim, we propose the fragment orbital localization index (FOLI)

$$D_i^F = \sqrt{\frac{D_i}{N_F^i}}, \tag{7.4}$$

which uses the Pipek delocalization measure,[194] defined in terms of *fragment* populations, $N_F^i = \sum_{A \in F} N_A^i$, as

$$D_i = \{\sum_F (N_F^i)^2\}^{-1}. \tag{7.5}$$

When the i-th orbital is perfectly localized on fragment F, $D_i^F = 1$, and the value increases gradually for OSLOs that are both less centered on fragment F and more delocalized. Let us mention that while $D_i^F = 1$ means perfect fragment localization, higher FOLI values may arise from different instances of delocalization. As example, $D_i^F = 2$ can be the results of 3 fragments with $D_i = 2.339$ via $N_{F_1} = 0.584$, $N_{F_2} = N_{F_3} = 0.208$ or 2 fragments with $D_i = 2$ via $N_{F_1} = N_{F_2} = 0.5$.

Now, how to select the N_{occ} most fragment-localized OSLOs from the set (redundant) of $M \times N_{occ}$ candidates? At a first glance, we ordered the OSLOs by decreasing FOLI value, selected the first N_{occ} ones and assigned them to their parent (originator) fragments. However, this procedure sometimes leads to linear dependencies among the selected OSLOs. For this reason, we proposed to perform the selection procedure iteratively (see Figure 7.6). In the first iteration, the algorithm selects the best fragment-localized LMO (smallest FOLI value) and projects it out from the occupied space for the next iteration. In the second iteration, first a new set of $M \times (N_{occ} - 1)$ LOs is constructed, followed by selecting and removing the best (freshly obtained) LO. The iterative procedure continues until a total of N_{occ} optimal fragment-localized orbitals are selected. For unrestricted single-determinant wavefunctions, the procedure is performed for the α and β occupied spaces independently, producing and assigning individual α and β OSLOs to each fragment. We modified the basic algorithm by introducing a tolerance value (typically of 10^{-3}) so that, in each iteration, all orbitals with D_i^F values within the tolerance are selected, symmetrically orthogonalized and projected out from the occupied space for the following iteration. We observed by applying this strategy that, for symmetric systems, the undesired situation of projecting out individual LOs and obtaining a symmetry-broken density-matrix for the next iteration is avoided. By performing the OSLO selection iteratively, we also observed that the fragment-localization of the non-selected orbitals is improved in the later iterations, which is a desirable side-effect.

Notice that no AIM definition is used to obtain the redundant set of LOs, just the minimization of the spread functional with respect to the atom/fragment center of charge. The population scheme is only necessary to select the best LOs of each iteration based on the FOLI value. Using fragment populations to generate the orbitals may result in different orbitals with different AIM methods, as seen in Pipek-Mezey localization.[195] As the final set of LOs exactly span the occupied space, they can also be used for other purposes such as fragment populations, ligand lability, embedding methods, QM/MM techniques and local correlation methods, among others. Alternative uses of the OSLOs have not been explored yet.

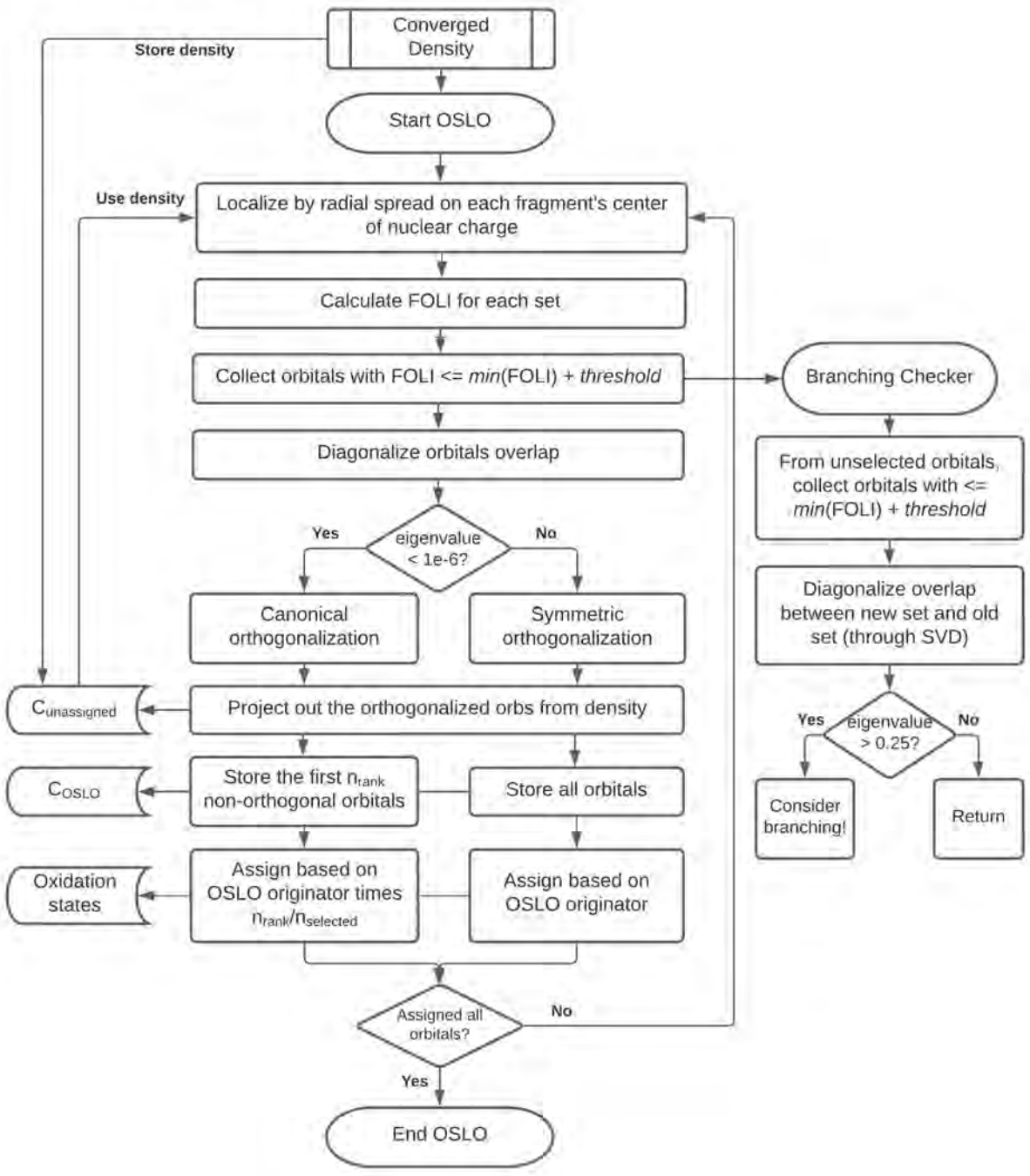

Figure 7.6: Iterative OSLO algorithm flowchart. The core and valence spectator orbitals (most fragment-localized) are projected out from the occupied space before the relevant orbitals for OSs purposes (least fragment-localized).

Some aspect of the procedure are worth to discuss in detail. First, the LOs obtained in the first iterations are basically the atomic core orbitals of the fragment atoms. Then, with the advance of the iterative process the *on-fragment* localized valence orbitals are produced, corresponding to orbitals not particularly involved in the bonding between fragments (spectator). In the last iterations, the least fragment localized molecular orbitals are produced and eventually selected, corresponding to bonds (or dative bonds) between fragments.

Interestingly, by first removing the more fragment-localized orbitals from the occupied space, the relevant across-fragment orbitals are then better localized on fragments, being thus their FOLI values *smaller* than those obtained in the first iteration using the whole occupied space. This means that the final result depends, to some extent, on the order in which the LOs are selected.

The resulting OS assignment can be affected when the FOLI-based selection is close-call. In such scenario, the algorithm flags when the OSLO procedure could *branch* into 2 (or more) paths, allowing then the user to explore the alternative outcomes. Let us consider the simple case of a single bond between fragments F and G. At the step of the iterative procedure that the bond LMO centered on F is produced, a similar one will be produced in the OSLOs associated with fragment G. The one with the lowest FOLI is the selected and projected out from the remaining occupied space, being this bond orbital in the next iteration absent from the new set of OSLOs obtained for both fragment F *and* G. In case that the F-G bond is very non-polar (rare in TM complexes), the D_i^F and D_i^G values would be very similar. Here, one can argue that choosing the LMO associated with G, instead of the one from F, would produce a plausible alternative solution. To detect these *borderline* cases, linear dependencies between the selected LMO and the first non-selected one (*second* lowest FOLI value) are checked at each iteration. It may occur that there are multiple selected and non-selected LOs if their FOLI values are within the tolerance. If near linear dependencies are found *and* the difference in D_i^F values is small, the algorithm will flag it. Then, the user can rerun the calculation toggling a branching flag, thus selecting the LMO with the somewhat larger FOLI value, and proceed to obtain a second distinct solution.

How to finally assign OSs from the obtained set of OSLOs? Let us recall that each of the selected LOs was generated from a fragment with a low FOLI value. This makes it natural to assign the LMO electrons based on the *originator* fragment. All results obtained are based on this assignment procedure (see below and Section 4.2), representing a "winner-takes-it-all" approach. However, once the optimal set of orthogonal fragment-localized orbitals are obtained, one can reevaluate the fragment populations for each orbital and reassign it either in a "winner-takes-it-all" fashion (again) or alternatively by allowing covalent assignments in non-polar cases, as described in Section 6.1.

As it was aforementioned, the AIM definition solely enters into the evaluation of the FOLI values, but its choice may affect which LOs are selected and in which order. Thus, we decided to make use of two very distinct atomic definitions to prove that different *but reasonable* choices work, in fact, very similarly. In particular, we selected the real-space TFVC (see details in Section 1.2.2), and we desired to perform a comparison with one of the most (if not the most) robust Hilbert-space methods. In our opinion, this is the Knizia IAO but, as it was already stated in Section 1.2.1, it presents some flaws. Then, we decided to also introduce a new Hilbert-space AIM definition based on the IAO formulism but using a universally applicable reference minimal basis obtained on-the-fly from appropriate free atom densities obtained with the same functional and basis set as the molecular calculation. This is achieved by using the AutoSAD functionality from Q-Chem,[174] termed the superposition of atomic densities (SAD) method, which is mostly employed in the construction of initial guesses for KS-DFT calculations. We termed the new AIM definition as IAO-AutoSAD.

For each atom type A, the IAO-AutoSAD procedure solves first a generalized eigenvalue problem

$$\mathbf{P}^A \mathbf{c}_\alpha^A = \mathbf{S}^A \mathbf{c}_\alpha^A \lambda_\alpha, \tag{7.6}$$

where $\mathbf{P}^A$ is the sphericalized and spin-averaged density matrix of the free-atom. The matrix has the dimension of the atom's full basis (rank N_A). Since many atoms have partly occupied degenerate orbitals, sphericalization is necessary for ensuring proper shell symmetry in the reference minimal basis. For simplicity and also avoiding ambiguity, we use the neutral atom's ground state. For open-shell atoms, we solve the unrestricted self-consistent field equations and the resulting α and β densities are spin-averaged and sphericalized. Then, the reference minimal basis on atom A is obtained by selecting the first M_A eigenvectors of eq. 7.6, where M_A is the rank of the minimal basis for A. The rank can be pre-established (e.g. one for H, five for C, etc) or can be inferred from the eigenvalues of 7.6 (by setting a threshold of 1/14 the whole f-shell of a f^1 electronic configuration is included).The set of selected column vectors $\{\mathbf{c}_\alpha^A\}$ defines an $N_A \times M_A$ transformation from the original basis to the minimal basis (MBS) $\mathbf{C}_{\mathrm{MBS}}^A$.

The molecular reference minimal basis has rank $M = \sum_A M_A$ with functions defined by the direct sum of the atomic transformations

$$\mathbf{T} = \bigoplus_A \mathbf{C}_{\mathrm{MBS}}^A. \tag{7.7}$$

With this, all quantities required to evaluate the IAOs using this MBS are available, being $\mathbf{s} = \mathbf{T}^\dagger \mathbf{S} \mathbf{T}$ and $\mathbf{S}_{sl} = \mathbf{T}^\dagger \mathbf{S}$ in concordance with Eqs. 1.65 and 1.66.

We tested the IAO-AutoSAD for a variety of rather small systems with light atoms to avoid the use of ECPs, and compared them with the obtained using the MinAO reference basis, observing very similar behaviour by using the MinAO and AutoSAD reference minimal basis. This settles the basis for using the IAO-AutoSAD procedure as Hilbert-space method in the OSLO algorithm and compare it against TFVC.

The performance of the OSLO approach has been evaluated for a variety of challenging systems (see below), and its robustness depending of the AIM definition used to evaluate the FOLIs is assessed by using both TFVC and IAO-AutoSAD AIMs. We report in Table 7.3 the OSs of the TM and the relevant ligand (in bold), together with the FOLI value of the last selected (least localized among the selected) OSLO and the difference in FOLI value (Δ-FOLI) of the last selected OSLO obtained using the fragment population of the originator and the fragment with the *second* largest population. It is important to remind that in the last iteration, when there is only one orbital left to assign, the same OSLO is produced from all fragments, being the comparison of FOLI values equivalent to the comparison of fragment populations of that particular OSLO.

Table 7.3: OSLO results obtained using the IAO-AutoSAD and TFVC (in parenthesis) AIMs for the battery of systems included in the study. OSs for TM, and selected ligand (L) in bold. Carbene types: Fischer (F), Schrock (S) and Grubbs (G). Abbreviations: tBu = tert-butyl, Cp = cyclopentadienyl, Ar = 2,6-diisopropylphenyl, Ar^1 = 2,6-dimethylphenyl, Cy = cyclohexyl, IMes = 1,3-Dimesitylimidazol-2-ylidene. $^{(a)}$ IAO-AutoSAD alternative solution. $^{(b)}$ TFVC results using tolerance value of 10^{-4}.

Complex	M OS	L OS	Δ-FOLI	Last FOLI
$[Ti\mathbf{O}_2]$	+4 (+4)	-2 (-2)	3.453 (3.367)	1.321 (1.372)
$[V\mathbf{O}_4]^{3-}$	+5 (+5)	-2 (-2)	1.548 (1.748)	1.466 (1.461)
$[Fe\mathbf{O}_4]^{2-}$	+6 (+6)	-2 (-2)	1.598 (1.682)	1.569 (1.623)
$[Re\mathbf{O}_4]^{-}$	+7 (+7)	-2 (-2)	1.806 (1.829)	1.470 (1.480)
$[Os\mathbf{O}_4]$	+8 (+8)	-2 (-2)	1.415 (1.363)	1.592 (1.609)
$[Ir\mathbf{O}_4]^{+}$	+9 (+9)	-2 (-2)	1.529 (1.084)	1.705 (1.742)
$[Pt\mathbf{O}_4]^{2+,(a)}$	+10 (+10)	-2 (-2)	1.023 (0.707)	1.859 (1.904)
$Fe\mathbf{Cp}_2$	+2 (+2)	-1 (-1)	1.800 (2.343)	1.313 (1.437)
Zn(**porphyrin**)	+2 (+2)	-2 (-2)	0.958 (1.470)	1.509 (1.319)
$[Ni(\mathbf{S_2C_2Me_2})_2]$	+2 (+2)	-1 (-1)	0.000 (0.000)	2.000 (2.245)
$[Ni(\mathbf{S_2C_2Me_2})_2]^{-}$ α	+2 (+3)	-1.5 (-2)	0.603 (0.913)	1.634 (1.656)
$[Ni(\mathbf{S_2C_2Me_2})_2]^{-}$ β			0.000 (0.110)	2.000 (1.901)
$[Ni(\mathbf{S_2C_2Me_2})_2]^{2-}$	+2 (+2)	-2 (-2)	1.085 (1.374)	1.482 (1.509)
$[Cu(\mathbf{CF}_3)_4]^{-}$	+3 (+3)	-1 (-1)	0.373 (0.728)	1.516 (1.531)
$[Cu(\mathbf{CF}_3)_4]^{-2}$ α	+2 (+2)	-1 (-1)	4.823 (4.845)	1.075 (1.152)
$[Cu(\mathbf{CF}_3)_4]^{-2}$ β		-1 (-1)	2.528 (2.867)	1.267 (1.270)
$[Cu(\mathbf{CF}_3)_4]^{-3}$	+1 (+1)	-1 (-1)	4.383 (4.581)	1.084 (1.145)
$Rh(\mathbf{SO}_2)Cl(PH_3)_2$ (L-type)	+1 (+1)	0 (0)	1.421 (1.209)	1.402 (1.509)
$Rh(\mathbf{SO}_2)Cl(CO)(PH_3)_2$ (Z-type)	+1 (+1)	0 (0)	1.064 (1.688)	1.606 (1.516)
$Ru(\mathbf{SO}_2)Cl(NO)(PH_3)_2$ (π-type) $^{(b)}$	0 (0)	0 (0)	0.514 (0.339)	2.432 (2.550)
$[Fe(CN)_5\mathbf{NO}]^{-2}$	+2 (+2)	+1 (+1)	0.981 (0.802)	1.573 (1.827)
$[Fe(CN)_5\mathbf{NO}]^{-3}$ α	+2 (+2)	0 (0)	0.839 (0.674)	1.688 (1.987)
$[Fe(CN)_5\mathbf{NO}]^{-3}$ β			2.638 (2.162)	1.375 (1.436)
$(CO)_5W{=}\mathbf{CHN(CH_3)_2}$ (1) (F)	0 (0)	0 (0)	3.069 (2.205)	1.920 (3.196)
$(CO)_5W{=}\mathbf{CHOCH_3}$ (2) (F)	0 (0)	0 (0)	1.860 (1.148)	2.037 (3.311)
$(CO)_5W{=}\mathbf{CF_2}$ (3) (F)	0 (0)	0 (0)	1.567 (0.893)	2.017 (3.232)
$(CO)_5W{=}\mathbf{CH_2}$ (4) (F)	0 (+2)	0 (-2)	0.612 (0.194)	2.279 (3.142)
$NAr(OtBu)_2W{=}\mathbf{CHtBu}$ (5) (S)	+6 (+6)	-2 (-2)	0.283 (0.659)	1.924 (1.933)
$NAr(OtBu)_2W{=}\mathbf{CH_2}$ (6) (S)	+6 (+6)	-2 (-2)	0.455 (0.806)	1.845 (1.908)
$NAr^1(OtBu)_2Mo{=}\mathbf{CHCMe_2Ph}$ (7) (S)	+6 (+6)	-2 (-2)	0.253 (0.565)	1.916 (1.917)
$NAr^1(OtBu)_2Mo{=}\mathbf{CH_2}$ (8) (S)	+6 (+6)	-2 (-2)	0.203 (0.487)	1.956 (2.018)
$NAr^1(OtBu)_2Mo{=}\mathbf{CHPh}$ (9) (S)	+6 (+6)	-2 (-2)	0.153 (0.430)	1.986 (2.042)
$PCy_3Cl_2Os{=}\mathbf{CH_2}$ (10) (G)	+2 (+4)	0 (-2)	0.048 (0.044)	2.089 (2.278)
$H_2IMesCl_2Os{=}\mathbf{CH_2}$ (11) (G)	+4 (+4)	-2 (-2)	0.192 (0.259)	2.375 (2.709)
$PCy_3Cl_2Ru{=}\mathbf{CH_2}$ (12) (G)	+2 (+2)	0 (0)	0.222 (0.150)	1.964 (2.199)
$H_2IMesCl_2Ru{=}\mathbf{CH_2}$ (13) (G)	+2 (+2)	0 (0)	0.276 (0.306)	2.013 (2.149)
$(PH_3)_2Cl_2Ru{=}\mathbf{CH_2}$ (14) (G)	+2 (+2)	0 (0)	0.241 (0.090)	1.961 (2.153)

The examination of the Δ-FOLI value allows to evaluate how clear-cut the OS assignment is: *the larger the better*. In general, we observe large Δ-FOLI values, being an indicator of very good orbital localization and, as consequence, a clear-cut OS assignment. Overall, the resulting OSs obtained by using both AIMs agree in 30 out of 33 cases. The disagreement appears for cases where the Δ-FOLI value is below 0.2. In such situation, one should probably question if a "winner-takes-it-all" assignment is chemically meaningful. In our opinion, performing an ionic assignment shares the philosophy of EOS, and the current definition of OS. However, these *borderline* cases will chemically behave more similar to an homologous system with the in-between OS than both extremes.

We proceed by discussing in detail some of the studied systems. General discussion can be found in Section 4.2. We start by the rather simple Ferrocene ($FeCp_2$) system, with valence OSLOs depicted in

Figure 7.7, as represents a nice example to show the utility of the OSLOs themself. In panels (a) to (c) from Figure 7.7 one can see the OSLOs of the cyclopentadienyl ligand (formally anionic). The fragment localized π LOs resemble the isolated anion's π delocalized MOs, highlighting the advantage of *fragment* localization over *global* localization. Visually equivalent orbitals were obtained by Senjean *et al.* using the recently introduced intrinsic fragment orbitals.[67] As one should expect, 3 d-type Fe OSLOs are also selected (occupied) with a clear-cut OS assignment based on a large Δ-FOLI gap.

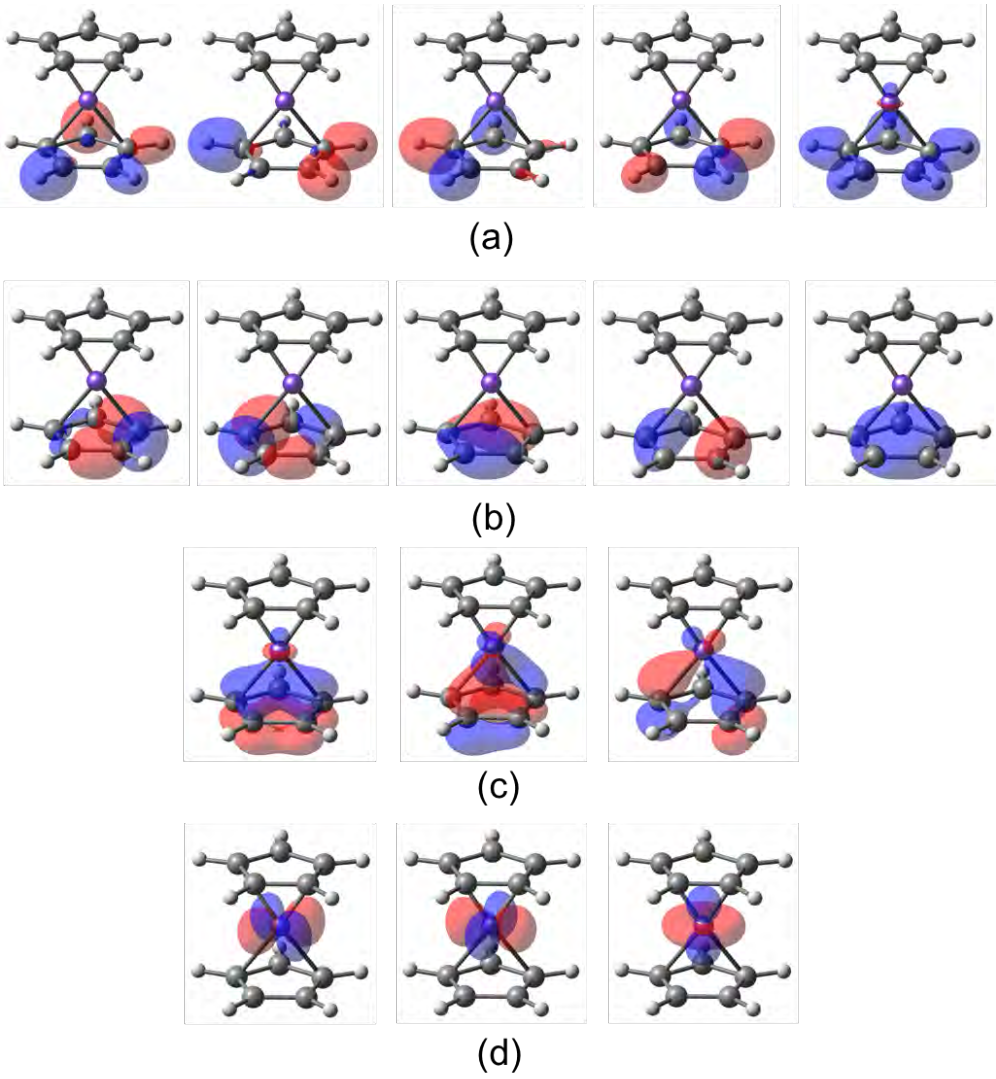

Figure 7.7: Valence OSLOs obtained for the $FeCp_2$ complex. (a) lower σ C-H, (b) σ C-C and (c) π OSLOs of the cyclopentadienyl ligand. (d) Fe 3d-type OSLOs. Selected isocontour value of 0.075 a.u.

A potential challenge for the algorithm is the characterization of systems containing non-innocent ligands. In this direction, we studied the nickel dithiolate complex redox series, $[Ni(S_2C_2Me_2)_2]^{n-}$ being $n = 0, 1, 2$. In the $n = 0$ case, the system is a closed-shell singlet, with most relevant OSLOs, together with their associated FOLI values, depicted in Figure 7.8. The Ni atom presents four well-localized d-type orbitals (Figure 7.8a), leading to the +2 OS. For each thiolate ligand, two σ OSLOs associated with the two S-Ni σ bonds and two S lone pairs are obtained (see Figure 7.8b). As we consider each thiolate as a fragment, these two sets of orbitals are not localized into individual S-Ni bonds and S lone pair, respectively, but form two in-phase

$(+,+)$ and out-of-phase $(+,-)$ LOs within the fragment. Here, the relatively large FOLI value (≈ 1.7) of the $\sigma(+,-)$ OSLO indicated partial contribution from the Ni center, which is smaller for the $\sigma(+,+)$ OSLO. As consequence, the FOLI value obtained for the latter is smaller (≈ 1.3). In addition, each thiolate exhibits a well localized π orbital on the two sp^2 carbon atoms, with FOLI ≈ 1. The last OSLO (Figure 7.8b bottom right) is a π orbital mostly delocalized over the two thiolate ligands. This visual inspection is consistent with the obtained FOLI ≈ 2 value. Importantly, we obtained a Δ-FOLI value of *exactly* zero using both AIMs, indicating a formal splitting of the electron pair between the two thiolate ligands (covalent assignment). Such electron assignment leads into two formally -1 thiolate moieties accompanied of a Ni(+2).

Two electron reduction to the system leads once again to a closed-shell species. Applying the OSLO algorithm leads to essentially the same valence LOs (four Ni's d-type LOs, two lone pairs and two σ S-Ni orbitals), in exception of the last delocalized orbital that is replaced by two well-localized π orbitals, one on each thiolate ligand (Figure 7.8c). The Δ-FOLI value larger than 1 clearly indicates that the reduction is ligand-based, being the system then characterized as a Ni(+2) with two formally -2 thiolate moieties.

The characterization of $[Ni(S_2C_2Me_2)_2]^-$ is more tricky. In this case, the system presents a doublet spin-state multiplicity (S = 1/2), being thus the α and β parts treated independently. According to OSLO, the α part is rather clear-cut (Δ-FOLI > 0.6), with similar LOs to the fully reduced ($n = 2$) species. Instead, the OSLOs of the β part depends of the AIM definition. In particular, when using the IAO-AutoSAD fragment populations the LOs obtained are comparable to those of the neutral species: four Ni's d-type LOs and a last π LMO delocalized over the two thiolate moieties, with FOLI ≈ 2 and Δ-FOLI $= 0$. These OLSOs suggest a mixed-valence situation with two partially-reduced thiolate ligands (formal OS of -1.5 each), from equal sharing of the last beta electron between the thiolates, and a Ni(+2). This OS assignment, as well as those for the closed-shell species, agrees with the experimentally reported evidences [196,197] and with the EOS results presented in Section 6.1. However, for this species the algorithm coupled with the TFVC AIM leads to a different scenario. In the iterative process, two equivalent π LOs centered on each thiolate and with significant contribution from the Ni center (see Figure 7.8d) are selected over the Ni d-type LMO (which also exhibits significant mixing with the ligands). The FOLI values are 1.901 and 2.011, respectively, indicating large delocalization of these last orbitals. As consequence, the picture obtained is two fully reduced thiolate (-2) ligands and a Ni(+3) (Δ-FOLI $= 0.11$). Note that such very small Δ-FOLI value argues for equal sharing of the last electron pair, recovering in that case the *correct* OS assignment.

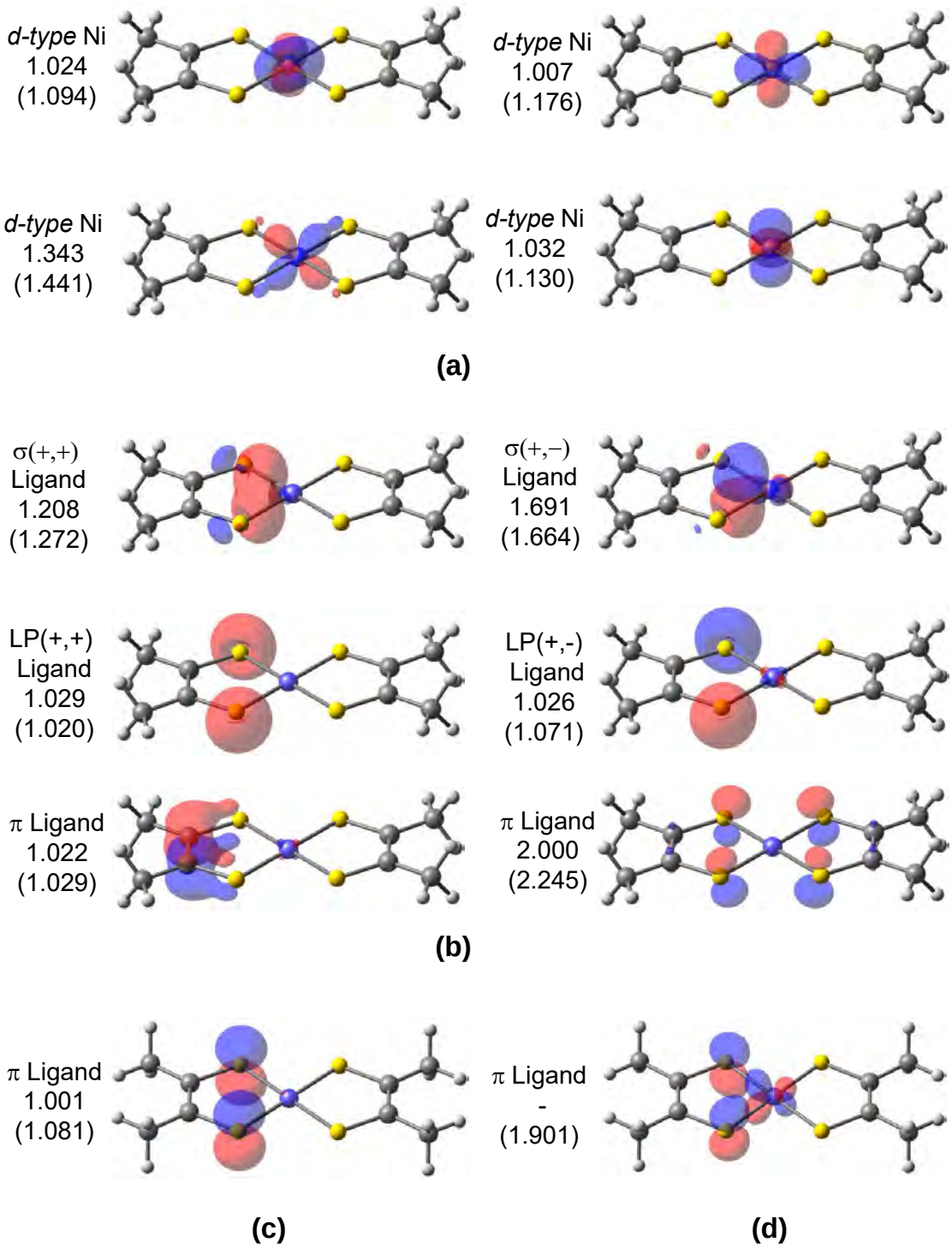

Figure 7.8: Valence LOs of the $[Ni(S_2C_2Me_2)_2]$ system with their associated FOLI values obtained using the IAO-AutoSAD and TFVC (in parenthesis) AIMs. (a) Ni *d*-type LOs, (b) ligand's σ, lone pair (LP) and π LOs. (c) Last localized ligand's π orbital for $[Ni(S_2C_2Me_2)_2]^{2-}$. (d) Last ligand's π LMO from the β-density of $[Ni(S_2C_2Me_2)_2]^{-}$ (TFVC AIM). Selected isocontour value of 0.075 a.u.

We also characterized the Cu OS in Naumann's ion, $[Cu(CF_3)_4]^{-}$,[198] and the role of the CF_3 ligands, which has been debated for more than 25 years.[199–204] In his original work, Snyder concluded that the

metal center is best described as Cu(+1) (d^{10}), instead of a Cu(+3) (d^8) based on frontier MOs analysis at the KS-DFT level.[199] The author states that the anion features an "inverted" ligand field,[204] where the lowest unoccupied molecular orbital (LUMO) exhibits dominant ligand character. This assignment has been questioned by others, who support the more conventional Cu(+3) assignment (with all CF_3 ligands formally -1).[200,201] Recently, Lancaster and coworkers presented experimental and computational arguments in favor of the d^{10} electronic configuration.[202,203] In fact, many arguments supporting both the Cu(+1) and Cu(+3) picture have been given, being in some cases not even the authors of the same manuscript all in agreement.[204]

This conflicting views are rooted in the relatively non-polar character of the Cu-C bond. According to LOBA, the Cu center is clearly in the formal +3 OS, but EOS depicted a close-call situation of Cu(+3) with R(%) = 51.7, supporting the *covalency* of the Cu-C bond (for detailed analysis see Section 6.1). The OSLO procedure also pointed towards a formal Cu(+3) with all ligands anionic, independently of the AIM definition (see Table 7.3). In particular, the algorithm yields four well-localized d-type orbitals from Cu (Figure 7.9a) and four equivalent ligand-centered LOs with non-negligible contribution from Cu, which describes the σ Cu-CF_3 interaction (Figure 7.9b). Interestingly, by applying a fragment-based localization it is observed mixing of the F p-type orbitals of the CF_3 moiety. The resulting LOs provide a much clearer picture compared to the PM ones at the same level of theory (see Section 6.1). Using both TFVC and IAO-AutoSAD leads into *virtually* the same FOLI values of the last OSLOs (≈ 1.5), being clearly polarized towards the ligand. Same chemical bonding picture with solely lower Δ-FOLI value obtained with IAO-AutoSAD (0.373), compared to TFVC (0.728).

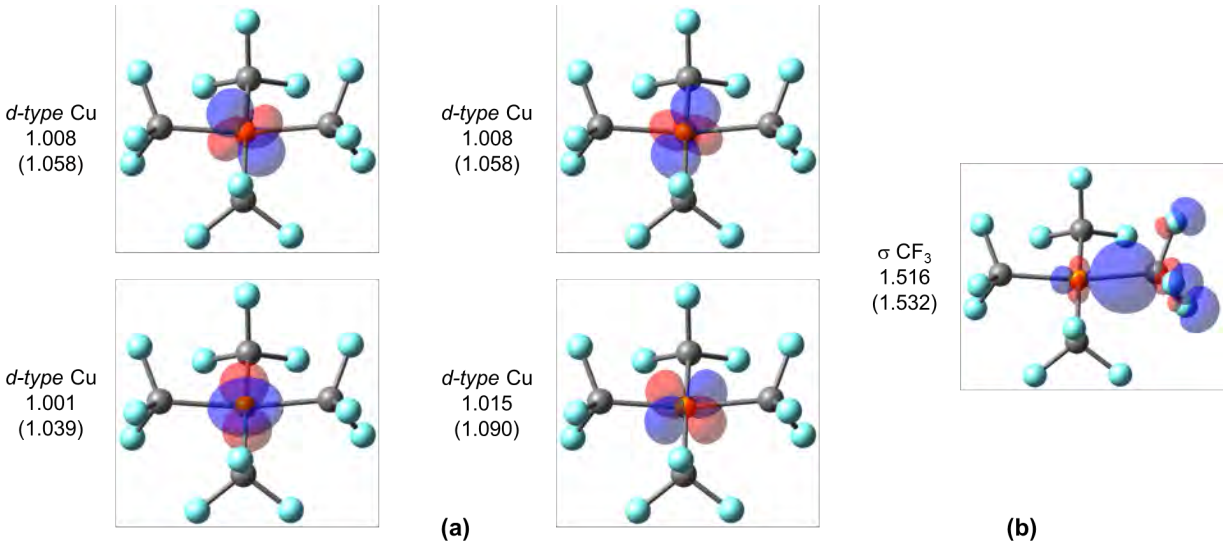

Figure 7.9: Selected LOs of $[Cu(CF_3)_4]^-$ together with the FOLI values for Cu (a) and CF_3 ligand (b) obtained with the IAO-autoSAD and TFVC (in parenthesis) AIMs. Selected isocontour value of 0.075 a.u.

As last examples, we tackle the TM-carbenes characterization as proved to be challenging systems from the OS perspective. For instance, in Section 4.1 we showed that using the centroids position of typically used orbital localization procedures (PM and NLMO), and assigning them electrons according to the closest-atom and basin-allegiance criteria, fail on its classification. Furthermore, EOS analysis often provides low R(%) values (close to 50), governed by almost equal occupancy values of the π EFOs from the TM and carbene unit. From the LOBA perspective, these systems are analyzed in Section 6.1 but, as spoiler, the obtained LOs are non-satisfying at all.

The OSLO scheme (using the IAO-AutoSAD AIM) correctly identifies all prototypical Fischer- and Schrock-type carbenes, while all Grubbs catalysts but **10** are pictured as formal neutral Fischer-type carbenes (see Table 7.3). Notice that the Δ-FOLI values are below 0.3 in almost all cases, and especially for nominal Schrock- and Grubbs-type carbenes, with FOLI values around 2.0. Such value indicates a large delocalization of the last orbital. In Figure 7.10 we depicted the OSLOs of two example systems, involving the carbene unit and the TM. One can observe that the FOLI values of the σ TM-carbene bonds (left) are noticeably smaller than those of the π ones (right). Moreover, the later exhibit a very similar contribution from both fragments. By simple visual inspection, it is clearly noted that the OSLO algorithm produces nice and chemically-interpretable LOs for both the σ and π bonding.

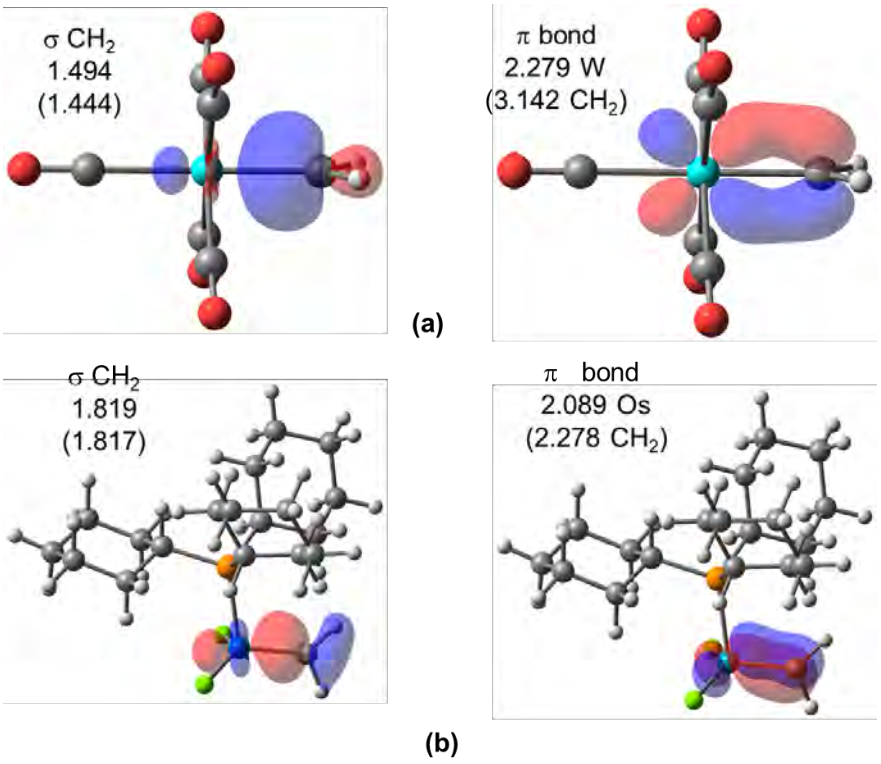

Figure 7.10: σ- and π-type OSLOs for (a) the Fischer-type $(CO)_5W{=}\mathbf{CH}_2$ TM-carbene (**4**), and (b) the Grubbs-type $PCy_3Cl_2Os{=}\mathbf{CH}_2$ TM-carbene (**10**). FOLI values of each LMO shown using the IAO-AutoSAD and TFVC (in parenthesis) fragment populations. Selected isocontour value of 0.075 a.u.

Focusing on the two cases depicted in 7.10, the IAO-AutoSAD and TFVC AIMs lead to different OS assignments, but yield almost identical sets of LOs. The σ TM-carbene OSLO belongs to the carbene moiety, with FOLI values of $\approx$ 1.5 and $\approx$ 1.8 for **4** and **10**, respectively. The origin of the discrepancies is the π TM-carbene OSLO. Since this orbital is the last selected in the OSLO procedure, its allegiance is based on the FOLI values from each fragment. For the Grubbs-type carbene **10**, TFVC provides FOLI values of 2.28 and 2.32 for the carbene moiety and TM, respectively, and the corresponding IAO-AutoSAD values are 2.14 and 2.09. As consequence, ionic assignment of the electron pair leads to a neutral CH_2 ligand according to IAO-AutoSAD, while anionic (-2) according to TFVC. Note that the Δ-FOLI values are in both cases below 0.05, which in fact is the smallest obtained in all systems evaluated. The genuinely covalent nature of this π bond precludes meaningful classification of this system as Fischer or Schrock: instead the electron pair is shared, similarly of the EOS scenario where the frontier EFOs are pseudo-degenerated in occupancy.

It is rather unexpected the different OS assignment obtained for system **4**, as both AIMs produce *virtually* the same set of OSLOs. With IAO-AutoSAD, this system is clearly characterized as a neutral Fischer-type carbene with a Δ-FOLI value of 0.61. However, TFVC yields not only to a reversed OS assignment, with small Δ-FOLI value (0.19), but also significantly higher FOLI values for the last π TM-carbene OSLO are obtained (3.34 and 3.14 for the TM and carbene moiety, respectively). To deepen in the origin of these results, we looked into the TFVC fragment populations, being for W and the carbene 0.66 and 0.76 electrons, respectively. Hence, the remaining 0.58 electrons belong to the formally spectator CO ligands, explaining the large FOLI value obtained. The IAO-AutoSAD fragment populations of W and the carbene are 1.03 and 0.64 electrons, respectively, being the electron pair more clearly on W.

Concluding this section, in this work we presented a new orbital localization procedure based on *molecular fragments* for oxidation states purposes. The fragments are *a priori* selected by the user, being in case of a TM complex the metal and each one of its ligands. The algorithm we propose selects the most strongly fragment-localized OSLOs iteratively and associates the electrons from each orbital with the parent fragment, being the OSs elucidation a side effect. To quantify the degree of locality of each OSLO (or *any* input orbital) on each fragment, we introduced a new index, namely the fragment orbital localization index (FOLI). Importantly, the orbital localization procedure is independent of the AIM definition, but the FOLI evaluation (used solely to *select* the OSLOs) requires fragment populations. Thus, we tested two different but robust population schemes, the TFVC and a new version of the IAOs that uses on-the-fly evaluation of the reference minimal basis based on superposition of atomic densities (IAO-AutoSAD), showing the robustness of the OSLO method independently of the AIM definition used.

The OSLO iterative procedure selects the orbital with lowest FOLI value on each iteration, so that the last OSLO produced has the largest FOLI value (and is least strongly fragment-localized) among the whole set. The Δ-FOLI value for the last localized molecular orbital measures the gap with the second smallest FOLI value among the fragments. Δ-FOLI formally measures how clear-cut the assignment has been performed. With the systems tested, a Δ-FOLI value larger than 0.5 usually indicates a clear OS assignment. Smaller values suggest large covalent character of the last OSLO, even though the shared-pared assignment is only invoked when the Δ-FOLI value is (almost) zero.

The results obtained with the OSLO procedure are in much better agreement with the expected Lewis structure than those obtained with other *global* localization schemes such as PM or NLMO (apart from straightforward cases). Some limitations found for the LOBA scheme (see Section 6.1), such as the TM-carbene characterization, are overcome.

Finally, the IAO-AutoSAD AIM performed well in combination with OSLO, even outperforming the real-space TFVC (conventionally used in the EOS framework). Thus, the IAO-AutoSAD represents a promising all-round general, fast, analytical, basis-set independent Hilbert-space AIM.

7.1.3 Effective oxidation states from the paired and unpaired density functions

One of the state-of-the-art OSs elucidation techniques is the EOS analysis.[43] As mentioned in Section 1.4, it relies on Mayer's effective fragment orbitals and its occupancy values. The EFOs are the orbitals of the fragment net density (see details in Section 1.3.2). In the real-space, the EFOs are obtained upon diagonalization of the MO matrix from Eq. 1.107, or, in the AO basis, of the $\mathbf{PS}^A$ matrix, where $\mathbf{P}$ is the first-order density matrix and $\mathbf{S}^A$ is the fragment net overlap matrix. Since $\mathbf{P}$ is readily available for most electronic structure methods, EOS is of most general applicability, from single-determinant to correlated wavefunctions. The

scheme also requires an underlying AIM definition that ultimately defines numerically the $\mathbf{S}^A$ values.

In the case of open-shell systems, the α and β electrons are treated separately, using the spin-resolved $\mathbf{P}^\alpha$ and $\mathbf{P}^\beta$ matrices to obtain two sets of EFOs for each fragment (see Section 1.3.2). Thus, when formally distributing the electrons over the molecular fragments, the number of both α and β electrons is conserved, as it should. However, this strategy precludes the coveted straightforward interpretation into genuine chemical terms, namely electron pairs. Dealing with separate α and β EFOs with unequal shapes (in particular with spin-contaminated wavefunctions) is clearly not satisfactory.

In a restricted open-shell description, the solution is to deal first with the doubly-occupied space to assign electron pairs, and then the singly-occupied one to assign the remaining (alpha) electrons. But single-determinant description of open-shell systems typically involves unrestricted MOs, where the spatial distribution of the α and β electrons differ. For instance, a recent study showed strong spin-polarization in the Fe-NO π-type interaction of a high spin S = 3/2 complex, which accumulated α-density on the metal and β-density on the nitrosyl ligand.[107] The authors pinpointed conceptual difficulties reconciling IUPAC's IA of electron pairs with the σ/π separation in such spin-polarized bonds. In their study the authors used both KS-DFT and CASSCF methods, and applied EOS analysis leading to quite consistent results. However, if the molecular system was in the singlet state the situation could have been different.

Unrestricted KS-DFT methods can readily capture spin-polarization in singlet spin-states by recurring to the so-called broken symmetry approach.[205–207] BS-DFT can describe diradicals, an extreme case of spin-polarization, resulting in a non-zero spin density. On the contrary, the latter vanishes when using a multireference wavefunction. In this case, the spin-polarization is introduced by populating the antibonding orbitals, while keeping the restricted framework. Consequently, the α and β parts of the density are exactly equivalent (as it should be for a singlet state), so the fate of both electrons resulting from any analysis is the same. This is the origin of the intrinsic limitation of the EOS scheme, being unable to characterize singlet diradical(oid) species from the proper multireference (e.g. CASSCF) wavefunctions (see details in Section 1.4). With this, the main objectives of this third project were:

1) To propose an new scheme, based on the EOS machinery, which is able to properly characterize singlet diradical(oid) species from a multireference (CASSCF) wavefunction.

2) To unify the treatment of spin-polarization within EOS.

To accomplish these goals, we proposed a new approach, namely uEOS, that fixes its intrinsic limitation (see Section 1.4) while keeping the essential ingredients of the original EOS scheme. In particular, uEOS extracts the EFOs from the paired and unpaired density functions, obtaining paired and unpaired EFOs, respectively, instead of α and β ones. Importantly, uEOS and EOS produce exactly the same results for restricted single-determinant wavefunctions as the unpaired density is trivially zero. Furthermore, the new scheme can be applied on equal footing for any single-determinant or correlated wavefunctions, unifying thus the treatment of spin-polarization. To evaluate its performance, we applied uEOS to a variety of systems including TM-based complexes with non-innocent ligands, a model system of an $[Fe_2S_2]$ cluster and the conflictive $[NaBH_3]^-$ anion.

The main idea is to obtain the EFOs from the paired and unpaired densities, instead of the α and β densities as it is commonly used in EOS. For that, one just needs to consider their matrix representations in

the AO basis, namely $\mathbf{P}^p$ and $\mathbf{P}^u$ instead of $\mathbf{P}^\alpha$ and $\mathbf{P}^\beta$. As a result, two sets of EFOs with their occupancies for each fragment are obtained.

Let us start by considering the dissociation of LiH in the singlet spin state, described with a FCI wavefunction. We show the evolution of the EFO occupancies for Li and H from the paired and unpaired density along the dissociation profile in Figure 7.11 (left). They both correspond to polarized 2s and 1s EFOs, respectively. The additional 1s EFO on Li from the paired density is not shown. For a better comparison between the relevance of the paired and unpaired EFOs, the occupancies of the paired EFOs have been halved.

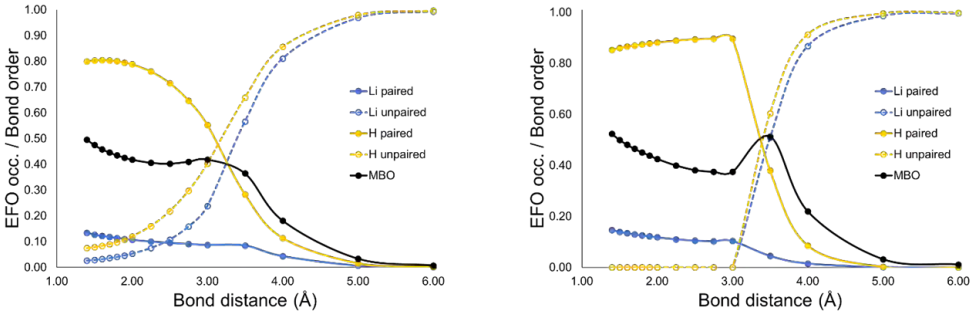

Figure 7.11: Occupancy of the EFOs and Mayer bond order (MBO) along the Li-H bond dissociation. FCI/def2-TZVP (left) and BS-DFT/def2-TZVP (right).

At large inter-atomic distances the unpaired density clearly dominates. The occupancy of both EFOs (dashed curve) is close to 1, clearly pointing towards the homolytic Li· + H· situation, with the unpaired electrons on each atom coupled as a singlet. As the inter-atomic distance shortens, the unpaired EFOs occupancy monotonically decrease, while the one of the paired EFOs increase, particularly that of the H moiety (solid lines). At around 3Å, the dominating paired and unpaired curves cross, very close to the maximum of the covalent bond order (black curve). At shorter distances, the occupancy of the unpaired EFOs is very small, and also that of the Li 2s EFO from the paired density, clearly indicating that the formal heterolytic assignment of the electron pair as Li(+1) + H(-1) is preferred. We performed the same type of analysis from a KS-DFT density obtained with the ωB97XD functional (Figure 7.11 (right)), obtaining a qualitatively similar picture even though the underlying wavefunction is completely different. At around 3.2Å, a BS solution is found and the occupancies of the paired EFOs drastically drop, in favor of the unpaired counterpart.

In the *ideal* case of an homolytic split of the Li-H bond, the occupancies of the paired EFOs should be zero, while the occupancies of the unpaired EFOs should be 1. On the contrary, a heterolytic split to form a formal Li(+1)/H(-1) should be put into correspondence a paired EFO on H with occupancy of 2, and zero occupancy of the paired EFO on Li and for the respective unpaired EFOs. The paired and unpaired occupancies of the EFOs obtained at FCI level of theory for several inter-atomic distances are gathered on Table 7.4. The sum of the absolute differences between the actual occupancy numbers and those of the ideal case leads to the overall deviation for the homolytic and heterolytic split of the Li-H bond, shown in the last two columns of Table 7.4. The deviations obtained along the dissociation profile are depicted in Figure 7.12.

Table 7.4: Occupancies of the paired and unpaired EFOs for Li and H in LiH in the ideal homolytic and heterolytic situations, and for several inter-atomic distances. Total deviations of the occupancies from the ideal homolytic and heterolytic pictures.

	Li		H		dev. homo	dev. hetero
	paired	unpaired	paired	unpaired		
Li·(0) / H·(0)	0	1	0	1	**0.00**	4.00
Li(+1) / H(-1)	0	0	2	0	4.00	**0.00**
LiH 1.6Å (eq.)	0.244	0.032	1.610	0.083	3.74	**0.75**
LiH 3Å	0.175	0.238	1.107	0.403	2.64	**1.71**
LiH 3.22Å	0.182	0.369	0.867	0.516	**2.16**	2.20
LiH 3.5Å	0.170	0.567	0.566	0.660	**1.51**	2.83

The smaller the deviation, the more faithful is a given string of occupancy numbers to the respective ideal situation. The maximum possible deviation is twice the number of electrons to be distributed. At equilibrium distance and up to 3Å distance, the formal Li(+1) / H(-1) picture is clearly preferred. At a distance of 3.5Å the deviation with respect to the homolytic split is now smaller, marking the beginning of the formal dissociation. In fact, it is easy to see that roughly at the turning point (at around 3.22Å), the sum of the two unpaired occupancies on Li and H is larger than the paired occupancy of H. A simpler *rule of thumb* is to compare the unpaired occupancies with half the paired occupancy.

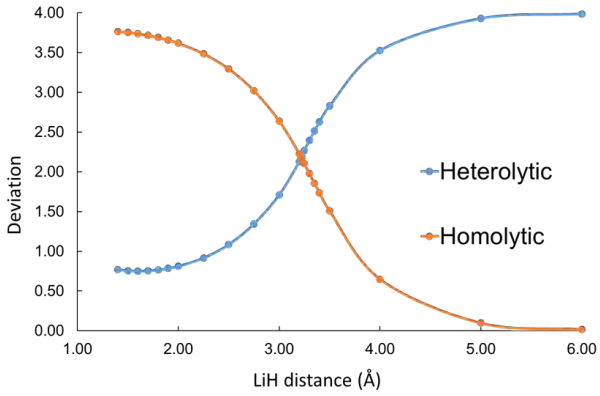

Figure 7.12: Deviation of the actual occupancy numbers of the EFOs from those of the ideal formal homolytic and heterolytic situations for the dissociation profile of the LiH system at the FCI/def2-TZVP level of theory.

This type of paired/unpaired information can be readily incorporated into a general scheme to assign OSs, namely uEOS analysis. In the same way as conventional EOS, one starts by defining the molecular fragments (i.e. metals and ligands). Then, the EFOs are obtained for each fragment using the paired and unpaired densities. As it was aforementioned, for that one just needs to consider their matrix representations in the AO basis, namely $\mathbf{P}^p$ and $\mathbf{P}^u$ instead of $\mathbf{P}^\alpha$ and $\mathbf{P}^\beta$. The EFOs are then sorted by decreasing occupancy and electron pairs are assigned to those EFOs from the paired density with higher occupancy, and individual electrons (usually of unknown spin) are assigned to EFOs of the unpaired density. However, while in EOS analysis the number of alpha and beta electrons is predefined, in uEOS the total (integer) number of paired and unpaired electrons is in general not known and must be inferred by comparing the occupancies of the respective EFOs.

Let us analyze the different situations one may encounter for a molecular system holding N electrons. In the case of a restricted single-determinant wavefunction, the unpaired density trivially vanishes, so $\mathbf{P}_u = 0$.

Accordingly, the uEOS procedure is applied using the total **P** matrix, from which $N/2$ pairs of electrons to the most populated EFOs are assigned. Thus, uEOS coincides with the conventional EOS scheme. Furthermore, only formal heterolytic cleavage of the bonds is allowed, in agreement with the "winner-takes-it-all" principle of the IUPAC's IA.[104,105] In the restricted open-shell single-determinant case, the uEOS procedure is applied for the paired and unpaired densities, separately. Since $u(\mathbf{r}) = \rho^s(\mathbf{r})$, the unpaired density holds exactly $N_\alpha - N_\beta$ electrons, being thus both the number of paired and unpaired electrons known. In this case, N_β pairs of electrons are assigned to the most occupied paired EFOs, and the remaining $N_\alpha - N_\beta$ electrons are individually assigned to the unpaired EFOs with larger occupancy values. However, for open-shell systems the use of unrestricted single-determinant wavefunctions is much more common. In that case, the unpaired density no longer coincides with the spin density due to spin contamination and therefore $\int u(\mathbf{r})d\mathbf{r} \geq N_\alpha - N_\beta$, being thus the (integer) number of unpaired electrons no longer predetermined. In such scenario, the paired and unpaired EFOs are ordered by decreasing occupancy number, independently, being the paired occupancies halved to be comparable with the unpaired ones, and pairs of electrons are assigned to the paired EFOs and individual electrons to the unpaired ones, until the total number of electrons is reached.

We illustrate the new procedure by considering the $[Fe(CN)_5NO]^{3-}$ complex in its $S = 1/2$ ground-state. The occupancy number of the paired and unpaired EFOs for the restricted open-shell and unrestricted wavefunctions are compiled in Table 7.5. The occupancies of the paired EFOs have been halved to allow a better comparison with that of the unpaired EFOs (see below). In the restricted case, a doublet leads to exactly one unpaired electron. The occupancy of the unpaired density (using both definitions) are 0.143, 0.816 and 0.010 for Fe, NO and each CN fragment, respectively. The unpaired electron is thus clearly assigned to the NO moiety. Afterwards, the EOS procedure is safely applied to the paired density and the remaining N_β pairs of electrons are assigned. The last electron pair is assigned to a 3d-type EFO sitting on Fe, with a (halved) occupancy of 0.690. The first unoccupied EFO sits on the NO moiety, with an occupancy of 0.233. The procedure finally results in the formal Fe(+2), NO(0) and CN(-1) picture. As far as the reliability of the uEOS assignation is concerned, one can simply replace in Eq. 1.113 the frontier occupancies of the alpha and beta parts by those of the paired and unpaired densities. This results in a clear cut assignation, with $R_p(\%) = 95.7$ and $R_u(\%) = 100$.

Table 7.5: Occupancy values of the selected paired and unpaired EFOs for the $[Fe(CN)_5NO]^{3-}$ anion with restricted open-shell and unrestricted wavefunctions.

	Fe			NO			CN	
Type	Rest.	Unrest.	Type	Rest.	Unrest.	Type	Rest.	Unrest.
				paired				
3d	0.851	0.854	π	0.994	0.993	π	0.989	0.989
3d	0.770	0.755	π	0.993	0.992	π	0.988	0.988
3d	0.690	0.602	3σ	0.880	0.876	3σ	0.790	0.788
3d	0.282	0.287	π^*	0.233	0.210	π^*	0.050	0.049
4s	0.254	0.253	π^*	0.151	0.138	π^*	0.044	0.041
				unpaired				
	0.143	0.175	π^*	0.816	0.813		0.010	0.012
		0.115			0.120			0.004
		0.031			0.004			

The EFO occupancies obtained with the unrestricted wavefunction are quite similar to the restricted open-shell ones, even though the spin contamination ($< S^2 > = 0.93$) is significant (see Table 7.5). Noticeably, the spin contamination induces a number of additional EFOs of the unpaired density with non-zero

occupancy. Their values are, however, very small (ca. 0.1) as compared to the occupancy of the last possible electron pair (0.602). Thus, the OS assignment coincides with the previously obtained.

Applying the conventional EOS analysis on the unrestricted wavefunction, thus considering the α and β electrons separately, also leads to the same OSs. The shape of the relevant EFOs is shown in Figure 7.13. Clearly, the spin-polarization induces a significant mismatch not only on the occupancies but also on the shape of the α and β EFOs. The 3σ and π^* EFOs of the α part are mixed so that it is not clear the nature of the EFO holding the unpaired α electron.

With uEOS, however, the picture obtained is much easier to interpret in terms of electron pairs. A single set of either singly or doubly occupied EFOs is obtained (Figure 7.13, bottom). The two π^* EFOs of the NO moiety are clearly identified in the paired part, together with the matching Fe's 3d EFOs that account for the Fe-NO bonding. The latter are clearly polarized towards the Fe, as shown by their respective occupancies. From the unpaired density, the only significantly populated EFO is a clear π^* on the NO moiety, similar to the (unoccupied) EFO of the paired part, altogether pointing to an undisputed NO(0) moiety. It is also interesting to note that for the other π Fe-NO bond, the shape of the paired and unpaired EFOs is strikingly similar, differing only by their occupancies. This appears to be a common feature of all systems studied thus far.

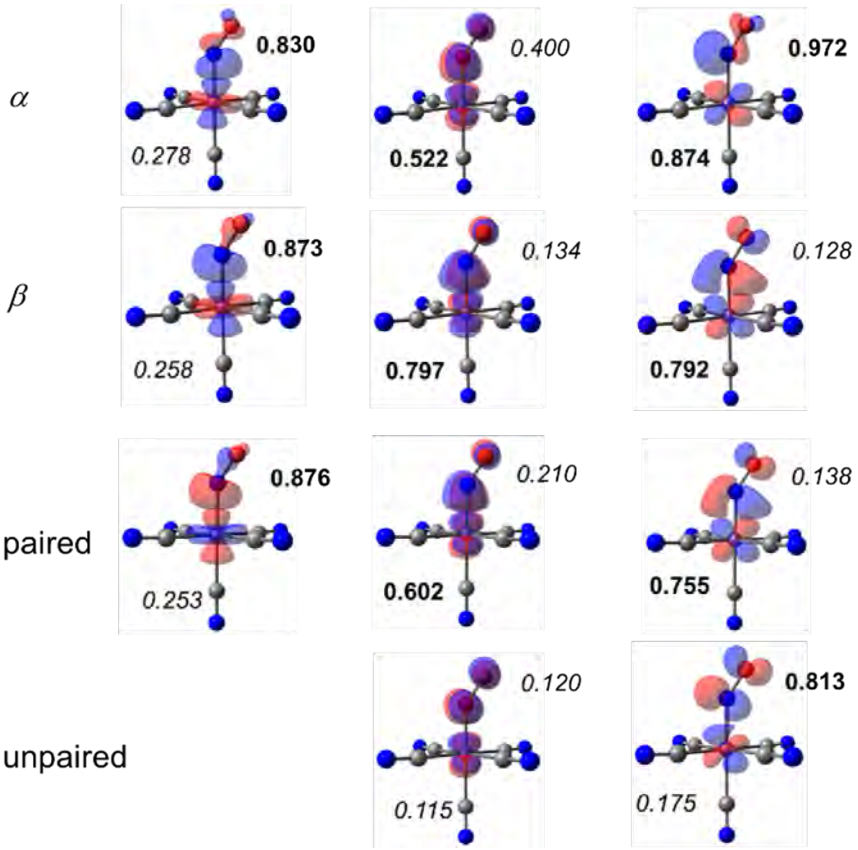

Figure 7.13: α/β (top) versus paired/unpaired (bottom) EFOs for the $[Fe(CN)_5NO]^{3-}$ anion from an unrestricted wavefunction, including their associated occupancies. EFOs considered occupied in bold and unoccupied in italics. Selected isocontour value of 0.1 a.u.

One may foresee situations where more than $N_\alpha - N_\beta$ EFOs of the unpaired density have occupancy

numbers larger than (half) the occupancy of the N_α pairs from the paired density. In the new scheme, this is an indication that one (or more) formal electron pairs must be homolytically split. This is indeed the case of mixed-valence compounds such as $[Ni(S_2C_2Me_2)_2]$. The occupancies of the paired and unpaired EFOs obtained for BS-DFT ($< S^2 > = 0.63$) and CASSCF(2,2) wavefunctions are collected on Table 7.6. Even though for this system in the singlet state $N_\alpha = N_\beta$, there is an EFO on each thiolate ligand with larger occupancy than that of the last electron pair from the paired density (a Ni 3d-type EFO). In the BS-DFT case, these occupancies are 0.554 and 0.484, respectively. The chemical bonding picture obtained at the CASSCF(2,2) level is somewhat clearer, with respective occupancies of 0.725 and 0.244, respectively. Hence, by the uEOS procedure each thiolate ligand is awarded an unpaired electron, and consequently the Ni center loses the last electron pair, becoming formally Ni(+2) and each thiolate -1. Applying conventional EOS to the BS-DFT wavefunction, one thiolate holds an extra α-electron and the other a β one, in line with their respective spin densities. For the CASSCF wavefunction, uEOS allocates an unpaired electron on each ligand.

A closed-shell description of this system leads to the undesired situation where two EFOs, one on each thiolate ligand, are degenerated in occupancy and there is only one electron pair left to assign. Then, a formal homolytic splitting of the electron pair is assumed on the basis of the degeneracy of the frontier EFOs, leading also to the abovementioned OS assignment (detailed analysis provided in Sections 6.1 and 4.2). Figure 7.14 shows again the same shape of the paired and unpaired EFOs. The occupancy values of the paired (frontier) EFO of the closed-shell wavefunction (2×0.531) is roughly decomposed in the uEOS treatment (CASSCF wavefunction) by an unpaired (0.725) and a paired (2×0.132) contribution (see Figure 7.14). Any asymmetry of the ligands would break that degeneracy and forbid the formal homolytic split in the closed-shell, unless artificially introduced, yielding an erroneous OS assignment. This would not be the case if one uses uEOS coupled with the proper multireference wavefunction.

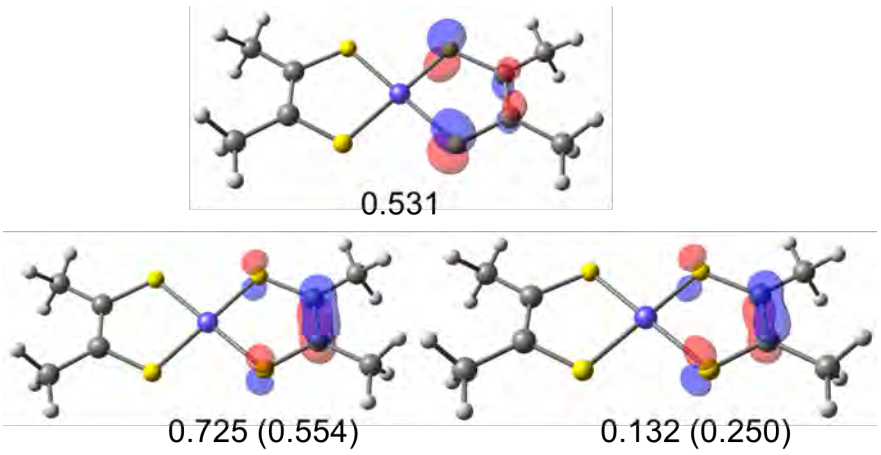

Figure 7.14: Frontier EFOs of the thiolate ligand in $[Ni(S_2C_2Me_2)_2]$. Paired EFO from a closed-shell wavefunction (top), unpaired (bottom-left) and paired (bottom-right) EFOs from a CASSCF(2,2) wavefunction. Occupancies from the BS-DFT in parenthesis. Selected isocontour value of 0.1 a.u.

We proceed by analyzing a modelled version of the smallest iron sulfur complex present in various metallaproteins, $[Fe_2S_2(SCH_3)_4]^{2-}$, and already studied computationally by several groups.[208–210] In its singlet ground-state, such system presents five unpaired electrons in each iron center antiferromagnetically coupled. By applying uEOS on a CASSCF(10,10) wavefunction on top of the reported geometry,[210] five 3d-type unpaired EFOs from each iron center are populated with occupancies larger than 0.8, recovering

thus the Fe(+3)/Fe(+3) picture. Upon one-electron reduction of the system, uEOS presents one 3d-type paired EFO (0.958) and four unpaired ones (0.961-0.934) on one of the Fe centers, while the other presents five 3d-type unpaired EFOs (0.955-0.864), leading into the asymmetric Fe(+2)/Fe(+3) assignment. The same OSs assignment is obtained with the less theoretically sound BS-DFT wavefunction.

Table 7.6: uEOS results for the systems studied at different levels of theory. Selected ligand (L) in bold. EFO occupancies and OSs from conventional EOS reported in Section 4.3. Paired and unpaired EFO occupancies obtained using Takatsuka's unpaired density function definition. WF = wavefunction, RO = restricted open-shell, BS = broken-symmetry, U = unrestricted. [a] Single unpaired electron split over the two equivalent ligands.

System	WF	$< S^2 >$	paired M/L	unpaired M/L	M OS	L OS	R(%)
$[Fe(CN)_5\mathbf{NO}]^{3-}$	RO-DFT	0.75	0.690/0.233	0.143/0.816	2	0	95.7
	U-DFT	0.93	0.602/0.210	0.175/0.813	2	0	89.2
$[Ni(\mathbf{S_2C_2Me}_2)_2]$	BS-DFT	0.63	0.484/0.250	0.065/0.554	2	-1	98.9
	CASSCF(2,2)	0.00	0.244/0.132	0.027/0.725	2	-1	100
$[Fe_2\mathbf{S}_2(SCH_3)_4]^{2-}$	BS-DFT	4.67	0.323/0.010 0.323/0.010	0.630/0.184 0.631/0.185	3/3	-2	94.6
	CASSCF(10,10)	0.00	0.227/0.008 0.227/0.008	0.856/0.083 0.856/0.083	3/3	-2	100
$[Fe_2\mathbf{S}_2(SCH_3)_4]^{3-}$	BS-DFT	4.60	0.399/0.010 0.933/0.016	0.614/0.169 0.801/0.162	2/3	-2	94.6
	CASSCF(11,10)	0.75	0.958/0.013 0.238/0.013	0.934/0.067 0.864/0.065	2/3	-2	100
$[Fe(CO)_3\mathbf{NO}]^{-}$	CASSCF(4,4)	0.00	0.321/0.301	0.337/0.342	0	-1	82.3
	CASSCF(10,10)	0.00	0.380/0.330	0.269/0.245	-2	+1	63.6

The new uEOS scheme clearly supersedes conventional EOS in the treatment of singlet states with marked multireference character. A paradigmatic example is the $[Fe(CO)_3NO]^-$ anion, studied in detail by several authors.[211–214] By combining spectroscopic features with theoretical considerations Klein *et al.* concluded that the most appropriate picture was a neutral Fe center with an anionic NO(-1) ligand, who exhibits two π- and no σ-type bonds with the metal.[213] Conventional EOS analysis struggles with this system, partly due its C_3v symmetry. When there are only two electron pairs left to assign, the NO moiety exhibits the expected two degenerated π^* EFOs with occupancies extremely close to that of a pair of degenerated 3d-type Fe EFOs, already indicating a strong covalent character of the Fe-NO bonds. Then, one necessarily ends with either the Fe(-2)/NO(+1) or Fe(-2)/NO(-3) OS assignments, no matter the underlying wavefunction being closed-shell single-determinant or CASSCF. On the contrary, with uEOS, if the unpaired density becomes dominant, the homolytic splitting of the two electron pairs can still be achieved, leading to the Fe(0)/NO(-1) picture suggested by Klein *et al.*[213] This is exactly what happens when analyzing the CASSCF(4,4) wavefunction. First, the total number of effectively unpaired electrons, N_D, is 1.50 (0.71 on both Fe and NO), indicating significant static correlation. The frontier EFOs of the paired and unpaired densities are strikingly similar in shape (see Figure 7.15), and correspond to the aforementioned d-type on Fe and $\pi*$-type on NO. The symmetry of the EFOs on each moiety also indicate that these are involved in two π-bonds. The key aspect for OS assignation are the corresponding occupancies obtained from the unpaired (0.337 and 0.342) and paired (0.321 and 0.301) densities. The larger value of the former calls for the formal homolytic splitting of the two Fe-NO bonds, and the consideration of the anion as a double diradicaloid.

It is interesting to assess the effect of increasing the active space, using for example a CASSCF(10,10) wavefunction. First, the number of effectively unpaired electrons increases up to 2.15. However, the occupancy of the relevant frontier unpaired EFOs actually decreases to 0.269 and 0.245 for Fe and NO, respectively. Thus, the increase in N_D originates from a number of additional EFOs on Fe with smaller but

non-negligible occupancy, a signature of the additional correlation introduced by enlarging the active space. At the same time, the occupancy of the EFOs from the paired density increases to 0.381 and 0.330 for Fe and NO, respectively. The picture originating from the uEOS procedure is now closer to a formal Fe(-2)/NO(+1) closed-shell scenario. This seems to indicate that using small active spaces tends to overestimate the static correlation of the Fe-NO bonds.

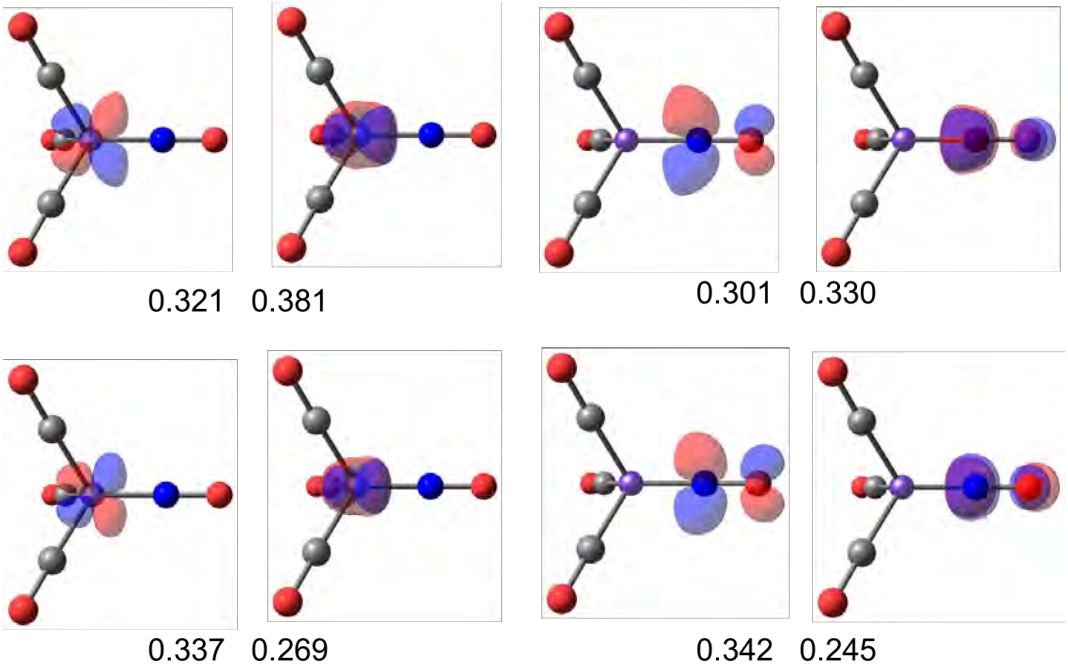

Figure 7.15: Frontier EFOs of the Fe (left) and NO (right) fragments of $[Fe(CO)_3NO]^-$ anion. (top) paired and (bottom) unpaired EFOs from a CASSCF(4,4) and CASSCF(10,10) wavefunction. Selected isocontour value of 0.1 a.u.

The last example to discuss is the $[NaBH_3]^-$ anion, which has generated strong debate in the recent literature about the nature of the Na-B bond.[94,215–217] The ground state is singlet, but the closed-shell wavefunction is not stable. The lowest energy solution at the single-determinant level is a broken-symmetry open-shell singlet. The corresponding $< S^2 >$ values are strongly dependent on the nature of the KS-DFT functional, being 0.29, 0.60 and 0.70 for BP86, PBE0 and M06-L functionals, respectively, using auc-cc-pVTZ as atomic basis set. Salvador *et al.* showed that the singlet CASSCF(8,8) wavefunction exhibits diradical(oid) character, due to the significant population of the σ^* Na-B bond orbital.[94] If the diradical character is large enough, the appropriate picture from an OS perspective would be Na(0)/BH_3(-1), in agreement with a formal homolytic cleavage of the Na-B bond. This is the picture one typically obtains with conventional EOS analysis over an approximate BS-DFT wavefunction (see below), as the spin-polarization provokes an excess of either α- or β-density on Na and the opposite on BH_3. However, as mentioned before, the conventional EOS analysis cannot account for such picture if the system is described by a proper multireference wavefunction, even in the case of a pure diradical.

According to uEOS, the frontier EFOs are associated to the Na-B bond, as expected. The shape and occupancies of the relevant EFOs (CASSCF) are depicted in Figure 7.16. The occupancies of the unpaired EFOs on Na (0.508) and BH_3 (0.459) are larger than that of the corresponding paired EFOs (0.316 and 0.189, respectively). Consequently, uEOS homolitically splits the Na-B electron pair, being thus the OS

assignment in line with its diradical character, i.e. best described as Na(0) and BH_3(-1).

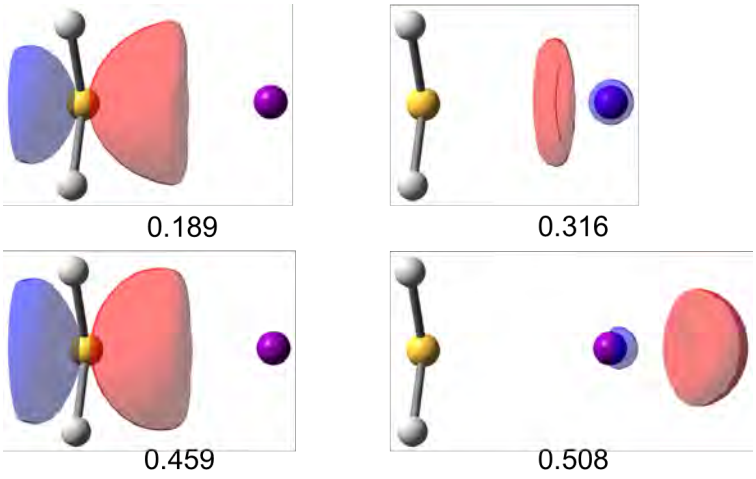

Figure 7.16: Frontier EFO of the BH_3 (left) and Na (right) fragments of $[NaBH_3]^-$ anion. Paired (top) and unpaired (bottom) EFOs, together with their occupancies, obtained from a CASSCF(8,8) wavefunction. Selected isocontour value of 0.1 a.u.

Remarkably, the shape of the singly occupied unpaired EFOs (Figure 7.16, bottom) is in striking agreement with the valence active orbitals of the covalent valence-bond wavefunction (i.e. Figure 2 left of Ref. [217]). The unpaired EFOs thus provide a picture fully consistent with the one put forward by Radenkovic *et al.*: a dominant diradical character but at the same time an enhanced electrostatic interaction induced by the charge-separation on the two fragments. [217] It does not support the interpretation of Pino-Rios *et al.* who considered both unpaired electrons on a formal Na(-1) fragment. [216]

The broken-symmetry solution using the local BP86 functional has a rather modest diradical character ($< S^2 > = 0.29$). As consequence, the EFOs of the unpaired density have too low occupancy number and all electrons are assigned from the paired density. The Na-B bond is heterolytically split towards the Na center, who exhibits the paired EFO with larger occupancy (0.444 vs 0.293 of the BH_3 moiety). This leads to the alternative formal Na(-1) and BH_3(0) assignment. This is in fact the best OS assignation using a modified B3LYP functional with exact exchange up to 20%. From that amount on or when using PBE0 and M06L functionals, the diradical character increases significantly, and the picture obtained with uEOS analysis is in line with the CASSCF(8,8) results. The frontier EFOs obtained with PBE0 and M06L methods are essentially the same as those of Figure 7.16, but the particular choice of DFT functional influences the occupancy numbers of the paired and unpaired EFOs.

Concluding this section, in this work we showed that considering the effectively paired and unpaired densities, rather than the spin-separated α and β ones, leads to much more consistent results in the framework of EOS analysis. Not only it accounts for the formal homolytic splitting of electron pairs in singlet diradical(oid) species, but it also affords a better picture of unrestricted wavefunctions in terms of electron pairs. The present strategy is not merely restricted to the framework of EOS and could be also incorporated in OS schemes based on orbital localization or in general wavefunction analysis techniques deriving from the first-order density matrix. Let us mention that alternative definitions of the unpaired density function exist, e.g. the proposed by Head-Gordon (Eq. 1.28). Using one or another definition of the unpaired density will

affect both the occupancy values and shapes (less) of the resulting EFOs. Thus, it may also affect the OSs assignments by uEOS. Exploratory work in this direction has been performed. The use of the Head-Gordon definition of the unpaired density within uEOS yields, in general, lower occupancy values of the unpaired EFOs but same shape under visual inspection. With this, in close-call scenarios, e.g. $[Fe(CO)_3NO]^-$ anion, the unpaired EFOs are not playing a role, being the electrons assigned to paired EFOs independently of the active space. Similar situation is present for the $[NaBH_3]^-$ anion, being the diradicaloid picture not resulting when applying uEOS on top of the CASSCF wavefunction. With this, it is clear that the Head-Gordon definition of the unpaired density yields unpaired EFOs with *too low* occupancy values for properly assigning OSs in the uEOS framework. Instead, Takatsuka's definition works perfectly at least for the systems tested. An extensive evaluation of the uEOS performance for even more sophisticated systems has not been yet performed. This avenue, together with defining a new unpaired density function for OSs purposes, are out of the scope of the Thesis and will be performed in the future.

7.2 On the development of energy decomposition schemes

7.2.1 Merging the energy decomposition analysis and interacting quantum atoms schemes

In Sections 1.5.1 and 1.5.2 we introduced the two major families of energy decomposition schemes: the energy decomposition analysis (and its variants) and the interacting quantum atoms approaches. Both EDA and IQA schemes have been extensively used to study the concept of chemical bond along the years, showing its usefulness in countless occasions. However, it is very rare the application of both schemes *together* to interpret the chemical bonding of a system. In this direction, several authors attempted to rationalize EDA-derived energy terms with the IQA obtained, and viceversa, but to date there is no study that shows the potential of both schemes when *synergistically* applied. In our opinion, both EDA and IQA schemes should be able to complement one to the other and for this reason the main objectives of this fourth project was:

1) To enrich the results obtained with the conventional EDA approach with the obtained from an IQA analysis.

To accomplish these goals, we propose to apply a fragment-based IQA decomposition to each of the EDA terms of the interaction energy. Thus, in this new methodology (see below), termed as EDA-IQA, the electrostatic, Pauli repulsion and orbital interaction energy terms are further decomposed into intra- and inter-fragment contributions. To illustrate its behaviour, we made use of the set of molecular complexes (described in Ref.[147]), which includes conventional hydrogen bonds, cation-dipole, cation-π, halogen-π and π-π interactions.

Considering again the formation of complex AB from fragments A and B (see Section 1.5.1), the application of Eqs. 1.68 and 1.71 to the complex final ground state (AB) readily affords the real-space decomposition of the interaction energy into both intra- and inter-fragment terms, namely

$$\Delta E_{Int} = \Delta\varepsilon_{Int,A} + \Delta\varepsilon_{Int,B} + \Delta\varepsilon_{Int,AB}, \tag{7.8}$$

where

$$\begin{aligned}\Delta\varepsilon_{Int,A} &= \varepsilon_A(AB) - E_A(A^0)\\ \Delta\varepsilon_{Int,B} &= \varepsilon_B(AB) - E_B(B^0)\\ \Delta\varepsilon_{Int,AB} &= \varepsilon_{AB}(AB).\end{aligned} \tag{7.9}$$

For clarity, in Eq. 7.9 we used the notation from Section 1.5.1 and omitted the explicit dependence of the EDA term on the reference states (A^0 and B^0). Here, $\Delta\varepsilon_{Int,A}$ and $\Delta\varepsilon_{Int,B}$ account for the energy gain/loss by the fragments when going from their isolated reference state to their *effective* state within the final complex. It is worth to note that in the context of real-space analysis, these contributions do not only originate from changes in the MOs upon complex formation, but also by the fact that the fragments share the physical space once the complex is formed (in intermolecular interactions the second effect should be dominant). Pendás, *et al.* refer to these terms as fragment's electronic deformation energies.[157] We will adopt this nomenclature, so that $\Delta\varepsilon_{Int,A} \equiv \Delta\varepsilon_{def.el,A}$ and $\Delta\varepsilon_{Int,A} \equiv \Delta\varepsilon_{def.el,A}$. On the other hand, the $\Delta\varepsilon_{Int,AB}$ term describes the energy gain upon complex formation that can be purely ascribed to inter-fragment interactions. The net interaction energy is thus seen as a balance between the prize the fragments must pay to share the physical space and be electronically prepared, and the gain originating from the new interactions that were absent before the complex formation.

Similarly, one can also obtain an analogous decomposition of the orbital interaction EDA term

$$\Delta E_{Orbint} = \Delta\varepsilon_{Orbint,A} + \Delta\varepsilon_{Orbint,B} + \Delta\varepsilon_{Orbint,AB}, \tag{7.10}$$

where

$$\begin{aligned}\Delta\varepsilon_{Orbint,A} &= \varepsilon_A(AB) - E_A(A^0B^0)\\ \Delta\varepsilon_{Orbint,B} &= \varepsilon_B(AB) - E_B(A^0B^0)\\ \Delta\varepsilon_{Orbint,AB} &= \varepsilon_{AB}(AB) - \varepsilon_{AB}(A^0B^0).\end{aligned} \tag{7.11}$$

In this case, the intra-fragment terms account for the net energy gain/loss upon relaxing the wavefunction from the intermediate state to the ground-state of complex AB. This relaxation comes with a change in the electron density. If the underlying AIM definition depends upon this scalar (e.g. QTAIM, TFVC or iterative Hirshfeld approaches), these terms contain also a contribution from the change on the boundaries of physical space going from AB to A^0B^0. The later could be removed by using the same AIM definition for states AB and A^0B^0. In the context of QTAIM that means integrating the density functions of state A^0B^0 on the atomic basins obtained from the AB state. In the case of overlapping AIM schemes, it implies using the same atomic weight functions throughout. Such strategies have been already used in the context of QTAIM and fuzzy atoms in in similar contexts.[83,157,218] In the present case, since by construction it is actually impossible to use the same AIM definition for the complex and the isolated fragments, we opt for using the AIM definition derived from each state.

The IQA decomposition of state (A^0B^0) readily affords an analogous decomposition of $\Delta E_{Pauli} + E_{Elec}$, by taking the isolated fragment states A^0 and B^0 as reference. On the other hand, since each term in ΔE_{Elec}

involves the electron density and/or potential from different fragments (see details in Section 1.5.1), one may argue that this term is entirely of intermolecular nature. In that case, ΔE_{Elec} would contribute solely to the inter-fragment term, namely

$$\begin{aligned}
\Delta\varepsilon_{Pauli,A} &= \varepsilon_A(A^0B^0) - E_A(A^0) \\
\Delta\varepsilon_{Pauli,B} &= \varepsilon_B(A^0B^0) - E_B(B^0) \\
\Delta\varepsilon_{Pauli,AB} &= \varepsilon_{AB}(A^0B^0) - \Delta E_{Elec}.
\end{aligned} \tag{7.12}$$

However, such a scheme is not satisfactory neither numerically nor conceptually. The main concern is that $\Delta\varepsilon_{Pauli,AB}$ thus defined mixes up real-space and Hilbert-space quantities, while in this case they behave quite differently. Indeed, as previously mentioned, there is no net charge-transfer between fragments A and B when building the intermediate state A^0B^0 according to Hilbert-space analysis (e.g. Mulliken and Löwdin populations add up to the number of electrons of each fragment). This is not the case when performing a real-space analysis, again because the fragments within the complex share the physical space

$$\int_{\Omega_A} \rho_A^0(\mathbf{r}_1)d\mathbf{r}_1 \neq N_A^0 \wedge \int_{\Omega_B} \rho_B^0(\mathbf{r}_1)d\mathbf{r}_1 \neq N_B^0. \tag{7.13}$$

Thus, the frozen density of isolated fragment A, when brought to the complex geometry, does not entirely belong to fragment A, and similarly for fragment B. For consistency, this effect should be taken into account when applying the real-space analysis to ΔE_{Elec} (Eq. 1.119). One should essentially ignore the original allegiance of the fragment frozen densities and treat the integrand in the exactly same manner as one does it with the electron-nuclear and the Coulombic contributions to the energy in the conventional IQA scheme

$$\begin{aligned}
\Delta\varepsilon_{Elec,A} &= \int_{\Omega_A} \rho_B^0(\mathbf{r}_1)\left[\sum_{i\in A}^{N_{At}} \frac{Z_i}{|\mathbf{r}_1-\mathbf{R}_i|} - \int_{\Omega_A} \frac{\rho_A^0(\mathbf{r}_2)}{|\mathbf{r}_1-\mathbf{r}_2|}d\mathbf{r}_2\right] d\mathbf{r}_1 = \int_{\Omega_A} \rho_B^0(\mathbf{r}_1)V_A^{0,net}(\mathbf{r}_1)d\mathbf{r}_1 \\
\Delta\varepsilon_{Elec,B} &= \int_{\Omega_B} \rho_A^0(\mathbf{r}_1)\left[\sum_{i\in B}^{N_{At}} \frac{Z_i}{|\mathbf{r}_1-\mathbf{R}_i|} - \int_{\Omega_B} \frac{\rho_B^0(\mathbf{r}_2)}{|\mathbf{r}_1-\mathbf{r}_2|}d\mathbf{r}_2\right] d\mathbf{r}_1 = \int_{\Omega_B} \rho_A^0(\mathbf{r}_1)V_B^{0,net}(\mathbf{r}_1)d\mathbf{r}_1.
\end{aligned} \tag{7.14}$$

Here we introduce the fragment net electrostatic potentials $V_A^{0,net}(\mathbf{r})$ and $V_B^{0,net}(\mathbf{r})$. They are different from the electrostatic potentials $V_A(\mathbf{r})$ and $V_A(\mathbf{r})$ because in the electronic term the integration is carried out within the fragment domain, rather than for the whole space. In the case of the inter-fragment contribution, one gets

$$\Delta\varepsilon_{Elec,AB} = -\left(\int_{\Omega_A} \rho_A^0(\mathbf{r}_1)V_B^{0,net}(\mathbf{r}_1)d\mathbf{r}_1 + \int_{\Omega_B} \rho_B^0(\mathbf{r}_1)V_A^{0,net}(\mathbf{r}_1)d\mathbf{r}_1\right) + \sum_{\substack{i\in A \\ j\in B}}^{N_{At}} \frac{Z_iZ_j}{|\mathbf{R}_i-\mathbf{R}_j|}. \tag{7.15}$$

The numerical value of this contribution will account to which extent the net potential of fragment A interacting with the density of B and vice versa compensate for the point charge nuclear repulsions. In any case, the additivity is conserved

$$\Delta E_{Elect} = \Delta\varepsilon_{Elec,A} + \Delta\varepsilon_{Elec,B} + \Delta\varepsilon_{Elec,AB}. \tag{7.16}$$

Then, subtracting these contributions from those originating from the IQA decomposition of $\Delta E_{Pauli} + \Delta E_{Elec}$ yield the appropriate real-space decomposition of the Pauli repulsion term

$$\begin{aligned}
\Delta\varepsilon_{Pauli,A} &= \varepsilon_A(A^0B^0) - E_A(A^0) - \Delta\varepsilon_{Elec,A} \\
\Delta\varepsilon_{Pauli,B} &= \varepsilon_B(A^0B^0) - E_B(B^0) - \Delta\varepsilon_{Elec,B} \\
\Delta\varepsilon_{Pauli,AB} &= \varepsilon_{AB}(A^0B^0) - \Delta\varepsilon_{Elec,AB}.
\end{aligned} \tag{7.17}$$

The final picture of the EDA analysis is completed by the inclusion of the preparation energies and, if required, a dispersion correction. In the case of the semiempirical dipole-dipole model of Grimme,[219] the dispersion correction is added to the interaction energy and has no influence in the intermediate steps. This won't be the case if one uses more involved density-dependent dispersion corrections such as VV10.[220] Finally, the basis set superposition error (BSSE) correction can be estimated a posteriori via the counterpoise formula[221,222] which is also additive

$$\Delta E_{BSSE} = E(A^A) + E(B^B) - \big(E(A^{AB}) + E(B^{AB})\big) \equiv \Delta E_{BSSE,A} + \Delta E_{BSSE,B}. \tag{7.18}$$

With this, the present approach affords a real-space fully additive decomposition into intra- (A or B) and inter-fragment (AB) contributions of all terms occurring in the EDA scheme.

To evaluate the behaviour and the information that the EDA-IQA can provide, we considered the set of intermolecular complexes (extracted from Ref.[147]) that essentially includes hydrogen bonded species, cation-dipole, cation-π halogen-π and π-π interactions. Except for the latter, one can identify electron donor and acceptor moieties, which translates in a certain charge-transfer upon complex formation. We will henceforth refer to fragment A as the acceptor of charge and fragment B as the donor of charge. To compact the discussion, here we focus solely on the dissociation profiles of six systems from the set, i.e. $H_2O\cdots H_2O$, $Li^+\cdots H_2O$, $NH_4^+\cdots H_2O$, $Li^+\cdots C_6H_6$, $C_6F_6\cdots F^-$ and $C_6F_6\cdots Br^-$, while the complete discussion of the results obtained is found in Section 5.1.

Starting by the electrostatic contribution of EDA (ΔE_{Elec}), Figure 7.17 gathers its evolution and the one of its IQA-decomposed terms, i.e. $\Delta\varepsilon_{Elec,A}$, $\Delta\varepsilon_{Elec,B}$ and $\Delta\varepsilon_{Elec,AB}$, along the dissociation pathway of the aforementioned systems. It is well-known that ΔE_{Elec} is favorable when the frozen densities of the two isolated fragments (A and B) are brought at the complex (AB) geometry.[223] This is reflected in Figure 7.17, being ΔE_{Elec} more negative as the inter-fragment distance shortens. Further insights are provided by the real-space decomposition of $\Delta\varepsilon_{Elec}$. According to Eq. 7.14, the $\Delta\varepsilon_{Elec,A}$ contribution originates from the net electrostatic potential of fragment A interacting with the density of fragment B within the domain of A. When A (acceptor of charge) is a cation, the positive net potential on A is enhanced as $N_{A^0} < Z_A$, and thus more ρ_{B^0} is able to penetrate into the fragment domain of A. As consequence, the $\Delta\varepsilon_{Elec,A}$ contribution becomes more negative. Figure 2 shows that $\Delta\varepsilon_{Elec,A}$ increases (in absolute value) as the interacting fragments come closer in all cases. This effect is larger for cationic acceptors than neutral ones, as observed in $H_2O\cdots H_2O$ or $C_6F_6\cdots F^-$ (Figure 2).

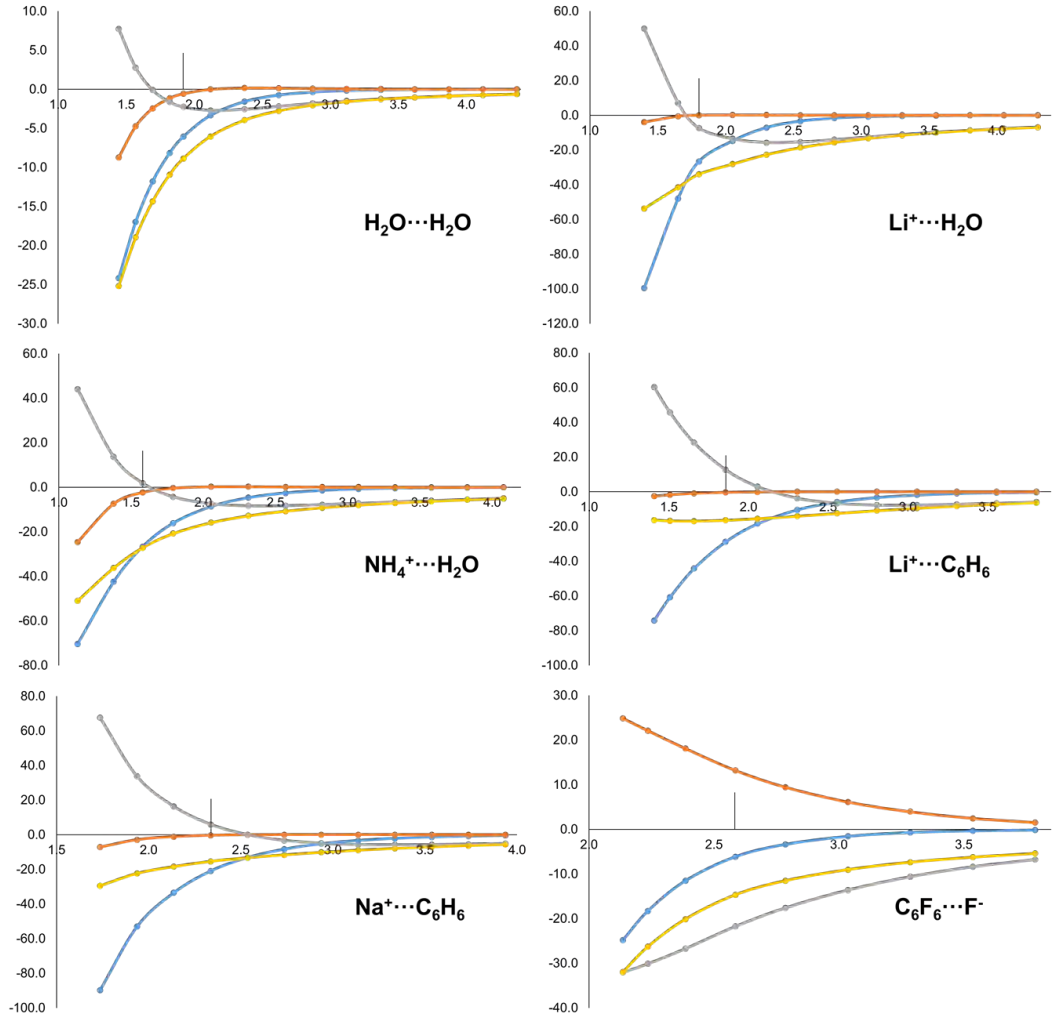

Figure 7.17: Energy evolution (in kcal/mol, y-axis) of ΔE_{Elec} (yellow) and its IQA-decomposed terms, i.e. $\Delta\varepsilon_{Elec,A}$ (blue), $\Delta\varepsilon_{Elec,B}$ (orange) and $\Delta\varepsilon_{Elec,AB}$ (grey), along the dissociation pathway (in Å, x-axis) of the selected molecular systems. Equilibrium distance marked with a vertical line

For fragment B (donor of charge), the situation is reversed. The electrostatic stabilization of B is very small, negligible in most cases, as the fraction of ρ_{A^0} that enters the domain of B is minimal. However, when B is anionic, since $N_{B^0} < Z_B$ its net electrostatic potential on B can be negative, and thus any ρ_{A^0} able to penetrate into B would lead to positive $\Delta E_{Elec,B}$ values. This effect is clearly seen with $C_6F_6 \cdots F^-$ (Figure 7.17). In all cases, the intra-fragment IQA terms tend asymptotically to zero when the A-B distance increases, being in agreement with the expected behavior since at large distances the fragments are essentially in their reference state. Consequently, $\Delta\varepsilon_{Elec,AB}$ tends to the overall ΔE_{Elec} value. However, $\Delta\varepsilon_{Elec,AB}$ becomes less favorable and even repulsive at very short distances. The $\Delta\varepsilon_{Elec,AB}$ value for a given complex at equilibrium may be positive (e.g. $Li^+ \cdots C_6H_6$) or negative ($Li^+ \cdots H_2O$), but the behavior of the components is very similar in both cases (see Figure 7.17). Still, the $\Delta\varepsilon_{Elec,AB}$ at equilibrium distance is very sensitive to the nature of fragments A and B. When both A and B are neutral, the electron-nuclear attraction compensate the nuclear-nuclear repulsion and the $\Delta\varepsilon_{Elec,AB}$ values are very small (ca. $\pm$ 2 kcal/mol). However, when B (donor) is anionic, the picture is completely different. As depicted in Figure 7.17, $\Delta\varepsilon_{Elec,AB}$ is negative and behaves opposite to the other systems, i.e. it becomes more negative as the

inter-fragment distance decreases. This fact can be explain by the second term on the r.h.s. of Eq. 7.15. Being B an anion, ρ_{B^0} holds an excess of electrons with respect to Z_B. In addition, the net potential of A in the domain of B is governed by the nuclear contribution (positive). Then, the closer the fragments, the larger the potential and consequently, the more negative the dominant term becomes.

The Pauli repulsion EDA term, ΔE_{Pauli}, originates from the intermediate state A^0B^0. Bickelhaupt and Baerends showed that the antisymmetrization of the frozen fragment densities to build A^0B^0 induces an electron density flow from the intermolecular region to the atomic regions.[223] The authors showed, upon the decomposition of ΔE_{Pauli} into kinetic and potential, that this contraction produces an increase of the kinetic energy and a decrease (more negative) of the potential energy. The latter is due to the fact that more density is accumulated at regions (close to nuclei) where the Coulombic potential is larger. The IQA decomposition of ΔE_{Pauli} yields a very similar picture. By definition, kinetic energy contributions only have intra-fragment character upon IQA decomposition, being thus captured by $\Delta\varepsilon_{Pauli,A}$ and $\Delta\varepsilon_{Pauli,B}$. The kinetic energy increase is so dominant that these terms are expected to be positive and increase along the shortening of the inter-fragment distance. This is exactly the behavior depicted in Figure 7.18. On the other hand, in all cases the $\Delta\varepsilon_{Pauli,AB}$ contributions are large and negative, and also become more favorable at shorter distances. The origin of its behavior is that, according to Eq. 7.17, this term does not explicitly contain energy differences between the intermediate and isolated fragment's states, as there is no inter-fragment term associate to the latter. Careful analysis indicates that the classical part of the potential energy differences cancels (particularly in the neutral complexes), so the inter-fragment exchange-correlation contribution becomes the dominant term. Notice that the aforementioned contraction effect also increases (makes more negative) the overall exchange-correlation energy of A^0B^0 with respect to that of A^0 and B^0. It might appear counterintuitive that a depletion of charge in the inter-atomic region leads nevertheless to a negative inter-fragment exchange-correlation. The simple explanation is that part of the exchange-correlation energy of the A^0B^0 state is assigned to inter-fragment character by the IQA decomposition, while, once again, there is no inter-fragment contribution from the isolated fragments to compensate for it.

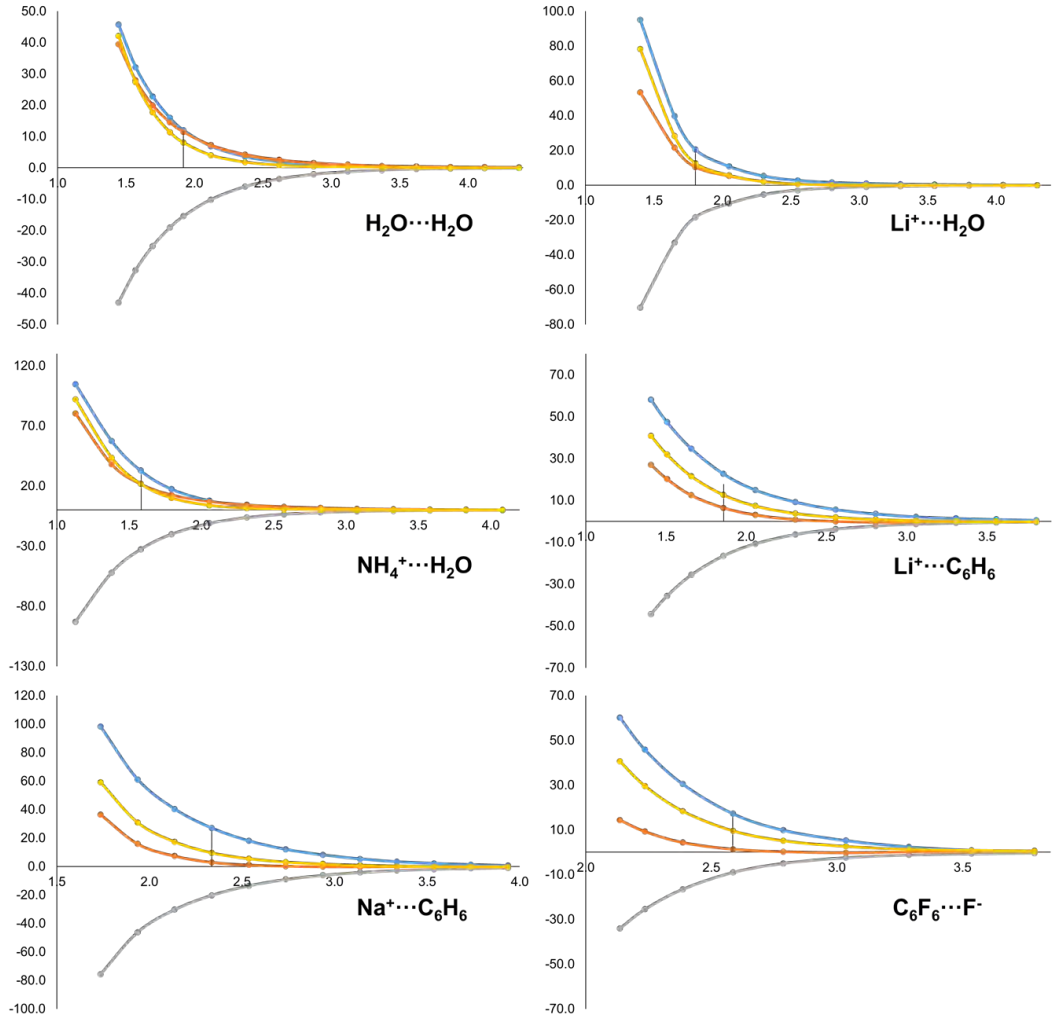

Figure 7.18: Energy evolution (in kcal/mol, y-axis) of ΔE_{Pauli} (yellow) and its IQA-decomposed terms, i.e. $\Delta\varepsilon_{Pauli,A}$ (blue), $\Delta\varepsilon_{Pauli,B}$ (orange) and $\Delta\varepsilon_{Pauli,AB}$ (grey), along the dissociation pathway (in Å, x-axis) of the selected molecular systems. Equilibrium distance marked with a vertical line

The orbital interaction from EDA, ΔE_{Orbint}, originates from the relaxation of the MOs of the complex's intermediate state A^0B^0 to the final complex's AB ground state. The orbital relaxation induces an enlargement of electron density in the inter-atomic (and thus intermolecular) region, making the inter-fragment exchange-correlation contributions of the AB ground state larger (in absolute value) compared to the ones from the intermediate state A^0B^0. This is reflected by $\Delta\varepsilon_{Orbint,AB}$, being more negative for all molecular systems, in exception of $C_6F_6\cdots F^-$, when the two fragments come closer (Figure 7.19). In case of anionic donors, $\Delta\varepsilon_{Orbint,B}$ is positive and increase at shorter distances, being compensated by negative (and similar) $\Delta\varepsilon_{Orbint,A}$ values. Thus, the ΔE_{Orbint} term is governed by $\Delta\varepsilon_{Orbint,AB}$. Interestingly, in case of the acceptor being NH_4^+ the $\Delta\varepsilon_{Orbint,A}$ values are much larger and negative, but once again compensated by the destabilization of the donor moiety.

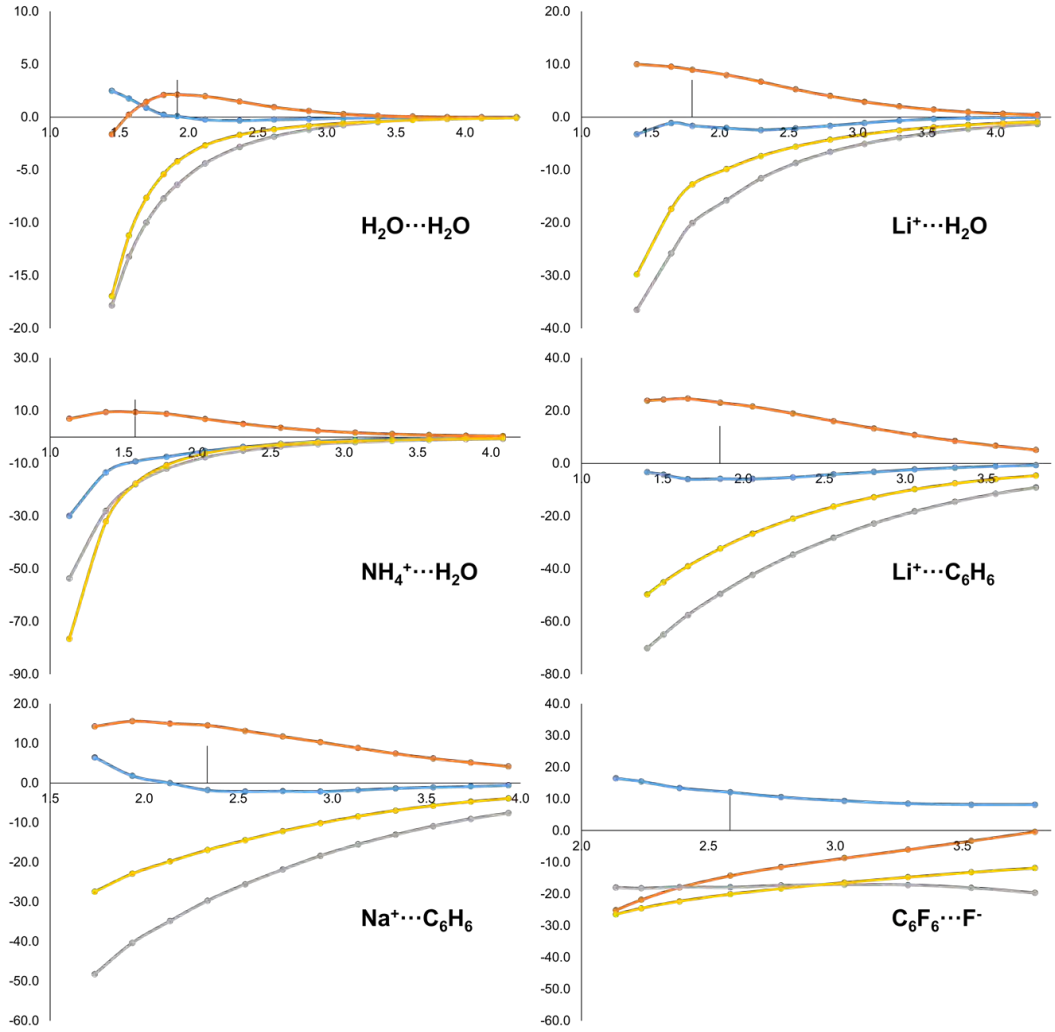

Figure 7.19: Energy evolution (in kcal/mol, y-axis) of ΔE_{Orbint} (yellow) and its IQA-decomposed terms, i.e. $\Delta\varepsilon_{Orbint,A}$ (blue), $\Delta\varepsilon_{Orbint,B}$ (orange) and $\Delta\varepsilon_{Orbint,AB}$ (grey), along the dissociation pathway (in Å, x-axis) of the selected molecular systems. Equilibrium distance marked with a vertical line

Finally, the interaction energy EDA term, ΔE_{Int}, originates from the difference in electronic structure of the complex AB ground-state with the isolated fragment's states A^0 and B^0 at the complex geometry. Thus, one expects negative ΔE_{Int} values while the interaction between fragments is favorable and positive when repulsive. Its intra- and inter-fragment IQA terms can be obtained upon decomposition of the aforementioned states or simply by adding the corresponding IQA terms from the decomposed electrostatic, Pauli repulsion and orbital interaction. The expected behavior is reflected in the dissociation profiles from Figure 7.20. In all cases, ΔE_{Int} is negative (and minimum) at equilibrium geometry and starts to be repulsive at close distances between fragments, except of $NH_4^+ \cdots H_2O$. Furthermore, it tends to zero upon dissociation, thus following the expected behavior. When the isolated fragment's wavefunctions relax to the ground-state of the complex, a part of the electron density from the donor B (and also from the acceptor, but lower) is sacrificed to form the AB interaction. This is captured by $\Delta\varepsilon_{Int,AB}$, being larger (more negative) at closer distances, and by $\Delta\varepsilon_{Int,B}$ and $\Delta\varepsilon_{Int,A}$, being larger (for the former) and positive (for the later) upon association. The $C_6F_6 \cdots F^-$ system is the exception, once again, where the behavior is reversed.

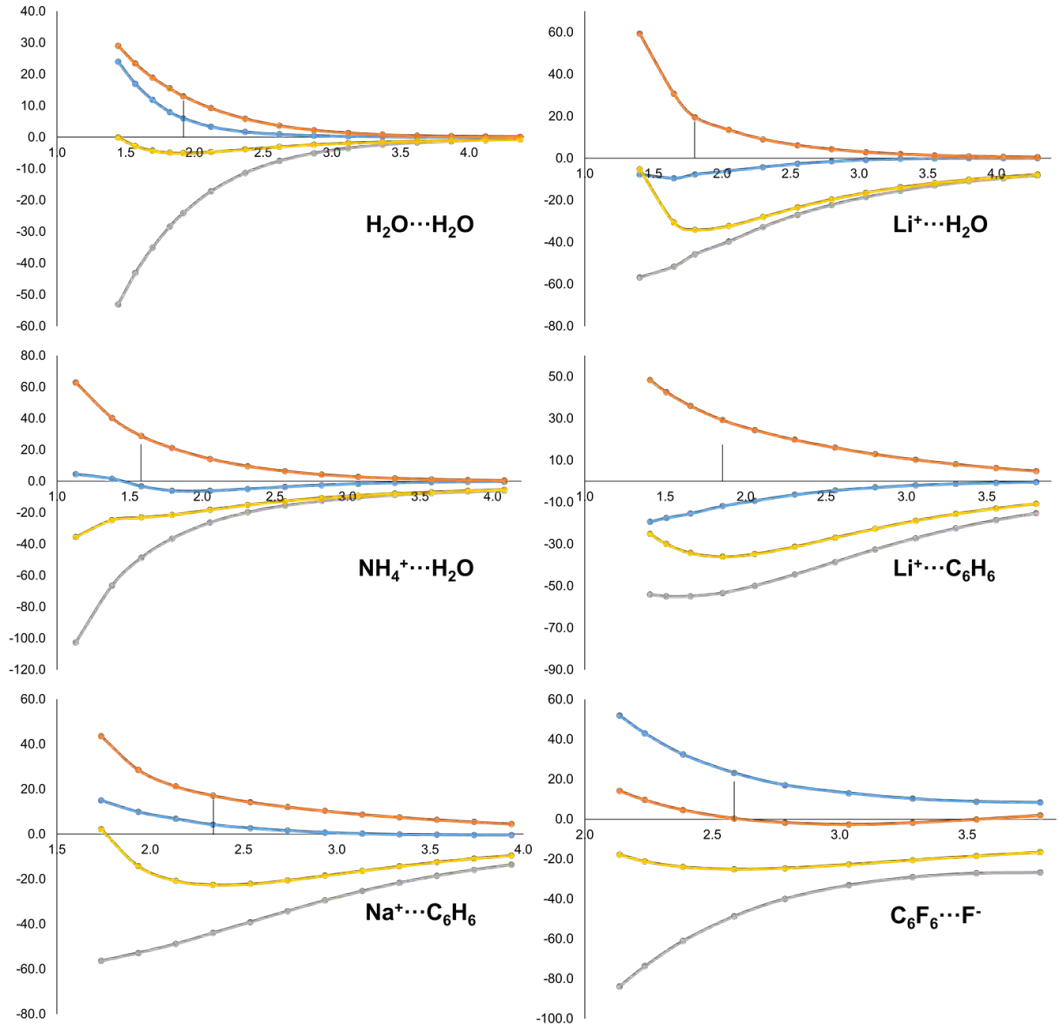

Figure 7.20: Energy evolution (in kcal/mol, y-axis) of ΔE_{Int} (yellow) and its IQA-decomposed terms, i.e. $\Delta\varepsilon_{Int,A}$ (blue), $\Delta\varepsilon_{Int,B}$ (orange) and $\Delta\varepsilon_{Int,AB}$ (grey), along the dissociation pathway (in Å, x-axis) of the selected molecular systems. Equilibrium distance marked with a vertical line

Concluding this section, in this work we showed that the application of an IQA decomposition on each of the EDA energy components can enrich the chemical bonding information from any molecular system. In particular, we illustrated the behavior of the intra- and inter-fragment IQA terms upon dissociation of a selected variety of donor-acceptor (non-covalently bonded) complexes, unveiling, for instance, that the EDA orbital interaction term is governed by its inter-fragment IQA contribution. Furthermore, we showed that the electrostatic energy from EDA, which is *formally* intermolecular, presents non-negligible intra-fragment contributions in veins of IQA (originated by the charge penetration from the electron density of one fragment into the atomic domains of the other).

7.2.2 Decomposition of the exchange-correlation energy from Kohn-Sham density functional theory into one- and two-center terms

As we showed in Section 1.5.2, in the IQA approaches the total energy is exactly (up to numerical integration error) decomposed into one- and two-center contributions.[224] The centers can be the individual atoms composing the system or groups of atoms, permitting the identification of energetic interactions between functional groups in the case of a molecular system, or individual monomers in a complex. The IQA schemes rely on the identification of the atom within the molecule, which in the case of IQA QTAIM is typically chosen.[47] It is important to stress that the real-space decomposition of properties such as the energy is not restricted to that particular atomic model (see details in Section 1.2.2).

Since the total energy can be expressed in terms of one- and two-electron density functions, it quite naturally decomposes into atomic and diatomic contributions by applying Eqs. 1.68 and 1.71, introduced in detail in Sections 1.2.2 and 3.1. However, contrary to electron distribution analyses (e.g. atomic populations, bond orders or local spins), the formulation of the molecular energy decomposition scheme depends upon how the total energy is obtained for each particular electronic structure method. Along the years, different formulations depending on the wavefunction-type have been introduced, being, curiously enough, the extension of the method to KS-DFT the most challenging. The main problem is that the KS-DFT exchange-correlation energy is a one-electron dependent (local) quantity, decomposing in the real-space into solely one-center terms. To date, there has been only two schemes that decompose the total KS-DFT exchange-correlation into both one- and two-center terms: the Salvador-Mayer (SM-IQA) and Francisco *et al.* (F-IQA) approximations (see details in Section 1.5.2).[48,51] Both methodologies have been applied along the years, independently, being a comparison between them non-existent.

The IQA schemes require to evaluate all the energy terms by numerical integration. Among the different energy terms, the Coulomb and exact-exchange energies are both the bottleneck, formally they are 6D integrals, and the major source of error (see Section 3.1). Increasing the grid size one can reduce the numerical error. However, then the calculation is much more expensive and generally unaffordable for large molecular systems. Thus, the development of algorithms that accurately integrates the aforementioned energy components at a low computational cost is still required. With this, the main objectives of this fifth project were:

1) To assess the performance of the aforementioned KS-DFT IQA schemes, comparing the atomic and diatomic exchange-correlation energy terms using functionals of different nature.

2) To derive a numerical procedure to improve the accuracy of the decomposition of the two-electron energy terms as they are the bottleneck of the IQA approach.

To accomplish these goals, first we proposed a strategy to *exactly* integrate the two-electron dependent energy terms in the real-space. This scheme, termed as the Zero Error Strategy (ZES), is based on reevaluating the one-center two-electron terms (major source of numerical error, see details in Section 3.1) playing with the rotation angles of the second set of grid points. Then, we performed a quantitative comparison between the two IQA schemes able to decompose the KS-DFT exchange-correlation energy into one- and two-center terms.

As previously mentioned, in the IQA schemes the two-electron contributions to the molecular energy,

namely Coulomb, Hartree-Fock exchange (and correlation, in the case of wavefunction methods) are both the bottleneck and the major source of numerical error. Formally, they scale N_{tot}^6, being N_{tot} the number of grid points (see Sections 1.2.2 and 3.1), albeit efficient algorithms achieving N_{tot}^4 scaling have also been introduced in the QTAIM framework.[166] As it was aforementioned, the decomposition of these energy terms is carried out by using two sets of atom-centered grid points, associated to the electron coordinates of electron 1 ($\mathbf{r}_1$) and 2 ($\mathbf{r}_2$), being the later rotated a given (preoptimized) value to minimize the number of points discarded on the integration, and thus also minimize the integration error (see Section 3.1).

We evaluated the integration error obtained using different angles, observing that appropriate rotation angles depend mostly upon the size of the angular grid. Another observation was that the two-center two-electron terms are contributing to the numerical error several orders of magnitude less than the one-center ones, while being rather unaffected by the rotation of the second grid.[163] Yet, the most relevant observation is depicted in Figure 7.21 (left). Here, the integration error in the two-electron B3LYP/cc-pVTZ energy of N_2 is shown with respect to the rotation angle of the second grid. The error is just defined as the difference between the sum of all one- and two-center contributions of the molecular two-electron energy and the exact (analytical) value, V_{ee}. One can see that, if the atomic grid provided is sufficiently large, there is always a rotation angle for which the overall two-electron integration error vanishes. Thus, a 30×74 (radial and angular points, respectively) atomic grid is clearly insufficient, and with the optimum rotation angle the error is still of approximately 15 kcal/mol. However, by using a 40×146 atomic grid the integration error first crosses the zero-error at around 0.18 rad and then again at 0.217 rad, close to the default rotation angle used in Ref.[46] By using larger atomic grids the zero-error line is crossed at smaller rotation angles. In addition, several poles are observed in the curves due to near singularities in r_{12}^{-1}. Noteworthy, using sufficiently large atomic grids such as 70×434 or 150×590, the shape of the curves is strikingly similar irrespective of the molecule. That is, the rotation angle that produces a zero-error in the two-electron energy lies within an extremely narrow range. This is illustrated in Figure 7.21 (right).

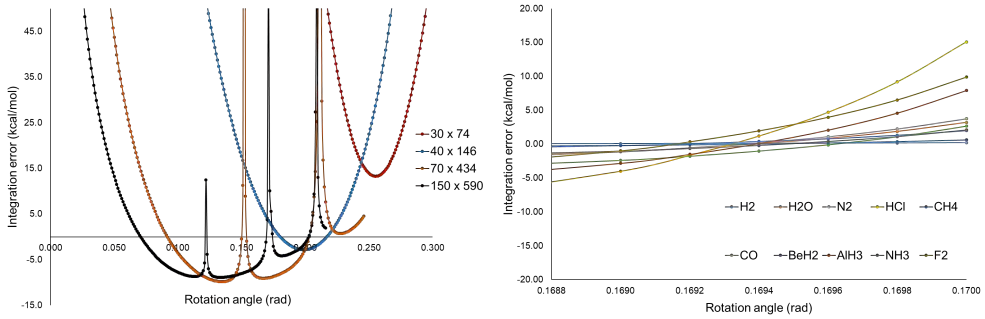

Figure 7.21: Two-electron integration error (kcal/mol) versus angular rotation of the electron 2 grid for N_2 using different grids (left) and for a variety of systems (right) using the 150×590 grid. All wavefunctions evaluated at the B3LYP/cc-pVTZ level of theory.

With these findings in mind, we propose a rather simple strategy to minimize the two-electron integration error in IQA schemes with overlapping atomic domains (see below). All that is required is V_{ee}, i.e. the exact two-electron energy of the molecular system. In the case of Hartree-Fock it comprises the Coulomb and exact-exchange terms. In correlated wavefunction methods, an additional correlation contribution coming from the cumulant of the RDM2 is also included. In KS-DFT it contains the Coulomb and the amount of exact-exchange that is actually used in the exchange functional definition. In a first step, the total two-

electron energy is decomposed into one- and two-center terms, as usual in the framework of IQA, with an associated integration error of

$$\delta V_{ee}^{(1)} = \sum_{A}^{N_{At}} E_A^{(1)} + \sum_{A,B>A}^{N_{At}} E_{AB} - V_{ee}, \tag{7.19}$$

where an appropriate rotation of the grid for $\mathbf{r}_2$ has been applied to compute the one-center (two-electron) terms. For instance, using a 150×590 atomic grid, a rotation of 0.169 rad performs very well (vide infra). Then, the process is repeated using a second rotation angle, but now *only* the one-center terms are reevaluated. This leads to another estimation of the two-electron energy, using the two-center terms evaluated in the previous step

$$\delta V_{ee}^{(2)} = \sum_{A}^{N_{At}} E_A^{(2)} + \sum_{A,B>A}^{N_{At}} E_{AB} - V_{ee}. \tag{7.20}$$

We proceed by introducing a damping between both estimates to impose the error on the two-electron energy to be zero

$$(1-\gamma)\delta V_{ee}^{(1)} + \gamma\, \delta V_{ee}^{(2)} = 0. \tag{7.21}$$

Substituting Eqs. 7.19 and 7.20 into Eq. 7.21 and rearranging, we obtain the following expression for the damping parameter γ

$$\gamma = \frac{\delta V_{ee}^{(1)}}{\sum_A^{N_{At}} \left(E_A^{(1)} - E_A^{(2)} \right)}, \tag{7.22}$$

and the corrected one-center terms

$$E_A \equiv E_A^{(1)} + \gamma(E_A^{(2)} - E_A^{(1)}). \tag{7.23}$$

It can be readily seen that the one- and two-center terms thus defined *exactly* reproduce the total two-electron energy.

Ideally, the applied rotation angles in the first and second step should be previously optimized to provide small deviations with respect to the exact two-electron energy and, most importantly, of opposite sign. In that case, the γ value lies between 0 and 1 and an actual damping (interpolation) is performed between the two estimates of V_{ee}. As such, a linear behaviour of V_{ee} with the rotation angle of the second grid is implicitly assumed. As mentioned before, we have found that a combination of 150×590 atomic grids and a rotation of 0.169 rad typically overestimates V_{ee} by 1-5 kcal/mol, while using a rotation of 0.170 rad in the second step leads to a somewhat larger underestimation of V_{ee}. In Table 7.7 we compiled the integration errors in V_{ee} for a set of 31 molecules obtained at B3LYP/cc-pVTZ level of theory (see Section 3.3 for further details). It can be seen that the two-electron integration errors in the first step are already rather small and negative, with the only exception of H_2 for which the error is merely 0.1 kcal/mol. For most applications these errors might be acceptable. The errors associated to the second step are somewhat larger but positive in all cases, so that the γ values that afford the exact decomposition are within the [0,1] range.

Table 7.7: Two-electron energy integration error for the first and second rotation (in kcal/mol) and optimal γ values at B3LYP/cc-pVTZ level of theory.

System	$\delta V_{ee}^{(1)}$	$\delta V_{ee}^{(2)}$	γ
C_2H_2	0.0	3.7	0.996
C_2H_4	-0.6	3.2	0.835
C_6H_6	-0.4	11.8	0.965
C_2H_6	-0.9	3.3	0.777
$HCONH_2$	-1.8	7.8	0.812
HCNO	-2.0	6.2	0.757
B_2H_6	-0.5	2.3	0.824
CO	-2.4	2.7	0.524
CO_2	-3.6	5.5	0.604
SO_2	-6.5	17.1	0.725
SO_3	-6.0	22.5	0.790
H_2	0.1	0.2	**1.619**
N_2	-1.1	3.8	0.769
NO^+	-2.6	2.8	0.515
CN^-	-2.0	2.3	0.533
LiF	-1.7	3.8	0.697
F_2	-1.0	9.9	0.909
LiH	-0.2	0.3	0.677
BeH_2	-0.2	0.6	0.779
BH_3	-0.2	1.2	0.838
CH_4	-0.2	2.0	0.903
NH_3	-1.0	2.2	0.686
H_2O	-1.1	3.2	0.745
HF	-1.5	3.8	0.724
NaH	-2.0	5.7	0.735
MgH_2	-2.6	6.5	0.713
AlH_3	-2.8	7.9	0.736
SiH_4	-2.7	9.7	0.780
PH_3	-3.8	10.2	0.727
H_2S	-3.8	12.8	0.771
HCl	-4.0	15.1	0.791

It is important to mention that with such (two-electron) zero-error scheme the two-center terms are evaluated solely once (in the first step). Previously, we observed that their value is rather unaffected by a rotation of the second grid and exhibit integration errors 2-3 orders of magnitude smaller than those of the one-center terms.[163] This is because there are no near singularities caused by small r_{12}^{-1} values and also because their contribution to the total two-electron energy is much smaller than that of the one-center terms, specially if heavy atoms are involved. Thus, it is only the much larger one-center terms that are slightly modulated to yield an overall exact decomposition of the two-electron energy.

The ZES could also be applied independently to each of the contributions to V_{ee}, namely Coulomb and exact-exchange (and correlation in case of correlated wavefunction methods), provided their exact value is known beforehand. However, we found that the behaviour of V_{ee} in the vicinity of the optimum rotation angles is very similar for HF, B3LYP and BP86 (see Section 5.2). Then, since the overall errors are very small anyway it is more efficient to apply the zero-error scheme only once to reproduce the exact V_{ee}. In this vein, Table 7.8 gathers the overall IQA integration error and γ values for our molecular test set at the HF, B3LYP and BP86 levels of theory. The same 150×590 atomic grid was used for the one-electron part of the energy. In almost all cases the overall integration error is below 0.1 kcal/mol. Upon the use of the ZES, the main source of numerical error becomes the one-electron atomic kinetic energy contributions, because of

the oscillatory character of the kinetic energy density near the nuclei. The worst case is the C_6H_6 molecule, with errors of up to 0.4 kcal/mol. Of course, the one-electron grid can still be further improved to decrease the residual integration error if necessary, by increasing the atomic grid size. More importantly, using the aforementioned 0.169 and 0.170 rad rotation angles for the two steps of the two-electron zero-error scheme resulted in the desired interpolation in almost all cases, disregarding whether V_{ee} contains any exact-exchange contribution.

Table 7.8: γ values and overall integration errors (in kcal/mol) for the test set computed with HF and the KS-DFT functionals BP86 and B3LYP coupled to the cc-pVTZ basis set.

	HF		BP86		B3LYP	
System	γ	Int. Err.	γ	Int. Err.	γ	Int. Err.
C_2H_2	1.028	0.0	0.980	0.0	0.996	0.0
C_2H_4	0.766	0.0	0.766	0.0	0.835	0.0
C_6H_6	0.941	-0.3	0.942	-0.3	0.965	-0.4
C_2H_6	0.772	0.0	0.805	0.0	0.777	0.0
$HCONH_2$	0.826	0.0	0.818	0.0	0.812	0.0
HCNO	0.888	0.0	**1.085**	0.0	0.757	0.0
B_2H_6	0.846	-0.2	0.848	-0.2	0.824	-0.2
CO	0.503	0.0	0.538	0.0	0.524	0.0
CO_2	0.583	0.0	0.630	0.0	0.604	0.0
SO_2	0.718	0.0	0.734	0.0	0.725	0.0
SO_2	0.808	0.0	0.802	0.0	0.790	0.0
H_2	**1.351**	0.0	**1.399**	0.0	**1.619**	0.0
N_2	0.746	0.0	**1.199**	0.0	0.769	0.0
NO^+	0.486	0.0	0.576	0.0	0.515	0.0
CN^-	0.483	0.0	0.657	0.0	0.533	0.0
LiF	0.701	0.0	0.710	0.0	0.697	0.0
F_2	0.930	0.0	0.922	0.0	0.909	0.0
LiH	0.669	0.0	0.705	0.0	0.677	0.0
BeH_2	0.674	0.0	**1.213**	0.0	0.779	0.0
BH_2	0.828	0.0	0.919	0.0	0.838	0.0
CH_4	0.959	-0.1	0.992	0.0	0.903	0.0
NH_3	0.691	0.0	0.699	0.0	0.686	0.0
H_2O	0.749	-0.1	0.751	0.0	0.745	0.0
HF	0.716	0.0	0.734	0.0	0.724	0.0
NaH	0.710	0.0	0.717	0.0	0.735	0.0
MgH_2	0.745	0.0	0.723	0.0	0.713	0.0
AlH_3	0.737	0.0	0.745	0.0	0.736	0.0
SiH_4	0.810	0.0	0.777	-0.1	0.780	-0.1
PH_3	0.726	0.0	0.732	0.0	0.727	0.0
H_2S	0.777	0.0	0.777	0.0	0.771	0.0
HCl	0.790	0.0	0.794	0.0	0.791	0.0

With this, the two-electron zero-error scheme smoothly worked for the molecular systems tested, obtaining most of the γ values within the [0,1] range using a system-independent fixed setup. In very few cases the corrected two-electron energy terms were obtained by extrapolation, but with γ values were still close to 1. Alternatively, in the case the γ value would be far off the [0,1] range, one could consider performing second grid rotations iteratively until the desired numerical conditions are fulfilled. We did not apply such strategy as the obtained results are good enough to avoid paying the increase in computational cost. It is worth to mention that the robustness of the ZES had already been put into stringent test. Some of us recently showed that the elements of α tensor can be expressed through the second derivative of a zero-th order field-dependent energy, so that an energy decomposition of the latter readily affords the decomposition of α.[83] Using very large atomic grids for the one-electron energy terms and the ZES for the two-electron part was

absolutely critical to obtain numerically converged atomic contributions to α. Overall, the ZES appears to be a promising strategy for obtaining accurate IQA energy decomposition terms for large molecular systems while keeping an affordable computational cost.

Once the integration setup is set, we proceed to evaluate the atomic and diatomic exchange-correlation energy terms obtained using the aforementioned F-IQA and SM-IQA schemes. We made use of the same molecular set for the comparison, being the numerical results found in Section 5.2. We evaluated the wavefunctions, and thus the IQA decompositions, at the HF, B3LYP and BP86 levels of theory using their own geometry-optimized structures. We exclusively focus on the exchange-correlation (xc) terms, as the remaining ones are exactly the same with both KS-DFT IQA approaches.

Focusing in the analysis of the diatomic xc components, with up to 43 values, the first observation is that all xc (exchange-only in case of HF) terms of chemically bonded atoms are negative, as it is well known for IQA decompositions. Their magnitude (in absolute value) is deeply connected with the covalent bond order, so that bonds with higher multiplicity tend to exhibit larger (more negative) diatomic xc contributions. Thus, the larger values are obtained for N_2, NO^+ and the C-C triple bond in C_2H_2. The diatomic xc terms obtained with B3LYP and BP86 correlate extremely well with the HF values, using either the F-IQA and SM-IQA formulations, as shown in Figure 7.22 (worst case exhibits $R^2 = 0.98$). It is more interesting to focus on how the contributions differ from each other in each case. With the F-IQA formulation, the diatomic xc components for B3LYP are systematically more negative than the HF ones with only two exceptions, namely F_2 and H_2S. In both cases this difference can be attributed to significant differences in the wavefunction itself (F_2 is poorly described at HF level and the shape of the atomic boundaries in H_2S was already found to change significantly from one method to another.[75]) This observation is a direct consequence of the scaling factors used in Eq. 1.140. The total xc energy in B3LYP contains both exchange and correlation contributions, whereas in HF it only contains exchange. Since the total xc value is more negative, the scaling factors are greater than 1 and hence all terms (both atomic and diatomic) become more negative. The picture obtained at the BP86 level is very similar. In fact, the mean unsigned deviation (MUD) between the BP86 and B3LYP xc components is merely 2.2 kcal/mol, whereas the respective MUD values with respect to HF are 14.5 kcal/mol and 14.2 kcal/mol, respectively. Different trends are observed with the SM-IQA formulation. Most of the B3LYP diatomic xc contributions (32 out of 43) are less negative than the HF ones. The differences are significant in the C-C and C-H bonds of the alkane series. However, the opposite trend is observed mainly for the systems with large (in absolute value) diatomic xc contributions, namely triple bonds like in acetylene, CO, N_2 or NO^+ (see Figure 7.22b). Similarly to F-IQA, the MUD between BP86 and B3LYP SM-IQA values is very small (3.5 kcal/mol). Thus, in general the F-IQA scheme pictures a bond between a pair of bonded atoms more covalent than the SM-IQA one.

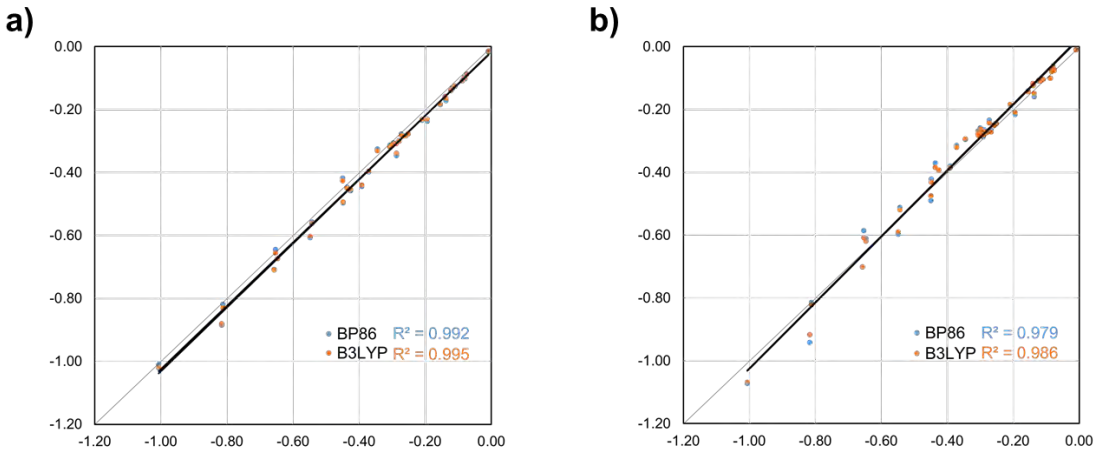

Figure 7.22: Correlations between diatomic Hartree-Fock exchange (x-axis) and KS-DFT exchange-correlation values (y-axis) for the molecular set using the F-IQA (a) and SM-IQA (b) approximations. Wavefunctions and IQA decompositions performed at the HF/cc-pVTZ and KS-DFT/cc-pVTZ levels of theory.

Concluding this Section, we first introduced a new strategy for the numerical integration of the two-electron energy contributions with *formally* zero-error. The ZES provided robust results for all molecular systems tested, obtaining in most cases γ values within the [0,1] range. Then, we performed a comparison between the two IQA schemes which decompose the total KS-DFT energy into one- and two-center contributions, i.e. the F- and SM-IQA methods. Upon correlation of both methodologies, none of them presented important flaws independently of the KS-DFT functional nature (pure, hybrid). The more negative diatomic exchange-correlation terms obtained with F-IQA pictures the bond between an atom pair more covalent than SM-IQA. This effect is compensated in the atomic deformation energies, but in none of the cases the tendencies observed between different bond multiplicities are broken. Thus, both decompositions are suitable for understanding the chemical bonding of new (or more complex) molecular systems.

7.3 Applying computational tools for chemical bonding characterization

7.3.1 Computational assignment of OSs beyond the IUPAC ionic approximation: OSs from the LOBA and EOS perspectives

In TM chemistry, the assignment of the metal (and ligand) OS is a crucial task for the classification, characterization and reactivity explanation (or prediction) of such compounds. However, it is not a trivial task in borderline cases, where the interesting chemistry arises. For this purpose, one can directly apply the IUPAC IA, which presents many flaws, or rely on the more sophisticated and specifically devoted computational tools (see Section 1.4). Currently, two of the state-of-the-art OS elucidation techniques are the LOBA and EOS analysis, which have been successfully applied by several groups in a wide range of chemical systems, proving their usefulness.[66,82,132–134] Both of them present some flaws, being the most relevant: the inflexibility of the population threshold to ionically assign the LOs electrons in the LOBA scheme, and the incapability to characterize singlet diradicals from CASSCF wavefunctions if the system is not symmetric for EOS. This

later limitation has been tackled in Section 4.3. To date, the performance of both LOBA and EOS schemes when applied together is unknown, as proper comparison between them is missing. With this, the main objectives of this sixth project were:

1) To increase the flexibility of the LOBA method when assigning the electrons from each LO, and opening the door to split the LMO electrons (covalent assignment) in case that LMO itself has shared-pair character.

2) To perform a comparison between the OS elucidation techniques LOBA and EOS for an extensive set of challenging molecular systems, against reference assignments performed by experimental evidences or from IUPAC's IA.

To accomplish these goals, we first reformulated the use of population analysis within LOBA by including the definition of an index which quantifies the clarity in our OS assignments. We support the idea of ionically assign the electrons of LOs in a "winner-takes-it-all" fashion. However, when the atomic populations are in a closed-call scenario, and the assignment could depend on the AIM definition used to extract them, there are two possibilities: rely on the AIM definition and ionically assign the electrons, in the direction of the OSLO and uEOS schemes (Sections 4.2 and 4.3, respectively), or considering the LMO shape and perform an ionic or covalent assignment based on chemical intuition. The introduced index softens the dependencies on population analysis method used (Mulliken, Löwdin, QTAIM or Hirshfeld, among others) and rigidity of using a single population value as threshold, increasing thus the robustness of the method. Secondly, we elucidated the OSs of 20 molecular systems of varying chemical nature and complexity using both LOBA and EOS. The collection of systems used is similar to the one in Section 4.2, and includes high-valence TM oxides, TM complexes with non-innocent ligands and TM carbene complexes, among others.

As mentioned above (see Section 1.4 for further details), the LOBA scheme requires the use of atomic populations. It assigns the electrons from a LMO if the atomic population on the TM (or a selected heavy element) surpass a given threshold. Prior studies showed that setting the threshold to 60% provides satisfactory results for systems with rather well-defined OS.[120,131,133] However, when evaluating compounds with non-trivial bonding scenarios, the number of LOs with atomic populations close to the borderline 50-70% region increase. Within this range, two different interpretations may arise from the same computational result and a small geometric change may interchange the electron assignment due to crossing the LOBA threshold. In such case, one could also doubt if performing an ionic assignment of the electrons from a LMO is the most appropriate philosophy when atomic populations are close to the threshold. Along the Thesis we made clear that we prefer a "winner-takes-it-all" fashion for single-determinant wavefunctions. In case of multireference wavefunctions, the electron pair might be homolytically split if specific conditions are found (see details in Section 4.3). However, as the properties of these *borderline* systems will resemble more to the intermediate chemical bonding picture, derived from applying a covalent assignment, we explore the possibility to covalently assign electrons (split of the electron pair between atoms/fragments) in the new defined index (see below).

Let us start by introducing a new clarity index (CI_a), which quantifies to which extend the LOBA OS assignments are clear-cut. First, we define the x quantity, extracted from the population analysis performed for every LMO as

$$x = \frac{abs(\lambda_M - \lambda_X)}{\lambda_M + \lambda_X}. \tag{7.24}$$

Here, λ_M corresponds to the electron population of the selected atom (e.g. the metal center, for the case of TM complexes), and λ_X is the electron population of the rest of the system. With this definition, x is bounded within the [0, 1] range, independently of the wavefunction being closed- or open-shell. As limits, the $x = 1$ case is when the LMO population is completely on either the selected atom M or on the rest of the molecular system X, while $x = 0$ corresponds to the $\lambda_M = \lambda_X$ scenario. Then, we define a parameter, namely P, corresponding to a threshold for ionicity, to separate the assignment of the electrons of a given LMO into two ranges depending on the x value obtained (Figure 7.23a): covalent when $0 < x < P$ and ionic when $P < x < 1$. In the ionic range, the LMO electrons are entirely assigned to M if $(\lambda_M - \lambda_X) > 0$ or to the rest of the molecular system X if $(\lambda_M - \lambda_X) < 0$. In the covalent range, also known as shared-pair range, the LMO electrons are equally split between the two moieties.

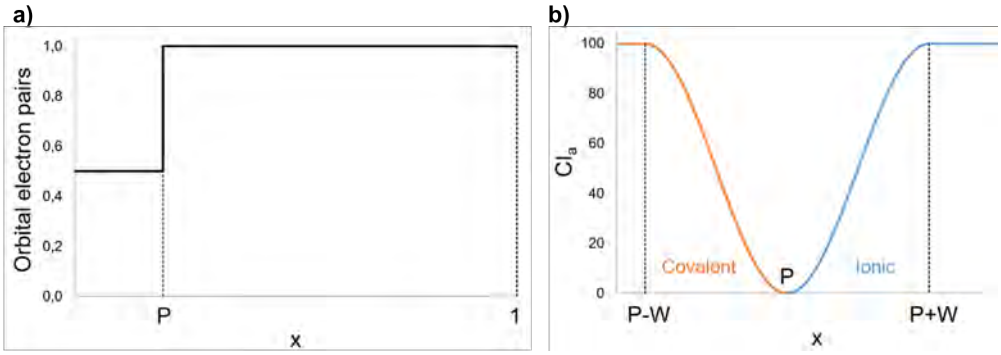

Figure 7.23: (a) Plot of the electrons assignment in a LMO for $x \in [0, 1]$, being x defined by Eq. 7.24. The covalent and ionic regimes for $0 < x < P$ and $P < x < 1$, respectively. (b) $CI_a(x)$ index representation.

To finally quantify to which extend the assignment is clear, we introduce a second parameter, namely W, which corresponds to the width for switching the electronic assignment from ionic to covalent. Using x, and the parameters P and W, we define the new clarity index (CI_a) where $a = i$ for ionic and $a = c$ for covalent assignments, in 3 different ranges; $CI_c = 100$ for $x \in$ [0, P−W], $CI_i = 100$ for $x \in$ [P+W, 1] and $CI_a = CI_a(x)$ within the $x \in$ [P−W, P+W] interval. Setting these conditions, a plausible $CI_a(x)$ expression is

$$CI_a(x) = 100\, cos^2\left(\pi\left(\frac{P + W - x}{2W}\right)\right), \tag{7.25}$$

which is a continuous and smooth function with a symmetrical shape (Figure 7.23b) and a rather simple mathematical expression. We propose to make use of the $P = 0.2$ and $W = 0.1$ values. The P choice corresponds to the x value for the original electron population threshold (60%), while the W value selected is based on the population threshold calibration calculations performed in the original LOBA work,[120] matching the region which minimizes the error on the OS assignment.

By definition, one obtains a CI_a value for each LMO which reflects the clarity of the electron assignment for that *particular* LO. In our opinion, the least-clearly assigned electrons determine how conclusive the final OS assignment is. For this reason, we select the lowest CI_a value as indicator of the *overall* OS assignment clarity.

We proceed on evaluating its performance, including strengths and weaknesses, compared to EOS, IUPAC's IA and reported experimental evidences. For this purpose, we use a collection of challenging systems when it comes to assign their OSs. A summary of the results, including the most relevant (from our point of view) systems is given below, while complete chemical bonding analysis is provided in Section 6.1.

Let us first discuss the relatively simple $(CH_3)_3NO$ molecule. As mentioned in Section 4.1, its dominant Lewis structure presents a single bond between a formal N(+1) and a O(-1) (octet rule fulfilled by N). Direct application of IUPAC's IA leads to the N(-1), O(-2) and three CH_3(+1) picture as all electron pairs from the σ N-C bonds are assigned to N and the ones from the N-O bond to oxygen, while EOS analysis provided the N(-3), O(0) and each CH_3(+1) OS assignments with R(%) = 55.7. We *artificially* quantified the weight of the chemical bonding picture from IUPAC's IA by manually assigning the electrons to the corresponding EFOs. Such non-*aufbau* electron assignment presents an $R(\%)$ value lower than 50, in particular $R(\%) = 44.3$. Analyzing the shape of the PM LOs obtained, there is no LMO corresponding to the π-type N-O bond. Instead, two lone pairs localized on the O atom are found. Such orbital picture also points to the aforementioned Lewis structure. We applied the LOBA scheme and depicted the shape of chemically relevant PM LOs, together with their Löwdin populations and CI_a values in Figure 7.24a. Visual inspection shows two lone pairs localized on O, one σ N-O and three σ C-N bond orbitals. According to the newly introduced index, both σ N-C and σ N-O bond LOs are covalently assigned with $CI_c = 100$. This OSs assignment is different from the obtained with both IUPAC's IA and EOS. The LOBA assignment of the σ N-O LMO can only be supported by EOS in case of occupancy degeneracy of the frontier EFOs, being one electron assigned to each EFO and mimicking the covalent assignment. However, EOS clearly assigned each CH_3 moiety as +1.

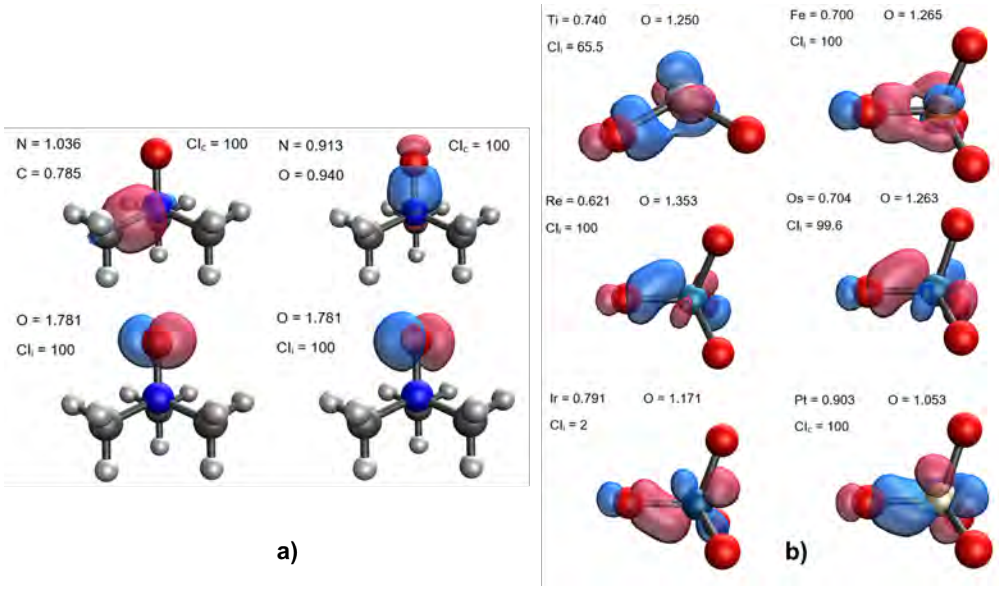

Figure 7.24: Selected chemically-relevant (valence) PM LOs for the $(CH_3)_3NO$ system (a) and the TM oxides TiO_2, FeO_4^{2-}, ReO_4^-, OsO_4, IrO_4^+ and PtO_4^{2+} (b), together with their associated Löwdin populations and CI_a values. Selected isocontour value of 0.3 a.u.

As first group of TM compounds, we evaluated the series of TM oxides, including TiO_2, FeO_4^{2-}, ReO_4^-, OsO_4, IrO_4^+ and PtO_4^{2+}, as in Sections 4.1 and 4.2. All methodologies tested coincide in the OS assignments, resulting in formal OSs up to +9 for Ir. The formal +10 OS from Pt is not supported by any scheme.

According to EOS at the current level of theory, the Pt presents the +6 OS with (once again) very low $R(\%)$ value (50.3). By using the reported geometry by Postils *et al.*[42] at the ωB97x-V/def2-TZVP level, we obtained a formal Pt(+2) with $R(\%) = 52.8$. Therefore, the disagreement on the OS assignment is mostly caused by geometrical differences. Nevertheless, it appears that the use of more sophisticated long-range corrected DFT functionals such as ωB97x-V, which include a density-dependent dispersion correction, may increase the ionic character of each bond by lowering the delocalization error. The more ionic the bonds, the more oxidized character of the metal center.

We depicted in Figure 7.24b the PM LOs corresponding to one of the σ TM-O bonds (for each complex). Due to symmetry, both the orbital picture and atomic populations are equal for all σ TM-O bonds. When going to higher valent compounds, the differences between atomic populations become less clear. This is also observed with the $R(\%)$ values close to 50 from EOS. For all systems, the electron pair from the σ M-O bonds is assigned to the O atom, as the difference on the atomic populations obtained is large enough, in exception of the PtO_4^{2+}. In that case, the newly introduced index supports the covalent assignment of each Pt-O pair with $CI_c = 100$. This assignment leads to a formal Pt(+6) and each O(-1), by symmetry. Interestingly, the Ir-based oxide is at the frontier between the covalent and ionic assignments, being of the former with a ridiculous $CI_i = 2$ value. In such scenario, the level of theory used or a small geometric change would easily flip the electron assignment for this system.

A second family of systems to discuss corresponds to the redox couple of nitroprusside anions $[Fe(CN)_5(NO)]^{n-}$, where $n = 2$ and 3. As previously mentioned (Section 4.3), the nitrossil (NO) is a simple non-innocent ligand which can present three different OSs, i.e. -1, 0 or +1, depending on its interaction with the metal center. For its OS assignment, IUPAC's statement is clear: the MNO segment should be linear for NO(+1) but bent for NO(-1).[105] In the $n = 2$ case, the geometry of the complex indicates a linear FeNO segment. Thus, according to the IUPAC rules the NO is formally +1. Then, direct application of the IUPAC IA characterizes each CN ligand as -1, leading to a formal Fe(+2) center. Applying the same rules, the bent geometry of the FeNO linkage in the $n = 3$ system is characteristic of NO(-1). However, the last system is properly characterized as neutral NO, which leads to a formal Fe(+2).[103] EOS analysis reproduced the reference OSs for both species with $R(\%) = 81.0$ and 74.0, respectively. Applying LOBA, all σ Fe-C LOs are ionically assigned to CN with $CI_i = 100$, thus leading to the expected CN(-1) ligands. For $n = 2$, the two LOs describing the Fe-N interaction (Figure 7.25a) are clearly assigned to Fe ($CI_i = 100$). This, together with a 3d-type LMO sitting on Fe, leads to the formal Fe(+2) assignment. Consequently, the NO moiety is characterized as +1.

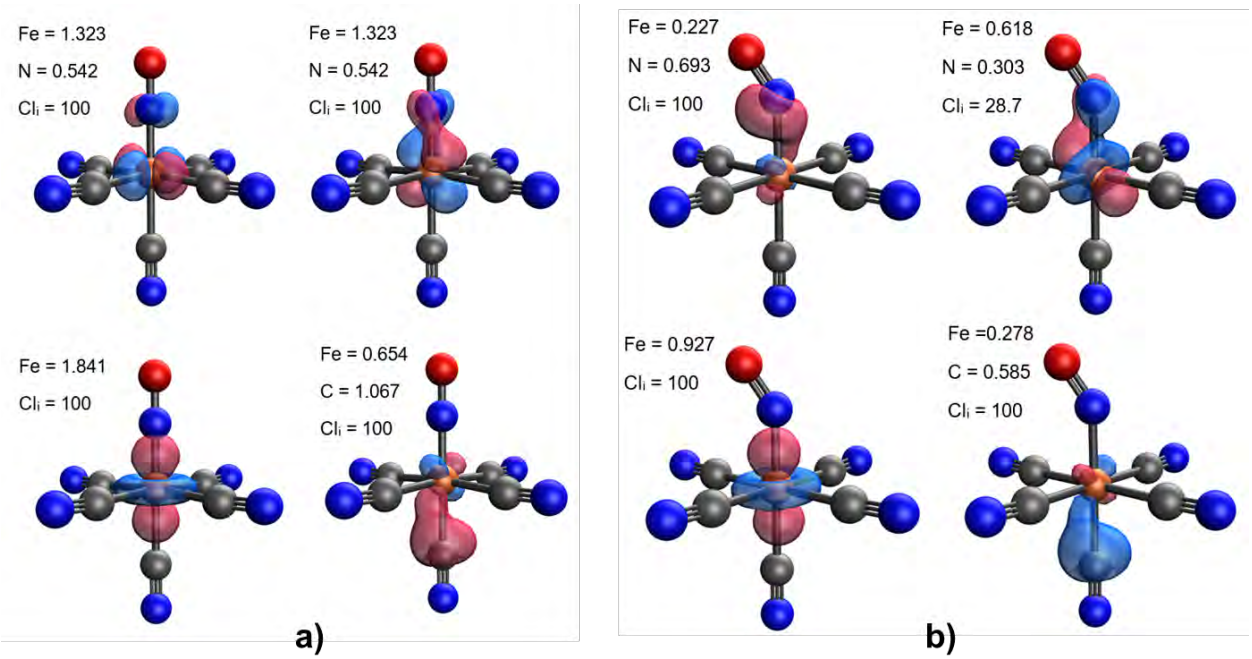

Figure 7.25: Selected valence PM LOs for the $[Fe(CN)_5(NO)]^{2-}$ (a) and $[Fe(CN)_5(NO)]^{3-}$ (b) systems, together with their associated Löwdin populations and CI_a values. Selected isocontour value of 0.3 a.u.

For the reduced species, with spin unrestricted LOs depicted in Figure 7.25b, the Fe center exhibits two α and three β 3d-type LOs, which, together with the assignment of the Fe-N interaction to the iron ($CI_i = 28.7$ (alpha)), leads to a formal Fe(+2). The CN ligands are also formally -1 for this system, being thus the NO ligand characterized as neutral. The results obtained in both cases are in perfect agreement with the reference values and EOS.

The last two compounds evaluated are within the TM-carbene family. In particular, we examined the Schrock-type compound, $Mo(=CH_2)(NC_8H_{10})(OtBu)_2$, and the Fischer-type complex, $W(=CF_2)(CO)_5$. As mentioned in Section 1.4, IUPAC's IA fails on elucidating the OS of the carbene moiety in the Fischer-type carbenes, assigning a formal -2 OS instead of the accepted value (0). EOS analysis properly characterized the carbene moiety as -2 for the Schrock-type compound with $R(\%) = 63.0$, and as neutral for the Fischer-type species with $R(\%) = 96.6$. The same OS assignment is obtained by applying the OSLO algorithm (see Section 4.2). We depicted the LOs associated with the σ and π TM-C interaction from the Fischer-type carbene, $W(=CF_2)(CO)_5$, in Figure 7.26a. According to LOBA, an ionic assignment with $CI_i = 100$ is obtained for the first, while the second has a covalent assignment with $CI_c = 74.1$. These assignments lead to a formally -1 carbene moiety, instead of the expected (0). For the Schrock-type complex, $Mo(=CH_2)(NC_8H_{10})(OtBu)_2$, we depicted the two LOs which describe the Mo=C bond in Figure 7.26b. In this case, both LOs are covalently assigned, with CI_c values of 33.1 and 91.4. As consequence, the carbene unit is characterized as neutral, which is the expected for a Fischer-type carbene, not an Schrock-type one. Here, the assignment of the two electron pairs from the Mo=C bond to the carbene moiety was expected.

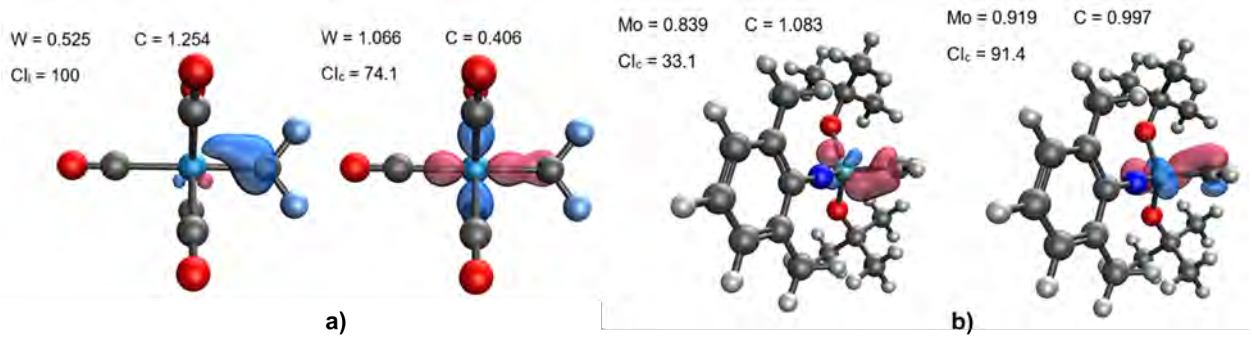

Figure 7.26: Selected valence PM LOs for the $W(=CF_2)(CO)_5$ (a) and $Mo(=CH_2)(NC_8H_{10})(OtBu)_2$ (b) TM carbenes, together with their associated Löwdin populations and CI_a values. Selected isocontour value of 0.3 a.u.

The use of EOS to characterize such compounds showed better performance than LOBA. For the latter, these systems showed its primary challenge: the difficulty to obtain clean LOs, at least with implementation present in the Q-Chem version used. Thus, the application (or development) of more robust orbital localization procedures is required before discarding the LOBA utility for this particular type of compounds, and in general.

To conclude this part, we examined the application of the computational methods to assign OSs, i.e. LOBA and EOS, to a series of compounds that present challenges in the OS assignment. We summarized the results obtained with both approaches for all compounds considered, together with their reference values, in Table 7.9. The OS is a chemically useful concept that, much like aromaticity or the chemical-bond itself, does not have a unique definition. Ultimately, all OS elucidation approaches will become ambiguous in regimes where the results approach the boundaries associated with a given assignment. This aspect is reflected, in our opinion, by the very useful $R(\%)$ index of the EOS procedure, and the newly introduced clarity index for LOBA. Such index, termed CI_a, approaches 100 away from the ionic/covalent boundary, and 0 when the boundary is approached from above or below.

We observed how both EOS and LOBA methods operate synergistically for assigning OSs. In the EOS approach, covalent assignments are rare, as there is no EFO occupancy difference range where the assignment is considered shared-pair. In contrast, the new LOBA scheme opens a range of atomic population differences, where the covalent assignment presents some weight. This is illustrated by the ostensibly simple molecule $(CH_3)_3NO$, for which the IUPAC IA, EOS and LOBA arrive at different results.

For the high-valence TM oxides culminating with IrO_4^+ and PtO_4^{2+}, which according to IUPÂC's IA present OSs of +9 and +10, respectively, are supported by EOS and LOBA up to the Ir-based system. The Pt(+10) is not obtained by any of the schemes tested. The same chemical bonding picture is obtained with the OSLO algorithm (Section 4.2). LOBA illustrates how delicate these high OSs are. With each TM-O bond equivalent, LOBA predicts Ir(+9) with low clarity (i.e. O(-2)), and Pt(+6) with higher clarity (i.e. O (-1)) as these systems traverse the ionic/covalent threshold.

Other challenging systems such as a Schrock- and a Fischer-type carbenes show impressive successes for EOS (and OSLO), and results that do not match conventional wisdom for LOBA. Relatively low CI_a values provide a warning that one should carefully inspect the LOs to assess the LOBA results. These systems illustrated that the primary challenge for the LOBA approach is that the orbitals in some systems do not localize cleanly. Furthermore, if the final goal is to properly scrutinize the OS of both the ligands and the

TM, one should incorporate the definition of fragments in the orbital localization procedure, for instance by using fragment populations instead of atomic ones in the localization functional. In this direction, we proposed an alternative fragment-based localization procedure, coupled with an iterative algorithm to select the *best* fragment-localized orbitals in Section 4.2.

Table 7.9: OS assignments of the atom/ligand marked in bold by the EOS and LOBA schemes, together with the $R(\%)$ and CI_a values (in parenthesis), respectively. [a] OS of Ru atom: +1 (EOS), +2 (LOBA), 0 (IUPAC's IA). [b] OS of the O atom: 0 (EOS), -1 (LOBA) and -2 (IUPAC's IA).

Molecule	EOS ($R(\%)$)	LOBA (CI_a)	IUPAC's IA / Other
$(CH_3)_3NO^a$	-3 (55.7)	+1 (100)	-1
TiO_2	+4 (92.6)	+4 (65.5)	+4
FeO_4^{2-}	+6 (68.9)	+6 (100)	+6
ReO_4^-	+7 (90.8)	+7 (100)	+7
OsO_4	+8 (76.1)	+8 (99.6)	+8
IrO_4^+	+9 (60.2)	+9 (2)	+9
PtO_4^{2+}	+6 (50.3)	+6 (100)	+10
$[Ni(S_2C_2Me_2)_2]^0$	+2 (55.7)	+2 (100)	+2
$[Ni(S_2C_2Me_2)_2]^{1-}$	+2 (65.7)	+3 (100)	+2
$[Ni(S_2C_2Me_2)_2]^{2-}$	+2 (82.4)	+2 (100)	+2
$[Fe(CN)_5(NO)]^{2-}$	+1 (80.9)	+1 (100)	+1
$[Fe(CN)_5(NO)]^{3-}$	0 (74.0)	0 (28.7)	0
$[Cu(CF_3)_4]^{1-}$	+3 (51.7)	+3 (100)	+1/+3
$[Cu(CF_3)_4]^{2-}$	+2 (78.5)	+2 (100)	+2
$[Cu(CF_3)_4]^{3-}$	+1 (100)	+1 (100)	+1
$Rh(SO_2)Cl(CO)(PH_3)_2$ (Z-type)	0 (84.0)	0 (100)	0
$Rh(SO_2)Cl(PH_3)_2$(L-type)[b]	0 (85.2)	0 (100)	0
$Ru(SO_2)Cl(NO)(PH_3)_2$ (π-type)	0 (50.3)	-1 (95.2)	0
$Mo(CH_2)(OtBu)_2(NC_8H_{10})$ (Schrock-type)	-2 (63.0)	0 (33.1)	-2
$W(CF_2)(CO)_5$ (Fischer-type)	0 (96.6)	-1 (74.1)	-2/0

Our results cannot be taken as an overall endorsement of any single approach to defining an OS, be it IUPAC's IA, EOS or LOBA. One can expect that all these methods will typically agree in straightforward cases (avoided here). In less straightforward cases, the comparison of the most sophisticated methods is instructive as a guide to complementary, and often convergent, ways to characterize complex bonding in the simplest possible way. When they differ, it is typically a signature of some interesting complexity, or otherwise, a limitation of one of the approaches.

7.3.2 Insights on the OSs and the TM-carbene interaction of the 1st and 2nd generation Grubbs-type olefin metathesis catalysts

Olefin metathesis is an extensively used reaction for the formation of carbon-carbon double bonds. This reaction commonly use Ru-based catalysts, which mechanism involves the formation of a four-membered metallacycle where the Ru center should exhibit a formal +4 OS, at least according to IUPAC's IA. Apart from the metallacycle, the characterization of the other intermediate species have also lead to some controversy.[110,225–229] In these systems, both the nature of the TM and its chemical environment (π donor/acceptor ligands) and the substituents on the carbene moiety are responsible for their electrophilic (Fischer) or nucleophilic (Schrock) character. The Ru=C moiety is often interpreted as a Fischer-type carbene, being thus the Ru formally in the +2 OS (Ru atom in a d^6 configuration),[230,231] whereas the ylidene ligand (either $=CH_2$ or =CHPh) is considered neutral. For Grubbs-type carbenes the distinction is not too clear, as the

alkyl groups of the ylidene ligand should furnish Schrock character to the carbene. For instance, the same compound (Grubbs 1st generation catalyst, with CAS number 172222-30-9) appears in the Sigma Aldrich catalogue with different nomenclatures (labelled as either Ru(+2) or Ru(+4)). With this, the main objective of this seventh project was:

1) To tackle the Ru(+2)/Ru(+4) debate in Grubbs catalysts, deepening into details about the different nature of the intermediates involved in the olefin metathesis reaction mechanism.

To accomplish this goal, we first reevaluated the reaction mechanism for the olefin methatesis reaction (Figure 7.27a), using 1st and 2nd generation Grubbs catalysts and ethylene as substrate, by means of KS-DFT calculations.[232] Then, we applied the EOS analysis on each species to examine the evolution of the Ru OS along the reaction mechanism. Moreover, we analyzed the chemical bonding picture of the homologous iron- and osmium-based catalysts as alternatives to the Ru-based ones.

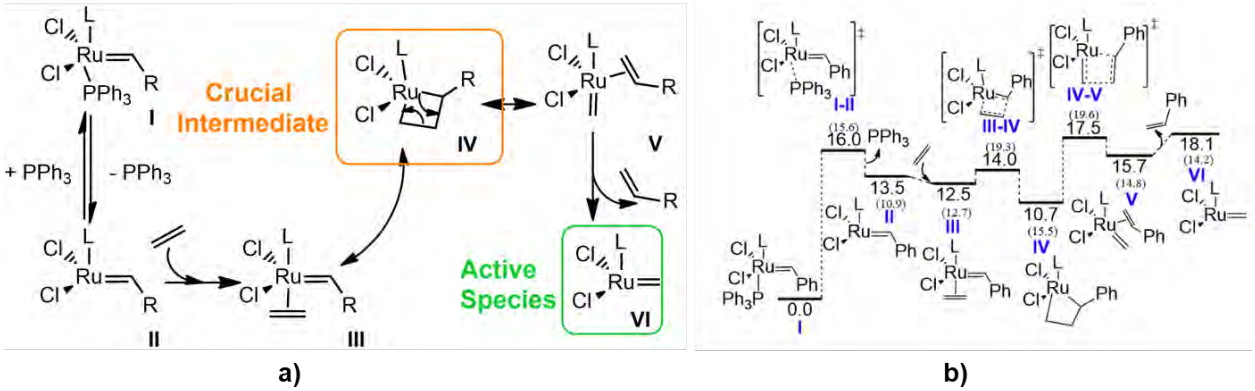

Figure 7.27: (a) Accepted mechanism for catalytic Ru-based olefin metathesis (R = H, Ph; L = NHC, phosphine).[232] (b) Relative Gibbs free energies (kcal/mol) of the first catalytic olefin metathesis cycle using the Ru-based 2nd generation Grubbs catalyst (L = SIMes) and ethylene as substrate. In parentheses we report the values for the 1st generation Grubbs catalyst (L = PPh_3). SIMes = 1,3-Bis(2,4,6-trimethylphenyl)-4,5-dihydroimidazol-2-ylidene.

First, we evaluated the mechanistic cycle of the aforementioned reaction using the Ru-based Grubbs catalyst, and its Fe- and Os-based homologous. All Ru and Os species are closed-shell singlet (low-spin) along the reaction pathway, as triplet and quintet spin-states are found higher in energy. Iron has the natural tendency to present high-spin configurations, finding that the ground state of the initial precatalyst **I** and the 14-electron (14*e*) species (**II** and **IV**) are triplet and quintuplet, respectively, despite the strong field character of the ligands. The Gibbs free energy results obtained at the M06/cc-pVTZ∼SDD//BP86/TZVP∼SDD level for the catalytic cycle are compiled in Figure 7.27b. The mechanism involving Ru and Os follows the same pathway, while significant differences for Fe are observed. In particular, the coordination intermediates **III** and **V** are absent.

Energetically, solely mentioning that for Os the metallacycle **IV** is 1.7 kcal/mol lower in energy (more stable) than **I**, whereas for Fe this difference amounts up to 31.1 kcal/mol. This energy wall will be difficult to surpass, resulting in a less active catalyst as stated previously.[233,234] We depicted the structural differences of species **IV** for the catalysts used in Figure 7.28. Moreover, the opening of the metallacycle, i.e. transition state **IV-V**, is the rate determining step (rds). However, we also considered the release of the styrene

subproduct via transition state **V-VI** since it is in competition.

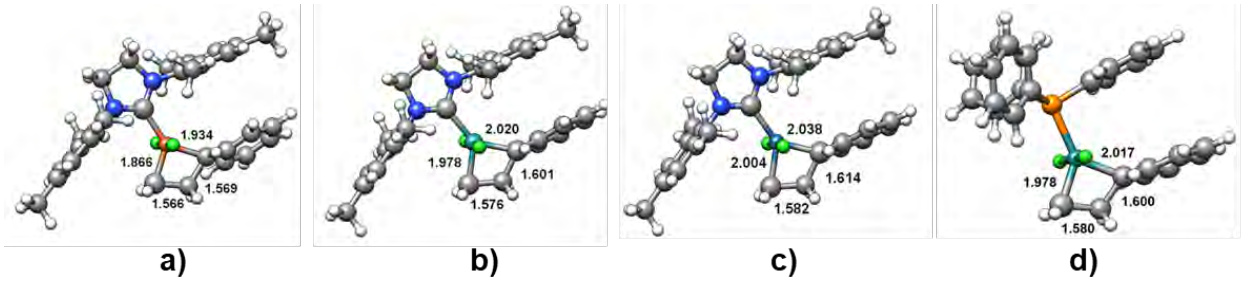

Figure 7.28: Metallacycle **IV** for the 2nd generation Grubbs-type TM-carbene with (a) Fe, (b) Ru and (c) Os as metal center and (d) 1st generation Ru-based one. Main distances reported in Å.

We elucidated the formal OSs of the TM and each one of the fragments for all species involved in the mechanistic cycle by means of the EOS analysis and gathered the results in Table 7.10. In all cases, the predicted OSs for the chlorine ligands is -1 and neutral (0) for both the phosphine and NHC ligands, being the later from the 2nd generation Grubbs-type catalysts.

Table 7.10: OS and R(%) index along the olefin metathesis reaction pathway for catalyst $MCl_2(L)(R_2)(=CHR_1)$. M = Fe, Ru, Os and L = SIMes, PPh_3.

	R_1	R_2	M OS	R_1 OS	R_2 OS	R_{Ru}(%)	R_{Fe}(%)	R_{Ru}(%)	R_{Os}(%)
						1st Gen.		2nd Gen.	
I	Ph	PPh_3	+2	0	0	62.3	65.9	64.3	63.8
I-II	Ph	PPh_3	+2	0	0	59.2	64.4	61.3	62.0
II	Ph	-	+2	0	-	59.0	50.0	60.5	57.1
III	Ph	Et	+2	0	0	62.0	-	63.7	63.5
III-IV	Ph	Et	+2	0	0	68.5	65.4	68.7	63.4
IV	$PhCH_2CH_2$	-	+2	0	-	53.1	54.7	50.8	44.1
IV-V	H	$PhCH_2$	+2	0	0	66.8	68.0	66.8	60.6
V	H	$PhCH_2$	+2	0	0	58.7	-	67.0	57.1
VI	H	-	+2	0	0	55.0	50.0	58.1	51.4

For all studied cases, EOS assigns the last electron pair to a d-type EFO on the TM and the first unoccupied hybrid lies on the carbene moiety (=CHR_1, Table 7.10). With this, the formal OS of the TM is +2, increasing its formal +4 character as the R(%) value decreases. From Fe to Os a direct trend can be established, highlighting the non-innocent role of the TM metal in the mechanism. We observe that the R(%) values for **IV** decrease from Fe to Os. In fact, for this system the R(%) values are close to 50 (worst-case scenario), being equally plausible the M(+2)/L(0) and M(+4)/L(-2) OS assignments. Increasing the metal size favours the M(+4)/L(-2) scenario. The M(+2)/L(0) combination is predominant along the reaction pathway, sharing with low contribution of the M(+4)/L(-2) since no R(%) value of any intermediate is higher than 65, in exception of **Fe-I** (65.9) and **Ru-V** (67.0). As general trend, the +4 OS on the metal center is more favoured for Os than Fe, being Ru in between. Let us mention that **Fe-II** breaks this trend, being plausibly caused by the fact that the ground state is the triplet spin-state instead of singlet.

To analyze the origin of the R(%) values obtained, we used the EFOs (and their occupancies) of first the rather simple species **II**, evaluating the formal Ru=CHPh double bond, and then the metallacycle **IV**. According to EOS, the formal OS of Ru in **II** is +2 with R(%) = 60.5, being in line with the Fischer-type carbene. The frontier EFOs (Figure 7.29a) unveil that the electrons from the π TM-carbene interaction are

associated to the carbene moiety (with occupancy of 0.522), while the ones from the σ TM-carbene bond are held by the Ru. Interestingly, one can observe a clear correspondence between the first unoccupied EFO (0.417), which corresponds to a d-type Ru orbital associated to the π bond with the carbene, and the aforementioned last occupied EFO (0.522). The sum of both occupancy numbers is almost (do not necessarily need to be) 1. Furthermore, an additional σ EFO on the C atom of the carbene ligand is obtained, being formally unoccupied. In case of occupying such EFO, which is clearly not the case, the carbene unit would be formally -2, and thus of Schrock-type. In the metallacycle **IV**, three EFOs presents very similar occupancies but only two electron pairs are left to be assigned (Figure 7.29b). Two of them are on the $(CH_2)_2$CHPh moiety with occupancies of 0.487 and 0.470, corresponding to the p-type EFOs on each of the C atoms that are forming σ bonds with the TM. In case that the two pairs of σ electrons of the Ru-C bonds are assigned to C, the two corresponding EFOs must be occupied being the $(CH_2)_2$CHPh moiety formally -2. Consequently, the Ru presents the +4 formal OS. However, there is a d-type Ru EFO with occupancy value in between that of these two EFOs (0.478), avoiding such a clear-cut assignment. Also, another d-type Ru EFO is present, with significantly smaller occupancy (0.437). Applying *strictly* the EOS scheme, following thus a "winner-takes-it-all" principle, the last electron pair goes to the Ru d-type EFO with 0.478 of occupancy, leading to a formal Ru(+2) and neutral $CH_2)_2$CHPh ligand. However, the Ru(+4) and $(CH_2)_2$CHPh(-2) assignment is almost equally plausible as the frontier EFOs are close to be pseudodegenerated (in occupancy). In fact, there are two electron pairs which can be considered to be equally distributed among the three *almost* pseudodegenerated EFOs, leading into nine possible different distributions of the electrons. Among them, solely one leads into the Ru(+4) assignment, being thus the chemical bonding picture closer to a formal Ru(+2), according to EOS.

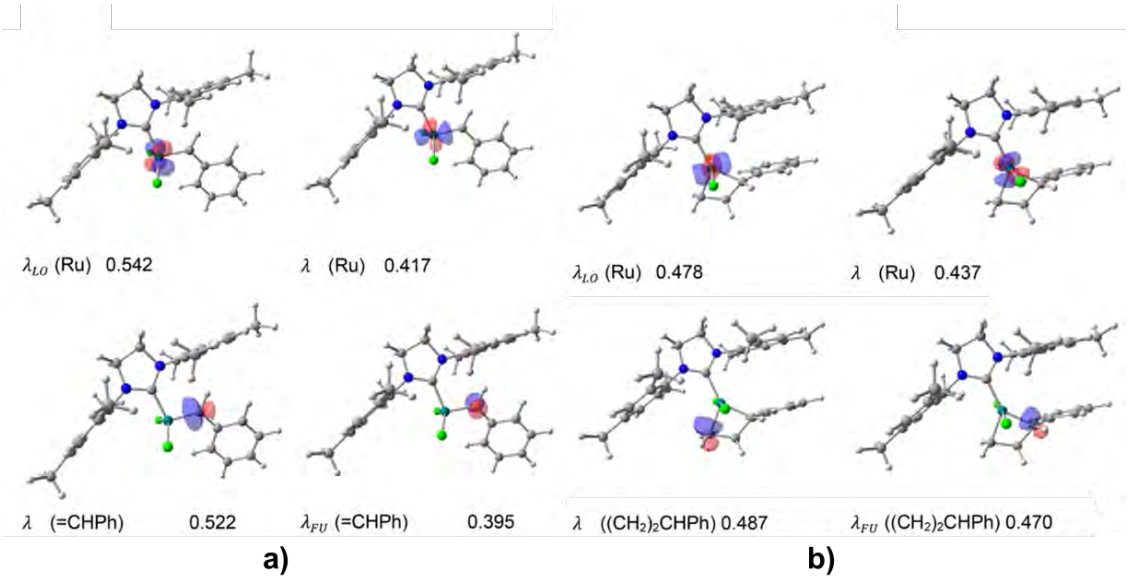

Figure 7.29: Frontier EFOs of species **II** (a) and **IV** (b) for the Ru-based 2nd generation Grubbs catalysts, together with their occupancy values (in electrons). Selected isocontour value of 0.1 a.u.

We also evaluated the robustness of the EOS approach by using a variety of KS-DFT functionals of different nature, namely GGA (BP86), hybrid-GGA (B3LYP) and meta-hybrid GGA (M06-2X), coupled with basis sets of different size (SVP, TZVP and cc-pVTZ). Very consistent results are obtained in all cases.

For instance, the Ru-based metallacycle **IV** presents R(%) values of of 50.8 for SVP and 51.0 for cc-pVTZ basis sets, whereas 50.0 (SVP, TZVP and cc-pVTZ) at the B3LYP level (See Table 7.11). The increase of the HF-type exchange in the functional expression, from 0% of BP86 to more than 50% of M06-2X, confirmed again the extreme robustness of the EOS analysis, obtaining for M06-2X R(%) values of 51.0 (SVP), 51.1 (TZVP) and 51.3 (cc-pVTZ) despite the overestimation of the Ru(+2) configuration that the HF-type exchange might induce.

Table 7.11: Metal OS and R(%) index of species **IV** obtained using different combinations of KS-DFT functional and basis set. M = Fe and Ru, L = Carbene moiety.

Functional	Basis set	Ru OS	L OS	R(%)	Fe OS	L OS	R(%)
BP86	SVP	+2	0	50.8	+2	0	54.7
	TZVP	+2	0	50.8	+2	0	54.7
	cc-pVTZ	+2	0	51.1	+2	0	54.7
B3LYP	SVP	+2	0	50.0	+2	0	57.6
	TZVP	+2	0	50.0	+2	0	59.4
	cc-pVTZ	+2	0	50.0	+2	0	59.3
M06-2X	SVP	+2	0	51.0	+2	0	100.0
	TZVP	+2	0	51.1	+2	0	100.0
	cc-pVTZ	+2	0	51.3	+2	0	100.0

Finally, no changes on the OS are observed when comparing 1st and 2nd generation Ru-based Grubbs-type carbenes. The R(%) values are slightly larger for the later, in exception of the metallacycle **IV** that the Ru(+4) character is larger. This is reflected in the energies, being 4.8 kcal/mol kinetically less demanding that the homologous from a 1st generation catalyst, and the closure and opening transition states 5.3 and 2.1 kcal/mol, respectively. Hence, the larger Ru(+4) character might explain, in agreement with Harvey *et al.*, the better performance of the 2nd generation Grubbs catalysts.[235]

To conclude this part, we showed that the metallic center in the metallacycle species **IV** presents character in between TM(+2) and TM(+4). The +2 OS is preferred for the rest of the reaction pathway, even thought low R(%) values were obtained. Our finding are in nice agreement with the trends proposed previously by theoretical groups.[236–238] Furthermore, the larger Ru(+4) character of the 2nd generation Grubbs-type catalysts reasonably explains their better catalytic performance compared to 1st ones. Finally, we proved the robustness of the EOS analysis by using a variety of KS-DFT of different nature, going from pure GGA to meta-hybrid GGA with more than 50% exact (HF) exchange.

7.3.3 Unveiling the electronic structure of the Bi(+1)/Bi(+3) redox couple on NCN and NNN pincer complexes

In the last decade, the synthesis and characterization of low-valent group 15 compounds, in particular the ones stabilized by pincer ligands, have gained interest due to their direct access to fine-tuning their reactivity by the coordination pattern. The use of pincer ligands with π-conjugated systems gives another channel to tailor the reactivity via conjugation with an empty p-orbital. Then, an occupied Bi p-orbital can interact with the π-system of the pincer ligand, forming a π-bonding orbital which can be located either at the Bi center or at the ligand, leading thus into the OSs of +1 or +3, respectively.

In 2007, Soran *et al.* described the synthesis of a Bi(+3) dihalide containing a NCN-type pincer ligand **I**

(see Figure 7.30a).[239] The complex presented a T-shaped $CBiCl_2$ core stabilized by two intramolecular dative N→Bi bonds. Afterwards, Simon *et al.* characterized the first examples of monomeric bismuthinidene **1**.[240] Interestingly, the use of 2,6-bis(ketimine)phenyl ligand ensured steric protection of the central Bi orbitals. Later on, Vránová *et al.* used similar ligands to access **2** and **3** via reduction of the corresponding chelated bismuth chlorides.[241,242] The authors proved and demonstrated that the reduction outcomes are influenced by the strength of the N→Bi interaction, leading to the rational design of an unprecedented two-coordinated bismuthinidene **II**.[241] The presence of the bismuth lone pair has been proven by the ability to coordinate various transition metal carbonyl moieties.[240] More recently, Cornella's group demonstrated the capacity of Bi-based compounds to be engaged in catalytic redox transformations making use of both the +1 and +3 OSs. Thus, system **2** resulted useful for the transfer hydrogenation of azoarenes and nitroarenes with ammonia-borane as transfer agent.[243] Mechanistic investigations suggested a Bi(+3) hydride as the key intermediate.

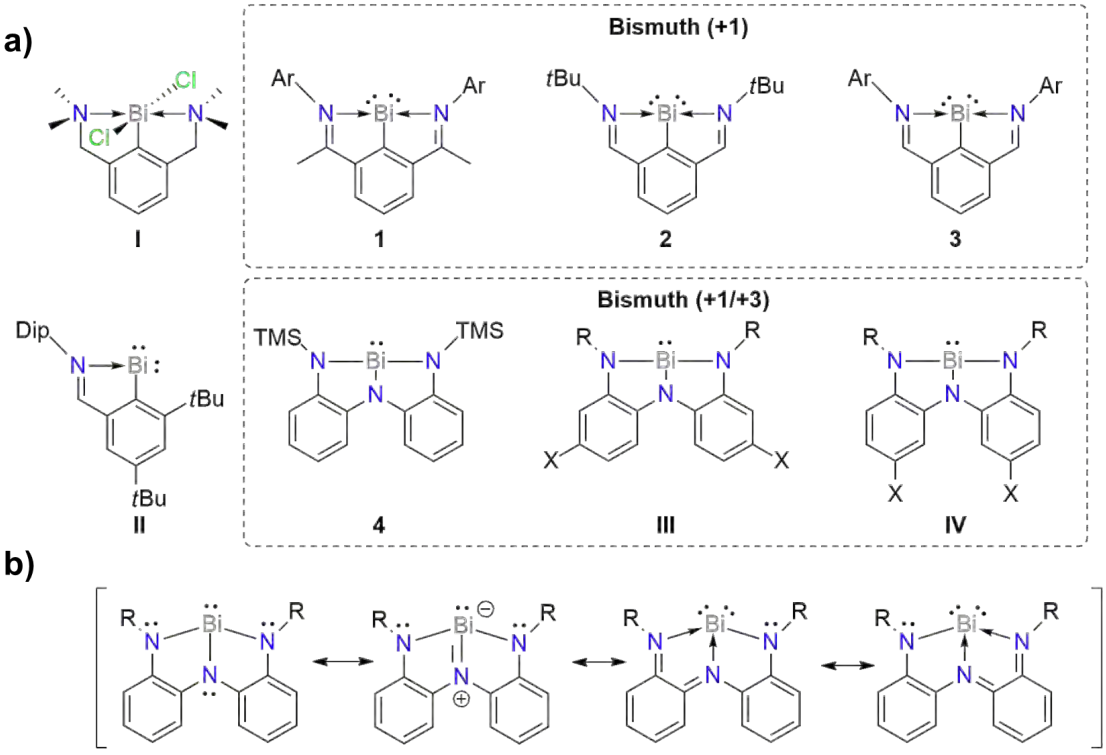

Figure 7.30: Bi-based complexes: **I**[239], **II**[241], **1** Ar = 2,6-$Me_2C_6H_3$[240], **2**, **3** Ar = 4-$Me_2NC_6H_4$[241,242], **4**[244], **III**, and **IV**[246]. Dip = 1,3-diisopropylphenyl, TMS = trimethylsilyl, tBu = tert-butyl (A). Possible resonance structures of the Bi-NNN system (B).

The first example of a planar geometry for bismuth triamides **4** was described in 2019 by Kindervater *et al.*[244] Such compound was tagged as "redox-confused" as presents significant Bi(+1) character but also exhibits reactivity similar to Bi(+3) electrophiles. The coordination of either pyridine N-oxide or $W(CO)_5$ revealed either a vacant or a filled Bi $6p_z$ MO. Noteworthy, the characterization of **4** as a Bi(+1) species was based on previous NCN-coordinated compounds. Nonetheless, its preparation uses Bi(+3) precursor without external reduction agents. This chemical behaviour points towards a rather ambiguous OS labelling, similar to the tackled in Section 6.2 regarding the Ru(+2)/Ru(+4) debate. With this, our main objective was:

1) To elucidate the electronic structure of a battery of Bi-based systems coordinated to different NCN and NNN ligands, tackling the Bi(+1)/Bi(+3) redox couple.

To accomplish this goal, we make use of the EFOs, both the shape and its associated occupancy values, and the EOS analysis. The use of EOS is justified considering that a redox couple involving closed-shell species, such as the Bi(+1)/Bi(+3), in combination with the absence of unpaired electrons/spin density makes the OS assignment particularly difficult with traditional approaches.[104,105] To date, EOS method has been successfully applied to a wide variety of systems, most of them involving TM complexes. However, EOS is of general applicability. Herein, we also extend the EOS scope into main-group chemistry. The systems considered in this work include monomeric bis(ketimine)phenyl (Bi-NCN) and triamide bismuthinidene (Bi-NNN), given their rather challenging and ambiguous bonding picture (see below). Thus, the description by different resonance structures (Figure 7.30b) may lead to either the +1 or +3 OS, which can be reduced to the question: does the Bi center possess one or two lone pairs?

We depicted in Figure 7.31 the optimized geometries of the studied Bi-based compounds. Both geometries and wavefunctions has been obtained at the B3LYP-D3(BJ)/def2-TZVPP level of theory (see details in Section 3.3). The obtained equilibrium geometries are in excellent agreement with the experimental ones, when available, or with the reported in previous computational studies.[240,241]

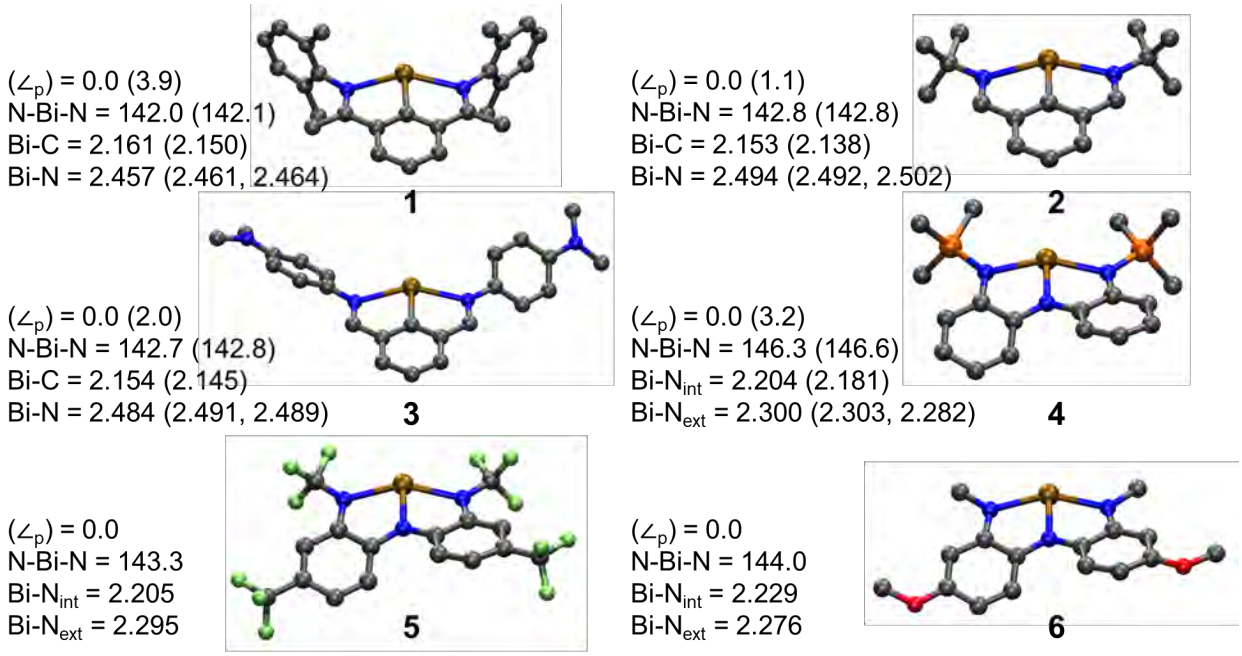

Figure 7.31: Optimized Bi-pincer complexes together with selected bond distances (Å) and bond angles (°). Experimental data (in parentheses) extracted from Refs. 240,241,244. Pyramidalization angle ($\angle_p$): N-C-N-Bi and N-N-N-Bi dihedral angles. Hydrogen atoms omitted for clarity.

First, we validated the EOS applicability to main-group compounds, using a set of 19 chemically diverse Bi-based systems. The resulting OS assignments are very clear in almost all cases ($R(\%) > 75$), and in perfect agreement with the expected OSs. The only significant exception is a dibismuthene species, for which the rather low $R(\%) = 58$ value emerges from the essentially unpolarised covalent nature of the Bi-Bi bond. Specific details about both the systems and results obtained are found in Section 6.3 and its supplementary

material.[245] After validation, we assigned the OS of both Bi and the NCN/NNN ligand of systems **1**-**6**, being the predicted OSs, the relevant EFO occupancies and R(%) values gathered in Table 7.12.

Table 7.12: Bi's and pincer ligand's (NCN or NNN) EFO occupancies and assigned OSs from systems **1**-**6**.

System	6s Bi	$6p_z$	π L	Bi OS	L OS	$R(\%)$
1	0.93	0.59	0.41	+1	-1	68.6
2	0.93	0.59	0.41	+1	-1	68.1
3	0.93	0.60	0.40	+1	-1	69.6
4	0.91	0.43	0.57	+3	-3	65.0
5	0.92	0.39	0.61	+3	-3	71.5
6	0.91	0.48	0.52	+3	-3	58.4

Starting by the relatively simple Bi-NCN system **2**, EOS assigns to Bi and NCN the +1 and -1 OSs, respectively, with $R(\%) = 68.1$. These values suggest a rather clear OS assignment, and the expected one, at the current level of theory. We depicted in Figure 7.32 the most relevant EFOs together with their occupancies. Since the EFOs maintain the σ-π separation, the respective electron distributions can be easily visualized, separately. The ligand exhibits three σ EFOs towards Bi with gross occupancies of 0.97, 0.86 and 0.70. The corresponding orbitals on Bi are formally unoccupied with occupancies of 0.03 (not shown), 0.14 and 0.30. Thus, by analyzing the EFOs the ligand is considered to have three σ lone pairs, which are coordinating to the Bi atom via dative bonds. The smaller the occupancy of the lone pair, the larger is the σ-donation *from* the ligand to the Bi center. This is usually reflected with an increase of the occupancy of the complementary Bi's σ EFO. The fact that the EFO with smaller occupancy is mainly localized on the C atom of the ring is in line with the better σ-donating ability of C- versus N-ligands. Regarding to the π-bonding, the NCN ligand exhibits five π EFOs with occupancies above 0.99, which essentially describe the five π occupied MOs of the free anionic ligand. An additional π EFO is present, which essentially corresponds to the LUMO of the free anionic ligand (Figure 7.32a). It exhibits an occupancy value of 0.41, smaller than that of the p-type EFO on Bi (0.59). As consequence, the EOS analysis considers the latter as occupied, resulting in a Bi(+1) assignment. Its partial Bi(+3) character originates in the π-bonding, due to the non-negligible occupancy of the ligand frontier π EFO. Replacing the tBu substituent of **2** by phenyl derivatives in **1** and **3** has a negligible effect on the EFOs shape and their occupancies. Overall, all these systems are consistently described as Bi(+1) and NCN(-1) species, which should not be surprising considering the nature of the ligand. From the isolated ligand perspective, the more plausible formal charge is the one that maintains the aromaticity of the 6-member ring, and that corresponds to the (-1) charge. In the hypothetical case the ligand would gain an electron pair upon system formation, the fragment would become formally -3. However, these extra electrons will be located at the π-system, breaking thus its Hückel aromaticity. The same would happen if the ligand transfers an electron pair to the Bi atom. Such scenario is rather unlikely considering that then the Bi would be formally -1.

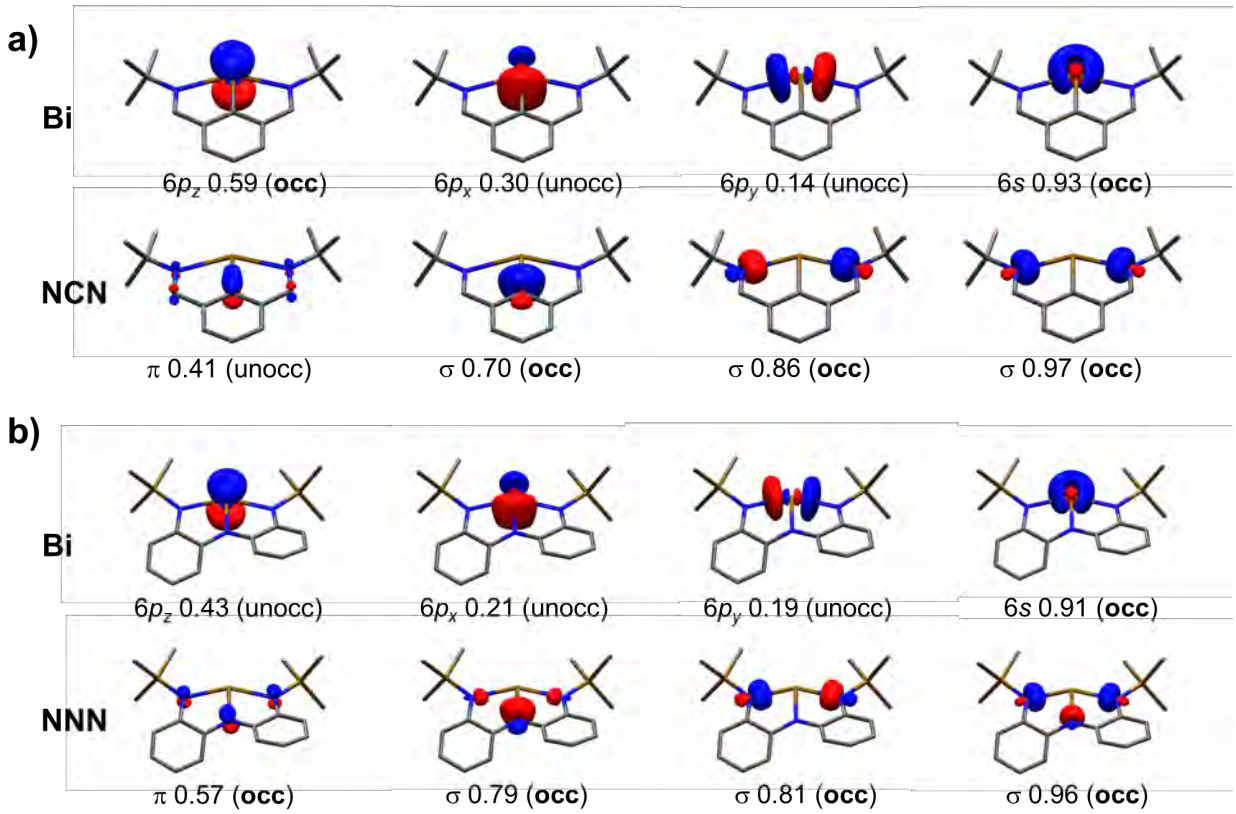

Figure 7.32: Selected relevant EFOs for systems **2** (a) and **4** (b), together with orbital symmetries, gross occupancies and EOS analysis: occupied (occ) and unoccupied (unocc). Selected isocontour value of 0.1 a.u. and hydrogen atoms omitted for clarity.

The triamide NNN ligand of compounds **4-6** presents an intriguing situation. Two anionic states for the NNN ligand are plausible, the associated with the Lewis structures depicted in Figure 7.30b. In the NNN(-3) case, and thus Bi(+3), each of the three N-coordinating atoms exhibits two lone pairs (with σ and π symmetry). In addition, each of the phenyl rings formally contains six π-electrons as outlined in Figure 7.30b (A). Instead, the NNN(-1) case is best represented by two resonant Lewis structures, where only one of the coordinating N atoms bears two lone pairs, and the remaining N atoms have one lone pair with a N→Bi interaction (Figure 7.30b. The former N atoms are conjugated with the aromatic rings and as a consequence their aromatic decreases. Nonetheless, there are up to 16 π-electrons that can delocalize among the phenyl rings, making the NNN(-1) state plausible. EOS analysis characterizes **4** as a Bi(+3) and a formal NNN(-3) ligand with $R(\%) = 65.0$, in contrast with the reported OS assignment.[244] We depicted the corresponding frontier EFOs in Figure 7.32b. Visual inspection of the EFOs illustrates that their shape is very similar to those obtained for the NCN-coordinated system **2**. The σ interaction is split, with occupancies of the ligand-centered EFOs being much higher (0.79, 0.81, 0.96) than those of the 6p-type hybrids on Bi (0.21, 0.19 and 0.04). The higher electronegativity of N (with respect to C) makes the ligand weaker σ-donor, so the 6p$_z$ occupancy of Bi is 0.21 rather than 0.30 as in **2**. The π-system shows EFOs analogous to the Bi-NCN system, but here the occupancy of the 6p$_z$ EFO on Bi (0.43) is smaller than that of the frontier π EFO on the ligand (0.57). Thus, the ligand formally keeps the electron pair. There are eight additional occupied π EFOs in the ligand, leading to the NNN(-3) and Bi(+3) OS assignment.

Marczenko *et al.* have explored the substituent effect on the NNN ligand.[246] Here, we consider two

extreme systems (**5** and **6**), where the -CF_3 and -OCH_3 substituents, respectively, induce opposite effects on the Lewis acid character of the Bi center. A higher Lewis acid character of Bi should be accompanied by a decrease of its $6p_z$ occupancy and hence a more marked Bi(+3) character. We performed EOS analysis on both systems and the occupancies of the $6p_z$ EFO on Bi decreases from 0.43 for **4** to 0.39 for **5**, and increases up to 0.48 for **6** (see Table 7.12). We observe the opposite trend for the occupancy of the ligand frontier π EFO. Note that the OS assignment within EOS relies mainly on the dissection of the π orbital occupancy (Figure 7.12, first column). In most of the cases, the relative occupancy of the π frontier EFOs on Bi and pincer ligand is quite similar. The extreme case is system **6**, where the occupancies are 0.48 for Bi and 0.52 for NNN, which is translated in a $R(\%)$ value close to 50 (54.8). Despite these small differences, EOS assigns the electron pairs to the ligand, leading thus into a formal Bi(+3). Note however, that for the OS assignment of Bi(+1), the occupancy dissection is not completely different from the one observed in **1**, where the $6p_z$ EFO from Bi has occupancy of 0.59.

The closed-call OS situation in these systems prompted us to further test the robustness of the assignments. We have studied both basis set and DFT functional dependence of the EOS results for prototypical systems **2** and **4**, being the results gathered in Table 7.13. The same OS assignments are obtained in all cases, with very small differences in the frontier EFO occupancies among the different KS-DFT functionals tested.

Table 7.13: Selected EFOs gross occupancies and EOS results for systems **2** and **4** evaluated with different KS-DFT functionals and basis sets. All wavefunction calculations have been performed on top of the B3LYP-D3(BJ)/def2-TZVPP optimized geometries.

	System **2**				System **4**			
Funct/Basis set	$6p_z$ Bi	π NCN	Bi OS	$R(\%)$	$6p_z$ Bi	π NNN	Bi OS	$R(\%)$
BP86/def2-SVP	0.57	0.43	+1	64.4	0.44	0.56	+3	62.3
BP86/def2-TZVP	0.57	0.43	+1	63.9	0.44	0.57	+3	63.1
BP86/def2-TZVPP	0.57	0.43	+1	63.8	0.43	0.57	+3	63.2
B3LYP/def2-SVP	0.60	0.41	+1	68.9	0.43	0.57	+3	64.1
B3LYP/def2-TZVP	0.59	0.41	+1	68.2	0.43	0.58	+3	64.9
B3LYP/def2-TZVPP	0.59	0.41	+1	68.1	0.43	0.58	+3	65.0
PBE0/def2-SVP	0.59	0.41	+1	68.8	0.42	0.58	+3	66.4
PBE0/def2-TZVP	0.59	0.41	+1	68.4	0.42	0.59	+3	66.9
PBE0/def2-TZVPP	0.59	0.41	+1	68.4	0.42	0.59	+3	67.0
M06-2X/def2-SVP	0.67	0.37	+1	75.8	0.39	0.61	+3	71.1
M06-2X/def2-TZVP	0.62	0.38	+1	74.6	0.37	0.63	+3	75.2
M06-2X/def2-TZVPP	0.62	0.38	+1	74.5	0.37	0.63	+3	75.4
ωB97x-D/def2-SVP	0.62	0.39	+1	72.9	0.40	0.60	+3	69.9
ωB97x-D/def2-TZVP	0.61	0.39	+1	72.7	0.40	0.60	+3	70.3
ωB97x-D/def2-TZVPP	0.61	0.39	+1	72.6	0.40	0.60	+3	70.4

Moreover, we compared the chemical bonding picture from EOS against the one provided by the NBO method applied in former studies.[241,244] The contributions of the most relevant NBOs involving Bi are summarized in Table 7.14.

Table 7.14: NBO results for systems **1**-**6**, including: NBO occupancies and orbital contributions. Population of the Bi $6p_z$ from the orbital contributions of the bonding and antibonding π C/N-Bi NBOs. [a] Enforced Lewis structure with lower non-Lewis density % value.

	$6p_z$ Bi	$\sigma_{C/N-Bi}$	$\sigma^*_{C/N-Bi}$	$\pi_{C/N-Bi}$	$\pi^*_{C/N-Bi}$
1	1.43	1.95, Bi-C(30/70%)	0.05, Bi-C(70/30%)	1.83, Bi-C(67/33%)	0.62, Bi-C(33/67%)
2	1.40	1.95, Bi-C(30/70%)	0.05, Bi-C(70/30%)	1.82, Bi-C(65/35%)	0.62, Bi-C(35/65%)
3	1.40	1.95, Bi-C(31/69%)	0.05, Bi-C(69/31%)	1.82, Bi-C(65/35%)	0.61, Bi-C(35/65%)
4[a]	1.00	1.95, Bi-N(16/84%)	0.13, Bi-N(84/16%)	1.78, Bi-N(27/73%)	0.71, Bi-N(73/27%)
5[a]	0.89	1.95, Bi-N(16/84%)	0.11, Bi-N(84/16%)	1.78, Bi-N(24/76%)	0.62, Bi-N(76/24%)
6[a]	1.12	1.95, Bi-N(16/84%)	0.16, Bi-N(84/16%)	1.80, Bi-N(32/68%)	0.80, Bi-N(68/32%)

NBO analysis leads in all cases to a 6s-type Bi lone pair with occupancy very close to 2 (electrons), as described by Vránová *et al.*[241] In systems **1**-**3**, the σ_{Bi-NCN} is represented by one lone pair on each N atom and a two-electron Bi-C bond polarized towards the ligand C atom. In addition, we obtain a bonding Bi-C π-bond polarized towards Bi with an occupancy of approximately 1.8, and the corresponding antibonding NBO with the reversed bond polarization and an occupancy of ca. 0.60. This clear Bi(+1) picture is in perfect agreement with the EOS results. It is worth to point out that our results for **3** differ from the reported ones for the same system,[241] where instead of a Bi-C π bond they obtain a fully-localized $6p_z$ orbital on Bi with an occupancy of 1.35. The later results are recovered by enforcing the NBO analysis to include of a Bi $6p_z$ lone-pair into the Lewis structure, with a non-Lewis density value (2.35%) somewhat larger than that of the default calculation (2.19%). Both pictures reconcile by quantifying the population of the Bi $6p_z$ NAO from the bonding and antibonding Bi-C π bonds (Table 7.14). Nonetheless, in our opinion, the two-electron bonding/antibonding NBO description permits a much closer connection with IUPAC's winner-takes-all principle (in line with LOBA).[120] The $6p_z$ lone pair picture also emerged by default for **4** with a low occupancy of 1.0, in perfect agreement with the results reported by Kindervater *et al.*[244] However, the default NBO analysis of **5** and **6** lead instead to a pair of bonding and antibonding Bi-N π bonds clearly polarized towards N from the NNN ligand, and to some minor differences in the σ-bonding involving Bi (lone pair vs strongly polarized bond).

According to Marczenko *et al.*[246] and EOS analysis, one would expect the Bi(+3) character of **4** to lie somewhat in between species **5** and **6**. This is precisely what can be inferred from the population of the calculated Bi $6p_z$ orbital on Table 7.14. We opted for an enforced NBO analysis for **4**-**6** leading to a picture analogous to that obtained for **1**-**3**, that is, including a pair of bonding and antibonding π Bi-N bonds and the two lone pairs on the N atoms. To our surprise, the non-Lewis density values were *smaller* than those obtained by the default calculations in all cases. So, it appears that different formal pictures (not necessarily associated with the lowest non-Lewis density value) can be obtained with NBO analysis by default, which hinders the comparison of the bonding situation among Bi-NCN and Bi-NNN systems. Considering the same NBO solution for all systems (which is also the one with lower non-Lewis density values) clearly confirms that the π Bi-C bond polarity in **1**-**3** (towards Bi) is completely reversed in the case of **4**-**6** (towards N). These results are in full agreement with EOS. A clear advantage of EOS is that it readily permits a straight comparison of the electronic structure of all systems on equal footing, independently of the dominant Lewis structure.

To further corroborate the relationship between the EFOs occupancies and the Lewis base properties, we computed the first and the second proton affinities (PA) for compounds **1**-**6** and compiled the results in Tables 7.15 and 7.16. Previous studies showed that PA_1 and PA_2 are sensitive probe for the presence of chemically available lone pairs of a molecule.[247–251] Thus, in theory such values provide information about

the location and the ability of the lone pairs to coordinate Lewis acids. The PA_1 of all systems, in exception of **5**, are higher than 220 kcal/mol, suggesting a highly basic nature. Note that the calculated PAs follow the trend of the Bi $6p_z$ EFOs occupancy. The highest PA_1 is for **3** (249.6 kcal/mol) with a $6p_z$ occupancy of 0.60. At the other extreme, system **5** presents $PA_1 = 188$ kcal/mol, and an occupancy of 0.39.

We applied EOS to systems **1**-**6**-(H^+), showing a clear Bi(+3), NCN/NNN(-1) and H(-1) assignment. Such situation results from the different electronegativities of Bi and H, which implies a formal oxidation of the Bi center to Bi(+3) while the H atom is pictured as a hydride. Bi(+3)-hydride **2**-(H^+) was postulated as intermediate in the catalytic dehydrogenation of ammonia-borane with **2**. This species was detected by high-resolution mass spectrometry, but all attempts for its isolation were unsuccessful.[243] Noteworthy, regardless the formal nature of the Bi center (+1 in **1**-**3** and +3 in **4**-**6**), we observe in all cases a full decay of the π EFO occupancy (< 0.05) of the ligand upon hydride formation. In **1**-**3**, Bi is electronically rich enough and readily provides the electron pair to form the hydride, thereby formally oxidizing to +3. In **4**-**6** it is mainly the NNN ligand who provides the electrons to form the hydride. Table 7.16 contains the computed PA_2 values, which are particularly important for testing the coordinating ability of the second lone pair and hence the Bi(+1) character. The values are relatively high (ca. 100 kcal/mol) and comparable to those reported for divalent ylidone E(0) compounds. The correlation with the Bi $6p_z$ occupancy of the deprotonated species is not as good as for PA_1. In fact, the second PA should probe the second available lone pair on Bi, which corresponds to a 6s-type EFO exhibiting a large and constant occupancy of ca. 0.90 for all species. This explains why the second PA is rather constant among the systems studied, no matter their formal OS is Bi(+1) or Bi(+3). System **5**, once again, is the only exception, for which both PAs are smaller than for the rest of systems. This finding are in line with its weakest Lewis basic character. Our calculations suggest that both Bi(+1) and Bi(+3) are able to coordinate two strongly polarizing Lewis acids. The second protonation is likely to be experimentally unachievable, considering that already the single Bi(+3)-hydride has not been isolated, yet. EOS clearly indicates only partial hydride character of the H moieties, as Bi remains with formal OS of +3 in all cases.

Table 7.15: First PA and bond dissociation energies including zero-point energy corrections (D_0) of systems **1**-**6** with one $W(CO)_5$ and $HNMe_2$ ligands. Bi's and Ligand (NCN or NNN) frontier EFOs occupancies and assigned OSs. $PA_1 = \Delta H(\mathbf{1}\text{-}\mathbf{6}) + \Delta H(H^+) - \Delta H(\mathbf{1}\text{-}\mathbf{6}\text{-}(H^+))$. Proton enthalpy +1.5 kcal/mol. All energies are in kcal/mol.

System	PA/D_0	6s Bi	$6p_z$ Bi	π L	Bi OS	L OS	$R(\%)$
1-(H^+)	244.2	0.92	0.34	< 0.05	+3	-1	75.8
1-($W(CO)_5$)	48.1	0.92	0.53	0.20	+1	-1	71.0
2-(H^+)	243.3	0.92	0.35	< 0.05	+3	-1	75.4
2-($W(CO)_5$)	52.0	0.92	0.54	0.19	+1	-1	73.4
3-(H^+)	249.6	0.92	0.36	< 0.05	+3	-1	75.5
3-($W(CO)_5$)	53.4	0.92	0.55	0.18	+1	-1	74.1
4-(H^+)	220.4	0.90	0.34	< 0.05	+3	-1	75.9
4-($W(CO)_5$)	38.7	0.90	0.48	0.31	+1	-1	65.6
4-($HNMe_2$)	12.1	0.90	0.28	0.74	+3	-3	97.4
5-(H^+)	188.0	0.91	0.36	< 0.05	+3	-1	73.7
5-($W(CO)_5$)	27.8	0.91	0.46	0.38	+1	-1	56.1
5-($HNMe_2$)	20.4	0.91	0.23	0.85	+3	-3	100
6-(H^+)	229.1	0.90	0.35	< 0.05	+3	-1	76.4
6-($W(CO)_5$)	41.9	0.90	0.51	0.25	+1	-1	73.0
6-($HNMe_2$)	8.0	0.90	0.36	0.63	+3	-3	77.3

Table 7.16: Second PA and bond dissociation energies including zero-point energy corrections (D_0) of systems **1**-**6** with two $W(CO)_5$ and $HNMe_2$ ligands. Bi's and Ligand (NCN or NNN) frontier EFOs occupancies and assigned OSs. $PA_2 = \Delta H(\textbf{1-6}\text{-}(H^+)) + \Delta H(H^+) - \Delta H(\textbf{1-6}\text{-}(H^+)_2)$. Proton enthalpy +1.5 kcal/mol. All energies are in kcal/mol. [a] Three pseudodegenerated EFOs (in occupancy), one from the NCN pincer ligand and two from H atoms (one each).

System	PA/D_0	6s Bi	$6p_z$ Bi	π L	Bi OS	L OS	$R(\%)$
1-$(H^+)_2$	103.1	0.69	0.33	< 0.05	+3	-1	50.0[a]
1-$(W(CO)_5)_2$	33.2	0.87	0.55	0.13	+1	-1	78.3
2-$(H^+)_2$	94.4	0.69	0.33	< 0.05	+3	-1	50.0
2-$(W(CO)_5)_2$	37.1	0.88	0.53	0.10	+1	-1	77.7
3-$(H^+)_2$	114.5	0.70	0.34	< 0.05	+3	+1	53.6
3-$(W(CO)_5)_2$	44.1	0.87	0.52	0.10	+1	-1	76.5
4-$(H^+)_2$	98.4	0.68	0.33	< 0.05	+3	-1	71.6
4-$(W(CO)_5)_2$	34.5	0.88	0.51	0.18	+1	-1	80.2
4-$(HNMe_2)_2$	16.4	0.88	0.18	0.87	+3	-3	100
5-$(H^+)_2$	62.5	0.69	0.34	< 0.05	+3	-1	67.6
5-$(W(CO)_5)_2$	30.7	0.88	0.51	0.20	+1	-1	77.0
5-$(HNMe_2)_2$	21.2	0.88	0.18	0.91	+3	-3	100
6-$(H^+)_2$	100.5	0.69	0.33	< 0.05	+3	-1	72.8
6-$(W(CO)_5)_2$	39.7	0.86	0.52	0.13	+1	-1	76.7
6-$(HNMe_2)_2$	11.3	0.88	0.21	0.83	+3	-3	100

We also considered the adducts with the electron-deficient $W(CO)_5$ species (**1-6**-$(W(CO)_5)$, as its synthesis is typically used as an experimental signature of Bi(+1) character, where the available $6p_z$ electrons of Bi are used to form a dative Bi→W bond. Hence, upon reaction with the $W(CO)_5$ Lewis acid, the Bi center should formally remain Bi(+1). Indeed, EOS results are in full agreement with these considerations. For instance, for **2**-$(W(CO)_5)$ EOS gives a clear Bi(+1), NCN(-1) and neutral $W(CO)_5$ assignment, with $R(\%) = 73.4$. The OS assignation is driven by newly formed bond, as the σ Bi-NCN interaction remains essentially unchanged. However, when bonded to the $W(CO)_5$ unit, the occupancy of the Bi $6p_z$ EFO slightly decreases from 0.59 (**2**) to 0.54 (**2**-$W(CO)_5$). Furthermore, the ligand frontier π EFO occupancy drops from 0.41 (**2**) to 0.19 (**2**-$W(CO)_5$). These electrons are used to populate the otherwise empty σ EFO on the $W(CO)_5$ moiety (0.29). Still, the large occupancy of the Bi $6p_z$ EFO indicates its predominant Bi(+1) character. The π-density of the NCN ligand is significantly altered, but still the ligand acts formally as spectator in both species. The aforementioned OS assignment of species **4**-**6** implies that the Bi $6p_z$ lone pair is formally absent, so they could potentially exhibit different reactivity towards a Lewis acid and protonation than **1**-**3**. However, adduct **4**-$W(CO)_5$ was observed and characterized by MS and NMR spectroscopy, which could be in an apparent contradiction to the Bi(+3) assignment.[252] Interestingly, the dissociation energies of the adducts **1**-**6** exhibit again excellent correlation with the Bi $6p_z$ occupancies of the precursor, no matter the formal OS of the Bi center. Thus, the smaller the occupancy, the smaller the D_0 value. Such behaviour is in line with a more pronounced Bi(+3) character.

Finally, we have also considered the coordination of systems **4**-**6** with one and two dimethylamine ($HNMe_2$) moieties. We obtained low D_0 values, suggesting a labile Lewis pair. The $HNMe_2$ release has been already observed (experimentally) by Kindervater *et al.* for the preparation of **4** from **4**-$(HNMe_2)_2$.[244] The authors argued that the deamination leads to a reduction of the original Bi(+3) to a Bi(+1) center, by a concomitant oxidation of the pincer ligand that would provide the electron pair. However, according to our calculations no change on Bi's OS is observed. EOS analysis of the mono and diaminated species points to an undisputed Bi(+3) and NNN(-3) assignment, especially for the diaminated ones. The NNN π EFO occupancy increases going from **4** (0.57) to **4**-$(HNMe_2)$ (0.74) and to **4**-$(HNMe_2)_2$ (0.87), indicating that it

is the π system of the ligand that collects the excess electrons coming from the σ-donating amines. This substantial occupancy change is concomitant with the structural deformation of the NNN ligand, pointing towards a certain dearomatization of the phenyl rings upon deamination, as noted by Kindervater *et al.*[244] Comparing the results for species **4**-**6**, we observe that the D_0 values decrease with the occupancy of the Bi $6p_z$ EFO, supporting the relationship between the EFO occupancies with the Lewis acid/base character.

To conclude this part, we shown that the EFOs and EOS analysis affords a scrutiny of the electronic structure of the Bi-based (main-group) complexes from ground-state properties, and without recurring to reference states. According to EOS, the Bi-NCN and Bi-NNN pincer complexes results in a different OS for the bismuth atom, being Bi(+1) and Bi(+3), respectively. However, regardless of the formal OS, all complexes are able to react with a series of Lewis bases and acids. The ambiphilic behaviour of these complexes is a direct consequence of the strong π-conjugation between the Bi and the pincer ligand. Finally, we quantitatively illustrated that this reactivity can be assessed by the occupancy of the Bi $6p_z$ EFO.

7.3.4 Characterizing the chemical bonding picture of main group compouds: the low-valent EL_2 (E = Mg, Be; L = NHC, cAAC) case

In the last two decades, the scope of the concept of OSs in main group chemistry has remarkably expanded.[253–255] Among them, stable singlet carbenes featuring non-oxidative electron-pair donation such as NHCs,[256] and cyclic(alkyl)(amino) carbenes (cAACs)[257,258] have been crucial to access low OSs. Regarding to the chemical bonding, the donor-acceptor interaction between the carbene and the central element, traditionally a TM, has been invoked.[259] Hence, the formal electron deficiency of the central atom is alleviated by σ-donation from the ligand, which is counterbalanced by a weaker π-backdonation.[259,260] Meanwhile the low-valent p-block compounds has substantially benefit from this bonding concept, little attention has been paid to this chemistry for s-block elements.[253]

The Group 2 chemistry is dominated by the +2 OS due to the hability of these elements to give the valence electrons. However, various experimental groups achieved the synthesis and characterization of lower in OS Mg- and Be-based compounds.[261–266] Among them, the dicoordinated neutral $Be(cAAC)_2$ reported by Braunschweig and co-workers, henceforth Be-cAAC^{Dip}, captivated our attention.[263] The Be-cAAC interaction was rationalized as donor–acceptor, acting the cAAC ligands as σ-donor to the empty Be(0) s-type orbital, which then has the p-type electrons available to strongly π-backdonate to the ligands. We depicted this interaction, cAAC→Be←cAAC, in Figure 7.33A.

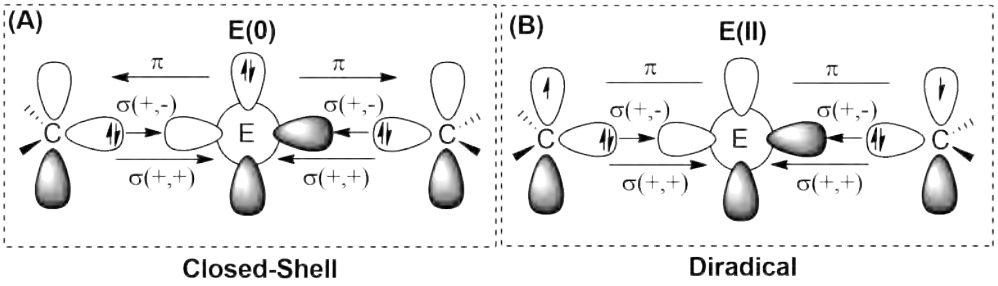

Figure 7.33: Schematic view of the orbital interactions in $E(0)L_2$ (L = NHC and cAAC): (A) donor-acceptor interaction in closed-shell singlet spin-state and (B) electron-sharing interaction in open-shell singlet spin-state (diradical). Notation "+,+" and "+,-"" stands for the in-phase and out-of-phase combination of lone pair orbitals.

The strongly pursued synthesis and characterization of a Mg(0)-based system has been recently achieved by Harder and co-workers, using an extraordinarily bulky ligand (BDI* = HC{C(tBu)N[2,6-(3-pentyl)-phenyl]}$_2$) to stabilize the Mg(+2) precursor.[264] In this case, the bonding situation differs from the previous systems, as the stability is driven by two Mg–Mg electron-sharing bonds rather than a donor-acceptor interaction.[267] For this species, the OS assignment is connected to MO theory picture.[268] The donor-acceptor interaction in a closed-shell singlet electronic configuration assumes an electronic structure preorganization of E(0) from the ground state ^{1}S (ns^2np^0) into the doubly excited singlet state ^{1}D (ns^0np^2) to interact with the σ-donor/π-acceptor ligands (Scheme 7.33A). Applying the IUPAC IA to the σ and π bonds could indeed lead to the 0 OS. Note, however, that the Be and Mg atoms are much less electronegative than the C itself, with electronegativity values of 1.57, 1.31 and 2.55 (according to Allen's electronegativity scale), respectively.[106] An alternative (and plausible) scenario is that upon bonding of the ligands, the metal center oxidizes, and its electron pair ends up at the ligands. Thus, a diradical(oid) species is formed, with chemical bonding picture represented in Figure 7.33B. Considering the three-center two-electron (3c-2e) nature of the system, the interaction between the unpaired electrons can be significant, and a rather low singlet-triplet gap would hint the diradical character of such compounds. However, distinguishing between the two chemical bonding pictures using single-reference methods is not straightforward, if not impossible, as the incomplete description of the spin-polarization can mislead the wavefunction analysis. With this, the main objective of this work was:

1) To elucidate the electronic structure and chemical bonding nature (donor-acceptor against diradical(oid)) of a variety of EL_2 systems, where E corresponds to Mg or Be and L to different NHC and cAAC ligands, including the low-valent E(0) systems recently accomplished experimentally.

To accomplish this goal, we included in the study NHC and cAAC ligands where the flanking groups have different stereoelectronic properties, i.e. methyl (Me) and 2,6-diisopropyl-phenyl (Dip). Then, we performed chemical bonding analysis at both the KS-DFT and multireference (CASSCF) levels of theory, including the use of the LSA, EOS and the analysis of the resulting NOs, together with their occupancy values, among others.

We performed geometry optimizations of all systems considering the closed-shell singlet (CSS), open-shell singlet (OSS) and triplet (T) spin states with a variety of KS-DFT functionals of different nature. The electronic ground states and the obtained adiabatic (spin-contamination corrected) singlet-triplet gap are

collected in Table 7.17. For the cAAC-substituted systems, we found open-shell singlet (broken-symmetry) solutions lower in energy than the closed-shell. In fact, the closed-shell B3LYP wavefunction for Be-cAAC^{Dip} is not stable. All tested KS-DFT functionals provided small singlet-triplet gaps (lower than 10 kcal/mol) independently of their nature (Table 7.17), hinting that the systems might present large multiconfigurational character.

Table 7.17: Ground state multiplicity and adiabatic (spin-corrected) singlet-triplet (S-T) gap obtained using a variety of (different in nature) KS-DFT functionals. CSS = closed-shell singlet, OSS = open-shell singlet, T = Triplet. ^{a} Vertical singlet-triplet gap.

	Ground State Multiplicity				ΔE_{S-T} Gap (kcal/mol)			
System	B3LYP	PBE0	M06-2X	ωB97x-D	B3LYP	PBE0	M06-2X	ωB97x-D
Mg-NHC^{Me}	CSS	CSS	CSS	CSS	10.9	7.8	7.5	12.1
Mg-NHC^{Dip}	CSS	CSS	CSS	CSS	13.3	11.1	0.9	14.2
Mg-cAAC^{Me}	OSS	OSS	T	OSS	3.3	3.2	-0.9	2.5
Mg-cAAC^{Dip}	OSS	OSS	T	OSS	2.4	2.2	-0.7	1.5
Be-NHC^{Me}	CSS	CSS	T	CSS	4.6	2.0	-3.4	2.1
Be-NHC^{Dip}	CSS	OSS	T	OSS	7.9	5.6	-5.5	9.0
Be-cAAC^{Me}	OSS	OSS	OSS	OSS	6.4	5.4	1.3	6.6
Be-cAAC^{Dip}	OSS	OSS	OSS	OSS	8.5	8.1	4.0	6.9
Be-NacNac^{Me}	CSS	CSS	CSS	CSS	30.2^a	29.5^a	33.8^a	30.5^a
Be-BDI*	CSS	CSS	CSS	CSS	35.7^a	32.5^a	29.3^a	34.7^a
Mg-NacNac^{Me}	CSS	CSS	CSS	CSS	38.3^a	34.7^a	37.6^a	36.6^a
Mg-BDI*	CSS	CSS	CSS	CSS	39.2^a	36.2^a	47.8^a	41.0^a

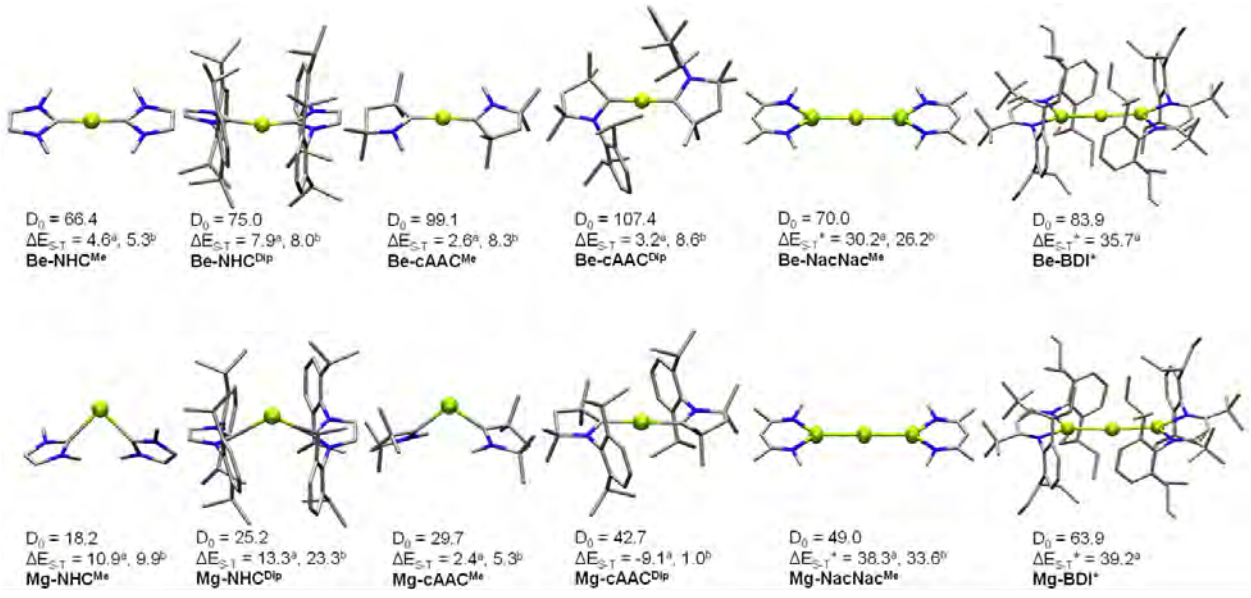

Figure 7.34: Optimized ground-state geometries (B3LYP/def2-SVP), dissociation energies (D_0) considering the $EL_2 \rightarrow E(0) + 2\times L(0)$ dissociation, and adiabatic singlet-triplet gap (ΔE_{S-T}) (B3LYP/def2-TZVPP^a, CASSCF/cc-pVDZ^b). *Vertical ΔE_{S-T} values. Energies reported in kcal/mol. Hydrogen atoms omitted for clarity.

In Figure 7.34 we displayed the ground-state geometries of the studied compounds, together with their dissociation energies (D_0), and adiabatic singlet-triplet gaps (ΔE_{S-T}), and in Table 7.18 we collected the main geometrical and electronic parameters. The calculated Be-C bond lengths slightly vary with the nature of the ligand (from 1.634 to 1.648Å), in good agreement with previous studies.[263,264,269] These bond

lenghts fall in the expected values for prototypical single and double bonds (1.77 and 1.57Å, respectively).[270] Furthermore, in all cases the bond angles are almost collinear (167.4-179.9 °), favoured by a strong delocalization on the C-Be-C π-system. On the other hand, the Mg-C distance are shorter than those reported by Couchman *et al.* for $Mg_2(NHC)_2$ and $Mg_2(NHC)_4$ systems.[271] However, note that the computed values are, in fact, longer than expected for a single bond Mg-C (2.14Å). Only for the Mg-cAAC^{Dip} compound the coordination distance is within the single and double bond range (1.99Å).[270] An appreciable coordination change is observed by the series of Mg-based compounds. Mg-cAAC^{Dip} exhibits an almost collinear angle ($\angle_{C-Mg-C}$ = 178.9 °), while the others possess a rather acute one (from 90.1 to 119.3 °). Similarly, the tilted coordination mode of MgL_2 (L = NHC^{Me}, NHC^{Dip} and cAAC^{Me}) can be rationalized with a different bonding situation. Here, the two electrons of Mg are not promoted from the s to the p orbital; instead the ligand donation into the Mg p-orbital, with a back-donation from the occupied s-orbitals into the carbene empty orbitals. The D_0 values indicate that the Mg-NHC^{Me} complex (18.2 kcal/mol) is much less stable than the Be-NHC^{Me} analogue (66.4 kcal/mol). The Be-cAAC^{Dip} is the most stable of the series (107.4 kcal/mol) and is about 60 kcal/mol more strongly bonded than Mg-cAAC^{Dip} (42.7 kcal/mol). The ionic dissociations ($EL_2 \rightarrow E(+2) + 2\times L(-1)$) are much less favoured than the neutral ones in all cases. This is in agreement with a donor-acceptor picture of Figure 7.33A. Note that this holds true even for Mg-cAAC^{Dip}, in which the OSS solution lies 11.4 kcal/mol below to the CSS one. Let us remark that the dissociation pattern of a system does not provide any information about its chemical bonding at the complex geometry, but may be informative of the stability of the compounds.

Table 7.18: Geometrical parameters (E = Mg or Be), fragment and inter-fragment local spin ($< S^2 >_f$ and $< S^2 >_{f_1-f_2}$), EOS results and $R(\%)$ index of the studied compounds in its ground state (GS) multiplicity. Local spin and EOS obtained at the CASSCF/cc-pVDZ//B3LYP-D3(BJ)/def2-SVP level using the TFVC atomic definition. [a] Evaluated at the B3LYP-D3(BJ)/def2-SVP level.

E-L_2 system	GS	d_{E-L}	$\angle_{L-E-L}$	$< S^2 >_E$	$< S^2 >_L$	$< S^2 >_{L_1-L_2}$	E OS	$R(\%)$
Be-H	CSS	1.331	180.0	0.04	0.02	0.00	+2	100
Be-NHC^{Me}	CSS	1.639	179.9	0.06	0.14	-0.11	+2	74.0
Be-NHCDip	CSS	1.648	167.4	0.08	0.22	-0.18	+2	73.8
Be-cAAC^{Me}	OSS	1.634	176.4	0.07	0.30	-0.26	+2	77.8
Be-cAAC^{Dip}	OSS	1.644	177.8	0.08	0.39	-0.35	+2	78.9
Be-NacNac^{Me}	CSS	2.541	180.0	0.07	0.06	-0.02	-2	86.7
Be-BDI^{*,a}	CSS	2.489	177.9	-	-	-	-2	73.0
Mg-H	CSS	1.699	180.0	0.05	0.03	-0.01	+2	100
Mg-NHC^{Me}	CSS	2.300	90.1	0.10	0.07	-0.02	0	100
Mg-NHC^{Dip}	CSS	2.347	119.3	0.09	0.07	-0.02	0	82.7
Mg-cAAC^{Me}	OSS	2.174	107.8	0.12	0.10	-0.04	0	80.0
Mg-cAAC^{Dip}	OSS	2.040	178.9	0.08	0.68	-0.64	+2	82.4
Mg-NacNac^{Me}	CSS	2.917	180.0	0.12	0.10	-0.02	0	59.0
Mg-BDI^{*,a}	CSS	2.800	175.4	-	-	-	0	59.9

To gain insight into the bonding situation, we first conducted EDA calculations coupled to the NOCV method on the broken symmetry solutions. The EDA method requires the use of reference states, and the ones which better represent the electronic structure of the resulting system is assumed to be the one that minimizes the orbital interaction energy component. We computed the EDAs for the Be-cAAC^{Dip} and Mg-cAAC^{Dip} systems considering two different fragmentation patters: donor-acceptor (Figure 7.33A) and diradical(oid) (Figure 7.33B). We summarized the results obtained in Table 7.19. The principal bonding picture that emerges from EDA features an E(0) with two neutral cAAC ligands. The orbital energy terms are -231.4 and -193.0 kcal/mol, for Be-cAAC^{Dip} and Mg-cAAC^{Dip}, respectively. Comparing with the E(+2) fragmentation, the orbital relaxation leads to a higher orbital interactions with values of -443.8 and -289.8 kcal/mol for Be-

cAAC^{Dip} and Mg-cAAC^{Dip}, respectively. The resulting energy-based OS assignment is in contrast with the derived from the EOS analysis (vide infra), and also from the previously suggested for similar model systems by Ponec and coworkers.[272] Both pictures can be reconciled by focusing on the electron flow associated with the orbital interactions rather than on the energy costs. Indeed, the EDA-NOCV approach provides this information as the eigenvalues of the deformation densities. In the π interaction channel, using the Be^0 in the ^{1}D reference state (Figure 7.35 (top)), 0.75α and 0.74β electrons are transferred from the starting electron pair of Be's p-orbital to the cAAC ligands, with a π-type symmetry fragment orbital. On the contrary, using a Be^{2+} reference (Figure 7.35 (bottom)), the electron flow from the ligands to the empty Be's p-orbital is merely 0.20σ and 0.22β electrons. Notice that the final result is similar in both cases: one ends with 0.49 and the other with 0.42 electrons on the Be p-orbital. However, the latter fragmentation leads an overall smaller electron flow. Thus, one may argue that the reference state for which a smaller electron flow among fragments is found, is the most appropriate reference state, at least to assign OSs. However, this is in contrast with the accepted criterion of choosing the reference states according to the minimum orbital interaction.[254,273] Hence the dichotomy: should we use energy or density criterion? One should recall that in the (revised) definition of OS from the IUPAC there is no mention of energetics, but it is essentially an electron count problem with the "winner-takes-it-all" principle.[105]

Table 7.19: EDA-NOCV of E-cAAC^{Dip} (E = Be and Mg) at the B3LYP-D3(BJ)/TZ2P level of theory. The lowest $\Delta E_{orb-corr}$ is high-lighted in bold. Reported energy values in kcal/mol. [a] The value in parenthesis gives the percentage contribution to the total attractive interactions $\Delta E_{elstat} + \Delta E_{orb} + \Delta E_{disp}$. [a] The values in parenthesis gives the percentage contribution to the total orbital interaction $\Delta E_{orb-corr}$.

	Be-cAAC^{Dip}		Mg-cAAC^{Dip}	
E-L$_2$ system	Be^0(^{1}D, $2s^02p^2$); $(cAAC)_2$ (CSS)	Be^{+2}(^{1}S, $2s^02p^0$); $(cAAC)_2^{2-}$ (OSS)	Mg^0 (^{1}D, $3s^03p^2$); $(cAAC)_2$ (CSS)	Mg^{+2} (^{1}S, $3s^03p^0$); $(cAAC)_2^{2-}$ (OSS)
ΔE_{int}	-287.1	-847.9	-222.6	-647.2
ΔE_{Pauli}	157.4	105.8	197.1	98.4
ΔE^a_{disp}	-10.5 (2.4%)	-10.5 (1.1%)	-16.1 (3.8%)	-16.1 (2.1%)
ΔE^a_{elstat}	-202.6 (45.6%)	-499.4 (52.4%)	-210.7 (50.2%)	-466.8 (60.4%)
ΔE_{orb}	**-231.4**	-401.4	**-193.0**	-241.6
ΔE_{orb-HF}	0.0	-42.4	-0.1	-48.2
$\Delta E^a_{orb-corr}$	**-231.4** (52.1%)	-443.8 (46.5%)	**-193.0** (46.0%)	-289.8 (37.5%)
$\Delta E^b_{orb-\sigma(+,+)}$	-18.3 (7.9%)	-45.7 (10.3%)	-13.8 (9.8%)	-41.9 (14.4%)
$\Delta E^b_{orb-\sigma(+,-)}$	-51.9 (22.4%)	-90.3 (20.3%)	-18.6 (9.7%)	-28.4 (9.8%)
$\Delta E^b_{orb-\pi}$	-150.7 (65.1%)	-211.6 (47.7%)	-152.0 (78.7%)	-119.5 (41.2%)
ΔE^b_{rest}	-10.4 (4.5%)	-53.9 (12.1%)	-8.6 (4.4%)	-51.8 (17.9%)
$< S^2 >$	0.571	0.571	0.942	0.942

Then, why does a smaller electron flow associated with the Be p-orbital have a more significant energy cost? The reason can be inferred again from the NOCV analysis. While the aforementioned electron flow to Be's p-orbital (empty) is just 0.20α and 0.22β electrons, the total electron displacement of this channel is approximately 1.8 electrons. Therefore, over 75% of the electron flow is associated with the internal reorganization of the fragment density, which certainly has an important energetic impact, but has no influence on the OS. This conundrum adds up to another related issue of EDA that was recently exposed by Salvador and coworkers: EDA cannot distinguish an electron-sharing interaction from a spin-polarized (diradicaloid) one.[94] This problem pops out whenever the closed-shell solution is not the ground-state (or unstable), which is precisely the case of most systems considered here. For all these reasons, we do not consider the combination of KS-DFT and the energy-based EDA criterion a reliable approach to elucidate the Be and Mg OSs in these systems. Instead, we prefer to rely on tools specifically devoted to elucidate

OSs from the analysis of the wavefunction itself, avoiding the use of reference states.

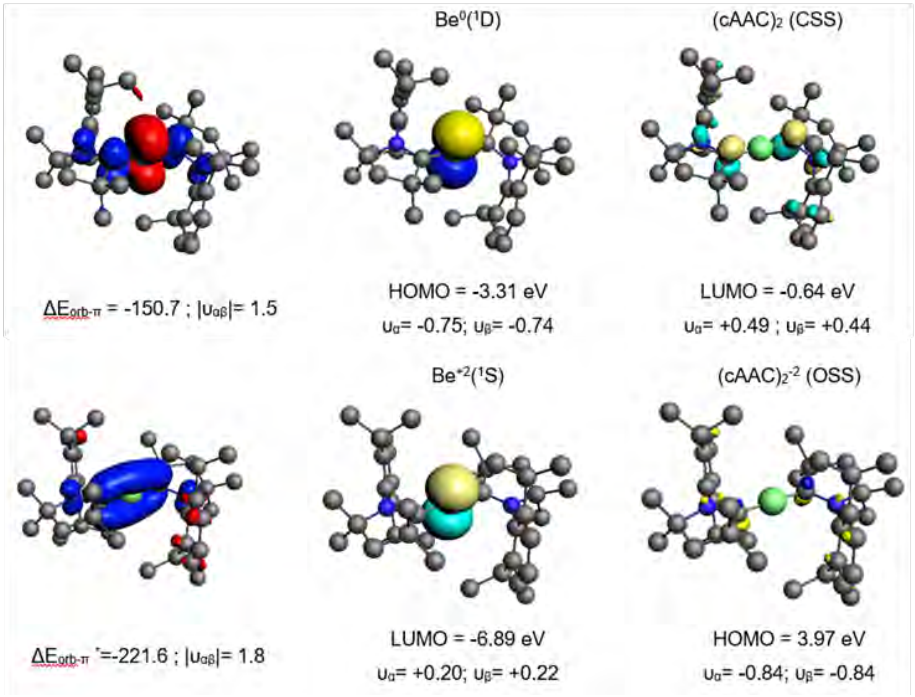

Figure 7.35: Deformation densities plot $\Delta\rho$ (isocontour value of 0.003) of the pairwise orbital interactions between $Be^0(^1D, 2s^02p^2)$ and $cAAC^{Dip}$ (top), and $Be^{+2}(^1S, 2s^02p^0)$ and $(cAAC^{Dip})_2^{2-}$ (bottom) within the Be-$cAAC^{Dip}$ system. Energies ΔE in kcal/mol and eigenvalues ν in a.u. Charge outflow in red and charge density accumulation in blue. Important interacting occupied and vacant orbitals of the fragments depicted with an isocontour value of 0.05. Occupied orbitals shown in blue and yellow, virtuals in cyan and pale yellow. Hydrogen atoms were omitted for clarity.

These systems are better described by a multireference (CASSCF) wavefunction. Visual inspection of the the CASSCF NOs and analysis of their occupancies already hint about the bonding situation, see as example Figure 7.36 (left). The complexes with an acute bond angle present a highest occupied natural orbital (HONO) and a lowest unoccupied natural orbital (LUNO) localized at the E atom with marked s-type, and p-type character, respectively. Instead, the frontier NOs of the linear complexes resemble the allyl π-system. Thus, the HONO is described as a π-system with in-phase combination π-(+,+,+), while the LUNO is the out-of-phase combination of the extremes π^*-(+,·,-) of the C-E-C p-type orbital lobes. The NO corresponding to the π-(+,-,+) combination has negligible occupancy. In Figure 7.36 we depicted the aforementioned NOs of systems Be-$cAAC^{Dip}$ (a) and Mg-$cAAC^{Dip}$ (b). Evaluating the occupancies of the NOs, they reveal that the HONO has significantly less than two π-electrons, precisely 1.62 (Be-$cAAC^{Dip}$) and 1.21 (Mg-$cAAC^{Dip}$). Note that the Mg has a weak contribution on the HONO as a consequence of lower overlap, which also justifies the geometry change throughout the series. In addition, the LUNO presents a significant occupancy, being 0.38 and 0.79 electrons for Be-$cAAC^{Dip}$ and Mg-$cAAC^{Dip}$, respectively. In the series of BeL_2, the LUNO occupancy varies within the 0.13-0.38 range. These results confirm our above hypothesis that the π-electrons are much more localized at the ligands than at the E center. As consequence, the complexes can also exhibit a different degree of diradical character.

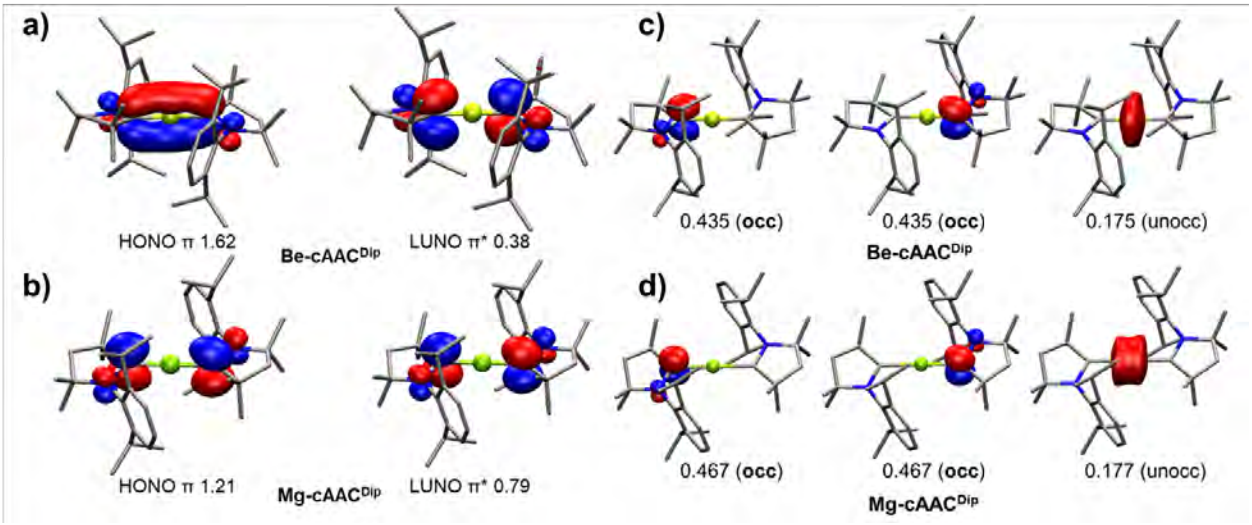

Figure 7.36: Frontier NOs and occupancies of the Be-cAAC^{Dip} (a) and Mg-cAAC^{Dip} (b) systems in the singlet spin-state, together with the frontier EFOs and their associated gross occupancies of Be-cAAC^{Dip} (c) and Mg-cAAC^{Dip} (d). Selected isocontour value of 0.05 a.u. for the NOs and 0.1 a.u. for the EFOs. Hydrogen atoms were omitted for clarity.

In this context, the cAAC-substituted compounds could be better interpreted as diradical(oid)s species. One of the practical manners to quantify the diradical(oid) character is from the NO occupancies.[274] However, if a system presents several NOs with significant occupancies, the usual underlying 2c-2e model is insufficient to describe the diradical character. Thus, we instead make use of the LSA which quantifies the presence of local spins on atoms/fragments and their couplings from correlated wavefunctions even in a singlet state (see details in Section 1.3.1). We gathered the LSA results in Table 7.18. For the NHC-coordinated systems, both the $< S^2 >_{NHC}$ and $< S^2 >_E$ values are below 0.15 in all cases, in exception of Be-NHC^{Dip} ($< S^2 >_{NHC} = 0.22$). Interestingly, in the cAAC-based compounds the $< S^2 >_{cAAC}$ values increase from 0.10 (Mg-cAAC^{Me}) to 0.68 (Mg-cAAC^{Dip}), and from 0.30 (Be-cAAC^{Me}) to 0.39 (Be-cAAC^{Dip}). In all cases, the $< S^2 >_E$ values are lower than 0.12, ruling out the presence of unpaired electrons at the central element. Thus, the chemical bonding picture points towards two unpaired spins, each one located at the π-system of the cAAC ligand, coupled antiferromagnetically. This coupling is supported by the $< S^2 >_{cAAC-cAAC}$ values obtained, being -0.64 (very close to the ideal -0.75, for a *perfect* diradical) for Mg-cAAC^{Dip}. The experimentally known Be-cAAC^{Dip} compound presents $< S^2 >_{cAAC}$ and $< S^2 >_{cAAC-cAAC}$ values of 0.39 and -0.35, respectively, indicating a pronounced (and obviously non-negligible) diradical character. Note that in the diradical(oid) scenario the formal OS of the central element E would be +2.

To confirm the chemical bonding picture, we elucidated the OSs of both the central element and each one of the ligands. For this aim, we applied the EOS analysis to the ground-state CASSCF wavefunctions. The resulting OSs, together with their associated $R(\%)$ values are gathered in Table 7.18. According to EOS, the nearly collinear systems (C-E-C angle $> 160^\circ$) are better characterized as E(+2), and thus each ligand formally -1. These findings are in line with the discussion above and also in agreement with the work of Ponec and coworkers.[272] We illustrated the situation from the EFO perspective in Figure 7.36 (right). In particular, the last occupied EFOs from Be-cAAC^{Dip} and Mg-cAAC^{Dip} correspond to π orbitals sitting on the cAAC ligands and with occupancy values of 0.435 and 0.467, respectively. As the frontier EFOs are pseudodegenerated in occupancy and from different fragments, the EOS analysis advocates for a homolytic

splitting of the last electron pair assigning one electron to each EFO. In this case, such electron assignment leads to the formal diradical(oid) picture (Figure 7.33B). In any case, the E(+2) assignment is unambiguous as the occupancy of the E last unoccupied EFO is very small. On the contrary, in the bent Mg system, EOS clearly points towards a genuine Mg(0) compound, even for a system like Mg-cAAC^{Me} with non-negligible diradicaloid character.

According to IUPAC's IA, the electron pair from an orbital (localized or not) should be assigned to the atomic orbital (and thus atom) with larger contribution. In our view, it represents a naïve and ambiguous point on the relationship between AO coefficients and OSs. This issue has already been discussed by Popp *et al.*[275] However, for the Be-cAAC^{Dip} system, one could simply focus on the π NO with a occupancy of 1.62 (Figure 7.36a) and assign an electron pair to the AO which contributes more. Nonetheless, it is not so obvious which is the contribution of a given fragment holding a set of non-orthogonal AOs to a MO or NO. One may consider an orthogonal basis instead, such as a Löwdin's variant implemented in pySCF.[175] The orbital coefficients of the $2p_z$ and $3p_z$ AOs of Be are 0.399 and -0.096 for Be-NHC^{Dip}, and 0.291 and -0.095 for Be-cAAC^{Dip}. For comparison, just the coefficient of the $2p_z$ AOs of each of the two contact carbon atoms of the ligands are 2×0.495 and 0.541 and 0.512 (non-symmetric orbital), respectively. The Be population of these NOs (i.e. sum of the square of the coefficients on an orthogonal basis) is merely 0.18 and 0.11, respectively, not too different from the DAFH and EFO occupancies discussed above.

Overall, the Mg/Be OS of +2 is a direct consequence of the strong electron π-accepting properties of the ligands. We consider interesting to contrast this analysis with the strong σ-donor and weak π-acceptor monoanionic β-diketiminate magnesium ligands. Optimization of the experimentally accomplished Mg-BDI* system lead to an almost collinear structure with an Mg-Mg-Mg angle 175.4°. We constructed a model of the system reducing the steric hindrance of the ligands, unaffecting in theory the electronic properties, obtaining formally the same structure but with a bond angle of 180°. However, the bond lengths are sharply lengthened from 2.800 (Mg-BDI*) to 2.917Å (Mg-NacNac). No OSS solutions were found for these systems. Thus, the CSS solution is the lowest in energy at the level of theory used. Furthermore, large vertical singlet-triplet gaps were obtained at both KS-DFT and CASSCF levels (above 25 kcal/mol). As expected, the ligand interaction with the central element is explained by the σ E-E NO with occupancy close to 1.90. The p- and π^*-type NO present occupancy values lower than 0.1, a fingerprint of dynamic, instead of static, correlation. EOS analysis yields a relatively straightforward Mg(0) assignment. Moving to the Be-based analogous, the Be-NacNac and Be-BDI* show no appreciable diradical character, with singlet-triplet gaps of 30.2 and 35.7 kcal/mol, respectively. According to EOS, these molecules formally bear a Be atom with an OS of -2.

Concluding this section, we examined the features of the structure and chemical bonding of the low-valent group 2 compounds depicted in Figure 7.34. Contrarily to the accepted understanding, beryllium still remains in the +2 OS territory. The strong σ-donor stabilized approach produces an internal electronic rearrangement furnishing diradical(oid) species with two unpaired electrons on the ligands. The magnesium analogues might present the neutral (low-valent) OS when the ligands are not too π-acid. However, the chemical bond is too weak to consider these molecules thermally stable. Interestingly, the EOS analysis suggests that the Mg-based ligands are key to accessing genuine low-valent compounds. Overall, our study give more insight into the peculiar features of the systems considered, suggesting also a promising beryllium in the (novel) -2 OS.

Chapter 8

Conclusions

The use of centroids of localized molecular orbitals (LMO) for the elucidation of formal oxidation states (OS) has been critically analyzed in this Thesis. We considered the conventional closest-atom criterion for the electron assignment, but also explored an alternative one that combines the centroid position with Bader's atomic basin: if the centroid of a LMO lies within the basin of atom A, the corresponding electrons are assigned to A. The new criterion, termed basin-allegiance, performed better than the closest-atom one for simple hydrides. In fact, the closest-atom criterion already fails to provide the correct OS in H_2O, but the new criterion fixes this failure. However, both schemes fail in the case of transition metal (TM) carbenes. Moreover, the particular choice of orbital localization has a non-innocent impact in the assignment using centroids with one or another criterion. Thus, this methodology proved to be unreliable as a general procedure to assign OS.

A new orbital localization procedure based on molecular fragments for oxidation state assignation purposes, termed oxidation states localized orbitals (OSLO), has been introduced. The fragments are (a priori) selected by the user, being in case of TM complexes the metal centers and each of the ligands. To quantify the degree of locality of each LMO (or any input orbital) on a given fragment, we introduced the fragment orbital localization index (FOLI). The proposed algorithm iteratively selects the most fragment-localized orbitals from a set of redundant LMOs generated on each fragment by minimizing the spread functional. The electrons of each LMO are associated to the parent fragment and thus the formal OS are obtained as a side effect. The OSLO method has been applied to a wide set of challenging systems, and the results obtained are in much better agreement with the expected Lewis structure than those obtained with other localization schemes such as Pipek-Mezey (PM) or natural localized molecular orbitals (NLMO), used in the context of the localized orbitals bonding analysis (LOBA) scheme. In particular, the limitations found for the use of centroids and LOBA (Sections 4.1 and 6.1, respectively) in the TM-carbene characterization are surpassed.

A generalization of the intrinsic atomic orbital (IAO) procedure from Knizia has been introduced, as a robust AIM method in the framework of Hilbert-space analysis. In the newly introduced IAO-AutoSAD approach, the reference minimal basis is obtained on-the-fly for each distinct atom using the actual molecular basis set from the eigenvectors of the free atom's sphericalized density. The IAO-AutoSAD scheme has been applied in the framework of the OSLO approach, with excellent results in agreement with real-space based AIM procedures.

An intrinsic limitation of the original effective oxidation state (EOS) scheme when it comes to assign OS in the case of diradical(oid) systems described by proper multireference wavefunctions has been rationalized. We show that the effective fragment orbitals (EFO) derived from the (effectively) paired and unpaired densities leads to much more consistent results in the framework of EOS analysis, as compared to the conventional treatment of the spin-separated α and β densities. The former readily accounts for the formal homolytic splitting of electron pairs in bonding situations governed by strong static correlation, superseding the original EOS scheme. Furthermore, the new approach, termed uEOS, also affords a much better chemical picture in terms of electron pairs from unrestricted wavefunctions, specially in the presence of large spin contamination.

The interacting quantum atoms (IQA) decomposition of each of the terms originated from the energy decomposition analysis (EDA) (i.e. electrostatic, Pauli repulsion, and orbital interaction) has been introduced. The EDA scheme has been implemented in a standalone code and linked to the in-house code APOST-3D. We find that the formally intermolecular electrostatic energy from EDA presents non-negligible intra-fragment contributions, originated from the charge penetration. Also, the behavior of the IQA terms upon dissociation of a selected variety of donor-acceptor (non-covalently bonded) complexes has been evaluated, unveiling, for instance, that the EDA orbital interaction term is governed by the inter-fragment IQA contribution (intra-fragment IQA terms tend to compensate each other). The new EDA-IQA methodology provides a richer energy decomposition scheme, and aims at bridging the gap between the two main distinct real-space and Hilbert-space methodologies.

A new strategy for the numerical integration of the IQA two-electron energy contributions in the framework of overlapping AIM has been introduced. With the so-called two-electron zero-error scheme (ZES), while the individual one- and two-center terms may bear some numerical error, their sum leads *exactly* to corresponding analytical value (e.g. Coulomb, exact exchange or correlation from the cumulant). The ZES exploits our observation that in two-electron numerical integrations, the rotation of the second grid has major effect in the accuracy of the one-center terms. It is found that, for a given atomic grid setup (e.g number of radial and angular grid points per atom), there is a rotation angle of the second grid for which the *sum* of all one- and two-center contributions is exact. The ZES algorithm exploits this observation, leading to robust one- and two-center energy components with essentially perfect additivity.

A comparison between the two main IQA realizations in the framework of Kohn-Sham density functional theory, namely F-IQA and SM-IQA (see Section 5.2), has been carried out. Disregarding the nature of the DFT functional (pure, hybrid), the energy terms provided by both schemes exhibit excellent correlation between each other and also as compared to the well-established Hartree-Fock diatomic exchange terms. The diatomic exchange-correlation terms obtained with SM-IQA are in general less negative than those from Hartree-Fock, thus better capturing the known effect of electron correlation upon covalent bonds. Both schemes perform in a similar manner for a large variety of molecules and different bond multiplicities, being thus suitable for understanding the chemical bonding of new (or more complex) molecular systems.

The application of computational methods to assign OSs, i.e. LOBA, EOS and OSLO, to a series of compounds that present challenges in the OS assignment has been performed, including high-valent TM oxides, TMs with non-innocent ligands, TM-carbenes of Fischer, Schrock and Grubbs (first and second generation) type and s-block and main-group based (Mg/Be and Bi respectively) compounds, among others.

The IUPAC assignation of high-valent TM oxides, culminating with IrO_4^+ and PtO_4^{2+}, are supported by all schemes up to the Ir-based system, with OS of +9. The Pt(+10) assignment is not obtained by any of the tested methodologies. LOBA illustrated how delicate these high OSs are. With each TM-O bond equivalent, LOBA predicts Ir(+9) with low clarity (i.e. O(-2)), and Pt(+6) with higher clarity (i.e. O (-1)) as these systems traverse the ionic/covalent threshold. This is also reflected by the EFO occupancies from EOS, where the Pt atom presented several d-type EFOs with occupancies too large to be considered empty compared to those of the oxygen atoms.

The closed-shell nickel dithiolate $[Ni(S_2C_2Me_2)_2]$ system proved to be challenging for all OS assignment techniques. According to EOS, the formal Ni(+2) OS, as experimentally characterized, is obtained by homolytic splitting of the last electron pair to assign among two degenerated (in occupancy) thiolate EFOs. With OSLO, in the last step of the iterative procedure the fragment-localized orbital obtained is perfectly delocalized among the two thiolate fragments, being invoked the homolitic splitting as in EOS. Such assignment, from both EOS and OSLO, would not be obtained in case the system is non-symmetric. Noticeably, with the newly developed uEOS formalism, two unpaired EFOs are obtained, each one of them sitting on each thiolate ligand, even for singlet state described by a proper CASSCF wavefunction, naturally leading to the Ni(+2) OS assignment.

The OS of the Cu center in Snyder's anion $[Cu(CF_3)_4]^-$ has been matter of discussion along the years, being characterized as both Cu(+1) due to its potentially inverted ligand field and Cu(+3). The orbital localization-based methodologies, i.e. LOBA and OSLO, clearly pointed into the Cu(+3) assignment, while EOS supported the +3 formal OS with rather low reliability index ($R(\%)$) value due to the high covalency of the Cu-C bond between the metal center and each of the CF_3 ligands.

The EOS and OSLO schemes clearly improved over previous methodologies (e.g. LOBA) in the characterization of Schrock- and Fischer-type carbenes. Our findings hinted that the primary challenge for the LOBA approach is the non-uniqueness of the localization procedure, and the fact that the orbitals in some systems do not cleanly localize into fragments. For the Ru-based Grubbs-type carbenes used as catalysts for olefin metathesis, the EOS analysis has been applied along the reaction pathway, showing that the metallic center in the metallacycle species presents character in between Ru(+2) and Ru(+4). For the rest of the reaction pathway, the +2 OS is preferred even thought low $R(\%)$ values were obtained. Moreover, the larger Ru(+4) character obtained for the 2nd generation Grubbs-type catalysts reasonably explained their better catalytic performance compared to 1st generation ones.

The low-valent Be-based (s-block) compounds with carbene (NHC and cAAC) ligands, which according to the previously accepted understanding are characterized as zero-valent Be(0) species, are better depicted as Be(+2) compounds according to the EOS analysis. The OS assignments were supported by the local spin analysis and the analysis of the relevant natural orbitals shape and occupancies obtained with the proper multireference wavefunction. Thus, their best fitting chemical bonding picture is the diradical(oid) one, where each ligand formally contains an unpaired electron. The Mg analogues might present the neutral (low-valent) OS if the ligands are not too π-acid, but the chemical bond is too weak to consider these molecules thermally stable. Interestingly, EOS suggested that the Mg-based ligands are key to access genuine low-valent compounds.

The Bi-based (main-group) complexes stabilized by pincer ligands (NCN and NNN) resulted in a different OS for the bismuth atom depending on the ligand. By analyzing the EFO occupancy values, the ability of these compounds to react with a series of Lewis bases and acids, regardless their formal OS, has been rationalized. EOS approach, applied also for the first time int he framework of the natural atomic orbital (NAO) basis, showed a more robust performance than the conventional natural bond orbital (NBO)

approach. This ambiphilic behaviour is a direct consequence of the strong π-conjugation between the Bi and the pincer ligand, and proper quantification can be achieved by the occupancy of the Bi $6p_z$ EFO.

Bibliography

[1] Ruedenberg, K.; Schwarz, W. H. E. *Pioneers of Quantum Chemistry*; ACS Symposium Series; American Chemical Society, 2013; Vol. 1122; Chapter 1, pp 1–45.

[2] Maksic, Z. B.; Cremer, D.; Surjan, P. R. *The Concept of the Chemical Bond: Theoretical Models of Chemical Bonding Part 2*; Springer-Verlag: Berlin Heidelberg, 1990.

[3] Pauling, L. *The Nature of the Chemical Bond and the Structure of Molecules and Crystals: An Introduction to Modern Structural Chemistry*; Cornell University Press: New York, 1960.

[4] Frenking, G.; Krapp, A. *Journal of Computational Chemistry* **2007**, *28*, 15–24.

[5] Schrödinger, E. *Annalen der Physik* **1926**, *384*, 361–376.

[6] Born, M.; Oppenheimer, R. *Annalen der Physik* **1927**, *389*, 457–484.

[7] Slater, J. C. *Physical Review* **1929**, *34*, 1293–1322.

[8] Handy, N. C. *Chemical Physics Letters* **1980**, *74*, 280–283.

[9] Knowles, P. J.; Handy, N. C. *Chemical Physics Letters* **1984**, *111*, 315–321.

[10] David Sherrill, C.; Schaefer, H. F. *Advances in Quantum Chemistry*; Academic Press, 1999; Vol. 34; pp 143–269.

[11] Roos, B. O. *Advances in chemical physics* **1987**, *69*, 399–445.

[12] Olsen, J.; Roos, B. O.; Jørgensen, P.; Jensen, H. J. A. *The Journal of Chemical Physics* **1988**, *89*, 2185–2192.

[13] McWeeny, R. *Reviews of Modern Physics* **1960**, *32*, 335–369.

[14] Takatsuka, K.; Fueno, T.; Yamaguchi, K. *Theoretica chimica acta* **1978**, *48*, 175–183.

[15] Ramos-Cordoba, E.; Salvador, P.; Reiher, M. *Chemistry – A European Journal* **2013**, *19*, 15267–15275.

[16] Head-Gordon, M. *Chemical Physics Letters* **2003**, *372*, 508–511.

[17] Kutzelnigg, W.; Mukherjee, D. *The Journal of Chemical Physics* **2002**, *116*, 4787–4801.

[18] Lain, L.; Torre, A.; Bochicchio, R. *The Journal of Chemical Physics* **2002**, *117*, 5497–5498.

[19] Hohenberg, P.; Kohn, W. *Physical Review* **1964**, *136*, B864–B871.

[20] Kohn, W.; Sham, L. J. *Physical Review* **1965**, *140*, A1133–A1138.

[21] Perdew, J. P.; Schmidt, K. *AIP Conference Proceedings* **2001**, *577*, 1–20.

[22] Becke, A. D. *The Journal of Chemical Physics* **1993**, *98*, 5648–5652.

[23] Lee, C.; Yang, W.; Parr, R. G. *Physical Review B* **1988**, *37*, 785–789.

[24] Becke, A. D. *Physical Review A* **1988**, *38*, 3098–3100.

[25] Dirac, P. A. M. *Mathematical Proceedings of the Cambridge Philosophical Society* **1930**, *26*, 376–385.

[26] Bloch, F. *Zeitschrift für Physik* **1929**, *57*, 545–555.

[27] Vosko, S. H.; Wilk, L.; Nusair, M. *Canadian Journal of Physics* **1980**, *58*, 1200–1211.

[28] Mardirossian, N.; Head-Gordon, M. *Molecular Physics* **2017**, *115*, 2315–2372.

[29] Lehtola, S.; Marques, M. A. L. *Journal of Chemical Theory and Computation* **2021**, *17*, 943–948.

[30] Teale, A. M. et al. *Physical Chemistry Chemical Physics* **2022**,

[31] Lewis, G. N. *Journal of the American Chemical Society* **1916**, *38*, 762–785.

[32] Coulson, C. A.; Lennard-Jones, J. E. *Proceedings of the Royal Society of London. Series A. Mathematical and Physical Sciences* **1939**, *169*, 413–428.

[33] Wiberg, K. B. *Tetrahedron* **1968**, *24*, 1083–1096.

[34] Mayer, I. *Chemical Physics Letters* **1983**, *97*, 270–274.

[35] Mayer, I. *Theoretica chimica acta* **1985**, *67*, 315–322.

[36] Mayer, I.; Salvador, P. *Chemical Physics Letters* **2004**, *383*, 368–375.

[37] Mayer, I. *Chemical Physics Letters* **2012**, *544*, 83–86.

[38] Mulliken, R. S. *The Journal of Chemical Physics* **1955**, *23*, 1833–1840.

[39] Maslen, E. N.; Spackman, M. A. *Australian Journal of Physics* **1985**, *38*, 273–288.

[40] Rousseau, B.; Peeters, A.; Van Alsenoy, C. *Chemical Physics Letters* **2000**, *324*, 189–194.

[41] Cho, M.; Sylvetsky, N.; Eshafi, S.; Santra, G.; Efremenko, I.; Martin, J. M. L. *ChemPhysChem* **2020**, *21*, 688–696.

[42] Postils, V.; Delgado-Alonso, C.; Luis, J. M.; Salvador, P. *Angewandte Chemie International Edition* **2018**, *57*, 10525–10529.

[43] Ramos-Cordoba, E.; Postils, V.; Salvador, P. *Journal of Chemical Theory and Computation* **2015**, *11*, 1501–1508.

[44] Mayer, I.; Hamza, A. *Theoretical Chemistry Accounts* **2001**, *105*, 360–364.

[45] Salvador, P.; Duran, M.; Mayer, I. *The Journal of Chemical Physics* **2001**, *115*, 1153–1157.

[46] Salvador, P.; Mayer, I. *The Journal of Chemical Physics* **2004**, *120*, 5046–5052.

[47] Blanco, M. A.; Martín Pendás, A.; Francisco, E. *Journal of Chemical Theory and Computation* **2005**, *1*, 1096–1109.

[48] Salvador, P.; Mayer, I. *The Journal of Chemical Physics* **2007**, *126*, 234113.

[49] Tognetti, V.; Joubert, L. *The Journal of Chemical Physics* **2013**, *138*, 024102.

[50] Tognetti, V.; Joubert, L. *Physical Chemistry Chemical Physics* **2014**, *16*, 14539–14550.

[51] Francisco, E.; Casals-Sainz, J. L.; Rocha-Rinza, T.; Martín Pendás, A. *Theoretical Chemistry Accounts* **2016**, *135*, 170.

[52] Guevara-Vela, J. M.; Francisco, E.; Rocha-Rinza, T.; Martín Pendás, A. *Molecules* **2020**, *25*.

[53] Feixas, F.; Matito, E.; Poater, J.; Solà, M. *Chemical Society Reviews* **2015**, *44*, 6434–6451.

[54] Grande-Aztatzi, R.; Mercero, J. M.; Matito, E.; Frenking, G.; Ugalde, J. M. *Physical Chemistry Chemical Physics* **2017**, *19*, 9669–9675.

[55] Pendás, A. M.; Blanco, M. A.; Francisco, E. *Journal of Computational Chemistry* **2009**, *30*, 98–109.

[56] Baker, J. *Theoretica chimica acta* **1985**, *68*, 221–229.

[57] Martin, F.; Zipse, H. *Journal of Computational Chemistry* **2005**, *26*, 97–105.

[58] Fonseca Guerra, C.; Handgraaf, J.-W.; Baerends, E. J.; Bickelhaupt, F. M. *Journal of Computational Chemistry* **2004**, *25*, 189–210.

[59] Löwdin, P. *The Journal of Chemical Physics* **1950**, *18*, 365–375.

[60] Reed, A. E.; Weinhold, F. *The Journal of Chemical Physics* **1983**, *78*, 4066–4073.

[61] Reed, A. E.; Weinstock, R. B.; Weinhold, F. *The Journal of Chemical Physics* **1985**, *83*, 735–746.

[62] Philips, J. J.; Hudspeth, M. A.; Browne, P. M.; Peralta, J. E. *Chemical Physics Letters* **2010**, *495*, 146–150.

[63] Lee, M. S.; Head-Gordon, M. *International Journal of Quantum Chemistry* **2000**, *76*, 169–184.

[64] Lu, W. C.; Wang, C. Z.; Schmidt, M. W.; Bytautas, L.; Ho, K. M.; Ruedenberg, K. *The Journal of Chemical Physics* **2004**, *120*, 2629–2637.

[65] Laikov, D. N. *International Journal of Quantum Chemistry* **2011**, *111*, 2851–2867.

[66] Knizia, G. *Journal of Chemical Theory and Computation* **2013**, *9*, 4834–4843.

[67] Senjean, B.; Sen, S.; Repisky, M.; Knizia, G.; Visscher, L. *Journal of Chemical Theory and Computation* **2021**, *17*, 1337–1354.

[68] Janowski, T. *Journal of Chemical Theory and Computation* **2014**, *10*, 3085–3091.

[69] Bader, R. F. W. *Chemical Reviews* **1991**, *91*, 893–928.

[70] Hirshfeld, F. L. *Theoretica chimica acta* **1977**, *44*, 129–138.

[71] Bultinck, P.; Van Alsenoy, C.; Ayers, P. W.; Carbó-Dorca, R. *The Journal of Chemical Physics* **2007**, *126*, 144111.

[72] Bultinck, P.; Cooper, D. L.; Van Neck, D. *Physical Chemistry Chemical Physics* **2009**, *11*, 3424–3429.

[73] Becke, A. D. *The Journal of Chemical Physics* **1988**, *88*, 2547–2553.

[74] Matito, E.; Solà, M.; Salvador, P.; Duran, M. *Faraday Discussions* **2007**, *135*, 325–345.

[75] Salvador, P.; Ramos-Cordoba, E. *The Journal of Chemical Physics* **2013**, *139*, 071103.

[76] De Proft, F.; Van Alsenoy, C.; Peeters, A.; Langenaeker, W.; Geerlings, P. *Journal of Computational Chemistry* **2002**, *23*, 1198–1209.

[77] Mandado, M.; Van Alsenoy, C.; Geerlings, P.; De Proft, F.; Mosquera, R. A. *ChemPhysChem* **2006**, *7*, 1294–1305.

[78] Bultinck, P.; Ayers, P. W.; Fias, S.; Tiels, K.; Van Alsenoy, C. *Chemical Physics Letters* **2007**, *444*, 205–208.

[79] Van Damme, S.; Bultinck, P.; Fias, S. *Journal of Chemical Theory and Computation* **2009**, *5*, 334–340.

[80] Pujal, L.; van Zyl, M.; Vöhringer-Martinez, E.; Verstraelen, T.; Bultinck, P.; Ayers, P. W.; Heidar-Zadeh, F. *The Journal of Chemical Physics* **2022**, *156*, 194109.

[81] Guillaumes, L.; Salvador, P.; Simon, S. *The Journal of Physical Chemistry A* **2014**, *118*, 1142–1149.

[82] Min, X.; Popov, I. A.; Pan, F.-X.; Li, L.-J.; Matito, E.; Sun, Z.-M.; Wang, L.-S.; Boldyrev, A. I. *Angewandte Chemie International Edition* **2016**, *55*, 5531–5535.

[83] Montilla, M.; Luis, J. M.; Salvador, P. *Journal of Chemical Theory and Computation* **2021**, *17*, 1098–1105.

[84] Ramos-Cordoba, E.; Salvador, P. *Physical Chemistry Chemical Physics* **2014**, *16*, 9565–9571.

[85] Ramos-Cordoba, E.; Salvador, P. *Journal of Chemical Theory and Computation* **2014**, *10*, 634–641.

[86] Karton, A.; Sylvetsky, N.; Martin, J. M. L. *Journal of Computational Chemistry* **2017**, *38*, 2063–2075.

[87] Clark, A. E.; Davidson, E. R. *The Journal of Chemical Physics* **2001**, *115*, 7382–7392.

[88] Alcoba, D. R.; Lain, L.; Torre, A.; Bochicchio, R. C. *Chemical Physics Letters* **2009**, *470*, 136–139.

[89] Mayer, I. *Chemical Physics Letters* **2009**, *478*, 323–326.

[90] Mayer, I.; Matito, E. *Physical Chemistry Chemical Physics* **2010**, *12*, 11308–11314.

[91] Alcoba, D. R.; Torre, A.; Lain, L.; Bochicchio, R. C. *Journal of Chemical Theory and Computation* **2011**, *7*, 3560–3566.

[92] Ramos-Cordoba, E.; Matito, E.; Mayer, I.; Salvador, P. *Journal of Chemical Theory and Computation* **2012**, *8*, 1270–1279.

[93] Ponec, R.; Ramos-Cordoba, E.; Salvador, P. *The Journal of Physical Chemistry A* **2013**, *117*, 1975–1982.

[94] Salvador, P.; Vos, E.; Corral, I.; Andrada, D. M. *Angewandte Chemie International Edition* **2021**, *60*, 1498–1502.

[95] Ramos-Cordoba, E.; Salvador, P.; Piris, M.; Matito, E. *The Journal of Chemical Physics* **2014**, *141*, 234101.

[96] Ramos-Cordoba, E.; Matito, E. *Journal of Chemical Theory and Computation* **2017**, *13*, 2705–2711.

[97] Martín Pendás, A.; Francisco, E. *Physical Chemistry Chemical Physics* **2021**, *23*, 8375–8392.

[98] Martín Pendás, A.; Francisco, E. *Physical Chemistry Chemical Physics* **2022**, *24*, 639–652.

[99] Mayer, I. *Chemical Physics Letters* **1995**, *242*, 499–506.

[100] Mayer, I. *The Journal of Physical Chemistry* **1996**, *100*, 6249–6257.

[101] Mayer, I.; Bakó, I.; Stirling, A. *The Journal of Physical Chemistry A* **2011**, *115*, 12733–12737.

[102] Mayer, I. *Chemical Physics Letters* **2013**, *585*, 198–200.

[103] Karen, P. *Angewandte Chemie International Edition* **2015**, *54*, 4716–4726.

[104] Karen, P.; McArdle, P.; Takats, J. *Pure and Applied Chemistry* **2014**, *86*, 1017–1081.

[105] Karen, P.; McArdle, P.; Takats, J. *Pure and Applied Chemistry* **2016**, *88*, 831–839.

[106] Mann, J. B.; Meek, T. L.; Allen, L. C. *Journal of the American Chemical Society* **2000**, *122*, 2780–2783.

[107] Monsch, G.; Klüfers, P. *Angewandte Chemie International Edition* **2019**, *58*, 8566–8571.

[108] Ampβler, T.; Monsch, G.; Popp, J.; Riggenmann, T.; Salvador, P.; Schröder, D.; Klüfers, P. *Angewandte Chemie International Edition* **2020**, *59*, 12381–12386.

[109] Schrock, R. R. *Journal of the American Chemical Society* **1974**, *96*, 6796–6797.

[110] Occhipinti, G.; Jensen, V. R. *Organometallics* **2011**, *30*, 3522–3529.

[111] Fischer, E. O.; Maasböl, A. *Angewandte Chemie International Edition in English* **1964**, *3*, 580–581.

[112] Resta, R. *Nature* **2008**, *453*, 735–735.

[113] Raebiger, H.; Lany, S.; Zunger, A. *Nature* **2008**, *453*, 763–766.

[114] Aullón, G.; Alvarez, S. *Theoretical Chemistry Accounts* **2009**, *123*, 67–73.

[115] Walsh, A.; Sokol, A. A.; Buckeridge, J.; Scanlon, D. O.; Catlow, C. R. A. *The Journal of Physical Chemistry Letters* **2017**, *8*, 2074–2075.

[116] Postils, V.; Company, A.; Solà, M.; Costas, M.; Luis, J. M. *Inorganic Chemistry* **2015**, *54*, 8223–8236.

[117] Catlow, C. R. A.; Stoneham, A. M. *Journal of Physics C: Solid State Physics* **1983**, *16*, 4321–4338.

[118] Jiang, L.; Levchenko, S. V.; Rappe, A. M. *Physical Review Letters* **2012**, *108*, 166403.

[119] Walsh, A.; Sokol, A. A.; Buckeridge, J.; Scanlon, D. O.; Catlow, C. R. A. *Nature Materials* **2018**, *17*, 958–964.

[120] Thom, A. J. W.; Sundstrom, E. J.; Head-Gordon, M. *Physical Chemistry Chemical Physics* **2009**, *11*, 11297–11304.

[121] Sit, P. H.-L.; Zipoli, F.; Chen, J.; Car, R.; Cohen, M. H.; Selloni, A. *Chemistry – A European Journal* **2011**, *17*, 12136–12143.

[122] Vidossich, P.; Lledós, A. *Dalton Transactions* **2014**, *43*, 11145–11151.

[123] Pipek, J.; Mezey, P. G. *The Journal of Chemical Physics* **1989**, *90*, 4916–4926.

[124] Boys, S. F. *Reviews of Modern Physics* **1960**, *32*, 296–299.

[125] Foster, J. M.; Boys, S. F. *Reviews of Modern Physics* **1960**, *32*, 300–302.

[126] Edmiston, C.; Ruedenberg, K. *Reviews of Modern Physics* **1963**, *35*, 457–464.

[127] Aquilante, F.; Bondo Pedersen, T.; Sánchez de Merás, A.; Koch, H. *The Journal of Chemical Physics* **2006**, *125*, 174101, doi: 10.1063/1.2360264.

[128] Høyvik, I.-M.; Jansik, B.; Jørgensen, P. *The Journal of Chemical Physics* **2012**, *137*, 224114.

[129] Glendening, E. D.; Landis, C. R.; Weinhold, F. *WIREs Computational Molecular Science* **2012**, *2*, 1–42.

[130] Reed, A. E.; Weinhold, F. *The Journal of Chemical Physics* **1985**, *83*, 1736–1740, doi: 10.1063/1.449360.

[131] Sundstrom, E. J.; Yang, X.; Thoi, V. S.; Karunadasa, H. I.; Chang, C. J.; Long, J. R.; Head-Gordon, M. *Journal of the American Chemical Society* **2012**, *134*, 5233–5242.

[132] Jurss, J. W.; Khnayzer, R. S.; Panetier, J. A.; El Roz, K. A.; Nichols, E. M.; Head-Gordon, M.; Long, J. R.; Castellano, F. N.; Chang, C. J. *Chemical Science* **2015**, *6*, 4954–4972.

[133] Panetier, J. A.; Letko, C. S.; Tilley, T. D.; Head-Gordon, M. *Journal of Chemical Theory and Computation* **2016**, *12*, 223–230.

[134] Van der Mynsbrugge, J.; Head-Gordon, M.; Bell, A. T. *Journal of Materials Chemistry A* **2021**, *9*, 2161–2174.

[135] Kermack, W. O.; Robinson, R. *Journal of the Chemical Society, Transactions* **1922**, *121*, 427–440.

[136] Ramos-Cordoba, E.; Salvador, P.; Mayer, I. *The Journal of Chemical Physics* **2013**, *138*, 214107.

[137] Ziegler, T.; Rauk, A. *Theoretica chimica acta* **1977**, *46*, 1–10.

[138] Mitoraj, M. P.; Michalak, A.; Ziegler, T. *Journal of Chemical Theory and Computation* **2009**, *5*, 962–975.

[139] Kitaura, K.; Morokuma, K. *International Journal of Quantum Chemistry* **1976**, *10*, 325–340.

[140] Khaliullin, R. Z.; Head-Gordon, M.; Bell, A. T. *The Journal of Chemical Physics* **2006**, *124*, 204105.

[141] Khaliullin, R. Z.; Cobar, E. A.; Lochan, R. C.; Bell, A. T.; Head-Gordon, M. *The Journal of Physical Chemistry A* **2007**, *111*, 8753–8765.

[142] Horn, P. R.; Head-Gordon, M. *The Journal of Chemical Physics* **2015**, *143*, 114111.

[143] Horn, P. R.; Mao, Y.; Head-Gordon, M. *Physical Chemistry Chemical Physics* **2016**, *18*, 23067–23079.

[144] Levine, D. S.; Horn, P. R.; Mao, Y.; Head-Gordon, M. *Journal of Chemical Theory and Computation* **2016**, *12*, 4812–4820.

[145] Schenter, G. K.; Glendening, E. D. *The Journal of Physical Chemistry* **1996**, *100*, 17152–17156.

[146] Reed, A. E.; Curtiss, L. A.; Weinhold, F. *Chemical Reviews* **1988**, *88*, 899–926.

[147] Phipps, M. J. S.; Fox, T.; Tautermann, C. S.; Skylaris, C.-K. *Chemical Society Reviews* **2015**, *44*, 3177–3211.

[148] Andrés, J. et al. *Journal of Computational Chemistry* **2019**, *40*, 2248–2283.

[149] Mayer, I. *International Journal of Quantum Chemistry* **1983**, *23*, 341–363.

[150] Mayer, I. *Chemical Physics Letters* **2000**, *332*, 381–388.

[151] Tognetti, V.; Silva, A. F.; Vincent, M. A.; Joubert, L.; Popelier, P. L. A. *The Journal of Physical Chemistry A* **2018**, *122*, 7748–7756.

[152] Casals-Sainz, J. L.; Guevara-Vela, J. M.; Francisco, E.; Rocha-Rinza, T.; Martín Pendás, a. *Journal of Computational Chemistry* **2020**, *41*, 1234–1241.

[153] Chávez-Calvillo, R.; García-Revilla, M.; Francisco, E.; Martín Pendás, a.; Rocha-Rinza, T. *Computational and Theoretical Chemistry* **2015**, *1053*, 90–95.

[154] Holguín-Gallego, F. J.; Chávez-Calvillo, R.; García-Revilla, M.; Francisco, E.; Pendás, A. M.; Rocha-Rinza, T. *Journal of Computational Chemistry* **2016**, *37*, 1753–1765.

[155] Fernández-Alarcón, A.; Casals-Sainz, J. L.; Guevara-Vela, J. M.; Costales, A.; Francisco, E.; Martín Pendás, A.; Rocha-Rinza, T. *Physical Chemistry Chemical Physics* **2019**, *21*, 13428–13439.

[156] Martín Pendás, A.; Francisco, E.; Blanco, M. A. *The Journal of Physical Chemistry A* **2006**, *110*, 12864–12869.

[157] Martín Pendás, A.; Blanco, M. A.; Francisco, E. *The Journal of Chemical Physics* **2006**, *125*, 184112.

[158] Racioppi, S.; Sironi, A.; Macchi, P. *Physical Chemistry Chemical Physics* **2020**, *22*, 24291–24298.

[159] Stroud, A. H. S. D. *Gaussian quadrature formulas*; Prentice-Hall: Englewood Cliffs, N.J., 1966.

[160] Lebedev, V. I.; Laikov, D. N. *Doklady Mathematics* **1999**, *59*, 477–481.

[161] Mentel, L. chemtools – A Python toolbox for computational chemistry, ver. 0.9.2. 2014.

[162] Pujal, L.; Tehrani, A.; Heidar-Zadeh, F. *Conceptual Density Functional Theory*; 2022; pp 649–661.

[163] Andrés, M. G. Towards an accurate Kohn-Sham Density Functional Theory Molecular Energy Decomposition scheme. Bachellor's thesis, Universitat de Girona, Departament de Química, 2016.

[164] Davidson, E. R. *Chemical Physics Letters* **1995**, *246*, 209–213.

[165] Pendás, A. M.; Blanco, M. A.; Francisco, E. *The Journal of Chemical Physics* **2004**, *120*, 4581–4592.

[166] Pendás, A. M.; Francisco, E.; Blanco, M. A. *Journal of Computational Chemistry* **2005**, *26*, 344–351.

[167] Francisco, E.; Menéndez Crespo, D.; Costales, A.; Martín Pendás, a. *Journal of Computational Chemistry* **2017**, *38*, 816–829.

[168] Kosov, D. S.; Popelier, P. L. A. *The Journal of Chemical Physics* **2000**, *113*, 3969–3974.

[169] Popelier, P. L. A.; Kosov, D. S. *The Journal of Chemical Physics* **2001**, *114*, 6539–6547.

[170] Popelier, P. L. A.; Joubert, L.; Kosov, D. S. *The Journal of Physical Chemistry A* **2001**, *105*, 8254–8261.

[171] Frisch, M. J. et al. Gaussian16 Revision C.01. 2016; Gaussian Inc. Wallingford CT.

[172] Glendening, E. D.; Landis, C. R.; Weinhold, F. *Journal of Computational Chemistry* **2013**, *34*, 1429–1437.

[173] Salvador, P.; Ramos-Cordoba, E.; Gimferrer, M. APOST-3D. 2019; Institute of Computational Chemistry and Catalysis, University of Girona: Girona.

[174] Epifanovsky, E. et al. *The Journal of Chemical Physics* **2021**, *155*, 084801.

[175] Sun, Q.; Berkelbach, T. C.; Blunt, N. S.; Booth, G. H.; Guo, S.; Li, Z.; Liu, J.; McClain, J. D.; Sayfutyarova, E. R.; Sharma, S.; Wouters, S.; Chan, G. K.-L. *WIREs Computational Molecular Science* **2018**, *8*, e1340.

[176] Frisch, M. J. et al. Gaussian09 Revision E.01. 2009; Gaussian Inc. Wallingford CT.

[177] Shao, Y. et al. *Molecular Physics* **2015**, *113*, 184–215.

[178] Yamaguchi, K.; Jensen, F.; Dorigo, A.; Houk, K. N. *Chemical Physics Letters* **1988**, *149*, 537–542.

[179] Shiozaki, T. *WIREs Computational Molecular Science* **2018**, *8*, e1331.

[180] te Velde, G.; Bickelhaupt, F. M.; Baerends, E. J.; Fonseca Guerra, C.; van Gisbergen, S. J. A.; Snijders, J. G.; Ziegler, T. *Journal of Computational Chemistry* **2001**, *22*, 931–967.

[181] Rodríguez, J. I.; Köster, A. M.; Ayers, P. W.; Santos-Valle, A.; Vela, A.; Merino, G. *Journal of Computational Chemistry* **2009**, *30*, 1082–1092.

[182] Wang, G.; Zhou, M.; Goettel, J. T.; Schrobilgen, G. J.; Su, J.; Li, J.; Schlöder, T.; Riedel, S. *Nature* **2014**, *514*, 475–477.

[183] Yu, H. S.; Truhlar, D. G. *Angewandte Chemie International Edition* **2016**, *55*, 9004–9006.

[184] Stoll, H.; Wagenblast, G.; Preuβ, H. *Theoretica chimica acta* **1980**, *57*, 169–178.

[185] Raimondi, M.; Famulari, A.; Specchio, R.; Sironi, M.; Moroni, F.; Gianinetti, E. *Journal of Molecular Structure: THEOCHEM* **2001**, *573*, 25–42.

[186] Nagata, T.; Takahashi, O.; Saito, K.; Iwata, S. *The Journal of Chemical Physics* **2001**, *115*, 3553–3560.

[187] Sax, A. F. *Journal of Computational Chemistry* **2012**, *33*, 1495–1510.

[188] de Silva, P.; Giebułtowski, M.; Korchowiec, J. *Physical Chemistry Chemical Physics* **2012**, *14*, 546–552.

[189] Horn, P. R.; Sundstrom, E. J.; Baker, T. A.; Head-Gordon, M. *The Journal of Chemical Physics* **2013**, *138*, 134119.

[190] Li, Z.; Li, H.; Suo, B.; Liu, W. *Accounts of Chemical Research* **2014**, *47*, 2758–2767.

[191] Mo, Y.; Bao, P.; Gao, J. *Physical Chemistry Chemical Physics* **2011**, *13*, 6760–6775.

[192] Mao, Y.; Loipersberger, M.; Horn, P. R.; Das, A.; Demerdash, O.; Levine, D. S.; Prasad Veccham, S.; Head-Gordon, T.; Head-Gordon, M. *Annual Review of Physical Chemistry* **2021**, *72*, 641–666.

[193] Giovannini, T.; Koch, H. *Journal of Chemical Theory and Computation* **2021**, *17*, 139–150.

[194] Pipek, J. *International Journal of Quantum Chemistry* **1989**, *36*, 487–501.

[195] Lehtola, S.; Jónsson, H. *Journal of Chemical Theory and Computation* **2014**, *10*, 642–649.

[196] Davison, A.; Edelstein, N.; Holm, R. H.; Maki, A. H. *Inorganic Chemistry* **1963**, *2*, 1227–1232.

[197] Lim, B. S.; Fomitchev, D. V.; Holm, R. H. *Inorganic Chemistry* **2001**, *40*, 4257–4262.

[198] Naumann, D.; Roy, T.; Tebbe, K.-F.; Crump, W. *Angewandte Chemie International Edition in English* **1993**, *32*, 1482–1483.

[199] Snyder, J. P. *Angewandte Chemie International Edition in English* **1995**, *34*, 80–81.

[200] Kaupp, M.; von Schnering, H. G. *Angewandte Chemie International Edition in English* **1995**, *34*, 986–986.

[201] Aullón, G.; Alvarez, S. *Theoretical Chemistry Accounts* **2009**, *123*, 67–73.

[202] Walroth, R. C.; Lukens, J. T.; MacMillan, S. N.; Finkelstein, K. D.; Lancaster, K. M. *Journal of the American Chemical Society* **2016**, *138*, 1922–1931.

[203] DiMucci, I. M.; Lukens, J. T.; Chatterjee, S.; Carsch, K. M.; Titus, C. J.; Lee, S. J.; Nordlund, D.; Betley, T. A.; MacMillan, S. N.; Lancaster, K. M. *Journal of the American Chemical Society* **2019**, *141*, 18508–18520.

[204] Hoffmann, R.; Alvarez, S.; Mealli, C.; Falceto, A.; Cahill, I., Thomas J.; Zeng, T.; Manca, G. *Chemical Reviews* **2016**, *116*, 8173–8192.

[205] Norman, J. G.; Ryan, P. B.; Noodleman, L. *Journal of the American Chemical Society* **1980**, *102*, 4279–4282.

[206] Noodleman, L. *The Journal of Chemical Physics* **1981**, *74*, 5737–5743.

[207] Noodleman, L.; Case, D. A. In *Advances in Inorganic Chemistry*; Cammack, R., Ed.; Academic Press, 1992; Vol. 38; pp 423–470.

[208] Noodleman, L.; Peng, C. Y.; Case, D. A.; Mouesca, J. M. *Coordination Chemistry Reviews* **1995**, *144*, 199–244.

[209] Sharma, S.; Sivalingam, K.; Neese, F.; Chan, G. K.-L. *Nature Chemistry* **2014**, *6*, 927–933.

[210] Presti, D.; Stoneburner, S. J.; Truhlar, D. G.; Gagliardi, L. *The Journal of Physical Chemistry C* **2019**, *123*, 11899–11907.

[211] Hieber, W.; Beutner, K. *Zeitschrift für Naturforschung B* **1960**, *15*, 323–324.

[212] Plietker, B.; Dieskau, A. *European Journal of Organic Chemistry* **2009**, *2009*, 775–787.

[213] Klein, J. E. M. N.; Miehlich, B.; Holzwarth, M. S.; Bauer, M.; Milek, M.; Khusniyarov, M. M.; Knizia, G.; Werner, H.-J.; Plietker, B. *Angewandte Chemie International Edition* **2014**, *53*, 1790–1794.

[214] Gruden, M.; Zlatar, M. *Theoretical Chemistry Accounts* **2020**, *139*, 126.

[215] Foroutan-Nejad, C. *Angewandte Chemie International Edition* **2020**, *59*, 20900–20903.

[216] Pino-Rios, R.; Inostroza, D.; Tiznado, W. *Angewandte Chemie International Edition* **2021**, *60*, 12747–12753.

[217] Radenković, S.; Shaik, S. S.; Braïda, B. *Angewandte Chemie International Edition* **2021**, *60*, 12723–12726.

[218] Bultinck, P.; Fias, S.; Van Alsenoy, C.; Ayers, P. W.; Carbó-Dorca, R. *The Journal of Chemical Physics* **2007**, *127*, 034102.

[219] Grimme, S. *WIREs Computational Molecular Science* **2011**, *1*, 211–228.

[220] Vydrov, O. A.; Van Voorhis, T. *The Journal of Chemical Physics* **2010**, *133*, 244103.

[221] Boys, S. F.; Bernardi, F. *Molecular Physics* **1970**, *19*, 553–566.

[222] Simon, S.; Duran, M.; Dannenberg, J. J. *The Journal of Chemical Physics* **1996**, *105*, 11024–11031.

[223] Bickelhaupt, F. M.; Baerends, E. J. *Reviews in Computational Chemistry*; Reviews in Computational Chemistry; 2000; pp 1–86.

[224] Guevara-Vela, J. M.; Francisco, E.; Rocha-Rinza, T.; Martín Pendás, A. *Molecules* **2020**, *25*.

[225] Vyboishchikov, S. F.; Frenking, G. *Chemistry – A European Journal* **1998**, *4*, 1428–1438.

[226] Frenking, G.; Sola, M.; Vyboishchikov, S. F. *Journal of Organometallic Chemistry* **2005**, *690*, 6178–6204.

[227] du Toit, J. I.; van Sittert, C. G. C. E.; Vosloo, H. C. M. *Monatshefte für Chemie - Chemical Monthly* **2015**, *146*, 1115–1129.

[228] Santamaria, J.; Aguilar, E. *Organic Chemistry Frontiers* **2016**, *3*, 1561–1588.

[229] Esteruelas, M. A.; González, A. I.; Lopez, A. M.; Onate, E. *Organometallics* **2003**, *22*, 414–425.

[230] Wu, Z.; Nguyen, S. T.; Grubbs, R. H.; Ziller, J. W. *Journal of the American Chemical Society* **1995**, *117*, 5503–5511.

[231] Katayama, H.; Nagao, M.; Ozawa, F. *Organometallics* **2003**, *22*, 586–593.

[232] Jean-Louis Herisson, P.; Chauvin, Y. *Die Makromolekulare Chemie* **1971**, *141*, 161–176.

[233] Poater, A.; Chaitanya Vummaleti, S. V.; Pump, E.; Cavallo, L. *Dalton Transactions* **2014**, *43*, 11216–11220.

[234] Poater, A.; Pump, E.; Vummaleti, S. V. C.; Cavallo, L. *Chemical Physics Letters* **2014**, *610-611*, 29–32.

[235] Tsipis, A. C.; Orpen, A. G.; Harvey, J. N. *Dalton Transactions* **2005**, 2849–2858.

[236] Sanford, M. S.; Love, J. A.; Grubbs, R. H. *Journal of the American Chemical Society* **2001**, *123*, 6543–6554.

[237] Adlhart, C.; Chen, P. *Angewandte Chemie International Edition* **2002**, *41*, 4484–4487.

[238] Adlhart, C.; Chen, P. *Journal of the American Chemical Society* **2004**, *126*, 3496–3510.

[239] Soran, A. P.; Silvestru, C.; Breunig, H. J.; Balázs, G.; Green, J. C. *Organometallics* **2007**, *26*, 1196–1203.

[240] Šimon, P.; de Proft, F.; Jambor, R.; Růžička, A.; Dostál, L. *Angewandte Chemie International Edition* **2010**, *49*, 5468–5471.

[241] Vránová, I.; Alonso, M.; Lo, R.; Sedlák, R.; Jambor, R.; Růžička, A.; Proft, F. D.; Hobza, P.; Dostál, L. *Chemistry – A European Journal* **2015**, *21*, 16917–16928.

[242] Vránová, I.; Kremláček, V.; Erben, M.; Turek, J.; Jambor, R.; Růžička, A.; Alonso, M.; Dostál, L. *Dalton Transactions* **2017**, *46*, 3556–3568.

[243] Wang, F.; Planas, O.; Cornella, J. *Journal of the American Chemical Society* **2019**, *141*, 4235–4240.

[244] Kindervater, M. B.; Marczenko, K. M.; Werner-Zwanziger, U.; Chitnis, S. S. *Angewandte Chemie International Edition* **2019**, *58*, 7850–7855.

[245] Gimferrer, M.; Danés, S.; Andrada, D. M.; Salvador, P. *Inorganic Chemistry* **2021**, *60*, 17657–17668.

[246] Marczenko, K. M.; Jee, S.; Chitnis, S. S. *Organometallics* **2020**, *39*, 4287–4296.

[247] Klein, S.; Tonner, R.; Frenking, G. *Chemistry – A European Journal* **2010**, *16*, 10160–10170.

[248] Takagi, N.; Shimizu, T.; Frenking, G. *Chemistry – A European Journal* **2009**, *15*, 3448–3456.

[249] Takagi, N.; Frenking, G. *Theoretical Chemistry Accounts* **2011**, *129*, 615–623.

[250] Takagi, N.; Shimizu, T.; Frenking, G. *Chemistry – A European Journal* **2009**, *15*, 8593–8604.

[251] Takagi, N.; Tonner, R.; Frenking, G. *Chemistry – A European Journal* **2012**, *18*, 1772–1780.

[252] Pang, Y.; Leutzsch, M.; Nöthling, N.; Cornella, J. *Journal of the American Chemical Society* **2020**, *142*, 19473–19479.

[253] Nesterov, V.; Reiter, D.; Bag, P.; Frisch, P.; Holzner, R.; Porzelt, A.; Inoue, S. *Chemical Reviews* **2018**, *118*, 9678–9842.

[254] Zhao, L.; Hermann, M.; Holzmann, N.; Frenking, G. *Coordination Chemistry Reviews* **2017**, *344*, 163–204.

[255] Frenking, G.; Hermann, M.; Andrada, D. M.; Holzmann, N. *Chemical Society Reviews* **2016**, *45*, 1129–1144.

[256] Hopkinson, M. N.; Richter, C.; Schedler, M.; Glorius, F. *Nature* **2014**, *510*, 485–496.

[257] Melaimi, M.; Soleilhavoup, M.; Bertrand, G. *Angewandte Chemie International Edition* **2010**, *49*, 8810–8849.

[258] Melaimi, M.; Jazzar, R.; Soleilhavoup, M.; Bertrand, G. *Angewandte Chemie International Edition* **2017**, *56*, 10046–10068.

[259] Dyker, C. A.; Bertrand, G. *Nature Chemistry* **2009**, *1*, 265–266.

[260] Zhao, L.; Pan, S.; Holzmann, N.; Schwerdtfeger, P.; Frenking, G. *Chemical Reviews* **2019**, *119*, 8781–8845.

[261] Green, S. P.; Jones, C.; Stasch, A. *Science* **2007**, *318*, 1754–1757.

[262] Jones, C. *Nature Reviews Chemistry* **2017**, *1*, 0059.

[263] Arrowsmith, M.; Braunschweig, H.; Celik, M. A.; Dellermann, T.; Dewhurst, R. D.; Ewing, W. C.; Hammond, K.; Kramer, T.; Krummenacher, I.; Mies, J.; Radacki, K.; Schuster, J. K. *Nature Chemistry* **2016**, *8*, 890–894.

[264] Jędrzkiewicz, D.; Mai, J.; Langer, J.; Mathe, Z.; Patel, N.; DeBeer, S.; Harder, S. *Angewandte Chemie International Edition* **2022**, *61*, e202200511.

[265] Wang, G.; Walley, J. E.; Dickie, D. A.; Pan, S.; Frenking, G.; Gilliard, J., Robert J. *Journal of the American Chemical Society* **2020**, *142*, 4560–4564.

[266] Czernetzki, C.; Arrowsmith, M.; Fantuzzi, F.; Gärtner, A.; Tröster, T.; Krummenacher, I.; Schorr, F.; Braunschweig, H. *Angewandte Chemie International Edition* **2021**, *60*, 20776–20780.

[267] Rösch, B.; Harder, S. *Chemical Communications* **2021**, *57*, 9354–9365.

[268] Dutton, J. L.; Frenking, G. *Angewandte Chemie International Edition* **2016**, *55*, 13380–13382.

[269] De, S.; Parameswaran, P. *Dalton Transactions* **2013**, *42*, 4650–4656.

[270] Pyykkő, P. *The Journal of Physical Chemistry A* **2015**, *119*, 2326–2337.

[271] Couchman, S. A.; Holzmann, N.; Frenking, G.; Wilson, D. J. D.; Dutton, J. L. *Dalton Transactions* **2013**, *42*, 11375–11384.

[272] Ponec, R.; Cooper, D. L. *Structural Chemistry* **2017**, *28*, 1033–1043.

[273] Hermann, M.; Frenking, G. *Chemistry - A European Journal* **2017**, *23*, 3347–3356.

[274] Bachler, V.; Olbrich, G.; Neese, F.; Wieghardt, K. *Inorganic Chemistry* **2002**, *41*, 4179–4193.

[275] Popp, J.; Riggenmann, T.; Schröder, D.; Ampβler, T.; Salvador, P.; Klüfers, P. *Inorganic Chemistry* **2021**, *60*, 15980–15996.